Enlightening Main Group Chemistry: Development and Synthesis of Novel Chromophores Based on Heavy Pnictogens

Dissertation

zur

Erlangung des Doktorgrades (Dr. rer. nat.)

der

Mathematisch-Naturwissenschaftlichen Fakultät

der

Rheinischen Friedrich-Wilhelms-Universität Bonn

vorgelegt von

André Korzun

aus

Quedlinburg

Bonn, 2026

Angefertigt mit Genehmigung der Mathematisch-Naturwissenschaftlichen Fakultät
der Rheinischen Friedrich-Wilhelms-Universität Bonn

Gutachter/Betreuer:	Prof. Dr. Alessandro Bismuto
Gutachter:	Prof. Dr. Manuel Alcarazo

Tag der Promotion: 28.05.2026
Erscheinungsjahr: 2026

Hiermit versichere ich, dass ich die vorliegende Arbeit unter Einhaltung der Regeln guter wissenschaftlicher Praxis selbstständig verfasst, sowie keine anderen als die angegebenen Quellen und Hilfsmittel benutzt und Zitate kenntlich gemacht habe. Künstliche Intelligenz (KI) wurde im Rahmen dieser Arbeit nur stellenweise zur Rechtschreibprüfung eingesetzt.

Table of Contents

Abbreviations **1**

1. Introduction **2**

1.1. Visible-light photocatalysis . . . 7

1.1.1. Energy transfer (EnT) catalysis . . . 8

1.1.2. Singlet oxygen . . . 11

1.1.3. Photoredox catalysis . . . 16

1.2. The chemistry of dipyrrins and their complexes . . . 22

1.2.1. Boron dipyrromethenes (BODIPY) . . . 24

1.2.2. BODIPY dyes in molecular sensing . . . 28

1.2.3. BODIPY dyes in photocatalysis . . . 29

1.2.4. Heavier analogues of BODIPY . . . 32

1.3. General aims . . . 39

2. The first antimony and bismuth analogues of BODIPY **41**

2.1. Project aims . . . 41

2.2. Ligand synthesis . . . 42

2.3. Synthesis of antimony dipyrrin complexes (SBDIPY) . . . 43

2.3.1. Complex stability . . . 47

2.3.2. Deviation from optimized conditions . . . 48

2.3.3. Modification of SBDIPY complexes . . . 53

2.3.4. Spectroscopic properties of SBDIPY chromophores . . . 57

2.4. Synthesis of bismuth dipyrrin complexes (BIDIPY) . . . 65

2.5. Halide abstraction . . . 73

2.6. Investigation of spectroscopic properties . . . 76

2.7. Computational investigation[141]† . . . 78

2.8. Conclusion and future work . . . 79

3. Evaluation of new dipyrrin ligands **81**

3.1. Overview and classification of tested ligands . . . 112

4. Photochemical applications of heavy pnictogen dipyrrins **114**

4.1. Project aims . . . 114

4.2. Energy transfer photocatalysis using pnictogen dipyrrins . . . 115

4.3. Theoretical considerations[174]‡ . . . 129

4.4. Mechanistic considerations . . . 130

4.5. Photocatalytic applications of SBDIPY chromophores 138
4.5.1. Oxidation of double bonds 138
4.5.2. Oxidation of sulfides 140
4.5.3. Photooxidation of benzylic amines 144
4.6. Photoredox applications of SBDIPY chromophores 147
4.7. Conclusion and future work 150

5. Reactivity studies of SBDIPY chromophores and molecular sensing applications 152
5.1. Molecular sensing in the context of organopnictogen chemistry 152
5.2. Oxidation and reduction of SBDIPY complexes 153
5.3. Redox-neutral reactivity of SBDIPY chromophores 157
5.3.1. Reactivity towards Lewis acids 157
5.3.2. Reactivity towards Lewis bases 180
5.3.3. Ligand exchange reactions of L7 SBDIPY complexes 184
5.4. Conclusion and future work 190

6. Experimental details 192
6.1. General information 192
6.2. Ligand synthesis (chapter 2) 196
6.3. Synthesis of SBDIPY complexes (chapter 2) 201
6.4. Synthesis of alkali dipyrrinato salts (chapter 2) 206
6.5. Synthesis of BIDIPY complexes (chapter 2) 208
6.6. Synthesis of other reagents (chapter 2) 211
6.7. Spectroscopic data of PnDIPY complexes (chapter 2) 214
6.8. Ligand synthesis (chapter 3) 215
6.9. Chapter 3: synthesis of alkali dipyrrinato salts 232
6.10. Synthesis of PnDIPY complexes (chapter 3) 235
6.11. Spectroscopic data of PnDIPY complexes (chapter 3) 252
6.12. Reagent synthesis (chapter 4) 253
6.13. Photocatalytic oxygenation reactions (chapter 4) 265
6.14. Syntheses (chapter 5) 273

References 279

I. Compound abbreviations 311

II. Appendix: Publications 313

III. Appendix: NMR spectra 314

IV. Appendix: Spectroscopic data **401**

V. Appendix: Electrochemical data **437**

VI. Appendix: X-ray crystallographic data **439**

List of abbreviations

[PC]	photocatalyst
10-CSA	(+)-10-camphorsulfonic acid
a.u.	arbitrary units
AlCF	tris(pentafluorophenyl)alane
anth	anthracene
approx.	approximately
Ar^{Br}	2-bromophenyl
Ar^{OMe}	2-methoxyphenyl
ATR	attenuated total reflection
BCF	tris(pentafluorophenyl)borane
BIA	free bromide ion affinities
BIDIPY	bismuth dipyrrin
BODIPY	4,4-difluoro-4-bora-3a,4a-diaza-*s*-indacenes
bpy	2,2′-bipyridine
CFL	compact fluorescent lamp
CPCM	conductor-like polarizable continuum model
CV	cyclic voltammetry
DABCO	1,4-diazabicyclo[2.2.2]octane
DDQ	2,3-dichloro-5,6-dicyano-1,4-benzoquinone
DET	Dexter energy transfer
Dipp	2,4-di(*iso*propyl)phenyl
DMA	9,10-dimethylanthracene
DMAc	*N,N*-dimethylacetamide
DMAP	4-(dimethylamino)pyridine
e.g.	*exempli gratia*
EnT	energy transfer
Eq.	equation
equiv.	equivalent(s)
Et	ethyl
FcH/FcH^+	ferrocene/ferrocenium
FRET	Förster resonance energy transfer
GADIPY	gallium dipyrrin
HAT	hydrogen atom transfer
HFIP	hexafluoro-2-propanol
HMDS	hexamethyldisilazane
HOMO	highest occupied molecular orbital
i.e.	*id est*
IC	internal conversion
ICT	intramolecular charge transfer
^{i}Pr	*iso*-propyl
IR	infrared
ISC	intersystem crossing
KHMDS	potassium bis(trimethylsilyl)amide
LED	light-emitting diode
LiHMDS	lithium bis(trimethylsilyl)amide
LMCT	ligand-to-metal charge transfer
LUMO	lowest unoccupied molecular orbital
max.	maximum
MeCN	acetonitrile
MeOH	methanol
Mes	2,4,6-trimethylphenyl
Mind	1,1,3,3,5,5,7,7-octamethyl-1,2,3,5,6,7-hexahydro-*s*-indacene
MLCT	metal-to-ligand charge transfer
$NaBArF_{24}$	sodium tetrakis[3,5-bis(trifluoromethyl)phenyl]borate
NaHMDS	sodium bis(trimethylsilyl)amide
NIR	near-infrared
NMR	nuclear magnetic resonance spectroscopy
PE	petroleum ether
PET	photoinduced electron transfer
Ph	phenyl
PHODIPY	phosphenium dipyrrin
PL	photoluminescence
PnDIPY	pnictogen dipyrrin
PODIPY	phosphorous dipyrrin
pyr	pyridine
rt	room temperature
SBDIPY	antimony dipyrrin
SCF	self-consistent field
SET	single electron transfer
SMD	solvation model density
SOC	spin-orbit coupling
SOMO	singly occupied molecular Orbital
TBA	tetrabutylammonium
TBS	*tert*-butyldimethylsilyl
^{t}Bu	*tert*-butyl
TEMPO	(2,2,6,6-Tetramethylpiperidin-1-yl)oxyl
TFA	trifluoroacetic acid
TfO^-	triflate anion
THF	tetrahydrofuran
TPA	tetrapropylammonium
Tr	trityl
Tripp	2,4,6-tri(*iso*propyl)phenyl
UV/Vis	ultraviolet-visible
vs	versus

1. Introduction

Light-induced chemical processes constitute the very basis for the existence of life as we know it and have become indispensable in many modern technologies.[1] The field of photochemistry represents an interface for a variety of scientific disciplines, which over the years have contributed to a significant progress in the understanding and application of excited state properties and light-driven processes.[1]

The word luminescence is derived from the latin word for light (*lumen*) and is used to describe the physical phenomenon of a spontaneous emission of radiation from either an electronically excited species or from a vibrationally excited species which is not in a thermal equilibrium with its environment.[2,3] Depending on the mode of excitation, various types of luminescence phenomena exist and have been well-documented.[3] The two types of luminescence that were of particular interest in the context of this thesis are photoluminescence, *i.e.* emission of photons caused by the absorption of light, and chemiluminescence, which describes a process in which the emission of photons is caused by a chemical reaction, such as oxidation or bond cleavage.[3]

Upon light absorption by a molecule, several photophysical processes are possible and can be visually simplified in a Perrin-Jablonski diagram (Figure 1).[3]

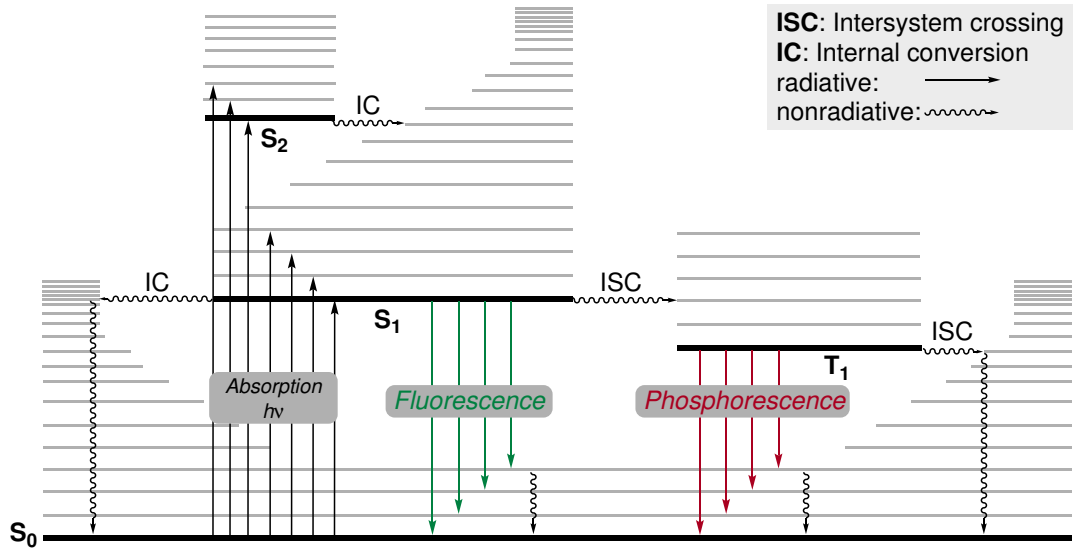


Figure 1: Simplified Perrin-Jablonski diagram. Black lines represent electronic energy levels, whereas grey lines indicate vibrational energy levels.[3,4]

The singlet ground state of the molecule is described by S_0, whereas S_1 and S_2 denote the first and second excited singlet states, respectively. These electronic energy levels are further partitioned into vibrational energy levels. Light absorption is generally depicted as vertical, upward-pointing arrows to illustrate the instantaneous nature

at which transitions between electronic states occur (circa 10^{-15} s).[4] Light absorption of a fluorophore, *i.e.* a molecule that emits fluorescence, generally results in the population of higher vibrational levels of either S_1 or S_2 state, from which molecules in the condensed phase readily fall back to the lowest vibrational level of S_1.[4,5] The nonradiative transition between two electronic states of the same spin multiplicity is called internal conversion (IC) and occurs within 10^{-9} s or less.[6] In solution, this process is normally accompanied by vibrational relaxation towards the lowest vibrational energy level, which can occur through deactivation with solvent molecules.[6] With fluorescence lifetimes typically being in the range of 10^{-8} s, IC is generally complete before any emission occurs, resulting in fluorescence emission from a thermally equilibrated excited state, which corresponds to the lowest energy vibrational state of S_1.[4] From here on, an $\mathrm{S}_1 \rightarrow \mathrm{S}_0$ relaxation can either proceed by fluorescence emission or nonradiative IC.[6] The emission of a photon proceeds as rapid as absorption (circa 10^{-15} s) but prior to that the excited molecules remain in the S_1 state for a variable time before emitting a photon or engaging in de-excitation process, such as IC or ISC. The lifetime of a singlet excited state lies in the range of 10^{-10}–10^{-7} s and depends on the properties of the molecule and the medium.[6] Moreover, the excited state population depletes exponentially which can be probed by short pulses of light to experimentally determine excited-state lifetimes (τ).[6] Lastly, the de-excitation process from an S_1 state to a T_1 triplet state is known as intersystem crossing (ISC) and plays a pivotal role in photocatalysis.[6–8] ISC is a nonradiative transition between two isoenergetic vibrational levels of two electronic states with different multiplicity and can occur sufficiently fast to compete with the other described de-excitations pathways from the S_1 state.[6] The resulting excited triplet state T_1 preferentially undergoes nonradiative decay to the ground state ($\mathrm{T}_1 \rightarrow \mathrm{S}_0$) in solution at ambient temperature, as opposed to the radiative de-excitation known as phosphorescence. This is mainly due to the $\mathrm{T}_1 \rightarrow \mathrm{S}_0$ transition being spin-forbidden, although it can occur to a small extent because of spin–orbit coupling, which results in an overall very low radiative rate constant. Since the radiative transition is intrinsically slow, collisions with solvent molecules favour de-excitation through ISC and vibrational relaxation to the lowest energy level of the S_0 state.[6] In contrast, low temperatures and/or a rigid medium can enhance radiative decay *via* phosphorescence.[6]

As mentioned before, a transition between different multiplicities (by ISC) is in principle forbidden but can be realized through spin-orbit coupling (SOC) contribution, which is favoured in the presence of heavy atoms, such as Br, Pb, Pt, etc.[6]

1. Introduction

The enhanced rate of SOC and consequently higher triplet state population associated with atoms of high atomic number is often referred to as the “heavy atom effect” and represents a crucial aspect in the development of new photocatalysts and phosphorescent materials.[7,9–11]

In recent years, the research and development of new long-lived phosphorescent materials has received considerable interest, especially due to the relevance in the field of optoelectronic devices.[12,13] Furthermore, this interest has also been noticeable in the field of main group chemistry, with many recent reports on phosphorescent compounds containing heavy p-block elements (Figure 2).[11,13] Particularly noteworthy is also the large amount of chromophores that incorporate heavy pnictogens, *i.e.* antimony and bismuth, into conjugated systems to promote phosphorescence through an increased singlet-triplet mixing.[11,13,14] An exemplary overview of selected main group compounds exhibiting phosphorescence emission is provided in Figure 2.

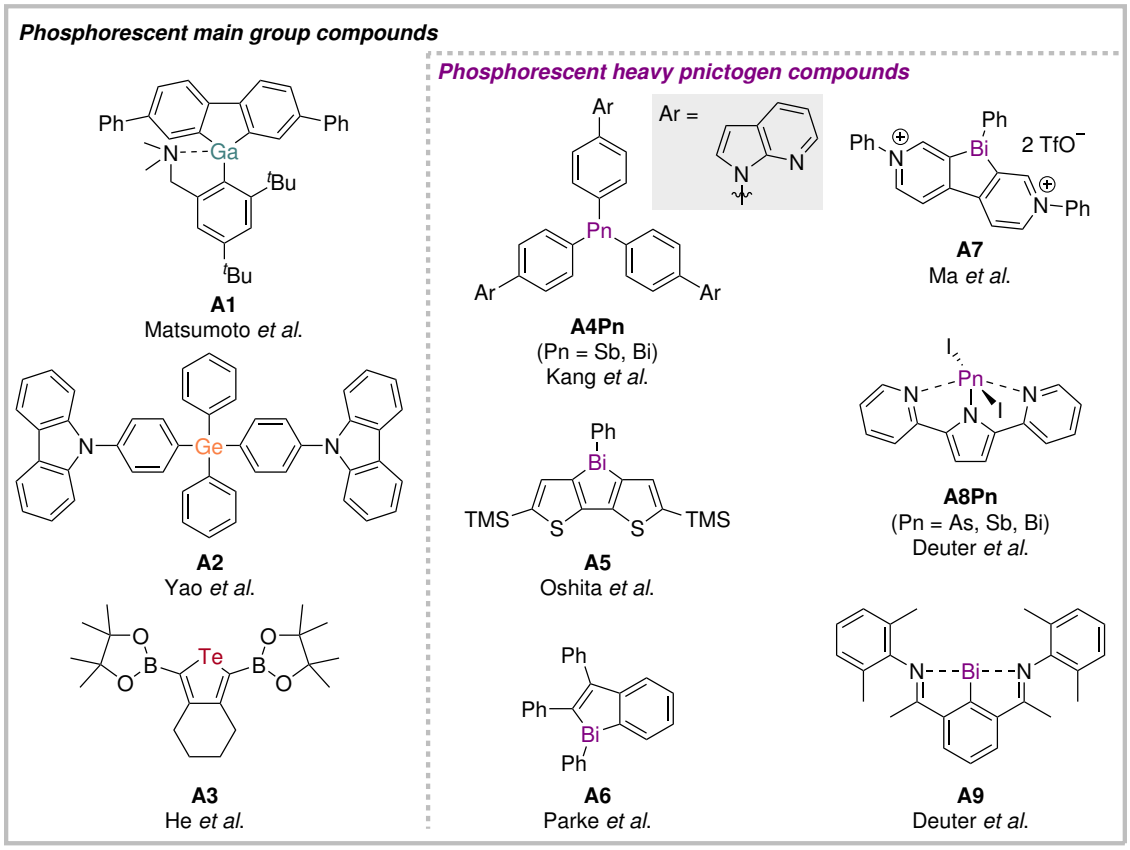


Figure 2: Selected examples of phosphorescent molecules containing heavy main group elements.[14–22]

In 2013, Matsumoto *et al.* reported the synthesis and characterization of several air- and moisture-stable gallafluorenes, such as compound **A1**.[15] The authors observed a phosphorescence emission in the visible-light region (578–684 nm) with lifetimes of several microseconds upon mixing gallafluorenes with one equivalent of tris(pentafluorophenyl)borane—a phenomenon that the authors assigned to the formation of a triplet exciplex.[15] In the field of heavy tetrel chemistry, Yao *et al.* developed an emissive germane **A2**, which displayed phosphorescence at 77 K and found further application as a host material for blue phosphorescent organic light emitting diodes.[16] In 2014, He *et al.* reported the synthesis of the first set of phosphorescent tellurophenes, *e.g.* **A3**, *via* a Zr/Te transmetalation reaction.[17] The presence of proximal pinacolborate side groups was identified as an important structural feature that enabled phosphorescence under ambient conditions.[17] Moreover, the authors reported additional applications of compound **A3** in the reversible on/off luminescence sensing of organic vapor and detection of fluoride ions.[17] Among other heavy main group elements, recent publications have highlighted antimony and bismuth as viable choices for the design of new phosphorescent materials.[11,14,18–20,22]

One of the earlier reported examples of heavy pnictogen-based phosphorescent compounds was presented by Kang *et al.* in 2002, introducing a triarylstibane (**A4Sb**) and a triarylbismuthane (**A4Bi**), which both displayed phosphorescence emission in the blue light region (456–494 nm) as the main radiative decay pathway in the solid-state and in a frozen CH_2Cl_2 matrix at 77 K.[18] The authors ascribed the photoluminescence characteristics of **A4Sb** and **A4Bi** to ligand-centred emissions with contributions from the lone-pair electrons of the heavy pnictogen atoms based on experimental data and DFT calculations.[18] Interestingly, although the heavy pnictogen compounds exhibited only phosphorescence at cryogenic temperatures, they also displayed considerably shorter excited state lifetimes as compared to the analogous triaryl phosphorus compound, which may stem from quenching through the heavy atoms.[18] Lastly, the authors also demonstrated the possibility of modifying the emission properties of **A4Bi** by oxidation with iodobenzene dichloride to the corresponding Bi(V) compound, thereby causing a bathochromic shift and an increased lifetime of the emission at 77 K.[18] Seminal work by Oshita *et al.* in 2010 underlined the potential of incorporating bismuth into a conjugated system to access phosphorescent materials.[19] The authors reported the synthesis and photophysical properties of a series of dithienobismoles akin to **A5**, which showcased phosphorescence emission in the solid-state even under air and at room temperature.[19] Building on this finding, Parke *et al.* reported the incorporation of bismuth into a conjugated hydrocarbon scaffold through Zr/Bi exchange to access a set of benzobismoles, such as **A6**, which exhibited phos-

phorescence emission in the visible-light region (600 nm) under ambient temperature and aerobic conditions.[14] Moreover, the authors were able to successfully install benzobismole units in high molecular weight polymers, thereby providing access bismuth-containing macromolecules with red light emission.[14] More recently, Ma *et al.* extended the library of bismuth containing heterocycles by reporting a series of bismoviologens akin to **A7**, which displayed phosphorescent emission in the visible-light region (550–590 nm) with lifetimes of several hundred nanoseconds under ambient conditions.[20] Furthermore, the authors showcased application of these novel compounds in electrochromic devices and as photocatalysts.[20]

In 2025, Deuter *et al.* reported a comparative study of three pnictogen diiodide complexes **A8Pn** (with Pn = As, Sb, Bi) bearing the 2,2'-(pyrrole-1-ide-2,5-diyl)bis(pyridine) ligand.[21] While only the arsenic complex **A8As** displayed weak fluorescence emission in CH_2Cl_2 at room temperature and in a glassy 2-MeTHF matrix at 77 K, no fluorescence was observed for the heavier congeners. Instead, all three complexes were found to display phosphorescence emission in frozen 2-MeTHF matrices at 77 K in the visible-light region (λ_{emi} = 584–612 nm) and lifetimes in the range of 60–219 ms with the highest phosphorescence quantum yield of the series determined for **A8Sb** (Φ_{phos} = 0.84). Additionally, the compounds showed a low activity as photosensitizers for singlet oxygen. Based on experimental and computational data, the authors attributed the photophysical properties of **A8Pn** to a combination of ligand effects (with contribution from pyrrolide and iodide substituents) and the heavy atom effect of the central pnictogen.[21] In 2025, Deuter *et al.* presented the first example of a low-valent bismuthinidine *N,C,N*-pincer complex (**A9**) with near infrared phosphorescence emission.[22] The authors reported a short phosphorescence lifetime of **A9** with just 5.2 ns at room temperature, which was enhanced to several hundred nanoseconds at cryogenic temperatures.[22] The unique emission properties of **A9** were attributed to the large spin-orbit coupling constant of bismuth and a metal-to-ligand charge transfer (MLCT) character of the first excited state based on computational investigations.[22]

1.1. Visible-light photocatalysis

Strongly influenced by technological advances in light sources, such as LEDs and CFLs, and the associated improvements in cost and energy efficiency, interest in the development of new photocatalytic reactions has grown significantly in recent years.[7] With visible light being a naturally available energy source, photocatalysis represents an important research field in the context of developing sustainable approaches for chemical transformations.[7] Although the term “visible-light photocatalysis" may suggest a process that is catalytic in photons, photocatalysis is more accurately described as the initiation or chemical reaction mediated by sub-stoichiometric amounts of a photocatalyst [PC] under visible light irradiation.[7,23] In general, photocatalysis can be categorized into two distinct working modes based on the redox behaviour of the photocatalyst. The first type is commonly referred to as photoredox catalysis, which utilizes the high redox activity of an excited state photocatalyst that undergoes a single electron transfer (SET) event with a suitable substrate to enable radical-based transformations.[24] The second mode is photosensitization, a term that is interchangeably used for energy transfer (EnT) catalysis and describes a process in which photochemical or -physical changes in one molecular entity are caused by an initial light absorption of another molecular entity (photosensitizer).[7,24,25] Conceptually, the term photoredox catalyst is used to describe compounds that can engage in SET chemistry, whereas photosensitizers are compounds that can undergo EnT upon excitation.[8,24] Nonetheless, it is important to point out that many photoredox catalysts can be utilized as photosensitizers and *vice versa*, depending on the nature of the excited states of catalyst and substrate, which may additionally complicate the interpretation of photocatalytic reactions and the involved mode(s) of action.[24] An overview of the applicability of both photochemical reaction modes (Figure 3) is provided in the following sections.

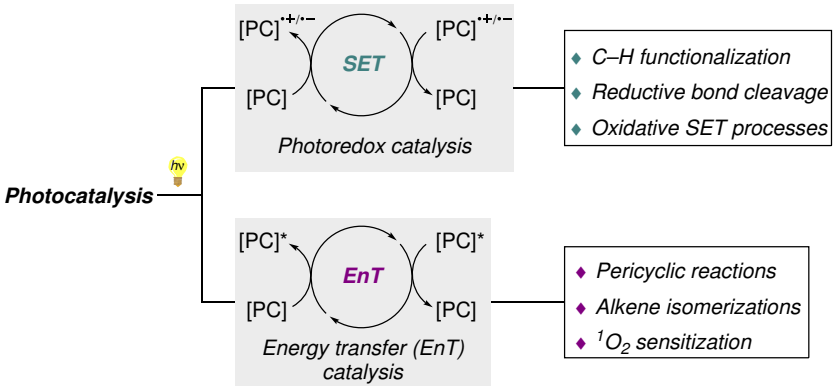


Figure 3: Overview of the main mechanistic pathways involved in molecular photocatalysis and exemplary reactivities thereof.[8,24]

1.1.1. Energy transfer (EnT) catalysis

The main principle of EnT catalysis is based on the energy transfer from an excited state molecule (D*) to an acceptor molecule (A) by deactivation to a lower-lying state.[26] In turn, the excited state acceptor (A*) can engage in follow-up reactivity. The previously introduced Perrin-Jablonski diagram provides a comprehensive description of the steps involved in EnT catalysis (Figure 4).[7,24] First, the photosensitizer, which is typically a transition metal complex or organic chromophore, is promoted from the S_0 ground state to an excited singlet state S_1 by light absorption. The S_1 excited state is rather short-lived and may undergo radiative or nonradiative de-excitation back to the S_0 ground state. However, inter-system crossing from S_1 to the triplet state T_1 yields an excited state with a significantly increased lifetime which is sufficient to engage in bimolecular quenching processes (Figure 4).[24]

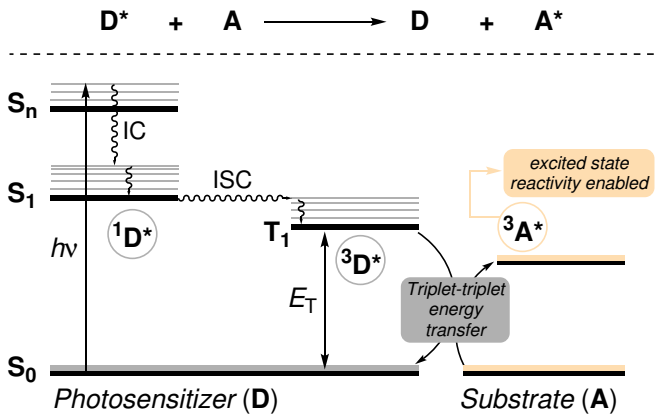


Figure 4: Main principles of EnT catalysis depicted in a simplified Perrin-Jablonski diagram. E_T shows the triplet state energy.[7,24]

In molecular photophysics two different interaction mechanisms have been considered for non-radiative EnT processes, namely Förster and Dexter energy transfer (Figure 5).[7,27–29] Förster resonance energy transfer (FRET) describes coulombic interactions consisting of long-range dipole-dipole interaction and short-range multipolar interactions, whereas Dexter energy transfer (DET) is characterized by a short range interaction involving intermolecular orbital overlap and electron exchange.[30] While for a singlet-singlet EnT both mechanism are relevant, triplet-triplet EnT only occurs on the basis of orbital overlap, thus following the mechanism described by Dexter.[29,30] A triplet-triplet EnT process *via* a Förster-type mechanism is disallowed as it poses a violation to the spin conversion rule, hence making DET the main mechanistic pathway for EnT photocatalysis.[7,31] Nonetheless, FRET represents a valuable tool for applications beyond photocatalysis, particularly in research areas such as

molecular interactions, structural biology and imaging techniques.[7,28]

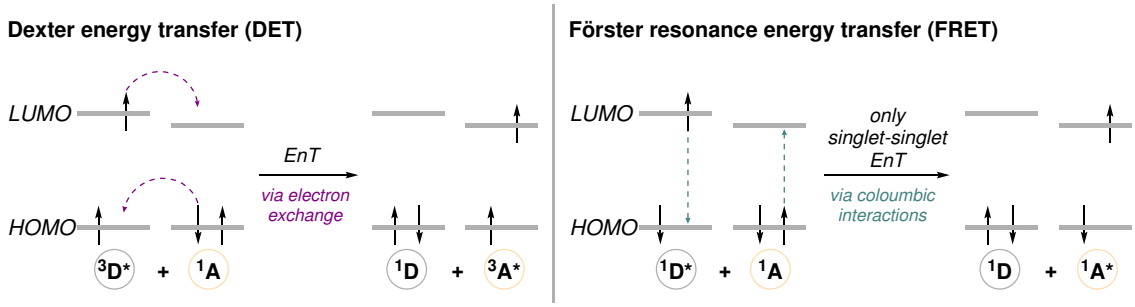


Figure 5: Schematic representation of the two mechanisms involved in EnT processes.[7,30]

Dexter-type EnT is governed by several factors that are especially relevant in the context of photocatalysis. As DET involves a (double) electron transfer, its rate can be described by Marcus theory and features an exponential decay with an increasing separation of photocatalyst (= donor, D) and substrate (= acceptor, A) as the mechanism relies on orbital overlap of the two.[7,32] Consequently, a key prerequisite for significant DET rates to enable EnT photocatalysis in solution is the formation of solvent-shared encounter complexes between donor and acceptor molecules, making it a predominantly diffusion-mediated process.[7] Moreover, the rate of EnT is controlled by thermodynamics, *i.e.* the involved triplet excited state energies of donor ($E_{T,D}$) and acceptor ($E_{T,A}$).[7] The resulting difference of excited state energies, given by

$$\Delta E_T = E_{T,A} - E_{T,D}, \tag{1}$$

provides an estimate to assess the feasibility of an EnT process (with $\Delta E_T < 0$ for exergonic EnT).[24] The most reliable method for determining triplet excited state energies (E_T) of photocatalysts and substrates is through the measurement of phosphorescence emission at cryogenic temperature (77 K) which allows direct determination of E_T by assignment of the (0,0) transition.[24]

An overview of commonly employed catalysts and substrates found in EnT photocatalysis with their corresponding triplet excited state energies (E_T) is provided in Figure 6. Various types of compounds can serve as suitable photocatalysts in EnT applications, ranging from common organic dyes such as methylene blue to aromatic carbonyls and transition metal complexes. EnT photocatalysts differ in the nature of their excited states, *i.e.* the associated E_T values and excited state lifetimes, as well as their operational wavelengths for excitation.[33]

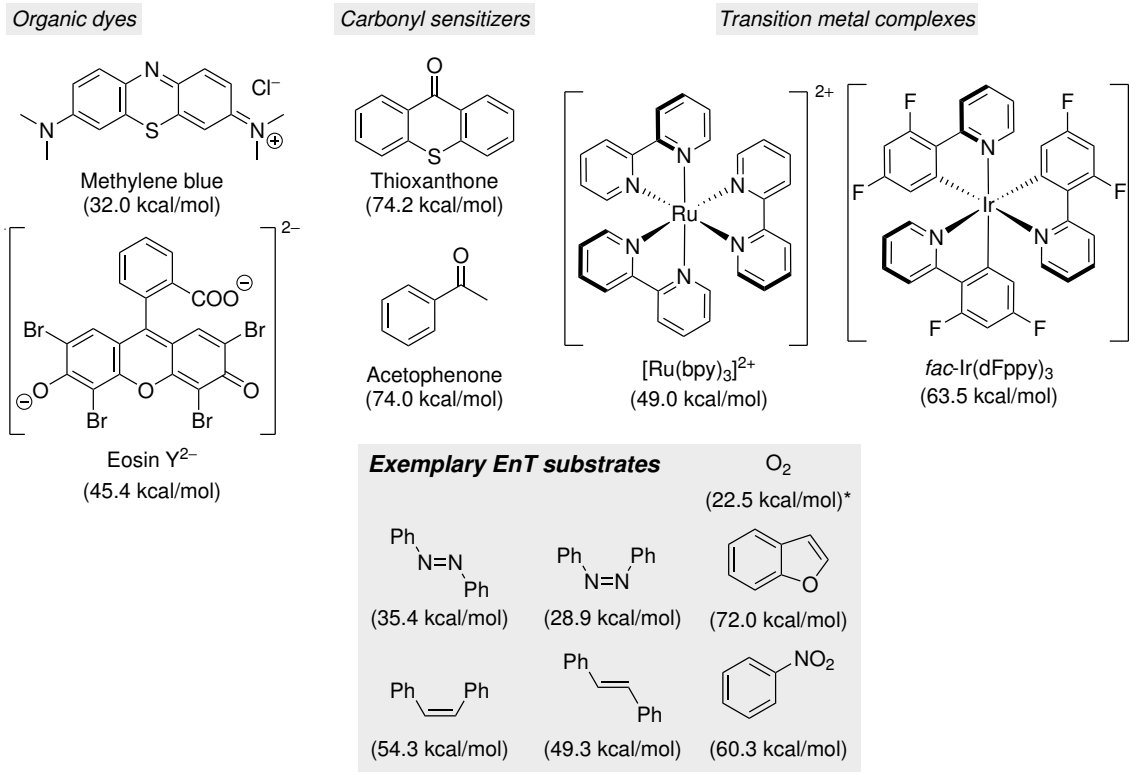
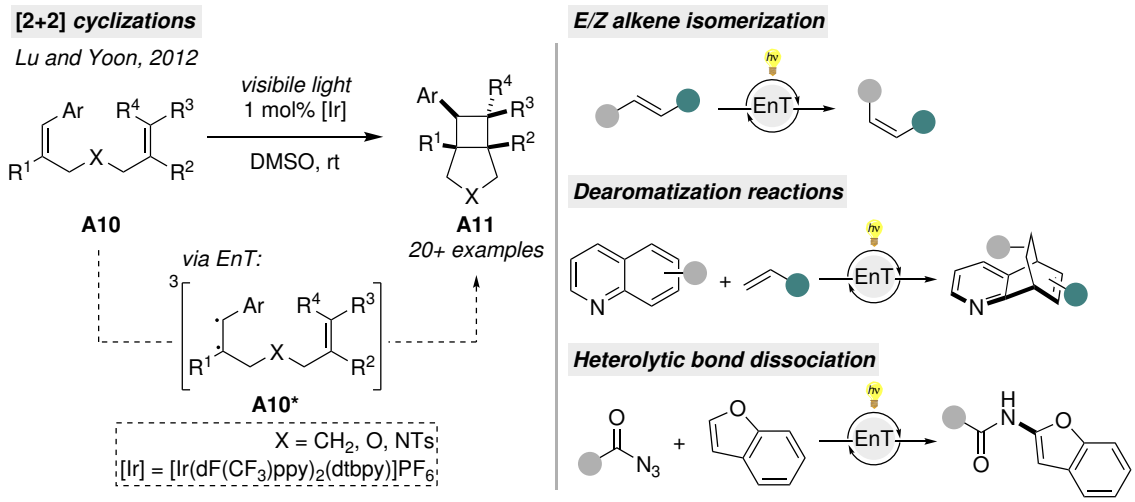


Figure 6: Selected examples of literature-known EnT photocatalysts and substrates with their respective triplet excited state energies (E_T) shown in round brackets. Value marked by (*) refers to the lowest $\mathrm{T}_0 \rightarrow \mathrm{S}_1$ transition in molecular oxygen.[7,24,34,35]

In order to engage in EnT processes, a photocatlyst requires a higher triplet excited state energy E_T than a chosen substrate to engage .[33] Moreover, it should possess a high ISC efficiency from S_1 to T_1 and a high molar absorption coefficient at the incident wavelength.[7] Lastly, the photocatalyst should be adequately photostable and inert to deleterious side-reactions with substrates in ground and excited state.[7]

EnT photocatalysis has recently gained renewed interest in literature, partially attributable to the pioneering work of Yoon and Lu, who reported a light-driven [2+2] cycloaddition reaction of various styrenes (**A10**) to form a library of cyclobutanes (**A11**) in the presence of transition metal photocatalysts (Scheme 1, left).[24,36] The transformation was proposed to proceed *via* an excited state triplet intermediate **A10***.[7] Importantly, this finding demonstrated the potential of EnT photocatalysis as a strategy to achieve photochemical transformations under visible light irradiation instead of otherwise harsh conditions and direct excitation with UV light.[36] Since then, the field of EnT photocatalysis has evolved further, with numerous new applications of organic and metal-based photocatalysts emerging in fields such as the photoisomerization of alkenes, dearomative cycloadditions and heteroatom dissociation strategies (Scheme 1, right).



Scheme 1: Various types of EnT photocatalysis applications.[24,36–38]

One of the earliest applications of EnT photocatalysis involves the excited state of molecular oxygen, namely singlet oxygen, which due to its relevance in the context of this thesis will be covered in a separate section.[24]

1.1.2. Singlet oxygen

The formation of a reactive metastable state of molecular oxygen through dye sensitization (EnT photocatalysis) was first identified in the 19th century by the seminal work of Kautsky and later assigned to the singlet excited state $^1\Delta_g$ by concurrent works of Foote and Wexler, as well as of Corey and Taylor.[39–41] From there on, photochemically generated reactive oxygen species (ROS) became an intensively studied field, leading to an improved understanding of the excited state properties of molecular oxygen in the presence of a photocatalyst.[42] As of today, two main interactions between a photocatalyst and ground state (triplet) oxygen have been postulated, which can be visualized by a simplified Perrin-Jablonski diagram (Figure 7).[43] The first pathway (*type I*) involves an SET from the photocatalyst to form a dioxygen radical anion, commonly refered to as superoxide ion due to its strongly oxidizing properties.[35,44] The second pathway (*type II*) proceeds *via* EnT photocatalysis, transitioning molecular oxygen from its ground state to either the first ($^1\Delta_g$) or second excited singlet state ($^1\Sigma_g^+$).[45] The $^1\Sigma_g^+$ state is unstable and rapidly decays to $O_2(^1\Delta_g)$ *via* a spin-allowed singlet-singlet transition.[45] As the decay from the $^1\Delta_g$ to the ground state is spin-forbidden, the $^1\Delta_g$ state is relatively long-lived and can be observed as a dim phosphorescence at 1270 nm.[35,43] The reactive singlet excited state of oxygen plays an important role in applications across multiple scientific disciplines, including photo-

sensitized oxygenation reactions, the photodynamic inactivation of viruses and cells, phototherapy for cancer and various other fields.[43,46]

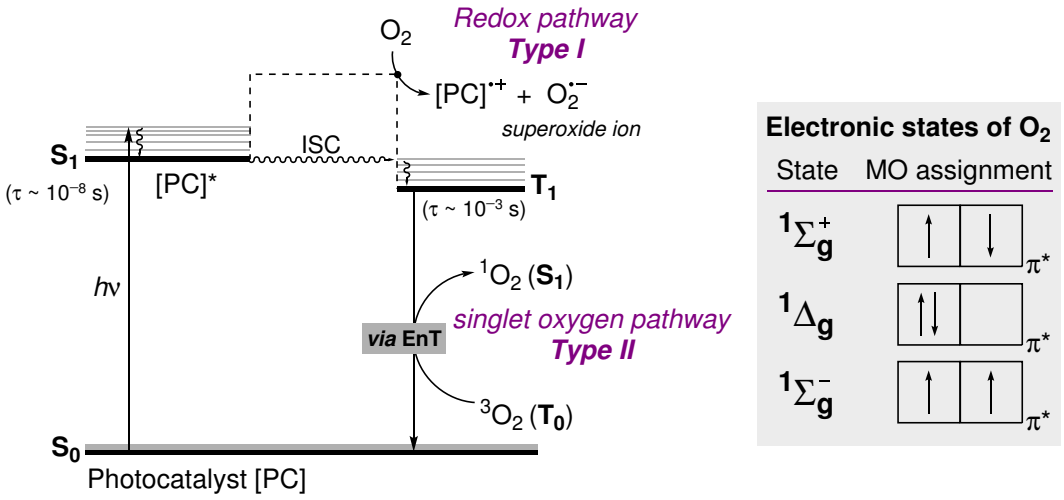


Figure 7: Simplified Perrin-Jablonski diagram description for generation of reactive oxygen species by sensitization with a photocatalyst [PC] and frontier orbital representation of molecular oxygen lowest singlet and triplet states.[35]

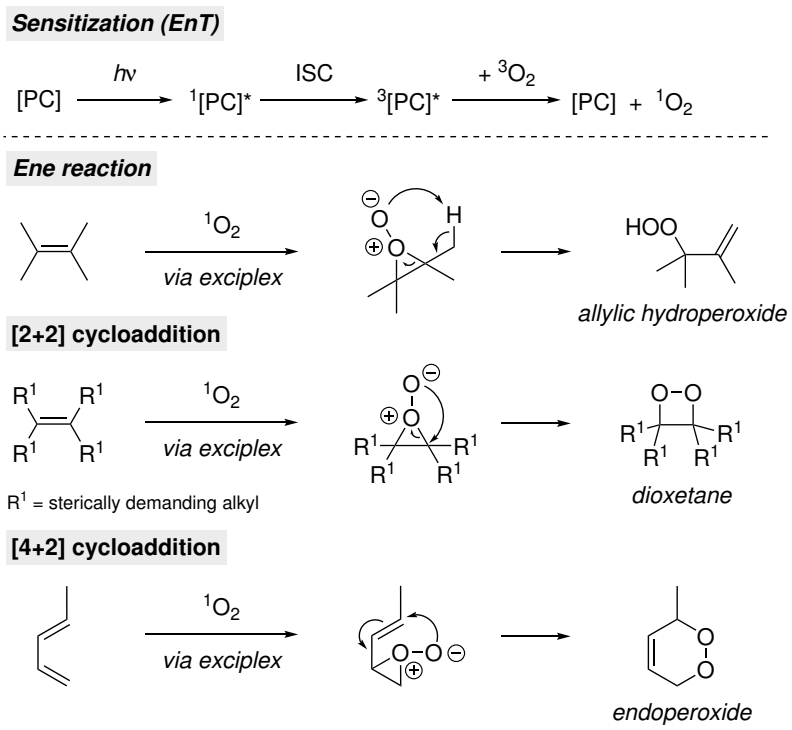
A common descriptor for the efficiency of photocatalytic $^1O_2$ production is the singlet oxygen quantum yield Φ_Δ which can be described by Eq. 2.[43,45]

$$\Phi_\Delta = p_S^{O_2} f_S^\Delta + \Phi_T p_T^{O_2} S_\Delta. \tag{2}$$

As both singlet and triplet excited states of the photocatalyst can contribute to $^1O_2$ sensitization, the factors $p_S^{O_2}$ and $p_T^{O_2}$ are used to describe the fractions of excited states S_1 and T_1 quenched by O_2, respectively. The efficiency of singlet oxygen generation further depends on the triplet quantum yield Φ_T in the presence of oxygen, the overall efficiency S_Δ of $O_2(^1\Delta_g)$ formation by O_2 quenching of T_1 states, whereas f_S^Δ denotes the efficiency of $O_2(^1\Delta_g)$ formation through S_1 quenching.[45] However, the contribution of S_1 quenching is in most cases negligible to the $^1O_2$ quantum yield, thus making sensitization *via* the excited triplet state the dominant process in the generation of $^1O_2$.[43] The singlet oxygen quantum yield is typically determined by direct measurement of the $^1O_2$ decay photoluminescence at 1270 nm using time-resolved or steady-state infrared luminescence spectroscopy, calorimetric techniques or quantitative analysis of photooxygenation reactions.[35]

Due to the increased reactivity of $^1O_2$ as compared to its ground state, singlet oxygen can enable a variety of oxidation reactions that can complement other established methods.[47] In fact, the most frequent use of $^1O_2$ in organic synthesis lies in the oxidation of alkenes, which offer several distinct reaction modes depending on the

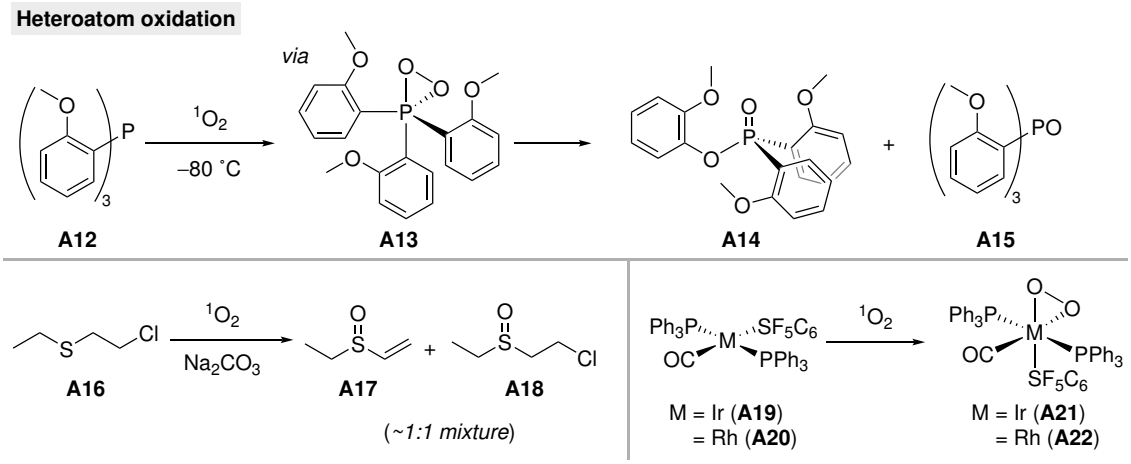
structure of the substrate.[47,48] The first interaction of $^1O_2$ with an alkene is the formation of an exciplex intermediate, which reacts further to form a hydroperoxide, dioxetane or endoperoxide depending on the reaction pathway (Scheme 2). The $^1O_2$ ene reaction is proposed to proceed via a stepwise mechanism and involves a suprafacial addition of the electrophilic oxygen and abstraction of hydrogen from the olefinic π-system.[49] Moreover, the hydrogen abstraction occurs preferentially at the sterically more encumbered side of an olefin, which is referred to as the *cis* effect.[49] The overall selectivity of the $^1O_2$ ene reaction is strongly dictated by steric and electronic effects, as well as potential hydrogen bonding interactions at the substrate.[49] The [2+2] cycloaddition reaction is observed with particularly electron rich alkenes and with those that contain no allylic hydrogens, resulting in the formation of dioxetane products which are most often thermally unstable compounds.[42] Lastly, the [4+2] cycloaddition of 1,3-dienes with $^1O_2$ yields synthetically versatile endoperoxide products. In all $^1O_2$ reaction types with alkenes, the control of stereo- and regioselectivity remains a challenge due to the small size of molecular oxygen.[42]



Scheme 2: Archetypal reactivities of singlet oxygen with unsaturated hydrocarbons.[42,47]

Owing to its electrophilic nature, $^1O_2$ readily reacts at electron pair bearing heteroatom centres, namely sulfur, selenium, phosphorous, nitrogen compounds and in some instances also with iridium and rhodium transition metal complexes (Scheme 3).[42] Contrary to unsaturated hydrocarbons, the interactions of $^1O_2$ with heteroatoms are dominated by physical quenching but can also lead to chemical quenching, which in

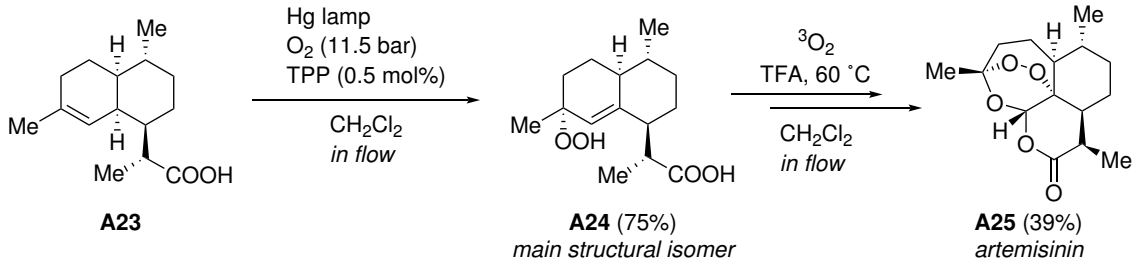
turn yields covalent adducts from the transfer of one or two oxygen atoms to the heteroatom.[42] A notable example for the reaction of $^1O_2$ with a pnictogen centre was reported by Selke and co-workers, who examined the photooxygenation of phosphine **A12** at low temperature in chloroform.[50] Under given conditions, the authors observed the formation of phosphinate **A14** phosphine oxide **A15**, which they were able to ascribe to the phosphadioxirane **A13** by low temperature ^{31}P and ^{17}O NMR spectroscopy.[50] Similarly to other heteroatoms, the photooxidation of organic sulfides is rather sluggish owing to the generally low quantum yields for sulfoxide formation.[42] The oxidation of organosulfur compounds has been proposed to undergo *via* the formation of a hydroperoxy sulfonium ylide which is in good agreement with experimental findings in the photoxygenation of chloroethyl ethyl sulfide (**A16**), yielding sulfoxides **A17** and **A18** in a 1:1 mixture.[42] The formation of the allylic sulfoxide **A17** has been proposed to proceed by β-elimination from a hydroperoxy sulfonium ylide intermediate.[51] Finally, organometallic complexes have displayed both physical and chemical quenching capabilities of $^1O_2$, with the possibility to react at the ligand or the metal centre.[42] Metal-centred reactivity was first demonstrated by Selke and Foote for Vaska's complex.[52] Further studies on thiolate substituted iridium (**A19**) and rhodium (**A20**) derivatives have indicated a preferential oxidation of the metal centre in presence of $^1O_2$, as opposed to other transition metal complexes where exclusively sulfur oxidation was observed.[42]



Scheme 3: Selected oxidation reactions of heteroatoms in the presence of $^1O_2$.[42]

The versatile reaction modes of $^1O_2$, as well as the comparably mild oxidation conditions, have made it an important reagent in the total synthesis of various natural products, which can also be used in flow reactors.[48] A 2012 report by Lévesque and Seeberger showcased the straight-forward synthesis of the antimalarial drug artemisinin (**A25**) from a porphyrin-sensitized macroflow photooxygenation of dihydroartemsinic

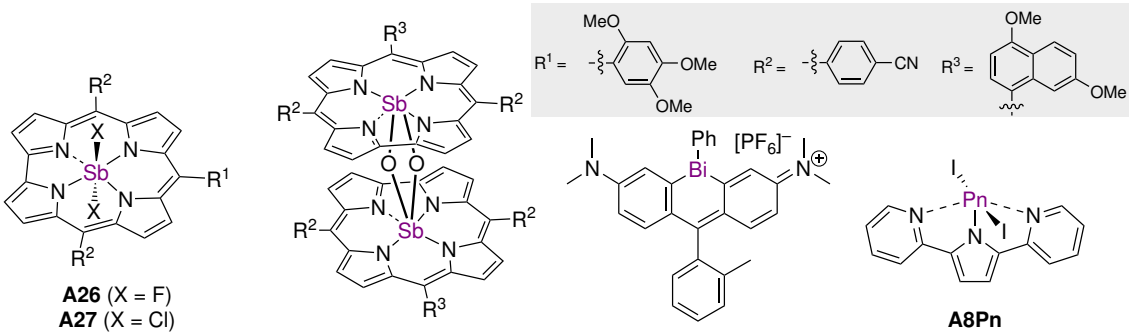
acid (**A23**, Scheme 4).[48,53] Acid **A23** was converted to a main structural isomer **A24** in good yield, which upon treatment with trifluoroacetic acid (TFA) and molecular oxygen yielded the artemisinin in moderate yield.[53]



Scheme 4: Synthesis of artemisinin using photosensitizer generated $^1O_2$ in a flow reactor (TPP = tetraphenylpophyrin, productivity: 0.49 mmol/min).[53]

Singlet oxygen is generally sensitized using organic dyes, such as methylene blue, rose bengal or porphyrins.[48] The low energy requirement (22.5 kcal/mol) makes it a convenient screening tool to assess the nature of a molecule's excited state and provides a good first indication for its potential use as a photocatalyst.[35] In the field of heavy-element-containing chromophores, only a few studies have investigated the influence of heavy central atoms in photochemical applications, with only a limited literature-presence particularly for group 15 elements.[54] The majority of literature-reported photosensitizers bearing a heavy central element feature a tetrapyrrolic ligand scaffold, such as corroles, porphyrins or phthalocyanines.[55–58] A 2005 report by Shiragami *et al.* showed the use of a silica gel supported Sb(V) porphyrin complex for sterilization of bacterial cultures under oxygen and light, indicating the formation of ROS, such as $^1O_2$.[59] More recently, tetrapyrrolic pnictogen complexes have been revisited in the context of EnT photocatalysis, *i.e.* oxygen sensitization. A recent study by Caliskanyürek *et al.* has highlighted the potential of antimony corrole complexes **A26**-**A28** to serve as photosensitizer for $^1O_2$ (Figure 8).[56] Especially the fluoride substituted antimony(V) complex **A26** was found to have the highest efficiency in $^1O_2$ generation (Φ_Δ > 0.95) of the series, marking it an interesting candidate for further photocatalytic applications.[56] A lower activity was observed in the case of a bis-μ_2-oxo-bridged dinuclear Sb(V) corrole **A29** reported by Mondal *et al.* (Figure 8), which displayed moderate $^1O_2$ efficiency in chloroform (Φ_Δ = 0.69).[57] Moreover, the authors stated that the $^1O_2$ efficiency of the mononuclear Sb(III) derivative were twice as low as **A29**.[57] In 2011, Reith *et al.* reported the synthesis and characterization of a Bi(III) corrole, which was identified as a potential $^1O_2$ photosensitizer, however, its $^1O_2$ efficiency was not disclosed.[58] In 2017, Hirayama *et al.* reported the synthesis and photophysical properties of a bismuth incorporated rhodamine chromophore analogue

A30.[60] The compound exhibited red-shifted absorption (λ_{abs} = 635 nm) and a more efficient $^1O_2$ generation (Φ_Δ = 0.66) than methylene blue under red light irradiation in acetonitrile. The authors further demonstrated the use of **A30** as a photosensitizer under subcellular conditions with several cell lines.[60] A recent report by Deuter *et al.* showcased another rare example of pnictogen complexes **A8Pn** without a tetrapyrrolic ligand scaffold but with the ability to generate $^1O_2$ under light irradiation. The authors observed comparably low $^1O_2$ generation for the arsenic complex **A8As** (Φ_Δ = 0.14) and the antimony complex **A8Sb** (Φ_Δ = 0.09), whereas the bismuth complex **A8Bi** displayed almost no activity (Φ_Δ < 0.01) in chloroform solutions at room temperature.



A26 (X = F)
A27 (X = Cl)
A28 (X = Br)
Caliskanyürek *et al.*

A29
Mondal *et al.*

A30
Hirayama *et al.*

A8Pn
(Pn = As, Sb, Bi)
Deuter *et al.*

Figure 8: Selection of literature reported heavy pnictogen-based $^1O_2$ photosensitizers $^1O_2$.[21,56,57,60]

1.1.3. Photoredox catalysis

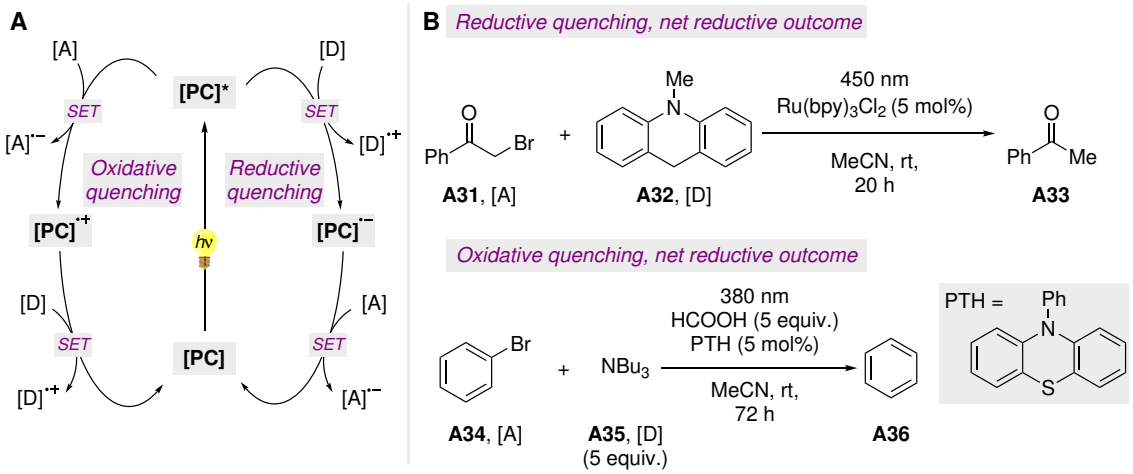
The second main category of modern photocatalysis is visible light photoredox catalysis. A characteristic trait of this field lies in the ability of metal complexes and organic dyes as photoredox catalysts to engage in single electron transfer processes with organic substrates upon excitation with visible light.[61–63] Commonly used photoredox catalysts are polypyridyl complexes of ruthenium and iridium akin to $Ru(bpy)_3^{2+}$ (tris(2,2'-bipyridine) ruthenium(II)), which have previously been described in the context EnT photocatalysis (*vide supra*).[61] Moreover, the use and development of new transition metal-free organic photoredox catalysts with strong reducing or oxidizing properties in the excited state, such as cyanoarenes or acridinium salts, have also attracted considerable interest in recent years.[63]

Most catalytic photoredox reactions proceed *via* one of the two mechanistic pathways upon excitation of the photocatalyst [PC] as shown in Scheme 5A.[8] In an oxidative quenching cycle the stronger reducing potential of the excited $[PC]^\star$ is harnessed by a suitable acceptor molecule [A], resulting in the formation of a radical ion pair

through single electron transfer (SET). The catalyst is subsequently regenerated in a consecutive SET with a suitable donor molecule [D], achieving catalyst turnover. In a reductive quenching cycle the reaction sequence of [D] and [A] is inverted as the photocatalyst is reduced to a radical anion in the first SET.[8] There are three possible outcomes for both quenching routes depending on the involvement of an external oxidant or reductant to achieve catalytic turnover: net oxidative, net reductive and net redox-neutral.[8]

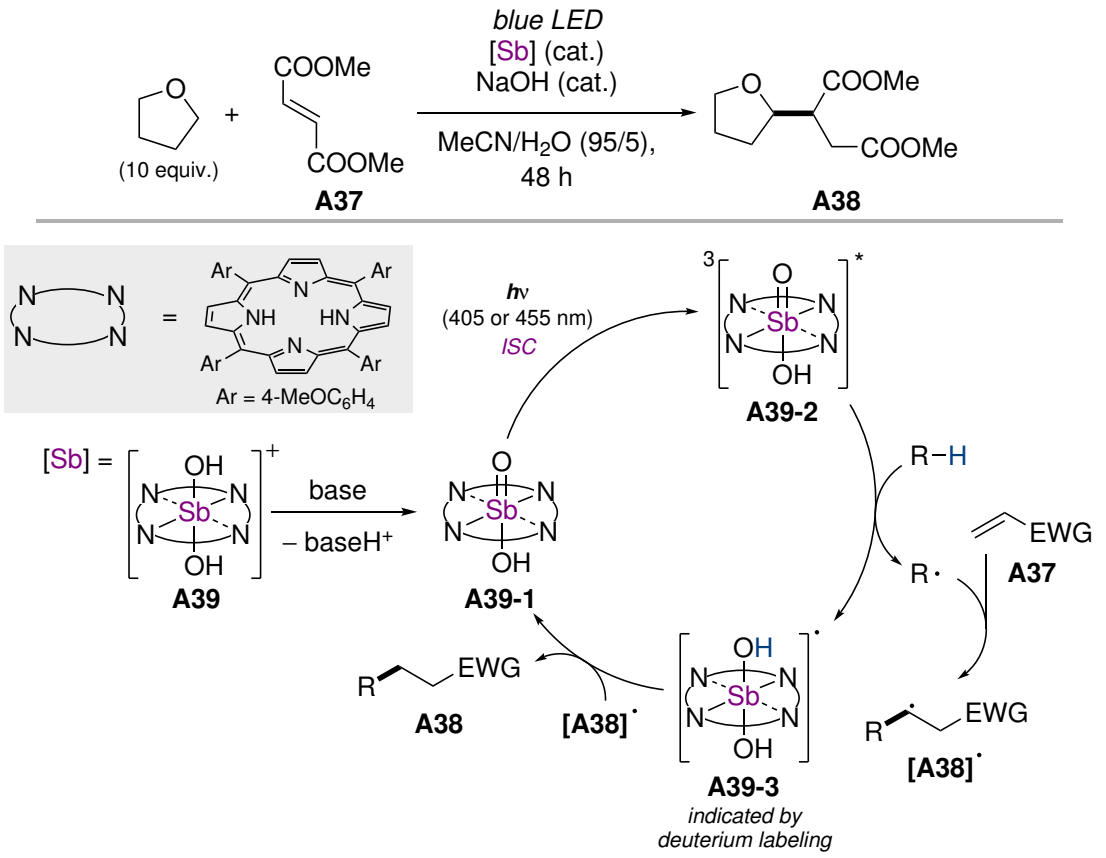
An early example of a transition metal catalysed photoredox reaction was shown by Fuzumiki *et al.* for the reductive dehalogenation of phenacyl bromide (**A31**) as acceptor in the presence of photocatalyst $Ru(bpy)_3^{2+}$ and stoichiometric reductant/donor 9,10-dihydro-10-methylacridine (**A32**, Scheme 5B).[64] Efficient conversion towards acetophenone (**A33**) was observed under visible light irradiation of the reaction mixture in acetonitrile, alongside the formation of the 10-methylacridinium monocation as by-product of the reductive quenching cycle.[61,64] An example of an oxidative quenching manifold in a metal-free catalytic photoredox system was demonstrated Discekici *et al.*, utilizing the highly reducing excited state properties of 10-phenylphenothiazine (PTH) as photocatalyst (Scheme 5B).[65] The authors reported a reductive dehalogenation reaction of alkyl and aryl halides, such as bromobenzene (**A34**), with an excess of tributylamine (**A35**) as donor, formic acid as proton source and PTH as photocatalyst under UV-light irradiation. With the given conditions, formation of benzene (**A36**) was reported in 85% yield, whereas no benzene was detected when employing tris(2-phenylpyridine)iridium (1 mol%) as photocatalyst under otherwise identical conditions, thus highlighting the potential of organophotoredox catalysts as viable alternatives to transition metal complexes in photoredox catalysis.

There have been continuous efforts to complement the predominant use of transition metal complexes in photochemistry by main group complexes.[66] However, an early perspective by Vogler *et al.* identified several challenges associated with the use of main group complexes in photochemical applications. First, the kinetic lability of main group complexes under irradiation in solution may hamper any reactivity and lead to decomposition.[66] A second important factor is the difference in the ability of transition metal complexes and main group compounds to undergo SET processes upon irradiation. While transition metal complexes readily engage in SET processes, main group compounds exhibit a high tendency to form diamagnetic compounds through the transfer of two electrons.[66] Finally, many main group compounds primarily absorb light in the UV region as they tend to be restricted by limited possible excitations, mainly relying on $s \rightarrow p$ and ligand-to-metal charge transfer (LMCT) transitions which makes them unsuitable for visible light applications.[66]



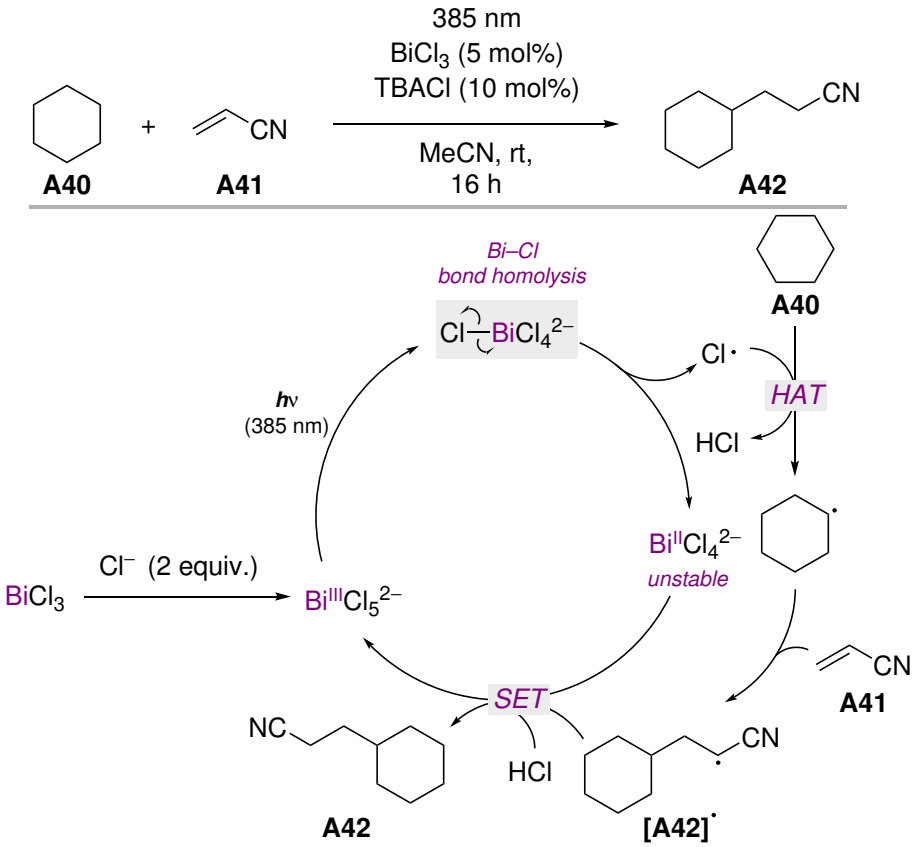
Scheme 5: Oxidative and reductive quenching modes in photoredox cataylsis ([PC] = photocatalyst, [A] = acceptor, [D] = donor; **A**). Exemplary applications of transition metal and organophotoredox catalysts (**B**).[63–65]

Nonetheless, recent developments in the field suggest that ligand design and reaction conditions can play an important role in enabling the photochemistry of main group elements, particularly for heavy pnictogen complexes. Seminal studies conducted by Inoue *et al.* have demonstrated the potential of Sb(V) tetraphenylporphyrin complexes as photoredox catalysts in the epoxidation reaction of various alkenes using water as the electron donor and oxygen source with methylviologen as an external oxidant.[67] Moreover, the authors also mentioned that similar reactivities were observed with high-valent porphyrin complexes of tin, germanium and phosphorous, potentially indicating an involvement of the ligand in the photochemical process.[67] The study was followed by several other investigations of the photochemistry of tetrapyrrolic Sb(V) complexes.[68–75] A more recent report by Capaldo *et al.* demonstrated the use of an Sb(V) porphyrin complex as a visible light photocatalyst for the redox-neutral coupling of THF with electron-poor olefins akin to **A37** (Scheme 6).[75] Based on additional computational and experimental studies, the authors proposed a mechanism featuring an initial deprotonation step from antimony complex **A39** to form oxo-complex **A39-1**. Light excitation of **A39-1** and subsequent ISC leads to the population of a triplet excited state with partial oxyl radical character **A39-2** which can perform hydrogen atom abstraction from THF to yield the corresponding radical which is subsequently trapped by alkene **A37** to afford **[A38]•**. According to computational analysis the antimony centre remains in the oxidation state of +V, indicating the formation of a ligand-centred radical complex **A39-3** that forms back **A39-1** through hydrogen atom transfer (HAT) to **[A38]•**, marking catalyst turnover (Scheme 6).[75]



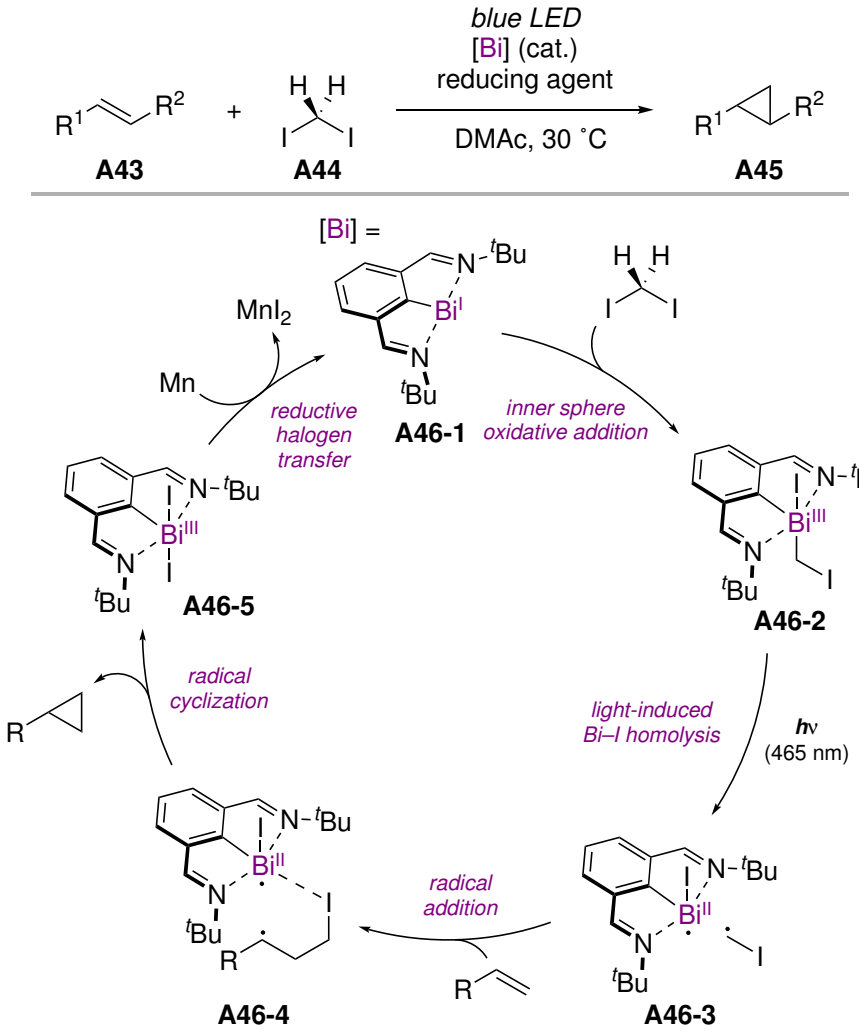
Scheme 6: Redox neutral C−H activation with an Sb(V)-oxo porphyrin complex.[75]

In recent years, bismuth compounds have also begun to emerge in photoredox applications, owing to the analogy between bismuth and transition metals.[76] A recent study by Birnthaler *et al.* illustrated the use of simple bismuth halide salts in LMCT photocatalysis to achieve net oxidative couplings of alkanes with electron-poor olefins, similar to the above-described reactivity of Sb(V) porphyrins.[77] UV irradiation of a MeCN solution containing an excess of an alkane, such as cyclohexane (**A40**), electron poor alkene **A41**, as well as catalytic amounts of $BiCl_3$ and tetrabutylammonium chloride (TBACl) resulted in the efficient conversion to the radical coupling product **A42** (Scheme 7).[77] Based on spectro-electrochemical analysis of a mixture of $BiCl_3$ and TBACl, the authors proposed a catalytic cycle for the reaction, involving an initial formation of a pentacoordinate bismuth(III) dianion, which undergoes Bi−Cl bond homolysis upon irradiation with UV light (Scheme 7).[77] The resulting electrophilic chlorine radicals readily engage in HAT with alkane substrate **A40**, which is subsequently trapped by the alkene **41** to generate radical **[A42]•**. The intermediate $BiCl_4^{2-}$ was found to be unstable in the absence of a coupling partner but undergoes SET with **[A42]•** and HCl to regenerate the catalyst.[77]



Scheme 7: Bismuth LMCT-photocatalysed radical coupling of alkanes with electron-deficient alkenes and proposed catalytic photoredox cycle.[77]

Recent studies by the Cornella group have showcased that the use of suitable ligands can further elevate photocatalytic applications of molecular low-valent bismuth chemistry through access to metal-to-ligand charge transfer (MLCT) transitions.[78–82] The group was able to utilize a robust bismuth(I) *N,C,N*-pincer complex in a diverse set of photoredox applications, including the C−N coupling of redox active elecrophile,[78], C(sp^2)–H trifluoromethylation,[83] reductive cyclopropanation reactions,[79], C(sp^2)−C(sp^2) couplings,[81] and heck-type coupling reactions.[82] These reactivities follow a common mechanistic template that can be visualized in the catalytic cycle proposed by Ni *et al.* in their 2024 report on bismuth-catalysed photoredox cyclopropenation reactions (Scheme 8).[79] The authors were able to demonstrate the efficient transformation of various olefins **A43** with carbenoid precursor **A44** to cyclopropanes **A45** under blue light, using catalytic amounts of a bismuthinidene *N,C,N*-pincer complex **A46-1** and stoichiometric reducing agent (Scheme 8).[79]

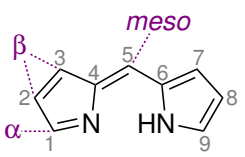


Scheme 8: Reductive cyclopropenation using a bismuthinidene *N,C,N*-pincer complex as photocatalyst and proposed mechanism.[79]

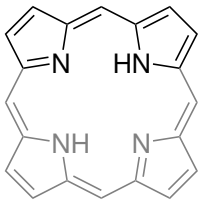
The catalytic cycle is initiated through the oxidative addition of the alkyl halide to the bismuth centre to form Bi(III) complex **A46-2** which can undergo Bi−I bond homolysis upon irradiation with a 465 nm LED lamp, resulting in the formation of a Bi(II) complex **A46-3** and an alkyl radical fragment. Radical addition with the olefin substrate, followed by radical ring-closing *via* a possible intermediate **A46-3** affords the cyclopropane product and Bi(III) complex **A46-5**. The catalyst **A46-1** is regenerated through the use of manganese as stoichimetric reductant (Scheme 8).[79] The oxidative addition and light-induced Bi−I bond homolysis is a common strategy featured in other photoredox applications of catalyst **A46-1**.[81–83] Moreover, the ligand system plays a crucial role in these transformations as it allows the population of ^{3}MLCT states that can engage in SET processes with suitable substrates.[80]

1.2. The chemistry of dipyrrins and their complexes

Dipyrrins are a class of bispyrrolic molecules that are well established as ligands in the field of chromophore chemistry. They consist of an azafulvene that is linked to a pyrrole unit through the pyrrolic 2-positions, thereby allowing delocalization of electron density across the entire scaffold (Figure 9).[84] The inception of dipyrrin chemistry dates back more than a century to the seminal report by Piloty in 1914, describing the first synthesis and structural proposal of dipyrrin dyes.[85] Based on the disclosed structure description of dipyrrin dyes, the origin of their strong colouration becomes evident as the π-conjugation of the bis-pyrrolic scaffold enables an efficient absorption of visible light through a $\pi \rightarrow \pi^{\star}$ transition.[86] Moreover, due to their structural and electronic similarities with porphyrins, dipyrrin dyes can be considered as "half-porphyrins".[86] The similarities also partially extend to the description and nomenclature of dipyrrin dyes, which was methodized in 1987 following the reported IUPAC guidelines and nomenclature for oligopyrrolic systems (Figure 9).[87] However, the 1- and 9-positions are often referred to as α-positions, 2-, 3-, 7- and 8-positions as β-positions, whereas the 5-position is commonly termed as the *meso*-position—a terminology coined by porphyrin chemistry.[84,87] Prior to the recommended IUPAC nomenclature, many different names have been used to describe dipyrrin dyes, which are still occasionally found.[84] In the context of this work, all molecules featuring the structural motif **A47**, will be referred to as "dipyrrins" or "dipyrromethenes".[84,88]



A47
Dipyrrin core



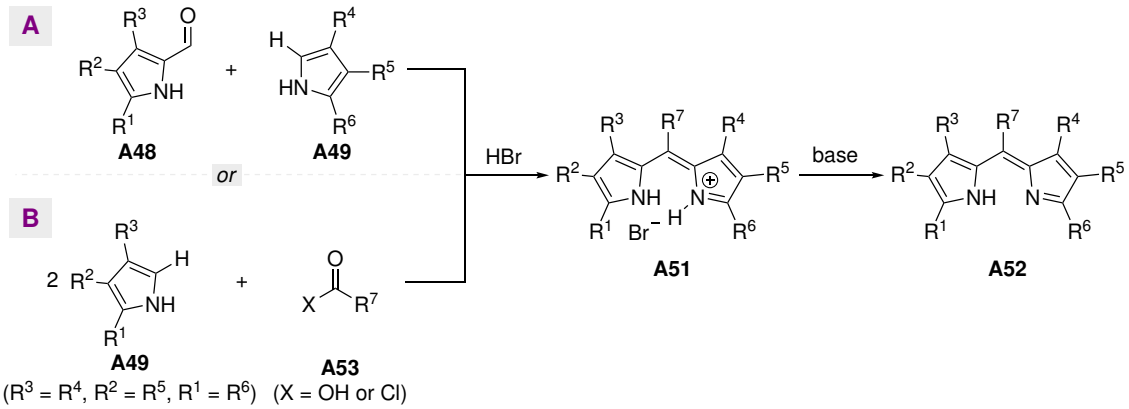
Porphyrin core

Figure 9: Structure of the dipyrrin core shown with IUPAC-recommended numbering scheme in grey and Fischer numeration in violet (left) and the structure of the porphyrin core (right).[84,87]

The stability of dipyrrins has been observed to be strongly affected by the number and type of substituents on the scaffold.[84] The first synthesis of the fully unsubstituted dipyrrin core (**A47**) was reported in 1977 by van Koeveringe and Lugtenburg, who were able to prepare dipyrrin **A47** through a Vilsmeyer-type reaction of 2-pyrrolecarbaldehyde and pyrrole at -60 °C using stoichiometric amounts of $POCl_3$, followed by neutralization with $Ca(OH)_2$.[89] However, isolation of the compound was not possible due to decomposition at temperatures above -30 °C caused by the

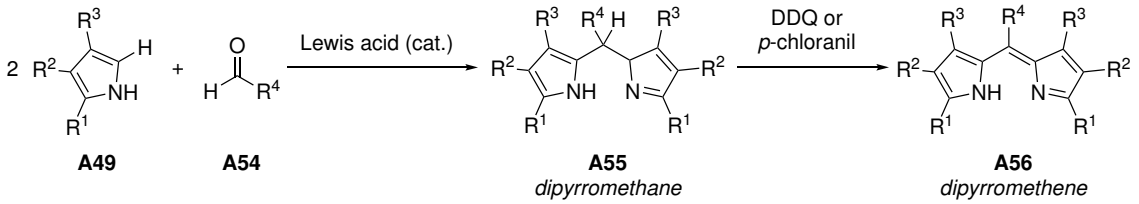
high susceptibility of the pyrrolic positions to undergo electrophilic or nucleophilic attack.[84,89] Consequently, alkyl substituents are often installed in the α- and β-positions of dipyrrins to prevent degradation. Moreover, incorporation of an aryl substituent in the *meso*-position also results in an improved stability, as the isolation of α- and β-unsubstituted dipyrrins becomes feasible.[84]

There are two common synthetic routes to access dipyrrin dyes: acid catalysed condensation of pyrroles (Scheme 9) and synthesis *via* the oxidation of dipyrromethanes (Scheme 10). The first strategy is often referred to as the MacDonald coupling, owing to its origins in porphyrin synthesis, and yields the salts of 5-unsubstituted dipyrrins (**A51**) by treating a mixture of 2-formyl pyrrole (**A48**) and a pyrrole without a substituent in the 2-position (**A49**) with HBr or phosporous(V) oxychloride (Scheme 9A).[84] The hydrohalido dipyrrin salt can easily be converted to the free-base form (**A52**) by treatment with a base and generally offers a higher stability than **A52**, which makes it a convenient precursor suitable for long-term storage. Additionally, the MacDonald coupling method allows the preparation of asymmetric dipyrrins as it relies on the complementary functionalities of the pyrrolic precursors.[84] Alternatively, *meso*-substituted dipyrrins (**A51**, where R^7 = alkyl or aryl) can be prepared from the condensation of two equivalents of pyrrole **A49** with one equivalent of carboxylic acid or acid halide (**A53**, Scheme 9B).



Scheme 9: General synthesis of dipyrrins *via* MacDonald coupling using 2-formyl pyrroles (A) or carboxylic acids/acid halides (B).[84]

A more versatile one-pot approach for the synthesis of *meso*-substituted dipyrrins involves the oxidation of dipyrromethanes (**A55**) as intermediates to access the corresponding free-base dipyrrins (**A56**, Scheme 10).[84] In this case, the dipyrromethane (**A55**) is first prepared through condensation of an aromatic aldehyde (**A54**) with two equivalents of pyrrole (**A49**) in the presence of a mild Lewis acid, followed by oxidation with stoichiometric amounts of 2,3-dichloro-5,6-dicyano-1,4-benzoquinone (DDQ) or *p*-chloranil (Scheme 10).[84]



Scheme 10: General synthesis of dipyrrins *via* oxidation of dipyrromethane.[84]

To date, dipyrrins have found numerous applications as building blocks in porphyrin synthesis and serve as highly versatile ligands for both transition metals and main group elements, usually resulting in complexes with strongly pronounced photophysical properties.[84,90] Main group element dipyrrin complexes, particularly those of boron, have received a considerable amount of attention due to their highly tunable properties and broad applicability across various fields of the natural sciences and will therefore be discussed in more detail.[91]

1.2.1. Boron dipyrromethenes (BODIPY)

Boron difluoride complexes featuring a dipyrrin ligand, *i.e.* 4,4-difluoro-4-bora-3a,4a-diaza-*s*-indacenes, are commonly abbreviated as “BODIPY” and constitute a prominent class of fluorophores that was first discovered by Treibs and Kreuzer in 1968.[91,92] BODIPY dyes are characterized by a fully conjugated and rigid π-system that can be further extended through addition of suitable substituents onto the dipyrrin framework.[91] In contrast to dipyrrin dyes, a different numbering scheme based on the analogy with the aromatic hydrocarbon *s*-indacene is used to describe BODIPY compounds (Figure 10).[93] However, the terms α-,β- and *meso*-postion are tantamount to the dipyrrin scaffold.[91] BODIPY dyes typically exhibit strong absorption in the UV-region and generally display sharp fluorescence emission bands with high quantum yields. Moreover, they showcase a considerably high stability under physiological conditions while maintaining their photophysical properties across a range of solvent polarities and pH values.[91]

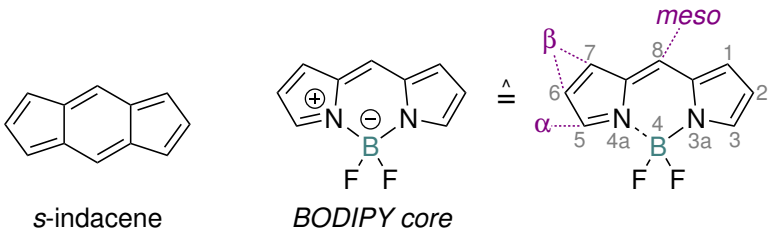
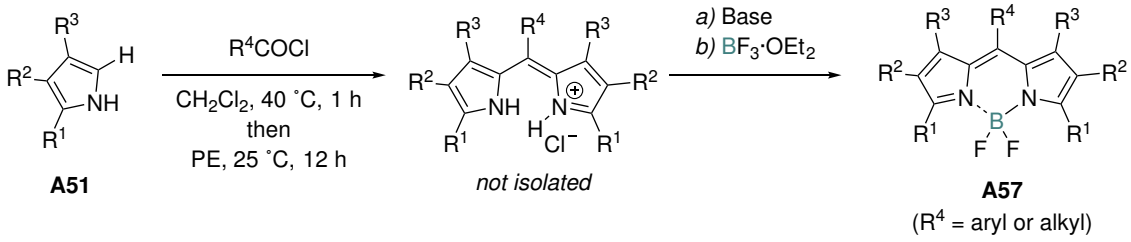


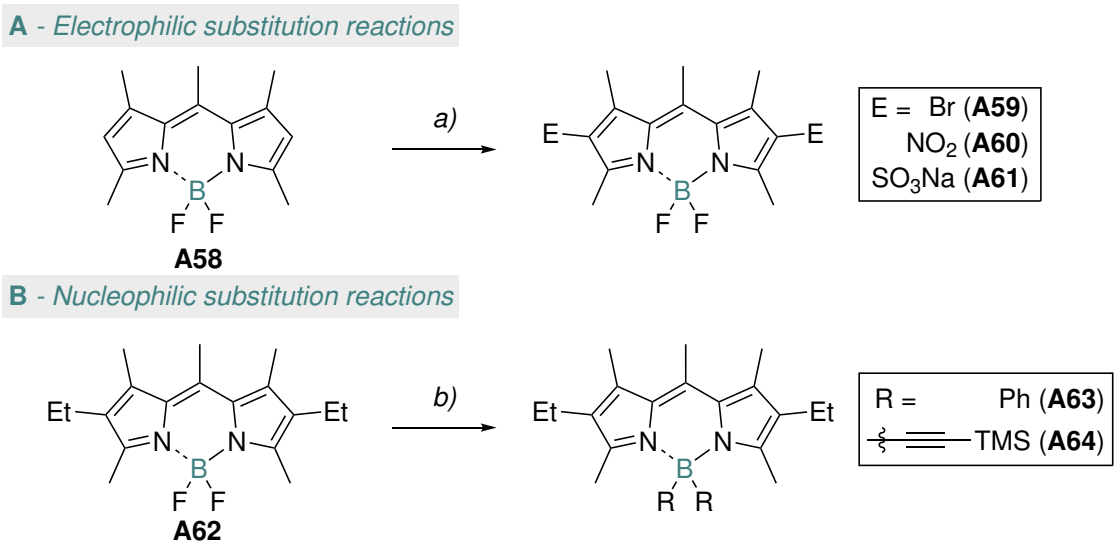
Figure 10: Structural analogy of *s*-indacene and the BODIPY core and corresponding numbering convention for BODIPY dyes.[91,93,94]

BODIPY dyes are most commonly synthesized without prior isolation of the dipyrrin ligand. Instead, a one-pot approach is often employed by first preparing the dipyrrin hydrohalido salt, which is then treated *in situ* with an excess of base and boron trifluoride diethyl etherate (Scheme 11).[91] Alternatively, the dipyrrin synthesis can be performed *via* a dyprromethane intermediate, followed by oxidation (see Scheme 10) and addition of base and boron trifluoride diethyl etherate.[91] Although the one-pot method provides direct access to BODIPY chromophores, a major drawback often lies in the tedious purification and ensuing low yields.[95]



Scheme 11: General one-pot procedure commonly employed for the synthesis of BODIPY dyes.[91,93]

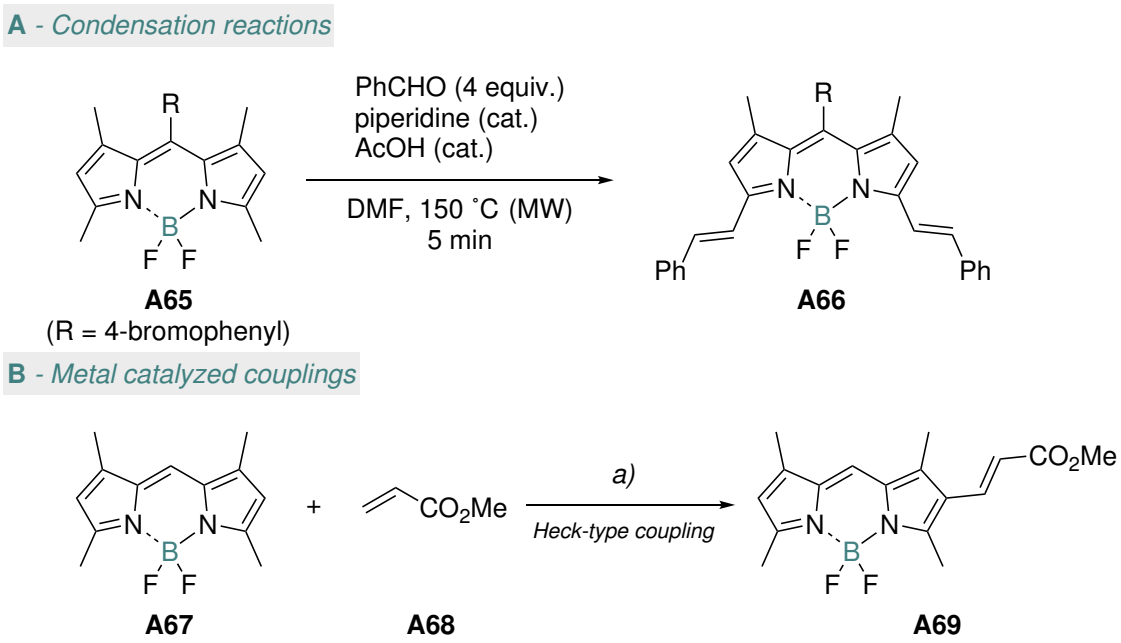
Owing to its high stability, the BODIPY core offers a multitude of possible modifications with virtually tailor-made properties. Examples include electrophilic substitution reactions which tend to occur in the 2- and 6-positions of the BODIPY core (Scheme 12A). Additionally, through adjustment of electrophile equivalents a di- or mono-substitution in the β-positions can be achieved.[91] Starting from alkyl-substituted BODIPY **A58**, electrophilic aromatic substitution has been successfully employed to prepare 2,6-dibromo BODIPY (**A59**), 2,6-dinitro BODIPY (**A60**) and 2,6-disulfonate BODIPY (**A61**).[91,96] Another possibilty to gain structural diversification of BODIPY chromophores is nucleophilic substitution at the boron centre (Scheme 12B). Nucleophilic substitution is possible with organolithium reagents, such as phenyllithium (for **A63**) or lithium acetylide (for **A64**), and Grignard reagents or other strong nucleophiles.[91,97,98]



Scheme 12: Electrophilc (A) and nucleophilic (B) substitution strategies for diversification of BODIPY chromophores. Conditions *a*: Br_2 (exc.) in CH_2Cl_2 at rt, 10 min (**A59**); HNO_3 (exc.) at 0 °C, 1.5 h (**A60**); HSO_3Cl (2.0 equiv) in CH_2Cl_2 at −50 °C to rt, treatment of precipitate with 2.1 equiv. of aqueous $NaHCO_3$ (**A61**); conditions *b*: Phenyllithium (2 equiv.) in diethyl ether at rt, 5 min (**A62**); *n*-BuLi (2.2 equiv.), trimethylsilylacetylene (2.2 equiv.) −78 °C to rt in THF (**A63**).[91,96–98]

Furthermore, the methyl substituents in 3-, and 5-position of the BODIPY core are acidic enough to undergo Knoevenagel-type condensations with aromatic aldehydes using acetic acid and piperidine as catalysts. In this way, tetramethyl-substituted BODIPYs, such as **A65**, afforded the distylryl modification **A66** in good yields under microwave irradiation in DMF (Scheme 13A). Finally, transition metal-catalysed couplings have also been successfully applied in BODIPY chemistry, with multiple variations of palladium cross-coupling reactions reported.[91] Thivierge *et al.* reported a Heck-type coupling that allowed the authors to extend the dipyrrin π-system in BODIPY **A67** through C−H functionalization with different acrylates **A68** (Scheme 13B).[99] The modification was observed to yield mono-substituted compound **A69** as the main product.

Both, metal-free and transition metal-catalysed methods can be implemented to achieve an extension of the π-conjugated chromophore system, thereby affording a bathochromic shift of the absorption and emission profile.[91]



Scheme 13: Metal free (A) and metal-catalysed (B) coupling reactions of BODIPY chromophores. Conditions *a*: methyl acrylate (5.0 equiv.), $Pd(OAc)_2$ (20 mol%), ^{t}BuOOBz (2.0 equiv.), AcOH/dioxane/DMSO (3/9/1), 35 °C, 5 days.[91,99,100]

The effect of substituents on the BODIPY core has been systematically studied in the past, particularly for the *meso*-substituent.[101] Based on experimental and computational data, three different scenarios can be assigned to the electronic interactions between the BODIPY core and a *meso*-substituent (Figure 11).[91] Depending on the relative energy gap between the first frontier molecular orbitals of the *meso*-substituent and the BODIPY core, no change in the fluorescence emission (Figure 11A) or fluorescence quenching due to photoinduced electron transfer (PET) can occur (Figure 11B, C). Additionally, a distinction is made between *a*-PET, in which the BODIPY core accepts an electron from the higher lying HOMO of the *meso*-substituent, and *d*-PET where the BODIPY core donates an electron to the lower-lying LUMO of the *meso*-substituent upon excitation.[91] This phenomenon is strongly dependent on solvent polarity and may be used for fluorescence-based sensing applications.[101]

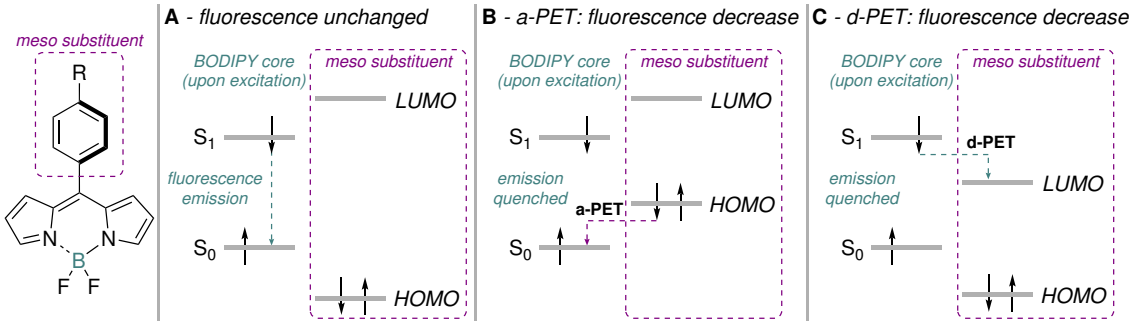


Figure 11: Influence of the *meso*-substituent on fluorescence emission intensities conceptualized by PET processes.[91,94]

1.2.2. BODIPY dyes in molecular sensing

The multitude of possible modifications has led to a large library of BODIPY chromophores with highly diverse chemical and photophysical properties. Based on this asset, several strategies have employed BODIPY chromophores in fluorescence-based and analyte-selective molecular sensing applications.[94] BODIPY sensors typically feature functional groups that readily engage in PET processes and are strongly affected by coordination of ions or chemical reactions that change the overall polarity of the chromophore. Another important effect that is relevant for fluorophores containing an electron-donating moiety that is conjugated to an electron-withdrawing group is the so-called photoinduced intramolecular charge transfer (ICT), which describes the charge separation in such fluorophores upon excitation leading to the population of an ICT state.[94] As for PET, this process can be strongly affected by polarity and ion-interactions but in contrast to PET results in a shift of the fluorescence emission.[94]

Sensors containing a BODIPY unit have been reported for various applications, ranging from pH-sensitive probes, cation- and anion-sensing to small molecule detection (Figure 12). BODIPY-based pH-indicators have been developed, utilizing the *a*-PET effect of the pH-sensitive *p*-(*N,N*-dimethyl)aniline functionality as *meso*-substituent in BODIPY dyes.[94] While the neutral form of BODIPY **A70** is nonfluorescent due to *a*-PET of the *meso*-substituent, protonation prevents PET, thus leading to a strong emission ("Fluorescence ON").[102,103] Different variations of BODIPY dyes containing crown-ethers have been developed for the selective detection of various (metal) cations.[94] An efficient probe for the detection of lead(II) ions has been synthesized by Mbatia *et al.*, utilizing an 18-membered crown-ether as a cation chelator in the chromophore backbone (**A71**).[104]

BODIPY **A71** was found to be essentially nonfluorescent ($\Phi \approx 0$) but displayed a drastically increased emission (Φ = 0.74) in the presence of lead(II) ions.[104] Detection of anions, such as fluoride, cyanide and hydrogenphosphate, has been explored by employing reactive functional groups.[94] Ekmekci *et al.* developed a BODIPY-based chemosensor **A72** that is mostly inert to inorganic anions but displays a large decrease in emission intensity in the presence of cyanide ions. The authors attributed this effect to the interaction of cyanide ions with the amide moiety of the sensor.[105] Lastly, Green *et al.* reported the synthesis and CO_2 detection properties of a BODIPY dye containing an iminophosphorane group (**A73**). The practically nonfluorescent BODIPY dye **A73** reacted in the presence of atmospheric CO_2 to form an isocyanate, leading to a significant increase in emission intensity.

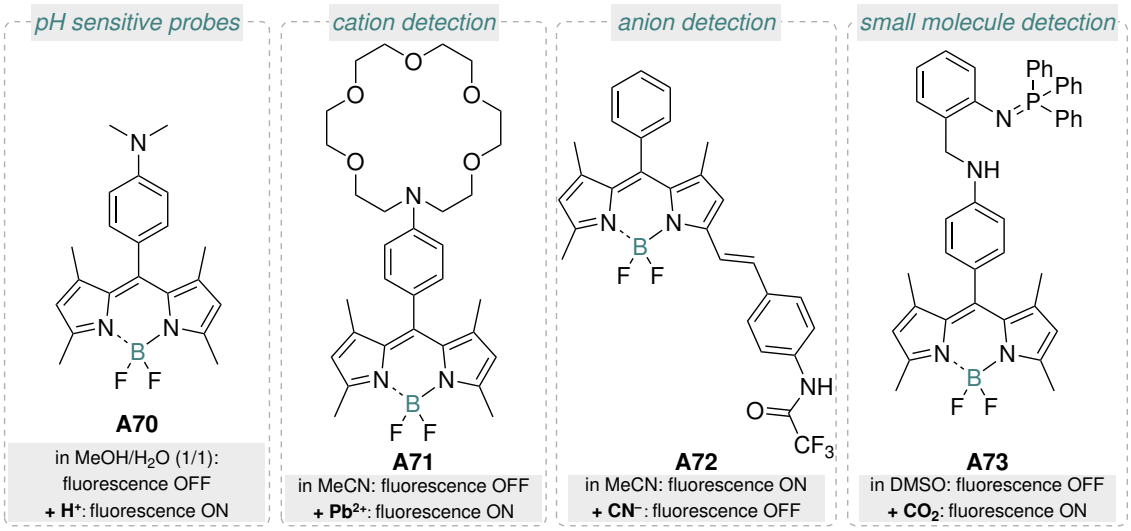


Figure 12: Examples of BODIPY fluorescence ON/OFF sensors.[94,102–106]

1.2.3. BODIPY dyes in photocatalysis

Owing to their pronounced photophysical properties, BODIPY dyes have also found applications as photocatalysts in EnT and photoredox catalysis, as well as in photodynamic therapy (PDT).[107,108] It is important to note, however, that specific modifications of the BODIPY core are required to accomplish significant photocatalytic activity, which can be categorized by two structural approaches (Figure 13).[107] The first strategy utilizes the heavy atom effect to enhance ISC from the first excited singlet state S_1 to the long-lived triplet excited state T_1 (Figure 13A). This is typically achieved through the incorporation of heavy halogens, *i.e.* iodine and bromine, as substituents on the BODIPY core (**A74**) or through coordination to transition metal complexes (**A75**).[109–111] The second approach involves BODIPY dyes whose struc-

ture allows for intramolecular charge separation by PET, resulting in the population of a highly polar excited state—typically referred to as a charge-transfer state (CT).[109] Common structural motifs that meet this criterion are donor-acceptor dyads, such as **A76**, and BODIPY dimers (**A77**, Figure 13B and C, respectively). Moreover, this approach enables the design of heavy-atom-free photocatalysts.[109]

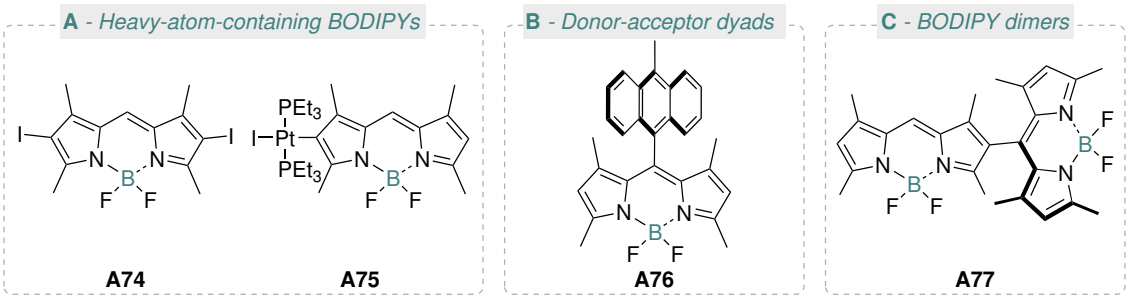
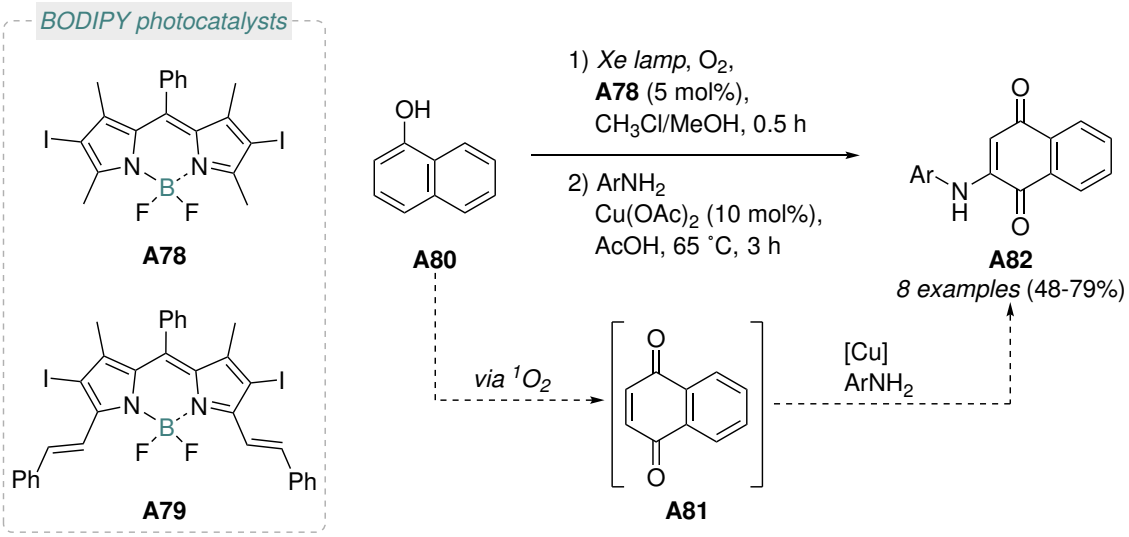


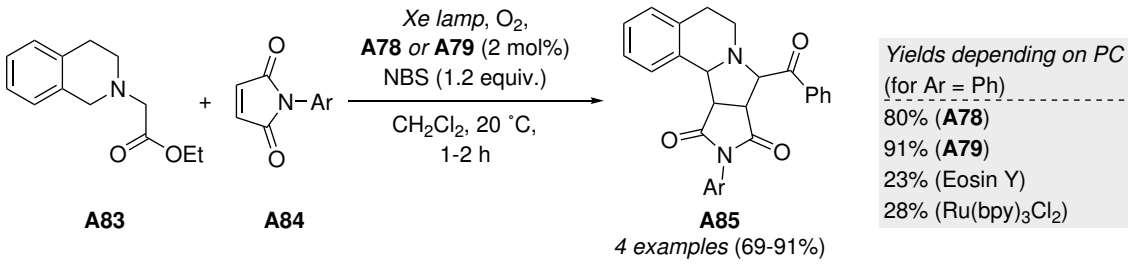
Figure 13: Examples of BODIPY-based photosensitizers.[109–111]

Applications of BODIPY dyes in molecular photocatalysis range from photoredox catalysis to EnT catalysis, mainly involving the photosensitization of singlet oxygen.[112] In this area of research, the group around Zhao has made considerable advancements in the field of BODIPY photocatalysis, mainly employing two iodine substituted BODIPY dyes **A78** and **A79** (Scheme 14). Using the halogenated BODIPY **A78** and a copper(II) salt, Huang *et al.* reported a one-pot photocatalysed procedure to access *N*-aryl-2-amino-1,4-naphthoquinones **A82** starting from 1-naphthols **A80**.[113] This reaction proceeds *via* the BODIPY-catalysed formation of $^1O_2$, resulting in the photooxygenation of **A80** to afford the corresponding 1,4-naphthoquinone **A81**, which undergoes C–H functionalization in the presence of aromatic amine and a copper(II) salt to yield **A82** in moderate to good yields (Scheme 14).[112,113]



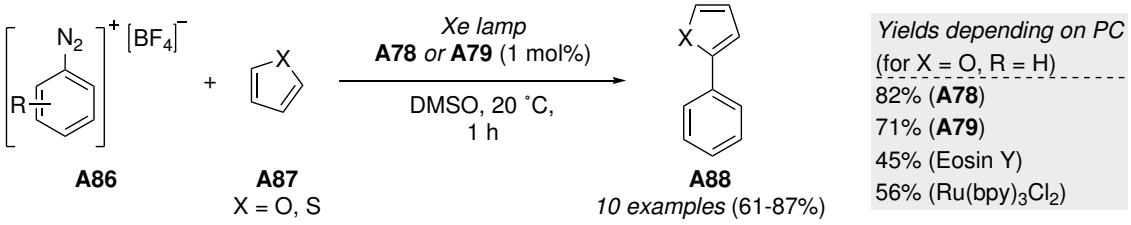
Scheme 14: Heavy-atom-substituted BODIPY photocatalysts (left) and use in one-pot photocatalysed synthesis of aminonaphthoquinones (right).[112–114]

Furthermore, Huang and Zhao reported the use of BODIPYs **A78** and **A79** as photocatalysts in the oxidation/[3+2] cycloaddition/aromatization sequence of tetrahydroisoquinolines **A83** with *N*-arly maleimides **A84** to form pyrrolo[2,1-*a*]isoquinolines **A85** in good yields (Scheme 15).[114] This transformation was first described by Zou *et al.* who proposed the photocatalytic formation of the superoxide radical anion as a key step in the mechanism using $Ru(bpy)_3Cl_2$ as a photocatalyst.[115] Interestingly, Huang and Zhao were able to demonstrate that photocatalysts **A78** and **A79** were more efficient under given conditions than the well-established photocatalysts Eosin Y or $Ru(bpy)_3Cl_2$.[114]



Scheme 15: Photocatalysed oxidation/[3+2] cycloaddition/aromatization to form isoquinolines **A85** and comparison of product yields with respect to photocatalysts (PC).[112,114]

Huang and Zhao were also able to show that BODIPYs **A78** and **A79** can be used as photocatalysts in the photoredox C–H arylation of heteroarenes **A87** with aryl diazonium salts **A86** *via* an oxidative quenching mechanism (Scheme 16).[114] The authors demonstrated a superior conversion towards the coupling products **A88** with BODIPY catalysts as compared to Eosin Y or $Ru(bpy)_3Cl_2$ under given conditions.[114]



Scheme 16: Photoredox catalysed arylation of furans and thiophenes.[112,114]

The overall high efficiency of BODIPY-dyes in photocatalytic reactions may be attributed to its often large molar absorption coefficient, making the viable choices for visible-light applications.[107,112] However, owing to the synthetic challenges involved in the multi-step synthesis of BODIPY photocatalysts, these compounds are still less commonly used and therefore arguably not as greatly studied in the context of photocatalysis as other commercially available dyes or metal complexes.[108,112,113]

1.2.4. Heavier analogues of BODIPY

Due to the success of BODIPY dyes across various research areas, a considerable interest in the synthesis and elucidation of photophysical properties of its heavier main group analogues ensued, particularly for dipyrrin complexes of the p-block elements.[84,116] Contrary to the synthesis of BODIPY dyes, which is often carried out in a one-pot approach (*vide supra*), the preparation of main group element dipyrrin complexes generally requires prior isolation of the free-base dipyrrin and careful choice of reaction conditions.[116] Mainly three different variations of main group element dipyrrin complexes can be found across literature: homoleptic and heteroleptic complexes, and dipyrrins featuring intramolecular chelating substituents.[116,117] Although all three variants have been reported for the group 13 complexes of aluminum, gallium and indium, this section will prioritize examples featuring the heavier triels gallium and indium over the well-established chemistry of aluminum dipyrrin complexes.[116]

Out of the p-block elements, triels represent the only literature-known examples where formation of homoleptic dipyrrin complexes has been observed (Figure 14).[116,118,119] Tris-homoleptic dipyrrin complexes bearing simple bidentate dipyrrins are typically prepared by treating the respective metal salt an excess of the ligand, thereby ensuring coordinative saturation of the metal centre.[116] In 2006, Thoi *et al.* reported the synthesis and spectroscopic characterization of the first homoleptic gallium (**A79Ga**) and indium (**A79In**) dipyrrin complexes.[118] The compounds were obtained in rather poor yields (approx. 20%) by stirring $Ga(NO_3)_3$ or $InCl_3$ with an excess of dipyrrin in MeCN.[118] UV/Vis analysis of the complexes showed two absorption maxima in the

visible-light region (400–500 nm), which the authors assigned to an excitonic coupling between two or more of the ligands bound to the metal centre.[118] Additionally, the authors computed the lowest-lying energy transitions to be ligand-centred ($\pi \rightarrow \pi^{\star}$). Both complexes were found to be weakly fluorescent (Φ < 10%).[118] The emission properties were further investigated using flash photolysis which revealed excited state lifetimes in the range of 45–80 μs for both compounds. Moreover, a decrease of lifetimes was observed in the presence of oxygen, thereby indicating quenching of the excited triplet states.[118] In 2018, Gutsche *et al*. were able to extend the scope of homoleptic gallium and indium dipyrrin complexes by employing various dipyrrin ligands and a post-functionalization strategy to afford a diverse set of homoleptic complexes *via* nucleophilic aromatic substitution with alcohols and thiocarbohydrates at the ligand backbone. Examples include the derivatives **A90Ga** and **A90In** shown in Figure 14.[119] Reported structural and spectroscopic features were similar to those shown by Thoi *et al*., with the complexes also displaying a split absorption profile.[116,118,119]

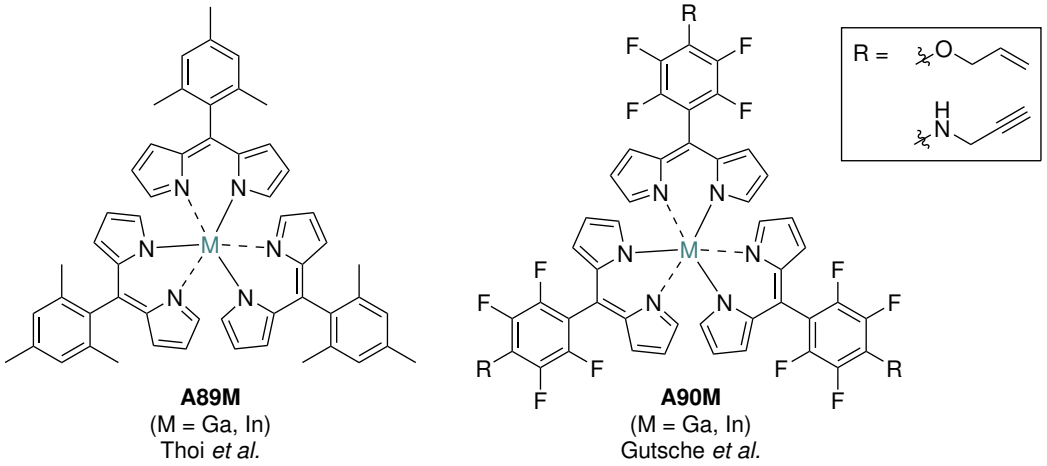


Figure 14: Literature-reported examples of homoleptic gallium and indium dipyrrin complexes.[118,119]

A considerably higher variety of heteroleptic triel dipyrrin complexes exists up to date (Figure 15).[116] A close analogue of the BODIPY core bearing a gallium dichloride unit was reported in 2019 by Wan *et al.* and termed “GADIPY” based on the analogy.[120] The authors were able to synthesize the GADIPY complex **A91** in 42% yield by treating a mixture of Ph_4PCl and $GaCl_3$ with an equimolar amount of lithium dipyrrinato salt in CH_2Cl_2.[120] The gallium complex exhibited comparable spectroscopic properties to the analogous BODIPY dye with a sharp absorption at λ_{abs} = 497 nm and strong emission at λ_{emi} = 505 nm (Φ = 0.91) in toluene.[120] More recently, Erlemeier *et al.* were able to synthesize a library of heteroleptic gallium (**A92Ga**, **A93Ga**) and

indium (**A92In**, **A93In**) dipyrrin complexes in two consecutive reports using a sterically shielded dipyrrin ligand.[121,122] The authors synthesized the alkyl-substituted complexes **A92M** by treating the free-base dipyrrin with the corresponding trialkyl triel reagent in toluene, whereas synthesis of the halide-substituted complexes **A93M** from the respective trihalide salts required prior ligand deprotonation with *n*-butyllithium.[121,122] All alkyl-substituted complexes **A92M** displayed comparable absorption properties with a main band at approximately 500 nm, but only the dimethyl-substituted gallium complex showed considerable fluorescence emission in solution (λ_{emi} = 539 nm, Φ = 0.51) and in solid state (λ_{emi} = 562 nm, Φ = 0.33). The other variants exhibited only low emission intensity (Φ < 0.02), suggesting significant quenching through the heavier central element and larger alkyl substituents.[121] In a consecutive 2025 report, the authors demonstrated that the dimethyl-substituted complexes **A92M** can be used as precursors to access dihalide complexes **A93M** and mixed-substituent complexes (monohalide, monomethyl) by treatment with HCl, bromine or iodine.[122] Compared to **A92M**, halide substituted dipyrrins **A93M** displayed a bathochromic shift in absorption and emission with considerably lower emission intensities in solution.[122]

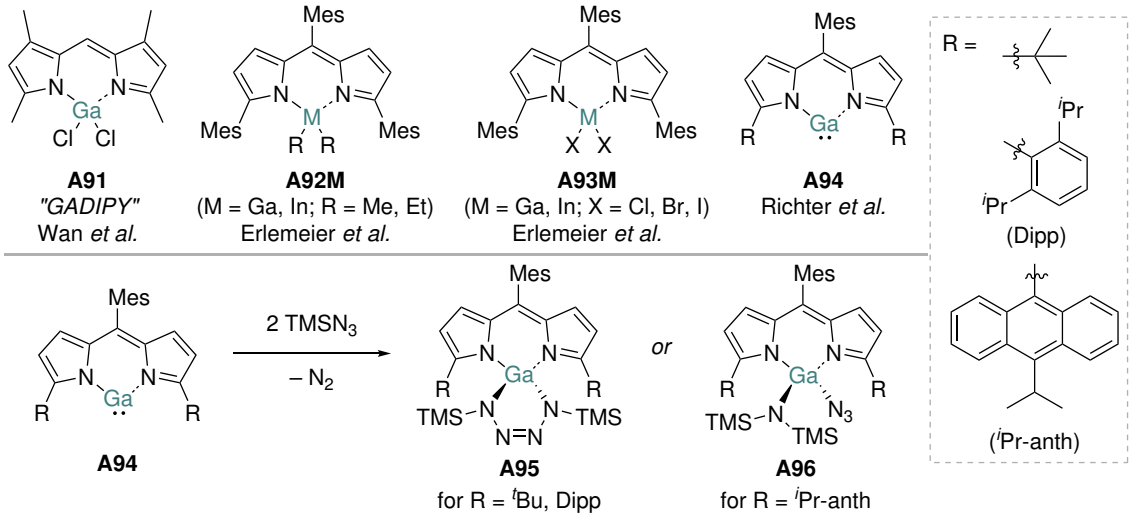
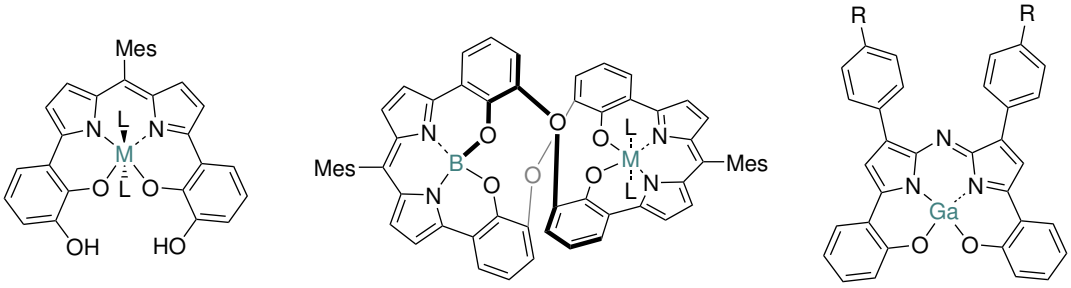


Figure 15: Literature-reported examples of heteroleptic gallium and indium dipyrrin complexes **A91**-**A92M** (top) and reactivity of low-valent gallium dipyrrin complexes (bottom).[120,121,123,124]

In two recent reports by Richter *et al.* diiodide-substituted GADIPY complexes were reduced using to the corresponding Ga(I) complexes **A94**.[123,124] For R = ^{t}Bu, reduction was achieved using K/KI (2.10 equiv.) in benzene at 60 °C for 7 days, whereas KC_8 (2.05 equiv.) was used for the reduction of complexes with R = Dipp or ^{i}Pr-anth in benzene at 50 °C over 3 days.[123,124] The low-valent gallium dipyrrins **A94** were observed to react with trimethylsilyl azide, affording different products depending on

the dipyrrin ligand. While ligands with less bulky substituents, *i.e.* R = ^{t}Bu and Dipp, resulted in the formation of a five-membered tetrazagallole **A95**, the bulkier ^{i}Pr-anth substituent gave acyclic product **A96**.[123,124]

Since the initial report by Kim *et al.* on the synthetis of tetracoordinate "N_2O_2" BODIPY dyes, the corresponding tetradentate dipyrrins bearing 2-phenol substituents in the α-positions have emerged as popular ligand choices for the stabilization of metal and main group centres utilizing the additional chelating effect of the bisphenolate moiety (Figure 16).[116,125] N_2O_2-dipyrrins have been used as ligands for several main group elements, including gallium and indium (Figure 16).[126] In 2019, Sumiyoshi *et al.* reported the first synthesis and spectroscopic characterization of well-defined gallium and indium bisphenolate dipyrrin complexes **A97M**.[126] The complexes were obtained with additional coordination of water or pyridine (pyr) in the apical positions of the central elements. Moreover, all reported triel N_2O_2-dipyrrins exhibited absorption in the visible-light region (λ_{abs} = 609–629 nm) with fluorescence emissions in the range of λ_{emi} = 636–652 nm and relatively short fluorescence lifetimes below 10 ns.[126] Notably, the additional hydroxide groups on the ligand scaffold allowed the authors to use complexes **A98M** as efficient fluorescence-based sensors for alkaline earth metal ions.[126] Using an expanded variant of the bisphenolate dipyrrin ligand featuring two tetradentate binding pockets Saikawa *et al.* reported the synthesis of heterodinuclear "N_4O_6" dipyrrin complexes **A98M**.[127] Similar to **A97M**, the complexes featured appical coordination of two methanol units to the Ga and In centres. While the compounds exhibited absorption in the visible-light region ($\lambda_{abs} \approx 614$ nm), the emission was virtually quenched ($\Phi < 0.01$).[127]



A97M
(M = Ga, In; L = H_2O, pyr)
Sumiyoshi *et al.*

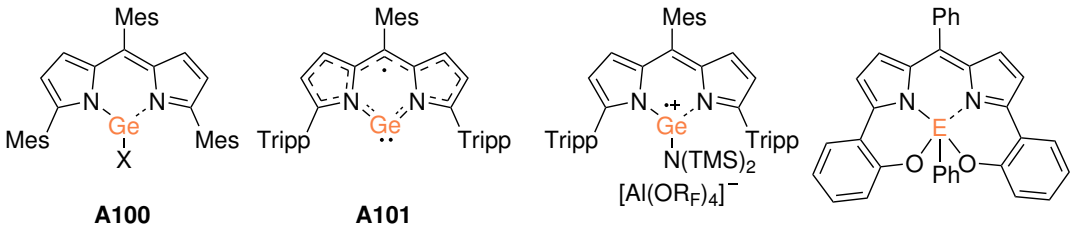
A98M
(M = Ga, In; L = MeOH)
Saikawa *et al.*

A99
R = H, Br, OMe, NMe_2
Godard *et al.*

Figure 16: Literature-reported examples of gallium and indium N_2O_2-dipyrrin complexes.[126–128]

Recently, Godard *et al.* reported a series of gallium N_2O_2-dipyrrins **A99** containing an bridging nitrogen in the ligand backbone. This modification of the ligand resulted in a significant bathochromic shift of the absorption (λ_{abs} = 609–629 nm) and emission (λ_{emi} = 782–802 nm) profile, extending into the near-infrared (NIR) region.[128]

Compared to triels, group 14 elements are considerably less represented in the field of dipyrrin chemistry. To date, mainly germanium dipyrrin complexes have been reported for group 14 elements in literature, with silicon and lead making only few appearances (Figure 17).[116] The group of Nagendran has made significant progress in the field of germanium dipyrrin chemistry, mainly using the same (or slightly modified versions of) mesityl-substituted ligand scaffold as employed for triel compounds **A92M** and **A93M**.[129–133] In 2014, Jha *et al.* reported the synthesis of a water-stable germylene dipyrrin **A100** (with X = Cl).[129] Halide exchange with an excess of CsF allowed the authors to isolate the fluoride-substituted analogue. Lastly, investigation of the spectroscopic properties of the two germylene variations revealed absorptions in the visible-light region (λ_{abs} = 517–524 nm), comparable to the findings reported for the analogous triel complexes **A93M**.[122,129] The compounds exhibited only weak fluorescence emission (λ_{emi} = 538–555 nm, Φ < 0.01) with short fluorescence lifetimes below 2 ns.[129] Recently, Dai *et al.* expanded the scope of available oxidation states in germanium dipyrrins by reporting the isolation of a Ge(I)-masked dipyrrin-based radical **A101** and a Ge(III)-centred radical cation **A102** using a sterically shielded ligand with Tripp-substituents (2,4,6-tri*iso*propylphenyl) in the α-positions.[134] The authors supported their findings with X-ray crystallography, EPR spectroscopy and computational studies.[134] The analogous Sn(I) compound to **A101** was later reported by Bao *et al.* further complementing the studies on heavy tetrel dipyrrins.[135]



A100
(X = Cl, F)
Jha *et al.*

A101
Dai *et al.*
(Tripp = 2,4,6-triisopropylphenyl)

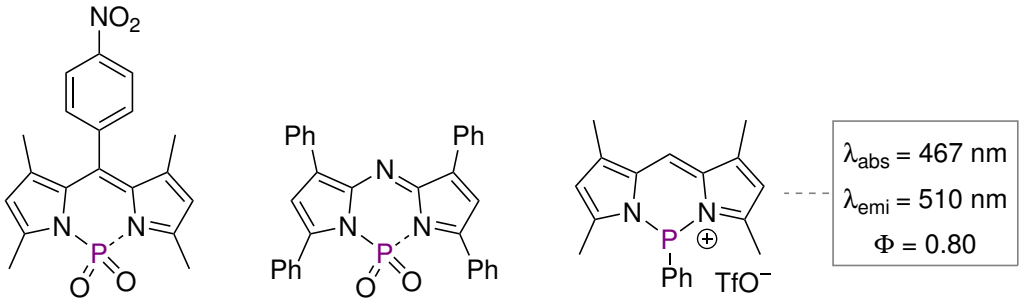
A102
Dai *et al.*

A103E
E = Si, Ge, Sn
Yamamura *et al.*

Figure 17: Literature-reported examples of group 14 dipyrrin complexes.[129,134,136]

Finally, Yamamura *et al.* demonstrated the use of N_2O_2-dipyrrins as suitable ligands for the stabilization of high-valent group 14 elements **A103E** (with E = Si, Ge, Sn).[136] These complexes featured structural geometries closely resembling a trigonal bipyramidal arrangement, in which the contribution of square-pyramidal character becomes more apparent with heavier central atoms. Additionally the compounds exhibited a bathochromic shift in absorption from Si (λ_{abs} = 612 nm) to Sn (λ_{abs} = 612 nm), as well as fluorescence emission in the upper visible-light region (λ_{emi} = 650–675 nm). Interestingly, the heavier element complexes **A103Sn** and **A103Ge** displayed stronger emission intensities (Φ = 0.22 for Sn, Φ = 0.12 for Ge) than the silicon complex **A103Si** (Φ < 0.03).[136]

Until very recently, dipyrrin complexes of group 15 elements (pnictogens) were severely rare and exclusively limited to examples with phosphorous as the central element (Figure 18).[120,137] In 2015, Jiang *et al.* reported the synthesis and spectroscopic characterization of "PODIPY" compound **A104** and "aza-PODIPY" **A105**.[137] The authors were able to prepare these compounds by treating the corresponding free-base dipyrrins with an excess of $POCl_3$ and triethylamine as base. The phosphorous-based dyes were observed to be water-soluble and exhibited visible-light absorption (λ_{abs} = 510 nm for **A104**, λ_{abs} = 625 nm for **A105**) in aqueous solution.[137] Compound **A104** displayed weak emission at λ_{emi} = 524 nm (Φ = 0.17), whereas aza-PODIPY showed a bathochromic shift with λ_{emi} = 661 nm (Φ = 0.08).[137] In 2019, Wan *et al.* reported the synthesis and spectroscopic investigations of cationic phosphorous dipyrrin **A106** "PHODIPY".[120] The authors synthesized **A106** starting from the corresponding lithium dipyrrinato salt, which was treated with $PhPCl_2$ (1.0 equiv.) and trimethylsilyl triflate (5.0 equiv.). However, they were only able to obtain **A106** containing approximately 19% of an unknown impurity.[120] Analysis of the crude compound revealed a main absorption band at λ_{abs} = 467 nm and an emission at λ_{emi} = 510 nm in CH_2Cl_2, affording an unusually large Stokes shift as compared to typical BODIPY dyes.[91,120]



A104
Jiang *et al.*

A105
Jiang *et al.*

A106 (*not isolated*)
Wan *et al.*

Figure 18: Literature-reported examples of phosphorous dipyrrin complexes.[120,137]

Only recently Liu *et al.* were able to synthesize antimony and bismuth dichloride complexes using a sterically-shielded dipyrrin ligand with Tripp-substituents in the α positions (Figure 19).[138] The authors employed the potassium dipyrrinato salt which upon treatment with stoichiometric amounts of pnictogen chloride salts in toluene gave the corresponding dipyrrin complexes of antimony (**A107Sb**) and bismuth (**A107Bi**) in good yields.[138] Both complexes exhibited a sharp absorption (λ_{abs} = 514 nm for **107Sb**, λ_{abs} = 513 nm for **107Bi**) and weak emission at λ_{emi} = 547 nm (Φ = 0.07) for **107Sb**, which was further red-shifted for the bismuth analogue (λ_{emi} = 568 nm, Φ < 0.01). The scope was later expanded to the arsenic complex **A107As** following the same procedure.[135] The arsenic complex displayed similar spectroscopic features as **107Sb**, albeit featuring a slight hypsochromic shift in absorption and emission.[135] Liu *et al.* further demonstrated that **A107Sb** can be reduced using sodium metal (2 equiv.) in toluene, yielding the monomeric stibinidine **A108**. Furthermore, this complex was found to undergo oxidative addition with diphenyldichalcogenides, such as diphenyl disulfide, affording Sb(III) complex **A109**.[138] Agou *et al.* recently reported two consecutive studies on N_2O_2-dipyrrin complexes of antimony and bismuth (Figure 19).

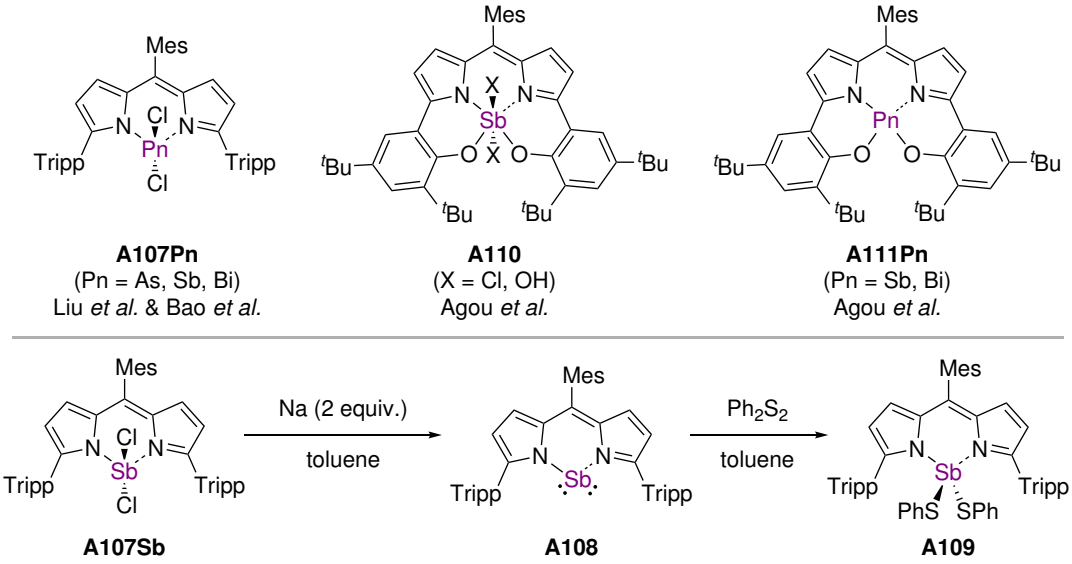


Figure 19: Recent literature-reported examples of pnictogen dipyrrin complexes.[135,138–140]

In their 2024 report, the authors described a rather unconventional synthesis and the photophysical properties of Sb(V) dipyrrin complexes **A110**.[139] The antimony dichloride complex (X = Cl) was obtained in moderate yield by treating the corresponding free-base dipyrrin with an excess of $SbCl_3$ in pyridine under oxygen atmosphere and white LED irradiation. Heating of the dichloride complex in a mixture of water and pyridine afforded the conversion to the dihydroxide (X = OH) in good yield.[139]

Compared to the free ligand, the Sb(V) dipyrrin complexes displayed a pronounced bathochromic shift in absorption (λ_{abs} = 627–643 nm). Interestingly, the dihydroxide complex exhibited intense fluorescence emission at λ_{emi} = 657 nm, whereas no emission was observed for the dichloride complex.[139] In 2025, Agou *et al.* used the same ligand scaffold to synthesize antimony (**A111Sb**) and bismuth (**A111Bi**) complexes, this time *via* deprotonation of the ligand with NaH (5 equiv.), followed by subsequent treatment with $SbCl_3$ (1.2 equiv.) or $BiBr_3$ (1.2 equiv.) in THF.[140] The complexes **A111Sb** and **A111Bi** exhibited absorption in acetone at λ_{abs} = 678 nm and λ_{abs} = 689 nm, respectively. However, only **A111Sb** exhibited weak emission at λ_{emi} = 724 nm ($\Phi \approx 0.01$).[140]

1.3. General aims

At the start of this doctoral work the field of heavy pnictogen dipyrrin complexes was virtually non-existent with only the previously described phosphorous compounds known at that time (Figure 18). However, the large Stokes shifts reported for phosphorous dipyrrins raised the question of whether this effect originates from the pnictogen centre or other unknown factors. Guided by this question, the first main milestone of this work was to develop a method to access the first heavy pnictogen analogues of BODIPY with antimony “SBDIPY” and bismuth “BIDIPY” as the central elements (Figure 20, *stage 1*). As outlined in the introductory section, the multifaceted field of dipyrrin ligands offers many possible ligand modifications that may allow the stabilization of heavier central elements.

Once isolation of heavy pnictogen dipyrrins (PnDIPY) is achieved, a thorough spectroscopic study of SBDIPY and BIDIPY complexes is required to obtain insight into the stability and photophysical properties of these compounds (Figure 20, *stage 2*). Moreover, in order to understand the influence of the heavy central atom, photoluminescence (PL) lifetimes need to be determined. At this stage, computational chemistry should be employed to provide additional support for experimental findings.

The heavy atom effect was identified as a key component in photocatalysts with BODIPY-based catalysts often featuring the incorporation of heavy atoms onto the ligand scaffold. In the case of PnDIPY complexes, however, the heavy atom is directly integrated as the central element of the chromophore, making these compounds interesting candidates for photocatalytic applications as this could enable the population of long-lived excited states. In this regard, combining the pronounced redox-properties of heavier pnictogens with the strong chromophore characteristics of dipyrrins may

enable applications of PnDIPY complexes in both photoredox catalysis and EnT photocatalysis (Figure 20, *stage 3*). Finally, heteroleptic PnDIPY complexes offer several opportunities for post-synthetic modifications, including the exchange of anionic ligands X as well as oxidation and reduction of the central element, which could enable additional variety in their chemical and spectroscopic properties.

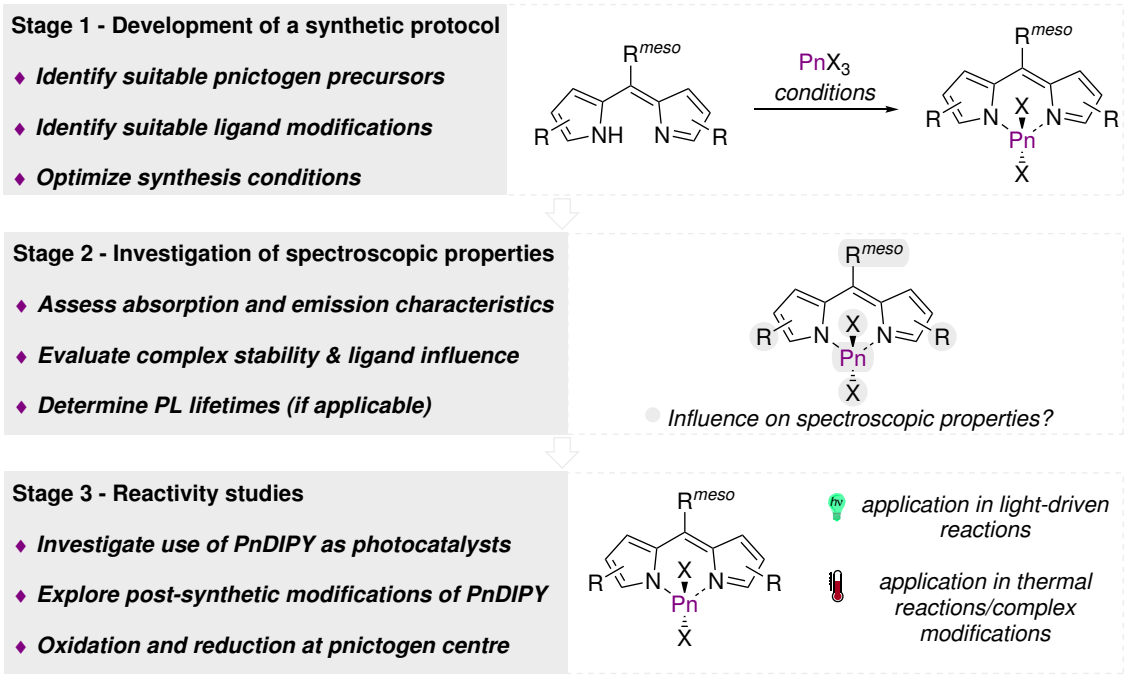


Figure 20: Conceptional guide to the goals within this thesis.

2. The first antimony and bismuth analogues of BODIPY

The data presented in the following chapter has been partially published in: A. Korzun, S. Crespi, C. Golz, A. Bismuto, *Chem. Sci.* **2023**, *14*, 6579-6584.[141] Theoretical studies were performed by Dr. Stefano Crespi and are included and indicated (†) in this thesis to complement the experimental work. All X-ray solid-state structures shown in this chapter were measured and refined by Dr. Christopher Golz or Dr. Gregor Schnakenburg if not otherwise noted.

2.1. Project aims

The dipyrrin scaffold is a well-established ligand for various transition metal ions and main group elements with boron complexes (BODIPY) being arguably the most prominent examples.[84] However, at the beginning of the project, dipyrrins have not yet been employed as ligands for heavier pnictogens. Encouraged by the gap in the literature, the aim of this project was to synthesize the first examples of heavy pnictogen dipyrrin complexes bearing antimony and bismuth as the central atoms ("SBDIPY" and "BIDIPY") in analogy to the widely popularized BODIPY chromophores (Figure 21). Beyond that, the goal was to study the influence of the *meso*-substituent in pnictogen dipyrrins and investigate the spectroscopic properties of these novel compounds. Finally, post-synthetic modifications of the halido-ligands were considered as options to increase structural variety.

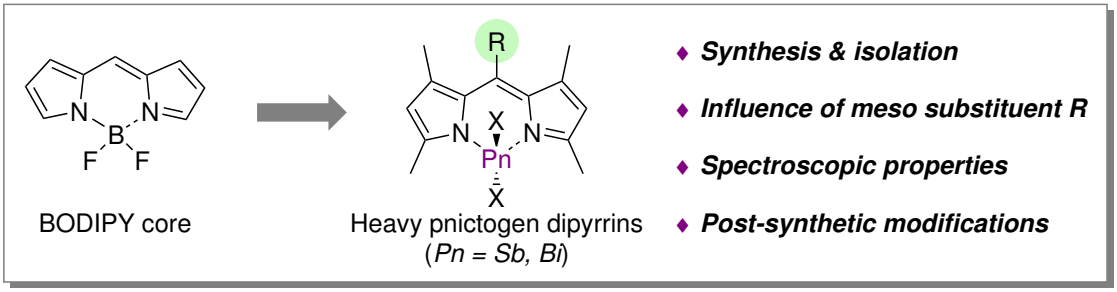
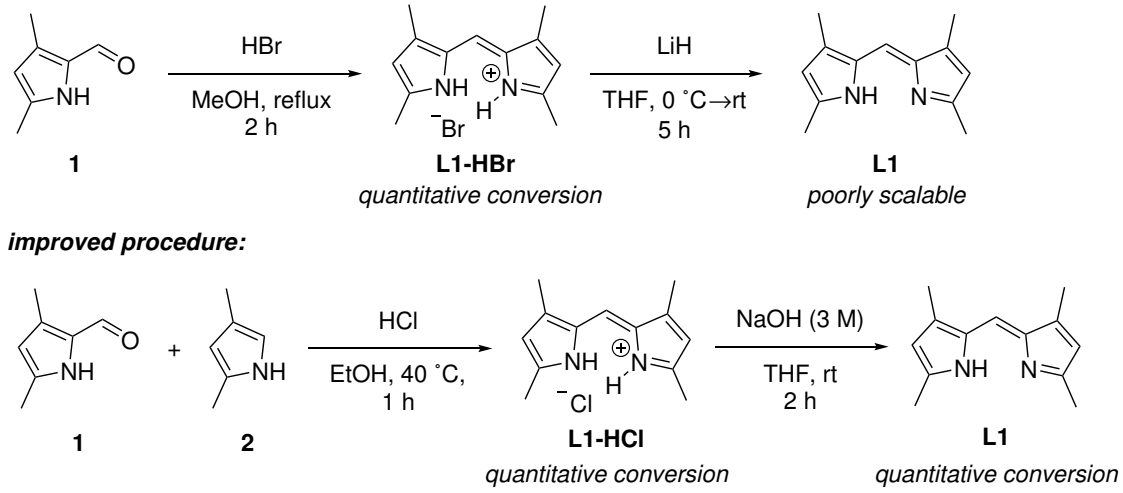


Figure 21: Summary of objectives within this chapter with the main focus lying on synthesis and characterization of novel pnictogen dipyrrin (PnDIPY) complexes.

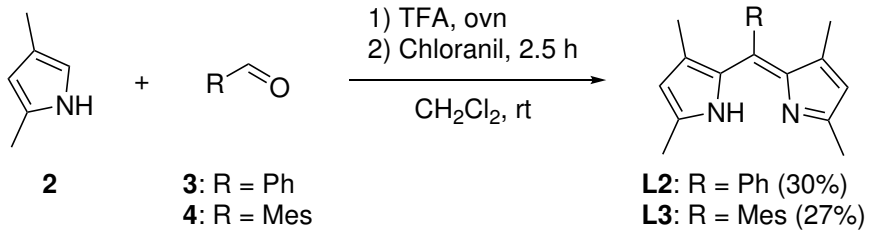
2.2. Ligand synthesis

The tetramethyl-substituted dipyrromethene **L1** was chosen as a model ligand for our study as it is already a well-established ligand for boron and a close derivative of the "BODIPY core".[91,142] The model dipyrrin **L1** was initially prepared *via* the HBr-salt **L1-HBr**, starting from pyrrole-2-carbaldehyde **1** (Scheme 17, top).[143,144] However, the deprotonation step involving LiH as a base was poorly scalable and therefore further optimized. A more convenient method was identified, starting from the HCl-salt **L1-HCl**, which was accessed by condensation of aldehyde **1** with 2,4-dimethylpyrrole (**2**) in the presence of hydrochloric acid (Scheme 17, bottom).[145] The resulting HCl-salt was then quantitatively converted to **L1** by treatment with aqueous NaOH solution (3 M). In this way, it was possible to improve the synthesis of **L1** to several grams of product in excellent yield.



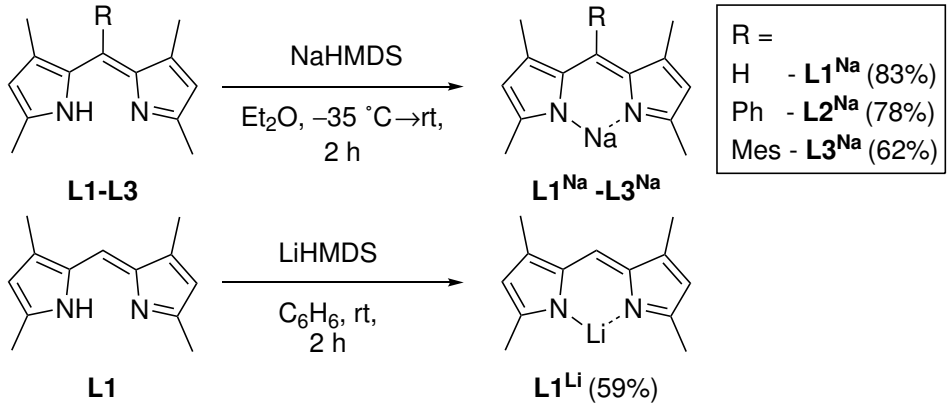
Scheme 17: Synthesis of dipyrrin ligand **L1**. First procedure (top) and improved approach (bottom).

In order to study the influence of the *meso*-position of the model dipyrrin, two derivatives of the ligand, **L2** and **L3**, were prepared *via* acid-catalyzed condensation of **2** with the respective aldehydes, followed by oxidation with chloranil in dichloromethane (Scheme 18). Compared to the unsubstituted ligand **L1**, the synthesis of *meso*-substituted ligands proceeded less selectively and involved laborious purification with overall poor yields, thus restricting the synthesis to small scale.



Scheme 18: Synthesis of *meso*-substituted dipyrrin ligands **L2** and **L3**.

Lastly, ligands **L1**-**L3** were converted to alkali salts using LiHMDS or NaHMDS in good to moderate yields (Scheme 19).[146] The alkali salts represent viable precursors for the synthesis of dipyrrin complexes as potential side-reactivity through additional base can be avoided.

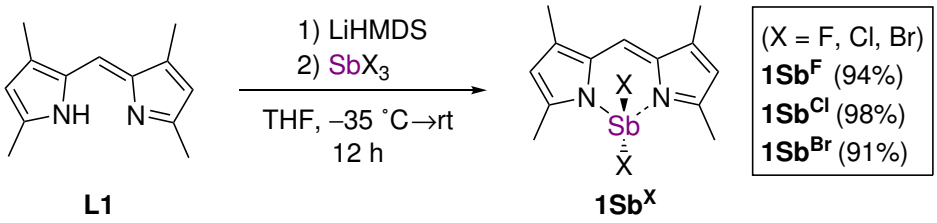


Scheme 19: Synthesis of sodium and lithium dipyrrinato salts of ligands **L1**-**L3**.

2.3. Synthesis of antimony dipyrrin complexes (SBDIPY)

The study was conducted by first prioritizing the synthesis of antimony dipyrrins (SBDIPYs) with model ligand **L1**. Antimony dipyrrins $\mathbf{1Sb^X}$ were successfully prepared by deprotonation of **L1** using LiHMDS as the base, followed by addition to a pre-cooled solution of antimony trihalide in THF (Scheme 20). Using LiHMDS as a base, a facile deprotonation of **L1** was observed on a milligram-scale, showing full conversion within few minutes (*circa* 10 min) by ^{1}H NMR spectroscopy in THF-d_8. Complexation to form SBDIPYs $\mathbf{1Sb^X}$ (X = F, Cl or Br) also proceeded smoothly, albeit requiring careful matching of reagent equivalents and maintaining strictly air- and moisture-free conditions. Using optimized synthetic procedures, complexes $\mathbf{1Sb^X}$ were obtained in excellent yields (Scheme 20). In the case of $\mathbf{1Sb^F}$, the best results were obtained when performing the reaction with a slight excess of base (1.10 equiv.) and equimolar amounts of **L1** and sublimed SbF_3. The reaction mixture was kept at −35 °C for 11 h

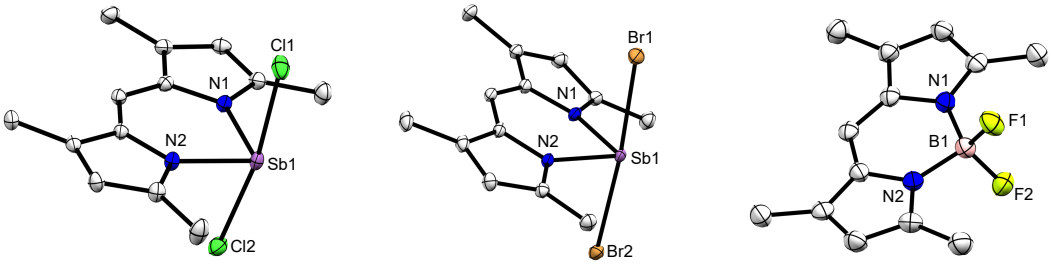
upon warming to room temperature for 1 h with a few drops of *n*-hexane to promote the formation of spectroscopically clean, micro-crystalline **1Sb^{F}**.



L1 **1Sb^{X}**

Scheme 20: Synthesis of SBDIPY complexes **1Sb^{X}**.

Single crystals of SBDIPYs **1Sb^{X}** suitable for X-ray analysis were grown from saturated solutions in THF/*n*-hexane mixtures. The X-ray solid-state structures of **1Sb^{Cl}** and **1Sb^{Br}** are in stark contrast to the analogous BODIPY **1B^{F}** as the lone pair on the pnictogen atom creates an entirely different coordination environment with the Sb-centers adopting a seesaw geometry (Figure 22). Furthermore, the structures of **1Sb^{Cl}** and **1Sb^{Br}** feature much more acute *N*,*N*-binding angles as compared to BODIPY **1B^{F}**, resulting in distorted six-membered rings in combination of Sb with the dipyrrin moiety (for **1Sb^{Cl}** N(1)−Sb−N(2) = 88.2(1)°, whereas **1B^{F}** N(1)−B−N(2) = 107.1°).[147] For both, boron and antimony complexes, the central atom is in a near planar conformation with **L1**. However, in the case of the antimony complexes the halido ligands occupy the axial positions of the coordination polyhedra with a small distortion away from the ideal value of 180° (Figure 22a & 22b).

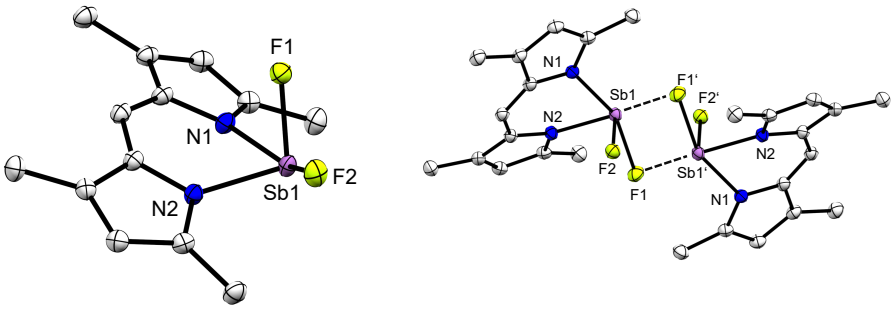


(a) 1Sb^{Cl} **(b) 1Sb^{Br}** **(c) 1B^{F}**

Figure 22: X-ray solid-state structures of **L1** dipyrrin complexes (a) **1Sb^{Cl}**, (b) **1Sb^{Br}** and (c) **1B^{F}** (*CCDC identifier WEPGUU*).[147] Hydrogen atoms were omitted for clarity and thermal ellipsoids were set to a 50% probability level.

SBDIPY **1Sb^{F}** represents the first direct group 15 analogue of BODIPY, bearing two fluoride handles on the central atom. Interestingly, this compound showed strong deviation from the seesaw geometry that was observed in the case of bromide- or chloride-substituted SBDIPYs as the X-ray solid-state structure of **1Sb^{F}** featured a highly distorted pseudo-octahedral geometry around the Sb-center. This geometrical perturbation was evidently caused by the strong Sb−F interaction, constituting a

dimeric arrangement of **1Sb^{F}** with two bridging fluorines (Figure 23). In fact, the dimer displayed a remarkably short Sb1−F1' distance of 2.862(2) Å and notably different Sb−N bonds (Sb1−N1 = 2.098(1) Å, Sb1−N2 = 2.249(1) Å) with the latter potentially being a result of a stronger *trans*-influence of the fluorido ligand. Compared to **1Sb^{Br}** and **1Sb^{Cl}**, the antimony centre in **1Sb^{F}** is significantly shifted out of the ligand plane, which is likely another consequence of the strong Sb−F interaction. To gain additional insight whether the distorted geometry observed in the solid-state structure was solely a consequence of crystal packing effects, the optimized geometries of **1Sb^{Cl}** and **1Sb^{F}** were computed in gas-phase, as well as with implicit solvation models, at the r^{2}SCAN-3c level of theory.[148],† For **1Sb^{Cl}**, an axial arrangement of halido ligands was favoured by a Gibbs free-energy of 10 kcal/mol over a distorted geometry. In contrast, only a 3 kcal/mol difference was obtained for **1Sb^{F}**, suggesting that the conformation seen in the X-ray solid-state structure may not arise exclusively from crystal-packing, but could also be influenced by an increased *trans*-influence.



(a) 1Sb^{F} **(b) 1Sb^{F}** dimer view

Figure 23: X-ray solid-state structure of (a) **1Sb^{F}** and (b) dimeric structure of **1Sb^{F}** (expanded short contacts). Hydrogen atoms were omitted for clarity and thermal ellipsoids were set to a 50% probability level.

Variable-temperature $^{19}F\{^{1}H\}$ NMR spectroscopy was used to elucidate the solution behaviour of **1Sb^{F}** (Figure 24). At 20 °C, a single sharp signal at −77.1 ppm was observed, indicating a fast exchange regime in which the fluoride substituents of **1Sb^{F}** interconvert rapidly as the equilibrium favours the monomer state. Decreasing the temperature caused the signal to broaden until a splitting into two signals at −66.5 ppm and −86.8 ppm occured at −40 °C, which signifies the presence of two non-equivalent fluorines. This observation hints toward a shift of the equilibrium toward a dimer structure or a higher aggregate conformation at lower temperature as the axial and bridging fluorides exhibit a different chemical environment upon aggregation. However, integration of the two signals at −80 °C revealed a ratio of circa 1:3, as opposed to the expected ratio of 1:1.

This discrepancy could originate from differences in relaxation times of both fluorine substituents.

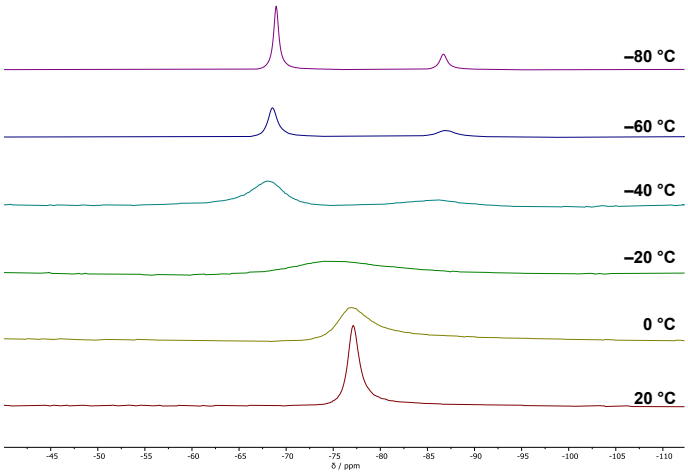
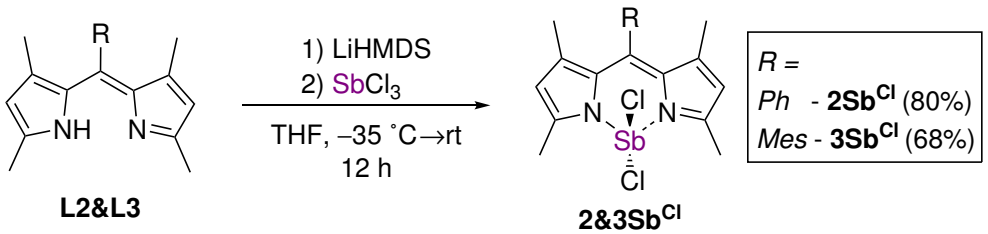


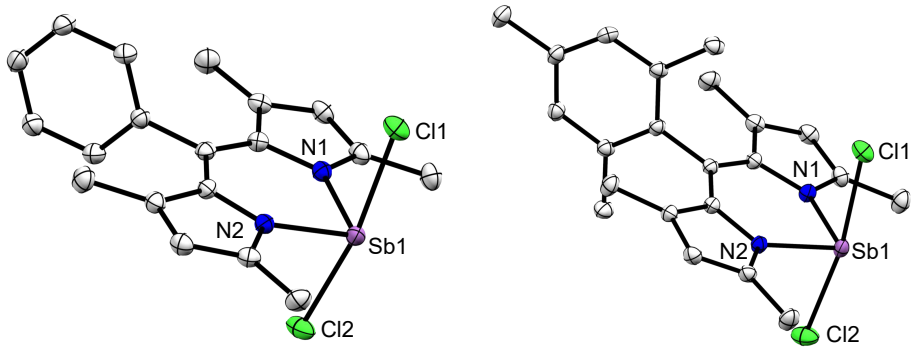
Figure 24: Stacked variable-temperature $^{19}F\{^{1}H\}$ NMR (377 MHz) spectra of **1Sb^{F}** in CD_2Cl_2. Measurement temperatures are shown on the right side.

In order to study the effect of the *meso*-position of the dipyrrin ligand on the chromophore properties, SBDIPY complexes **2Sb^{Cl}** and **3Sb^{Cl}** were synthesized starting from the respective ligands **L2** and **L3**. Fortunately, the previously employed synthetic protocol for the synthesis of SBDIPYs **1Sb^{X}** was also applicable for the *meso*-substituted ligands, giving chlorido complexes **2Sb^{Cl}** and **3Sb^{Cl}** in good yields (Scheme 21).



Scheme 21: Synthesis of SBDIPY complexes **2Sb^{Cl}** and **3Sb^{Cl}**.

Single crystals of these two SBDIPY complexes were grown from a mixture of THF and *n*-hexane and analyzed by X-ray diffraction (Figure 25). Key structural parameters of both complexes are very similar to those of **1Sb^{Cl}**, hinting at a minor influence of the chosen *meso*-substiteunts on the steric and electronic properties of the ligand.



(a) 2Sb^{Cl} **(b) 3Sb^{Cl}**

Figure 25: X-ray solid-state structures of (a) **2Sb^{Cl}** and (b) **3Sb^{Cl}**. Hydrogen atoms were omitted for clarity and thermal ellipsoids were set to a 50% probability level.

For comparison, a selection of relevant structural parameters obtained from X-ray solid-state structures of SBDIPY complexes are provided in Table 1.

Table 1: Selected bond lengths and angles for SBDIPY complexes. The mean plane (MPLN) is defined by the five atoms included in the binding pocket of the dipyrrin ligands.

	X1−Sb−X2 (°)	N1−Sb−N2 (°)	avg. Sb−X (Å)	Sb−N1 (Å)	Sb−N2 (Å)	MPLN··Sb (Å)
1Sb^{Br}	175.2(1)	86.4(1)	2.733(1)	2.085(2)	2.082(2)	0.410(3)
1Sb^{Cl}	170.7(1)	88.2(1)	2.560(1)	2.086(1)	2.079(1)	0.053(2)
1Sb^{F}	80.4(1)	81.1(1)	1.968(2)	2.248(2)	2.097(2)	0.759(2)
2Sb^{Cl}	170.1(1)	88.0(1)	2.552(1)	2.059(1)	2.063(1)	0.102(2)
3Sb^{Cl}	171.1(1)	87.4(1)	2.556(1)	2.063(1)	2.055(1)	0.261(2)

2.3.1. Complex stability

As previously noted, the synthesis of SBDIPY chromophores required strictly air- and moisture-free conditions to avoid formation of various possible decomposition products, involving the re-protonation of ligand **L1** evident from broad, downfield shifted N−H signals in the ^{1}H NMR spectrum. Especially for the synthesis of SBDIPY **1Sb^{F}**, several attempts were required to avoid minor amounts of complex decomposition products. To test the air-stability of isolated SBDIPYs **1Sb^{Cl}** and **1Sb^{F}** the compounds were exposed to air, both in solid-state and solution. Interestingly, ^{1}H NMR spectroscopy of **1Sb^{Cl}** and **1Sb^{Br}** showed only minor amounts of decomposition products upon 24 h exposure as a solid to air whereas **1Sb^{F}** was fully decomposed to a new product with a single ^{19}F NMR resonance at −70.8 ppm. The same result was also obtained upon exposure of a dichloromethane solution of **1Sb^{F}**, whereas solutions of

1Sb^{Cl} and **1Sb^{Br}** showed increased amounts of decomposition product under air as compared to the solid samples. In all cases, the formation of a single decomposition product with a broad singlet around 13.5 ppm was seen by ^{1}H NMR spectroscopy, indicating the presence of a cationic 1*H*-pyrrolium salt akin to **L1-HX** (with X = Br or Cl). For **1Sb^{F}** pronounced changes in the ^{19}F NMR spectrum were also noted after 24 h at room temperature in CD_2Cl_2 solution with two new signals present at −72.2 ppm and −75.1 ppm (Figure 26). As the respective ^{1}H NMR spectrum showed only small amounts (circa 20%) of decomposition after 24 h, changes in the ^{19}F NMR data may stem from aggregation dynamics as observed in the solid-state structure of **1Sb^{F}**.

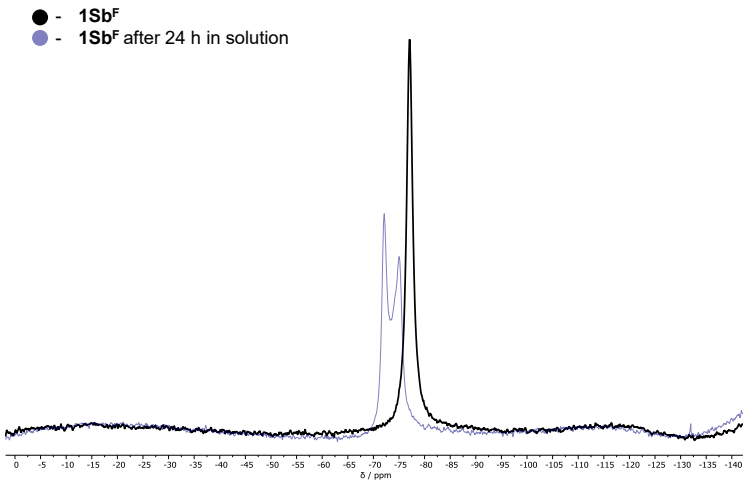


Figure 26: Superimposed ^{19}F NMR spectra of **1Sb^{F}** in CD_2Cl_2 (377 MHz), immediate measurement (black) and after 24 h in CD_2Cl_2 at room temperature (light blue).

More information on complex stabilities is provided in section 2.3.4.

2.3.2. Deviation from optimized conditions

In order to gain additional insight into the intricacies of SBDIPY synthesis, several attempts using procedures deviating from the above described “optimized” conditions were carried out. As a result, several surprising outcomes were obtained which will be discussed in the following section. In the case of $SbCl_3$ or $SbBr_3$ as the antimony precursors, no side-reactivity was observed by ^{1}H NMR spectroscopy with a slight excess of LiHMDS (1.10 equiv.) and Sb-halide (1.15 equiv.), yielding respective SBDIPY complexes as crystalline red solids in THF at room temperature. To assess the possibility of coordinating multiple dipyrrin ligands to antimony, the hitherto successful protocol was adjusted to 2.05 equivalents of **L1** and 2.10 equivalents of LiHMDS, as examples with other heavy main group elements, such as indium or tin, have been

previously reported.[149,150] In this way *in situ* generated **L1^{Li}** was allowed to react with 1.00 equivalent of antimony chloride, resulting in an immediate colour change from light orange to dark red. Unlike for **1Sb^{Cl}**, however, no downfield shift of the aromatic signals was observed in the crude ^{1}H NMR spectrum of the reaction mixture. Instead, the outcome was rather unselective with the main signals showing very close resemblance to **L1^{Li}**. Due to the presence of a fine coloured precipitate, it is likely that a part of the dipyrrinato salt reacted to form **1Sb^{Cl}** or other insoluble oligomers, while unreacted dipyrrinato salt **L1^{Li}** remained in solution, among non-definable impurities (Figure 27).

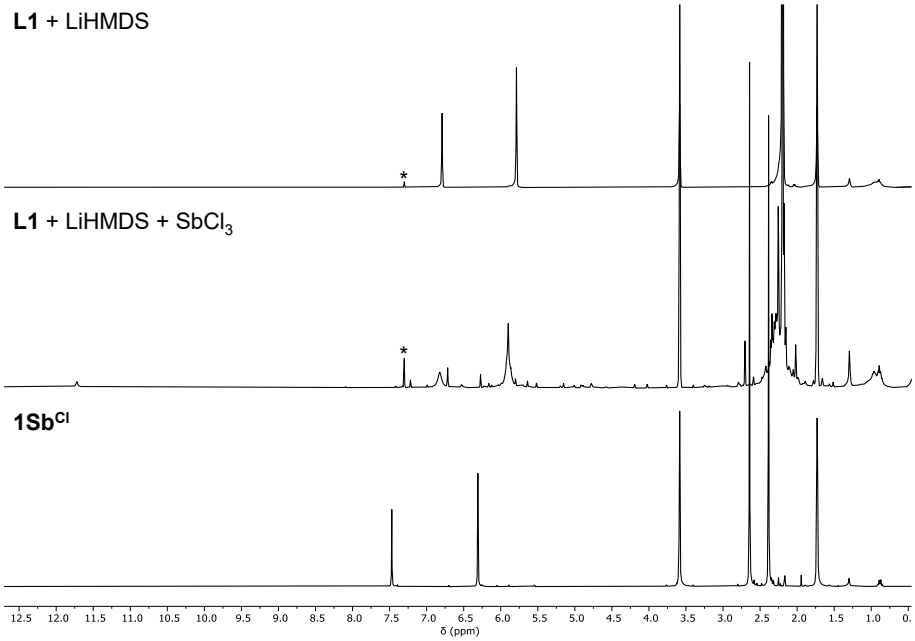
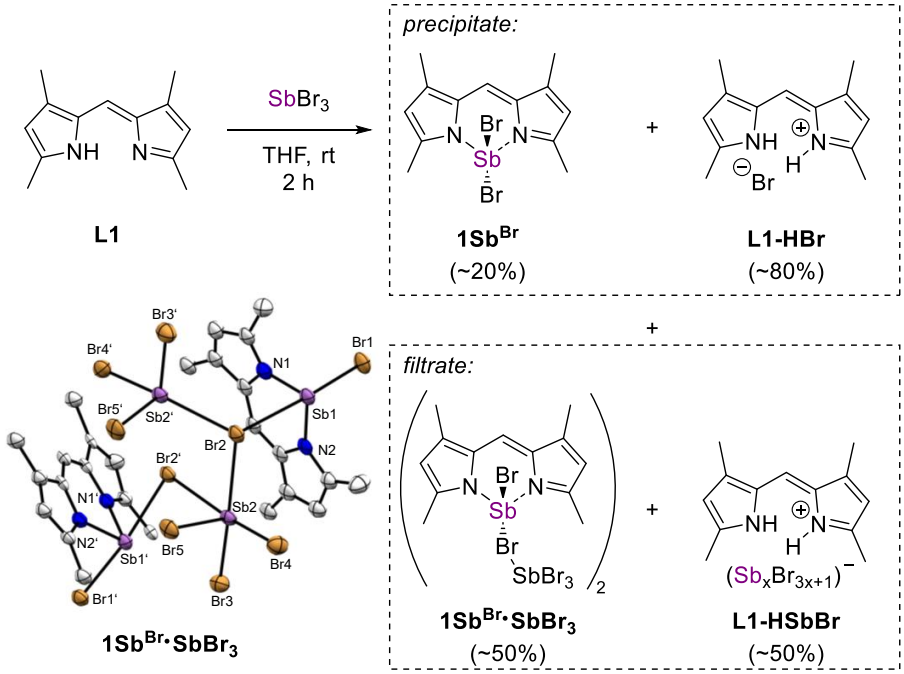


Figure 27: Stacked ^{1}H NMR (400 MHz) spectra of **L1** and LiHMDS, after reaction with $SbCl_3$ (ratio 2:1) and comparison to **1Sb^{Cl}** in THF-d_8 (in order from top to bottom). The sign (*) marks benzene.

When performing the synthesis of **1Sb^{Br}** in the absence of a base, multiple products were identified based on ^{1}H NMR spectroscopy and X-ray diffraction analysis (Scheme 22). Addition of 1.00 equivalent of $SbBr_3$ to a THF solution of **L1** yielded a red amorphous precipitate as the quantitatively main product. Upon washing with THF and drying under reduced pressure, ^{1}H NMR spectroscopy of the solid revealed a mixture of two products; **1Sb^{Br}** (∼20%) and **L1-HBr** (∼80%), which was confirmed by data of independently synthesized compounds. Furthermore, the components of the THF filtrate were determined by ^{1}H NMR spectroscopy as a circa 1:1 mixture of two different products, which were identified as the ligand antimonate salt **L1-HSbBr** and the adduct **1Sb·SbBr$_3$**. Both were crystallized from a saturated dichloromethane solution. The asymmetric unit of **1Sb·SbBr$_3$** comprises a dimeric structure in which two

$SbBr_3$ groups are situated between two units of **1Sb^{Br}**. This arrangement resembles a pyramidal $[Sb_2Br_8]^{-2}$ diantimonate which bridges two ligand-supported stibenium fragments of **1Sb^{Br}** as indicated by a considerably elongated antimony bromine distance of Sb1−Br2 = 3.0187(3) Å and a pyramidal geometry around Sb2 with nearly 90° angles between neighboring bromines.[151]



Scheme 22: Reaction of **L1** without addition of base. Yields refer to relative fraction based on ^{1}H NMR integration. X-ray solid-state structure of **1Sb·SbBr$_3$** is depicted with omitted hydrogen atoms and thermal ellipsoids set to a 50% probability level.

Due to the difficulties involved in the isolation of **1Sb^{F}**, the synthesis was also attempted starting from **L1^{Li}**, which was added to a slight excess of SbF_3 (1.50 equiv.) in THF at −35 °C and warmed to room temperature over the course of one hour. This led to the formation of a fine crystalline, precipitate which matched the unit cell parameters of previously described **1Sb^{F}**, further implying that this route presents a viable option to access **1Sb^{F}**. Upon addition of extra SbF_3 (circa 1.00 equiv.) to the THF mother liquor, a new crop of single crystals was obtained after one week at −35 °C. Interestingly, analysis of these single crystals by X-ray diffraction revealed an oligomeric structure of **1Sb^{F}** which is bridged by SbF_3 units (Figure 28). Compared to **1Sb^{F}**, the adduct displays slightly elongated average Sb−F bond lengths of 2.083(2) Å and exhibits a pseudo-bipyramidal geometry at Sb1 with a slightly more acute angle of ∠(F1−Sb−F2) = 160.4(1)° as compared to **1Sb^{Cl}** and **1Sb^{Br}**. As a consequence of the different geometry, the bond lengths in the adduct structure *d*(Sb1−N1) = 2.068(3) Å and *d*(Sb1−N1) = 2.061(3) Å are in contrast to those found

with **1Sb^{F}** and display better agreement with the Sb−N bond lengths seen with the other SBDIPYs. This finding is further supported by a drastically smaller antimony to ligand mean plane distance of 0.305(3) Å, which together with the above-mentioned observations suggests a stabilizing effect coming from the bridging SbF_3 units. The SbF_3 units feature a distorted square pyramidal geometry, having three covalent Sb−F bonds and two weakly bound fluorides (F1 and F2') featuring Sb−F distances slightly below the sum of van der Waals radii (<3.53 Å).[152,153]

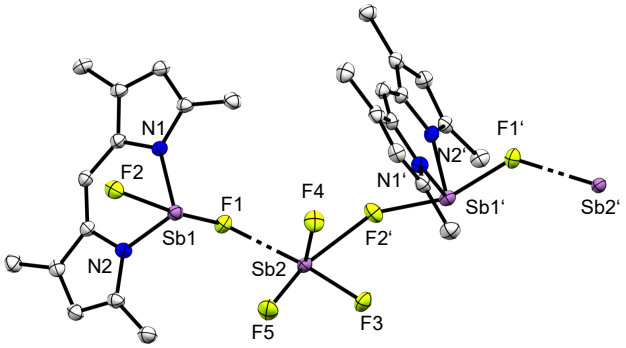
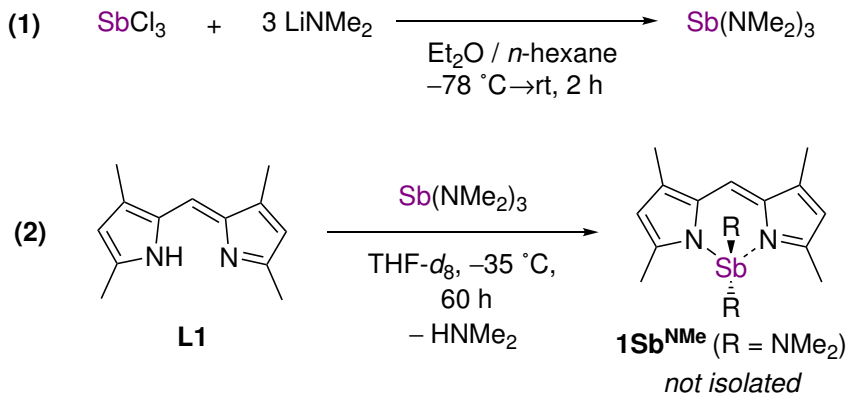


Figure 28: X-ray solid-state structure of SbF_3-adduct of **1Sb^{F}**. Hydrogen atoms were omitted for clarity and thermal ellipsoids were set to a 50% probability level.

As a last modification of the synthetic procedure other antimony precursors were evaluated to access SBDIPY chromophores featuring different anionic ligands besides halides. First, tris(dimethylamino)antimony ($Sb(NMe_2)_3$) was prepared with the goal of synthesizing the respective bis(amido)-antimony dipyrrin. This antimony precursor can be considered as a base due to the labile Sb−N bond that readily undergoes ligand exchange with amines or alcohols. This approach has found recent success in the synthesis of several antimony amide complexes, as complexation is facilitated by avoiding the use of an additional base for ligand deprotonation.[154,155] Tris(dimethylamino)antimony was prepared according to literature and reacted with **L1** in cold THF-d_8 (Scheme 23).[156]



Scheme 23: Synthesis of $Sb(NMe_2)_3$ (1) and synthesis of SBDIPY complex **1Sb^{NMe}** (2).

A gradual colour change from yellow to orange-red was observed upon mixing of both reagents. Immediate measurement of the ^{1}H NMR spectrum revealed the formation of one major new compound featuring drastically highfield-shifted signals of the pyrrolic ^{1}H resonance at 5.55 ppm and the methene proton at 4.16 ppm (Figure 29). Due to the presence of residual ^{1}H NMR signals of **L1** and $Sb(NMe_2)_3$, the sample was kept at −35 °C for 60 hours before removal of solvent and dimethyl amine as the reaction by-product under reduced pressure, resulting in a light orange solid. Analysis by ^{1}H NMR spectroscopy showed a reasonably clean spectrum that is in agreement with the proposed structure of **1Sb^{NMe}**. However, it is unusual to see that the NMe_2 groups show two different ^{1}H resonances (broad singlet at 2.71 ppm and singlet at 2.19 ppm) which both integrate as 6 protons, hinting at a potential dynamic behaviour in solution, thereby causing a reduced molecular symmetry. Contrary to other SBDIPYs, the obtained product was fully soluble in *n*-hexane which could stem from the decreased polarity of the amido ligands. Unfortunately, structural proof through X-ray diffraction analysis remains missing as no suitable single crystals were obtained from slow evaporation of *n*-hexane or THF solutions at toom temperature.

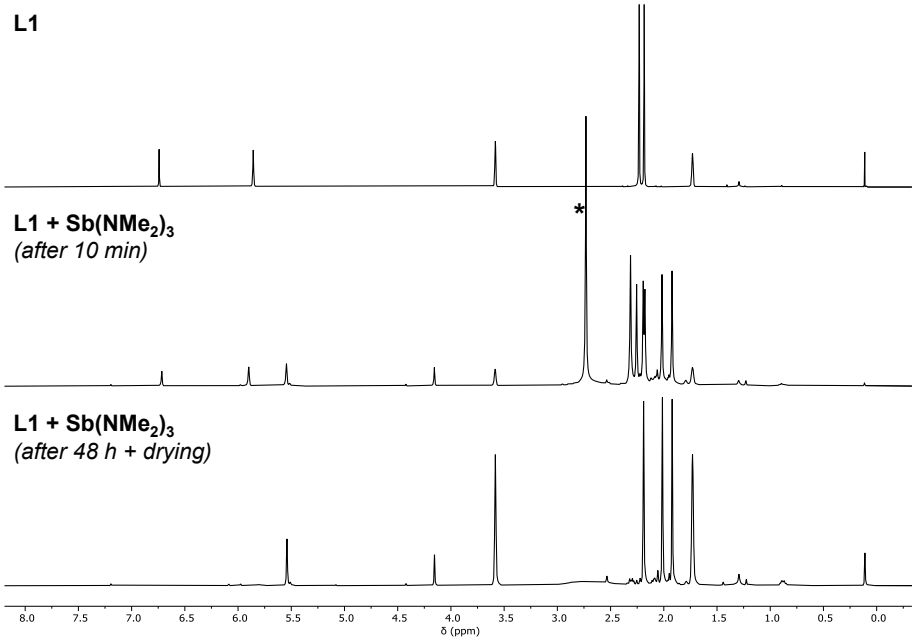
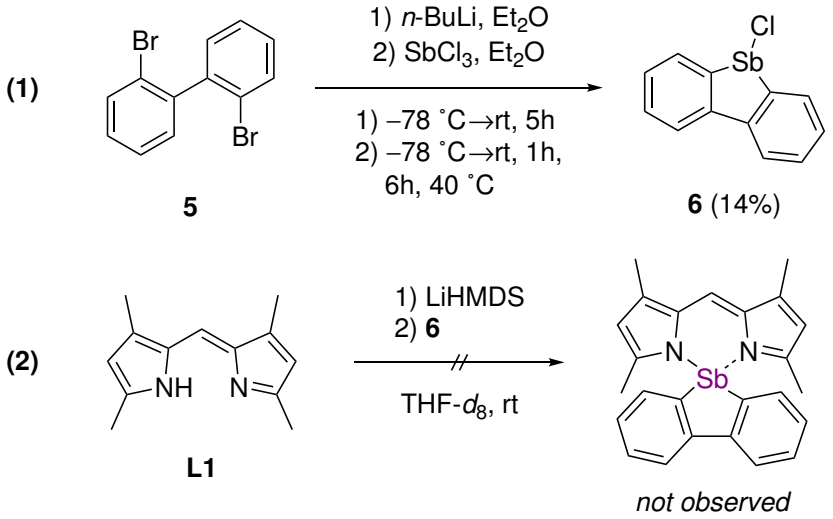


Figure 29: Stacked ^{1}H NMR spectra of **L1** (400 MHz, top), immediately after addition of $Sb(NMe_2)_3$ (300 MHz, middle) and after 60 h at −35 °C and drying, in THF-d_8 (the sign * marks $Sb(NMe_2)_3$). *Note: ^{1}H NMR spectrum of **L1** was recorded by A. Bismuto.*

As the second precursor, stibol **6** was prepared from dibromobiphenyl **5** following a literature-reported procedure (Scheme 24).[157] Despite multiple attempts, the yield after recrystallization of **6** was significantly lower compared to the one reported in

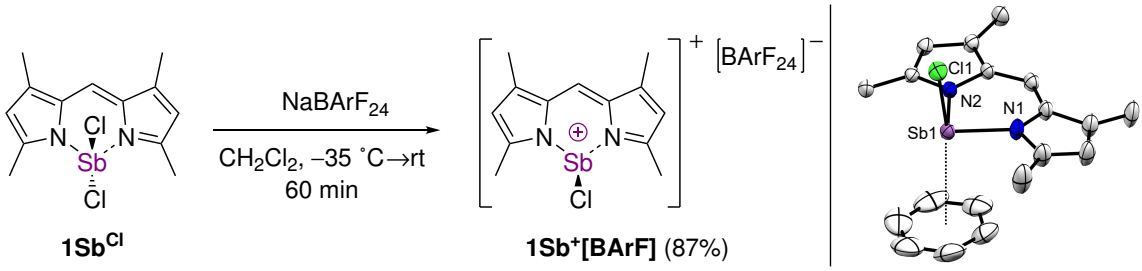
literature, potentially owing to the quality of reagents used.[157] Employing stibol **6** as the antimony source for the synthesis of the corresponding SBDIPY complex was envisioned to form a more strained system with potentially enhanced photoluminescence characteristics. However, addition of an equimolar mixture of LiHMDS and **L1** in THF at −35 °C to **6** did not result in any reaction based on ^{1}H NMR data. Even heating the sample to 70 °C did not lead to any appreciable changes in the ^{1}H NMR spectrum. Most likely, the reaction to form the corresponding SBDIPY complex is inhibited by the imposed geometry of **6**, disfavoring complexation with a bidentate ligand such as **L1**.



Scheme 24: Synthesis of stibol **6** (1) and unsuccessful ligand exchange reaction with **L1** (2).

2.3.3. Modification of SBDIPY complexes

Several reactivities were tested to diversify available SBIDIPY chromophores by modifying the substituents at the antimony centre. The first considered option was the halide abstraction from **1Sb^{Cl}** to obtain a cationic stibenium complex by using a weakly coordinating anion. Indeed, upon mixing of **1Sb^{Cl}** and $NaBArF_{24}$ in CH_2Cl_2 an immediate change in colour and selective transformation based on ^{1}H NMR spectroscopy were observed. Full conversion based of the reaction was noted already within one hour and the cationic SBDIPY **1Sb$^+$[BArF]** was isolated in good yield (Scheme 25). Suitable single crystals of **1Sb$^+$[BArF]** were grown from a mixture of CH_2Cl_2/benzene and X-ray diffraction analysis revealed coordination of the aromatic solvent to positively charged antimony centre (Scheme 25).

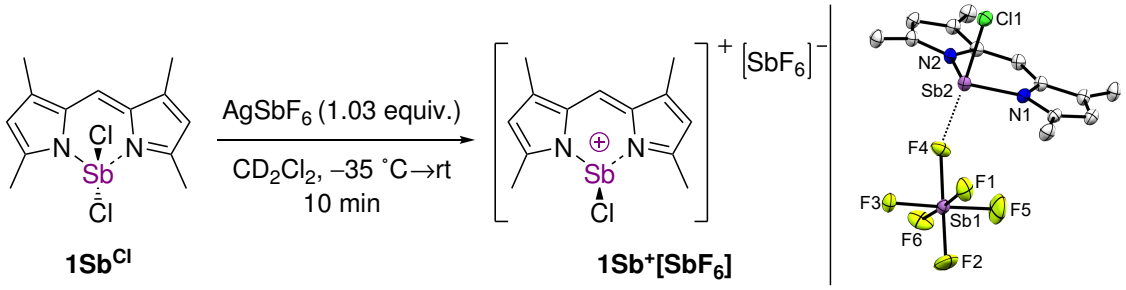


1Sb^{Cl} **1Sb^{+}[BArF]** (87%)

Scheme 25: Synthesis of **1Sb^{+}[BArF]** (left) and X-ray solid-state structure of **1Sb^{+}[BArF]** (right). Hydrogen atoms, non-coordinating benzene and $BArF_{24}^{-}$ counterion were omitted for clarity, and thermal ellipsoids were set to a 50% probability level.

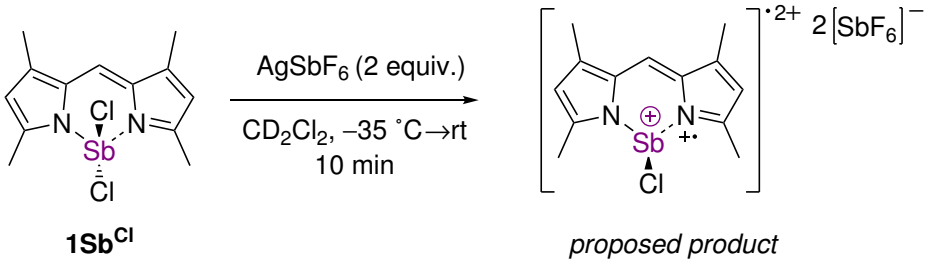
The coordination of benzene can be interpreted as a η^3 binding mode as the solvent molecule has a distance of 3.212(1) Å from its centroid to Sb with the shortest Sb−C distance of 3.250(4) Å and the longest being 3.702(5) Å. Moreover, having an average Sb−N bond length of 2.057(3) Å and Sb−Cl bond length of 2.368(2) Å, the stibenium complex features bond lengths that are noticeably shorter than the parent complex **1Sb^{Cl}**. The solution colour of **1Sb^{+}[BArF]** in THF was also strikingly different as compared to **1Sb^{Cl}** and will be further discussed in section 2.3.4. Interestingly, performing the reaction under identical conditions but with 2.00 equiv. of $NaBArF_{24}$, a second halide abstraction was not observed by ^{1}H NMR spectroscopy, thus indicating that only single halide abstraction can be achieved by using weakly coordinating anions as in $NaBArF_{24}$.

Halide abstraction was also attempted by reacting **1Sb^{Cl}** with $AgSbF_6$ (Scheme 26). The reaction immediately proceeded as indicated by a change in colour from orange to light red, precipitation of AgCl and a selective shift in the ^{1}H NMR spectrum. However, isolation of the proposed product **1Sb^{+}[SbF$_6$]** was unsuccessful due to gradual sample decomposition related to protonation of the ligand. Nonetheless, single crystals were obtained from a mixture of CH_2Cl_2/Et_2O, which confirmed the formation of a stibenium complex by X-ray diffraction analysis (Scheme 26). Interestingly, the solid-state structure of **1Sb^{+}[SbF$_6$]** featured an evident secondary interaction between the stibenium centre and fluorine F4 of the hexafluoroantimonate counterion with an Sb−F distance of 2.779(4) Å that is well below the sum of van der Waals radii (<3.53 Å).[153]



Scheme 26: Reaction of **1Sb^{Cl}** in the presence of $AgSbF_6$ (left) and X-ray solid-state structure of **1Sb^{+}[SbF$_6$]** (right). Hydrogen atoms and molecule disorder in SbF_6 counterion were omitted for clarity, and thermal ellipsoids were set to a 50% probability level.

Notably, the reaction of **1Sb^{Cl}** with 2.00 equiv. of $AgSbF_6$ resulted in a ^{1}H NMR spectrum with severely broadened signals, potentially resulting from a single-electron oxidation by $AgSbF_6$ to give an NMR-silent radical dication.[158,159] Unfortunately, attempts tp obtain single crystals of the product from CH_2Cl_2/Et_2O and CH_2Cl_2/*n*-hexane mixtures at room temperature were unsuccessful. Nonetheless, with dative interactions to solvent or counterion present in both solid-state structures of **1Sb^{+}[BArF]** and **1Sb^{+}[SbF$_6$]**, the increased coordination capability of the stibenium ion is highlighted as compared to the parent complex **1Sb^{Cl}**. This finding may arise from a higher Lewis acidity and vacant coordination site at the antimony centre, thus also possibly contributing to an increased instability of the SBDIPY complex (Scheme 27). It was further noted that halide abstraction of **1Sb^{F}** with $NaBArF_{24}$ gave a significantly less selective outcome based on ^{1}H NMR spectroscopy, likely due to the lower stability of **1Sb^{F}**.



Scheme 27: Proposed reaction of **1Sb^{Cl}** with 2.00 equiv. $AgSbF_6$.

Despite the limited solvent-stability of **1Sb^{Cl}** several reagents were tested with respect to ligand exchange of the chlorido ligands in **1Sb^{Cl}** through different monoanionic ligands, thereby potentially improving stability and changing the spectroscopic properties of the SBDIPY chromophore. Salt metathesis of **1Sb^{Cl}** in the presence of an excess of AgF (2.50 equiv.) to give **1Sb^{F}** was unsuccessful with no reaction besides slow decomposition observed even upon heating to 40 °C and sonication in CD_2Cl_2.

Similarly, no reaction was noted for **1Sb^{Cl}** in the presence of 1.00 equiv. NaN_3 in THF-d_8 at room temperature, as well as upon irradiation with 456 nm light for 30 minutes. On the contrary, **1Sb^{Cl}** reacted vigorously with $LiAlH_4$ as a hydride source, resulting in gas evolution and rapid decomposition of the complex to an insoluble black precipitate even at −78 °C. As "hard" nucleophiles seemed less suitable for the ligand exchange, softer alkali organyls were considered as more promising options. However, reaction of **1Sb^{Cl}** (40 mg, 0.10 mmol, 1.00 equiv.) with mesityllithium (30 mg, 0.22 mmol, 2.20 equiv.), resulted in the formation of the lithium dipyrrinato salt **L1^{Li}** as the main dipyrrin-related product as evidenced by ^{1}H NMR spectroscopy. Mesityllithium was fully consumed over the course of 1 hour at room temperature with two new singlets appearing at 6.86 ppm and 6.80 ppm in the ^{1}H NMR spectrum. The major signal at 6.86 ppm can likely be attributed to chloromesitylstibane whereas the minor one 6.80 ppm originates from trimesitylstibane (Figure 30).[160] These findings illustrate the rather weak Sb−N bonds within SBDIPY chromophores as exchange of the dipyrrin ligand appeared to be the preferred pathway over halide substitution at the antimony centre.

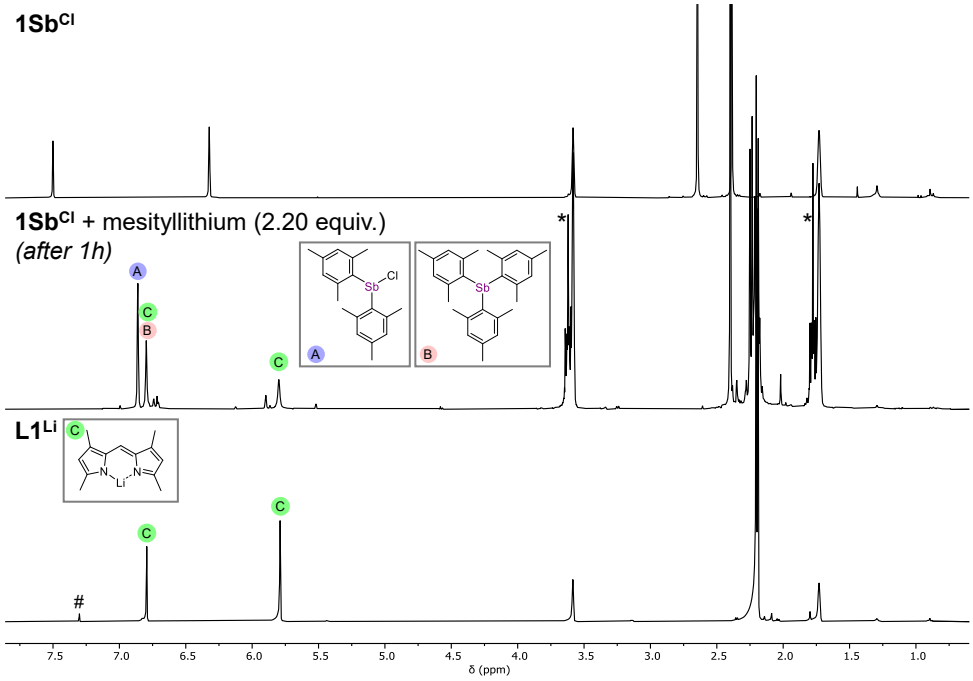


Figure 30: Stacked ^{1}H NMR spectra of **1Sb^{Cl}** (300 MHz, top), reaction aliquot of **1Sb^{Cl}** (1.00 equiv.) with mesityllithium (2.20 equiv.) after 1 h (300 MHz, middle) and comparison to **L1^{Li}** spectrum, all in THF-d_8. Reaction products are marked by colours, while the sign (*) marks THF and (#) marks benzene.

Compared to boron dipyrrins, the respective pnictogen complexes could also access central atoms with the oxidation state of +V. Therefore, oxidation of **1Sb^{F}** was at-

tempted with XeF_2 (1.05 equiv.) in CD_2Cl_2 at −35 °C. Immediately upon addition of the oxidant, a colour change from orange to brown was observed. Analysis by ^{1}H NMR spectroscopy revealed a slight shift (downfield and highfield) of all **1Sb^F**-related signals but also circa 30% complex decomposition visible as a broad singlet at 12.30 ppm. The ^{19}F NMR resonance of **1Sb^F** was slightly shifted to −72.7 ppm, similar to what was observed after keeping **1Sb^F** in solution for extended time, and thus indicating an unsuccessful oxidation of the Sb-centre as it would involve a more pronounced shift in the ^{19}F NMR spectrum. Unfortunately, no further structural proof was obtained.

Modification of the antimony centre was impeded due to the sensitive nature of SBDIPY complexes, readily resulting in gradual sample decomposition. Therefore, additional kinetic or electronic stabilization through the dipyrrin ligand should be introduced to obtain a more robust platform for reactivity screening.

2.3.4. Spectroscopic properties of SBDIPY chromophores

In order to get an initial overview of the spectroscopic properties of SBDIPY chromophores, the absorbance spectrum of **1Sb^{Cl}** was recorded for a selection of solvents (Figure 31).

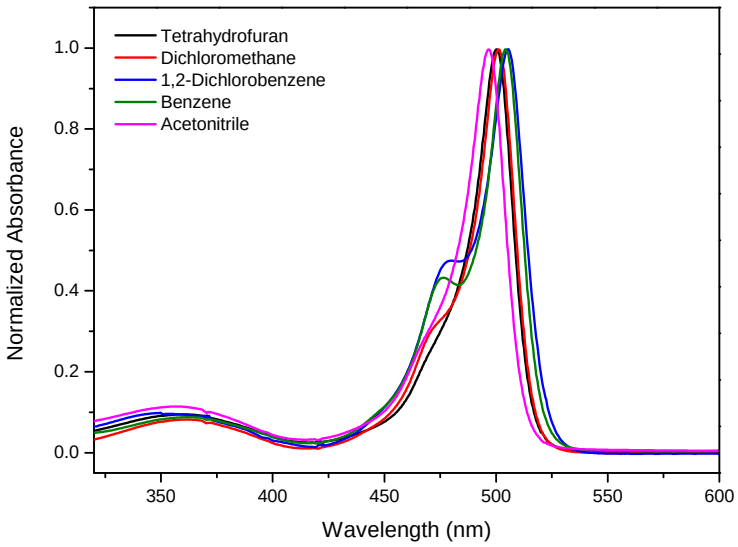


Figure 31: Normalized absorbance spectra of **1Sb^{Cl}** in various solvents at room temperature.

The absorbance spectrum of **1Sb^{Cl}** displayed a similar profile as **1B^F** with one main band at λ_{abs} = 501 nm in CH_2Cl_2, while also showing a slight hypsochromically shifted shoulder (circa 470 nm), which is usually attributed to a vibronic transition.[161] Interestingly, this shoulder appeared more pronounced in benzene and 1,2-dichlorobenzene.

In order to evaluate whether this behaviour could originate from sample degradation, a series of UV/Vis spectra were recorded for a THF solution of **1Sb^{Cl}** over 19 hours (Figure 32). The time course measurement revealed a steady increase of a new band at λ_{abs} = 468 nm, hinting at a potential decomposition event taking place.

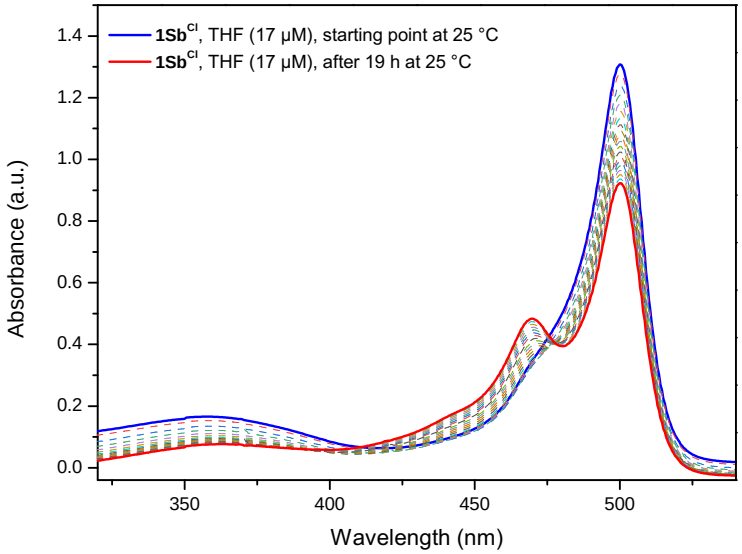


Figure 32: UV/Vis time course measurement of **1Sb^{Cl}** in THF (17 µM) at 25 °C. The first absorbance spectrum is displayed in blue and the spectrum after 19 hours is shown in red.

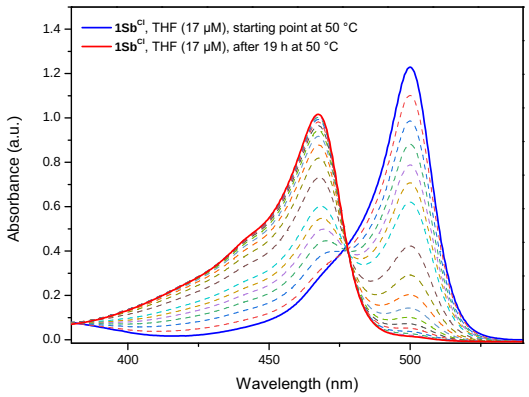
To obtain more insight into this phenomenon, time-resolved UV/Vis measurements of fresh **1Sb^{Cl}** samples were carried out in THF over the same time interval but at different temperatures (50 °C, 40 °C, 10 °C and 0 °C). Indeed a much faster sample degradation was observed at 40 °C or higher with an approximately full conversion to the second band at λ_{abs} = 468 nm after 19 hours (Figure 33a). In contrast to that, measurements at temperatures below 25 °C showed no decrease in decomposition rate (Figure 33b and 33c). According to the Beer-Lambert law (equation 3), sample absorbance A is directly proportional to the concentration c of the absorbing compound, molar absorption coefficient ϵ and optical path length l.[162]

$$A = \epsilon l c. \tag{3}$$

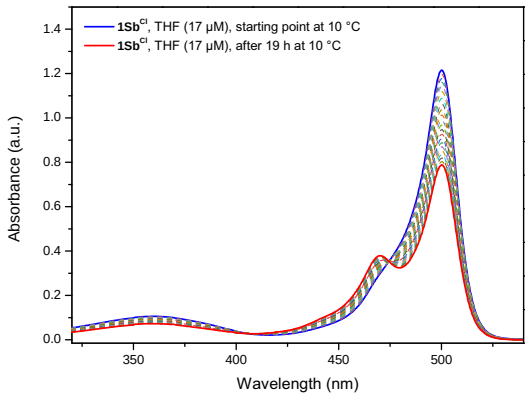
Based on this, information on the reaction order can be obtained by plotting $\ln A_n$ against the time t (where A_n refers to the normalized absorbance of the sample).[163] The general integrated form of the first-order rate law is given as

$$\ln\left(\frac{[Sb]}{[Sb]_0}\right) = -kt, \tag{4}$$

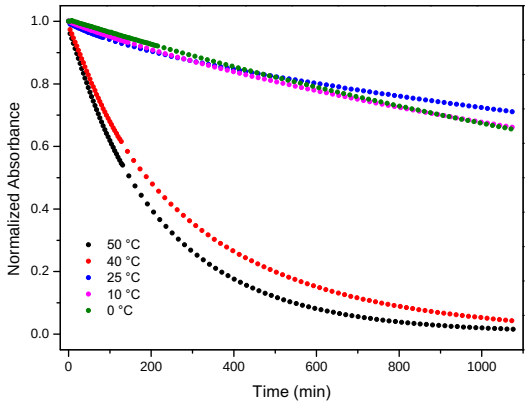
where $[Sb]_0$ refers to the initial concentration, $[Sb]$ to the actual concentration of **1Sb^{Cl}** and k to the rate constant. As concentration and absorbance are in a linear relationship, a first-order reaction will give a straight slope $-k$ when $\ln \frac{A}{A_0}$ is plotted against the time t (with A being the absorbance and A_0 the initial absorbance). As shown in Figure 33d, the decomposition of **1Sb^{Cl}** is in good agreement with first-order kinetics, therefore excluding a dimerization reaction as a cause and hinting at a potential intramolecular decomposition process.



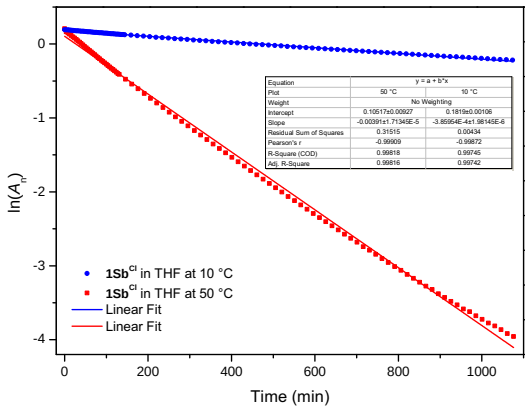
(a) 1Sb^{Cl} at 50 °C (THF).



(b) 1Sb^{Cl} at 10 °C (THF).



(c) Absorbance decay of **1Sb^{Cl}** at varying temperatures.



(d) Reaction order analysis.

Figure 33: Investigation of temperature dependency of **1Sb^{Cl}** in THF. Time-resolved UV/Vis spectra of **1Sb^{Cl}** at 50 °C (a) and 10 °C (b) in THF. Graphical analysis of sample degradation (c and d).

The decomposition band at λ_{abs} = 468 nm was found to bear a striking resemblance to the UV/Vis spectrum of **L1-HCl** (Figure 34), suggesting a ligand protonation as the decomposition pathway. However, the cause of decomposition remains unclear, with possibilities being trace amounts of water or acid present in the solvent. Unfortunately, meticulous attempts to purify solvents, silylation of glassware and addition of 1,8-bis(dimethylamino)naphthalene ("Proton Sponge") did not lead to notable improvements.

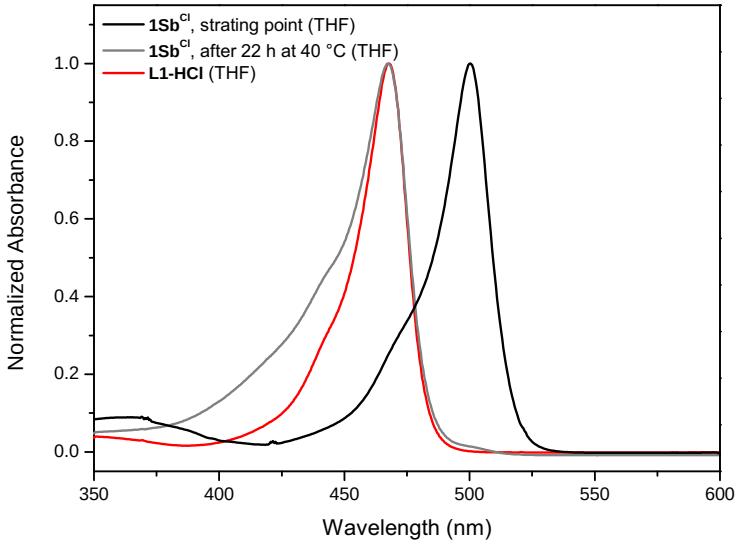
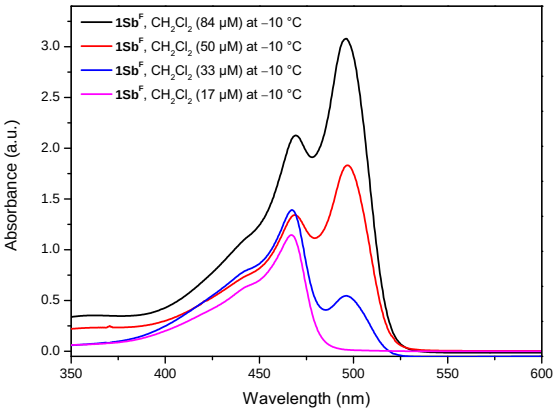


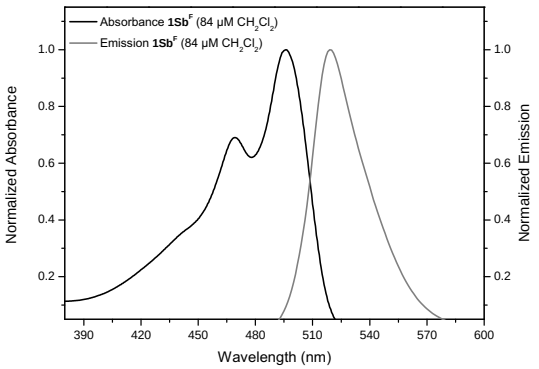
Figure 34: Comparison of normalized UV/Vis spectra of **L1-HCl** (red), **1Sb^{Cl}** (black) and **1Sb^{Cl}** after 22 hours at 40 °C (grey); all in THF at 25 °C.

Furthermore, it is worth pointing out that reported spectra of the previously mentioned PHODIPY (**A106**, see section 1.2.4) show a significant fraction of a similar band at λ_{abs} = 467 nm, therefore indicating a similar decomposition occurring with the phosphorous compound. SBDIBY chromophore **1Sb^{Cl}** showed fluorescence emission at λ_{emi} = 516 nm, which almost fully diminished upon sample decomposition with maximum absorption at λ_{abs} = 468 nm. Using **1B^{F}** as a reference, the relative quantum yield of **1Sb^{Cl}** was determined as Φ_{rel} = 3%. The comparatively low quantum yield of **1Sb^{Cl}** emphasizes the effect of a heavy element core in a fluorophore on possible radiative decay pathways in contrast to the BODIPY analogue. Nonetheless, no phosphorescence or solid-state emission was detected for **1Sb^{Cl}** at room temperature.

Moreover, the stabilities of the other halido complexes **1Sb^{Br}** and **1Sb^{F}** were evaluated using UV/Vis spectroscopy. Interestingly, the absorption spectra of **1Sb^{F}** displayed a concentration dependency, displaying either a single band at λ_{abs} = 467 nm at low concentrations (17 μM) or a mixture of two species with absorption maxima at λ_{abs} = 467 nm and λ_{abs} = 496 nm at higher concentrations ($>$33 μM). However, it is important to note that these measurements were carried out at $-$10 °C as the hysochromically shifted band gradually decomposed to the one at λ_{abs} = 467 nm due to the low stability of **1Sb^{F}**. Furthermore, the concentration dependency, suggests that aggregation may contribute to stabilizing the emitting species.



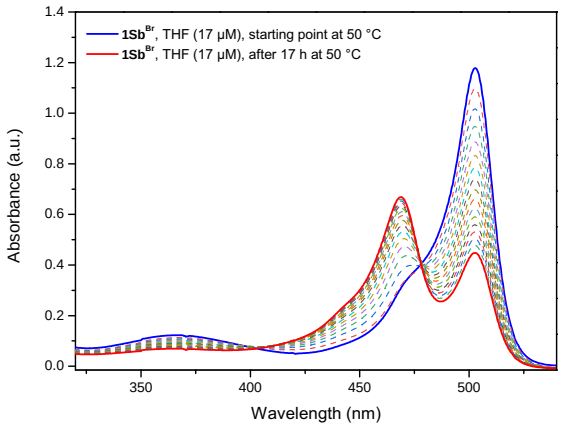
(a) UV/Vis spectra of **1Sb^{F}** (CH_2Cl_2).



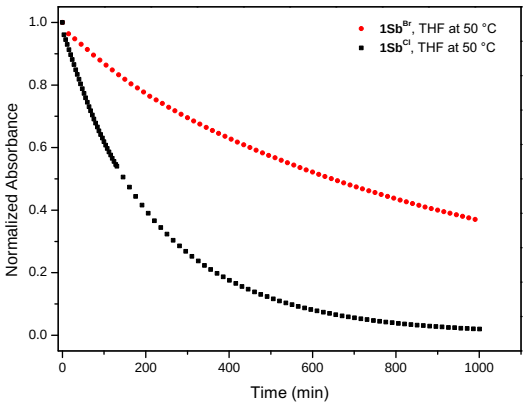
(b) Normalized absorbance and emission of **1Sb^{F}** .

Figure 35: UV/Vis spectra of **1Sb^{F}** at varying sample concentrations (a) and normalized absorption and emission spectra of **1Sb^{F}** (b); both in CH_2Cl_2 at −10 °C. The emission was recorded at an excitation wavelength of 460 nm.

Lastly, the spectroscopic properties of **1Sb^{Br}** were investigated to compare with the other halido complexes. Time-resolved UV/Vis spectra of **1Sb^{Br}** showed a similar decomposition speed at 10 °C as compared to **1Sb^{Cl}**, whereas a significantly higher stability at elevated temperatures was noted, thus underlining the influence of the bromido ligand on complex stability (Figure 36).



(a) 1Sb^{Br} at 50 °C (THF).



(b) Absorbance decay of **1Sb^{Cl}** and **1Sb^{Br}** (50 °C).

Figure 36: UV/Vis stability analysis of **1Sb^{Br}** in comparison to **1Sb^{Cl}**.

Besides affecting complex stability, the bromide substituents also caused a decrease in fluorescence emission as compared to **1Sb^{Cl}**, having a relative quantum yield of just Φ_{rel} = 0.5% for **1Sb^{Br}**. This observation was expected as a consequence of fluorescence quenching through the internal heavy atom effect.[164] An overview of the absorption and emission of the different halide variants **1Sb^{X}** is shown in Figure 37

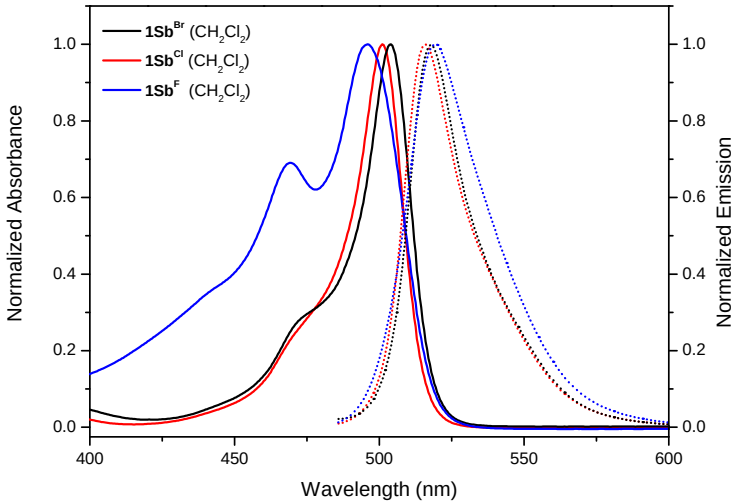


Figure 37: Overview of normalized absorbance and emission spectra of SBDIPYs **1Sb^{X}** in CH_2Cl_2. The emission was recorded at an excitation wavelength of 460 nm.

The effect of halide abstraction was clearly visible in the difference of absorption and emission parameters between **1Sb^{+}[BArF]** and **1Sb^{Cl}**. The stibenium complex displayed a bathochromic shift in absorption (λ_{abs} = 513 nm) and only a slight shift in emission (λ_{emi} = 518 nm), making it the SBDIPY chromophore with the smallest Stokes shift (Figure 38). Due to sample instability, the photoluminescence quantum yield of **1Sb^{+}[BArF]** was unfortunately not determined.

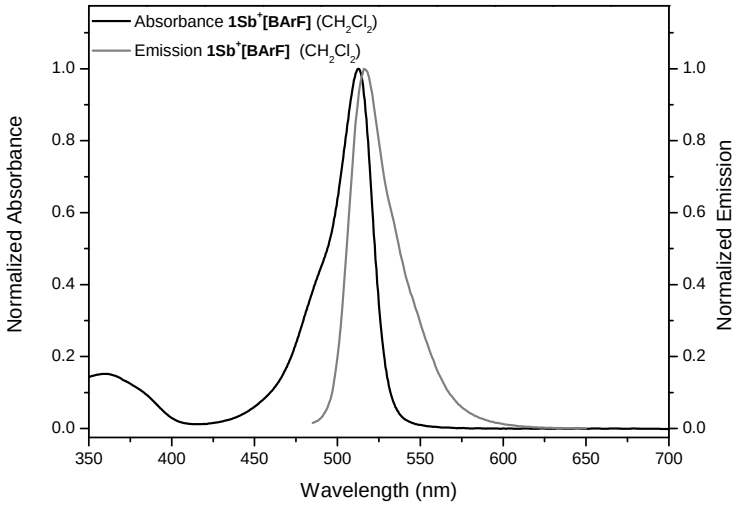
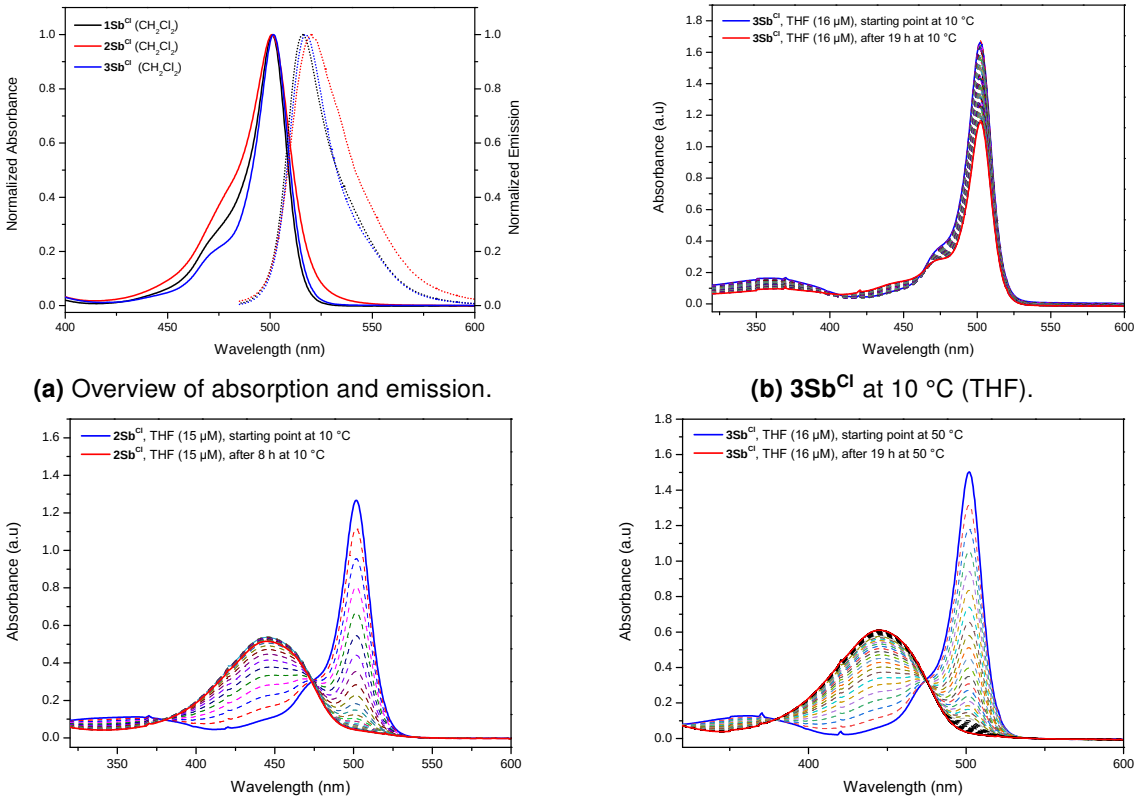


Figure 38: Normalized absorbance and emission spectra of **1Sb^{+}[BArF]** in CH_2Cl_2. The emission was recorded at an excitation wavelength of 460 nm.

Lastly, SBDIPYs **2Sb^{Cl}** and **3Sb^{Cl}** were tested to examine the influence of different *meso*-substituents on the optical properties of the antimony complexes. Both SBDIPY modifications, **2Sb^{Cl}** and **3Sb^{Cl}**, showed insignificantly shifted absorption maxima at λ_{abs} = 501 nm in CH_2Cl_2 and slightly different emission maxima at λ_{emi} = 520 nm (**2Sb^{Cl}**) and λ_{emi} = 523 nm (**3Sb^{Cl}**). However, the fluorescence emission intensity was found to be drastically reduced for **2Sb^{Cl}** (Φ_{rel} well below 1%) and slightly lowered for **3Sb^{Cl}** (Φ_{rel} = 1%) due to nonradiative quenching of the excited state by rotation of the *meso*-substituent. While the mesityl substituent is sterically restricted, a stronger quenching effect was observed for the freely rotating phenyl group, which has been previously described with BODIPY.[165] Based on these minor changes with respect to the Stokes shift, only a minor energetic contribution of the *meso*-substituents to the HOMO-LUMO gap of SBDIPY chromophores can be assumed. Furthermore, time-resolved UV/Vis spectroscopy confirmed no improvement in terms of complex stability through the introduction of a *meso*-substituent. For **2Sb^{Cl}**, a rapid decomposition was observed in THF at 10 °C with the main absorption band at λ_{abs} = 502 nm fully transforming into a new, unknown product with a maximum absorption at λ_{abs} = 445 nm within 8 hours (Figure 39a). Complex **3Sb^{Cl}** showed decent stability in THF at 10 °C (Figure 39b) but decomposed rapidly at elevated temperature (50 °C), giving a new band with maximum absorption at λ_{abs} = 445 nm, thus indicating a similar decomposition event as for **2Sb^{Cl}**. Overall, these findings suggest no meaningful improvement through introduction of a *meso*-substituent in terms of emission efficiency and complex stability.



(a) Overview of absorption and emission.

(b) 3Sb^{Cl} at 10 °C (THF).

(c) 2Sb^{Cl} at 10 °C (THF).

(d) 3Sb^{Cl} at 50 °C (THF).

Figure 39: Comparison of absorption and emission of chloride-substituted SBDIPYs in CH_2Cl_2 (a) and UV/Vis stability analysis of *meso*-substituted SBDIPYs in THF at 10 °C and 50 °C (b-d). The emission was recorded at an excitation wavelength of 460 nm.

An overview of relevant spectroscopic properties of SBDIPY chromophores is provided in Table 2.

Table 2: Spectroscopic data of SBDIPY complexes.

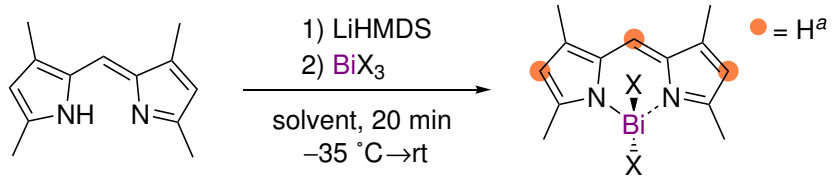
Complex	max. Absorption λ_{abs} (nm)	max. Emission[a] λ_{emi} (nm)	Stokes shift (cm^{-1})	Quantum yield Φ_{rel}
1Sb^{Cl}	501	516	580	0.025
1Sb^{Br}	504	518	536	0.004
1Sb^{F}	496	522	1004	–[b]
2Sb^{Cl}	501	520	729	–[b]
3Sb^{Cl}	501	523	840	0.011
1Sb^{+}[BArF]	513	518	188	–[b]

[a]Emission recorded at excitation wavelength λ_{exc} = 460 nm. [b]Quantum yield not determined due to sample instability.

Several important conclusions can be extracted from the data described above. First of all, contrary to the earlier work on PHODIPY (**A106**, see section 1.2.4) which Smith and co-workers assigned a maximum absorption at λ_{abs} = 467 nm, time-resolved UV-Vis spectroscopy strongly indicated this band to stem from a ligand-related decomposition product akin to **L1-HCl**.[120] Thus, the group 15 centre has likely only very little contribution to the extent of the Stokes shift as compared to the analogous BODIPY chromophore. Moreover, pnictogen dipyrrins were found to be significantly less stable, which is likely a consequence of larger element radii and electrophilicity, resulting in more facile sample degradation.[166] Lastly, very little fluorescence emission intensity was observed with all new SBDIPY chromophores, possibly owing to the quenching effect of the heavy central element. However, no phosphorescence or solid-state emission was detected for **1Sb^{Cl}** at room temperature.

2.4. Synthesis of bismuth dipyrrin complexes (BIDIPY)

The synthesis of bismuth dipyrrin complexes (BIDIPYs) was initially attempted using the previously reported procedure for SBDIPY synthesis. Despite successful application to the synthesis of SBDIPY chromophores, isolation of the desired BIDIPY failed with multiple ligand variants **L1**-**L4** and starting from $BiCl_3$ or $BiBr_3$, due to the formation of ligand-related byproduct. Such byproduct could potentially stem from reprotonation through HMDS to the N−Bi bond which can ultimately lead to complex degradation and undesired side-reactivity as indicated by ^{1}H NMR spectroscopy. An overview of failed attempts to isolate BIDIPY chromophores using the protocol shown in Scheme 28 is given in Table 3.



Scheme 28: General procedure for attempted BIDIPY synthesis (X refers to a generic monoanionic substituent, as specified in Table 3).

Table 3: Screening of reaction conditions for BIDIPY complex formation. NMR spectra of crude samples were recorded after solvent removal under reduced pressure and washing with *n*-hexane.

Entry	Ligand (mmol)	Bi source (mmol)	Solvent (NMR solvent)	^{1}H chemical shift of H$^\alpha$ (ppm)[a]	Estimated impurity[b] (%)
e1	**L1** (0.10)	$Bi(OAc)_3$ (0.098)	THF (CD_2Cl_2)	7.14 (s, 1H) 6.40 (s, 2H)	15
e2[c]	**L1** (0.10)	$BiBr_3$ (0.098)	THF (CD_2Cl_2)	7.12 (s, 1H) 6.43 (s, 2H)	68
e3[d]	**L1** (0.020)	$BiCl_3$ (0.020)	THF (CD_2Cl_2)	7.11 (s, 1H) 6.38 (s, 2H)	11
e4[e], [f]	**L1** (0.11)	$BiCl_3$ (0.050)	THF (THF-d_8)	6.66 (s, 1H) 5.98 (s, 2H)	8
e5[g]	**L1** (0.001)	$Bi(HMDS)_3$ (0.001)	C_6D_6 (C_6D_6)	*no reaction*	–
e6[f], [g]	**L1** (0.040)	$Bi(NMe_2)_3$ (0.040)	C_6D_6 (C_6D_6)	6.16 (s, 2H) 4.32 (s, 1H)	10

[a]See Scheme 28 for H$^\alpha$ reference. [b]Estimation based on relative integration of H$^\alpha$ resonances in crude ^{1}H NMR spectra. [c]Increased amount of impurity due to air leak during handling. [d] LiHMDS substituted for NaHMDS. [e]Best result obtained without any additional work-up; otherwise higher impurity level observed. [f]Product isolation unsuccessful as sample showed gradual decomposition based on ^{1}H NMR spectroscopy. [g]No additional base used.

In all attempts, besides entry *e5*, a shift of the dipyrrin ^{1}H NMR signals upon reaction with a bismuth source was observed, thus indicating formation of the respective BIDIPY complex. The largest amount of decomposition product was observed for entry *e2* which was likely caused by an air leak during sample work-up. Nonetheless, suitable single crystals were grown from this reaction mixture, revealing an unexpected bismuth dipyrrin complex that likely originated from sample degradation (Figure 40). The solid-state structure featured one dipyrrin **L1** covalently bound to a $BiBr_2$ core, which is further bound to a bismuthate unit $[BiBr_5]^{2-}$ *via* weak halogen

interactions. Furthermore, the unit cell contains two protonated **L1** ligand cations. From mixing **L1-HBr** and $BiBr_3$ in a 1:1 ratio in THF under air, a similar structure was revealed by X-ray diffraction analysis from single crystals of the reaction mixture. The solid-state structure featured a polymeric bismuthate anion $[Bi_2Br_8]_n^{2-}$ and a protonated cationic ligand **L1** (Figure 40). In this case, the unit cell also contained molecules of water which showed secondary interactions with **L1** and bromide substituents via H-bonding.

Unlike for antimony, the reaction of 2.05 equivalents of deprotonated **L1** with $BiCl_3$ led to a more selective outcome based on ^{1}H NMR spectroscopy with the main species appearing highfield-shifted. Due to the larger size of the central element this observation might signify coordination of multiple dipyrrin units to a single bismuth centre.[166] Despite several attempts, isolation of the reaction product was unsuccessful as gradual decomposition was observed by ^{1}H NMR spectroscopy. Similarly to the antimony analogue, **L1** reacted in the presence of $Bi(NMe_2)_3$ resulting in a rather clean conversion to a new product with significantly highfield-shifted ^{1}H resonances (entry *e6*). In order to probe whether substitution of the remaining dimethylamido ligands could be achieved, 1.00 equiv. of 2,3-naphthalenediol was added to the reaction mixture *e6*. Unfortunately, this led to the instantaneous back-formation of **L1**.

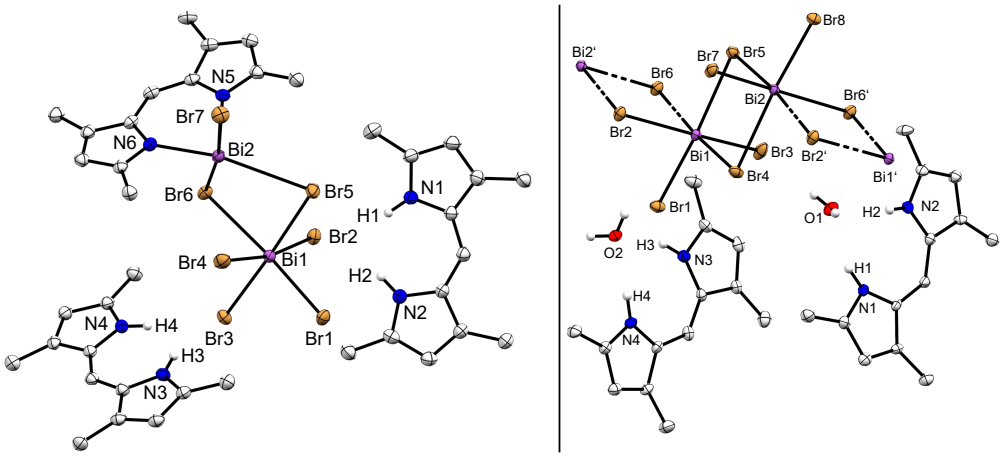
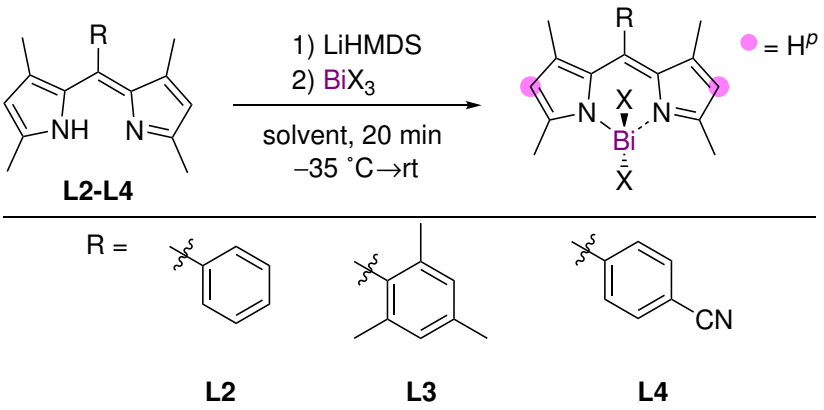


Figure 40: X-ray solid-state structure obtained from mixing **L1-HBr** and $BiBr_3$ (left) and from reaction mixture of entry *e2* (right). Non-nitrogen bound hydrogen atoms and CH_2Cl_2 (left structure) were omitted for clarity, and thermal ellipsoids were set to a 50% probability level.

Although all of the above described data gave strong indications for the formation of BIDIPY complexes, purification and isolation of the desired products remained particularly challenging as washing of the crude product with non-polar solvents (*n*-hexane, *n*-pentane or benzene) and filtration through celite® did not lead to notable improvements.

In order to determine whether the *meso*-substituent could improve the synthesis of BIDIPY complexes, ligands **L2**-**L4** were evaluated in NMR-scale reactions in THF (Scheme 29). An overview of the tested reaction conditions is given in Table 4. With the exception of entry *e7*, ^{1}H NMR spectra were recorded in THF-d_8 without performing any additional work-up beforehand. For entries *e8*-*e11*, ^{1}H NMR spectra of ligand and base mixtures were recorded prior to reaction with the bismuth halide to ensure a successful ligand deprotonation.



Scheme 29: General procedure for attempted BIDIPY synthesis featuring *meso*-substituted ligands **L2-L4** (X refers to a generic monoanionic substituent, as specified in Table 4). *Note:* **L4** *was synthesized by A. Bismuto.*

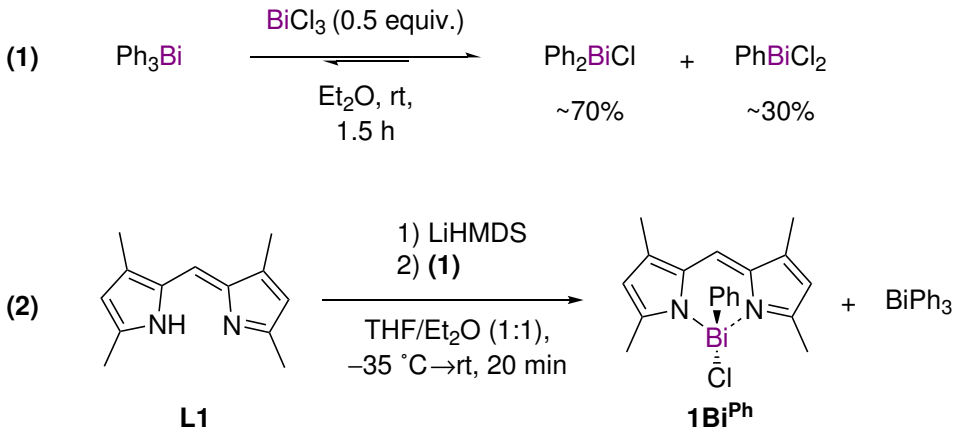
Table 4: Screening of reaction conditions for Bi complex formation featuring ligands bearing *meso*-substituents **L2**-**L4**. All reactions performed using 0.020 mmol of ligand and bismuth halide and 0.021 mmol of LiHMDS.

Entry	Ligand	Bi source	Solvent	^{1}H chemical shift of H^p (ppm)[a]	Estimated impurity[b] (%)
e7[c]	**L2**	$BiCl_3$	THF	6.30 (s, 2H)	18
e8	**L2**	$BiBr_3$	THF-d_8	6.16 (s, 2H)	15
e9	**L3**	$BiBr_3$	THF-d_8	6.19 (s, 2H)	20
e10	**L4**	$BiCl_3$	THF-d_8	6.20 (s, 2H)	12
e11	**L4**	$BiBr_3$	THF-d_8	6.16 (s, 2H)	5

[a]See Scheme 29 for H^p reference. [b]Estimation based on relative integration of H^p resonances in crude ^{1}H NMR spectra. [c]^{1}H NMR data recorded in CD_2Cl_2 after work-up.

Entries *e7*-*e11* presented a similar problem as observed for BIDIPY synthesis using **L1** as all attempts with *meso*-substituted ligands featured decomposition-related impurities. Here, the choice of bismuth precursor appeared rather negligible as similar amounts of impurities were estimated for $BiCl_3$ and $BiBr_3$ based on ^{1}H NMR data.

One particularly interesting finding was made for the reaction of **L1**^{Li} with $PhBiCl_2$, resulting in the formation of a mixed BIDIPY complex (Scheme 30). The proposed molecular structure of **1Bi**^{Ph} was further supported by X-ray diffraction analysis of a single crystal obtained from the reaction mixture. This result was rather serendipitous as the initial goal was to prepare a diphenyl substituted Bi(III) dipyrrin starting from Ph_2BiCl. Synthesis of diphenyl bismuth chloride was performed according to Barton *et al.*[167] However, the etheral reaction mixture was mistakenly used for the next step, which contained a mixture of $PhBiCl_2$ and Ph_2BiCl based on retroactive ^{1}H NMR analysis.[168]



Scheme 30: Redistribution reaction between $BiPh_3$ and $BiCl_3$ (1). Attempted synthesis of **1Bi**^{Ph} (2).

NMR analysis of the reaction mixture after a work-up consisting of solvent removal under reduced pressure, washing with *n*-hexane and filtration through celite® revealed a mixture of three compounds which were identified as **1Bi**^{Ph}, **L1** and $BiPh_3$ (Figure 41). Unfortunately, removal of **L1** and triphenylbismuth was ineffective through celite® filtration and several *n*-hexane washings, suggesting a potential interaction between the two compounds as well as the need of a different purification method. After 12 h a slight increase of **L1** and $BiPh_3$ was noted based on ^{1}H NMR spectroscopy, thus indicating slow decomposition of **1Bi**^{Ph} in solution. The solid-state structure of **1Bi**^{Ph} featured a distorted square pyramidal geometry around bismuth with two μ_2-bridging chlorido ligands and **L1** occupying the equatorial position whereas the phenyl group is in apical position (Figure 41). Interestingly, the bismuth centre is significantly shifted out of the dipyrrin ligand plane by 1.174(3) Å, possibly due to steric effects.

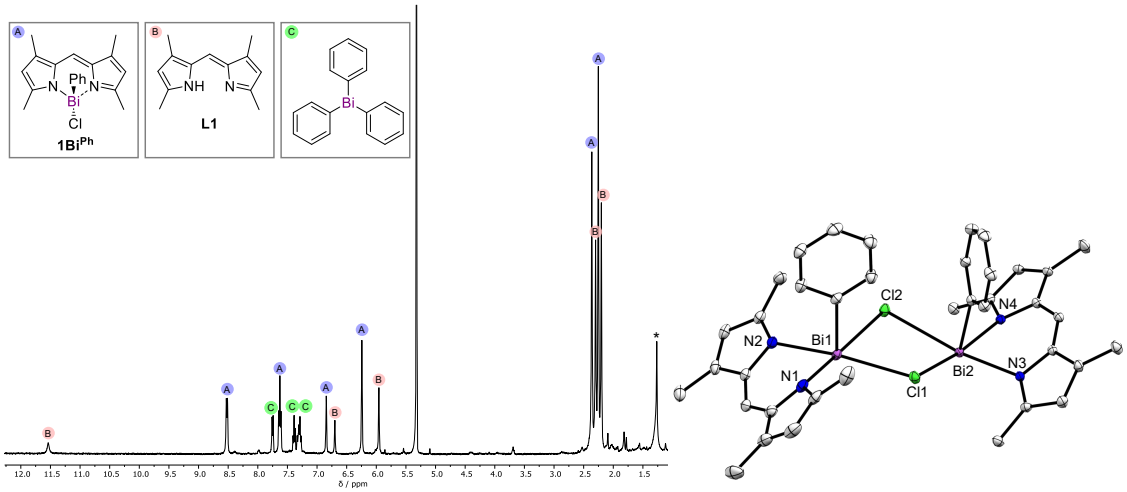
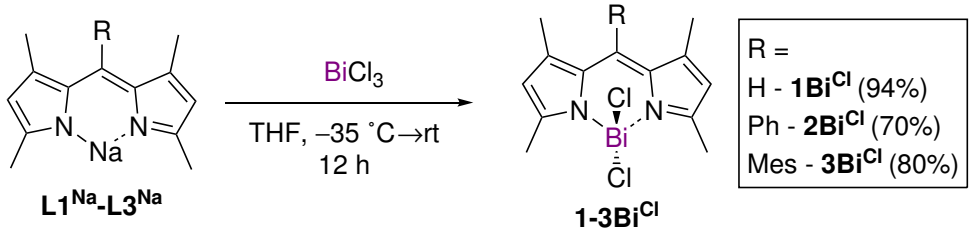


Figure 41: ^{1}H NMR spectrum (400 MHz) of reaction mixture obtained from attempted synthesis of **1Bi^{Ph}** in CD_2Cl_2 (left). Assignments of identified compounds to ^{1}H resonances are shown by colours and (*) marks *n*-hexane. X-ray solid-state structure of **1Bi^{Ph}** obtained from the reaction mixture (right). Hydrogen atoms were omitted for clarity and thermal ellipsoids were set to a 50% probability level.

As the presence of hexamethyldisilazane was suspected as a potential cause for BIDIPY decomposition, a different approach was chosen. Therefore, isolated sodium dipyrrinato **L1^{Na}**-**L3^{Na}** (see section 2.2, Scheme 19) were tested as suitable precursors to access the corresponding BIDIPY complexes. Indeed, reaction of equimolar amounts of sodium dipyrrinato salt with $BiCl_3$ or $BiCl_3$-mesitylene complex led to a clean conversion of the desired BIDIPYs **1**-**3Bi^{Cl}** in THF (Scheme 31).[169] Over the course of 12 h at room temperature, the bismuth complexes precipitated as crystalline solids from the reaction mixtures and were isolated in good yields. NMR data of the BIDIPY complexes showed THF despite thorough drying under reduced pressures, suggesting dative interaction between the ether function and the bismuth centre.



Scheme 31: Successful procedure for the synthesis of BIDIPY complexes **1Bi^{Cl}**-**3Bi^{Cl}**.

Suitable single crystals for X-ray diffraction analysis of all new BIDIPY complexes were obtained from *n*-hexane/THF mixtures. As already observed by NMR spectroscopy, a coordination of π-donating solvents, *i.e.* THF or 1,4-dioxane, was present in the X-ray solid-state structures of **1Bi^{Cl}** (Figure 42). As for antimony, a bending of the chlorido

ligands of **1Bi^{Cl}** was observed, hence deviating from an ideal Cl1−Bi1−Cl2 bond angle of 180°. In the case of the BIDIPY complexes this observation can be clearly attributed to halogen bonding within the symmetric units of the measured solid-state structures. The bending is further increased through ether coordination, as seen from the solid-state parameters of **1Bi^{Cl}**.

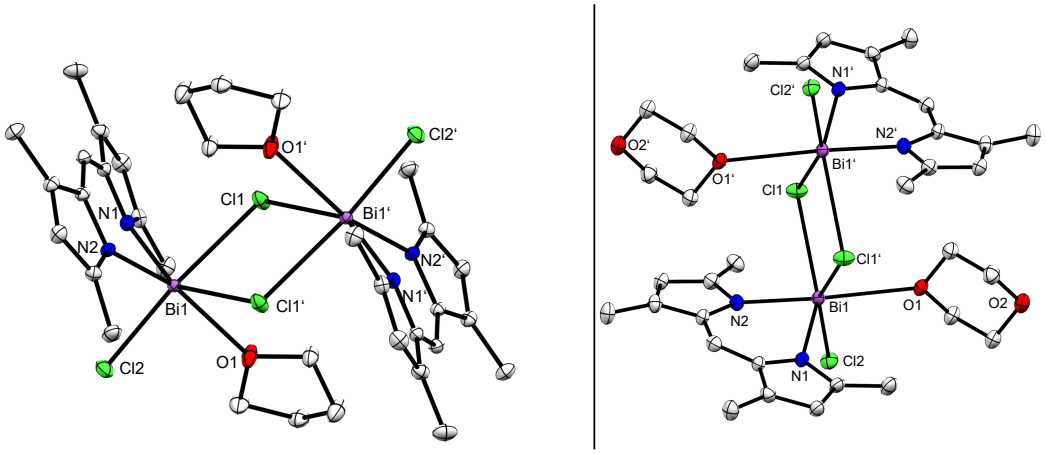


Figure 42: Symmetric unit representation of X-ray solid-state structure of **1Bi^{Cl}** obtained from a THF/*n*-hexane mixture (left) and from a 1,4-dioxane/*n*-hexane mixture (right). Hydrogen atoms were omitted for clarity and thermal ellipsoids were set to a 50% probability level.

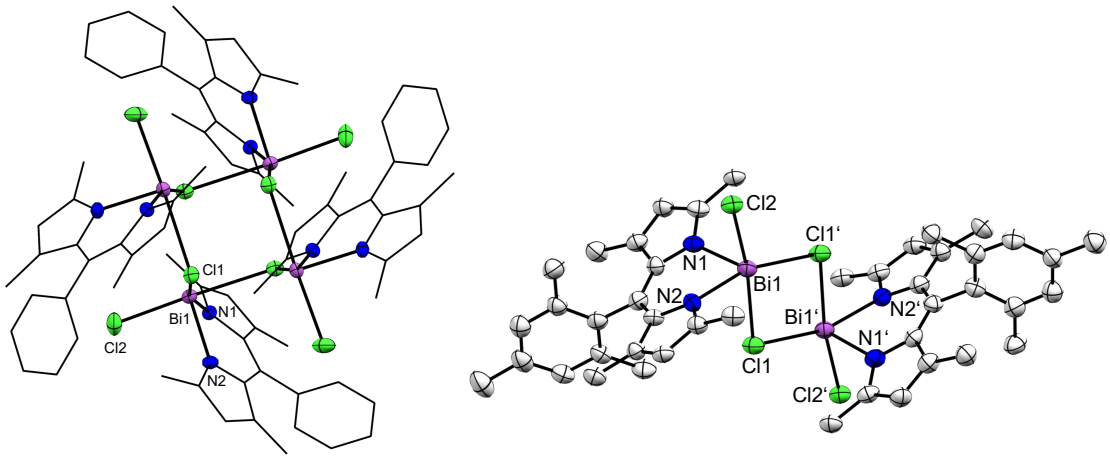
For complex **2Bi^{Cl}**, a symmetric unit consisting of a halogen μ_2-bridged tetramer was found (Figure 43a). In contrast to the other BIDIPY complexes, the asymmetric unit of **3Bi^{Cl}** featured more than one BIDIPY molecule due to the core Bi1−Cl1−Bi1'−Cl1' subunit not being perfectly symmetric (Figure 43b). An overview of important solid-state parameters of BIDIPY complexes is presented in Table 5.

Table 5: Selected bond lengths and angles for BIDIPY complexes. The mean plane (MPLN) is defined by the five atoms included in the binding pocket of the dipyrrin ligands.

	Cl1−Bi−Cl2 (°)	N1−Bi−N2 (°)	avg. Bi−Cl[a] (Å)	Bi−N1 (Å)	Bi−N2 (Å)	MPLN··Bi (Å)
1Bi^{Cl} [b]	153.4(1)	81.5(1)	2.703(1)	2.256(2)	2.269(2)	0.758(2)
1Bi^{Cl} [c]	152.8(1)	81.7(2)	2.715(2)	2.242(5)	2.244(5)	0.753(7)
1Bi^{Ph}	–	79.9(1)	2.929(1)	2.310(2)	2.318(2)	1.174(3)
2Bi^{Cl}	170.8(1)	80.2(1)	2.705(1)	2.218(2)	2.204(2)	0.814(3)
3Bi^{Cl}	165.3(1)	80.6(2)	2.690(2)	2.223(7)	2.218(7)	0.748(10)

[a] Including Cl1 and Cl2. [b] Data for THF adduct structure. [c] Data for 1,4-dioxane adduct structure.

Overall, all analyzed BIDIPY complexes exhibited comparable bond parameters, with **1Bi^{Ph}** being an exception due to the different geometry around bismuth induced by the phenyl group. All solid-state structures displayed two similar Bi1−N bond lengths but a more acute N1−Bi1−N2 bond angle and a larger distance between ligand mean plane and central atom as compared to SBIDIPY complexes. These findings are comparable with the deviation observed for **1Sb^{F}**, thus indicating strong intermolecular halogen interactions as a cause for the geometrical perturbations.

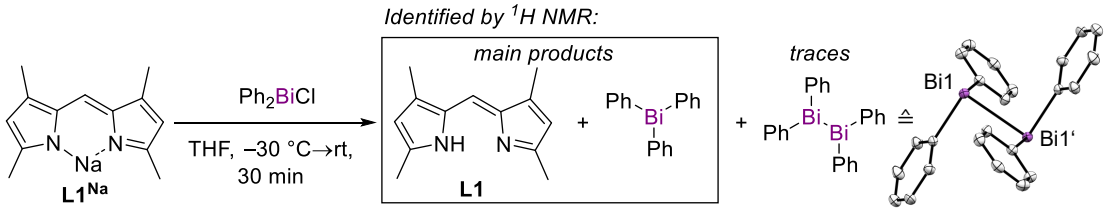


(a) 2Bi^{Cl} **(b) 3Bi^{Cl}**

Figure 43: Symmetric unit representation of X-ray solid-state structure of (a) **2Bi^{Cl}** with the carbon-framework of the ligand depicted as wireframes. X-ray solid structure of (b) **3Bi^{Cl}**. Hydrogen atoms were omitted for clarity and thermal ellipsoids were set to a 50% probability level for both.

Synthesis of the fluoride-substituted BIDIPY was attempted starting from **L1^{Li}** or **L1^{Na}** and 2.00 equiv. of BiF_3 in THF but no reaction was observed due to the insolubility of the bismuth salt even at reflux. Unfortunately, halogen exchange of **1Bi^{Cl}** with an excess of AgF in CD_2Cl_2 was also unsuccessful.

Encouraged by the promising NMR data and X-ray solid-state structure obtained from the attempted synthesis of **1Bi^{Ph}**, diphenylbismuth chloride was reacted with **L1^{Na}**. A gradual colour change from yellow-orange to red was observed for the 1:1 reaction of **L1^{Na}** with Ph_2BiCl in THF (Scheme 32). ^{1}H NMR analysis of the crude product in C_6D_6 hinted at the formation of **L1** and triphenylbismuthane $BiPh_3$ as the main products. Moreover, a single crystal of the dibismuthane Bi_2Ph_4 was obtained from a benzene/*n*-hexane mixture of the crude product, indicating that reduction of Bi(III) to Bi(II) may occur in the presence of **L1^{Na}**. Nonetheless, the dibismuthane was only visible in trace amounts by ^{1}H NMR.[170]

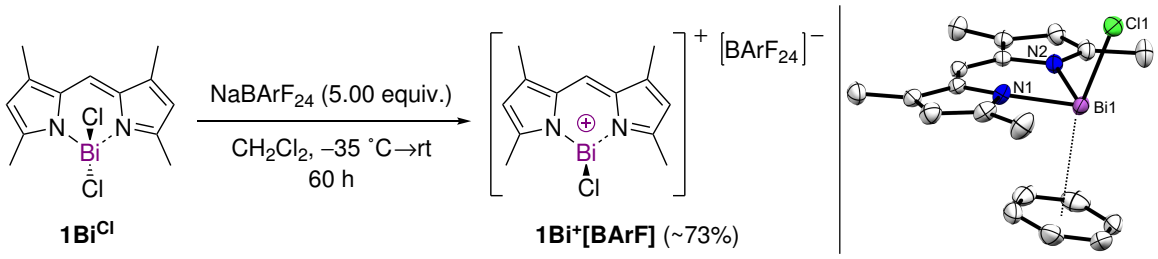


Scheme 32: Reaction of Ph_2BiCl with sodium dipyrrinato salt **L1^{Na}**. X-ray solid-state structure of Bi_2Ph_4 is shown on the right. Hydrogen atoms were omitted for clarity and thermal ellipsoids were set to a 50% probability level.

The exact mechanism for the formation of $BiPh_3$ and Bi_2Ph_4, however, is unclear as the proton source involved in the formation of **L1** remained unknown.

2.5. Halide abstraction

Based on the previous success with SBIDIPY complexes, halide abstraction from **1Bi^{Cl}** was targeted as a reactivity to modify the coordination environment of BIDIPY complexes. Straightaway, addition of $NaBArF_{24}$ to CH_2Cl_2 solution of **1Bi^{Cl}** resulted in a slow change of colour from red to dark red and a selective shift by ^{1}H NMR spectroscopy (Scheme 33). Single crystals were obtained from the CH_2Cl_2 after slow evaporation mixed with benzene, which further confirmed the structure of the bismuthonium complex **1Bi$^+$[BArF]** (Scheme 33). It is important to point out that the formation of **1Bi$^+$[BArF]** required a much longer reaction time and an excess of $NaBArF_{24}$ (5.00 equiv.) as compared to **1Sb$^+$[BArF]**. Unfortunately, despite multiple synthesis attempts and thorough washing with *n*-pentane and *n*-hexane/benzene, the desired product was obtained with impurities (ca. 10%).



Scheme 33: Synthesis of **1Bi$^+$[BArF]** (left) and X-ray solid-state structure of **1Bi$^+$[BArF]** (right). Hydrogen atoms and $BArF_{24}^-$ counterion were omitted for clarity, and thermal ellipsoids were set to a 50% probability level.

Unlike the antimony analogue, the X-ray solid-state structure of **1Bi$^+$[BArF]** displayed not only apical coordination of benzene to the bismuth centre but also a weak interaction of the latter with two fluorides of the $BArF_{24}^-$ counterion, resulting in an overall

pseudo-octahedral coordination environment around the bismuth (Figure). This finding underlines the extended coordinating ability of bismuth as compared to antimony due to the difference in size and electrophilicity.[171]

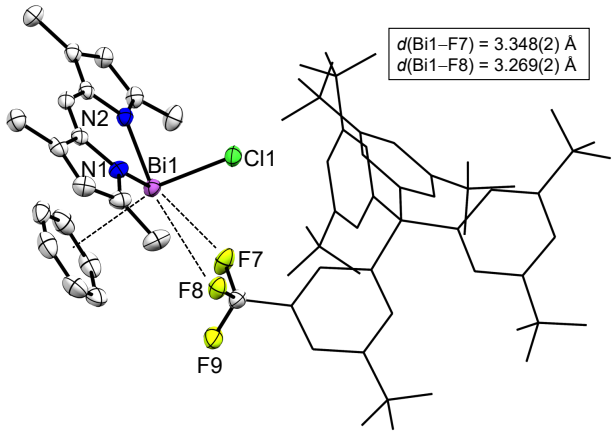


Figure 44: X-ray solid-state structure of **1Bi$^+$[BArF]** with weak interactions highlighted by dashed lines. Hydrogen atoms were omitted for clarity and thermal ellipsoids were set to a 50% probability level. Aside from the selected trifluoromethyl group, the $BArF_{24}^-$ counterion is depicted as wireframe.

As for SBIDIPY, salt metathesis reaction of **1Bi^{Cl}** was further attempted with $AgSbF_6$. Addition of an equimolar amount of $AgSbF_6$ to a cold solution of **1Bi^{Cl}** in CH_2Cl_2/1,4-dioxane mixture led to a gradual colour change from red to dark red. After 30 min at room temperature the solvent was removed under reduced pressure and the crude product analyzed by ^{1}H NMR spectroscopy. The ^{1}H NMR spectrum displayed two compounds in an approximate ratio of 1:1 (Figure 45). First, a species with slightly downfield-shifted ^{1}H resonances (H^a at 7.33 and 6.62 ppm) was present which likely stems from the bismuthonium complex **1Bi$^+$[SbF$_6$]**. The second set of ^{1}H resonances displayed a broad singlet at 9.87 ppm which is likely attributed to protonated ligand **L1-HX** (with unknown anion X) resulting from complex decomposition. Unfortunately, filtration of the mixture through celite® did not lead to any notable improvements with respect to sample purity. Nonetheless, suitable single crystals for X-ray diffraction analysis were obtained through slow evaporation of a CH_2Cl_2/1,4-dioxane mixture of the crude product at room temperature, confirming the presence of a bismuthonium complex **1Bi$^+$[SbF$_6$]** (Figure 46).

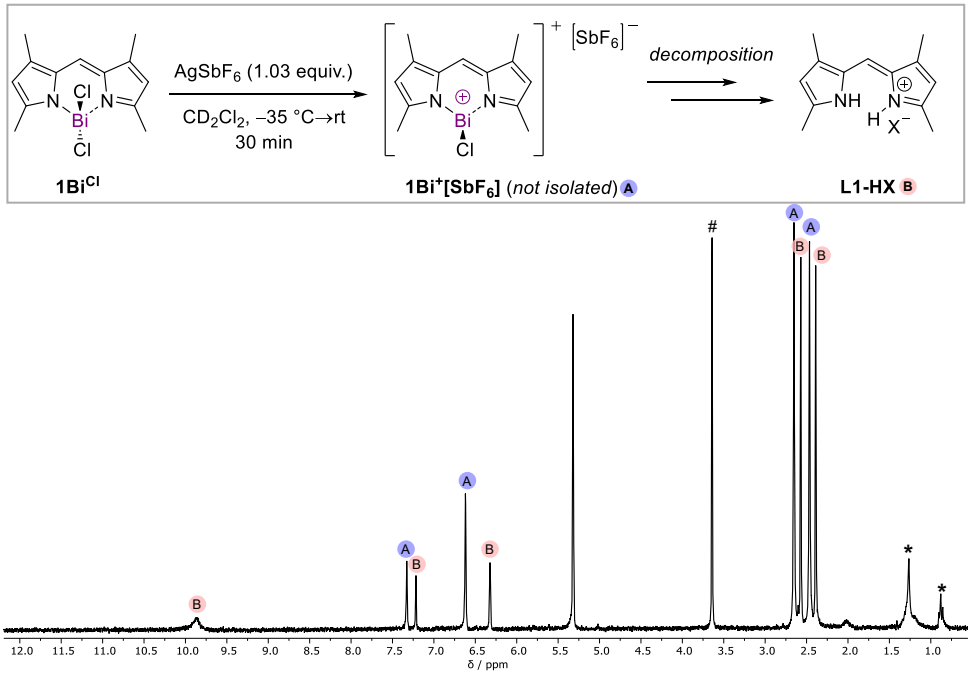


Figure 45: Reaction of **1Bi^{Cl}** with $AgSbF_6$. ^1H NMR spectrum (300 MHz) of crude product in CD_2Cl_2; the sign ($^{\#}$) marks coordinated 1,4-dioxane whereas * marks *n*-hexane.

The solid-state structure of **1Bi$^+$[SbF$_6$]** contained one coordinated 1,4-dioxane molecule per symmetric unit bridging two **1Bi$^+$[SbF$_6$]** complexes. Furthermore, the solid-state structure featured well-visible secondary interactions between fluorides of the SbF_6^- anion and the bismuth centre. Due to disorder in the SbF_6^- unit, the number of coordinated fluorides was only estimated as one (d(Bi−F) = 2.853(10) Å), thus resulting in an overall pseudo-trigonal bipyramidal geometry around bismuth.

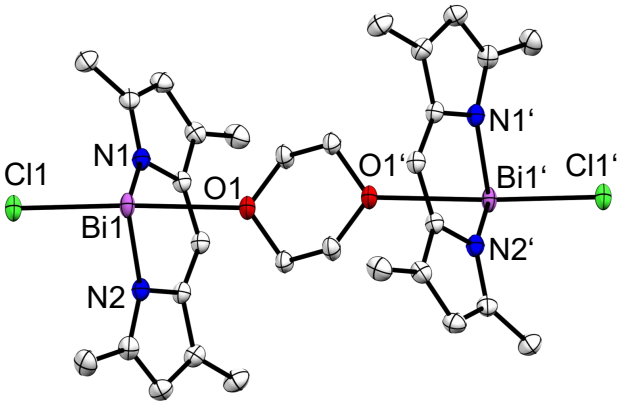


Figure 46: Symmetric unit representation of X-ray solid-state structure of **1Bi$^+$[SbF$_6$]**. Hydrogen atoms and SbF_6^- counterions were omitted for clarity, and thermal ellipsoids were set to a 50% probability level.

2.6. Investigation of spectroscopic properties

First attempts to obtain UV/vis data for BIDIPY complexes were unsuccessful as full decomposition was observed for all isolated Bi-complexes at low concentrations (circa 16 μM) in CH_2Cl_2, resulting in the absorption spectra shown in Figure 47.

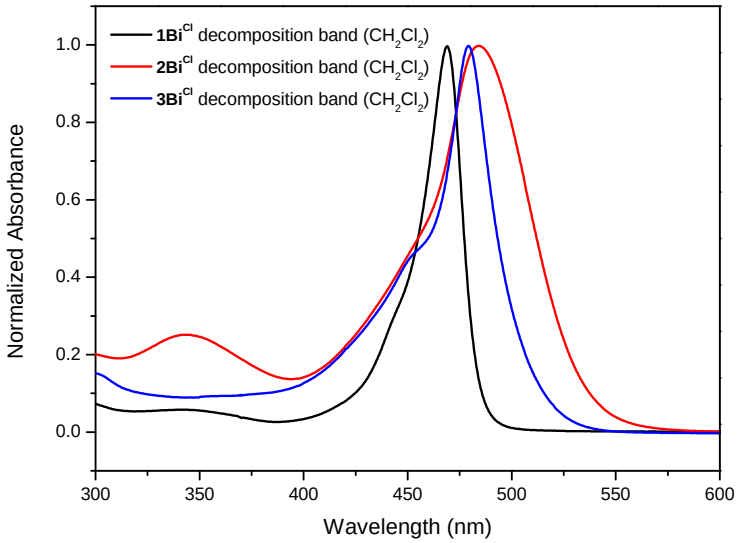


Figure 47: Overview of normalized absobance spectra of fully decomposed BIDIPY complexes **1Bi^{Cl}**-**3Bi^{Cl}** in CH_2Cl_2 at room temperature.

In order to prevent decomposition, stock solutions of all BIDIPY chromophore were handeled at −35 °C and measurements of UV/Vis spectra were conducted at 5 °C while also using samples with increased concentrations (circa 0.2 mM) as aggregation effects were hypothesized to have a non-negligible effect on solution stability of BIDIPYs. In this way, the spectra depicted in Figure 48 were obtained, displaying absorption maxima in the region of λ_{abs} = 505 nm in CH_2Cl_2, similar to the SBDIPY analogues, albeit showing a hypsochromically shifted broader shoulder.

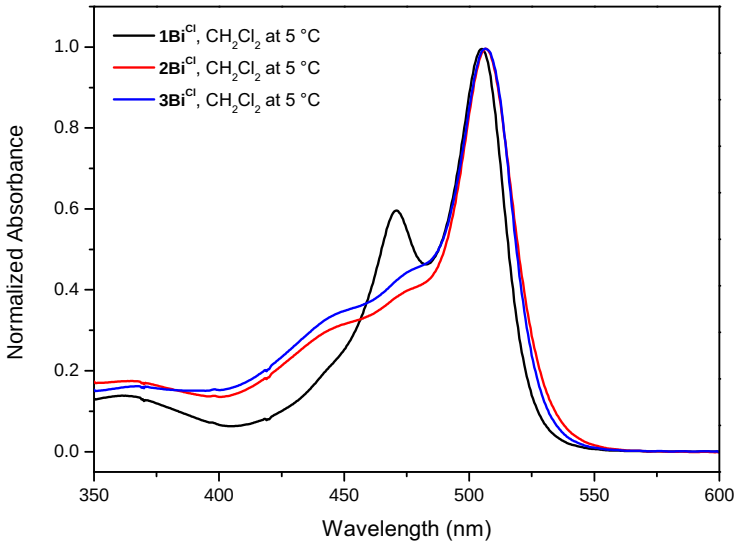


Figure 48: Overview of normalized absorbance spectra of BIDIPYs **1Bi^{Cl}**-**3Bi^{Cl}** in CH_2Cl_2 at 5 °C.

For complexes **1Bi^{Cl}** and **2Bi^{Cl}** no appreciable emission was detected in solution, while **3Bi^{Cl}** displayed very weak emission at λ_{emi} = 535 nm (Figure 49). Overall, the spectroscopic properties of BIDIPY complexes were more difficult to evaluate as compared to SBIDIPY chromophores due to a more pronounced decomposition.

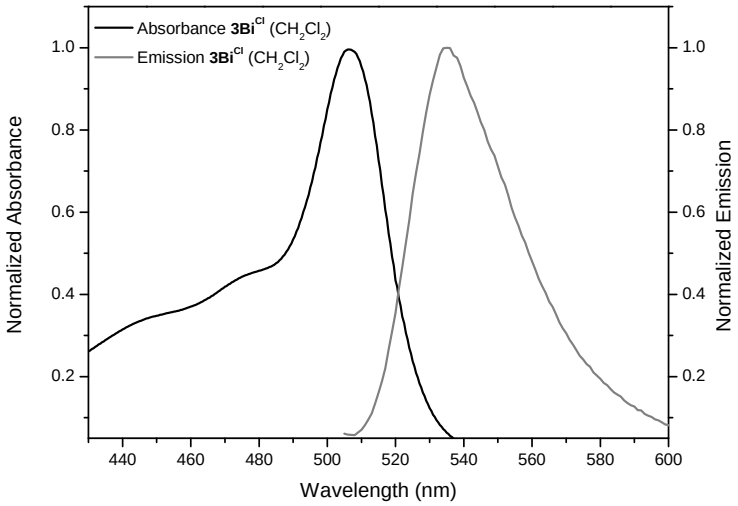


Figure 49: Normalized absorbance and emission spectra of **3Bi^{Cl}** in CH_2Cl_2 at 5 °C.

2.7. Computational investigation[141]†

In order to get additional insight into the electronic properties of the novel SBDIPY and BIDIPY chromophores, the first electronic transitions of **L1** dipyrrin complexes with different main group centres were computed at the CPCM-SCS-CIS(D)/def2-TZVPP//r^{2}SCAN-3c level using CH_2Cl_2 or toluene in the implicit CPCM solvent model as featured in the ORCA software package (Figure 50).[141,148,172,173] In addition to the experimental evidence for both SBDIPY and BIDIPY complexes, the estimated transition energies and the contributing frontier molecular orbitals match well with the $\pi \rightarrow \pi^\star$ of BODIPY **1B^F**. The calculated transition energies accentuate a minimal influence of the type of central atom and the halogens on the transition character. This outcome was further fitting for the literature-reported GADIPY (**A91**) and PHODIPY (**A106**) chromophores, for which also a negligible effect of the central atoms on the Stokes shift was found.

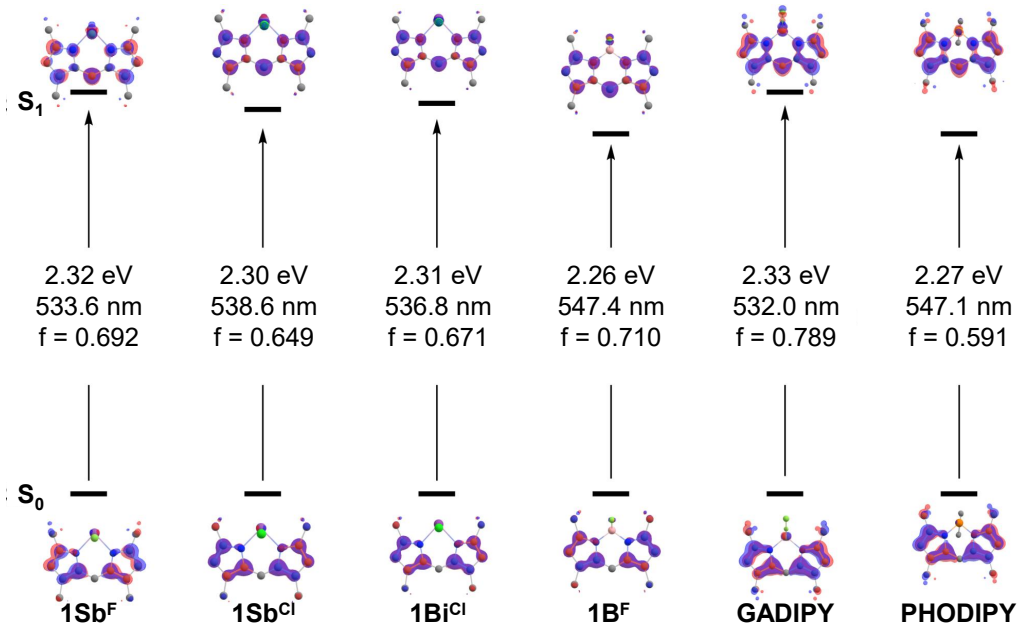


Figure 50: Computed first electronic transitions of selected main group dipyrrin complexes at the CPCM-SCS-CIS(D)/def2-TZVPP//r^{2}SCAN-3c level. The Natural Transition Orbitals contributing to the main $\pi \rightarrow \pi^*$ excitations are shown with predicted energies and oscillator strengths.[141]†

2.8. Conclusion and future work

This chapter covered the initial progress made in the field of heavy pnictogen dipyrrin complexes and described the successful development of two methods to access antimony and bismuth-based BODIPY analogues, SBDIPY and BIDIPY (Figure 51). For SBDIPY chromophores, a one-pot procedure was established for the synthesis of complexes bearing different halide substituents **1Sb^{X}** (X = F, Cl and Br), as well as for ligand variations with different *meso*-substituents (**L1**-**L3**). In this way, the first direct antimony analogue of BODIPY, **1Sb^{F}**, was successfully isolated and characterized, revealing unforeseen aggregation behaviour both in solid-state and solution. The synthesis of SBDIPY chromophores with substituents other than halides was found to be challenging and requires further investigation of possible Sb(III) precursors, such as aryl antimony dihalides. Oxidation of SBIDIPY complexes or attempts of complex synthesis starting from Sb(V) sources were unsuccessful, thus preventing access to higher oxidation state SBDIPYs. An alternate route to synthesize BIDIPY complexes using Na-dipyrrinato salts (**L1^{Na}**-**L3^{Na}**) was developed as sample decomposition was observed with the previously described method (Figure 51).

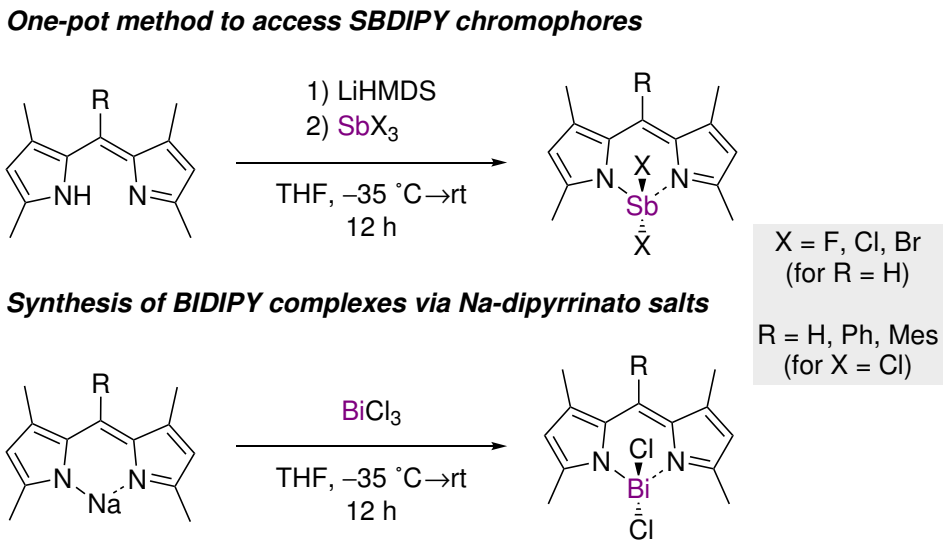


Figure 51: General reaction scheme for the synthesis of pnictogen dipyrrin complexes starting from antimony and bismuth halides.

The isolated bismuth complexes displayed an increased instability in solution based on NMR and UV/vis data but also featured striking halide aggregation in solid-state structures. Respective SBDIPY complexes showed more promising spectroscopic properties as some displayed notable fluorescence emission. Nonetheless, all SBDIPY chromophores showed a gradual decomposition to a protonated ligand byproduct **L1-HX**, potentially caused by trace amounts of water in solution. The decom-

position was observed to be most pronounced for **1Sb^{F}** and slower in the case of **1Sb^{Br}**. These findings complicate further applications of pnictogen dipyrrins and require changes of the ligand scaffold to improve complex stability (Figure 52). Once more robust chromophores are developed, the new heavy pnictogen dipyrrin complexes can be tested as photocatalysts since BODIPYs have shown promising properties in this direction.[112] With regard to photochemistry, the effect of the heavy central atom is particularly interesting to further explore. Therefore, improvement of the stability pnictogen dipyrrin complexes and evaluation of their use as photocatylsts was targeted as the project aim of the following chapter.

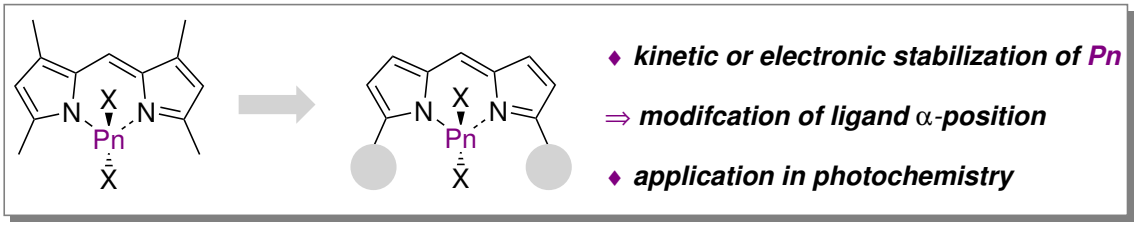


Figure 52: Outlook on enhanced complex stability through ligand modification and aim for the following chapter.

3. Evaluation of new dipyrrin ligands

The data presented in the following chapter has been partially published in: A. Korzun, M. J. McKee, H. Neugebauer, O. Green, G. Schnakenburg, S. Grimme, N. Kornienko and A. Bismuto, *Inorg. Chem.* **2025**, *64*, 15667-15679.[174] All X-ray solid-state structures shown in this chapter were measured and refined by Dr. Gregor Schnakenburg if not otherwise noted.

A set of α-substituted dipyrromethenes was selected as synthetitc targets to evaluate the suitability of different ligand variations for the formation and stabilization of pnictogen dipyrrin complexes (Figure 53).

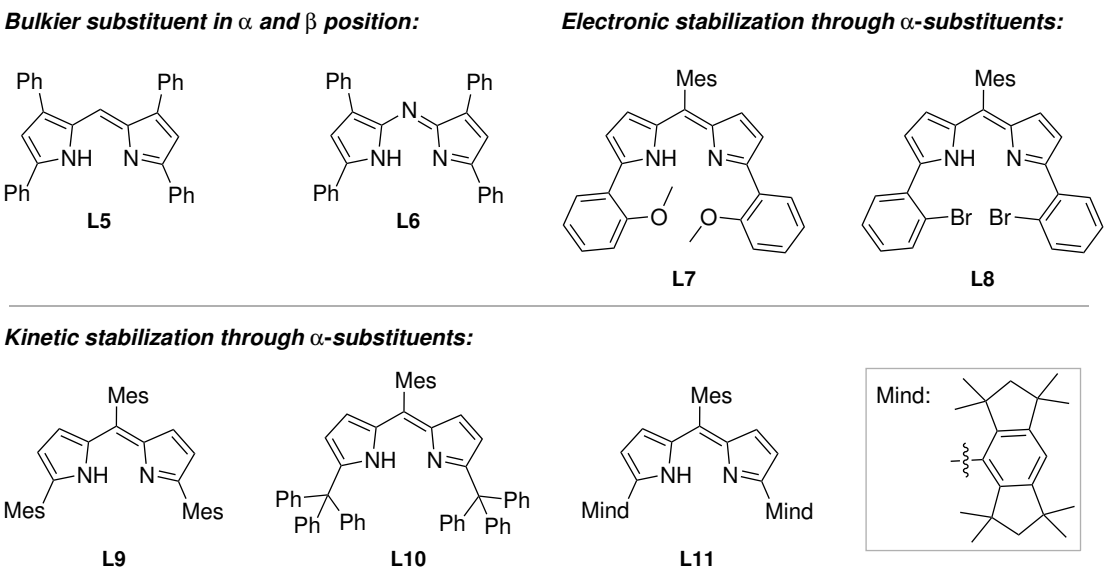
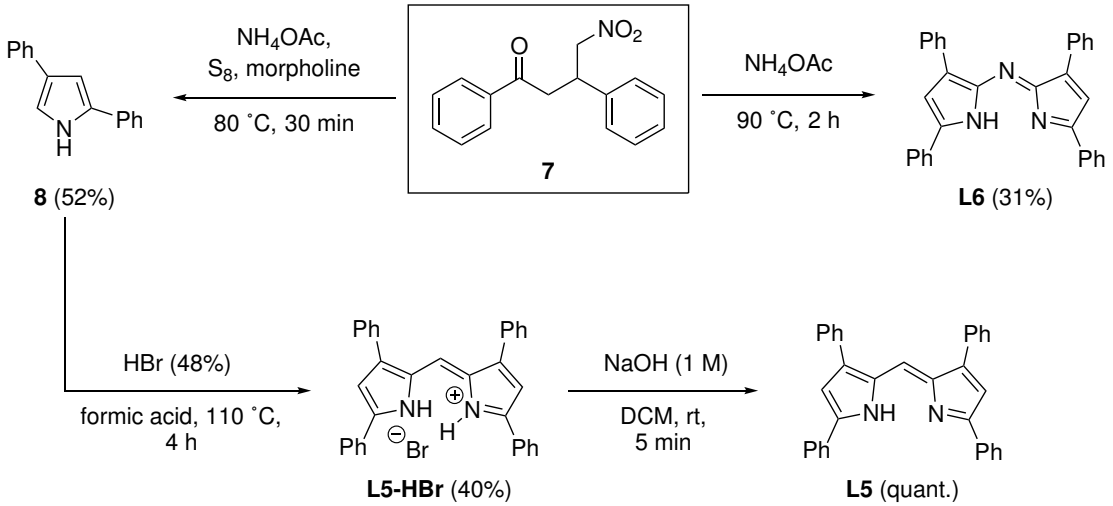


Figure 53: New ligand targets for the synthesis of pnictogen dipyrrin complexes.

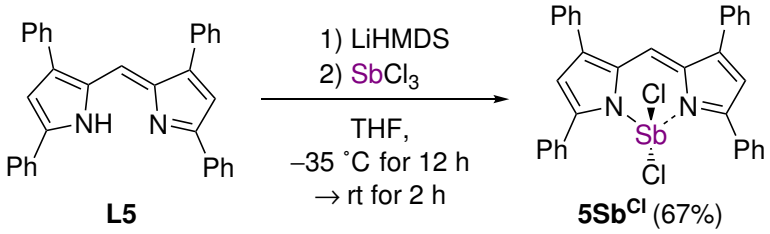
Dipyrromethenes **L5** and **L6** are literature-known ligands mainly used as BODIPY dyes.[175,176] The ligands feature bulkier substituents than **L1** in both α- and β-positions. Furthermore, **L6** is an azadipyrromethene variation of **L5**, thus having a slightly decreased donor strength and a bathochromic shift in absorption due to the *meso*-nitrogen.[177] Both, **L5** and **L6**, were prepared starting from 4-nitro-1,3-diphenylbutan-1-one **7** (Scheme 34). The condensation of **7** with an excess of ammonium acetate gave direct access to **L6** in poor yield.[178] In the presence of morpholine and sulfur, however, the reaction of **7** with ammonium acetate led to the formation of **8** in moderate yield.[179] Using formic acid and aqueous HBr (48%), condensation of pyrrole **8** gave **L5-HBr** in moderate yield. Treatment of the HBr-salt with an aqueous NaOH solution (1 M) resulted in a quantitative conversion to the free base **L5**. The overall

yields for both ligands were slightly lower as compared to literature due to complications during sample purifications.[177–179]



Scheme 34: Synthesis of **L5** and **L6**.

As the isolation of Sb-dipyrrin complexes had been more facile as compared to the analogous bismuth complexes, the synthesis of new SBDIPY chromophores was prioritized with the selected dipyrromethene variations. Fortunately, the previously successful protocol for SBDIPY synthesis was also applicable for dipyrrin **L5**, affording antimony complex **5Sb^{Cl}** in good yield (Scheme 35).



Scheme 35: Synthesis of **5Sb^{Cl}**.

As a consequence of the extended π-conjugation through the phenyl substituents, SBDIPY chromophore **5Sb^{Cl}** displayed a bathochromic shift as compared to **1Sb^{Cl}**. The SBDIPY complex exhibited a maximum absorption at λ_{abs} = 556 nm and a single emission at λ_{emi} = 602 nm in CH_2Cl_2, resulting in a Stokes shift of 1374 cm^{-1} (Figure 54). The Stokes shift of **5Sb^{Cl}** is considerably larger than the one recorded for **1Sb^{Cl}**. Moreover, time-resolved UV/Vis spectroscopy of **5Sb^{Cl}** in CH_2Cl_2 revealed a gradual change to a new band with slight bathochromic shift and higher relative absorbance, thus indicating the formation of a new species with higher molar absorptivity (Figure 54). Once again, the newly formed band at λ_{abs} = 560 nm showed a significant overlap with the absorption maximum of **L5-HBr** (λ_{abs} = 562 nm), which

suggests a similar decomposition process as observed for **1Sb^{Cl}** in THF.

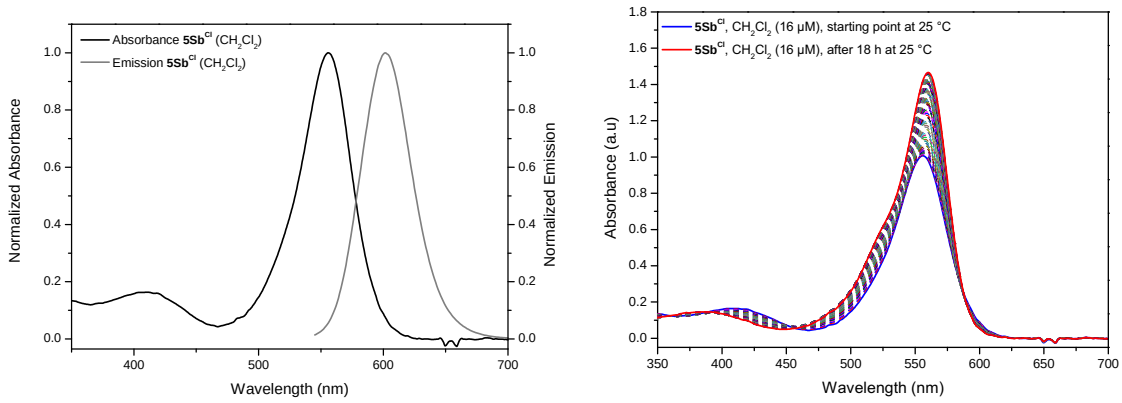
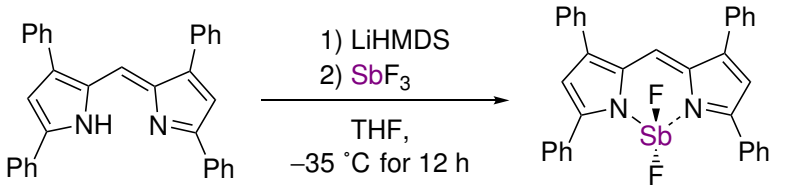


Figure 54: Normalized absorption and emission (λ_{exc} = 520 nm) profile of **5Sb^{Cl}** in CH_2Cl_2 (left) and UV/Vis stability analysis of **5Sb^{Cl}** in CH_2Cl_2 (right).

As a final proof-of-concept, the synthesis of the hitherto difficult to isolate fluoride-substituted SBDIPY complex was attempted (Scheme 36). Despite successful complexation based on ^{1}H NMR findings, however, the complex **5Sb^{F}** could not be isolated in analytically pure form due to the presence of protonated side-product throughout multiple attempts. Similarly to the observed decomposition of **1Sb^{F}** but significantly downfield shifted, ^{19}F NMR of **5Sb^{F}** displayed two broad signals at −162 ppm and −186 ppm, further indicating that the observed impurity in the ^{1}H NMR of **5Sb^{F}** resulted from decomposition. Unfortunately, no suitable single crystals for X-ray diffraction analysis were obtained, leaving the structural differences between **L5** and **L1** SBDIPY complexes unknown. Besides the shift in absorption and emission, however, only a minor effect of **L5** on complex stability can be assumed based on UV/Vis and NMR data.



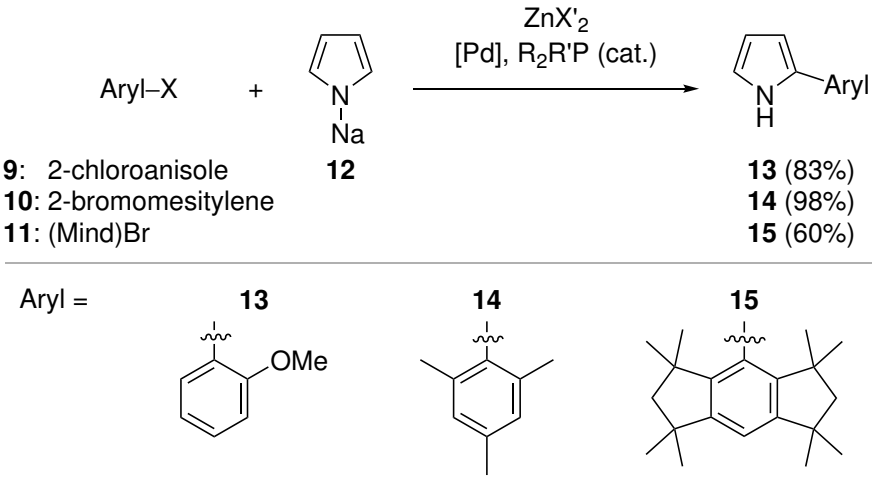
L5 **5Sb^{F}**

unselective, not isolable

Scheme 36: Synthesis of **5Sb^{F}**.

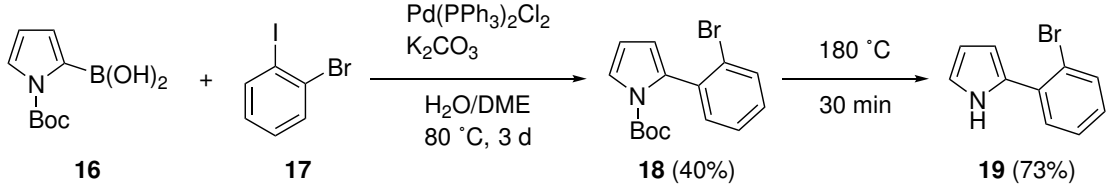
In contrast to **L5**, complexation of $SbCl_3$ with **L6** was found to be unproductive. Although deprotonation of the ligand in THF-d_8 underwent smoothly in the presence of LiHMDS, addition to an equimolar amount of $SbCl_3$ resulted in no change in the ^{1}H NMR spectrum. Ultimately, this resulted in the back-formation of **L6** after several days.

Due to the higher effort involved in the synthesis and purification of the ligands, as well as no notable improvements with respect to stability and isolation of Sb dipyrrins, **L5** and **L6** were not further considered. Instead, α-substituted dipyrrins **L7**-**L11** were prepared with the aim of achieving improvements in complex stability. Dipyrromethenes **L7**-**L11** were prepared following a two-step protocol. First, pyrroles with substituents in the 2-position were synthesized, followed by a one-pot condensation reaction and oxidation with 2,3-dichloro-5,6-dicyano-1,4-benzoquinone (DDQ) to obtain dipyrrins **L7**-**L11**. Pyrroles **13**-**15** were prepared in good yields utilizing a Negishi-type coupling reaction of aryl halides **9**-**11** and sodium pyrrolide **12** in the presence of a zinc(II) salt and catalytic amounts of a palladium complex and phosphine ligand (Scheme 37).[180]



Scheme 37: Palladium-catalysed cross-coupling to access aryl-substituted pyrroles.

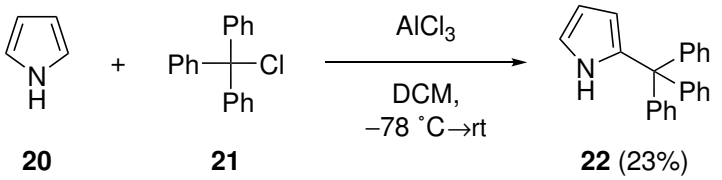
In order to access bromophenyl-substituted pyrrole **19**, a different synthetic route had to be employed.[181] Starting from boronic acid **16** and 1-bromo-2-iodobenzene **17**, Boc-protected pyrrole **18** was obtained in moderate yield *via* a palladium-catalysed cross-coupling reaction (Scheme 38). Heating of **18** to 180 °C under a stream of argon resulted in a selective conversion to pyrrole **19** in good yield (Scheme 38).



Scheme 38: Reaction scheme for synthesis of pyrrole **19**.

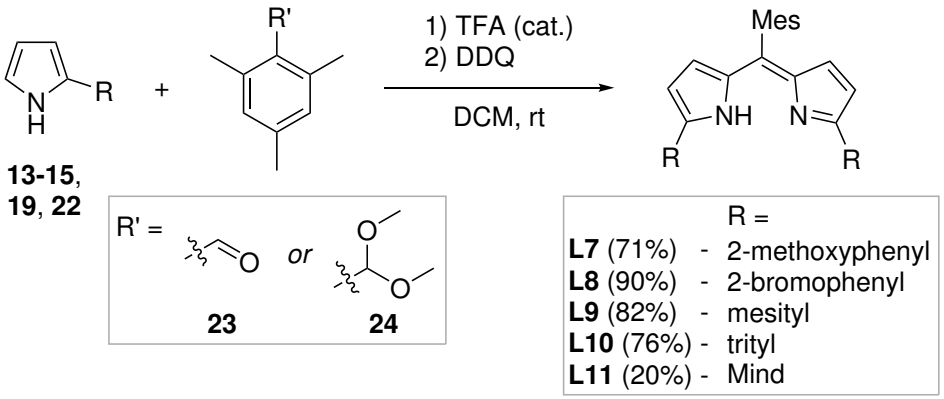
Lastly, trityl-substituted pyrrole **22** was prepared using Friedel-Crafts alkylation of 1*H*-pyrrole **20** with trityl chloride **21** in the presence of $AlCl_3$ (Scheme 39). The target compound was isolated in rather poor yield due to polymeric by-products that

substantially complicated the work-up and purification.



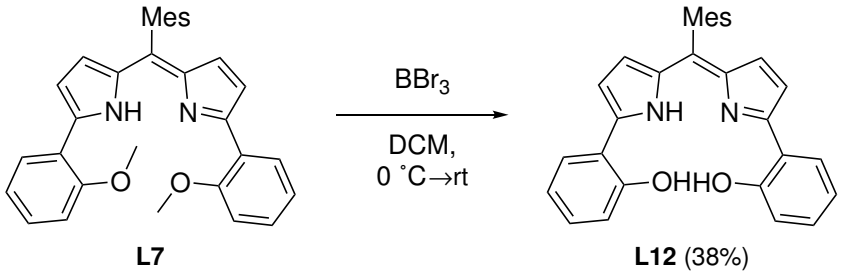
Scheme 39: Reaction scheme for synthesis of pyrrole **22**.

In the subsequent step, all substituted pyrroles were condensed with mesitaldehyde **23** or mesitaldehyde dimethyl acetal **24** using a catalytic amount of an acid, followed by oxidation with DDQ in a one-pot reaction to yield the respective dipyrrin ligands (Scheme 40). It is worth pointing out that for the synthesis of **L8**-**L10** acetal-protected mesitaldehyde **24** was used as an improvement in yield and purification was observed especially for **L8** compared to using **23** as a starting material. Possibly, the poor yield of **L11** could be increased by employing **24** instead of **23** for the condensation reaction.



Scheme 40: General reaction scheme for one-pot procedure to access dipyrrin ligands **L7**-**L11**.

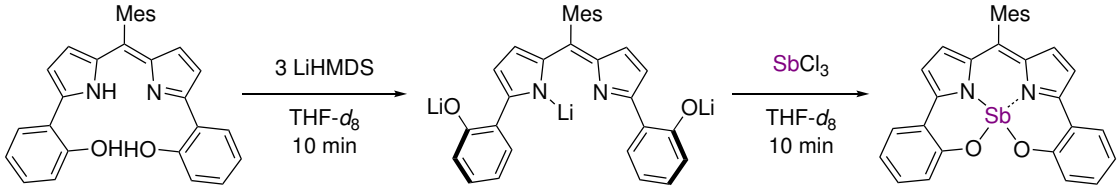
Dipyrromethene **L7** has thus far only been used as a ligand for BODIPY dyes but it has been more commonly utilized as a precursor in the synthesis of the trianionic "N_2O_2"-dipyrrin **L12**.[182,183] Ligand **12** was also prepared as part of this study *via* a demethylation reaction of **L7** in the presence of BBr_3 (Scheme 41).[183] The N_2O_2-dipyrrin motif has found widespread use as a ligand for transition metals, such as Zr,[184] Ti,[184] Co,[185] Cu,[186], Au,[186], Pt,[187] etc.,[188] as well as for various main group elements, such as Al,[183] Ga,[126] In,[126] Si,[136,189] Ge,[136,184] and Sn.[136,184] Significant contributions in this field have been made by the Nabeshima group who have recently also reported the incorporation of antimony into a N_2O_2-dipyrrin.[139,140]



L7 **L12** (38%)

Scheme 41: Synthesis of "N_2O_2"-dipyrrin **L12**.

Prior to the report of the first antimony N_2O_2-dipyrrin by Agou *et al.*, synthesis of tetracoordinate SBDIPY **12Sb** was attempted on NMR-scale using LiHMDS as a base (Scheme 42).[139,140]



L12 **L12^{Li}** **12Sb**

Scheme 42: Attempted synthesis of "N_2O_2" SBDIPY complex **12Sb**.

Fortunately, addition of 3.10 equivalents of LiHMDS to a THF-d_8 solution of **L12** led to the full deprotonation of the ligand, evident by the disappearance of the N−H ^{1}H resonance at 11.35 ppm (Figure 55). Combining the deprotonated ligand with a solution of $SbCl_3$, resulted in an immediate colour change to light blue and a selective shift of ^{1}H resonances, likely indicating the formation of **12Sb**. Interestingly, after reaction with $SbCl_3$, the ^{1}H and ^{13}C resonances of the mesityl CH_3 groups were split into three signals instead of the usually observed two, thus hinting at a more restricted rotation of the mesityl substituent upon complexation. This phenomenon was also observed for a similar system in the recent study conducted by Agou *et al.*[140]

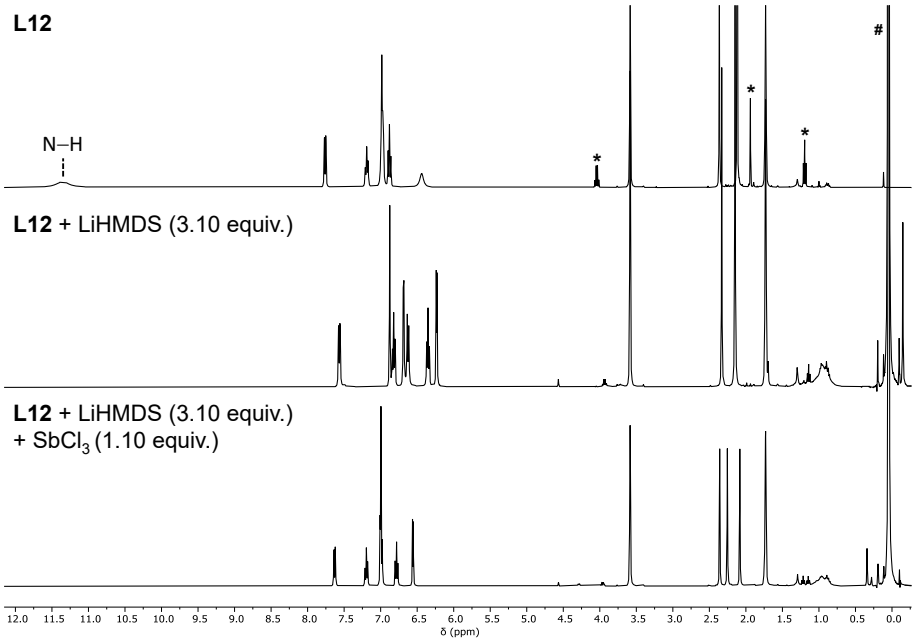


Figure 55: Stacked ^{1}H NMR spectra (400 MHz, THF-d_8) of **L12** (top), after addition of 3.10 equiv. LiHMDS (middle), followed by addition to 1.10 equiv. $SbCl_3$ (bottom). The sign (*) marks ethyl acetate, whereas (#) marks HMDS.

However, isolation of the target compound **12Sb** turned out to be difficult as removal of HMDS-related impurities by washing of the crude product with *n*-hexane was ineffective with the target compound appearing to be also partially soluble. Consequently, the presumed product **12Sb** was obtained only in a moderate yield (51%) and with trace amounts of HMDS-related impurities still present. Further structure elucidation was unfortunately not possible as crystallization attempts from THF, benzene or toluene solutions at room temperature were unsuccessful. As seen in the recent report of Agou *et al.*, a better approach to complexation could be realized by using a hydride base, such as NaH or KH, to minimize potential interactions of the product with residual amine.[140] Nonetheless, the moderate yields reported by the authors, suggest an overall cumbersome complexation with antimony and bismuth.[140] A preliminary attempt at synthesizing **12Sb** with NaH (5.00 equiv.) as a base in THF-d_8 showed rather selective conversion towards the presumed complex **12Sb** and should be tested on larger scale (Figure 56).

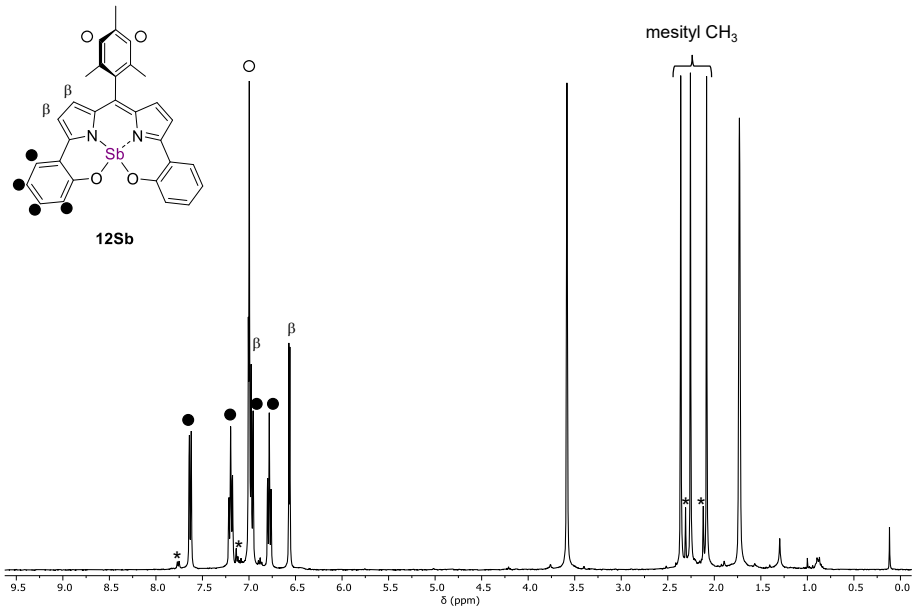


Figure 56: ^{1}H NMR (THF-d_8, 400 MHz) of crude product obtained from reaction of **L12** (20 mg, 0.045 mmol, 1.00 equiv.), NaH (5 mg, 0.23 mmol, 5.00 equiv.) and $SbCl_3$. THF (circa 5 mL) was added to **L12** and base at 0 °C. Upon warming to room temperature over the course of 40 min, the reaction mixture was cannula filtered onto a THF solution of $SbCl_3$ at 0 °C and the reaction mixture was evaporated to dryness. The sign (*) marks an unknown **L12**-related impurity while signals of presumed complex **12Sb** are assigned by signs.

Since **12Sb** showed a strikingly different colour in solution as compared to the ligand (**L12**), the compounds were analyzed by UV/Vis and photoluminescence spectroscopy (Figure 57). Both compounds showed a sharp absorption in the UV-region and a broad band consisting of two close-lying maxima in the visible region. The dipyrrin **L12** showed a maximum absorption at λ_{abs} = 541 nm, whereas **12Sb** displayed a significant bathochromic shift by 3287 cm^{-1} with a maximum at λ_{abs} = 658 nm. Furthermore, while no appreciable emission was detected for **L12**, **12Sb** featured a sharp emission at λ_{emi} = 697 nm.

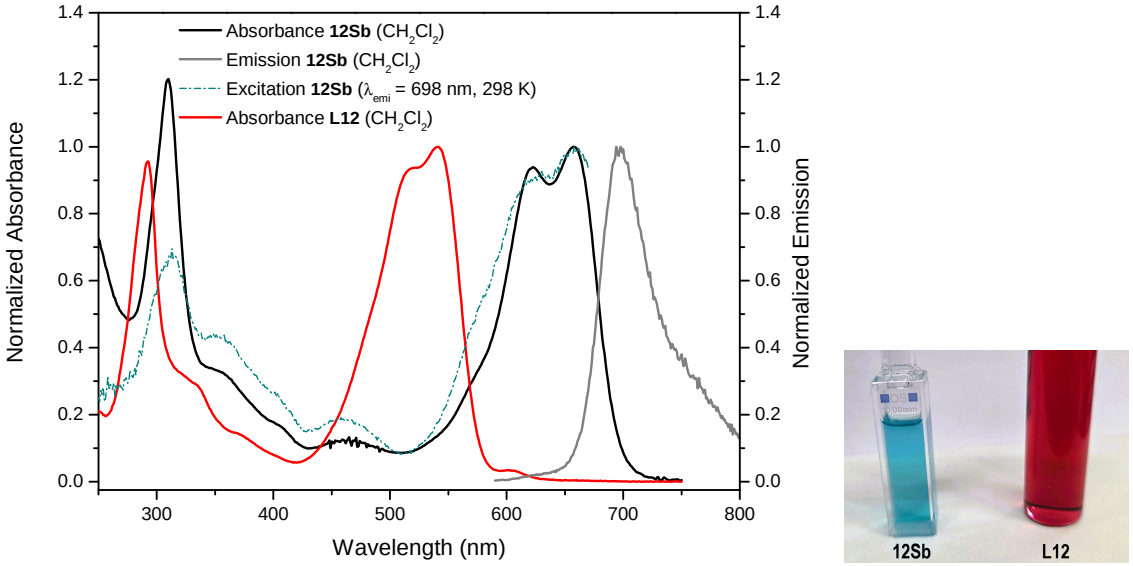
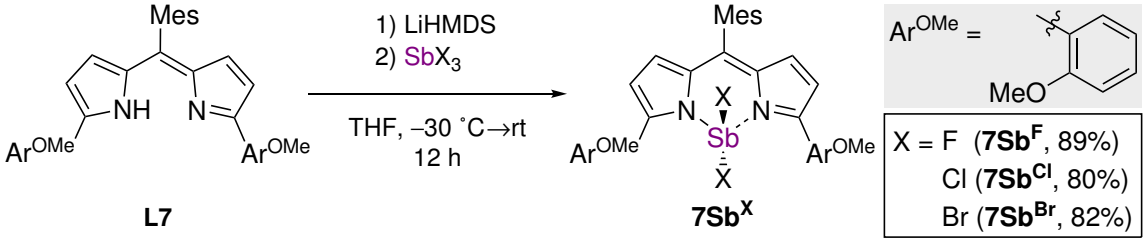


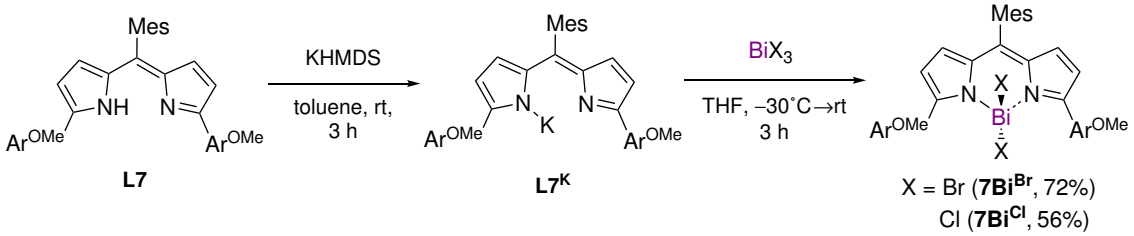
Figure 57: Normalized absorbance and emission spectra of **12Sb** and **L12** in CH_2Cl_2. The emission spectrum was recorded at an excitation wavelength of 570 nm, whereas the excitation spectrum (dashed line) was recorded at λ_{emi} = 698 nm. All spectra were recorded at 298 K (left). Photograph of CH_2Cl_2 solutions of **12Sb** and **L12** (right).

Overall, **L12** offers an interesting option to access antimony dipyrrin complexes with strongly red-shifted absorption and emission features. However, due to the difficulties encountered during synthesis and purification the focus was instead shifted onto the precursor dipyrrin **L7**. As compared to the trianionic, tetracordinate ligand **L12**, **L7** is formally bidentate and monoanionic but features two aryl ethers that can coordinate through π-donation of the oxygen atoms. Using the previously established procedure, the complexation of dipyrromethene **L7** proceeded smoothly with different antimony halides SbX_3 (X = F, Cl, Br), giving the respective SBDIPY complexes **7Sb^X** in good yields (Scheme 43).



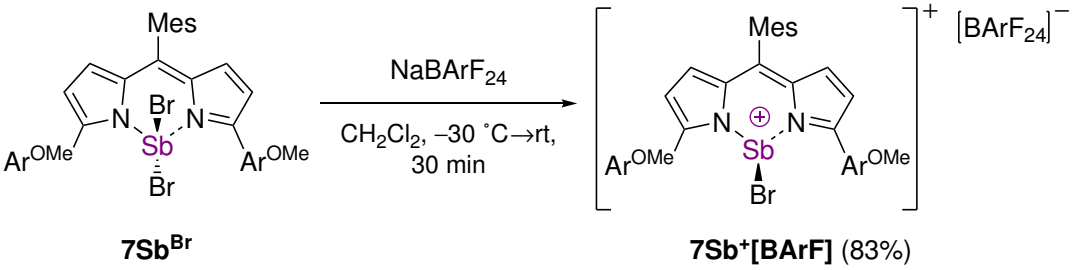
Scheme 43: Synthesis of SBDIPY complex **7Sb^X**.

Similar to the method reported by Liu *et al.*, the potassium salt **L7^K** was prepared by treating **L7** with KHMDS in toluene and subsequently reacted with a bismuth halide to yield the BIDIPY complexes **7Bi^{Br}** and **7Bi^{Cl}** in moderate yields (Scheme 44).[138]



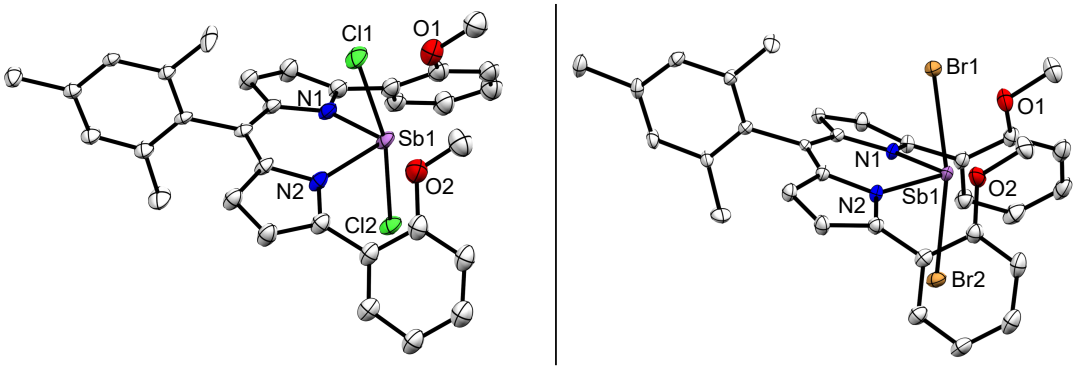
Scheme 44: Two-step synthesis of BIDIPY complex **7Bi^{Br}** and **7Bi^{Cl}**.

Based on previous success with SBDIPY complex **1Sb^{Cl}**, halide abstraction from **7Sb^{Br}** with $NaBArF_{24}$ was performed. Indeed, addition of the borate salt to a CH_2Cl_2 solution of **7Sb^{Br}** led to a selective formation of the stibenium complex **7Sb^{+}[BArF]** (Scheme 45).



Scheme 45: Synthesis of stibenium complex **7Sb^{+}[BArF]**.

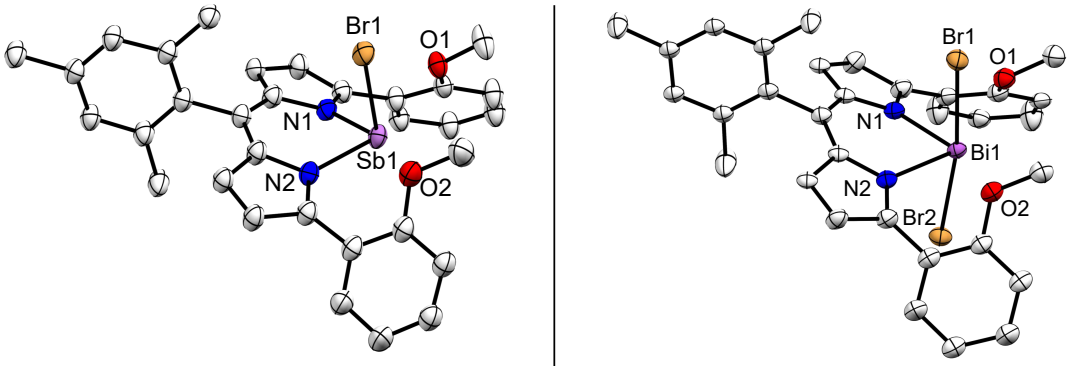
Single crystals of all new pnictogen dipyrrin complexes featuring ligand **L7** were grown from saturated solutions of THF/*n*-hexane, with exception of **7Sb^{+}[BArF]**, which was crystallized by slow evaporation of a CH_2Cl_2/*n*-dodecane mixture, and analyzed by X-ray diffraction. As envisaged, the solid-state structures of SBDIPY complexes **7Sb^{Cl}** and **7Sb^{Br}** (Figure 58) displayed evident secondary interactions between the antimony centre and the pending ether functions of the anisole substituents as the experimental Sb−O distances were below the sum of van der Waals radii (<3.58 Å).[153]



(a) 7Sb^{Cl} **(b) 7Sb^{Br}**

Figure 58: X-ray solid-state structures of (a) **7Sb^{Cl}** and (b) **7Sb^{Br}**. Hydrogen atoms were omitted for clarity and thermal ellipsoids were set to a 50% probability level.

Interestingly, unlike **1Sb^{+}[BArF]**, stibenium complex **7Sb^{+}[BArF]** displayed no solvent coordination in the solid-state structure, which appeared to be compensated by a smaller average Sb−O distance ($d_{\mathrm{Sb-O}}$ = 2.682(9) Å) as compared to the parent complex **7Sb^{Br}**, thus indicating stronger coordination of the pending ether functions (Figure 59a). Secondary interactions were also evident in the solid-state structure of **7Bi^{Br}**, showcasing even lower average Pn−O distances than the corresponding SBDIPY complexes (Figure 59b). This finding is in line with the previously observed coordination of ethereal solvents in solid-state structures of **1Bi^{Cl}** and further emphasizes the tendency of bismuth to form hypervalent coordination complexes.[190] Unfortunately, no suitable single crystals of complex **7Bi^{Cl}** were obtained.



(a) 7Sb^{+}[BArF] **(b) 7Bi^{Br}**

Figure 59: X-ray solid-state structures of (a) **7Sb^{+}[BArF]** and (b) **7Bi^{Br}**. Hydrogen atoms and $BArF_{24}$ anion (in case of **7Sb^{+}[BArF]**) were omitted for clarity and thermal ellipsoids were set to a 50% probability level.

The fluoride substituted complex **7Sb^{F}**, however, was found to be an exception to this trend, as the solid-state structure revealed one anisole substituent being twisted side-

ways due to halogen bridging (Figure 60). Consequently, one ether function showed a clear interaction with the antimony centre ($d_{\mathrm{Sb-O}}$ = 2.731(2) Å) while the other remained non-coordinate. This finding is in agreement with the structural features found with SBDIPY **1Sb^{F}**, as also **7Sb^{F}** displayed a strongly distorted geometry around the central antimony atom (Figure 60). Antimony was shifted out of the ligand mean plane by 1.020(4) Å and showed a similarly acute ∠(F1−Sb−F2) angle as **1Sb^{F}**.

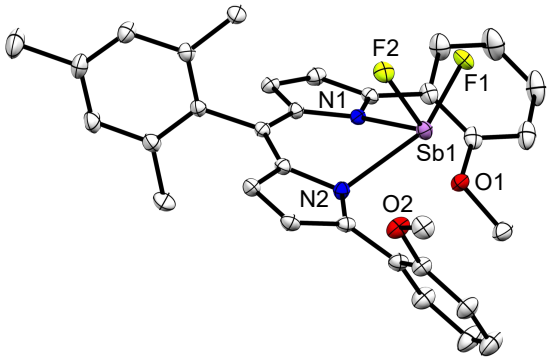


Figure 60: X-ray solid-state structure of **7Sb^{F}**. Hydrogen atoms were omitted for clarity and thermal ellipsoids were set to a 50% probability level.

Overall, the structural parameters of pnictogen dipyrrins with ligand **L7** were similar to those observed for the **L1** complexes, albeit showcasing slightly more acute antimony-halogen and -nitrogen bond angles, as well as a slightly larger offset of the central atom from the ligand mean plane. These subtle changes may arise from the more electron-rich ligand system **L7**. Selected structural data of the new SBDIPY complexes are shown in Table 6.

Table 6: Selected bond lengths and angles for **L7** pnictogen complexes. The mean plane (MPLN) is defined by the five atoms included in the binding pocket of the dipyrrin ligands.

	X1−Pn−X2 (°)	N1−Pn−N2 (°)	avg. Pn−X (Å)	avg. Pn−N (Å)	avg. Pn−O (Å)	MPLN··Pn (Å)
7Sb^{Br}	167.6(1)	86.4(2)	2.734(1)	2.090(3)	2.905(3)	0.500(4)
	166.9(1)[a]	87.2(2)[a]	2.742(1)[a]	2.096(3)[a]	2.849(4)[a]	0.434(6)[a]
7Sb^{Cl}	167.0(1)	86.7(3)	2.570(3)	2.133(6)	2.817(7)	0.396(11)
	163.4(1)[a]	87.6(3)[a]	2.559(2)[a]	2.119(5)[a]	2.763(6)[a]	0.545(13)[a]
7Sb^{F}	84.9(1)	78.5(1)	1.950(2)	2.274(2)	3.867(2)	1.020(4)
7Bi^{Br}	171.6(2)	82.6(8)	2.814(4)	2.265(15)	2.728(14)	0.66(4)
	167.1(2)[a]	84.2(8)[a]	2.731(13)[a]	2.262(15)[a]	2.792(1)[a]	0.55(4)[a]
7Sb^{+}[BArF]	–	85.9(4)	2.510(2)	2.102(10)	2.682(9)	0.700(15)

[a] Parameters of second independent molecule (if applicable).

The secondary interactions observed in the solid-state structures were promising preliminary indications of a more robust ligand framework for the incorporation of heavy elements. Next, the spectroscopic properties of new SBDIPY chromophores bearing ligand **L7** were evaluated in CH_2Cl_2. UV/Vis spectroscopy analysis of the complexes revealed a single main absorption band in the visible region with **7Sb^{F}** being the exception. Similarly to **1Sb^{F}**, **7Sb^{F}** displayed two bands with the major one at λ_{abs} = 555 nm, gradually converting to a second band at λ_{abs} = 601 nm, which correlated to an unknown, non-emitting species (Figure 61). This observation can likely be attributed to a decrease in complex stability which is caused by the geometry distortion of the complex due to antimony-fluoride interactions. Also interesting to note is that the UV/Vis spectrum of **7Sb^{F}** featured a strong absorption in the UV-region, possibly resulting from an $S_0 \rightarrow S_2$ transition.

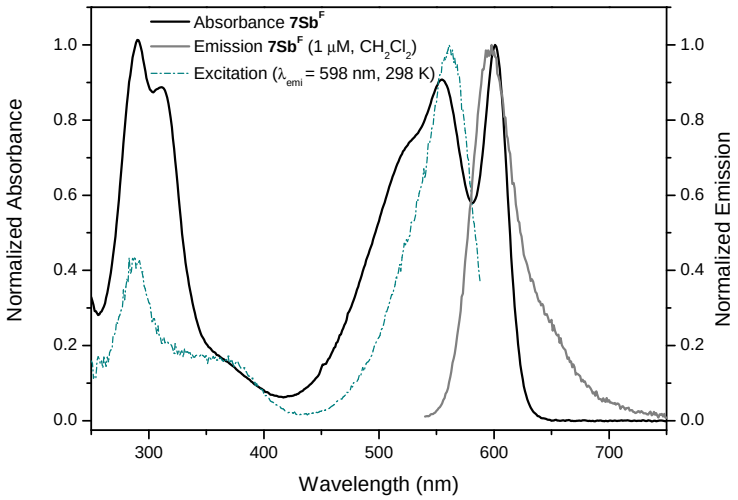


Figure 61: Normalized absorbance and fluorescence emission spectra of **7Sb^{F}** in CH_2Cl_2. The emission spectrum was recorded at an excitation wavelength of 520 nm, whereas the excitation spectrum (dashed line) was recorded for λ_{emi} = 598 nm. Absorbance and emission spectra were measured at 288 K, whereas excitation was recorded at 298 K.

Furthermore, the complexes **7Sb^{Br}** and **7Sb^{Cl}** showed a considerably higher degree of fluorescence emission as compared to SBDIPY complexes of ligand **L1**. Once again, the chloride substituted complex displayed a higher relative quantum yield (Φ_{rel} = 37%) than the bromide analogue **7Sb^{Br}** (Φ_{rel} = 5%), whereas unfortunately no quantum yield of **7Sb^{F}** was determined due to sample degradation. Interestingly a slight bathochromic shift in absorption and emission was noted for the stibenium complex **7Sb^{+}[BArF]**, as well as an increase in emission intensity (Φ_{rel} = 26%) as compared to the parent complex **7Sb^{Br}**. The BIDIPY complex **7Bi^{Br}** displayed only very low PL emission, having a relative quantum yield below 1%, which is likely a consequence of quenching through the heavy central atom. Lastly, it is worth pointing out that shifts

of the emission maxima of all Sb-complexes were observed above sample concentrations of 1 μM, alongside a slight mismatch of absorption and excitation spectra. This effect strongly suggests an aggregation of the chromophores at increased concentrations and was found to play a pivotal role in further studies (see chapter 4). An overview of the spectroscopic features of **L7** pnictogen dipyrrins is provided in Table 7.

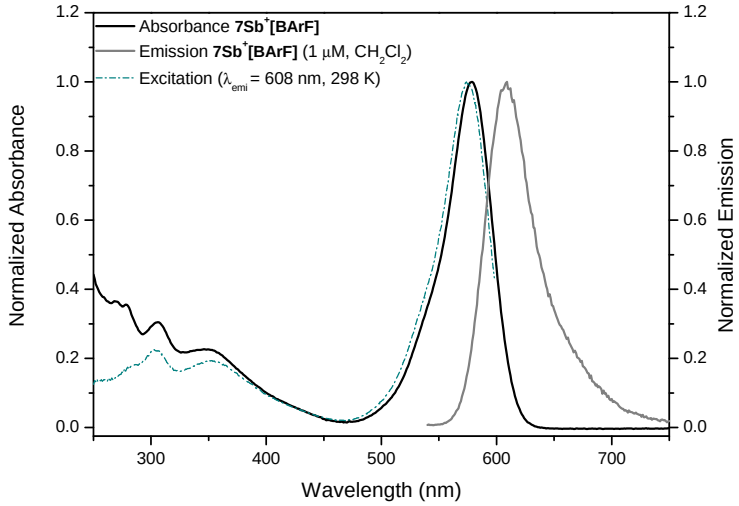


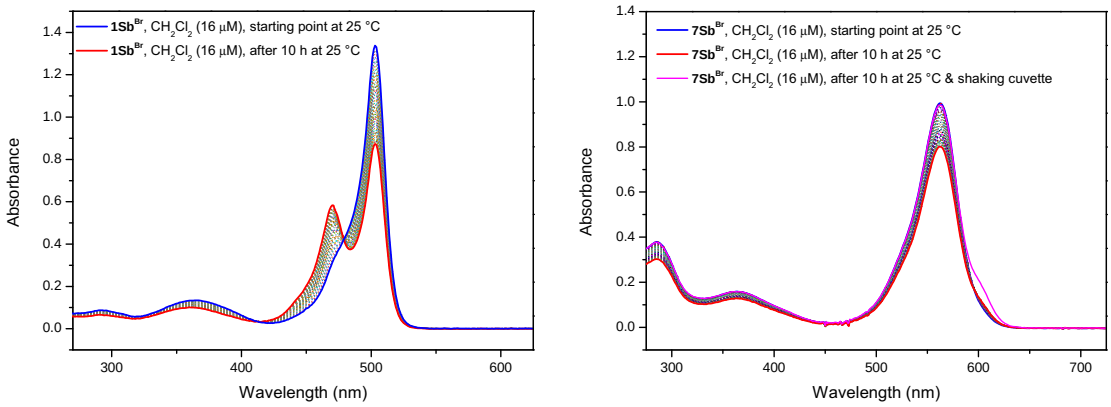
Figure 62: Normalized absorbance and fluorescence emission spectra of **7Sb$^+$[BArF]** in CH_2Cl_2. The emission spectrum was recorded at an excitation wavelength of 520 nm, whereas the excitation spectrum (dashed line) was recorded for λ_{emi} = 608 nm. All spectra were measured at 298 K.

Table 7: Spectroscopical data for pnictogen dipyrrin complexes of ligand **L7**.

Complex	max. Absorption λ_{abs} (nm)	max. Emission [a] λ_{emi} (nm)	ϵ ($M^{-1}cm^{-1}$)	Quantum yield Φ_{rel}
7Sb^{Br}	563	597 (602[b])	62790	0.05
7Sb^{Cl}	560	597 (601[b])	75120	0.37
7Sb^{F}	555, 601	598 (593[b])	–[c]	–[c]
7Bi^{Br}	561	590	84610	0.005
7Sb$^+$[BArF]	577	608 (616[b])	54860	0.26

[a]Emission recorded at excitation wavelength λ_{exc} = 520 nm. [b]Refers to emission maximum with higher sample concentration (16 μM). [c]Quantum yield and ϵ not determined due to sample instability.

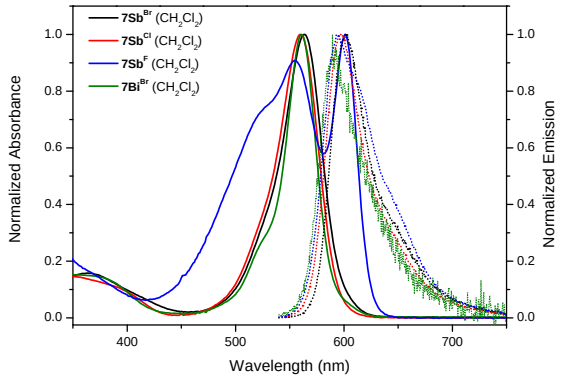
More importantly, however, time-resolved UV/Vis spectroscopy of the new SBDIPY chromophores revealed a clear improvement with respect to complex stability in solution. Furthermore, the direct comparison of **1Sb^{Br}** and **7Sb^{Br}** under equal conditions disclosed **7Sb^{Br}** to have a significantly increased stability in solution, showing only traces of sample degradation after 10 h at room temperature (Figure 63).



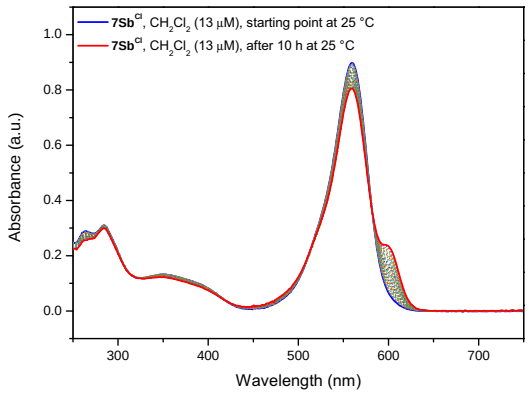
(a) 1Sb^{Br} **(b) 7Sb^{Br}**

Figure 63: Comparison of time-resolved UV/Vis spectra of **1Sb^{Br}** (a) and **7Sb^{Br}** (b) over the course of 10 h in CH_2Cl_2 at room temperature.

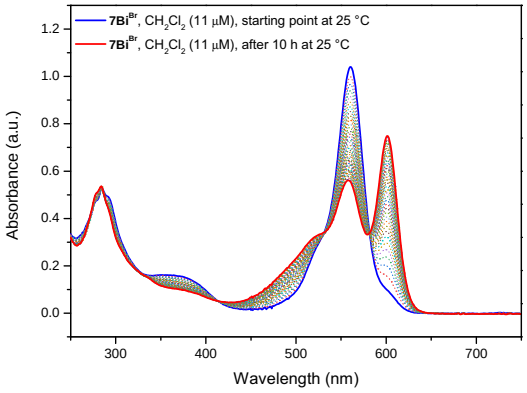
As expected from previous findings, the stability of **7Sb^{X}** dipyrrins decreased with respect to the size of the halide substituent (Br > Cl > F). An overview of the conducted time-resolved measurements is given in Figure 64.



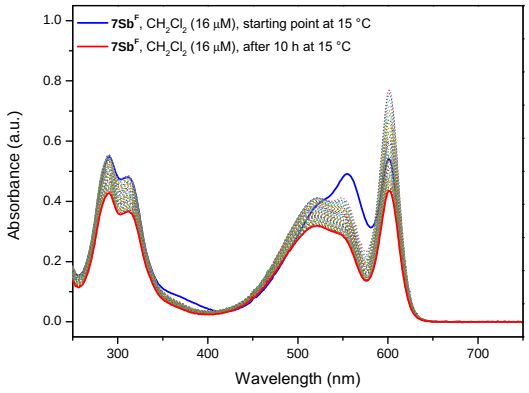
(a) Overview of absorption and emission in CH_2Cl_2.



(b) 7Sb^{Cl} at 25 °C (CH_2Cl_2).



(c) 7Bi^{Br} at 25 °C (CH_2Cl_2).



(d) 7Sb^{F} at 15 °C (CH_2Cl_2).

Figure 64: Comparison of absorption (solid line) and emission (λ_{exc} = 520 nm, dotted line) of **L7** pnictogen complexes in CH_2Cl_2 (a) and UV/Vis stability analysis of pnictogen dipyrrins in CH_2Cl_2 over the course of 10 h (b-d).

For the most stable SBDIPY complex, **7Sb^{Br}**, additional solvents were screened by UV/Vis spectroscopy (Figure 65). The compound showed negligible differences in acetone, THF, CH_2Cl_2 and toluene with respect to the main absorption band. In acetonitrile, however, a notable hypsochromic shift was observed, which is unlikely an electronic/solvatochromic effect but rather resulted from a chemical reaction.[191]

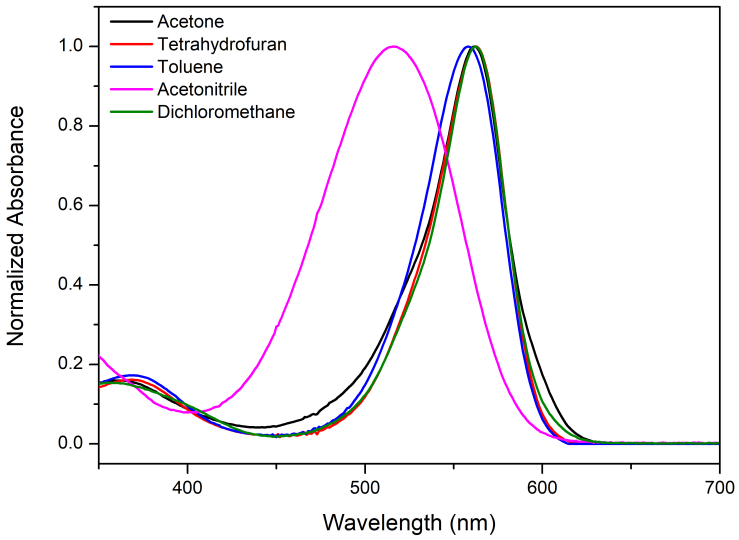
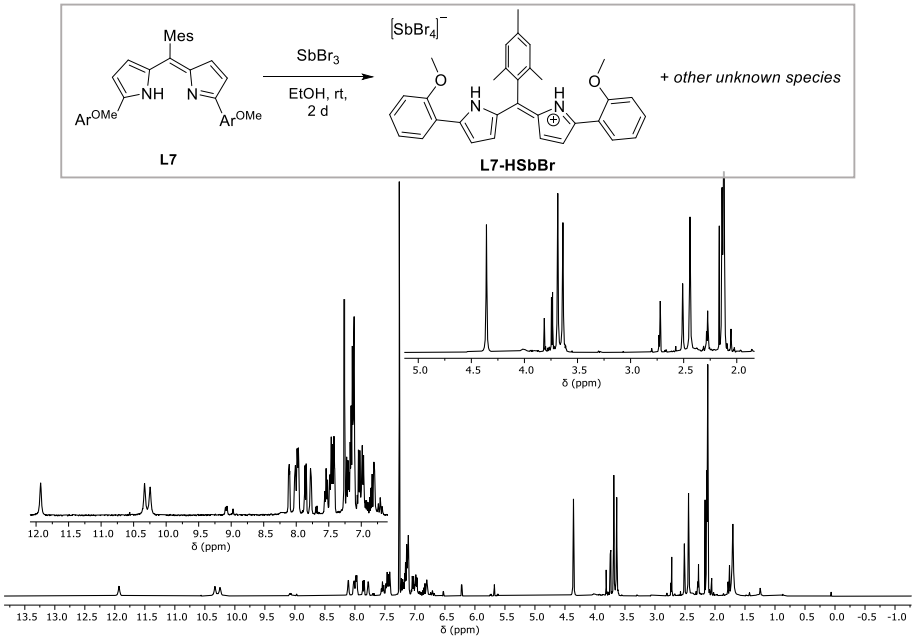


Figure 65: Normalized UV/Vis absorbance spectra of **7Sb^{Br}** in a selection of different solvents at 15 °C.

Complex **7Sb^{Br}** remained stable, both as a solid and in CD_2Cl_2 solution, upon exposure to air for 24 h, only showing traces of ligand re-protonation after extended time in solution. In order to obtain more information on the ligand protonation as a potential decomposition product, **L7** was reacted with $SbBr_3$ in a protic solvent and under air according to Scheme 46. Addition of $SbBr_3$ to an ethanol solution of **L7** resulted in an immediate colour change from red to dark blue. The mixture was stirred at room temperature for 2 days, affording a dark blue precipitate. The solid was filtered off and washed with additional ethanol and *n*-pentane. Analysis by ^{1}H NMR revealed a complicated mixture of multiple protonated species (Scheme 46). Attempts at purification by recrystallization of the solid in CH_2Cl_2 led to negligible changes in the ^{1}H NMR. Based on the number of ^{1}H resonances associated with the methoxy functions of the ligand (between 4.5-3.5 ppm), the mixture contained a minimum of three species that were dissimilar to **L7**.



Scheme 46: Reaction of **L7** with $SbBr_3$. ^1H NMR (400 MHz, $CDCl_3$) of crude product after attempted recrystallization in CH_2Cl_2.

Single crystals from the reaction mixture were obtained from a solution of CH_2Cl_2 and analyzed by X-ray diffraction, confirming the identity of one the products as the antimonate salt **L7-HSbBr** (Figure 66). Interestingly, the solid-state structure of **L7-HSbBr** displayed a contortion of both pyrroles along the bridging methene unit, which represents a rarely observed dipyrrin conformation.[84] A similar effect has been previously described for protonated dipyrrins with tetrahalozinc anions in the solid-state.[192] Moreover, **L7-HSbBr** displayed orientation of both ether functions towards the N−H of the pyrroles due to hydrogen bonding with the oxygen atoms.

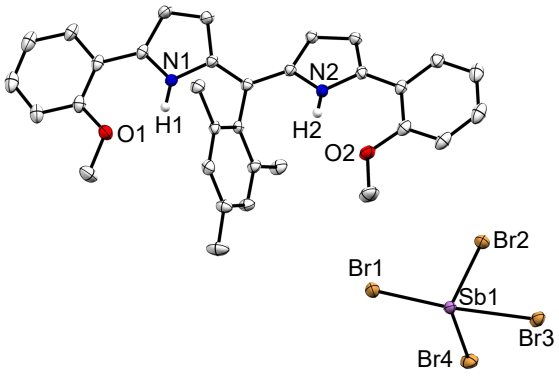


Figure 66: X-ray solid-state structure of **L7-HSbBr**. Non-nitrogen bound hydrogen atoms were omitted for clarity and thermal ellipsoids were set to a 50% probability level.

Qualitatively similar results were obtained upon reaction of **7Sb^{Br}** with 1.00 equiv. of (+)-10-camphorsulfonic acid (10-CSA) as a Brønsted acid in non-dry $CDCl_3$. Using

dry CD_2Cl_2 a slightly more selective outcome was observed, albeit still displaying two downfield-shifted ^{1}H resonances which can be attributed to pyrrolic N−H functions (Figure 67). These findings further reinforce the assumption that decomposition of **7Sb^{Br}** is mainly enabled under acidic conditions. It is also important to note, however, that this process is not acid-catalysed as **7Sb^{Br}** remained mostly intact when reacted with sub-stoichiometric amounts of 10-CSA.

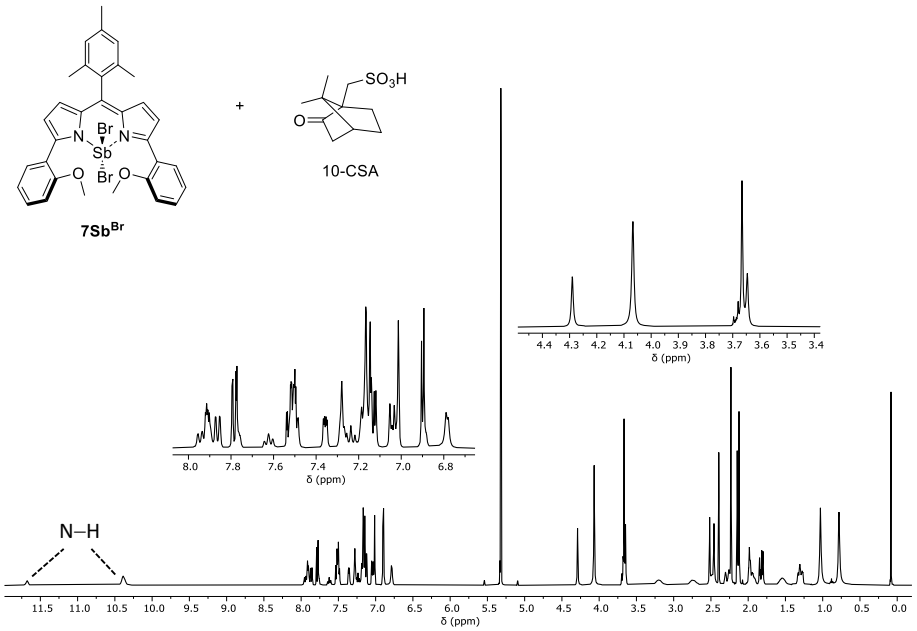
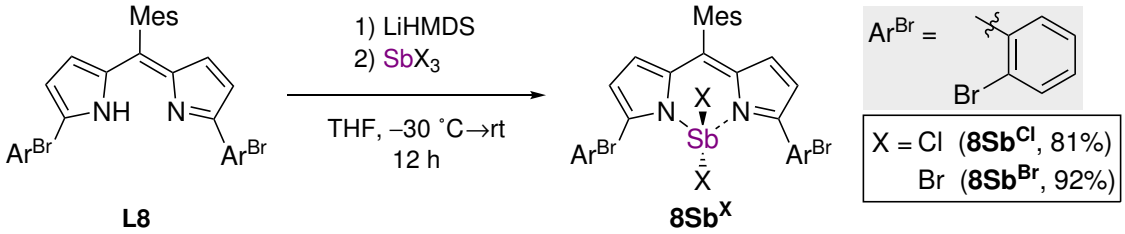


Figure 67: ^{1}H NMR of **7Sb^{Br}** upon addition of camphorsulfonic acid (1.00 equiv.) in CD_2Cl_2.

Furthermore, deliberate hydrolysis of **7Sb^{Br}** was attempted by treating a CH_2Cl_2 solution of the complex with an excess of $BaCl_2{\cdot}2\ H_2O$. However, no changes of the starting material were observed after sonication of the reaction mixture, possibly owing to the low solubility of the barium salt. Yet, treatment of the mixture with water and extraction with CH_2Cl_2, yielded exclusively **L7** as confirmed by ^{1}H NMR. Despite decomposition under more forcing conditions, the above discussed findings firmly support the envisaged improvements in complex stability through dipyrrin **L7**. Therefore, pnicotgen complexes of dipyrrin **L7** were categorized as promising candidates for further photochemical applications which will be discussed in chapter 4.

Next, the viability of dipyrromethene **L8** as a ligand for antimony and bismuth was tested. Compound **L8** has not been reported in literature yet and features additional possibilities for synthetic modifications through the 2-bromophenyl substituents on the ligand scaffold. Since the bromine atoms are in direct proximity of the chromophore's π-system, an additional heavy atom effect is also to be expected.

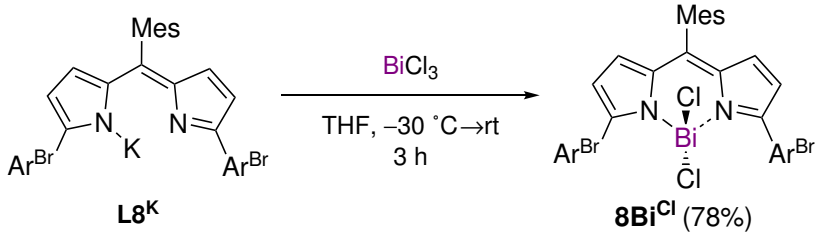
Using the previously employed protocol for complexation, **L8** SBDIPY complexes **8Sb^{Br}** and **8Sb^{Cl}** were isolated in good yields (Scheme 47).



L8 **8Sb^{X}**

Scheme 47: Synthesis of SBDIPY complex **8Sb^{X}** (X = Cl, Br).

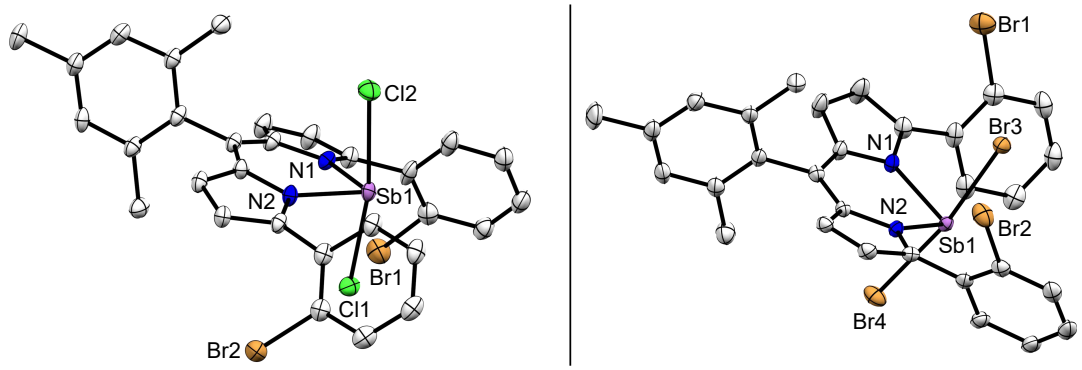
Following the previously described method, BIDIPY complex **8Bi^{Cl}** was prepared as an additional proof-of-concept (Scheme 48). As before, a potassium dipyrrinato salt **L8^{K}** was used to access the bismuth complex in good yield.



L8^{K} **8Bi^{Cl}** (78%)

Scheme 48: Synthesis of BIDIPY complex **8Bi^{Cl}**.

Single crystals of **L8** pnictogen complexes were grown from saturated solutions of THF/*n*-hexane and analyzed by X-ray diffraction (Figures 68 and 69). In contrast to complexes of ligand **L7**, no interaction between the central atom and the functional groups on the phenyl substituents was present in the solid-state structures. Regarding bond lengths and angles, **8Sb^{Br}** and **8Sb^{Cl}** were very similar to complexes **7Sb^{Br}** and **7Sb^{Cl}**, respectively, but displayed slightly smaller offsets from the ligand mean plane, which may arise from coordination of the aryl ethers to the pnictogen centre.



(a) 8Sb^{Cl} **(b) 8Sb^{Br}**

Figure 68: X-ray solid-state structures of **L8** SBDIPY complexes (a) **8Sb^{Cl}** and (b) **8Sb^{Br}**. Hydrogen atoms were omitted for clarity and thermal ellipsoids were set to a 50% probability level.

Although for both, bismuth and antimony complexes, the phenyl groups appear to be slightly bent towards the central atoms, this is likely only due to crystal packing effects as the distances between aryl centroids and pnictogen atoms were found to be too large to be considered significant. While for solid-state structures of SBIDPY complexes the 2-bromophenyl substituents were oriented in the same direction (“syn”), the BIDIPY solid-state structure displayed an opposing orientation of the 2-bromophenyl groups (“anti”). As previously noted, this behaviour is likely due to crystal packing effects as no significant interactions with the bromide function were present and rotation of the 2-bromophenyl groups is therefore less hindered. The solid-state structure of **8Bi^{Cl}** exhibited equatorial coordination of THF which was restricted in the case of **7Bi^{Br}** through additional ligand coordination.

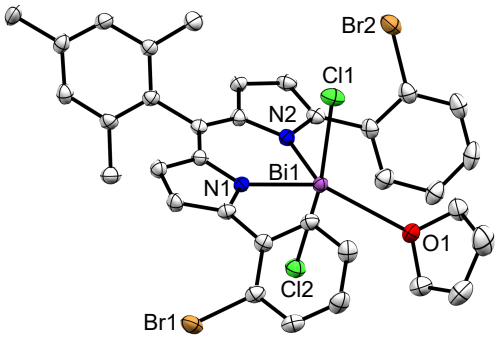


Figure 69: X-ray solid-state structure of **8Bi^{Cl}**. Hydrogen atoms and non-coordinating THF were omitted for clarity and thermal ellipsoids were set to a 50% probability level.

Selected structural parameters of SBDIPY complexes **8Sb^{Br}**, **8Sb^{Cl}** and BIDIPY complex **8Bi^{Cl}** are summarized in Table 8.

Table 8: Selected bond lengths and angles for **L8** pnictogen complexes. The mean plane (MPLN) is defined by the five atoms included in the binding pocket of the dipyrrin ligands.

	X1−Pn−X2 (°)	N1−Pn−N2 (°)	avg. Pn−X (Å)	avg. Pn−N (Å)	MPLN··Pn (Å)
8Sb^{Br}	171.6(1)	85.7(1)	2.696(1)	2.096(2)	0.347(3)
8Sb^{Cl}	168.7(1)	86.3(2)	2.528(2)	2.099(5)	0.342(8)
8Bi^{Cl}	172.1(1)	82.2(2)	2.658(2)	2.232(4)	0.166(6)

Because of the electronic effect of the different functional groups on the phenyl substituent, **8Sb^{X}** dipyrrins displayed a slight hypsochromic shift in absorption and emission as compared to **7Sb^{X}** complexes (Figure 70). A single main absorption at λ_{abs} = 532 nm (**8Sb^{Cl}**) and λ_{abs} = 535 nm (**8Sb^{Br}**) was recorded. Both complexes showed appreciable emission at λ_{emi} = 569 nm (**8Sb^{Cl}**) and at λ_{emi} = 572 nm (**8Sb^{Br}**) respectively. It is worth pointing out that aggregation effects were not considered this time, as above-described spectroscopic data refers to 16 μM samples.

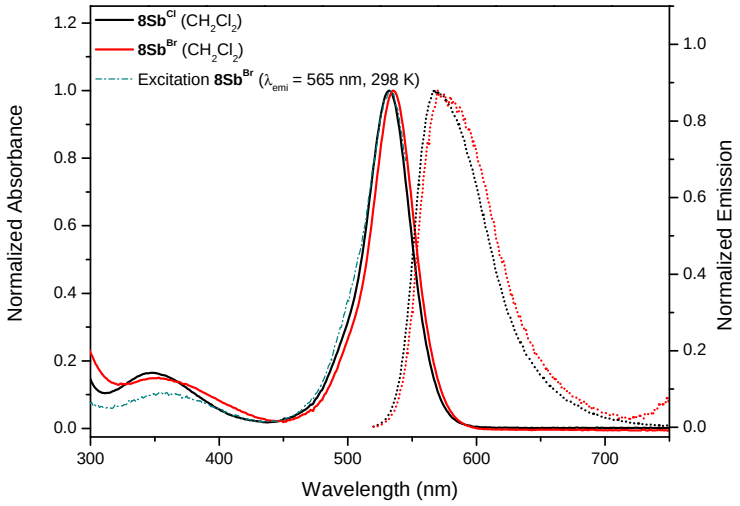


Figure 70: Normalized absorbance (solid line) and fluorescence emission (dotted line) spectra of **8Sb^{Br}** and **8Sb^{Cl}** in CH_2Cl_2 (recorded at λ_{exc} = 500 nm). Excitation spectrum of **8Sb^{Br}** (dashed line) was recorded for λ_{emi} = 565 nm. All spectra were measured at 298 K.

The bismuth complex **8Bi^{Cl}** displayed a slight bathochromic shift in absorption with λ_{abs} = 537 nm and a very weak emission at λ_{emi} = 596 nm (Figure 71). The low emission intensity can be attributed to the quenching effect of the heavy central atom, as well as the presence of the bromide moieties on the chromophore scaffold.

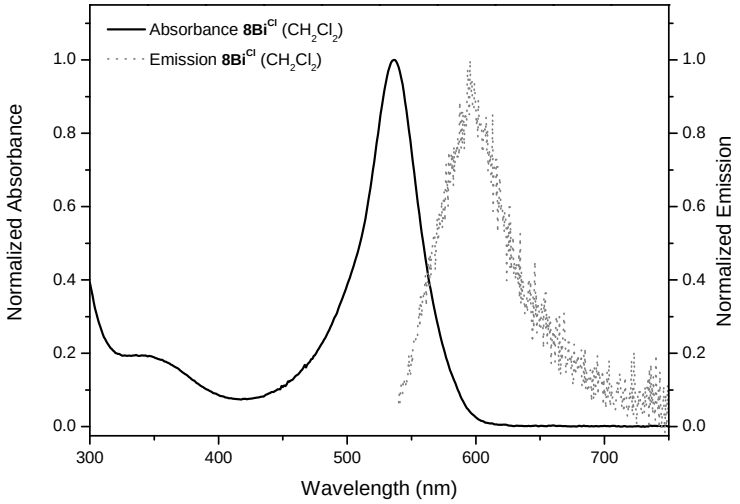
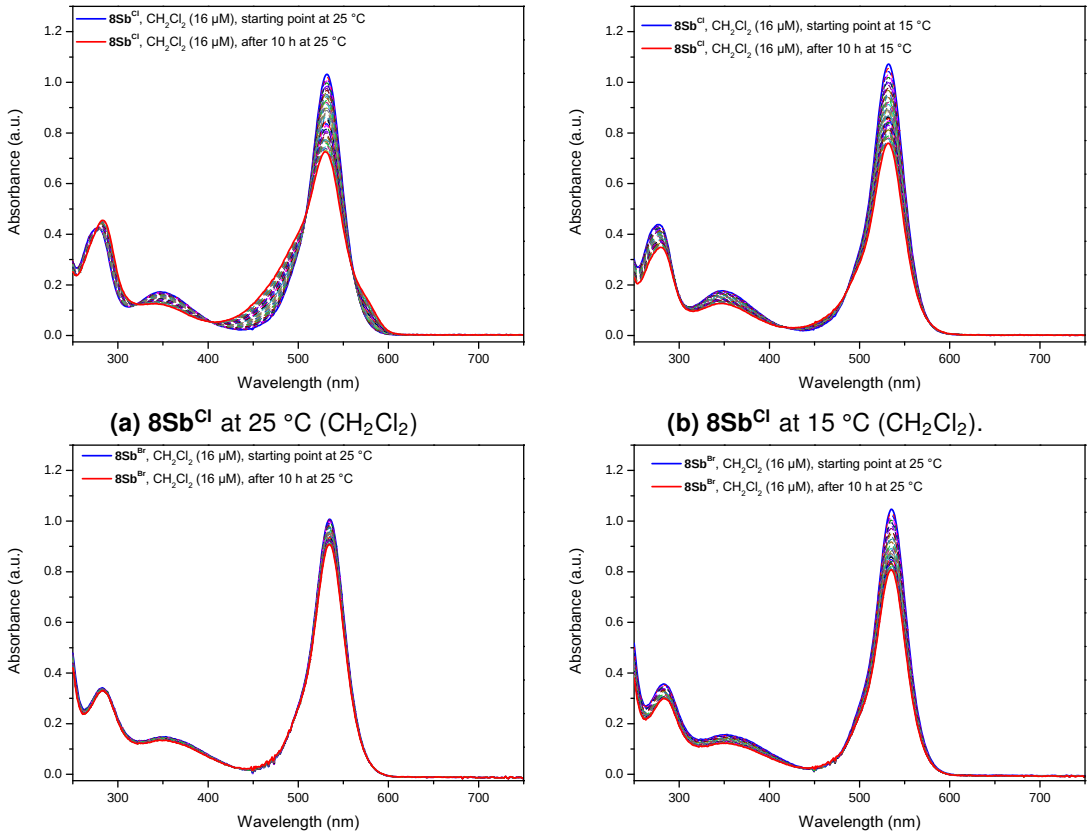


Figure 71: Normalized absorbance (solid line) and fluorescence emission (dotted line) spectra of **8Bi^{Cl}** in CH_2Cl_2 (measured at λ_{exc} = 500 nm). The spectra were recorded at 298 K.

The stability of both SBDIPY complexes was analyzed by time-resolved UV/Vis spectroscopy, denoting a high stability in the case of **8Sb^{Br}**, whereas **8Sb^{Cl}** was found to be more prone to decomposition above 15 °C, marked by a noticeable broadening of the main band at λ_{abs} = 532 nm (Figure 72). The slightly increased absorbance decrement of **8Sb^{Br}** at 15 °C as compared to the measurement series at 25 °C may stem from precipitation as observed for **7Sb^{Br}** and could potentially be avoided through sample agitation.



(a) 8Sb^{Cl} at 25 °C (CH_2Cl_2)

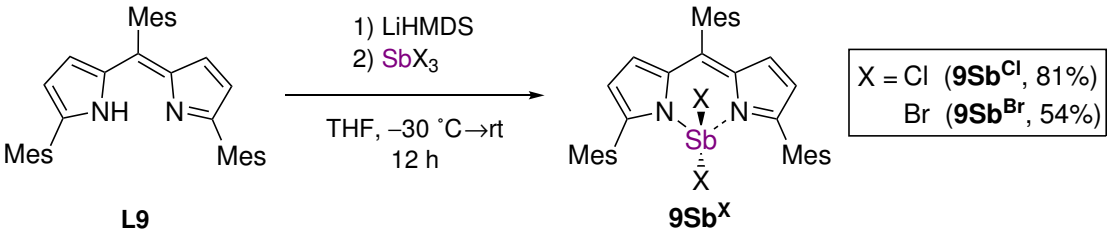
(b) 8Sb^{Cl} at 15 °C (CH_2Cl_2).

(c) 8Sb^{Br} at 25 °C (CH_2Cl_2).

(d) 8Sb^{Br} at 15 °C (CH_2Cl_2).

Figure 72: UV/Vis stability analysis of **8Sb^{Cl}** (a-b) and **8Sb^{Br}** (c-d) in CH_2Cl_2 over the course of 10 h (b-d) at 25 °C and 15 °C.

Synthesis and isolation of SBDIPY complexes with **L9** underwent smoothly, following the established procedure (Scheme 49).[i] Complex **9Sb^{Cl}** was isolated in good yield while a slightly lower yield was obtained for **9Sb^{Br}** due to incomplete precipitation of **9Sb^{Br}** during synthesis and work-up, resulting in a slight loss of product.



L9 **9Sb^{X}**

Scheme 49: Synthesis of SBDIPY complex **9Sb^{X}** (X = Cl, Br).

Due to the close resemblance of **L9** with the ligand system used by Su and co-workers, however, these complexes were not considered for further applications.[138]

[i] Synthesis and NMR characterization of these compounds was performed by L. Mohr during a research internship.

Nonetheless, spectroscopic analysis of **9Sb^{Br}** in toluene revealed an important piece of information that was yet unseen for SBDIPY complexes **7Sb^{X}** and **8Sb^{X}** (Figure 73). Complex **9Sb^{Br}** exhibited a single absorption band at λ_{abs} = 515 nm. Upon excitation at 515 nm, the **9Sb^{Br}** sample displayed emission at λ_{emi} = 550 nm, as well as a second, more intense signal at λ_{emi} = 738 nm, accounting for the hitherto largest observed Stokes shift with SBDIPY chromophores of 5867 cm^{-1}. Heavier triel complexes of ligand **L9** were also reported to show a bathochromic shift in emission by Erlemeier *et al.*, but not to the same extent as seen for **9Sb^{Br}**.[193] Second order diffraction can be excluded as a cause of this unexpected finding as the spectrometer was equipped with a fully automated order sorting filter wheel. The excitation spectrum recorded for λ_{emi} = 738 nm showed good agreement with the absorbance of **9Sb^{Br}**, albeit showing a slight broadening and the shape of two maxima in the region of 515 nm, thus hinting at potential aggregation effects. Fascinatingly, the emission at λ_{emi} = 738 nm was attributed to phosphorescence emission as the lifetime decay was significantly increased (τ = 30.6±0.4 µs). Such dual emission behavior is considerably rare and mainly found for chromophores that incorporate heavy elements, such as tin, lead or bismuth.[194–197]

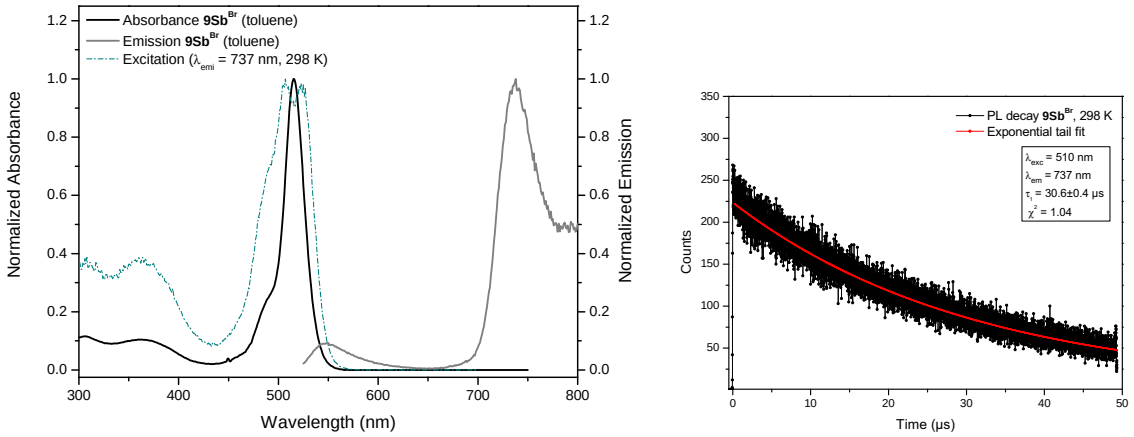


Figure 73: Normalized absorbance and fluorescence emission spectra of **9Sb^{Br}** in toluene (16 µM, left). The emission spectrum was recorded at an excitation wavelength of 515 nm, whereas the excitation spectrum (dashed line) was recorded for λ_{emi} = 737 nm. Photoluminescence lifetime decay of **9Sb^{Br}** in toluene (right). All spectra were recorded at 298 K.[ii]

Moreover, dual fluorescence and phosphorescence emission has been reported for platinum-tethered BODIPY chromophores by Winter and co-workers, who assigned this phenomenon to emission from BODIPY-centred $^{1}\pi\pi^{*}$ and $^{3}\pi\pi^{*}$ states.[198] Inter-

[ii] The photoluminescence decay was limited to a time range of 50 µs by the pulsed LED light source and should be independently verified using a microsecond flashlamp. Nonetheless, the exponential tail fit presents a good preliminary estimate for the PL lifetime of **9Sb^{Br}**.

estingly, a second emission band was not observed for **9Sb^{Cl}** (λ_{abs} = 511 nm and λ_{emi} = 541 nm) at 298 K which implies that the bromide substituents play a meaningful role in enabling phosphorescence at given temperature (Figure 74). In order to understand whether this is related to the sample temperature, additional measurements at cryogenic temperature should be carried out.

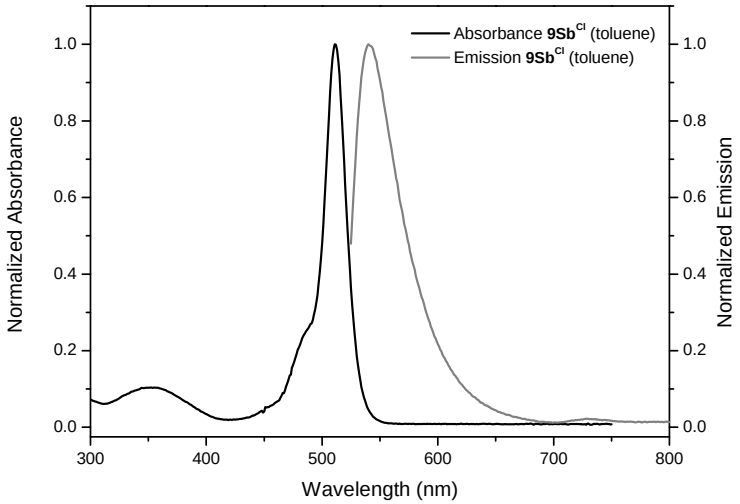
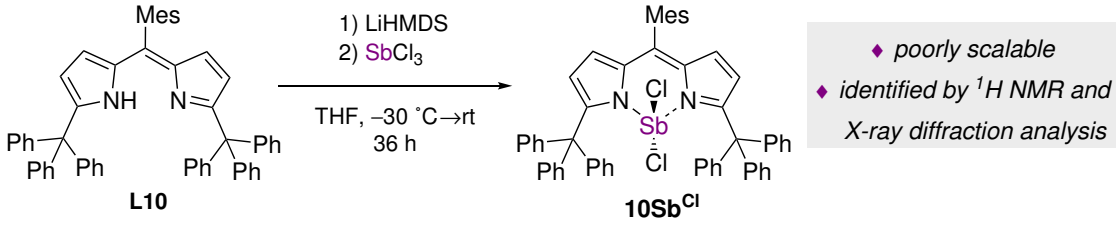


Figure 74: Normalized absorbance and fluorescence emission spectra of **9Sb^{Cl}** in CH_2Cl_2 (16 μM). The emission spectrum was recorded at an excitation wavelength of 510 nm.

Based on the spectroscopic findings for **9Sb^{Br}**, a dual emission could also be present for other α-substituted dipyrrin complexes with an $SbBr_2$ core (*e.g.* **7Sb^{Br}**) but may lie outside of the detectable wavelength region of the detection window of the spectrometer (800 nm).

Finally, dipyrrins offering enhanced steric protection in the α-postions, **L10** and **L11**, were evaluated as ligands for antimony and bismuth. Complexation of $SbCl_3$ with **L10** was first tested on small scale (0.07 mmol) following the established procedure. A gradual change of colour was observed upon combining a mixture of **L10** (50 mg, 67 μmol, 1.00 equiv.) and LiHMDS (11 mg, 68 μmol, 1.02 equiv.) in THF (0.7 mL) with $SbCl_3$ (16 mg, 70 μmol, 1.04 equiv.) in THF (0.3 mL) at −30 °C and allowing the reaction mixture to warm to room temperature for 12 h. Upon layering the reaction mixture with *n*-hexane, a small amount of orange crystalline solid (circa 15 mg) was obtained after 24 h at room temperature. The solid was analyzed by ^{1}H NMR and X-ray diffraction, which both supported a successful complexation towards **10Sb^{Cl}** (Scheme 50). Unfortunately, however, ligand exchange reaction of $SbCl_3$ with **L10** proceeded with lower selectivity at larger scale, resulting in partial back-formation of **L10**. This outcome can likely be attributed to a sluggish deprotonation step of **L10** in the presence of LiHMDS, as incomplete deprotonation (approximately 40%) was

observed on larger scale (0.45 mmol) after 10 h at −30 °C and an additional 2 h at room temperature by ^{1}H NMR aliquot in THF-d_8.



Scheme 50: Synthesis of SBDIPY complex **10Sb^{Cl}**.

The solid-state structure of **10Sb^{Cl}** displayed several striking differences as compared to the previously described SBDIPY structures (Figure 75). Firstly, it should be noted that one phenyl group per trityl substituent was found to be sufficiently close to the antimony centre to enable considerable π-interactions. Both phenyl centroids have an average distance of 3.317(2) Å to the antimony centre, having each three carbon atoms at a distance below the sum of Van der Waals radii, thus allowing interaction in an η^3-fashion.[153] Second, the halide substituents showed increased bending towards the ligand plane with a Cl1−Sb−Cl2 bond angle of 153.5(1)°, which is likely a consequence of the close proximity of the phenyl groups to the central atom. Furthermore, complex **10Sb^{Cl}** featured slightly larger average Sb−N bond lengths ($d_{\mathrm{Sb-N}}$ = 2.141(2) Å) and a wider N1−Sb−N2 bond angle of 93.5(1)° in comparison to the previously described SBIDPY complexes.

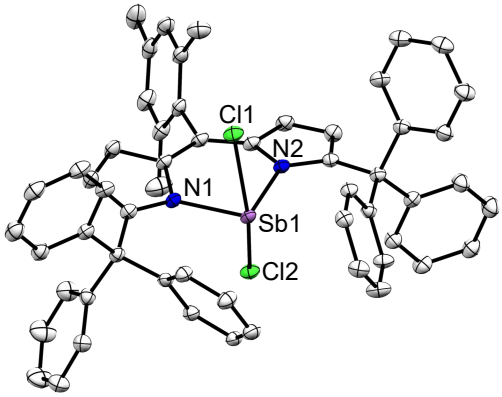
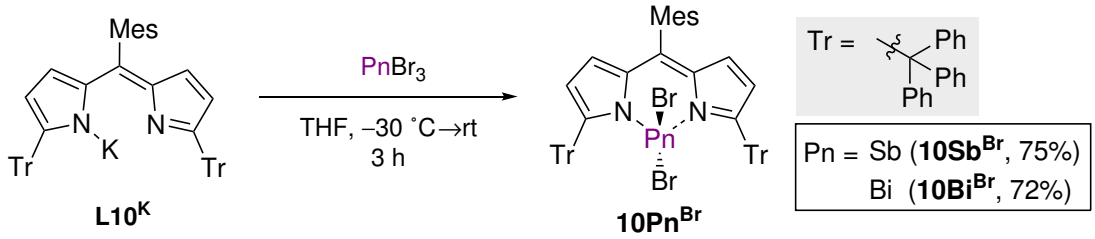


Figure 75: X-ray solid-state structure of **10Sb^{Cl}**. Hydrogen atoms and non-coordinating THF were omitted for clarity and thermal ellipsoids were set to a 50% probability level.

Due to the difficulties encountered for *in-situ* deprotonation of **L10** with LiHMDS, the potassium dipyrrinato salt **L10^{K}** was first prepared and subsequently reacted with $SbBr_3$ or $BiBr_3$, selectively yielding the respective pnictogen dipyrrin complexes **10Pn^{Br}** in good yields (Scheme 51). Complexes **10Pn^{Br}** were found to be poorly solu-

ble in non-polar solvents and only moderately soluble in polar ones, such as CH_2Cl_2, possibly owing to the trityl substituents.



Scheme 51: Synthesis of **L10** pnictogen dipyrrin complexes **10Pn^{Br}**.

Both pnictogen complexes featured a sharp absorption at λ_{abs} = 523 nm (**10Sb^{Br}**) and λ_{abs} = 525 nm for **10Bi^{Br}** (Figure 76). While **10Sb^{Br}** showed notable emission at λ_{emi} = 545 nm, the photoluminescence of the bismuth analogue was found to be significantly quenched (λ_{emi} = 544 nm) and consequently had to be recorded using an increased emission bandwidth setting. Moreover, the bismuth complex displayed hints of a second emission signal in the region of 750 nm. Given the overall low emission intensity, this finding would need to be verified through additional measurements at cryogenic temperatures.

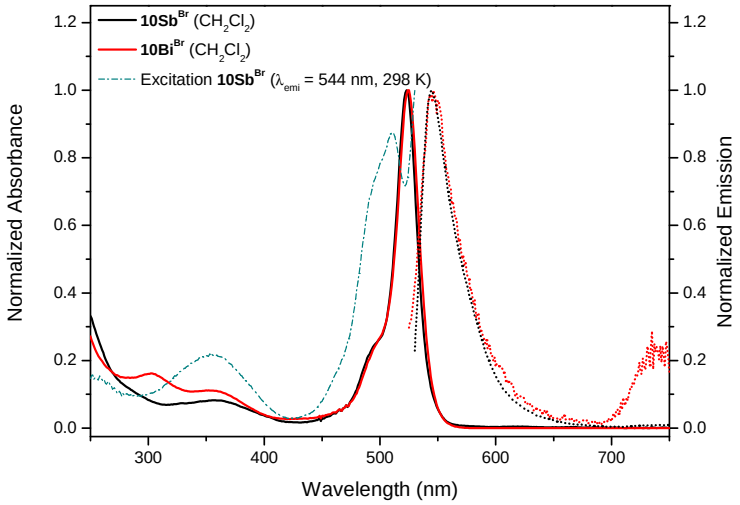


Figure 76: Normalized absorbance (solid line) and fluorescence emission (dotted line) spectra of **10Sb^{Br}** and **10Bi^{Br}** in CH_2Cl_2 (recorded at λ_{exc} = 510 nm, 5.0 nm emission bandwidth for **10Bi^{Br}**). Excitation spectrum of **10Sb^{Br}** (dashed line) was recorded for λ_{emi} = 544 nm. All spectra were measured at 298 K using 16 μM samples.

The stability of SBDIPY chromophore **10Sb^{Br}** was evaluated in CH_2Cl_2 at 298 K using time-resolved UV/Vis spectroscopy (Figure 77). Fortunately, the complex displayed a remarkable stability over a period of 20 hours. A similarly high degree of stability was observed for **10Bi^{Br}**, as no spectroscopic changes were noted upon brief exposure of a CH_2Cl_2 sample. The enhanced stability of **10Pn^{Br}** dipyrrins can be attributed to the sterically encumbered pnictogen centre as well as the choice of halide substituents and showcase a significant improvement in relation to pnictogen complexes bearing tetramethyl-substituted dipyrromethenes.

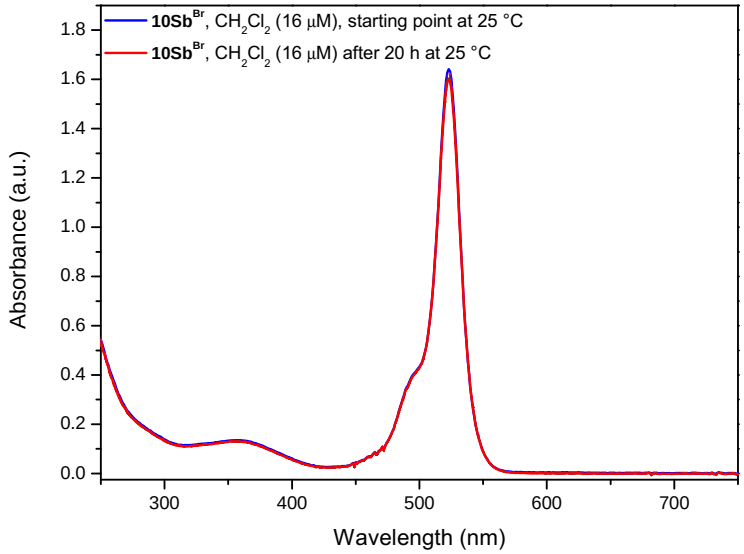
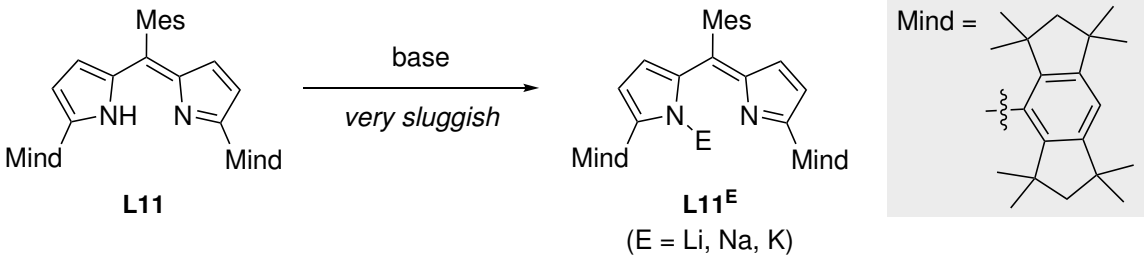


Figure 77: UV/Vis stability analysis of **10Sb^{Br}** in CH_2Cl_2 over the course of 20 h.

For the last steric protection option considered, **L11**, the general procedure for SBIDIPY synthesis was found to be completely unproductive. Similarly to **L10**, this observation was linked to the even more sluggish deprotonation of **L11**. Thus, several bases were screened to find optimal conditions to form an alkali dipyrrinato salt **L11^{E}** (Scheme 52). An overview of the reaction conditions is provided in Table 9.



Scheme 52: General reaction scheme for deprotonation of **L11**.

Table 9: Screening of reaction conditions for deprotonation of **L11**. All entries were set up for 0.11 mmol of **L11** at most.

Entry	Base	Conditions	Deprotonation[a]
e1	LDA (2.50 equiv.)	C_6D_6 at 25 °C	36% after 40 min 100% after 24 h
e2	KHMDS (1.05 equiv.)	C_6D_6 at 25 °C	5% after 30 min
e3	KHMDS (2.20 equiv.)	C_6D_6 at 25 °C	70% after 4 h $>$99% after 24 h[b]
e4	NaH (33.3 equiv.)	THF at 25 °C	$>$99% after 24 h[c]
e5	LiPh (1.20 equiv.)	C_6H_6 25 °C	$>$99% after 17 h[c]

[a]Deprotonation yield estimated by relative integrals in ^{1}H NMR. [b]After 3 additional days under Ar atmosphere back-formation of **L11** was noted by ^{1}H NMR. [c]Successfully isolated product.

The overall results of trials *e1*-*e5* showed that an extended time was required to achieve complete deprotonation of dipyrrin **L11**. Moreover, besides entry *e5*, an excess of base was needed to achieve a decent reaction rate. Although an excess of lithium diisopropylamide (LDA) and alkali bis(trimethylsilyl)amides gave full conversion to the corresponding alkali dipyrrinato salts **L11^{E}** after extended time, separation of remaining base and amine by-product from **L11^{E}** was not possible. Unsurprisingly, reaction of $SbBr_3$ in C_6D_6 with the mixture obtained in entry *e1* was unproductive as unwanted side-reactivity with the excess of base may occur. Ultimately, back-formation of **L11** was observed with an excess amount of $SbBr_3$. More promising approaches were realized with NaH and phenyllithium (entries *e4* and *e5*) as the resulting by-products and excess of base were easily separable from **L11^{E}**, thus enabling isolation of the alkali salts in these instances. Unfortunately, however, neither sodium nor lithium dipyrrinato salt could be used to access the respective SBDIPY complex. The reaction progress of **L11^{Na}** in the presence of $SbCl_3$ was monitored in THF-d_8 over 6 hours (Figure 78). Immediate formation of **L11** and gradual appearance of a new compound with downfield-shifted pyrrolic ^{1}H resonances, most likely assigned to SBDIPY **11Sb^{Cl}**, was observed over time. The cause of ligand protonation is not clear but may stem from trace impurities in solvent or $SbCl_3$. In addition to a slow colour change from orange to red, a fine red precipitate was observed after a few hours. After 6 hours the THF-d_8 solution contained approximately 71% SBDIPY complex, 24% **L11** and 5% **L11^{Na}** based on relative integrals of pyrrolic ^{1}H signals. However, the overall signal intensity decreased over this time frame with respect to residual THF due to the precipitation of an unknown reaction component. The precip-

itate was insoluble in alkanes and only sparsely soluble in CD_2Cl_2. ^{1}H NMR analysis of the precipitate revealed a mixture (circa 1:1 ratio) of ligand **L11** and an unknown compound—presumably **11Sb^{Cl}** as the signal set did not feature an additional N−H ^{1}H resonance.

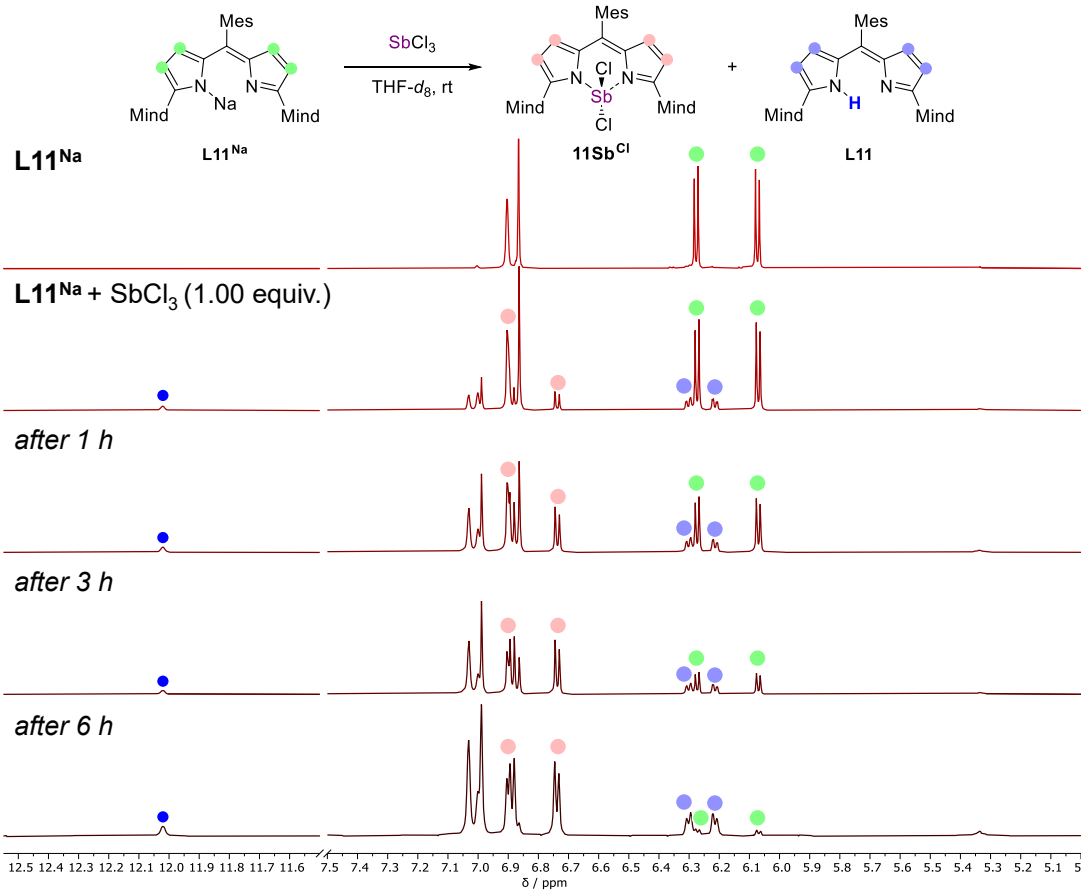


Figure 78: Reaction of **L11^{Na}** in the presence of $SbCl_3$ with colour-coded assignment of pyrrolic ^{1}H resonances. Aromatic region of ^{1}H NMR spectra (300 MHz) of the mixture in THF-d_8 are depicted below after given reaction times and are shown in descending order.

Unfortunately, isolation of **11Sb^{Cl}** remained unsuccessful as separation of the presumed product from **L11** was not possible. In order to see whether smaller main group elements could coordinate to the dipyrrin binding pocket of **L11**, other precursors were reacted with **L11^{Na}** ($BF_3{\cdot}OEt_2$) or **L11^{Li}** ($GeCl_2{\cdot}$(1,4-dioxane)). However, in all cases back-formation of **L11** was observed as the main reaction outcome. These findings were rather surprising given the fact that a similar dipyrrin ligand has been used by Betley and co-workers to access Cu(I) complexes.[199] Nonetheless, the authors used forcing conditions (72 h up to 110 °C), a reactive precursor (mesitylcopper) and extensive purification to obtain the target compound, which may all be necessary factors that need to be fulfilled for the synthesis of main group complexes of **L11**. The

challenging coordination environment of **L11** is also well-visible from solid-state data, which projects a much more encapsulated binding pocket as for other dipyrrins used in this work. Employing the structural parameters obtained from solid-state structures, the buried volumes of **L9** (V_{bur} = 66.5%) and **L11** (V_{bur} = 74.8%) were calculated (3.5 Å radius around centre, H atoms omitted), further emphasizing the excessively high degree of steric shielding in **L11** (Figure 79).[200]

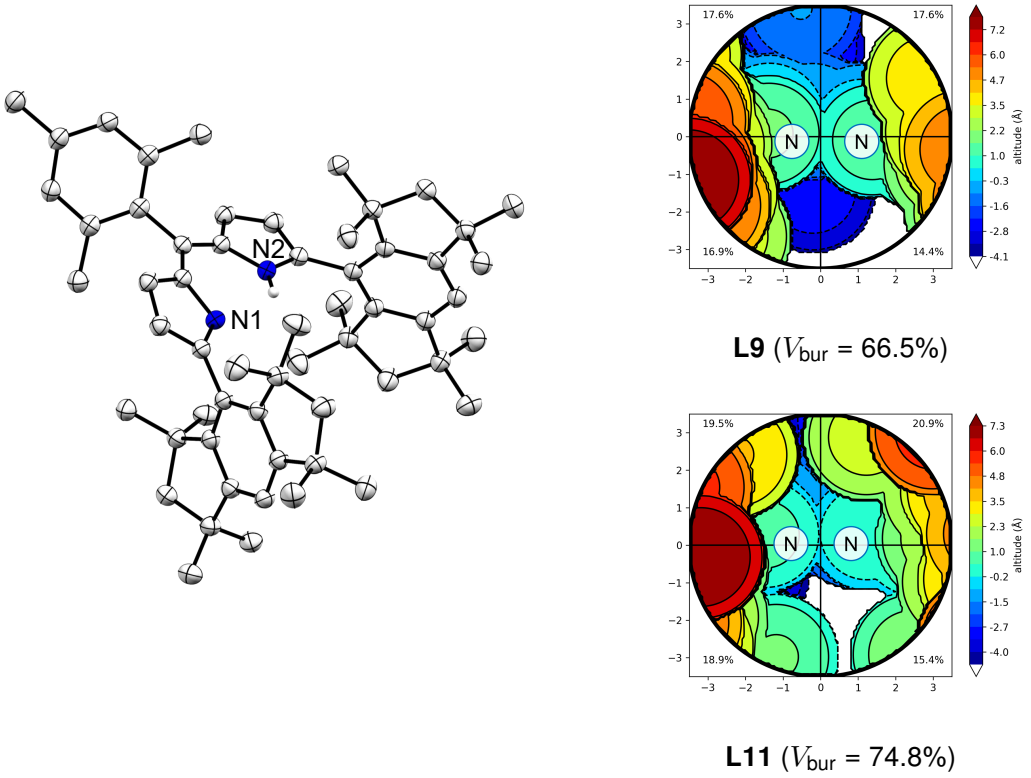


Figure 79: X-ray solid-state structure of **L11** (a). Non-nitrogen-bound hydrogen atoms were omitted for clarity and thermal ellipsoids were set to a 50% probability level. Buried volume plots (3.5 Å radius around centre, atomic radii scaled by 1.17 and H atoms omitted) of **L9** (b) and **L11** (c).[200]

An additional comparison of buried volumes with ligand **L10** would be desirable, however, this would require a set of crystallographic data of the free-base dipyrrin to ensure a suitable comparison with the other dipyrrins in the absence of coordination effects from a central atom.

3.1. Overview and classification of tested ligands

A series of dipyrromethenes **L5**-**L12** was successfully synthesized and evaluated as ligands for antimony and bismuth with the aim of improving the solution stability of pnictogen dipyrrin complexes (Figure 80).

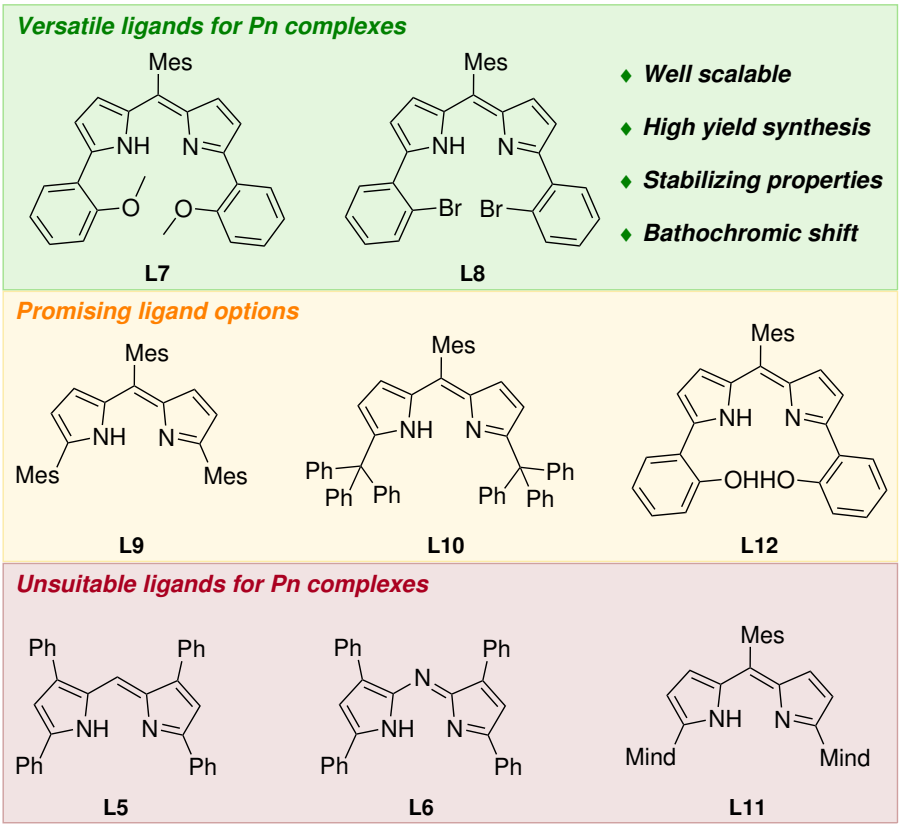


Figure 80: Overview of tested ligands in pursuance of more stable heavy pnictogen dipyrrin complexes.

The least amount of success was found with ligands **L11** and **L6** due to difficulties in synthesis and isolation of pnictogen dipyrrins. In this regard, dipyrrin **L5** was slightly more suitable as SBDIPY complex **5Sb^{Cl}** was successfully isolated. However, UV/Vis analysis of the complex showed a gradual decomposition of the complex in CH_2Cl_2. More promising ligand options were found with **L9**, **L10** and **L12** as the SBDIPY complexes thereof displayed a high stability and/or interesting spectroscopic properties (large Stokes shift and dual emission). Due to the close resemblance of **L9** and **L12** to already reported examples, as well as difficulties encountered for larger scale synthesis with **L10** and **L12**, the synthesized pnictogen dipyrrins were not considered for further applications.[138–140] Nonetheless, especially **L12** pnictogen complexes are promising candidates for photoredox or molecular sensing applications as the rigid tetracoordinate ligand scaffold could enable reactivity through the vacant apical coor-

dination sites. Overall, dipyrrins **L7** and **L8** proved to be the most suitable options from the considered scope, as the synthesis of ligands and pnictogen complexes could be easily carried out on gram scale. The new SBDIPY complexes also showed a considerable increase in solution stability as compared to SBDIPY complexes of **L1**-**L3**. Based on theses findings, **L7** and **L8** pnictogen complexes were selected as targets to explore further applications and reactivity of PnDIPY complexes.

Due to the increased stability of heavier halide substituted PnDIPY complexes compared to those with lighter halide substituents, the synthesis of PnDIPY complexes starting from antimony and bismuth triiodide should be investigated. Previous studies in the field have indicated a contribution iodide substituents to a higher SOC rate, which could also benefit the excited state lifetimes of PnDIPY complexes.[21]

4. Photochemical applications of heavy pnictogen dipyrrins

The data presented in the following chapter has been partially published in: A. Korzun, M. J. McKee, H. Neugebauer, O. Green, G. Schnakenburg, S. Grimme, N. Kornienko and A. Bismuto, *Inorg. Chem.* **2025**, *64*, 15667-15679.[174] Theoretical studies were performed by Dr. Hagen Neugebauer (Grimme group) and are included and indicated (‡) in this thesis to complement the experimental work. Cyclic voltammetry studies were conducted in collaboration with Morgan J. McKee and Prof. Dr. Nikolay Kornienko. Electrochemical data was evaluated by Morgan J. McKee and is included to complement the presented experimental work. All X-ray solid-state structures shown in this chapter were measured and refined by Dr. Gregor Schnakenburg.

4.1. Project aims

Owing to the heavy atom effect, molecular heavy pnictogen photochemistry has recently seen a surge in interest with exciting new developments emerging in the field of bismuth-catalysed photoredox chemistry,[78,80–83] alongside sporadic reports on pnictogen-based photosensitizers.[21,56,57,60] In order to evaluate the potential of the new generation of more stabilized PnDIPY complexes **7Pn^{X}** and **8Pn^{X}** to serve as photocatalysts, this chapter aims to investigate the light-driven reactivity of these complexes in the context of EnT photocatalysis and photoredox catalysis (Figure 81).

Once a photocatalytic mode of action has been determined for PnDIPY complexes, additional mechanistic and computational studies would be carried out in order to identify the role of the heavy central pnictogen in photocatalytic transformations.

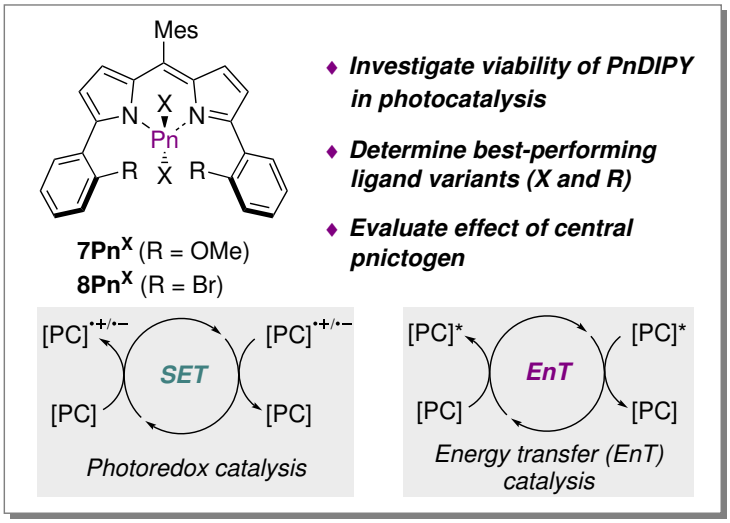
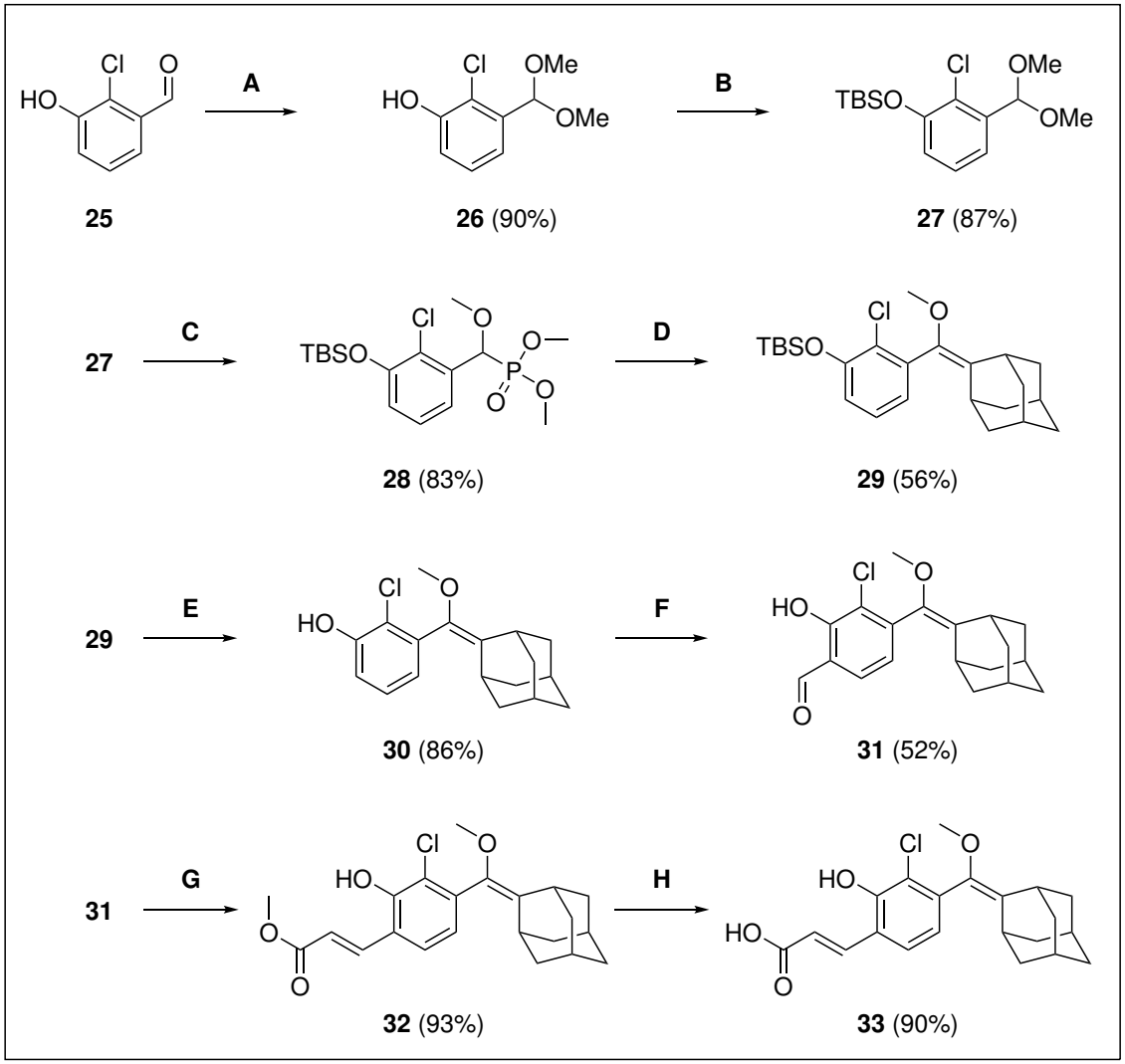


Figure 81: Conceptual project aim within this chapter.

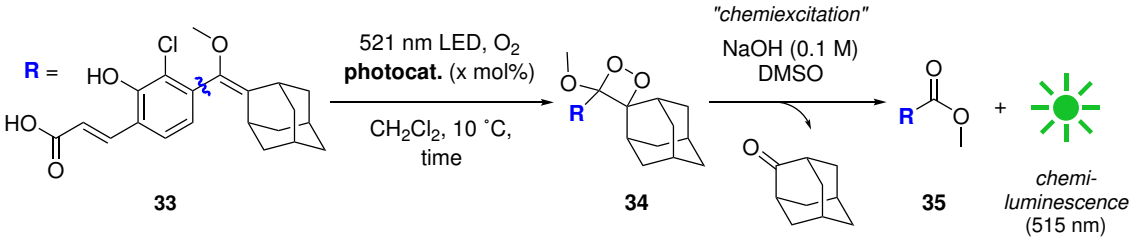
4.2. Energy transfer photocatalysis using pnictogen dipyrrins

In order to probe the ability of stabilized pnictogen dipyrrin complexes, **7Pn^{X}** and **8Pn^{X}**, to partake in triplet energy transfer (EnT) photocatalysis, singlet oxygen ($^1O_2$) reactivity was envisaged as an informative screening option. The formation of $^1O_2$ in the presence of a pnictogen dipyrrin would confirm the population of a sufficiently long-lived excited state with enough energy (>22.5 kcal/mol) to generate $^1O_2$ under irradiation, thus also fulfilling the minimal requirements for EnT photocatalysis.[33,35,201,202] A particularly effective method for qualitative $^1O_2$ detection was presented by Hananya and Green *et al.*, who developed a $^1O_2$ responsive luminophore (**33**).[203] Encouraged by the convenient use and possibility to internally compare the efficiency of different photosensitizers, $^1O_2$ probe **33** was prepared in a multi-step synthesis with an overall yield of 14%, following literature-reported protocols (Scheme 53).[203–206]



Scheme 53: Synthesis of singlet oxygen probe “SOCL" (**33**). The following reaction conditions were used: (**A**) $CH(OCH_3)_3$ (1.60 equiv.), *n*-Bu_4NBr_3 (5 mol%) in methanol for 6 h at rt, (**B**) imidazole (1.20 equiv.), TBSCl (2.00 equiv, TBS = *tert*-butyldimethylsilyl) in CH_2Cl_2 for 2 h at rt, (**C**) $P(OCH_3)_3$ (1.30 equiv.), $TiCl_4$ (1.20 equiv.) in CH_2Cl_2 for 2 h at 0 °C, (**D**) LDA (2 M in THF, 1.50 equiv.), adamantan-2-one (1.50 equiv.) in THF for 20 min at −78 °C and 12 h at rt, (**E**) TBAF (1.10 equiv.) in THF for 4 h at rt, (**F**) $MgCl_2$ (2.20 equiv.), NEt_3 (2.20 equiv.), paraformaldehyde (8.00 equiv.) in MeCN for 24 h at 94 °C, (**G**) methyl (triphenylphosphoranylidene)acetate (1.10 equiv.) in CH_2Cl_2 for 30 min at rt, (**H**) NaOH (2.10 equiv) in THF/H_2O (4:1) for 4 h at 60 °C.

In the presence of singlet oxygen, the probe **33** reacts to form a dioxetane **34** (Scheme 54). Upon treatment with a base, **34** decomposes to adamnatanone and benzoate ester **35**, accompanied by chemoluminescence emission in the form of green light, thus confirming the presence of $^1O_2$. The general approach shown in Scheme 54 was applied to a selection of pnictogen dipyrrins to assess their ability to serve as a photosensitizer for $^1O_2$. Preliminary experiments were carried out using a mixture of **33** in CH_2Cl_2 (2.67 mM, 1.00 mL) and dipyrrin chromophore (10 mol%) under an oxygen atmosphere. The solution was irradiated for 30 minutes under green light whereupon the crude concentrated under reduced pressure. Following this protocol, SBDIPY chromophores with ligands **L1**, **L7** and **L8** exhibited bright chemiluminescence upon quenching with NaOH solution (Scheme 54), thus giving qualitative evidence for the $^1O_2$ sensitization in the presence of SBDIPY chromophores.



Scheme 54: mechanism of singlet oxygen detection of probe **33**.

Based on the positive preliminary $^1O_2$ screening, reaction conditions and setup were adjusted to quantify dioxetane **34** formation using a luminometer. First trials were conducted using the bromide substituted SBDIPYs **7Sb^{Br}** and **8Sb^{Br}** as photocatalysts. A Schlenk tube containing probe **33** (0.85 mM in 2.5 mL CH_2Cl_2) and photocatalyst (0.005 mol%) frozen in liquid nitrogen and degassed once before backfilling with O_2 (circa 0.2 bar overpressure). The reaction mixture was then irradiated with a 521 nm LED light source at 10 °C and a total of five aliquots of the crude mixture were taken over the course of 5 minutes, while maintaining an O_2 atmosphere (experimental setup is shown in Figure 82).

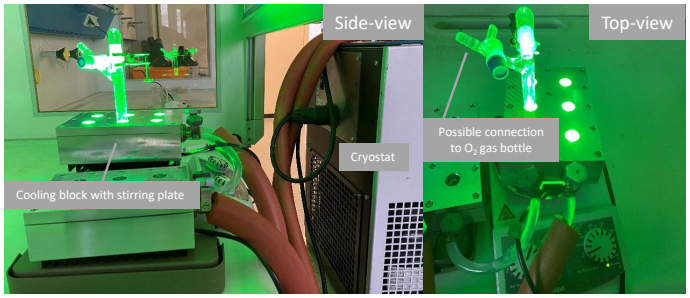


Figure 82: Experimental setup used for photocatalytic applications throughout this chapter. Connection to O_2 gas bottle was only used for experiments involving **33**.

Aliquots were diluted with a 1:1 mixture of DMSO and 0.1 M aqueous NaOH solution to give approximately 1 μM samples. The resulting chemiluminescence of **35** was immediately monitored over a 5 minute window using a luminometer. Photoluminescence decay plots after set sample irradiation times (15 s, 30 s, 1 min, 2 min and 5 min) of reaction aliquots with **7Sb^{Br}** and **8Sb^{Br}** as catalysts showed a gradual increase in photoluminescence intensity, with the latter complex exhibiting approximately twice the intensity (Figure 83).

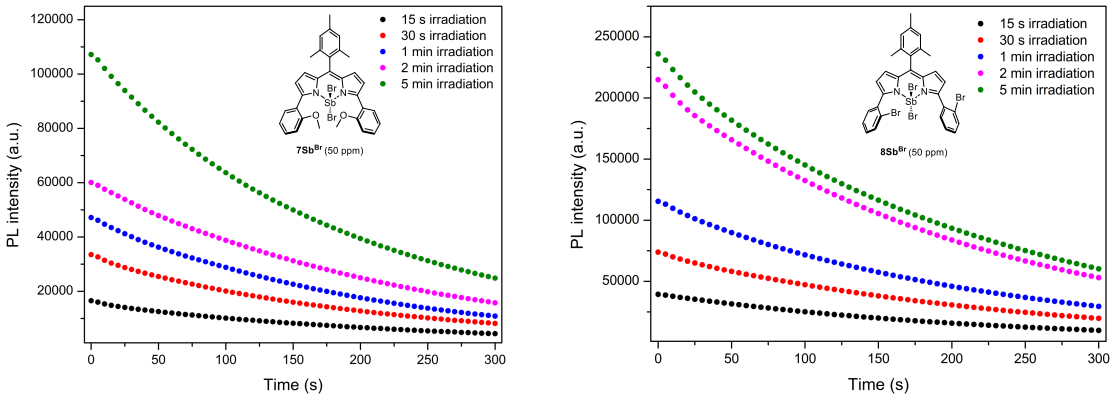


Figure 83: Time-dependent chemiluminescence decay of **35** upon irradiation of **33** in CH_2Cl_2 in the presence of 50 ppm photocatalyst: (a) **7Sb^{Br}** and (b) **8Sb^{Br}**. Photoluminescence intensity of aliquots was analyzed after given irradiation times.

As verified by an independent control sample without photocatalyst, the increase in photoluminescence intensity can indeed be attributed to the presence of SBDIPY chromophores (Figure84a). As an additional control reaction, the $^1O_2$ trapping experiment was also performed with ligand **L8** (0.005 mol%), which showed a substantial increase in photoluminescence intensity over time, thus signifying a notable photocatalytic activity of the dipyrrin **L8**.

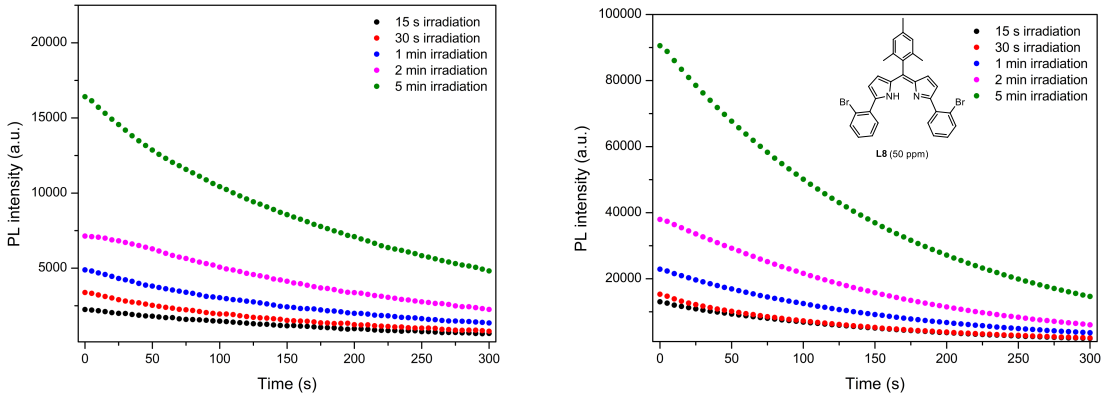


Figure 84: Time-dependent chemiluminescence decay of **35** upon irradiation of **33** in CH_2Cl_2 in the presence of photocatalyst: (a) **L8** (50 ppm) and (b) no additive. Photoluminescence intensity of aliquots was analyzed after given irradiation times.

Further measurements were conducted for the whole series of **L7** pnictogen complexes, using 100 ppm of catalyst for each trial. Contrary to **L8**, the free dipyrrin **L7** showed almost no activity as compared to the blank (Figure 85a), which is likely due to the inefficient population of any long-lived excited states in the absence of heavy atom substituents on the chromophore. However, a similarly low increase in photoluminescence intensity was recorded for complexes **7Sb^{F}** and **7Bi^{Br}** (Figure 85c-d). This may stem from complex decomposition, which these two complexes were found to be the most susceptible to. Moreover, decomposition can be possibly further facilitated through deaggregation at very low complex concentrations. Consequently, the activity of **7Sb^{F}** and **7Bi^{Br}** needed to be re-evaluated at higher catalyst loading (see Table 10). Nonetheless, complex **7Sb^{Cl}** displayed a slightly increased activity as compared to the ligand, thus indicating slight photosensitization by the SBDIPY complex, likely owing to a higher stability as compared to the above discussed complexes (Figure 85b).

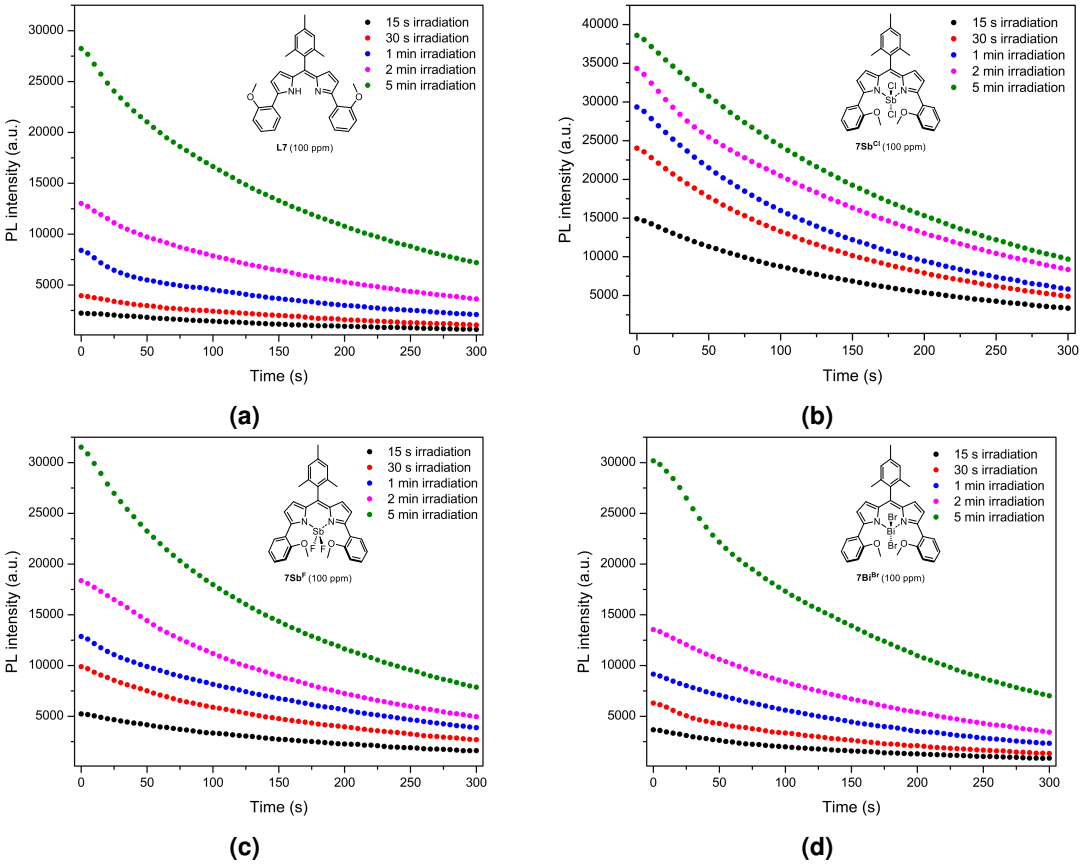


Figure 85: Time-dependent chemiluminescence decay of **35** upon irradiation of **33** in CH_2Cl_2 in the presence of 100 ppm photocatalyst: (a) **L7**, (b) **7Sb^{Cl}**, (c) **7Sb^{F}** and **7Bi^{Br}**. Photoluminescence intensity of aliquots was analyzed after given irradiation times.

Reassessment of **7Sb^{Br}** using a catalyst loading of 100 ppm demonstrated a superior efficiency as a photosensitizer compared to the other tested **L7** complexes but also pointed out an apparent error susceptibility of the given method as maximum PL intensity of experiments conducted with 50 ppm and 100 ppm were in a similar range (Figure 86a). This finding is rather contradictory as higher turnover to **34** is expected with increased catalyst loading and is likely attributed to experimental error. Possible error sources in this case may be differences in oxygen saturation of the reaction system due to improper adjustment of the gas connection or leaks in the system. With such short reaction times, this could have notable consequences, as the formation of $^1O_2$ is diffusion-controlled.[201] In addition to measurement inaccuracies when taking aliquots, another reason for the deviation could be the gradual decomposition of **34** under insufficient cooling, thus causing a lowering in recorded PL intensity. Finally, **1Sb^{Br}** was also tested as a photosensitizer but showed no detectable activity as compared to the blank (Figure 86b). As for **7Sb^{F}** and **7Bi^{Br}**, the lack of activity could be due to complex decomposition, which might be promoted by deaggregation effects.

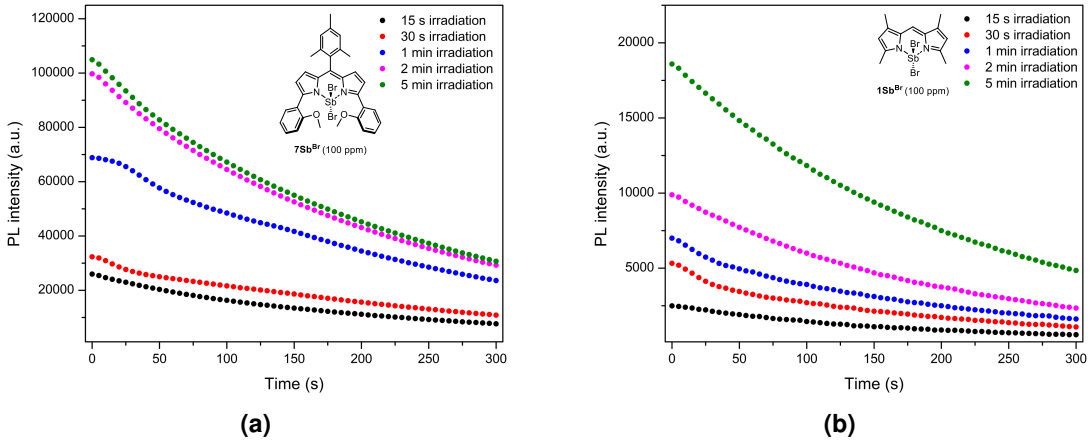
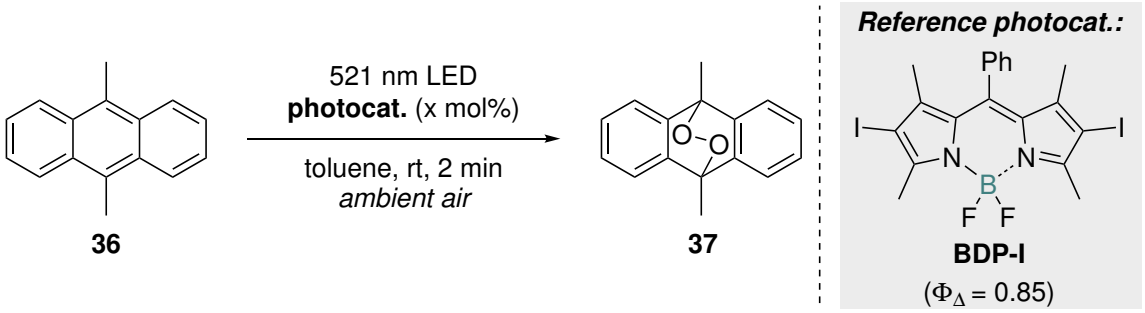


Figure 86: Time-dependent chemiluminescence decay of **35** upon irradiation of **33** in CH_2Cl_2 in the presence of 100 ppm photocatalyst: (a) **7Sb^{Br}** and (b) **1Sb^{Br}**. Photoluminescence intensity of aliquots was analyzed after given irradiation times.

Since **7Sb^{Br}** showed a superior activity as a photosensitizer within the series of **L7** dipyrrins and the activity of the free ligand **L7** appeared negligible, an attempt was made to determine the $^1O_2$ quantum yield (Φ_Δ) of **7Sb^{Br}** using a literature-reported protocol.[207,208] The $^1O_2$ quantum yield was estimated using an air-saturated toluene solution of 9,10-dimethylanthracene (**36**) with an absorbance around 1.5. To this solution the photosensitizer **7Sb^{Br}** or reference photocatalyst **BDP-I** was added and its absorbance adjusted to approximately 0.1 at an incident wavelength of 521 nm.[208,209] In the presence of $^1O_2$ compound **36** forms the endoperoxide **37**, which successively results in a decrease of UV/Vis absorption caused by a loss of aromaticity in **36** (Scheme 55).



Scheme 55: Photocatalytic oxidation of **36** under air in the presence of a $^1O_2$ photosensitizer (left). Reference photocatalyst **BDP-I** with literature-reported Φ_Δ^{ref} value (right).[208,209]

The above described reaction mixtures with **7Sb^{Br}** or **BDP-I** as photocatalysts were irradiated under 521 nm light for 30 seconds, followed by immediate measurement of the corresponding UV/Vis spectrum. This process was repeated five times for a total irradiation time of 2 minutes, resulting in a pronounced decrease of the absorption bands of **36** (Figure 87). Measurements for both, reference and **7Sb^{Br}**, were carried out in triplicates and the absorbance of **36** at 379 nm was plotted against the irradiation time (Figure 87). It should be noted that, due to inconsistencies observed in the luminometer study, it was decided to conduct the experiment under ambient air and using aerated toluene. Given the short exposure of **7Sb^{Br}** to air, no signs of decomposition were identified in the UV/Vis spectra of the reaction mixture (Figure 87, right).

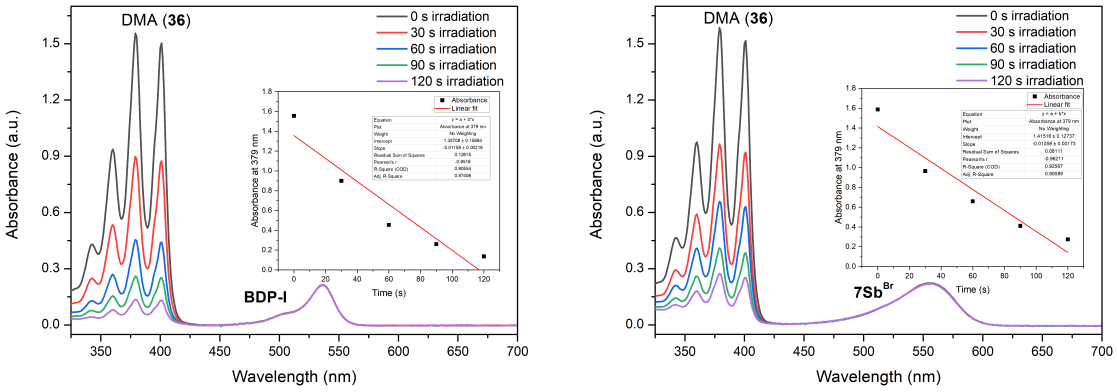


Figure 87: UV/Vis spectra and linear regression analysis of absorbance decrease at 379 nm of 9,10-dimethylanthracene (DMA, **36**) in the presence of **BDP-I** (left) and **7Sb^{Br}** (right) after given irradiation times in toluene at room temperature and under ambient air.

Based on the collected data, the relative $^1O_2$ quantum yield of **7Sb^{Br}** (Φ_Δ) was calculated using equation 5.

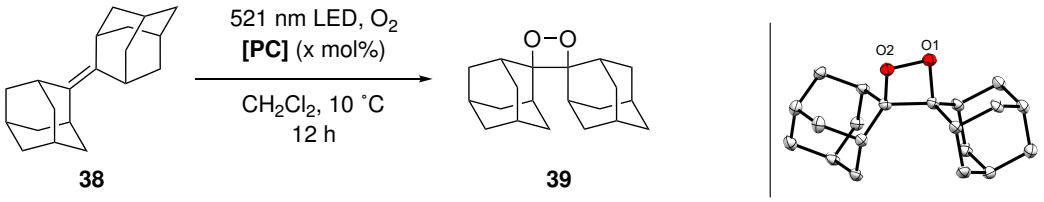
$$\Phi_\Delta = \Phi_\Delta^{\mathrm{ref}} \cdot \frac{m}{m_{\mathrm{ref}}} \cdot \frac{\mathrm{I}_{\mathrm{abs}}^{\mathrm{ref}}}{I_{\mathrm{abs}}}. \tag{5}$$

Here, the superscript "ref" is ascribed to reference sample **BDP-I**, m is the slope of the linear fit of the absorbance decay of **36** at 379 nm against time and $\mathrm{I}_{\mathrm{abs}}$ denotes the correction factor which is given by

$$\mathrm{I}_{\mathrm{abs}} = 1 - 10^{-\mathrm{OD}}, \tag{6}$$

where OD refers to the optical density of the sample at an incident wavelength of 521 nm. Following the above-described procedure, the relative singlet oxygen yield of **7Sb^{Br}** was determined as a mean value with standard error of $\Phi_\Delta = 0.76 \pm 0.02$. The value lies in the upper range of commonly used porphyrin-based photosensitizers and ranks among the highest reported values for Sb-based systems.[56,57,210,211]

With clear evidence for the photocatalytic activity of pnictogen dipyrrins, synthetic applications involving $^1O_2$ reactivity were targeted. Adamantylideneadamantane (**38**) was selected as a convenient substrate for the optimization of reaction conditions as the room temperature stable dioxetane **39** forms selectively in the presence of $^1O_2$ (Scheme 56) and can be easily distinguished from the starting material by ^{1}H NMR spectroscopy (Figure 88).



Scheme 56: Photocatalytic oxidation of **38** under an oxygen atmosphere (left). X-ray solid-state structure of **39** (right). Hydrogen atoms were omitted for clarity and thermal ellipsoids were set to a 50% probability level.

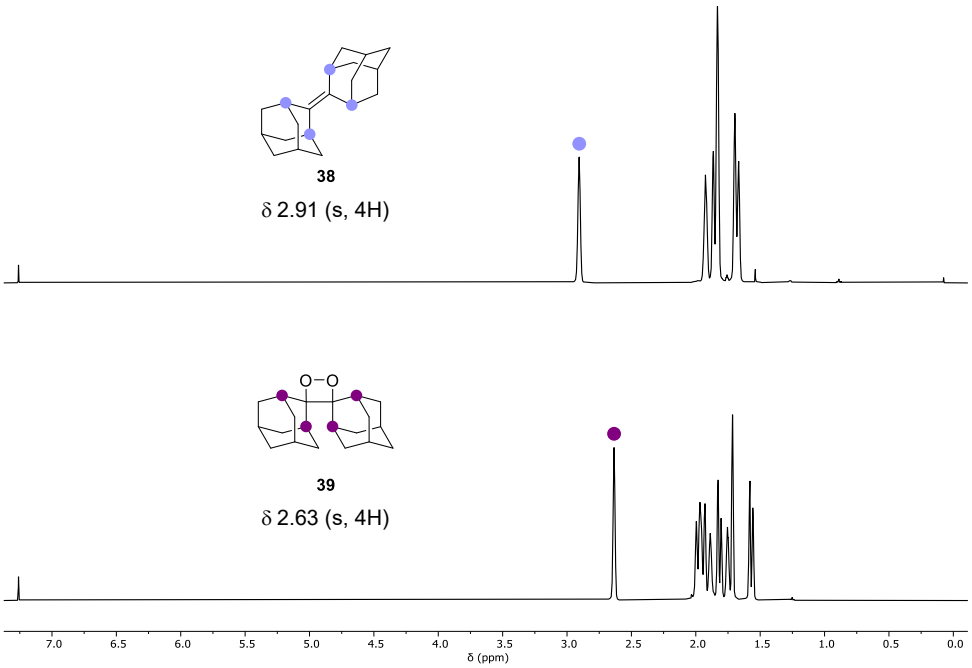


Figure 88: Comparison of ^{1}H NMR spectra of **38** (400 MHz) and **39** (500 MHz) in $CDCl_3$. Characteristic ^{1}H resonances of both compounds are visually marked.

The oxidation of **38** was evaluated for a series of **L7** complexes (Table 10, entries *e1-e12*) and further supported through control experiments *c1-c6* (Table 10). The conversion of **38** was monitored by ^{1}H NMR, using 1,3,5-trimethoxybenzene as an internal standard. It should be noted that the oxidation of **38** proceeded selective with only trace amounts of adamantan-2-one observed as a decomposition product of **39** in a few cases.

Table 10: Catalyst screening of **L7** dipyrrins for oxidation reaction of **38** under irradiation and control experiments and (*c1-c8*).

Entry	Photocatalyst [PC]	Catalyst loading (mol%)	^{1}H NMR conversion[a]
e1	**7Bi^{Br}**	10	24%
e2	**7Sb^{F}**	10	83%
e3	**7Sb^{F}**	5	15%
e4	**7Sb^{Cl}**	5	25%
e5	**7Sb^{Br}**	10 to 0.025	>99%
e6	**7Sb^{Br}**	0.01	55%
e7	**7Sb^{Br}**	0.005	40%
e8[b]	**7Sb^{Br}**	0.5	50%
e9[c]	**7Sb^{Br}**	0.025	62%
e10	**7Sb^{+}[BArF]**	1	>99%
e11	**7Sb^{+}[BArF]**	0.025	>25%
c1	None	–	0%
c2	**L7**	10	0%
c3	$SbBr_3$	10	0%
c4[d]	**7Sb^{Br}**	10	0%
c5[e]	**7Sb^{Br}**	10	0%
c6[f]	**7Sb^{Br}**	100	0%
c7[g]	**7Sb^{Br}**	0.5	>99%
c8	**L7** + $SbBr_3$ (1:1)	0.05	38%
c9	**L7** + $SbBr_3$ (1:1)	0.005	4%

[a] ^{1}H NMR conversion was estimated using 1,3,5-trimethoxybenzene (0.20 equiv.) as an internal standard. [b] Reaction stopped after 30 minutes. [c] Experiment performed at room temperature. [d] Experiment performed without irradiation. [e] Experiment performed with 1.00 equiv. of DABCO. [f] Experiment performed under Ar atmosphere. [g] Experiment performed in the presence of 1.00 equiv of TEMPO.

The screened reaction conditions of the photocatalytic oxidation of **38** revealed several notable details. First, as expected from previous studies using probe **33**, complexes **7Bi^{Br}**, **7Sb^{F}** and **7Sb^{Cl}** showed significantly lower conversion towards dioxetane **39** (entries *e1*-*e4*) as compared to **7Sb^{Br}** at catalyst loadings of 10 or 5 mol% (entry *e5*). Interestingly, no conversion of the starting material **38** was observed without addition of a photocatalyst and in the presence of **L7** (10 mol%) (entries *c1* and *c2*), thus indicating that pnictogen dipyrrins **7Bi^{Br}** and **7Sb^{F}** also function as photocatalyst but likely require sufficiently high concentrations to prevent sample degradation. This was not given in previously discussed luminometer studies, which were likely hampered by the low concentrations of photosensitizers. Based on this information, however, complexes **7Bi^{Br}**, **7Sb^{F}** and **7Sb^{Cl}** were classified as ineffective photocatalysts.

Dipyrrin **7Sb^{Br}** on the other hand displayed outstanding catalytic activity, reaching quantitative conversion of **38** at a catalyst loading of only 250 ppm (0.025 mol%) while still showing activity with just 50 ppm of **7Sb^{Br}**. Based on catalyst concentration and ^{1}H NMR conversion of **38**, a TON value of 5500 was determined for entry *e7*.

Additional control reactions *c3*-*c8* were performed to verify the role of **7Sb^{Br}** as a $^{1}O_2$ photosensitizer. The oxidation of **38** did not proceed without irradiation (entry *c4*) or in the presence of 1.00 equiv. of 1,4-diazabicyclo[2.2.2]octane (DABCO, entry *c5*) under otherwise identical conditions. DABCO is known for quenching $^{1}O_2$, which further highlighted the importance of $^{1}O_2$ as a reactive oxygen species in this reaction.[212] Moreover, **7Sb^{Br}** and **38** were dissolved in CD_2Cl_2 and irradiated under argon atmosphere for 12 h to see whether the compounds react in the absence of oxygen (entry *c6*). However, no changes were observed based on ^{1}H NMR data. In contrast, quantitative conversion towards **39** was observed in the presence of **7Sb^{Br}** and 1.00 equiv. of radical trap (2,2,6,6-Tetramethylpiperidin-1-yl)oxyl (TEMPO), thus indicating none or neglible single-electron processes involved in the photooxygenation of **38** (entry *c7*).

Finally, no reaction was observed in the presence of $SbBr_3$ as photocatalyst (entry *c3*). Instead, in the presence of $SbBr_3$ and ligand **L7**, considerable conversion of the starting material was noted with low catalyst loadings (entries *c8* and *c9*). Consequently, the mixture of $SbBr_3$ and ligand **L7** was independently analyzed under inert conditions by ^{1}H NMR. As for **L1**, addition of 1.00 equiv. of $SbBr_3$ to a THF solution of **L7** led to the formation of multiple compounds based on ^{1}H NMR analysis in CD_2Cl_2 (Figure 89). Moreover, the ^{1}H NMR spectrum of the $SbBr_3$ and **L7** mixture displayed appreciable overlap with data of the previously discussed reaction of **7Sb^{Br}** with 10-CSA (Chapter 3). The reaction of ligand **L7** and antimony halide resulted

in a slightly less selective outcome, yielding at least three different species base on ^{1}H NMR spectroscopy. As observed in the reaction of **L1** with $SbBr_3$, formation of the respective SBDIPY complex may also occur in the case of **L7**, but was not definitively verifiable due to signal overlap in the aromatic region of the ^{1}H NMR data. Overall, the successful photooxygenation of **38** in the presence of **L7** and $SbBr_3$ suggests that either trace amounts of complex **7Sb^{Br}** or an unknown ligand-related compound, such as antimonate **L7-HSbBr**, serve as $^1O_2$ photosensitizers for entries *c8* and *c9*.

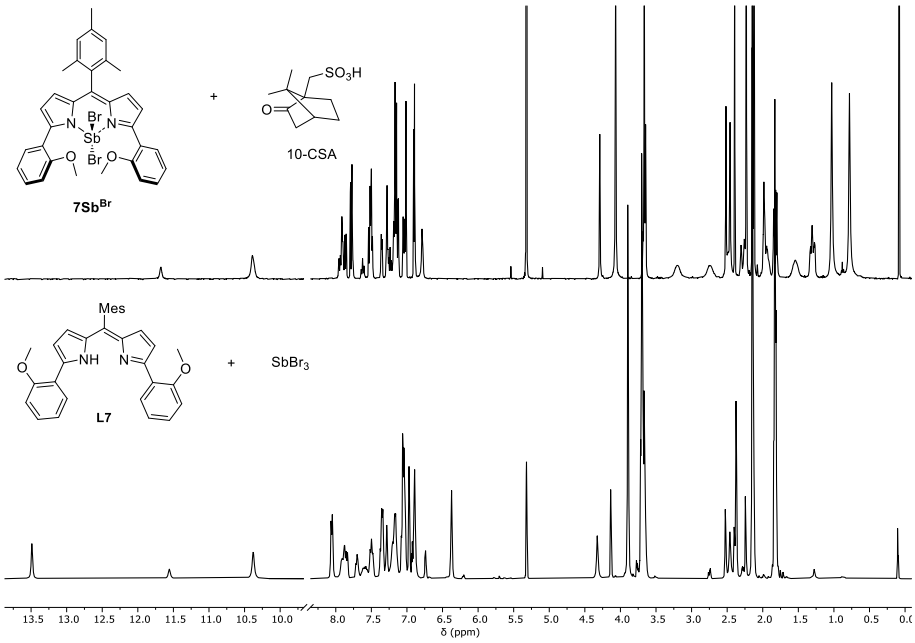


Figure 89: Comparison of crude ^{1}H NMR spectra (400 MHz, CD_2Cl_2) of **7Sb^{Br}** in the presence of 1.00 equiv. 10-CSA (top) and crude product obtained by mixing equimolar amounts of $SbBr_3$ and **L7** for 10 h in THF at −30 °C (bottom).

Besides **7Sb^{Br}**, stibenium complex **7Sb$^+$[BArF]** also displayed a considerable catalytic activity, albeit performing worse than the neutral complex **7Sb^{Br}** at lower catalyst loading (entry *e10* and *e11*). This outcome may result from a higher decomposition susceptibility of **7Sb$^+$[BArF]** as compared to **7Sb^{Br}** under given conditions but could also relate to a lower excited-state lifetime.

Besides **L7** pnictogen complexes, several other dipyrrin-related compounds were screened as photocatalysts for the oxidation reaction of **38** (Table 11).

Table 11: Additional catalyst screening for oxidation reaction of **38** under irradiation.

Entry	Photocatalyst [PC]	Catalyst loading (mol%)	^{1}H NMR conversion[a]
e12	**8Sb^{Cl}**	5	57%
e13	**8Sb^{Cl}**	0.5	traces
e14	**8Sb^{Br}**	0.005	74%
e15	**L8**	0.005	45%
e16	**1Sb^{Br}**	0.1	>99%
e17	**1Sb^{Br}**	0.025	50%
e18	**7B^{F}**	0.01	>99%

[a] ^{1}H NMR conversion was estimated using 1,3,5-trimethoxybenzene (0.20 equiv.) as an internal standard.

Antimony complexes of dipyrrin **L8** were found to have a slightly higher acitivity than the respective **L7** complexes. Complex **8Sb^{Cl}** displayed a slightly higher conversion of **38** than **7Sb^{Cl}** but was ineffective at lower catalyst loadings (entries *e12* and *e13*), likely due decomposition. The analogous bromide substituted SBDIPY **8Sb^{Br}**, however, showed an even higher conversion of **38** at a catalyst loading of 50 ppm than the hitherto best-performing SBDIPY complex **7Sb^{Br}** (entry *e14*). The overall higher turnover observed in entries *e12-e14* could be attributed to the additional heavy atom effect associated with ligand **L8**, which promotes ISC to an excited triplet state as a key step in the photosensitization of $^1O_2$. In contrast to **L7**, however, the dipyrrin **L8** exhibited significant activity as a photosensitizer even at a low catalyst loading (entry *e15*), which led to an ambiguity of the previously discussed results for **7Sb^{X}** complexes as the catalytic activity can no longer be clearly assigned to the SBDIPY chromophores. Surprisingly, despite the previously discouraging results for **1Sb^{Br}** using probe **33**, the first-generation SBDIPY chromophore displayed significant photocatalytic activity (entry *e16*). Nonetheless, the conversion decreased at lower catalyst loading (entry *e17*), which is consistent with previous findings and thus further indicates a concentration-dependent stability of the active photosensitizer.

Finally, the highest conversion of **38** at lowest overall catalyst loading was observed for BODIPY chromophore of ligand **L7**, **7B^{F}**. This finding was particularly surprising as, unlike other commonly found BODIPY-based photocatalysts, **7B^{F}** does not contain any heavy atoms, which are often essential to access long-lived excited triplet states and are therefore relevant for photocatalysis.[107,108,112] Nonetheless, recent studies

have also highlighted heavy-atom-free strategies for the design of BODIPY-based photocatalysts.[107–109,112] These approaches rely on enhancing ISC efficiency through the introduction of geometric contortion in the chromophore, as well as through electronic effects in structures that feature donor and acceptor moieties.[108,109] In this regard, the twisting of the 2-methoxyphenyl groups in **L7** dipyrrins may contribute significantly to a population of excited charge-transfer state that have a sufficient longevity to partake in EnT processes. In order to gain additional insight into this matter, the photoluminescence lifetimes of both **7Sb^{Br}** and **7B^{F}** were recorded (Figure 90).

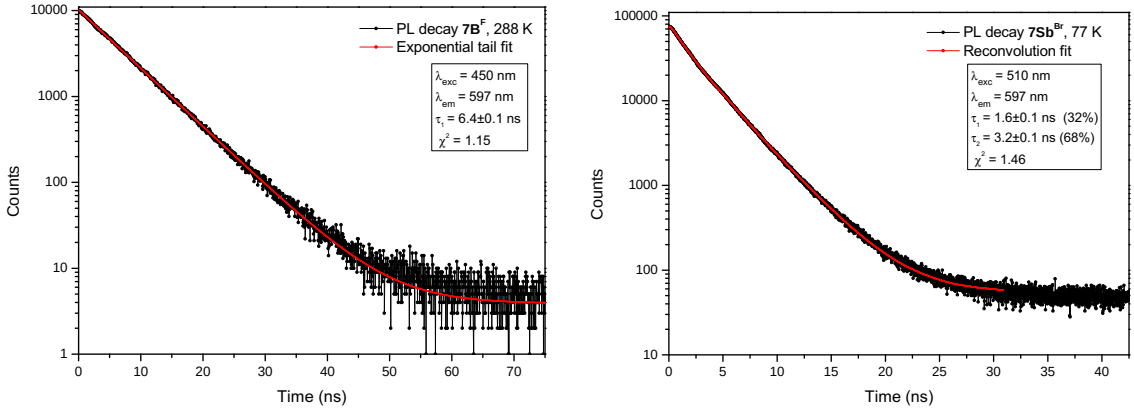


Figure 90: Photoluminescene decays and exponential fit functions for **7B^{F}** at 288 K in CH_2Cl_2 (left) and **7Sb^{Br}** at 77 K in toluene (right).

The biexponential luminescence lifetime of **7Sb^{Br}** was determined as τ_2 = 3.2 ns (68%) and τ_1 = 1.6 ns (32%) in toluene at 77 K, which is considerably lower than values found for BODIPY photosensitizers.[113] The luminescence lifetime of the corresponding BODIPY chromophore **7B^{F}** (λ_{emi} = 597 nm) was found to be slightly higher with a value of τ = 6.4 ns in CH_2Cl_2 at 288 K. This value is in the same range as reported fluorescence lifetimes of comparable BODIPY chromophores with 2-methoxyphenyl substituents, but still rather short in comparison to common BODIPY photosensitizers.[113,213] On a similar note, strained systems, such as B−N functionalized anthracenes, have been reported to display luminescence lifetimes in the nanosecond regime while simultaneously being $^1O_2$ photosensitizers.[214] In conclusion, the determined luminescence lifetimes of **7Sb^{Br}** and **7B^{F}** indicate no phosphorescence emission in both cases. As the presence of triplet excited states presents an important prerequisite for the sensitization of $^1O_2$, possible non-radiative singlet to triplet transitions were investigated by means of theory.[201,215]

4.3. Theoretical considerations[174]‡

In order to obtain more insight into the electronic structures of **7Sb^{Br}**, the energy gaps between ground state and first excited singlet and triplet states ($S_0 \rightarrow S_1$, $S_0 \rightarrow T_1$, $S_1 \rightarrow T_1$) were calculated using the (ω = 0.15) ωB97X-D4[216–218]/def2-QZVPP[219] //B97-3c[220] level of theory, further employing the SMD solvation model[221] for CH_2Cl_2 in the ORCA software package.[174,222–224] Absorption energies were first calculated using a TD-DFT approach but were found to be in poor agreement with experimental data (Table 12). As an alternative method to TD-DFT, a ΔSCF approach was applied as it has been shown to yield improved accuracy for excited-state applications.[225,226] The S_1 state was calculated on the same DFT level by ΔUKS as previous results obtained from TD-DFT indicated the HOMO-LUMO excitation to fit the $S_0 \rightarrow S_1$ transition. Following the ΔSCF procedure, energy values were obtained as differences of the SCF energies, *i.e.*

$$\Delta E(S_0 \rightarrow S_1) = E(S_1) - E(S_0). \tag{7}$$

The results obtained in this way were in better agreement with the experimental data than TD-DFT calculations, showing differences below 3 kcal/mol (Table 12).[174] The electronic transitions considered in **7Sb^{Br}** and **7Bi^{Br}** were identified as being ligand-centred.

Table 12: Calculated absorption energies on the (ω = 0.15) TDA-ωB97X-D4/def2-QZVPP //B97-3c+SMD(CH_2Cl_2) TD-DFT level of theory labeled as "TD-DFT". Absorbance and emission values calculated on the ωB97X-D4/def2-QZVPP//B97-3c level of theory (Absorbance) and ωB97X-D4/def2-QZVPP for emission (optimized in S_1 state). The S_1 state was accessed using ΔUKS; these values are labeled as "ΔUKS". Experimental data are provided for comparison.[174]‡

Compound (data set)	Absorbance ($S_0 \rightarrow S_1$)	Emission ($S_1 \rightarrow S_0$)
7Sb^{Br} (TD-DFT)	2.62 eV / 473 nm	–
7Sb^{Br} (ΔUKS)	2.10 eV / 591 nm	1.92 eV / 647 nm
7Sb^{Br} (exp.)	2.20 eV / 563 nm	2.08 eV / 597 nm
7Bi^{Br} (TD-DFT)	2.66 eV / 466 nm	–
7Bi^{Br} (ΔUKS)	2.13 eV / 582 nm	1.94 eV / 638 nm
7Bi^{Br} (exp.)	2.21 eV / 561 nm	2.10 eV / 590 nm
7Sb^{+}[BArF] (ΔUKS)	2.02 eV / 613 nm	1.84 eV / 672 nm
7Sb^{+}[BArF] (exp.)	2.15 eV / 577 nm	2.04 eV / 608 nm

In order to gain information on the potential presence of an excited triplet state, the vertical electronic transition $\mathrm{S}_0 \rightarrow \mathrm{T}_1$ was calculated as 35.5 kcal/mol (Figure 91), which provides a sufficiently high energy for the sensitization of $^1O_2$ (22.7 kcal/mol).[35] Moreover, calculated ground state triplet gap $\Delta E(\mathrm{S}_0 \rightarrow \mathrm{T}_1)$ (805 nm) lies outside of the wavelength range detected by the spectrometer. Considering the spectroscopic data of **9Sb^{Br}**, a phosphorescence emission could also be present for **7Sb^{Br}**. Moreover, the calculated energy gap $\Delta E(\mathrm{S}_0 \rightarrow \mathrm{T}_1)$ provides an estimate for the triplet excited state energy (ΔE_T) for **7Sb^{Br}** which ranks at the lower end of literature-known EnT photocatalysts.[7]

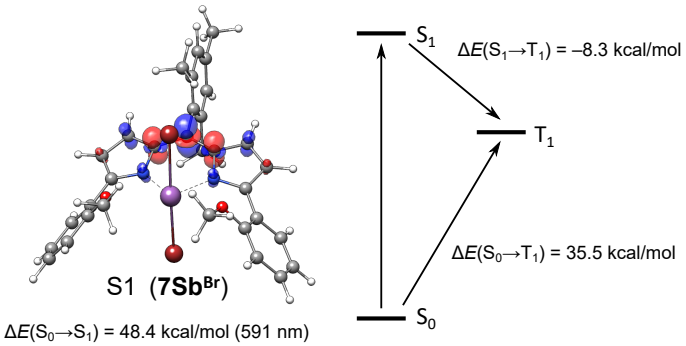


Figure 91: Electron difference-density plot of the $\mathrm{S}_0 \rightarrow \mathrm{S}_1$ HOMO-LUMO transition, accessed by ΔUKS (left). Electron density decrease and increase is shown by red and blue surfaces respectively (isovalues set to 0.005 au). Energy gap of $\Delta E(\mathrm{S}_0 \rightarrow \mathrm{S}_1)$ was calculated vertically on the S_0 geometry, and $\Delta E(\mathrm{S}_1 \rightarrow \mathrm{T}_1)$ and $\Delta E(\mathrm{S}_0 \rightarrow \mathrm{T}_1)$ were computed adiabatically using optimized geometries of the respective electronic states (right).[174]‡

4.4. Mechanistic considerations

Another question that arose with regard to SBDIPY photocatalysts was whether the central element could be involved in the observed reactivity as the presence of a redox-active ligand and a heavy pnictogen centre may lead to unusual redox behaviour upon irradiation. To obtain more information on this subject, cyclic voltammetry (CV) measurements of selected **L7** dipyrrins were carried out with and without irradiation of the electrochemical cell at 521 nm using a circular LED reactor (Figure 92).

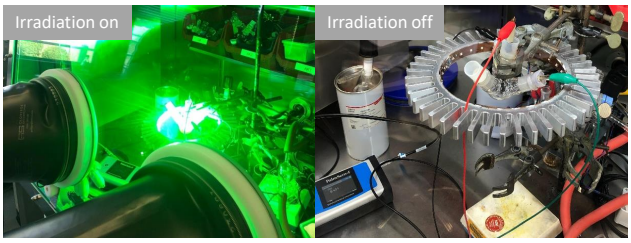


Figure 92: Experimental setup used for CV study of **L7** dipyrrins under argon atmosphere and with (left) and without irradiation (right).

All measurements were conducted with $TBAPF_6$ in dry CH_2Cl_2 (0.1 M) in an argon-filled glovebox to ensure a moisture- and oxygen-free environment. Complex **7Sb^{Br}** displayed two pronounced redox events—an irreversible redox event at approx. −1.25 V vs FcH/FcH^+ and a quasi-reversible second redox couple at −1.90 V (Figure 93). Moreover, irradiation of the electrochemical cell with green light led to the emergence of a new redox wave at approx. −1.00 V alongside a slight increase in current response, hinting at a change in the electronic structure of **7Sb^{Br}**.

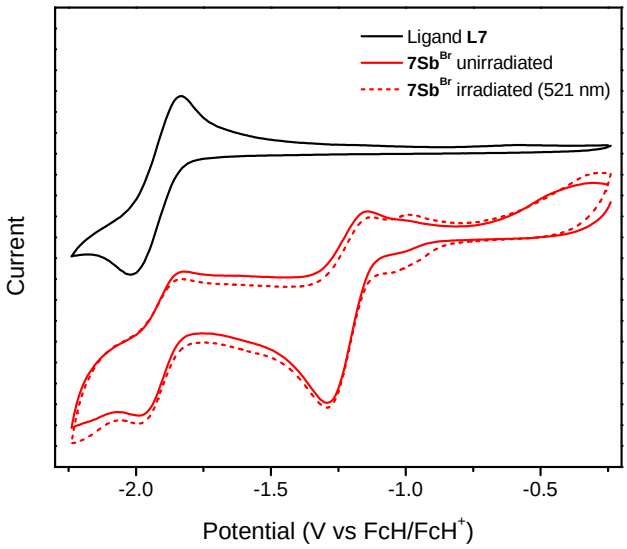


Figure 93: Qualitative comparison between cyclic voltammograms of ligand **L7** and **7Sb^{Br}** (both 1 mM) without (solid line) and with irradiation under a green LED light source (dashed line). The measurements were conducted in a CH_2Cl_2 solution of $TBAPF_6$ (0.1 M) at a scan rate of 100 mV/s.

In comparison, ligand **L7** featured only a single quasi-reversible redox event also at −1.90 V, indicating that in the case of **7Sb^{Br}** the second redox event is ligand-centred. For the bismuth complex **7Bi^{Br}** a cyclic voltammogram comparable to the data of **7Sb^{Br}** was obtained, albeit displaying an overall higher irreversibility with no clear return peak of the first reduction at −1.34 V and a significantly broader second redox event around −2.04 V (Figure 94). Moreover, comparison of **7Sb^{Br}** with the **L1**

analogue **1Sb^{Br}** revealed strikingly different electrochemical behaviours with **1Sb^{Br}** exhibiting only a single irreversible reduction at −1.59 V (Figure 94). This finding is likely correlated with the different electronic structures of the two dipyrrin ligands.

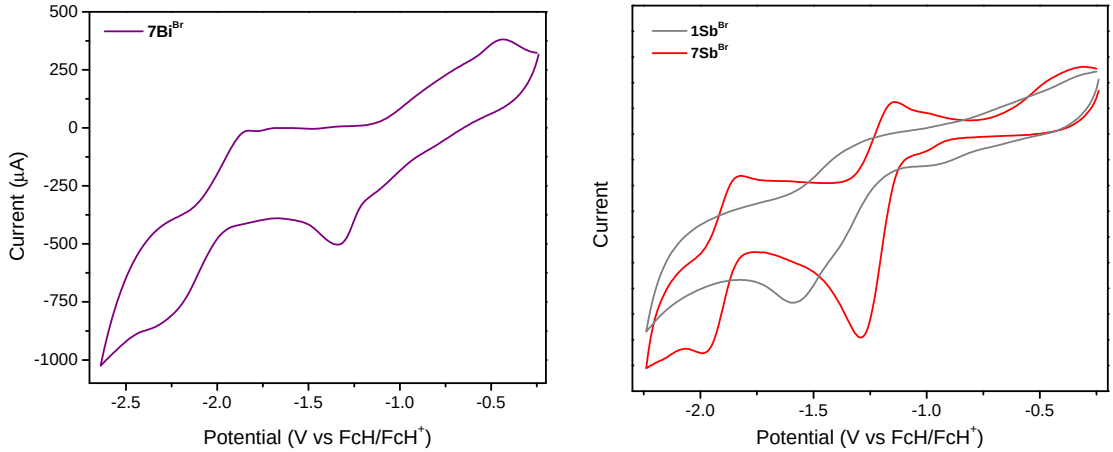


Figure 94: Cyclic voltammogram of **7Bi^{Br}** (left) and qualitative comparison of cyclic voltammograms of **1Sb^{Br}** and **7Sb^{Br}** (right). All measurements were conducted at a 1 mM analyte concentration in a CH_2Cl_2 solution of $TBAPF_6$ (0.1 M) using a scan rate of 100 mV/s.

Given the ambiguous nature of the first redox event found for **7Sb^{Br}**, the redox potentials of **7Sb^{Br}** were computed on the (ω = 0.15) ωB97X-D4/def2-QZVPP//B97-3c+SMD(CH_2Cl_2) level of theory to discern between ligand- and metal-centred redox events.‡ The respective redox potentials were calculated employing the Nernst equation with the ferrocene/ferrocenium (FcH/FcH^+) redox couple as a reference (explicitly calculated on the same level of theory).[174]‡The first calculated reduction potential was found to be in excellent agreement with the experimentally observed cathodic peak potential at E_{red} = −1.29 V. The single-electron reduction was identified to be centred on the dipyrrin ligand as indicated by the singly occupied molecular orbitals (SOMO, Figure 95). However, the calculated value of the second reduction was in poor agreement with the experimentally observed cathodic peak potential at E_{red} = −2.00 V, thus indicating a deviation from a simple two electron reduction of the complex. Indeed, when taking the dissociation of bromide substituents from complex **7Sb^{Br}** into account, the calculated reduction potential (E_{red} = −2.01 V) fitted substantially better to the experimental cathodic peak potential, thus identifying the dissociation of two bromide ions as a possible side reaction under reducing conditions (Figure 95).‡

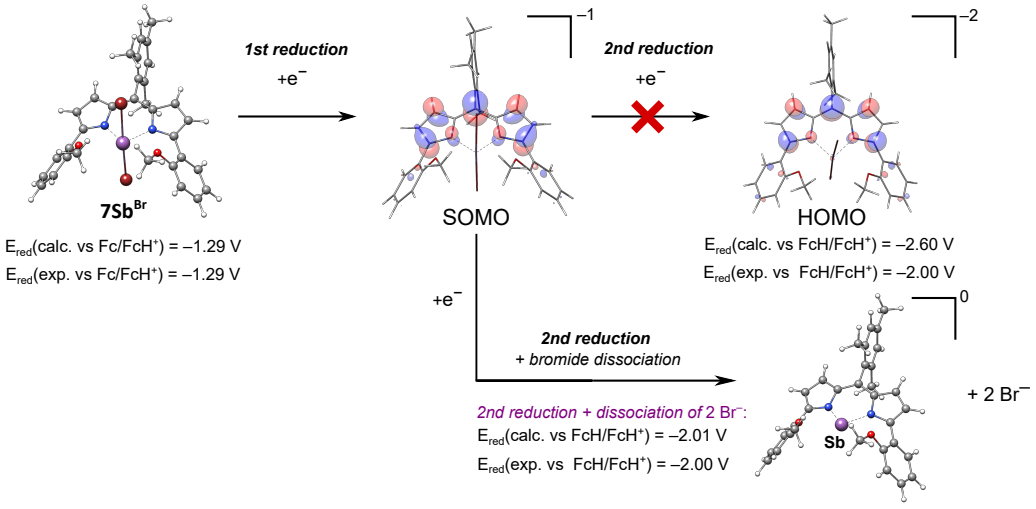


Figure 95: Comparison of calculated reduction potentials E_{red} (calc.), obtained on the (ω = 0.15) ωB97X-D4/def2-QZVPP//B97-3c+SMD(CH_2Cl_2) level of theory, with experimental cathodic peak potentials E_{red} (exp.).[174]‡

As the origin of the new redox event upon irradiation of **7Sb^{Br}** was still unclear, bromide ion dissociation from **7Sb^{Br}** was considered as a possible light-driven reaction. Thus, the stepwise dissociation of bromide ions from **7Sb^{Br}** was calculated in the ground state S_0 and for the first excited singlet and triplet states S_1 and T_1, respectively (Figure 96).‡ The dissociation of a single bromide ion was calculated to be endergonic with ΔG = 19.4 kcal/mol in the ground state S_0.‡ However, when considering the first excited states as starting points and using the excitation energies for the vertical $S_0 \rightarrow S_1$ and $S_0 \rightarrow T_1$ transitions as estimates, dissociation of a single bromide ion to yield the free stibenium complex **7Sb^{+}** becomes thermodynamically feasible with negative changes in Gibbs free energies (Figure 96).‡ Nonetheless, these energies were found to be not sufficient to enable a second bromide ion dissociation as calculated Gibbs free energies were endergonic.‡[174]

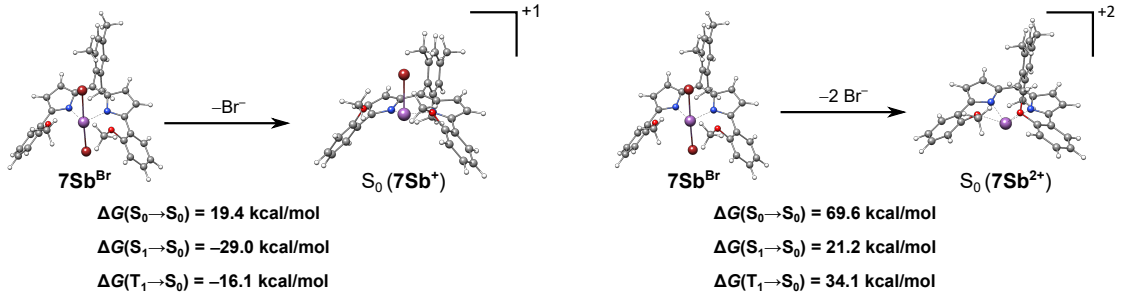


Figure 96: Calculated Gibbs free energies for bromide ion dissociation from **7Sb^{Br}** calculated on the (ω = 0.15) ωB97X-D4/def2-QZVPP//B97-3c+SMD(CH_2Cl_2) level of theory in the ground state and corrected for vertical transition energies of first excited states ($S_0 \rightarrow S_1$ and $S_0 \rightarrow T_1$).‡[174]

Moreover, the dissociation of bromide ions was also examined upon single-electron reduction to mimic CV conditions. Starting from the monoanionic complex (S = $\frac{1}{2}$), a single bromide dissociation was calculated to be endergonic by ΔG = 8.1 kcal/mol (Figure 97).‡ However, considering the dianionic complex (S = 0) as a starting point, the stepwise dissociation of two bromide ions becomes feasible with slightly negative changes in respective Gibbs free energies (Figure 97).‡

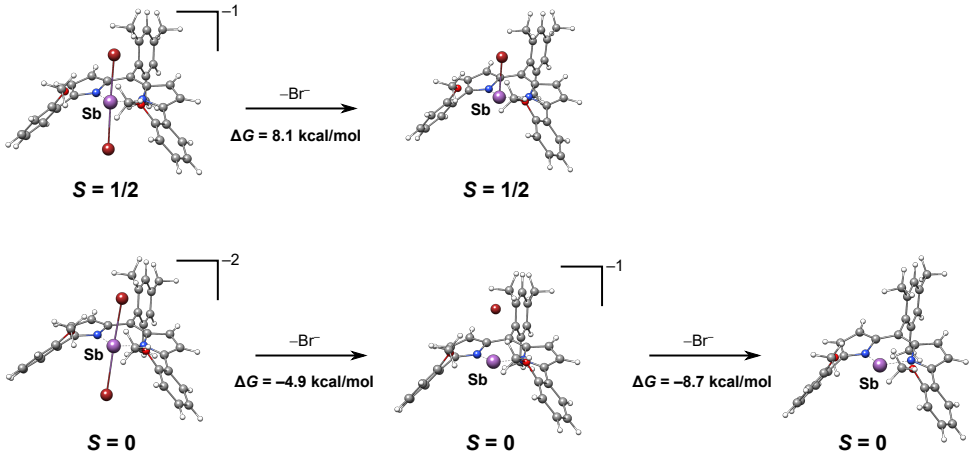


Figure 97: Calculated Gibbs free energies for bromide ion dissociation from anions of **7Sb^{Br}** calculated on the (ω = 0.15) ωB97X-D4/def2-QZVPP//B97-3c+SMD(CH_2Cl_2) level of theory.[174]‡

Finally, the redox potential of the free stibenium complex **7Sb^{+}** was calculated as E_{red} = -0.80 V, which is in good agreement with the experimental redox wave observed upon irradiation (approx. -1.00 V). In summary, the electrochemical behaviour of **7Sb^{Br}** was interpreted as two consecutive ligand-centred single-electron reductions, which may be coupled to a dissociation of bromide ions from the charged complex (Figure 98). Upon irradiation of the electrochemical cell, bromide ion dissociation from **7Sb^{Br}** can be hypothesized to occur prior to reduction, as dissociation from the first excited states complex was estimated to be thermodynamically feasible and showed considerable overlap with independently recorded CVs of **7Sb^{+}[BArF]** (Figure 99). Interestingly, complex **7Sb^{+}[BArF]** displayed an increase in the cathodic peak current upon irradiation, which may arise from a photoexcited species that is more readily reduced than the ground state complex (Figure 99).[174]

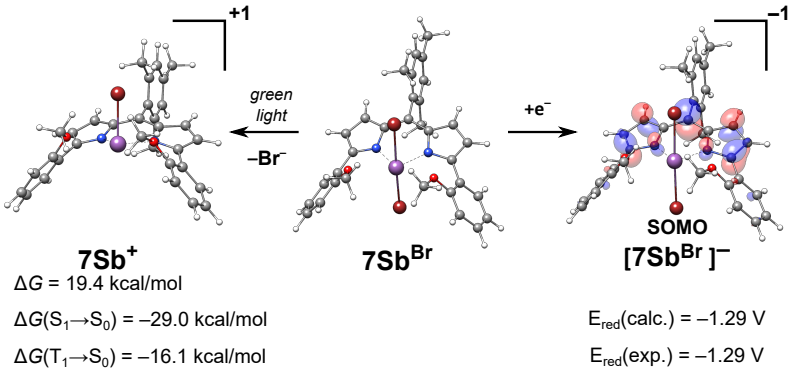


Figure 98: Summary of computational results in the context of electrochemical studies of **7Sb^{Br}**. Calculated ΔG for dissociation of bromide ions are shown with and without irradiation (left) and First reduction potential of **7Sb^{Br}** vs FcH/FcH$^+$ with the corresponding depiction of the highest SOMO upon single-electron reduction (isovalue of 0.05 a.u., right).[174]‡

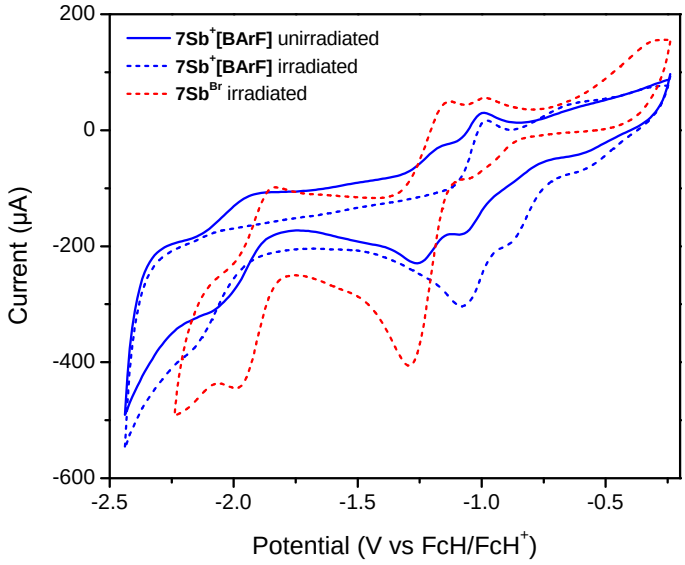


Figure 99: Qualitative comparison between cyclic voltammograms of **7Sb^{Br}** and **7Sb$^+$[BArF]** (both 1 mM) without (solid line) and with irradiation under a green LED light source (dashed line). The measurements were conducted in a CH_2Cl_2 solution of $TBAPF_6$ (0.1 M) at a scan rate of 100 mV/s.

Due to the previously observed photocatalytic activity of the 1:1 mixture of **L7** and $SbBr_3$, the combined reagents were also examined by CV as an additional control experiment. Interestingly, compared to the CV of **L7**, the reagent mixture displayed an additional irreversible redox event at approx. -1.08 V vs FcH/FcH$^+$ (Figure 100). The two redox events seen for the mixture of **L7** and $SbBr_3$ showed a similar shape to the redox couples in **7Sb^{Br}** but were found at shifted potentials, indicating a different electrochemical behavior. Nonetheless, the first redox event displayed by the mixture showed also slight similarity with the new redox wave observed upon irradiation of

7Sb^{Br}, thus indicating potential resemblance with the newly formed species. Given the complicated nature of the mixture of **L7** and $SbBr_3$ based on ^{1}H NMR spectroscopy, it is not possible to specify the exact origin of the redox couple at −1.08 V. It is certain, however, that the redox event must be caused by the interplay of the antimony halide and dipyrrin ligand **L7** and is likely ligand-centred.

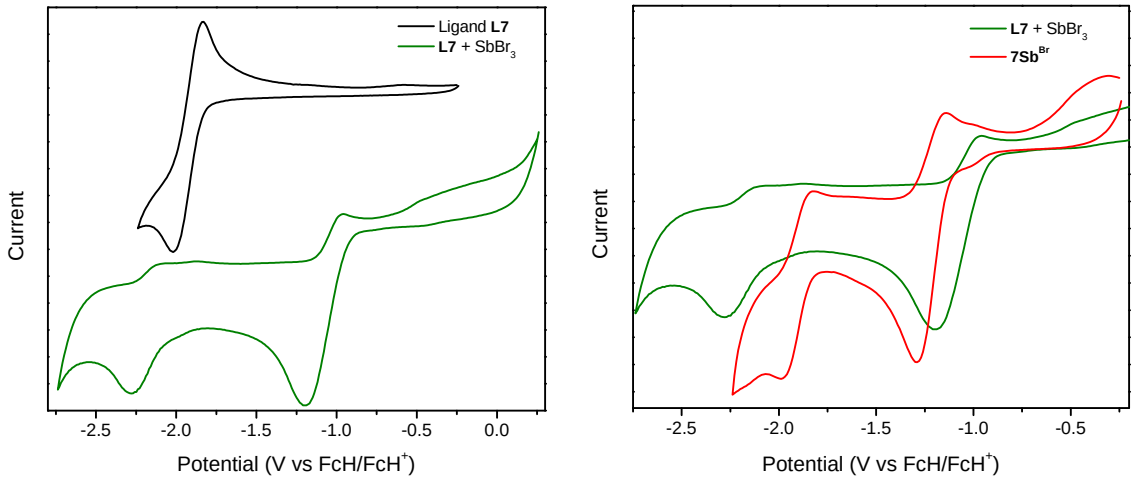


Figure 100: Qualitative comparison between cyclic voltammograms of **L7** and a 1:1 mixture of **L7** and $SbBr_3$ (left) and comparison between cyclic voltammograms of the mixture with **7Sb^{Br}** and **7Sb$^+$[BArF]** upon irradiation (right). The measurements were conducted at a 1 mM analyte concentration in a CH_2Cl_2 solution of $TBAPF_6$ (0.1 M) using a scan rate of 100 mV/s.

Finally, the potential interaction of **7Sb^{Br}** with an alkene was investigated under irradiation. Although CV studies of **7Sb^{Br}** in the presence of model alkene **38** indicated a potential interaction of the two compounds under electrochemical conditions, no supporting data through additional computational or experimental studies was obtained.[174] More specifically, neither the neutral complex **7Sb^{Br}**, nor stibenium complex **7Sb$^+$[BArF]** showed any changes by ^{1}H NMR spectroscopy in the presence of equimolar amounts of **38** upon irradiation of the reaction mixtures under an argon atmosphere with green light over the course of several hours. This observation was also true for less sterically encumbered alkene substrates, *i.e.* cyclohexene (4.00 equiv.) in the presence of **7Sb$^+$[BArF]** and styrene in the presence of **7Sb^{Br}** (5 mol%). Notably, no reactivity was observed towards the [2+2] cycloaddition product of styrene, which has been previously described for metal-based photocatalysis and organophotocatalysis.[36,227] This finding further implies that **7Sb^{Br}** does not possess an energetically suitable excited state to undergo energy transfer catalysis with alkenes.

In an attempt to gain insight into the fate of **7Sb^{Br}** during catalysis, photooxygenation of **38** was performed with equimolar amounts of **7Sb^{Br}** in an oxygen-filled J-Young NMR tube in CD_2Cl_2 (Figure 101). After 4 hours of irradiation a new set of signals appeared in the aromatic region, increasing in intensity after additional 8 hours of irradiation. Nonetheless, upon a total of 12 hours, **7Sb^{Br}** was still present (above 50%) and the alkene had fully reacted to **39** and trace amounts of 2-adamantanone. Based on ^{1}H NMR data, one main new species related to **7Sb^{Br}** formed upon prolonged irradiation under an oxygen atmosphere (Figure 101). The newly formed compound showed a distinct singlet at 6.47 ppm and a set of broad downfield-shifted ^{1}H resonances, indicating a protonation of the ligand backbone. However, the newly formed species did not match with any previously observed data with respect to **L7** (see Chapter 3) and attempts at isolation of the compound remained unsuccessful. Consequently, the true nature of the photocatalytically active compound remains unclear for **7Sb^{Br}** as it could also serve as a pre-catalyst. Nonetheless, since the complex remains mostly intact during the photooxygenation reactions according to NMR and UV/Vis data, it can be assumed that the neutral complex serves as an energy transfer photocatalyst.

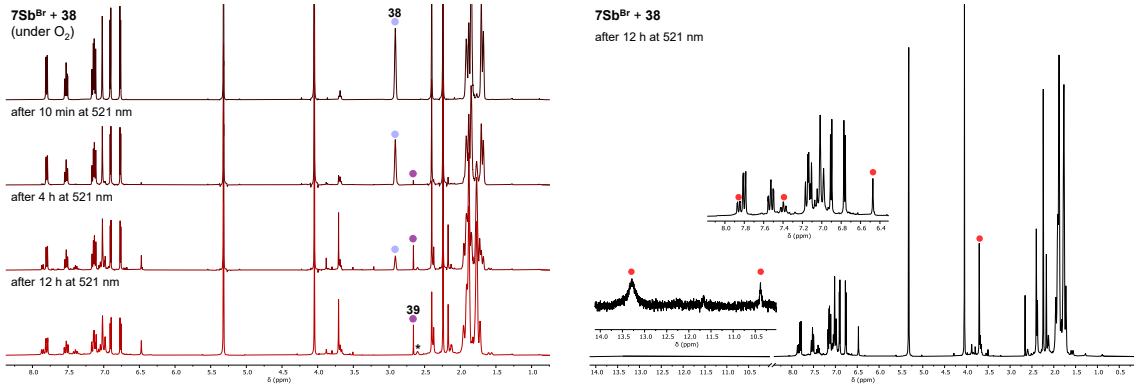


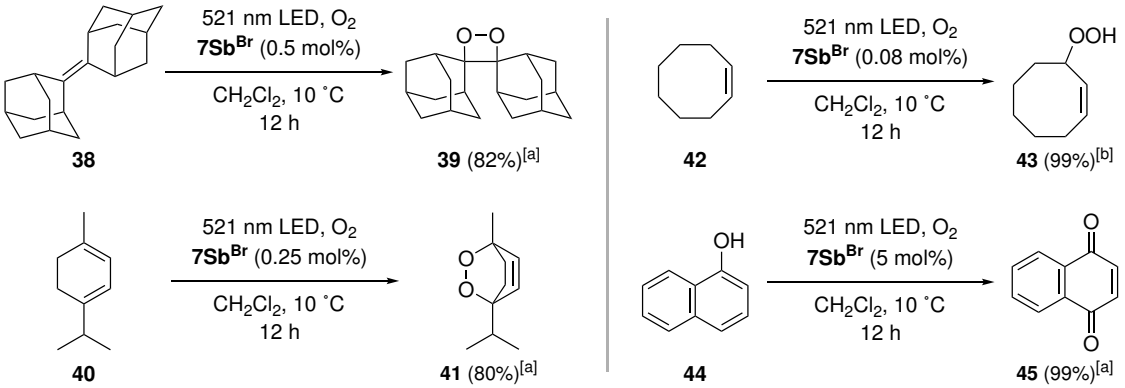
Figure 101: Fate of **7Sb^{Br}** photocatalyst throughout oxidation of **38**. Stacked ^{1}H NMR spectra of a 1:1 mixture of **7Sb^{Br}** and **38** under an oxygen atmosphere after given irradiation times (left, **38** and **39** marked by colours while adamantan-2-one is marked by *), and zoom-in of ^{1}H NMR spectrum after 12 h with new signals related to **7Sb^{Br}** marked in red (right).

4.5. Photocatalytic applications of SBDIPY chromophores

Having obtained theoretical insights into the light-enabled properties of **7Sb^{Br}**, the applicability of the SBDIPY photocatalyst was evaluated for various $^1O_2$-based oxidation reactions, which will be discussed in the following sections.

4.5.1. Oxidation of double bonds

Encouraged by the initial success found in the photocatalytic oxidation of alkene **38**, the scope was expanded to several other substrates containing carbon-carbon double bonds. The oxidation products shown in Scheme 57 were isolated in high yields. As the oxidation reactions were performed on a larger scale (between 0.75 mmol and 0.30 mmol) than the initial photocatalyst screening, a slightly higher catalyst loading was required to ensure sufficient turnover. While the photooxygenation of alkenes **38**, α-terpinene (**40**) and cyclooctene (**42**) required only low catalyst loading to achieve a high conversion, a slightly higher concentration of **7Sb^{Br}** was needed to effectively oxidize 1-naphthol (**44**) to the corresponding quinone **45**. This is likely due to the loss of aromaticity which makes the [4+2] addition slightly more challenging. The substrate scope shown in Scheme 57 nicely illustrates the synthetic utility of $^1O_2$, as it can be used to access oxygen-containing heterocycles or hydroperoxide in ene-type reactions.[48]



Scheme 57: Photocatalytic oxidation of alkenes under an oxygen atmosphere. [a]Refers to isolated yield while [b]refers to conversion based on ^{1}H NMR analysis of crude sample.

Moreover, several other unsaturated hydrocarbons were tested that exhibited a low selectivity or no conversion with regard to the photooxygenation reaction in the presence of **7Sb^{Br}** (Figure 102).

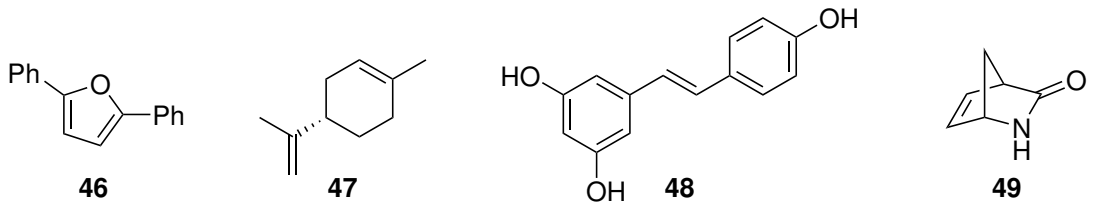


Figure 102: Scope of less successful substrates. Reactions were tested using 0.30 mmol of substrates **46** and **47** with 0.08 mol% of **7Sb^{Br}** while reactions of substrates **48** and **49** (both 0.15 mmol) were performed with a 10 mol% and 5 mol% catalyst loading.

Besides the oxidation reaction of (*E*)-resveratrol (**48**), which displayed poor solubility in CH_2Cl_2, all reactions were carried out in CH_2Cl_2 (with 0.1 M substrate concentration) at 10 °C and were irradiated for 12 h with green light. For both, 2,5-diphenylfuran (**46**) and (+)-limonene (**47**), full conversion of the starting materials was observed at a catalyst loading of 0.08 mol% **7Sb^{Br}**, however resulting in a low selctivity in both cases. Furans have been reported to undergo [4+2] cycloaddition with $^1O_2$ to form the respective endo-peroxide product, which readily undergoes many possible decomposition pathways, thus resulting in a particularly complex reaction outcome.[228] For **47** the situation is arguably even more complicated, as the starting material gives a mixture of regio- and diasteriomeric hydroperoxides upon photooxygenation.[229] In this case, a thorough analysis of the product mixture would require first a reduction of the peroxides to the corresponding alcohols and purification by high-performance liquid chromatography.[230,231] Compared to the first two examples provided in Scheme 102 the stilbenoid (*E*)-Resveratrol (**48**) showed only a low conversion towards a mixture of several literature-known photooxygenation products **50**-**52**, which were identified by ^{1}H NMR analysis (Figure 103).[232] The low conversion of the starting material may be due to the poor solvent compatibility of **7Sb^{Br}** and CD_3CN.

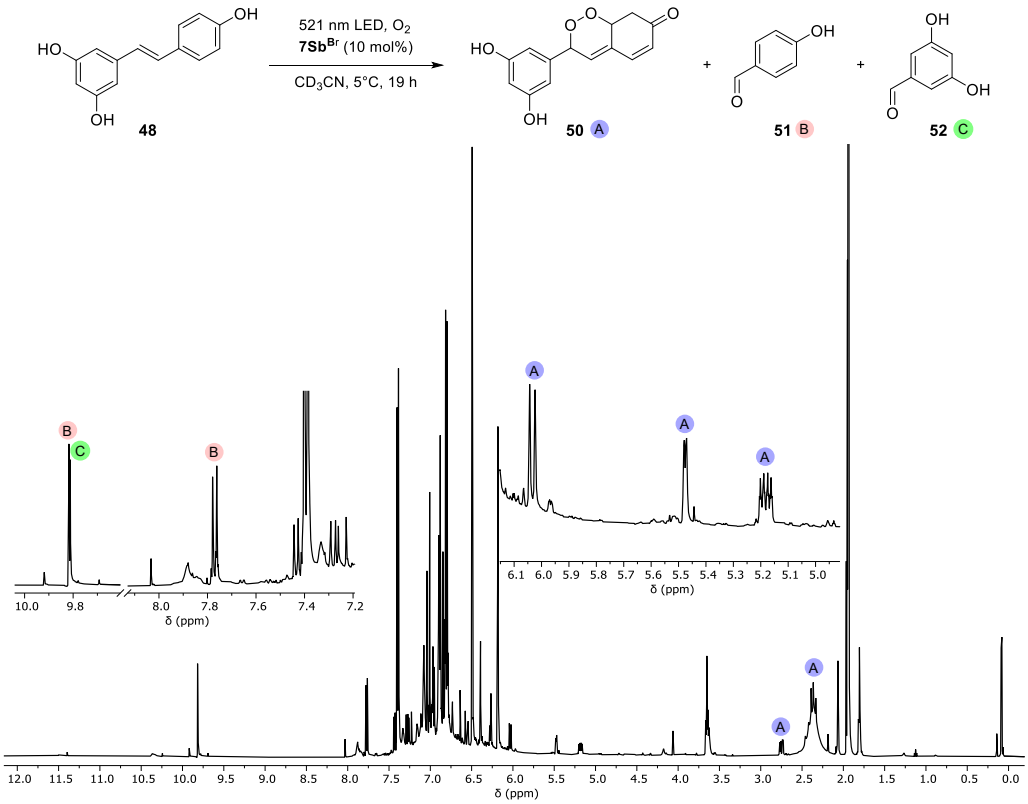
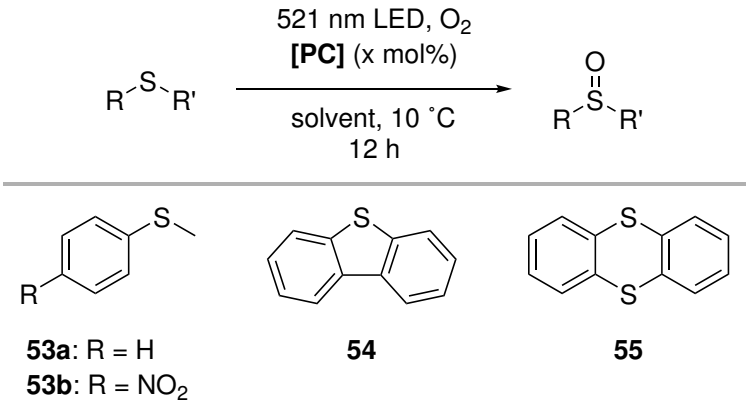


Figure 103: Crude reaction mixture obtained upon irradiation of a CD_3CN solution of **48** (0.15 mmol) and **7Sb^{Br}** (10 mol%) in an oxygen-filled J-Young NMR tube. Identifiable ^1H resonances of products are assigned by colours.[232]

Finally, substrate **49** showed no reactivity in the presence of **7Sb^{Br}** (5 mol%) and oxygen under prolonged irradiation, likely due to the amine function which can effectively quench $^1O_2$ prior to any reactivity.[233]

4.5.2. Oxidation of sulfides

Due to its high electrophilicity, singlet oxygen can be used as a mild oxidant for organic sulfides.[35] Therefore, the applicability of photocatalyst **7Sb^{Br}** was evaluated for the oxidation of several selected sulfides (Scheme 58). Various reaction conditions were screened to optimize the oxidation of selected sulfides using SBDIPY photocatalysts (Table 13).



Scheme 58: Photocatalytic oxidation of organic sulfides to sulfoxides and selected substrate scope.

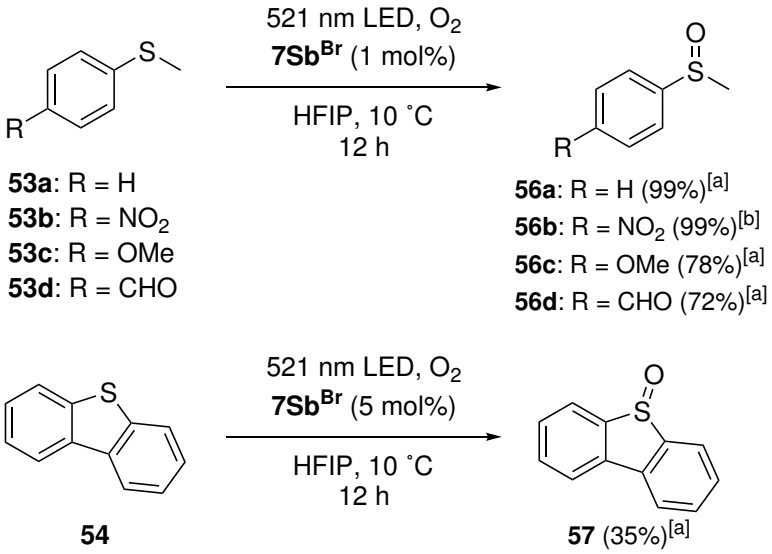
Table 13: Reaction condition screening for photocatalytic oxidation of sulfides to sulfoxides. All reactions conducted with 0.30-0.15 mmol of sulfide in given solvent (0.1 M) at 10 °C for 12 h.

Entry	Photocatalyst	sulfide	solvent	Catalyst loading (mol%)	^{1}H NMR conversion[a]
e1	**7Sb^{Br}**	**53a**	CH_2Cl_2	10	93%
e2	**8Sb^{Cl}**	**53a**	CH_2Cl_2	10	40%
e3	**7Sb^{Br}**	**53a**	CH_2Cl_2	1	63%
e4	**7Sb^{Br}**	**53b**	CH_2Cl_2	1	0%
e5	**7Sb^{Br}**	**54**	CH_2Cl_2	1	0%
e6	**7Sb^{Br}**	**54**	CH_2Cl_2	5	0%
e7	**7Sb^{Br}**	**55**	CH_2Cl_2	1	0%
e8	**7Sb^{Br}**	**55**	MeOH	1	0%
e9	**7Sb^{Br}**	**53b**	HFIP	5	99%[b]
e10	**7Sb^{Br}**	**53b**	HFIP	5	99%[b]
e11	**7Sb^{Br}**	**54**	HFIP	5	35%[b]
e12	**7Sb^{Br}**	**55**	HFIP	5	20%[c]

[a] ^{1}H NMR conversion was estimated based on relative integrals of starting material and product. [b] Isolated yield. [c] Irradiation for 24 h.

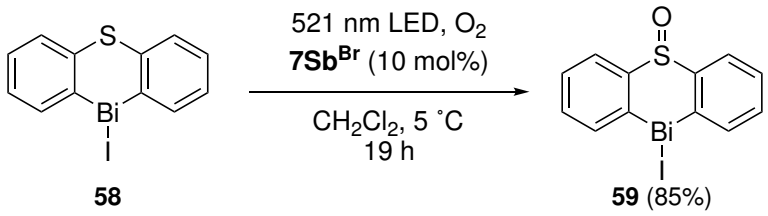
Despite dichloromethane being a suitable solvent choice for the photocatalytic oxidation of unsaturated hydrocarbons, its use was found to be limited in the oxidation of sulfides. Although moderate ^{1}H NMR conversion was observed for thioanisole (**53a**) as a substrate while requiring comparatively high catalyst loading of **7Sb^{Br}** and

8Sb^{Cl} (entries *e1-e3*), this was not the case for other tested sulfide substrates (entries *e4-e8*). The low conversion towards respective sulfoxides can be attributed to the poor choice of solvent, as dichloromethane among other aprotic solvents, has been reported to be inefficient in this transformation due to physical quenching of $^1O_2$ through sulfides.[234] In contrast, protic solvents, *e.g.* methanol or hexafluoroisopropanol (HFIP), have been found to be more suitable options for the photooxygenation of sulfides, as solvent molecules may stabilize relevant intermediates.[234–236] Moreover, recent studies by Forchetta *et al.* have highlighted the effectiveness of HFIP as a solvent for photooxygenation reactions due to its high oxygen solubility.[236,237] Indeed, performing the photocatalytic oxidation of sulfides **53**-**55** in HFIP resulted in significantly increased conversion towards the respective sulfoxides (entries *e10-e12*). With this information in hand, various thioanisole derivatives were prepared in high yields using **7Sb^{Br}** as a photocatalyst (Scheme 59). However, the oxidation remained challenging for the heterocyclic substrates dibenzothiophene (**54**) and thianthrene (**55**), resulting in a low isolated yield for the sulfoxide **57**.



Scheme 59: Scope of photooxygenation of organic sulfides under optimized reaction conditions. All reactions were performed starting from 0.30 mmol of sulfide. [a]Isolated yield. [b]Reaction was performed with 5 mol% catalyst loading.

Besides organic sulfides **53**-**55**, several more complex structures containing sulfide moieties were tested as substrates in the photooxygenation reaction. Surprisingly, despite using CH_2Cl_2 as a solvent, 10-iodophenothiabismine (**58**) showed a selective conversion to the corresponding sulfoxide **59** using a catalyst loading of 10 mol% (Scheme 60). This result was particularly interesting as various other oxidants led to unselective outcomes or no conversion to **59**.[iii]

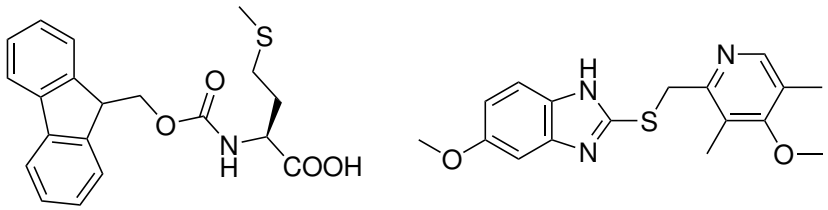


58 **59** (85%)

Scheme 60: Photooxygenation of 10-iodophenothiabismine (**58**) in the presence of **7Sb^{Br}**.[iv]

No reactivity was observed for Fmoc-Met-OH (**60**) and omeprazole sulfide (**61**), likely due to the presence of amine functions which cause an increased quenching of $^1O_2$ (Figure 104).[233]

Unreactive substrates



60 **61**

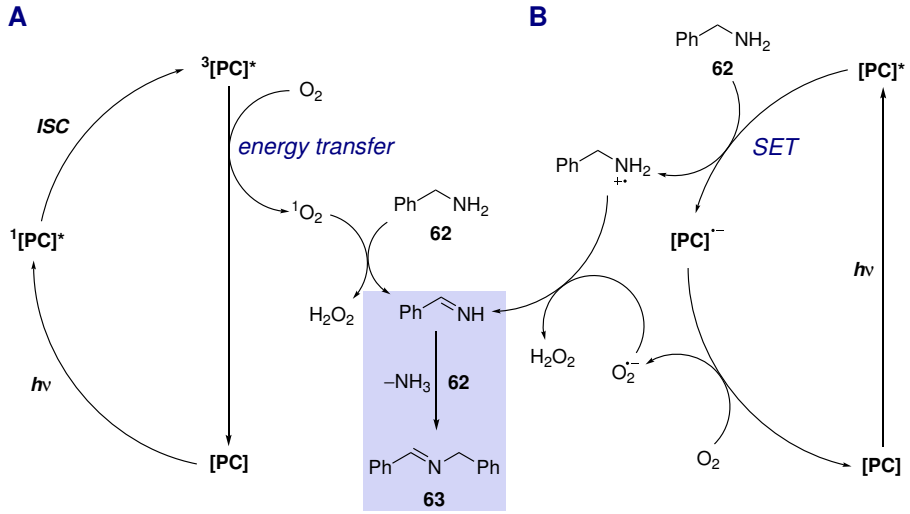
Figure 104: Unreactive photooxygenation substrates using photocatalyst **7Sb^{Br}**.

[iii] Purification and characterization of **59** was performed by G. Pugliese. Screening of other oxidants was also carried out and analyzed by G. Pugliese.

[iv] Isolated product was obtained by G. Pugliese with respect to 0.20 mol starting material.

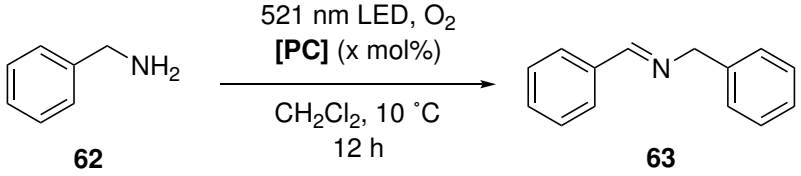
4.5.3. Photooxidation of benzylic amines

The photooxidation of benzylamines using various singlet oxygen photosensitizers has been demonstrated to be a viable method to access a multitude of imines.[113,238–243] The reaction has been proposed to proceed *via* two mechanistic pathways which both feature H_2O_2 as a common byproduct.[241,243,244] The first option involves the formation of an exciplex with partial charge transfer between amine and $^1O_2$.[241] Such an intermediate has been also hypothesized to play a role in the physical and chemical quenching of $^1O_2$ in the presence of amines with the latter being a possible route to access the condensation product (Scheme 61A).[241] The second option on the other hand involves a single-electron transfer to yield the oxidation product *via* a radical mechanism (Scheme 61B).[241,244]



Scheme 61: Possible pathways involved in the photooxidation of benzylamine (**62**): energy transfer pathway (A) and radical mechanism (B, adapted from [241]).

The photooxidative coupling of benzylamine (**62**) was chosen as a model reaction to evaluate the applicability of SBDIPY complexes (Scheme 62). Conversion towards the coupling product (*E*)-*N*-benzyl-1-phenylmethanimine (**63**) was estimated using 1,3,5-trimethoxybenzene as an internal standard in ^{1}H NMR spectroscopy (Table 14).



Scheme 62: Model reaction for catalyst screening of the oxidative coupling of benzylic amines.

Table 14: Catalyst screening for the photocatalytic oxidative coupling of benzylic amines to imines. All reactions were conducted with 0.15 mmol of **62** in CH_2Cl_2 (0.1 M) at 10 °C for 12 h.

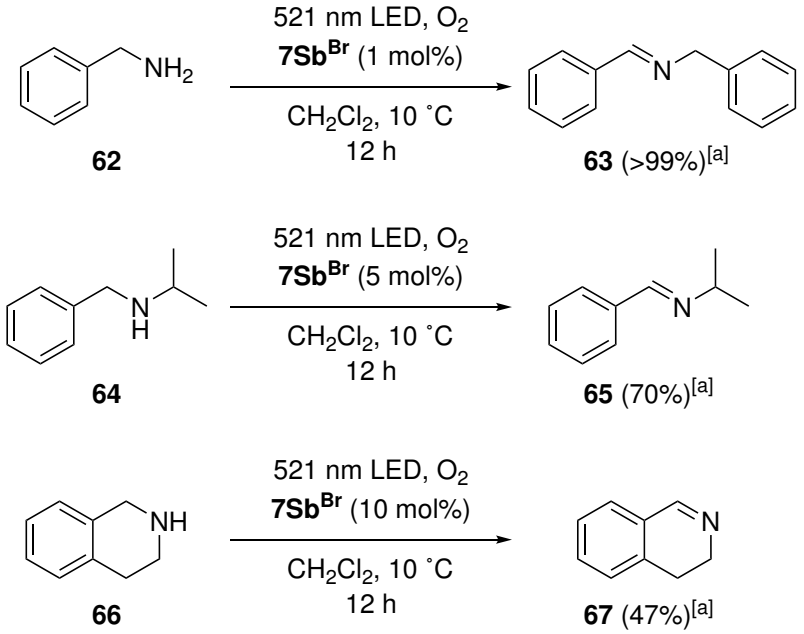
Entry	Photocatalyst	Catalyst loading (mol%)	^{1}H NMR conversion[a]
e1	**7Sb^{Br}**	2.5	>99%
e2	**7Sb^{Br}**	1	>99%
e3	**7Sb^{Br}**	0.1	40%
e4	**7Sb^{Br}**	0.05	20%
e5	**L7**	10	traces
e6	$SbBr_3$	0.1	traces
e7	**8Sb^{Cl}**	2.5	>99%
e8	**8Sb^{Cl}**	0.1	>99%
e9	**8Sb^{Cl}**	0.005	>99%
e10	**8Sb^{Br}**	0.5	>99%
e11	**8Sb^{Br}**	0.005	>99%
e12	**L8**	10	>99%
e13	**L8**	0.5	>99%
e14	**L8**	0.005	>99%

[a] ^{1}H NMR conversion was estimated using 1,3,5-trimethoxybenzene (0.20 equiv.) as an internal standard.

The photocatalyst **7Sb^{Br}** showed quantitative conversion to the target compound **63** at catalyst loadings as low as 1 mol%. However, it did not reach comparable efficiency at low concentrations, in contrast to its performance in the photooxygenation of unsaturated hydrocarbons (entries *e1*-*e4*). Control experiments using **L7** and $SbBr_3$ as catalysts afforded only trace amounts of **63** (well below 5%), thereby confirming that **7Sb^{Br}** or related secondary product(s) serve as active photocatalysts in this transformation (entries *e5*, *e6*).

In addition to **7Sb^{Br}**, SBDIPY complexes **8Sb^{Cl}** and **8Sb^{Br}** were also tested as photocatalysts. Surprisingly, both complexes exhibited outstanding catalytic activity in the photooxidation of **62**, achieving quantitative conversion at catalyst loadings as low as 50 ppm. However, control reactions using catalytic amounts of ligand **L8** showed an equally high conversion to **63** as for the antimony complexes **8Sb^{X}** (entries *e12*-*e14*). As the presence of **L8** was confirmed after reaction completion by ^{1}H NMR

spectroscopy, the observed catalytic activity of **8Sb^{X}** is likely attributable to the dipyrrin ligand. In contrast, no ^{1}H NMR signals of ligand **L7** were detected after the completed reaction using **7Sb^{Br}** as the catalyst (entry *e1*). Instead, the residual ^{1}H resonances indicated a more complicated fate of the catalyst in this case. Due to the indistinct catalytic activity between Sb-complexes and ligand, only **7Sb^{Br}** was used as a catalyst for further photooxidation reactions of benzylic amines (Scheme 63).



Scheme 63: Scope of oxidative amine coupling using photocatalyst **7Sb^{Br}**. [a] ^{1}H NMR yield with respect to 1,3,5-trimethoxybenzene (0.20 equiv.) as internal standard.

The overall applicability of **7Sb^{Br}** as photocatalyst for oxidative coupling of amines was rather deficient due to the overall low conversion and high required catalyst loadings as compared to literature-reported studies.[113,239,240] This may be caused by catalyst deactivation through the reactive byproducts of the photooxidation reactions (hydrogen peroxide and ammonia). Only very low conversion to the respective imine (approximately 5% at 1 mol% catalyst loading) was observed for the more electron-deficient benzylamine **68**, whereas no reaction at a catalyst loading of 5 mol% was observed with 4-cyanobenzylamine (**69**) as the substrate (Figure 105).

Unreactive substrates

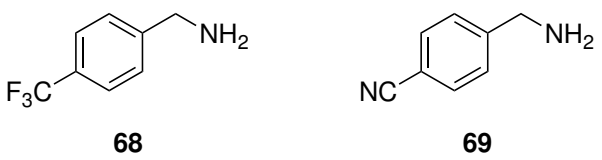
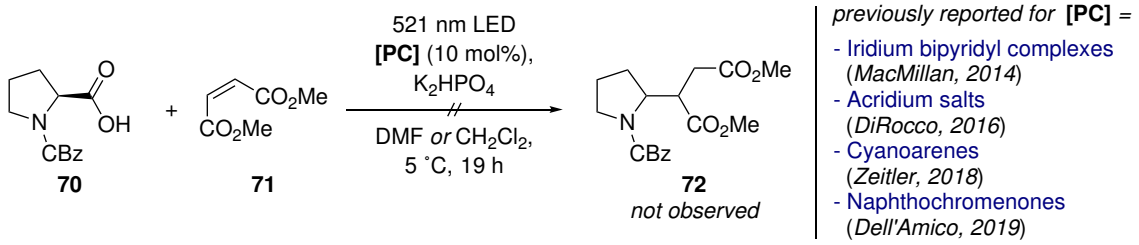


Figure 105: Unreactive benzylamines in photooxidation reaction using photocatalyst **7Sb^{Br}**.

4.6. Photoredox applications of SBDIPY chromophores

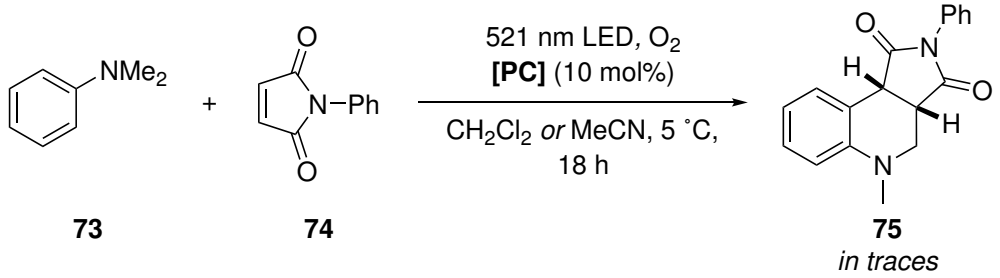
Research on photoredox chemistry has received considerable attention in recent years due to the resurgence of metal- and organocatalysed photoredox reactions as synthetic tools to access new reactivity *via* single-electron transfer (SET) processes.[61,62,245] In this regard, photoredox catalysis provides access to radical species under considerably mild conditions, using light as the main source of energy.[62,245] Upon light excitation, the photoredox catalyst generally undergoes photoinduced electron transfer (PET) in the presence of an electron donor or acceptor, resulting in a reductive or oxidative quenching of the respective substrate.[245] This process is mostly governed by the exited state redox properties of the catalyst, which can significantly influence its light-driven reactivity.[245]

In order to obtain insight into the applicability of SBDIPY chromophores as photoredox catalysts, several literature-reported reactions were tested by exchanging the original catalyst with SBDIPY chromophore **7Sb^{Br}** or **8Sb^{Cl}**. The Giese-type coupling of protected proline **70** with dimethyl maleate (**71**) has been adapted from previous work by Mateos *et al.*, who were able to achieve high yields of the decarboxylative coupling product **72** using naphthochromenone photocatalysts.[63] Unfortunately, formation of the target compound was not observed in the presence of **7Sb^{Br}** or **8Sb^{Cl}** as photocatalyst (Scheme 64).



Scheme 64: Attempted Giese-type coupling reaction using **7Sb^{Br}** and **8Sb^{Cl}** as photocatalysts (**[PC]**). Literature-reported catalysts for the reaction are listed on the right side.[63,246–248]

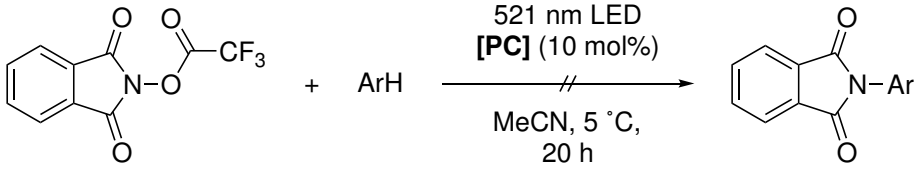
Next, a Povarov-type addition of *N,N*-dimethylaniline (**73**) to phenylmaleimide (**74**) was attempted in the presence of **7Sb^{Br}** or **8Sb^{Cl}** as photocatalysts (Scheme 65). Such reactivity has been previously reported for organophotoredox- and metal-based catalysts.[63,249,250] In the case of both SBIDIPY catalysts and either solvent (CH_2Cl_2 or MeCN) trace amounts of the desired product **75** were detected by ^{1}H NMR spectroscopy, showing a characteristic ddd signal at 3.52 ppm.[249] However, since a significant amount of both starting materials remained at the end of the reaction (product formation below 5% based on relative integration of ^{1}H NMR resonances), background reactivity can not be ruled out.



73 **74** **75** *in traces*

Scheme 65: Povarov-type addition reaction using **7Sb^{Br}** or **8Sb^{Cl}** as photocatalysts (**[PC]**).[251]

The usage of redox-active esters as viable reagents for C−H imidation reactions under photoredox conditions has been explored by Ooi and co-workers, using a thioxanthone catalyst under UV irradiation.[251] Using modified reaction conditions, the applicability of SBDIPY complexes as photoredox catalysts in the presence of redox-active ester **76** and arene (benzene or trifluorotoluene) was tested (Scheme 66). Unfortunately, no formation of the imidation products **77** and **78** was observed by ^{19}F NMR spectroscopy, indicating that a more strongly reducing photocatalyst is required.



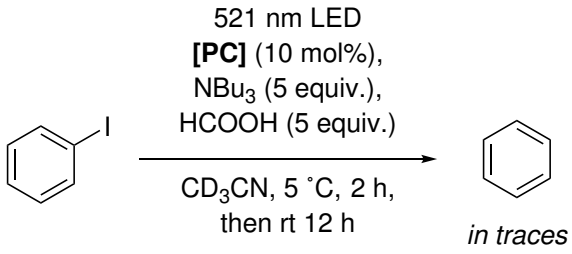
76

77 (Ar = Ph)
78 (Ar = $PhCF_3$)
not observed

Scheme 66: Attempted C−H imidation of benzene and trifluorotoluene using **7Sb^{Br}** or **8Sb^{Cl}** as photocatalysts (**[PC]**).[65]

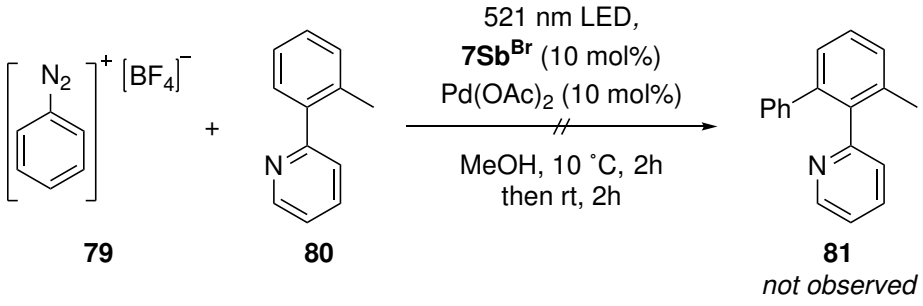
In contrast to that, the reductive dehalogenation of iodobenzene using SBDIPY photocatalysts **7Sb^{Br}** or **8Sb^{Cl}** showed a very slow conversion to benzene (trace amounts) under the conditions shown in Scheme 67. The procedure was originally reported by

de Alaniz and co-workers who were able to perform efficient dehalogenation of aryl halides using the highly reducing 10-phenylphenothiazine (PTH) photocatalyst.[65] Although the reaction did not proceed in the absence of a photocatalyst, the stability of SBDIPY chromophores under the given acidic conditions is highly unlikely, making the low reaction progress difficult to attribute to a well-defined catalyst.



Scheme 67: Dehalogenation of iodobenzene using **7Sb^{Br}** or **8Sb^{Cl}** as photocatalysts (**[PC]**).

Finally, seminal work by Sanford and co-workers disclosed the possibility of combining photoredox catalysis with transition-metal catalysed C−H functionalization reactions.[252] The authors employed tris(bipyridine)ruthenium(II) chloride as a photoredox catalyst to generate aryl radicals from diazonium salts, which were utilized to perform Pd-catalysed C−H arylation.[252] The coupling of benzenediazonium tetrafluoroborate (**79**) with 2-(*o*-tolyl)pyridine (**80**) was tested under adapted conditions, using **7Sb^{Br}** as a photocatalyst under green light irradiation (Scheme 68). Unfortunately, no formation of the coupling product **81** was observed by ^{1}H NMR spectroscopy, thus indicating that generation of aryl radicals was not possible with **7Sb^{Br}** as catalyst. Once again, this finding emphasizes the fact that SBDIPY chromophores likely do not possess a sufficiently reducing excited state to partake in SET chemistry.



Scheme 68: Attempted Pd-catalysed C−H arylation using **7Sb^{Br}** as photocatalyst.

Overall, the SBDIPY complexes **7Sb^{Br}** and **8Sb^{Cl}** showed very limited applicability in the field of photoredox catalysis with only few indications of possible activity. However, it should be noted that photoredox catalysis often requires conditions that may not be compatible with SBDIPY chromophores due to their susceptibility to ligand

protonation. The above-discussed results strongly suggest that the main photocatalytic regime of SBDIPY complexes is based on energy transfer as the excited state redox properties are not well-suited to undergo SET processes.

4.7. Conclusion and future work

This chapter laid the groundwork for photocatalytic applications of heavy pnictogen dipyrrin (PnDIPY) complexes. Bromide substituted SBDIPYs **7Sb^{Br}** and **8Sb^{Br}** were identified as excellent photosensitizers for the photooxygenation of unsaturated hydrocarbons *via* the formation of $^1O_2$. The applicability of SBIDIPY complexes as energy transfer photocatalysts was further verified in the photooxidation of organic sulfides and benzylamines. While **7Sb^{Br}** exhibited a significantly increased catalytic activity in comparison to the dipyrrin ligand **L7**, ambiguity was found in the case of **L8** Sb-complexes as the ligand also showed significant photocatalytic activity. Consequently, the focus was shifted onto complex **7Sb^{Br}**, which was further investigated by CV and computational studies with respect to its redox properties and behaviour under light. These mechanistic investigations revealed a mostly ligand-based redox chemistry in **7Sb^{Br}**, which may undergo bromide dissociation under reducing conditions, as well as under light irradiation (Figure 106).

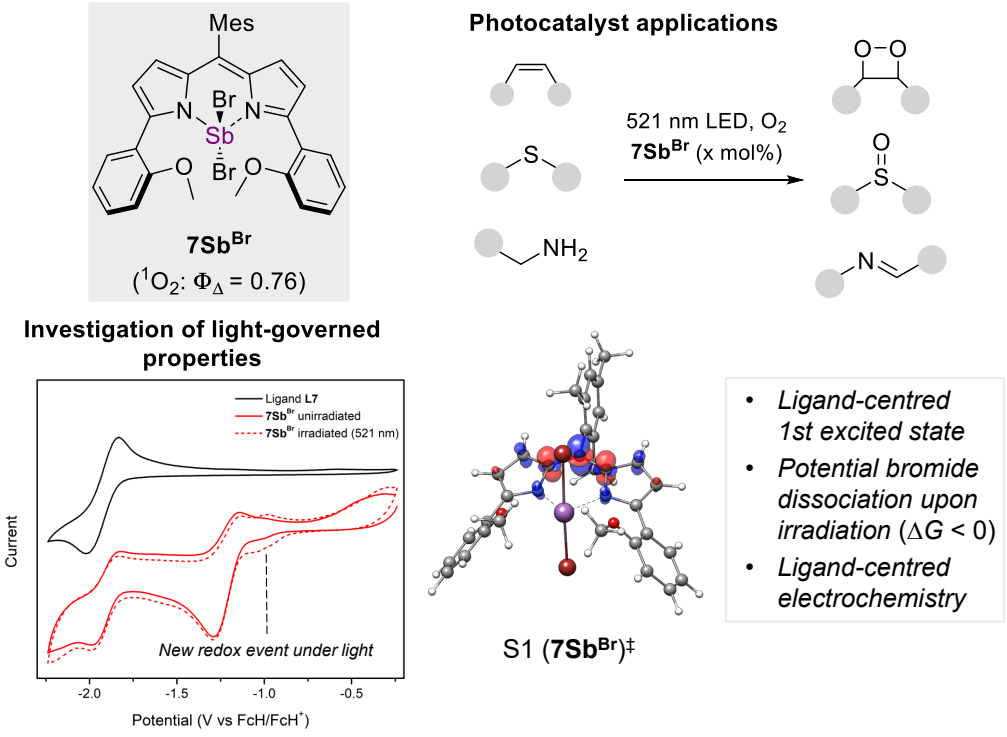


Figure 106: Summary of heavy pnictogen dipyrrins as photocatalysts.[174]

The potential of SBDIPY chromophores to engage in SET processes was found to be negligible based on the evaluated photoredox reactions. This area of research requires additional testing and should also be assessed using different dipyrrin complexes, such as **12Sb** or **10Pn^{Br}**. Moreover, iodide-substituted PnDIPY complexes, which were not prepared within the scope of this work, should also be targeted due to their potentially different excited state properties and possibility to undergo homolytic cleavage of the Pn−I bond under irradiation.[82] As the redox properties of dipyrrin complexes appeared to be predominantly ligand-based and complex stability under conditions required for photoredox applications was not vested, further changes with respect to the ligand scaffold should be considered.

5. Reactivity studies of SBDIPY chromophores and molecular sensing applications

---

The data presented in the following chapter has been partially published in: A. Korzun, P. C. Brehm, G. Schnakenburg and A. Bismuto, *Organometallics* **2026**, *45*, 81-89.[253] Theoretical studies were performed by Dr. Philipp C. Brehm and are included and indicated (◇) in this thesis to complement the experimental work. All X-ray solid-state structures shown in this chapter were measured and refined by Dr. Gregor Schnakenburg if not otherwise noted.

5.1. Molecular sensing in the context of organopnictogen chemistry

The broad applicability of main group compounds in the field of molecular sensing has been previously introduced for BODIPY chromophores. In this context, the reactivity of pnictogen compounds has likewise enabled various approaches to molecular sensing across a wide range of analytes. One of the most widely utilized examples is the Gutmann-Beckett method which uses the experimentally determinable ^{31}P NMR shift of triethylphosphine oxide in the presence of a Lewis acid as a metric to evaluate the effective Lewis acidity of an additive.[254–257] The ^{31}P NMR shift occurs as a result of the interaction between the Lewis basic oxygen atom in phospine oxide and the respective Lewis acid and has been used to compare different Lewis acids (Figure 107).[257] Recently, the groups of Baumgartner and Caputo applied the same concept to dithienophosphole oxide chromophores, but instead of ^{31}P NMR spectroscopy utilized the emission properties of these compounds as a tool to quantify relative Lewis acid strength (Figure 107).[258,259] In contrast to the ^{31}P NMR shift, the authors assessed relative Lewis acidity based on a shift in the PL emission resulting from the formation of fluorescent Lewis adducts.[258,259]

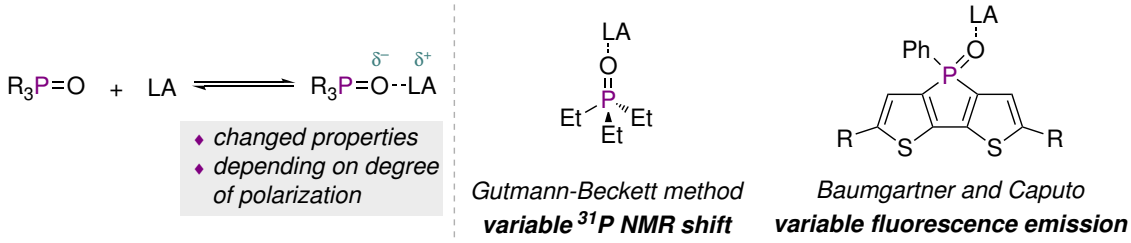


Figure 107: Phosphorous-based methods for estimation of effective Lewis acid strength.[257,258]

In the field of organoantimony chemistry, seminal works of the Gabbaï group have demonstrated the potential of high-valent stibonium compounds to serve as photoluminescent anion probes.[260–262] The authors developed a nonemissive organoantimony compound that displayed a “turn-on” fluorescence response in the presence of ppm levels of fluoride ions in aqueous systems (Figure 108).

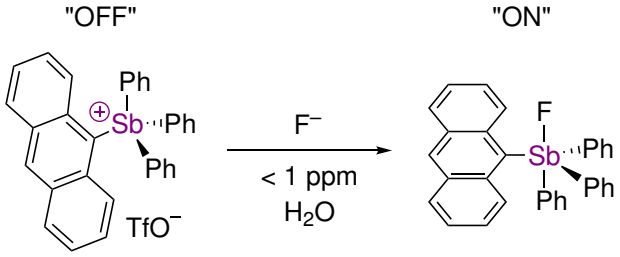


Figure 108: Antimony(V) turn-on sensor for fluoride ions.[261]

The objective of this chapter is to investigate redox-based and redox-neutral reactivity of the **L7** SBDIPY chromophores and explore potential applications in the context of molecular sensing using PL spectroscopy as the analytical method of choice.

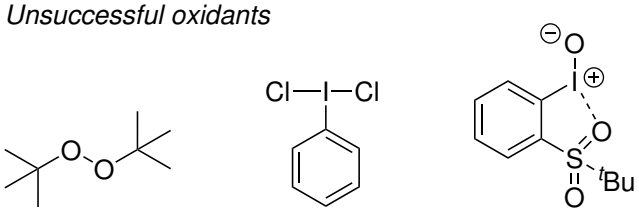
5.2. Oxidation and reduction of SBDIPY complexes

Having established a general overview of the redox properties of **7Sb^{Br}** by means of cyclic voltammetry, both oxidation and reduction of the chromophore were pursued to investigate potential resulting changes in the photophysical properties. First, the ability to undergo an oxidative addition reaction of **7Bi^{Br}** was tested using benzyl bromide as a substrate. However, no reactivity was observed in CD_2Cl_2 at room temperature, upon prolonged irradiation (40 min at 521 nm) and after heating at 40 °C for 1 h. Moreover, SBDIPY **7Sb^{Br}** showed no reactivity towards N_2O or ammonia-borane (10 equiv.) over the course of 3 h in THF at room temperature. While prolonged stirring (24 h) of **7Sb^{Br}** in the presence of ammonia-borane resulted in an unselective decomposition of the starting material, potentially owing to the hydrogenation of the Sb−N bonds or

other deleterious side-reactivity, no reactivity of **7Sb^{Br}** in the presence of N_2O was observed after prolonged time, irradiation at 521 nm for 1 h and heating to 65 °C (2 h). These findings suggest a low nucleophilicity of the pnictogen centre in PnDIPY complexes, which makes them unable to undergo oxidative addition even with polarized bonds.[263] This is possibly due to the low availability of the mostly *s*-character lone pair on the pnictogen centre, as well as an unsuitable geometry in oxidation state +III PnDIPY complexes.[263,264] The ability of pnictogen dipyrrins to engage in oxidative addition could potentially be enhanced through further steric and electronic tuning of the substituents at the pnictogen centre with the aim of decreasing the singlet-triplet gap, *e.g.* through the introduction of stronger σ-donor substituents.[263] Another possible option to increase the propensity of oxidative addition is the reduction of the pnictogen centre to the oxidation state of +I, which has been previously demonstrated by Liu *et al.*[138]

Lastly, the oxidation of **7Sb^{Br}** to the oxidation state of +V was attempted using an organic peroxide and hypervalent iodine reagents (Scheme 69). Addition of 3.00 equiv. of di-*tert*-butyl peroxide (**82**) to a CD_2Cl_2 solution of **7Sb^{Br}** yielded no reaction with **7Sb^{Br}** based on ^{1}H NMR spectroscopy, which was still the case after UV irradiation (40 min at 290 nm) and heating at 80 °C for 1 h. Unfortunately, no reactivity of **7Sb^{Br}** was also observed in the presence of hypervalent iodine reagents **83** (1.00 equiv.) or **84** (1.20 equiv.) in CD_2Cl_2 over a prolonged time (24 h) at room temperature.

Unsuccessful oxidants



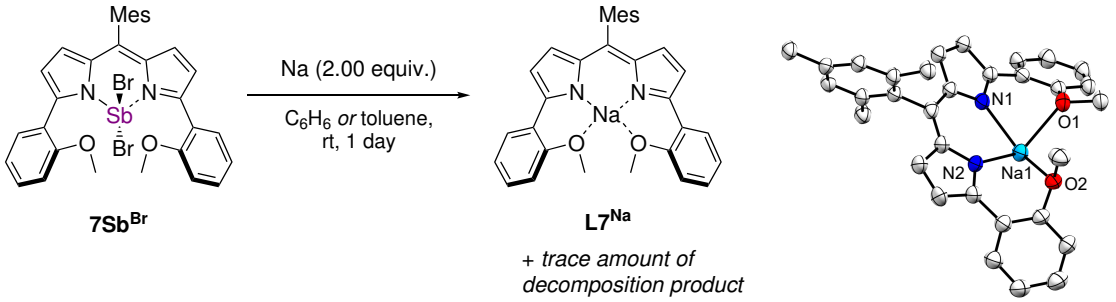
82 **83** **84**

Scheme 69: Unsuccessful oxidants for the oxidation **7Sb^{Br}**.

It became apparent at an early stage that neither the first-generation SBDIPYs (**1Sb^{X}**) nor **L7** and **L8** SBDIPY chromophores were well-suitable candidates to attempt reduction of the antimony centre due to their rather poor solubility in non-polar solvents such as toluene or benzene, which are commonly employed in reduction reactions. Moreover, the previously described CV and DFT studies of **7Sb^{Br}** indicated a predominantly ligand-centred reduction chemistry, which may prohibit a reduction at the antimony atom. The hitherto only literature-known example of a low-valent heavy pnictogen dipyrrin featured a sterically more protecting ligand that enabled access to a dipyrrin-ligated stibinidene, starting from the corresponding dichloride SBDIPY in

the presence of 2 equivalents of sodium.[138] Moreover, Liu *et al.* revealed that attempts to isolate the pnictinidene complexes using other reducing agents, such as KC_8, magnesium or $KHBEt_3$, were unsuccessful, thereby implying that the reduction is inherently challenging to perform in a selective manner.[138]

Despite all odds, the reduction of **7Sb^{Br}** was tested with several reducing agents. First, the successful procedure of Liu *et al.* was adapted for **7Sb^{Br}**.[138] Sodium (2.00 equiv.) was added as the reducing agent to suspensions of **7Sb^{Br}** (0.07 mmol) in benzene and in toluene, and the reaction mixtures were stirred for 24 h at room temperature. Unfortunately, in both cases the formation of the sodium dipyrrinato salt as the major product, alongside trace amounts of decomposition product as indicated by a strongly downfield-shifted N−H resonance around 14 ppm, was identified by ^{1}H NMR spectroscopy (Scheme 70). Moreover, suitable single crystals for X-ray diffraction analysis were obtained of from the benzene reaction mixture, further confirming the identity of **L7^{Na}** (Scheme 70).



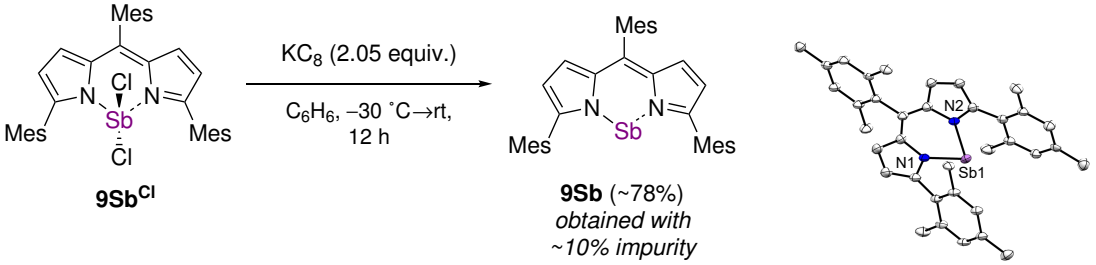
7Sb^{Br} **L7^{Na}** *+ trace amount of decomposition product*

Scheme 70: Attempted reduction of **7Sb^{Br}** in toluene or benzene, yielding **L7^{Na}** as the major product (left). X-ray solid-state structure of **L7^{Na}** (right). Hydrogen atoms and non-coordinating benzene were omitted for clarity and thermal ellipsoids were set to a 50% probability level.

Furthermore, unselective decomposition of **7Sb^{Br}** was observed upon addition of cobaltocene (2.00 equiv.) or KC_8 (2.00 equiv.) to a THF solution of the SBDIPY complex and stirring at room temperature for 2 days. Lastly, attempted reduction *via* addition of the hydride source $NaHBEt_3$ to a THF solution of **7Sb^{Br}** at −78 °C resulted in rapid decomposition of the starting material upon warming to 0 °C, yielding an insoluble black precipitate. These findings are consistent with the previously discussed CV data, suggesting that a ligand-centred reduction is favoured, which precludes successful reduction at the antimony centre.

Based on the above described findings, low-valent chemistry with **L7** dipyrrins appears to be difficult to access and requires further investigation under milder conditions. However, more promising results were obtained using the sterically shielded

SBDIPY **9Sb^{Cl}**, which is also conveniently well-soluble in non-polar solvents such as benzene. Addition of a 0.1 M benzene solution of **9Sb^{Cl}** (0.43 mmol, 1.00 equiv.) onto a frozen suspension of KC_8 (2.05 equiv.) in benzene (0.5 mL) resulted in a gradual colour change from orange to dark red upon warming to room temperature over the course of 12 h (Scheme 71). Filtration of the reaction mixture and subsequent drying of the filtrate under reduced pressure afforded a dark red solid (78% assuming quantitative reduction). Analysis of the solid by ^{1}H NMR spectroscopy in C_6D_6 revealed a mixture of two compounds with the major one displaying substantially downfield shifted ^{1}H resonances in the aromatic region as compared to the starting material and the potassium dipyrrinato salt, whereas the second compound was assigned as a ligand-related impurity (approx. 10%) due to the presence of a downfield-shiftet N−H resonance at 13.2 ppm. Structure elucidation by X-ray crystallography confirmed the successful reduction of **9Sb^{Cl}** to the corresponding antimony(I) complex (Scheme 71).



Scheme 71: Reduction of **9Sb^{Cl}** in benzene (left). X-ray solid-state structure of **9Sb** (right). Hydrogen atoms were omitted for clarity and thermal ellipsoids were set to a 50% probability level.[v]

The increased steric hindrance of the ligand and the higher solubility of its PnDIPY complexes in non-polar solvents make the **L9** dipyrrin complexes the most suitable candidates for further pursuits in low-valent main group chemistry among the presented examples. Nonetheless, a strategy for the purification of **9Sb** still needs to be developed, *e.g.* by washing with a suitable solvent or recrystallization, in order to obtain analytically pure compound.

The reactivity of **9Sb** was briefly investigated, using the crude product (containing approximately 10% impurity) to test oxidative addition of **9Sb** to iodobenzene. Surprisingly, treatment of a C_6D_6 solution of **9Sb** with an excess of iodobenzene resulted in an immediate colour change of the sample. Moreover, while trace amounts of the impurity and iodosobenze were visible by ^{1}H NMR spectroscopy, the signals related to **9Sb** were completely vanished, indicating the formation of a paramagnetic antimony

[v] single crystals were obtained by L. Mohr from an independently prepared reaction mixture that matched the one described above.

compound as no precipitation was observed (Figure 109). This finding could indicate reactivity distinct from the anticipated oxidative addition and may arise from redox non-innocence of the ligand backbone. Furthermore, EPR spectroscopy should be performed to verify the presence of a paramagnetic species and probe its electronic structure. The molecular structure of the reaction product remains purely speculative, as unfortunately no single crystals were obtained from the reaction mixture.

The chemistry of low-valent dipyrrin pnictinidenes is still at an early stage and requires additional investigation and reactivity screening to paint a clearer picture of the properties of these compounds.

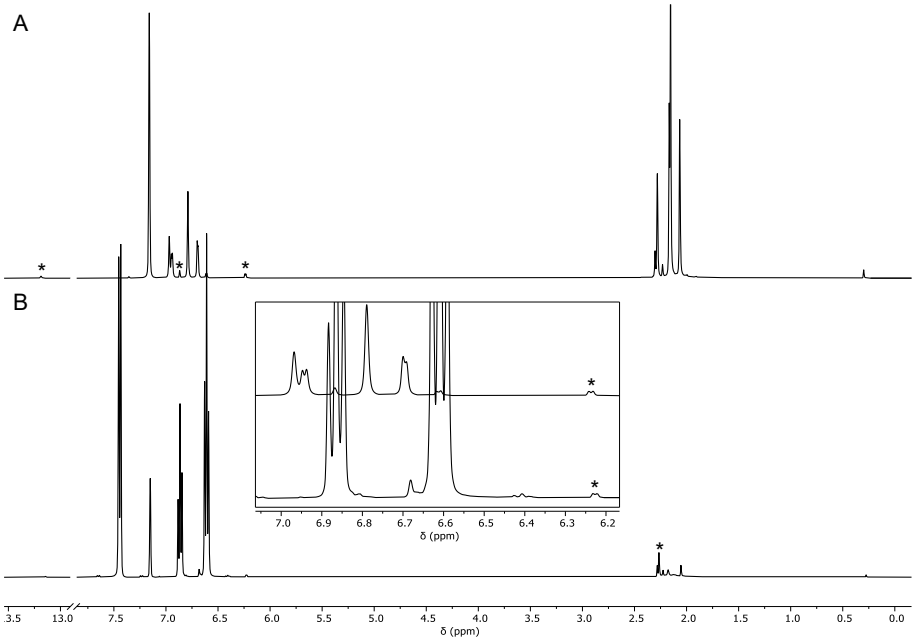
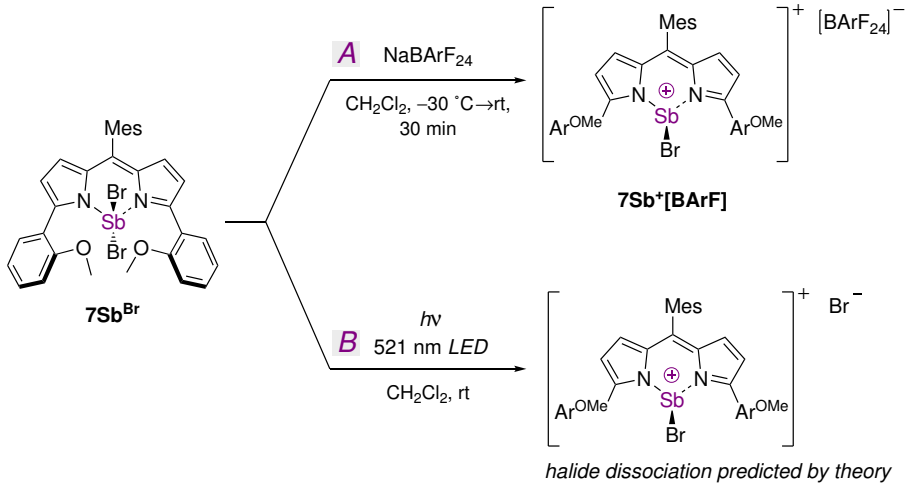


Figure 109: Stacked ^{1}H NMR (400 MHz) spectra of **9Sb** (A) and **9Sb** immediately after addition of excess iodobenzene (B). **L9**-related impurity is indicated by (*).

5.3. Redox-neutral reactivity of SBDIPY chromophores

5.3.1. Reactivity towards Lewis acids

Previous chapters have outlined the propensity of SBDIPY chromophores to engage in halide abstraction chemistry to form *N,N*-ligated stibenium complexes such as **7Sb^{+}[BArF]** (Scheme 72A). Moreover, the dissociation of one bromide ion from **7Sb^{Br}** has been predicted by theory to occur upon green light irradiation and was further indicated by CV experiments of **7Sb^{Br}** under light (Scheme 72B).[174]



Scheme 72: Halide abstraction from SBDIPY **7Sb^{Br}** using weakly coordinating anion salt (A) and proposed light-induced dissociation pathway (B).

The halide lability in **7Sb^{Br}** prompted the question of whether this behaviour could be further exploited using Lewis acids in the context of molecular sensing. Accordingly, the heterolytic Sb−Br bond cleavage was evaluated in the presence of different Lewis acids. Initial test reactions were conducted using tris(pentafluorophenyl)borane (BCF) and $AlBr_3$ as neutral Lewis acids. Addition of 1.00 equiv. of the Lewis acid to a dichloromethane solution of **7Sb^{Br}** resulted in an evident colour change from magenta to dark purple. Moreover, a selective shift of the original ^{1}H NMR signals was observed for **7Sb^{Br}**, with the changes appearing distinct for each Lewis acid (Figure 110). For both tested Lewis acids a downfield shift of pyrrolic ^{1}H resonances (H^{py}) was observed while ^{1}H signals of the ligand's anisole substituents (H^{Ar}) converged. This observation was in line with spectroscopic findings for the previously isolated and characterized stibenium complex **7Sb$^+$[BArF]**. Notably, the shift of ^{1}H resonances was significantly more pronounced for $AlBr_3$ as an additive, which may be attributable to an interaction of the Lewis acid with the pending methoxy groups aside from halide abstraction as bromomethane was observed by ^{1}H NMR spectroscopy (singlet at 2.65 ppm).[vi] Furthermore, a selective shift in the presence of the Lewis acid additives was also seen by ^{13}C{^{1}H} NMR spectroscopy, thus providing two viable options for detection of the tested Lewis acids.

[vi] good agreement with reported data in CCl_4, National Institute of Advanced Industrial Science and Technology. SDBS Web: `https://sdbs.db.aist.go.jp` (accessed 09.02.26). SDBS No.: 5236, Spectral code: HPM-02-884.

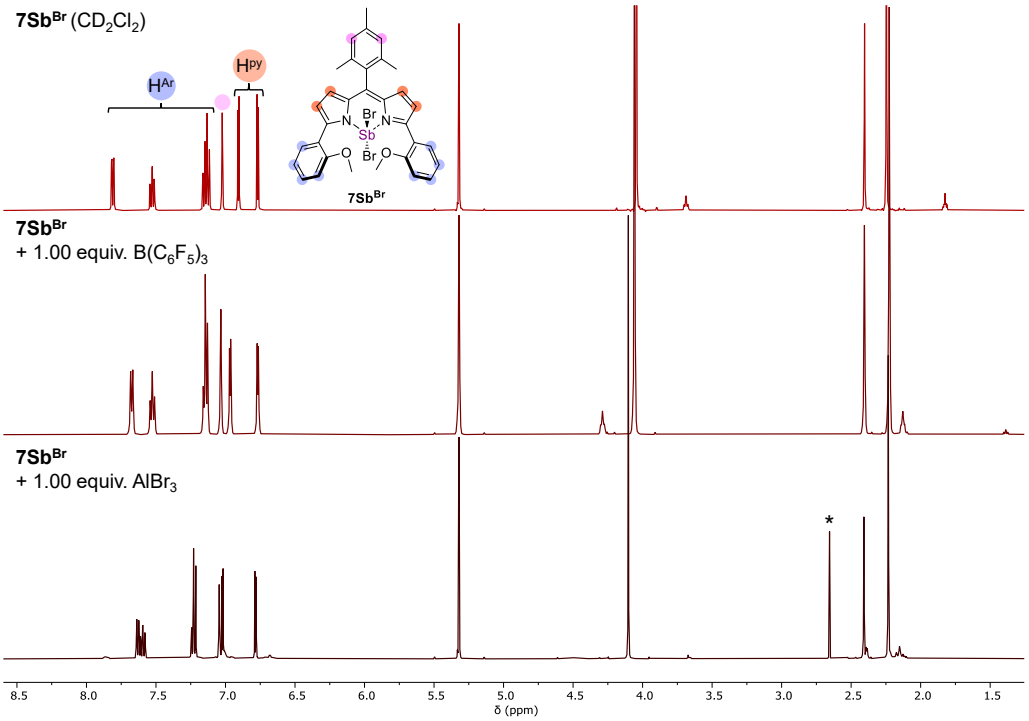
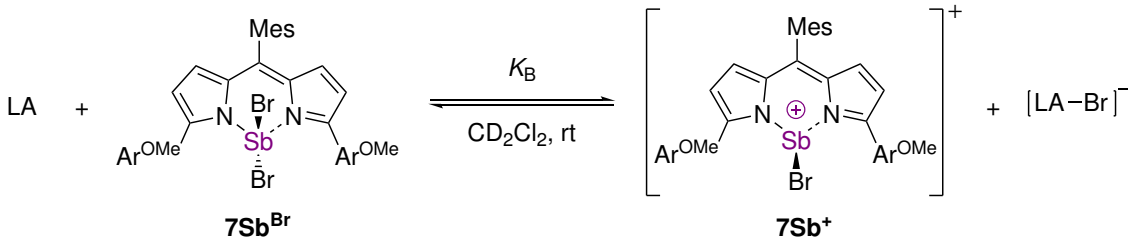


Figure 110: Stacked ^{1}H NMR (500 MHz) spectra of **7Sb^{Br}** (top) upon addition of 1.00 equiv. of BCF (middle) and upon addition of 1.00 equiv. $AlBr_3$ (top) in CD_2Cl_2. The sign (*) marks bromomethane.

Following the method reported by Ofial and co-workers, a ^{1}H NMR titration experiment with varying Lewis acid concentrations (BCF or $AlBr_3$) was conducted in order to estimate the equilibrium constants K_B of the halide abstraction reaction (Scheme 73).[265] The method was well-applicable for BCF as an additive, giving an experimentally determined value of K_B = 156±30 M^{-1} (Figures 111 and 112).



Scheme 73: Proposed reaction scheme for the equilibrium between **7Sb^{Br}** and **7Sb^{+}** in the presence of a Lewis acid.

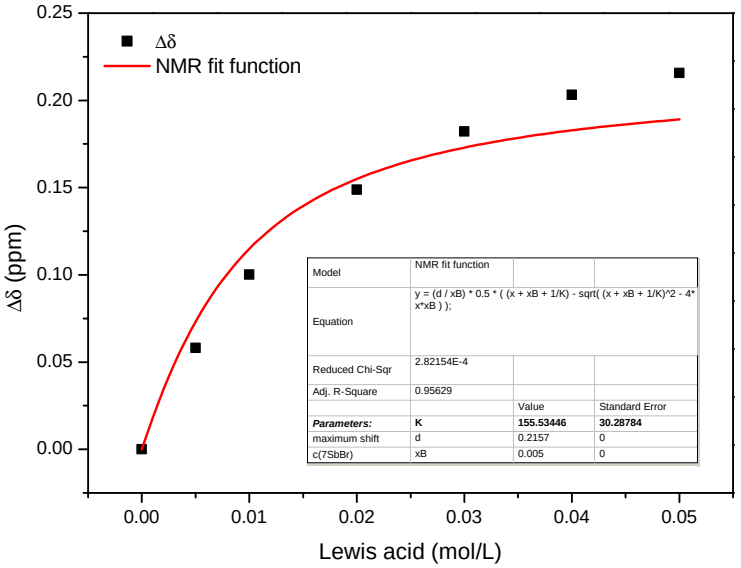


Figure 111: NMR titration plot of **7Sb^{Br}** in the presence of varying amounts of BCF. The chemical shift difference $\Delta\delta$ was determined with respect to the ^{1}H resonance of **7Sb^{Br}** at 7.80 ppm (dd) and referenced to CD_2Cl_2 (Figure 112). The non-linear fit function was derived from literature-reported studies.[265]

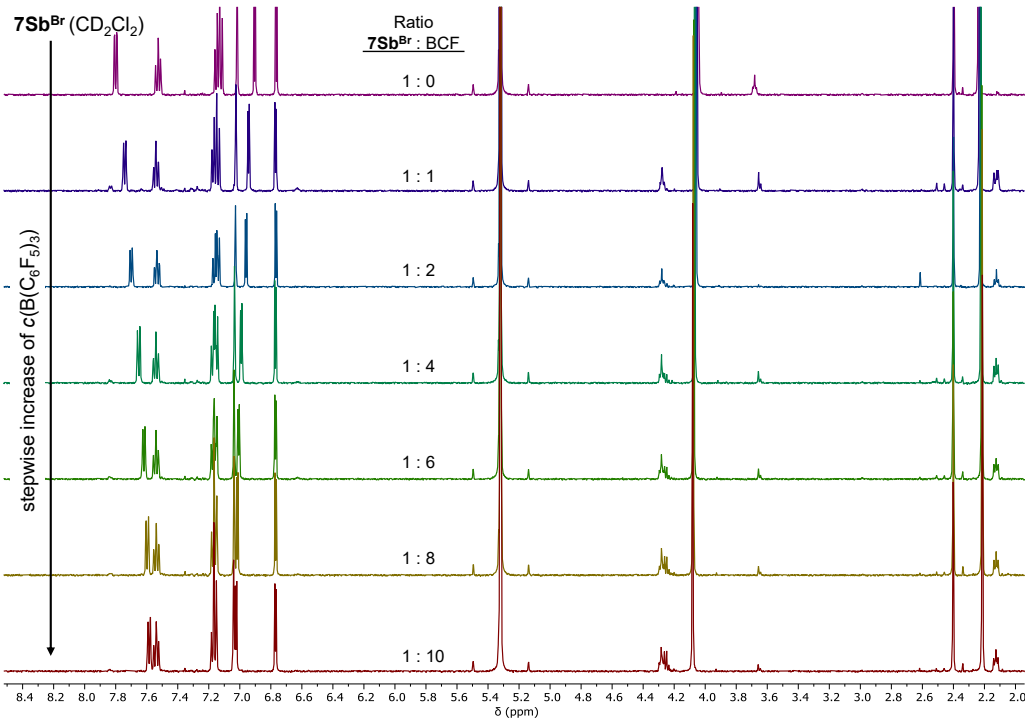


Figure 112: Stacked ^{1}H NMR spectra (500 MHz, CD_2Cl_2) of **7Sb^{Br}** (0.005 M) upon stepwise increase of BCF concentrations (top to bottom).

However, the method was not applicable for $AlBr_3$ as additive due to competitive demethylation of **7Sb^{Br}**, which was apparent through the disappearance of the ^{1}H resonance of the methoxy groups at 4.04 ppm in the presence of excess amounts of

Lewis acid, alongside the formation of CH_3Br (singlet at 2.65 ppm). Moreover, excess $AlBr_3$ led to unforeseen structural changes of the complex above 1.00 equiv. which ultimately led to decomposition of the complex (Figure 113). Moreover, it should be noted that a strong discoloration of the **7Sb^{Br}** solution was observed with a significant excess of $AlBr_3$ (circa 8.0 equiv.). These samples also exhibited the appearance of a new ^{1}H resonance at 3.04 ppm which may be attributed to the formation of chloromethane from CH_2Cl_2, possibly resulting from dechlorination with a strongly Lewis-acidic intermediate.[vii]

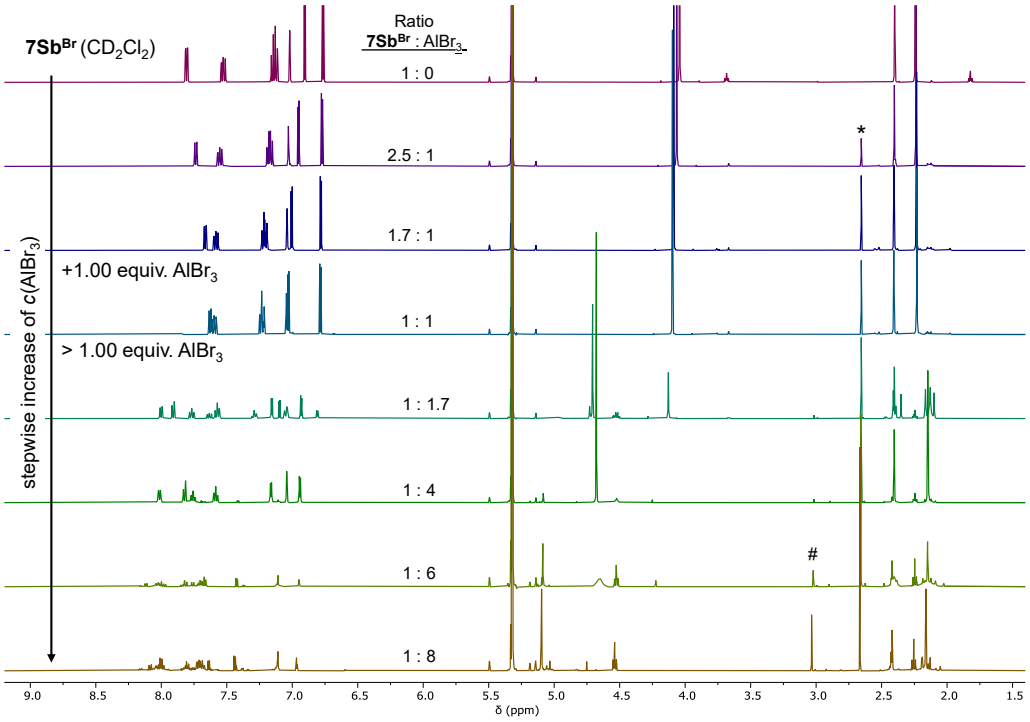


Figure 113: Stacked ^{1}H NMR spectra (500 MHz, CD_2Cl_2) of **7Sb^{Br}** (0.005 M) upon stepwise increase of $AlBr_3$ concentrations (top to bottom). Bromomethane is marked by ($\star$), whereas chloromethane is marked by ($\#$).

Next, other aluminum halides AlX_3 (X = Cl or I) were tested as additives to see whether a similar effect as for $AlBr_3$ could be observed. Indeed, addition of one equivalent of $AlCl_3$ or AlI_3 to a CD_2Cl_2 solution of **7Sb^{Br}** resulted in a very similar signal pattern by ^{1}H NMR, which displayed only slightly different chemical shifts of the pyrrolic protons H^{py} (Figure 114). Subtle changes between the additives were also visible by $^{13}C\{^1H\}$ NMR (Figure 115).

[vii] good agreement with reported data in CCl_4, National Institute of Advanced Industrial Science and Technology. SDBS Web: `https://sdbs.db.aist.go.jp` (accessed 09.02.26). SDBS No.: 9566 Spectral code: HPM-02-883.

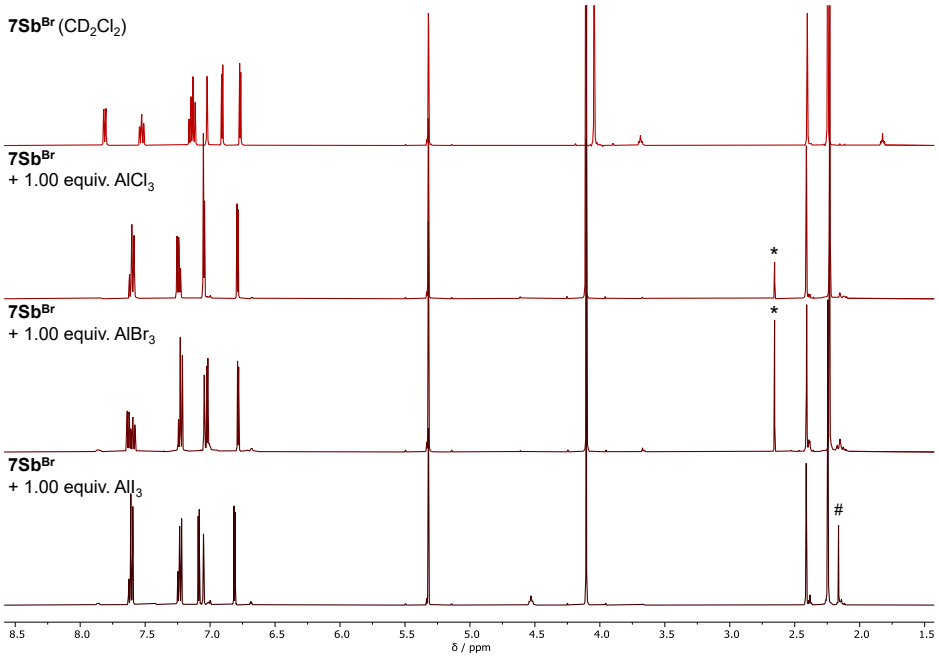


Figure 114: Stacked ^{1}H NMR spectra (500 MHz, CD_2Cl_2) of **7Sb^{Br}** (0.02 mmol) upon addition of 1.00 equiv. of AlX_3 (X = Cl, Br or I). Bromomethane is marked by (*), whereas iodomethane is marked by (#).

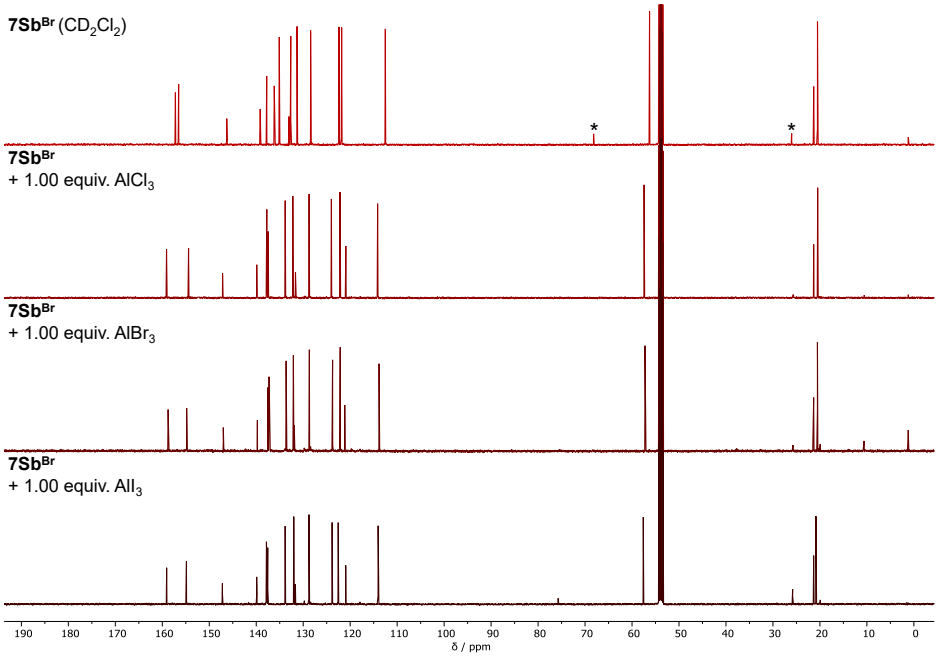


Figure 115: Stacked $^{13}C\{^{1}H\}$ NMR spectra (126 MHz, CD_2Cl_2) of **7Sb^{Br}** (0.02 mmol) upon addition of 1.00 equiv. of AlX_3 (X = Cl, Br or I). The sign (*) marks THF.

Interestingly, while upon addition of 1.00 equiv. of $AlCl_3$ the formation of bromomethane was observed by ^{1}H NMR, addition of 1.00 equiv. of AlI_3 resulted in the formation of iodomethane, indicating that partial halogen exchange may occur between the halide

source and **7Sb^{Br}**.[viii] Addition of a second equivalent to **7Sb^{Br}** resulted in complex decomposition for all three aluminum salts, displaying a disappearance of the ^{1}H resonance of the methoxy group of the ligand alongside an increase of the halomethane peaks (Figure 116). In the case of $AlCl_3$ as additive, the increased amount of Lewis acid resulted in the formation of CH_3Cl and CH_3Br based on ^{1}H NMR data. The decomposition of **7Sb^{Br}** in all three cases is likely caused by demethylation of the ligand, leading to a highly reactive intermediate that readily undergoes deleterious follow-up reactivity (Scheme 74).

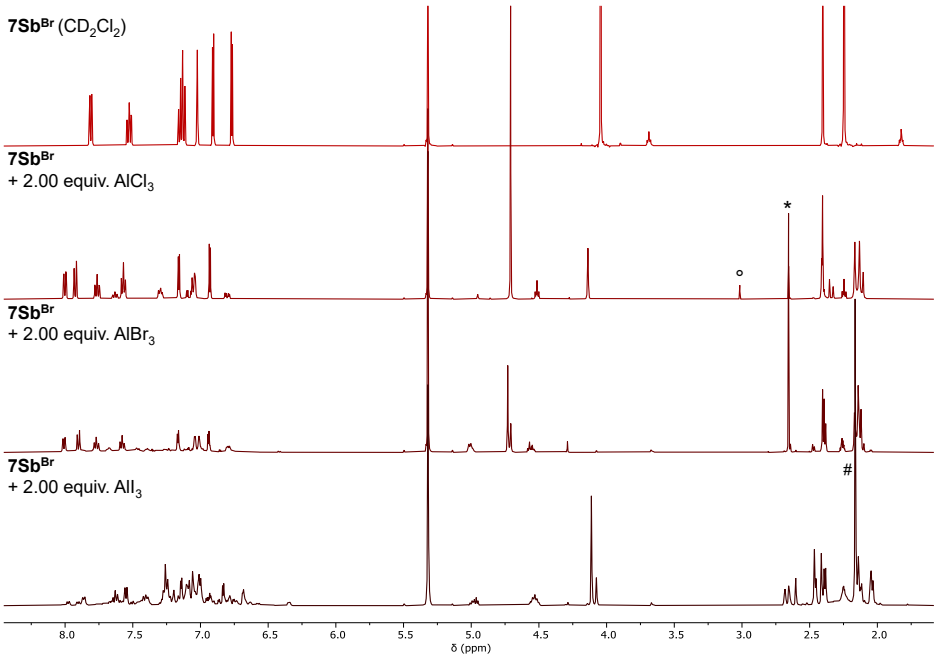
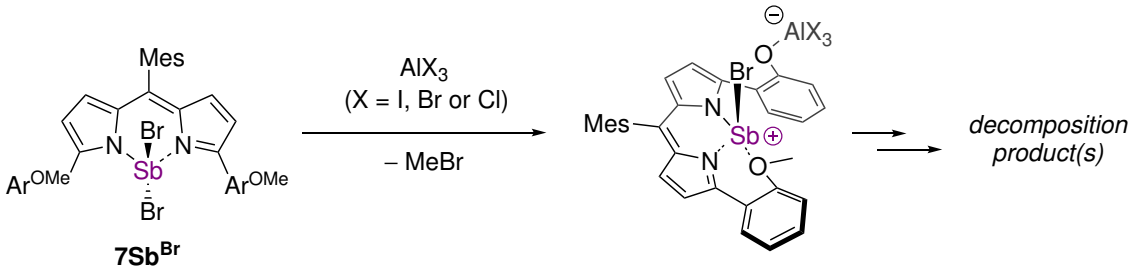


Figure 116: Stacked ^{1}H NMR spectra (500 MHz, CD_2Cl_2) of **7Sb^{Br}** (0.02 mmol) upon addition of 2.00 equiv. of AlX_3 (X = Cl, Br or I). The sign (°) marks CH_3Cl, (*) marks CH_3Br and (#) marks CH_3I.



Scheme 74: Proposed demethylation decomposition pathway of **7Sb^{Br}** in the presence of aluminum halides.

[viii] good agreement with reported data in $CDCl_3$, National Institute of Advanced Industrial Science and Technology. SDBS Web: `https://sdbs.db.aist.go.jp` (accessed 09.02.26). SDBS No.: 3048 Spectral code: HPM-00-217.

In contrast to aluminum halides as “hard” Lewis acids, “softer” ones, such as $GeBr_2$·(1,4-dioxane), $SbBr_3$ or $[RhCl(CO)_2]_2$, caused only small NMR shifts of **7Sb^{Br}**, with no deleterious reactivity observed in the presence of an excess of Lewis acid. In the case of rhodium carbonyl chloride, addition of excess amounts caused no further chemical shift in the ^{1}H NMR spectrum beyond the one observed upon addition of 0.50 equiv. of $[RhCl(CO)_2]_2$ (Figure 117). Based on the assumption that softer Lewis acids do not result in a complete halide abstraction from **7Sb^{Br}**, but instead form halogen bridged adducts with the SBDIPY complex, this finding indicates the formation of a 1:1 adduct between **7Sb^{Br}** and the rhodium complex.

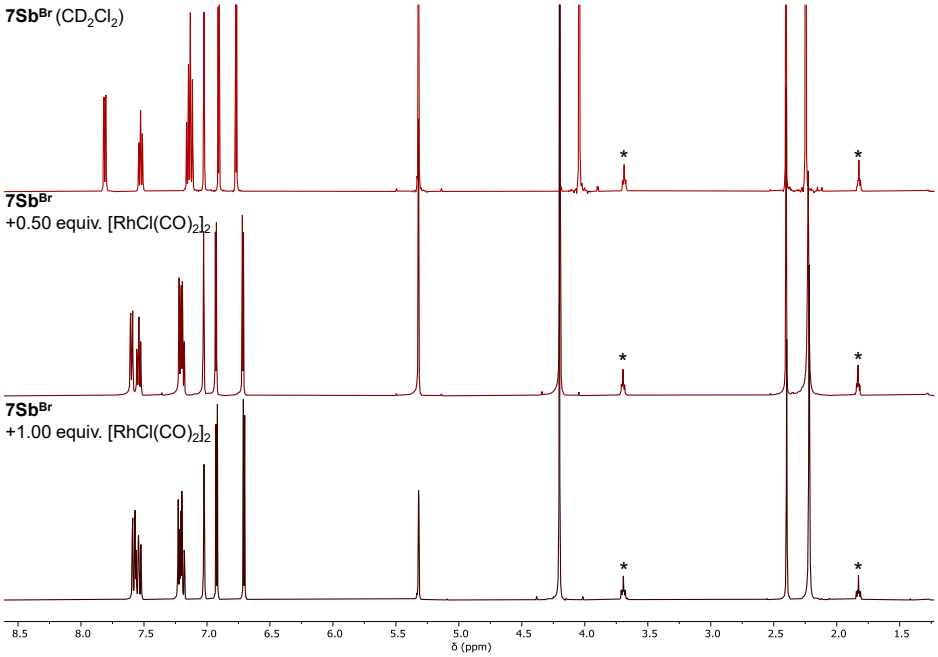
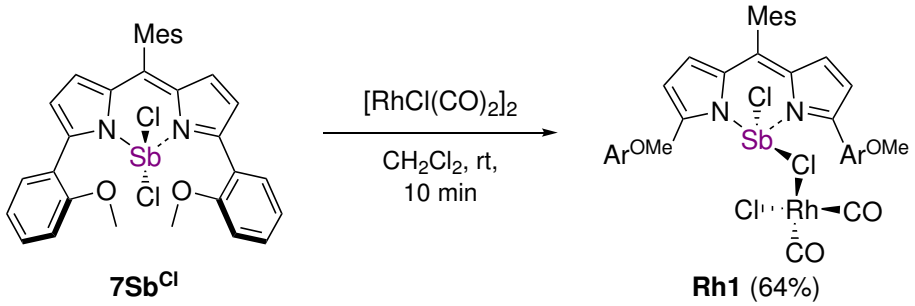


Figure 117: Stacked ^{1}H NMR spectra (500 MHz, CD_2Cl_2) of **7Sb^{Br}** (0.02 mmol) upon addition of 0.50 equiv. of $[RhCl(CO)_2]_2$ (middle) and 1.00 equiv. of $[RhCl(CO)_2]_2$ (bottom). The sign (*) marks THF.

Single crystals of the reaction mixture above were obtained and analyzed by X-ray diffraction, confirming the identity of a 1:1 adduct between **7Sb^{Br}** and a $[RhCl(CO)_2]$ fragment.[253] Moreover, the reaction was performed on larger scale using **7Sb^{Cl}** instead of **7Sb^{Br}** to prevent halide scrambling and the corresponding adduct **Rh1** was isolated in good yield (Scheme 75).



7Sb^{Cl} **Rh1** (64%)

Scheme 75: Synthesis of **7Sb^{Cl}** adduct **Rh1**.

Suitable single crystals of **Rh1** for X-ray diffraction were obtained by slow evaporation of a CH_2Cl_2 and *n*-dodecane mixture. The compound represents a rare example of a heteronuclear μ_2-bridged rhodium complex (Figure 118). This description is further supported by an observed reduction of carbonyl-stretching frequencies from four in rhodium carbonyl chloride to only two in the solid-state infrared (IR) spectrum of **Rh1** ($\tilde{\nu}$(CO) = 2075 cm^{-1}, 2004 cm^{-1}).[266]

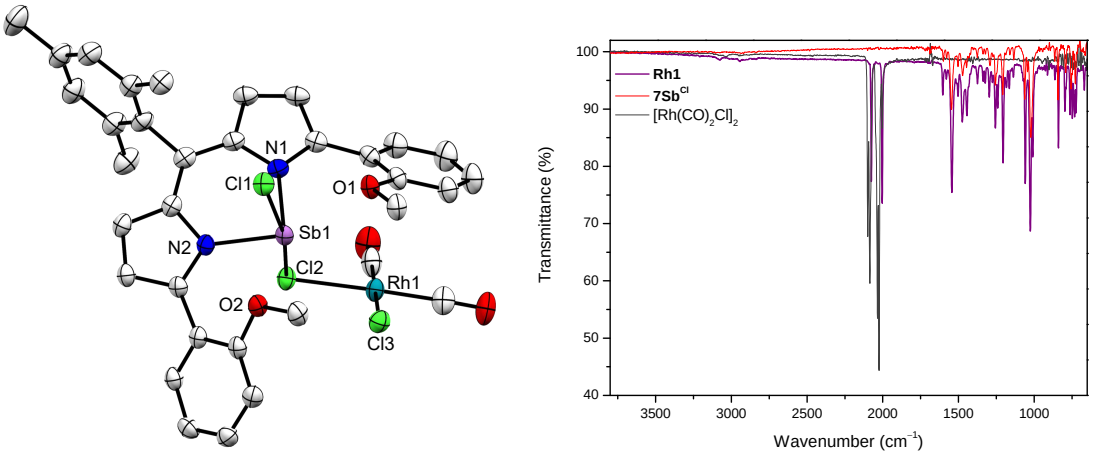
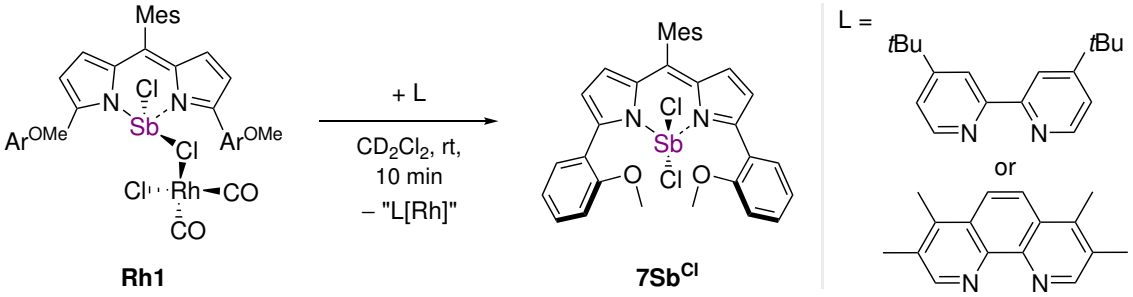


Figure 118: X-ray solid-state structures of **Rh1** (left). Hydrogen atoms were omitted for clarity and thermal ellipsoids were set to a 50% probability level. Solid-state infrared spectra (right) of **Rh1** (purple), **7Sb^{Cl}** (red) and rhodium carbonyl chloride (dark grey).

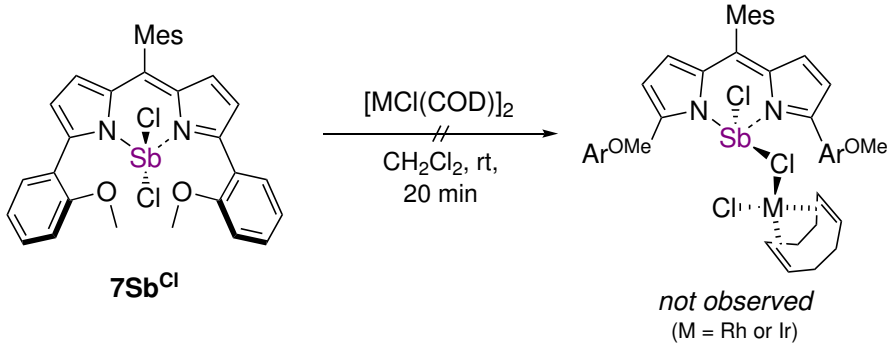
The structural parameters of **Rh1** are very similar to those previously described for **7Sb^{Cl}**, with the main difference being two distinctively different Sb−Cl bond lengths in **Rh1** (Sb1−Cl1 = 2.434(1) Å, Sb1−Cl2 = 2.889(1) Å) which is likely caused by the interaction with the Lewis acidic rhodium centre. Moreover, the [$RhCl_2(CO)_2$] unit in **Rh1** displayed a square planar geometry, thus indicating a redox-neutral reaction to form **Rh1** as the metal centre remained in a d^8 configuration. Attempts at ligand exchange of the rhodium-bound carbonyls with bidentate ligands such as bipyridine or phenanthroline was unsuccessful, as back-formation of **7Sb^{Cl}** was observed in the presence

of extra ligand by ^{1}H NMR spectroscopy (Scheme 76). This finding emphasizes the weak dative interaction of the **7Sb^{Cl}** unit and the rhodium centre present within **Rh1**.



Scheme 76: Reaction of **Rh1** in the presence of bidentate ligands L = 4,4'-di-*tert*-butyl-2,2'-dipyridyl or 3,4,7,8-tetramethyl-1,10-phenanthroline.

Interestingly, no reaction of **7Sb^{Cl}** was observed in the presence of iridium or rhodium cyclooctadiene (COD) complexes which underlines the fact that a π-acidic ligand, *i.e.* CO, needs to be present on rhodium for the metal centre to act as halogen acceptor (Scheme 77).



Scheme 77: Attempted adduct formation starting from metal cyclooctadiene complexes (M = Ir, Rh).

For the additives $GeBr_2$·(1,4-dioxane) and $SbBr_3$ a maximum chemical shift was observed upon addition of 2.00 equiv. of the respective Lewis acid which may indicate the formation of 1:2 adducts between **7Sb^{Br}** and the Lewis acid. However, it could also imply a stronger capability of the Lewis acids to engage in halide abstraction reactivity, which would be in line with the slightly more downfield-shifted H^{py} signals in case of these two additives (Figure 119).

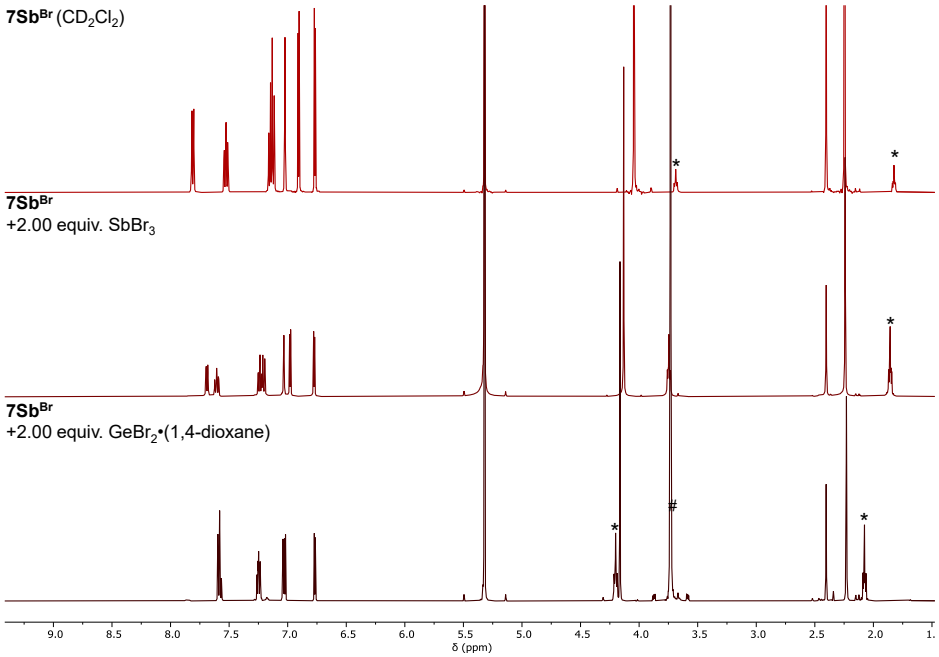
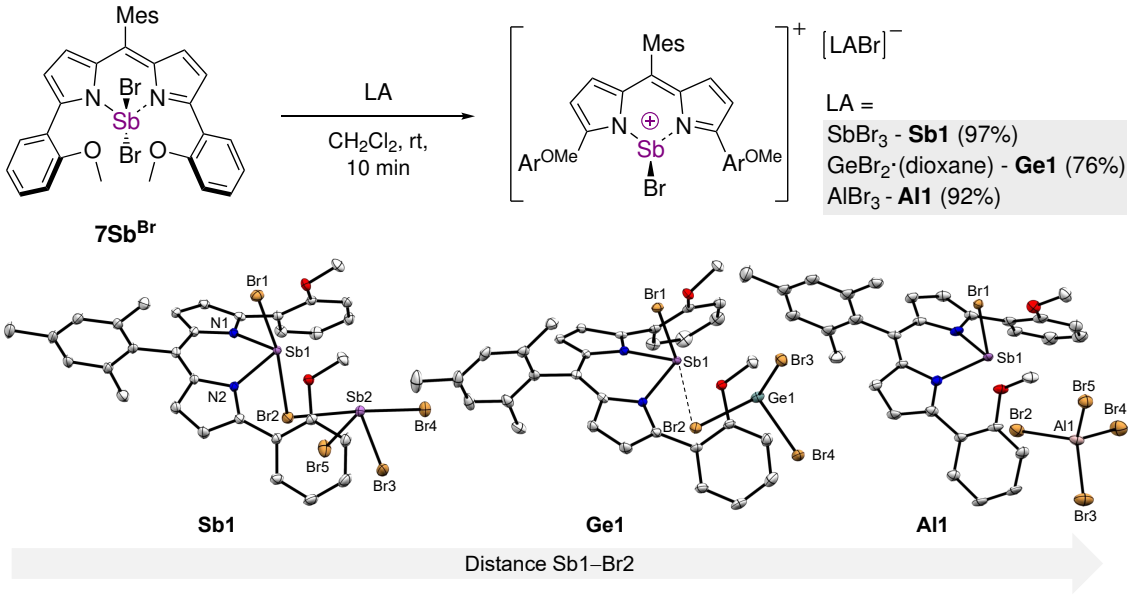


Figure 119: Stacked ^{1}H NMR spectra (500 MHz, CD_2Cl_2) of **7Sb^{Br}** (0.02 mmol) upon addition of 2.00 equiv. of $SbBr_3$ (middle) and 2.00 equiv. of $GeBr_2$·(1,4-dioxane) (bottom). The sign (*) marks THF and (#) marks 1,4-dioxane.

As for **Rh1**, synthesis of 1:1 adducts was performed with the other screened Lewis acids on larger scale and in good yields (Scheme 78). The molecular structures of the isolated compounds were further confirmed by X-ray diffraction analysis (Scheme 78). Interestingly, the Sb1−Br2 distances found in the solid-state structures of **Sb1**, **Ge1** and **Al1** portrayed a clear trend with increasing Sb1−Br2 distances for stronger Lewis acid additives. Moreover, this finding aligns well with previously discussed NMR data, as more pronounced chemical shifts were observed for stronger Lewis acids. In addition to changes in Sb1−Br2 distances, a slight decrease of the average Sb−O distances became apparent with increasing Lewis acid strength, which may be due to bond polarization by the Lewis acid and the consecutive formation of a more electropositive stibenium centre in the case where dative interaction between Br2 and Sb1 becomes negligible (*e.g.* in **Al1**).[153] Selected X-ray solid-state data is provided in Table 15.



Scheme 78: Synthesis of Lewis acid adducts of **7Sb^{Br}** and X-ray solid-state structures of **7Sb^{Br}** Lewis acid adducts; sorted by Sb1−Br2 distance. Hydrogen atoms were omitted for clarity and thermal ellipsoids were set to a 50% probability level.

Table 15: Selected bond parameters of **7Sb^{+}[BArF]**, **7Sb^{Br}** and its adduct complexes.

Structure	Sb1−Br2 (Å)	avg. Sb−O (Å)
7Sb^{Br}	2.761(1)	2.92(2)
7Sb^{+}[BArF]	–	2.68(1)
Sb1	2.954(1)	2.75(9)
Ge1	3.088(1)	2.75(3)
Al1	3.739(1)	2.67(2)

Based on the observed reactivity of BCF in the presence of **7Sb^{Br}**, the neutral triel Lewis acids triphenylborane (BPh_3) and tris(pentafluorophenyl)alane (AlCF) were tested as additives. While, **7Sb^{Br}** displayed a distinct ^{1}H and $^{13}C\{^{1}H\}$ NMR shift upon addition of 1.00 equiv. of AlCF, no reaction was observed in the case of BPh_3, which may be due to its lower Lewis acidity (Figures 120 and 121).[265] Moreover, a selective chemical shift was also observed for the fluoride-substituted SBDIPY **7Sb^{F}** in the presence of 1.00 equiv. BCF, indicating that the proposed halide abstraction reactivity is not only limited to **7Sb^{Br}**.

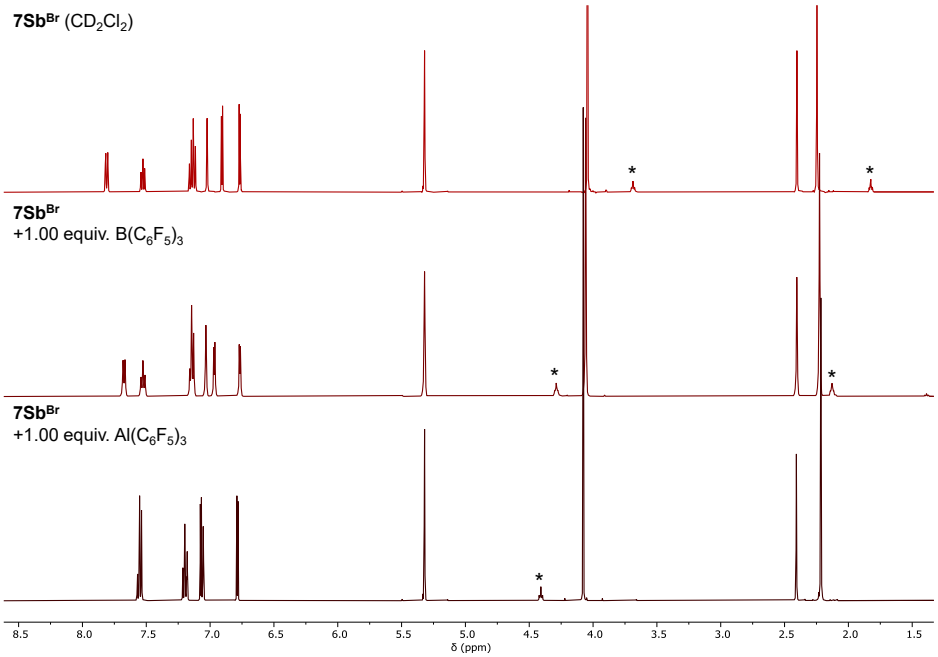


Figure 120: Stacked ^{1}H NMR spectra (500 MHz, CD_2Cl_2) of **7Sb^{Br}** (0.02 mmol) upon addition of 1.00 equiv. of BCF (middle) and 1.00 equiv. of AlCF (bottom). THF is marked by the sign (*).

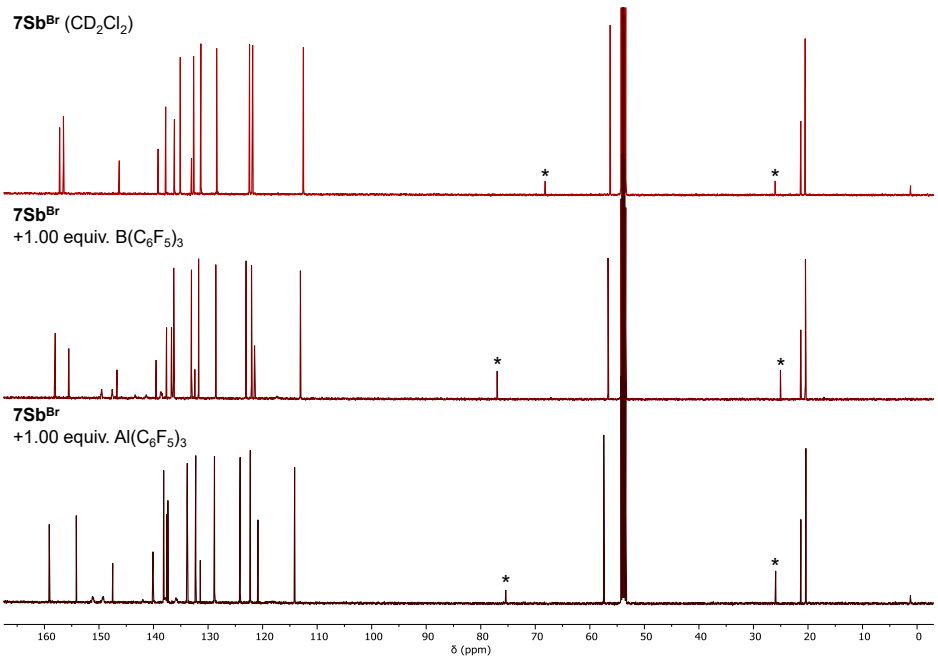


Figure 121: Stacked $^{13}C\{^{1}H\}$ NMR spectra (126 MHz, CD_2Cl_2) of **7Sb^{Br}** (0.02 mmol) upon addition of 1.00 equiv. of BCF (middle) and 1.00 equiv. of AlCF (bottom). THF is marked by the sign (*).

Due to the evident colour changes of **7Sb^{Br}** in the presence of Lewis acids, the reactivity was further investigated using UV/Vis and PL spectroscopy as convenient options for the detection of changes resulting from interactions of **7Sb^{Br}** with additives. Toluene was chosen as a more inert solvent alternative to dichloromethane for the spectroscopic additive screening in order to minimize any potential solvent interaction. As expected, the addition of incremental amounts of BCF or $AlBr_3$ caused significant changes in the absorption and emission profiles of **7Sb^{Br}**. Stepwise addition of $AlBr_3$ resulted in a depletion of the overall emission intensity with a concurrent conversion of the maximum absorbance (λ_{abs} = 556 nm) to a more intense band at λ_{abs} = 607 nm (Figure 122). Additionally, an evident splitting into two distinct absorbance and emission maxima was observed upon addition of 1.00 equiv. of the Lewis acid, indicating the presence of two spectroscopically unlike species. Beyond the addition of 2.00 equiv. of $AlBr_3$ no significant spectroscopic changes were observed, indicating full conversion of the starting complex **7Sb^{Br}**.

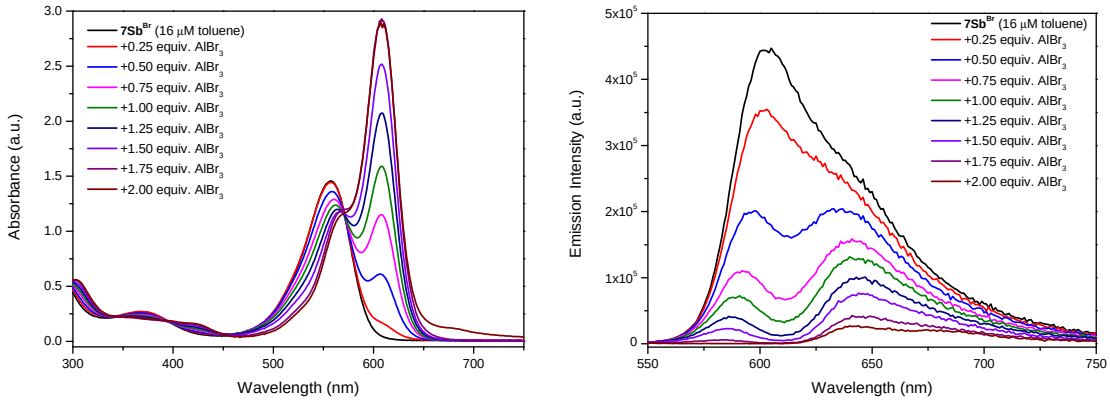


Figure 122: Spectroscopic changes upon addition of incremental amounts of $AlBr_3$ to a toluene solution of **7Sb^{Br}** (16 μM): UV/Vis spectra (left) and PL emission spectra (right).

In contrast to $AlBr_3$, the addition of BCF to a **7Sb^{Br}** sample resulted in a boost of the overall PL emission intensity alongside the emergence of two distinct absorbance and emission maxima that remained also at higher additive concentrations (Figure 123). Similarly to $AlBr_3$, the presence of BCF resulted in a bathochromic shift of the absorbance and full spectroscopic conversion was reached upon addition of approximately 2.00 equiv. of BCF. Interestingly, compared to **7Sb^{Br}** the SBDIPY complex **9Sb^{Br}** appeared to be insensitive to the addition of Lewis acids as no changes in the absorption and emission profiles were seen in the presence of excess BCF (10 equiv.), whereas addition of 1.00 equiv. of $AlBr_3$ only resulted in a subtle broadening of the absorption band and slight increase in emission. This is likely due to the more sterically shielded ligand in **9Sb^{Br}** which effectively disfavours halide abstraction.

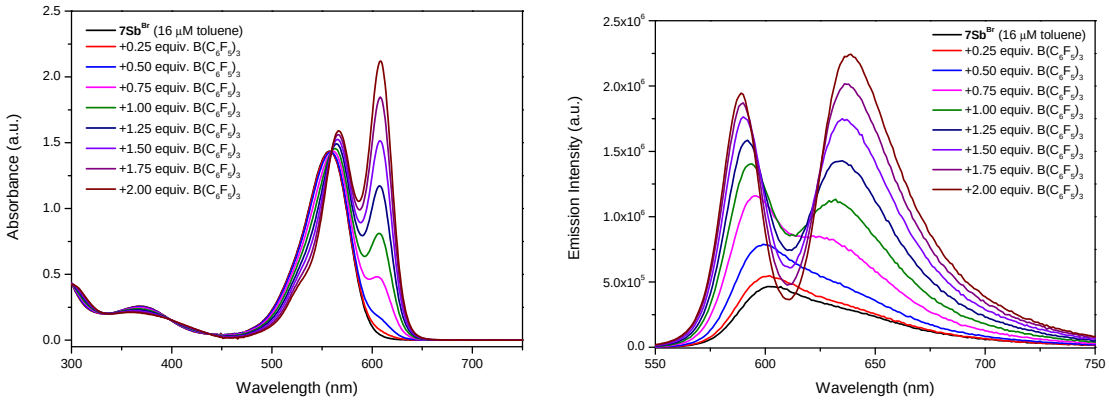


Figure 123: Spectroscopic changes upon addition of incremental amounts of BCF to a toluene solution of **7Sb^{Br}** (16 μM): UV/Vis spectra (left) and PL emission spectra (right).

In order to validate whether full spectroscopic conversion is caused by a second halide abstraction from **7Sb^{Br}**, the reactivity of **7Sb^{+}[BArF]** was evaluated in the presence of BCF and $AlBr_3$ (Figure 124). Interestingly, **7Sb^{+}[BArF]** exhibited no changes in its absorption and emission profiles upon addition of an excess of BCF, whereas addition of 1.00 equiv. of $AlBr_3$ resulted in an immediate colour change from magenta to blue which appeared as a new band with maximum absorbance at λ_{abs} = 607 nm. These findings highlight multiple interesting details. First, BCF is likely not capable of engaging in two consecutive halide abstraction reactions from **7Sb^{Br}**. Thus, the observed spectroscopic changes of **7Sb^{Br}** in the presence of BCF may stem from the reaction equilibrium of a single halide abstraction. The enhanced emission is further in line with comparison of experimental data for **7Sb^{Br}** (ϕ_{rel} = 0.05) and stibenium complex **7Sb^{+}[BArF]** (ϕ_{rel} = 0.26). Second, **7Sb^{+}[BArF]** and **7Sb^{Br}** possibly share a common decomposition product in the presence of excess amounts of $AlBr_3$ as the corresponding absorption bands match. Based on NMR spectroscopy evidence, it can be hypothesized that the decomposition is caused by demethylation of the ligand scaffold after a single halide abstraction from **7Sb^{Br}**.

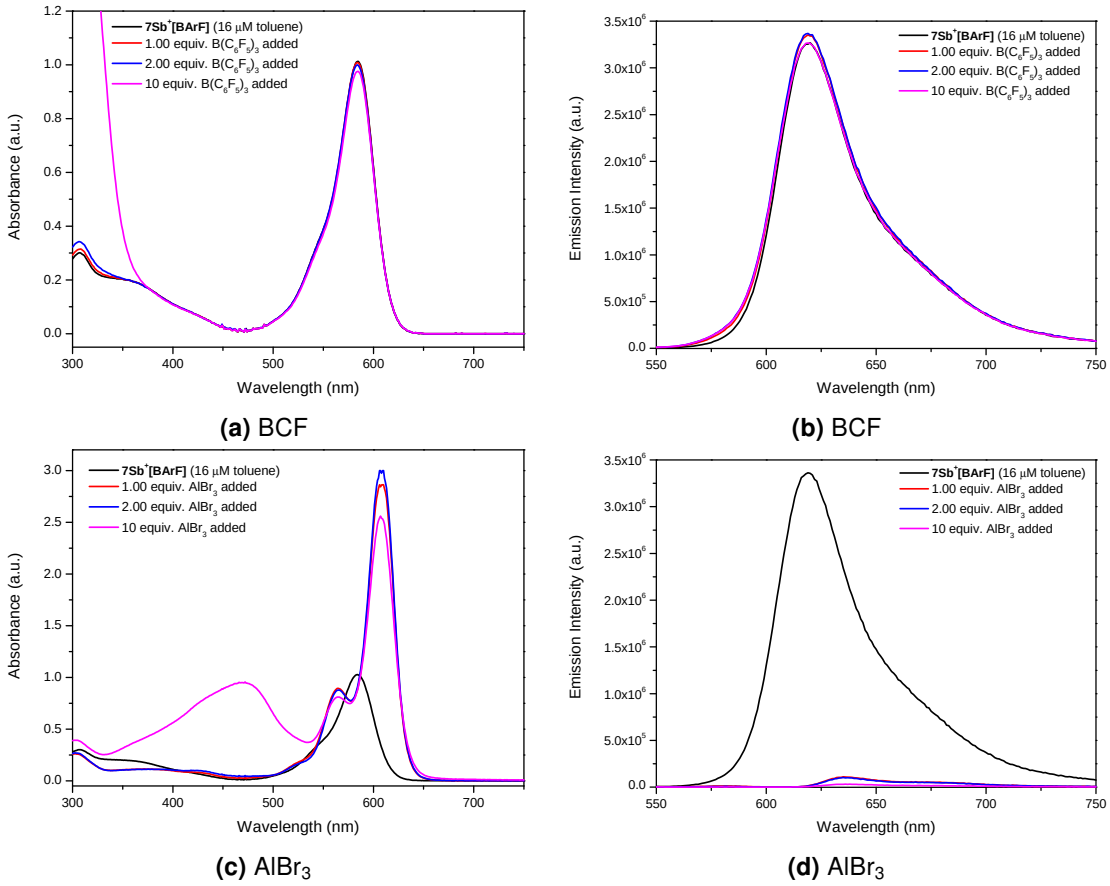
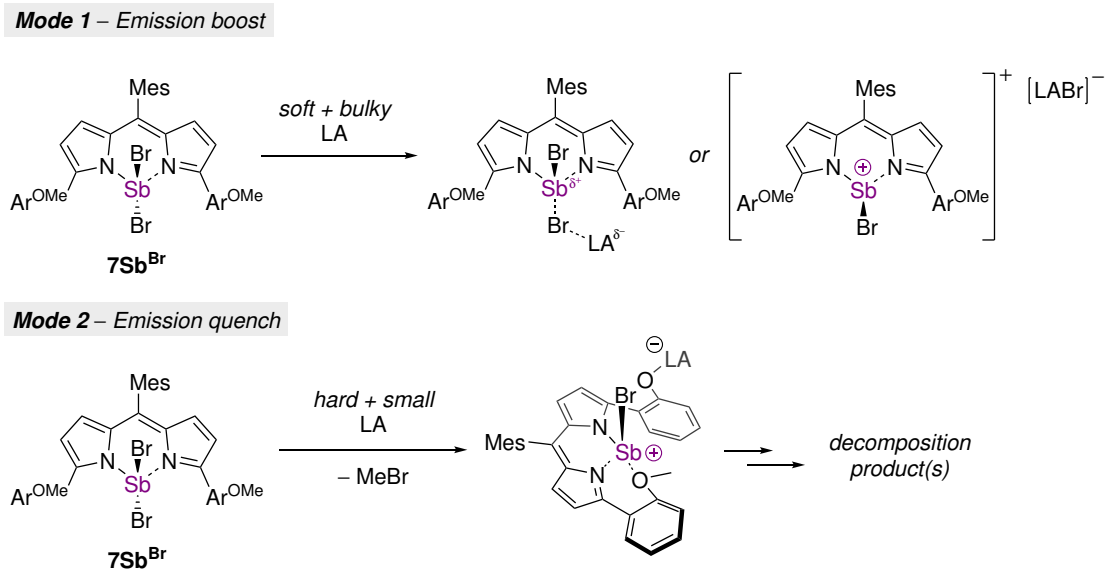


Figure 124: UV/Vis and PL emission spectra upon addition of increasing amounts of BCF (a and b), and upon addition of increasing amounts of $AlBr_3$ (c and d) to toluene solutions of **7Sb⁺[BArF]** (16 μM).

The observations described so far can be categorized into two proposed reaction modes of **7Sb^{Br}** in the presence of Lewis acids. *Mode 1* describes the emission boost that likely originates from a pure halide abstraction reactivity, enabled by sterically hindered additives of sufficient Lewis acidity (Scheme 79). In contrast, *Mode 2* occurs in the presence of strong and small Lewis acids which engage in a single halide abstraction from **7Sb^{Br}**, but also undergo a collateral demethylation of the ligand scaffold which results in complex decomposition and an effective emission quenching (Scheme 79). It should also be noted that the sensitivity towards Lewis acid additives is influenced by the concentration of **7Sb^{Br}**, possibly due to aggregation effects as spectroscopic changes upon addition of stoichiometric amounts of BCF were negligible at a 2 μM **7Sb^{Br}** concentration in toluene.



Scheme 79: Proposed reactivity modes of **7Sb^{Br}** in the presence of Lewis acids.

Both modes are apparent to the naked eye upon addition of stoichiometric amounts of Lewis acid (Figure 125).

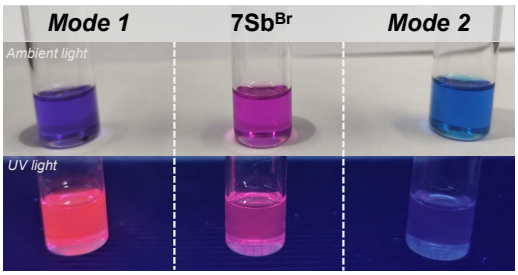


Figure 125: Photographs of **7Sb^{Br}** sample in toluene after addition of 2.00 equiv. of BCF (*Mode 1*) or 2.00 equiv. of $AlBr_3$ (*Mode 2*). The top image was taken under ambient light whereas the bottom one was taken under a 366 nm light source.

Overall, the above described findings make a good case for the use of **7Sb^{Br}** in Lewis acid and potentially molecular sensing applications. As BODIPY chromophores are a prominent class of compounds in the field of molecular sensing, the analogous BODIPY compound **7B^{F}** was also evaluated for its sensitivity towardss Lewis acids such as BCF and $AlBr_3$.[267] Surprisingly, titration experiments of **7B^{F}** at equal concentrations (16 μM) in toluene displayed a drastically hampered sensitivity as compared to SBDIPY complex **7Sb^{Br}** (Figure 126). The addition of excess BCF resulted in negligible changes of the absorption and emission profiles of **7B^{F}**, aside from a decrease in signal intensity due to dilution. However, surplus amounts of $AlBr_3$ (>2 equiv.) caused a visible colour change of **7B^{F}** from bright magenta to a faint blue tone, resulting in a new absorbance maximum at λ_{abs} = 633 nm and weakened corresponding

emission at λ_{abs} = 684 nm. As for the SBDIPY complex, this decomposition event is likely caused by the demethylation of the ligand scaffold through the Lewis acid additive. Moreover, the lack of reactivity in the presence of BCF suggests that fluoride abstraction from **7B^{F}** is not feasible under given conditions.

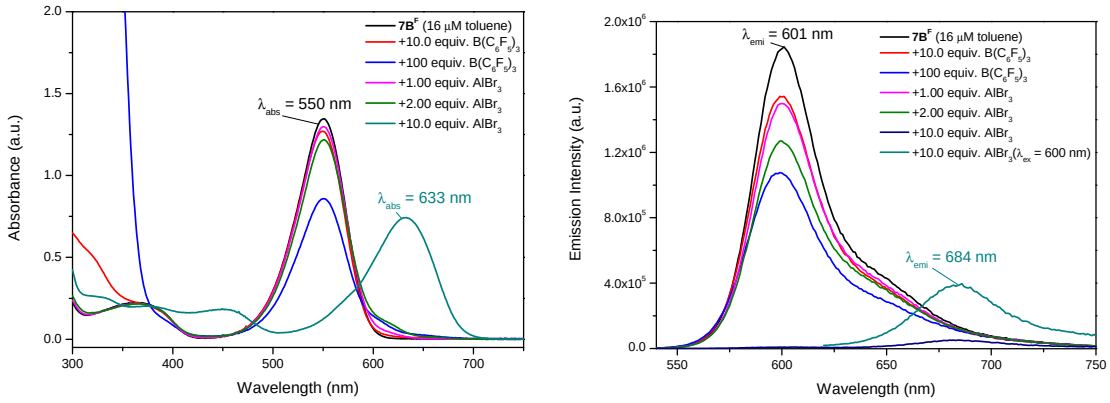


Figure 126: Spectroscopic changes upon addition of incremental amounts of BCF or $AlBr_3$ to a toluene solution of **7B^{F}** (16 µM): UV/Vis spectra (left) and PL emission spectra (right).

In order to obtain more information on the scope of application of **7Sb^{Br}** as a molecular sensor, an additional qualitative screening of Lewis acid additives was conducted. Each Lewis acid was added stepwise (with a total of 1.00, 2.00 and 10.0 equiv.) and the resulting absorbance and emission maxima, as well as the effect on the overall emission intensity were documented upon addition of 10 equiv. of additive and are summarized in Table 16. In order to gain additional insight into the halide abstraction tendencies of the tested Lewis acids, free bromide ion affinities (BIA) were computed on the Pr^{2}SCAN69-D4/def2-QZVPP(CPCM(CH_2Cl_2)) level of theory (Table 16).[268]◇ Moreover, using the **7Sb^{Br}**/**7Sb^{+}** (donor-free cation) pair as a reference point, the bromide abstraction energies were calculated for each additive (Table 16).◇

Table 16: Overview of additive effects on UV/Vis and PL properties of **7Sb^{Br}** in toluene (16 μM) with computed free bromide ion affinities (BIA) of each additive and computed bromide abstraction energies from **7Sb^{Br}** to the Lewis acid.[a]◇

Additive	Absorbance maximum λ_{abs} (nm)[b]	Emission maximum λ_{emi} (nm)[b]	Emission change	BIA (kJ/mol)	Bromide abstraction energy (kcal/mol)
BBr_3	606	640	decrease	−175.1	1.5
$AlCl_3$	603	640	decrease	−283.2	−19.7
$AlBr_3$	607	641	decrease	−290.2	−20.0
AlI_3	610 (max), 632	615, 661 (max)	increase	−290.7	−18.5
$GaCl_3$	592	630	increase	−272.1	−17.4
$InCl_3$	557	597	increase	−288.5	−17.4
$AlMe_3$	532, 582 (max)	566, 598 (max)	increase	−178.5	−1.5
$B(C_6F_5)_3$	568, 609	588, 638 (max)	increase	−209.8	6.0
$Al(C_6F_5)_3$	604	631	increase	−324.5	−16.4
BPh_3	557	602	none	−116.4	18.6
$GeBr_2$·(1,4-diox.)	561, 607 (max)	590, 640 (max)	decrease	−202.8	−3.7
$SbBr_3$	557	602	slight decrease	−156.2	10.2
$SbCl_3$	556, 605 (shoulder)	593, 640 (shoulder)	increase	−149.8	10.4
$ZnCl_2$	568	623	increase	−227.1	−0.2
$HgCl_2$	556	598	increase	−157.4	12.5

[a] Emission change, absorbance and emission maxima are provided upon addition of 10 equiv. of each respective additive. [b] In the case of two maxima, the more intense one is indicated by (max).

Experimental data showed an overall good agreement with the two previously described sensing modes of **7Sb^{Br}**. Addition of hard Lewis acids, such as BBr_3, $AlCl_3$ or $AlBr_3$, resulted in a significant decrease in emission intensity, whereas addition of softer Lewis acids, such as $ZnCl_2$, $GaCl_3$ and sterically more shielded triaryl triels, caused a notable increase in emission intensity. Based on the calculated BIA values, the two sensing modes of **7Sb^{Br}** are governed by an interplay of Lewis acidity and bromide ion affinities of additives. In order to enable *Mode 1* (emission boost) a soft Lewis acid with high BIA is required, whereas *Mode 2* (emission decrease) is caused by demethylation with hard Lewis acids. Moreover, the recurrence of the emission band at $\lambda_{emi} \approx 640$ nm suggests a common or similar decomposition product in the case of demethylation reactivity and a concurrent emission decrease. Despite being hard Lewis acids, the additives $AlMe_3$ and AlI_3 represent two exceptions to the trends described above, as an increase in emission intensities was observed in these cases (Figure 127). For $AlMe_3$ this observation could stem from a ligand exchange of bromide to methyl at the antimony centre or potential follow-up reactivity that leads to the formation of a more strongly emissive Al-dipyrrin. Interestingly, addition of AlI_3 initially showed a decrease of emission, which reverted to a dramatic increase when 10 equiv. of AlI_3 was added. Indeed, this strikingly different behaviour is likely linked to follow-up reactivity and, as mentioned above, may be caused by the formation of a more strongly emissive, red-shifted Al-dipyrrin complex.

Furthermore, ligand exchange of the bromide substituents with chloride salts that are soft Lewis acids of low BIA, such as $SbCl_3$ and $HgCl_2$ is highly probable as these additives resulted in the formation of new absorbance and emission maxima which were found to be in good agreement with data of **7Sb^{Cl}** (λ_{abs} = 555 nm and λ_{emi} = 598 nm). In line with these findings, addition of $SbBr_3$ to **7Sb^{Br}** caused only very minor changes in absorbance and emission, displaying a slight shoulder at λ_{abs} = 610 nm with an added excess of the Lewis acid, thus showing a very sluggish halide abstraction as indicated by the low BIA value. For triphenylborane as the Lewis acid with the highest bromide abstraction energy and lowest BIA value no spectroscopic changes were observed in the presence of **7Sb^{Br}**, which is in accordance with the previously discussed NMR spectroscopy data.

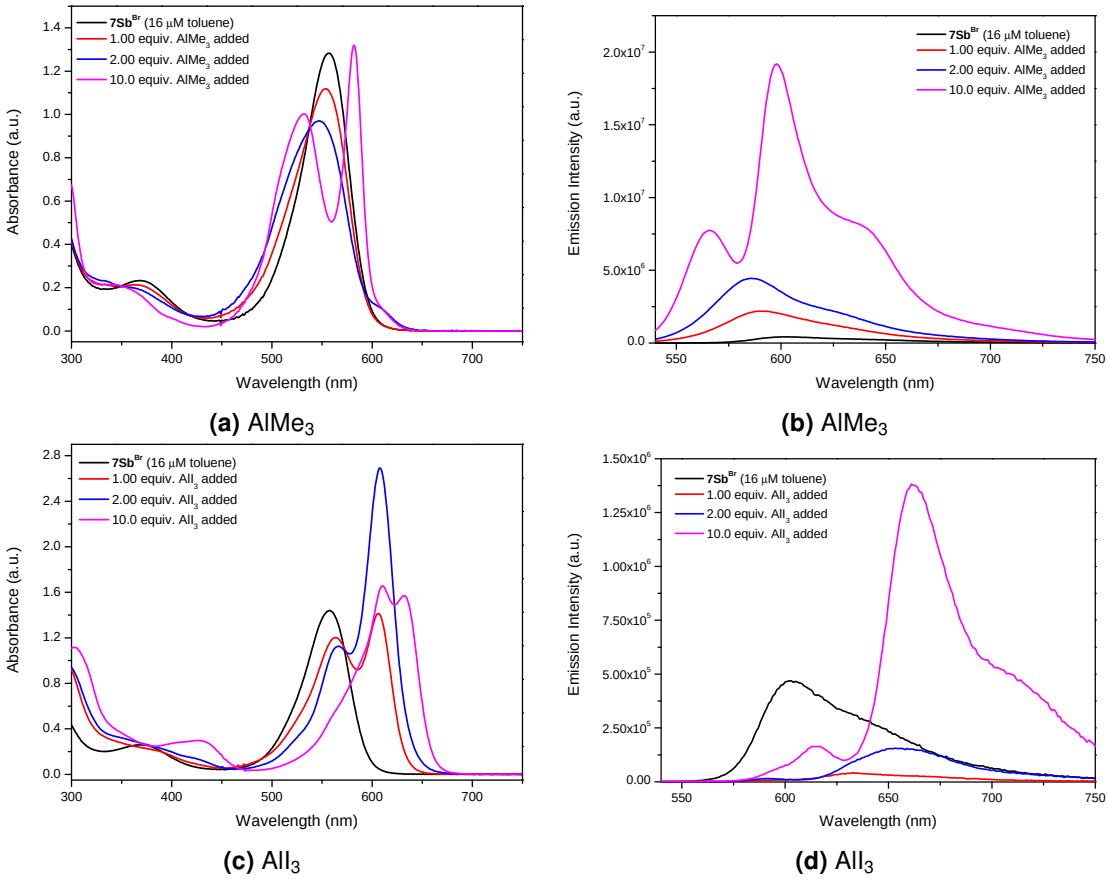


Figure 127: UV/Vis (left) and PL emission spectra (right) upon addition of increasing amounts of $AlMe_3$ (a and b), and upon addition of increasing amounts of AlI_3 (c and d) to toluene solutions of **7Sb^{Br}** (16 μM).

Lastly, the reactivity of **7Sb^{Br}** towards Brønsted acids was revisited using (+)-10-camphorsulfonic acid (10-CSA) in the context of spectroscopic sensing. Unexpectedly, the addition of a CH_2Cl_2 solution of 10-CSA caused a broadening of the main absorption band, alongside a slight emission increase without the formation of any new band (Figure 128). This observation does not align well with the previously proposed sensing modes of **7Sb^{Br}** and would require further investigation. However, based on the fact that no new band in the emission spectrum appeared, **7Sb^{Br}** likely remains in tact under given conditions and could potentially also be used for sensing of Brønsted acids.

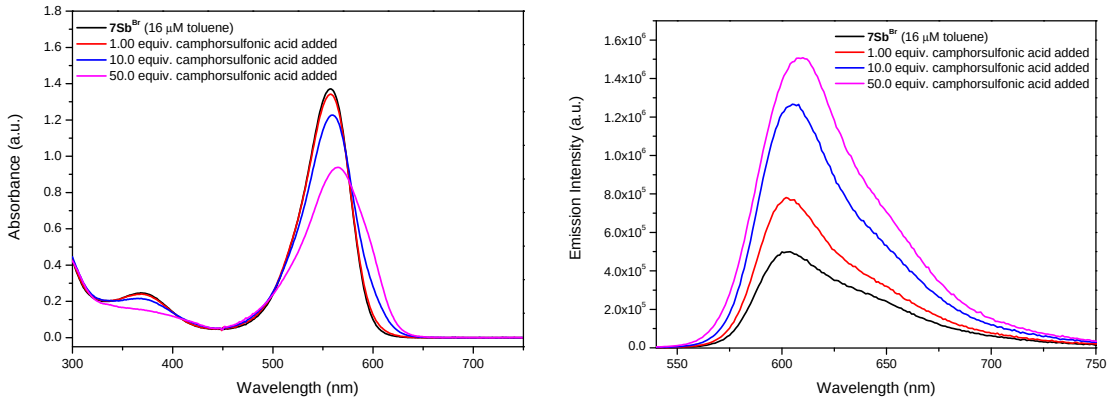


Figure 128: Spectroscopic changes upon addition of incremental amounts of 10-CSA to a toluene solution of **7Sb^{Br}** (16 μM): UV/Vis spectra (left) and PL emission spectra (right).

Computational studies were conducted to provide additional insight into electronic structure of 1:1 Lewis adducts with **7Sb^{Br}** and the connected halide abstraction reactivity.◇ Thus, the molecular structures of 1:1 adducts of $AlBr_3$ (**Al1**) and BCF (**BCF1**) were on the r^{2}SCAN-3c level of theory, accounting for solvents effects by employing the CPCM (CH_2Cl_2).[148,269]◇ Optimized geometries were found to be in good agreement for **7Sb^{Br}** and **Al1**. Final single point energies were calculated on the ωB97X-D4[216–218]/def2-QZVPP[219](ω = 0.15) level of theory.◇ Comparison of frontier molecular orbitals demonstrated that the HOMO and LUMO of **7Sb^{Br}** and adduct **Al1** are considerably similar with both displaying mostly ligand-centred electron densities with π-symmetry (Figure 129).

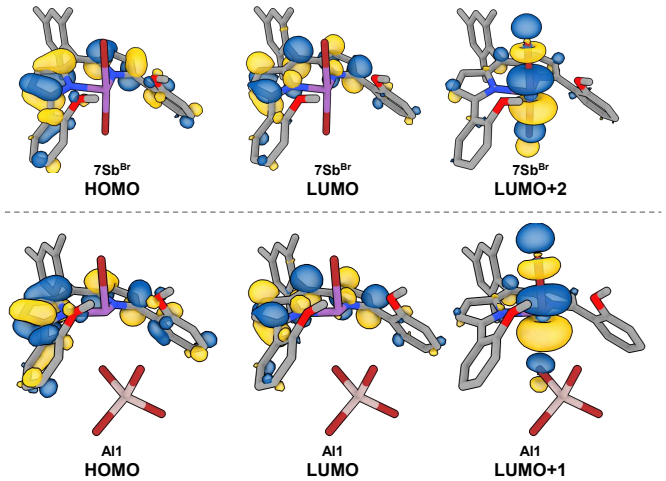
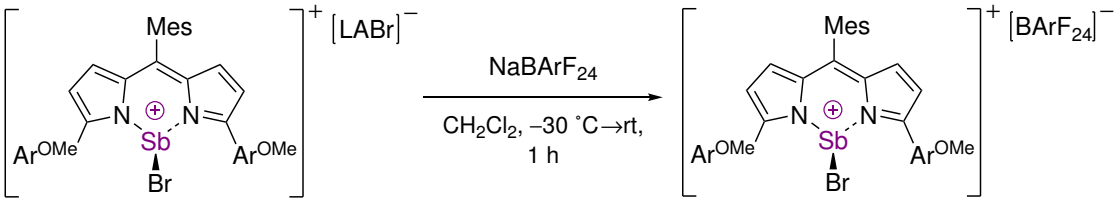


Figure 129: Comparison of selected frontier molecular orbitals (depicted at an isovalue of 0.04 a.u.) of **7Sb^{Br}** (top) and **Al1** (bottom).[253]◇

While the HOMO-LUMO gap of **7Sb^{Br}** was determined as 5.34 eV, it is only slightly reduced in the case of **Al1** with a HOMO-LUMO gap of 5.27 eV, thus indicating only minor electronic effects upon coordination of $AlBr_3$. Moreover, the LUMO+2 in **7Sb^{Br}** displays significant Br−Sb−Br antibonding character, having a HOMO-LUMO+2 gap of 7.59 eV.◇ In the case of **Al1**, the $AlBr_3$ coordination appeared to have a considerable effect on the $\sigma^{\star}$(Br−Sb−Br) orbitals, as LUMO+1 is stabilized by 0.53 eV compared to **7Sb^{Br}**.◇ Although BCF and $AlBr_3$ have considerably different BIA values, the borane was found to have a similar effect on the electronic structure of **7Sb^{Br}** upon coordination.[253]

Since halide abstraction form **7Sb^{Br}** generally resulted in a bathochromic shift of the absorption, ΔSCF calculations were performed to compute absorption energies for adduct **BCF1** as 608 nm and **Al1** as 612 nm, whereas the absorption energy of the donor-free, fully separated ion **7Sb^{+}** was calculated as 627 nm.◇ The apparent redshift is in good agreement with experimental data. Lastly, a second halide abstraction with both additives was investigated computationally.◇ While coordination of a second equivalent of $AlBr_3$ appeared feasible for **Al1**, indicating the potential occurrence of a second halide abstraction with $AlBr_3$, BCF showed no interaction with **7Sb^{+}**.[253] This information further supports the assumption that the emission increase is caused by the formation of the **7Sb^{+}**/$[BrBCF]^{-}$ ion pair in solution which correlates well with the increased emission of **7Sb^{+}[BArF]** vs **7Sb^{Br}**.[253]

On a similar note, a second halide abstraction of **Al1** or **Ge1** was not achieved by allowing the adducts to react with 1.00 equiv of $NaBArF_{24}$ in CH_2Cl_2. Instead, a quantitative formation of **7Sb^{+}[BArF]** was observed by ^{1}H NMR spectroscopy (Scheme 80).

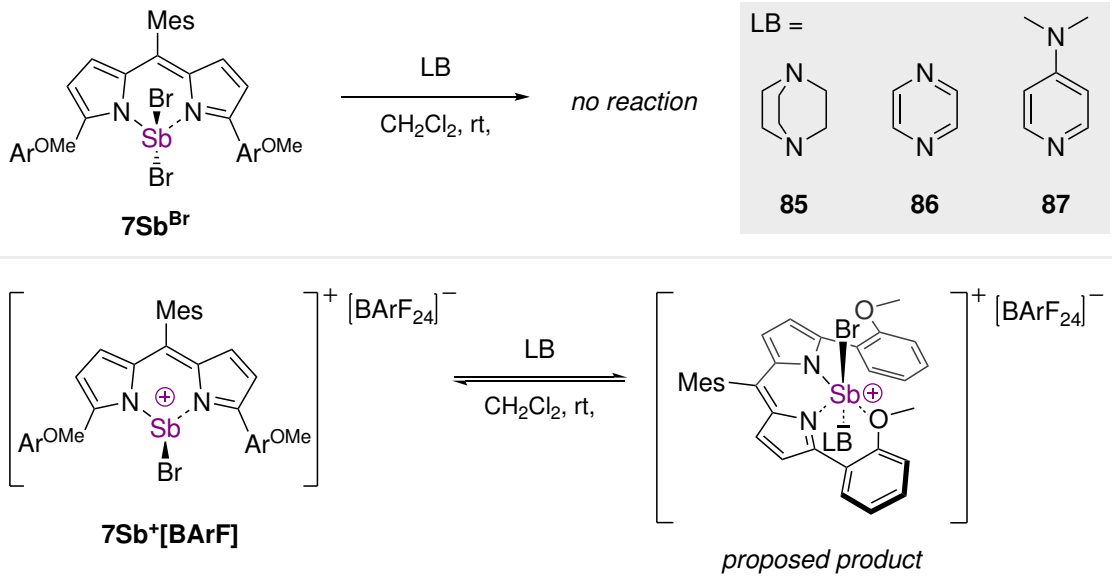


Ge1 *or* **Al1** **7Sb^{+}[BArF]**

Scheme 80: Reaction of Lewis acid adducts **Al1** and **Ge1** in the presence of $NaBArF_{24}$.

5.3.2. Reactivity towards Lewis bases

Besides Lewis acids, the reactivity of **L7** SBDIPY chromophores towards Lewis bases was briefly evaluated. While **7Sb^{Br}** displayed no reaction towards Lewis base additives based on ^{1}H NMR, a selective shift was observed in the case of **7Sb^{+}[BArF]** (Scheme 81). Unlike **7Sb^{Br}**, the stibenium complex **7Sb^{+}[BArF]** can likely react as a Lewis acid due to the more electropositive antimony centre, allowing the formation of adducts as shown in Scheme 81. While **7Sb^{Br}** appears to be coordinatively saturated, the proposed reactivity of **7Sb^{+}[BArF]** is further favoured by the vacant apical coordination site.



Scheme 81: Reactivity of **7Sb^{Br}** and **7Sb^{+}[BArF]** towards Lewis bases **85**-**87**.

The addition of 1.00 equiv. of a nitrogen-centred Lewis base, such as DABCO (**85**), pyrazine (**86**) or 4-dimethylaminopyridine (DMAP, **87**), resulted in a selective ^{1}H and ^{13}C{^{1}H} NMR shift, which was distinct for each additive (Figures 130 and 131). Moreover, the consecutive addition of Lewis base ensued further shifting of the aromatic ^{1}H resonances, thus suggesting an equilibrium between the starting material and the Lewis adduct similarly to what was observed for **7Sb^{Br}** in the presence of Lewis acids.

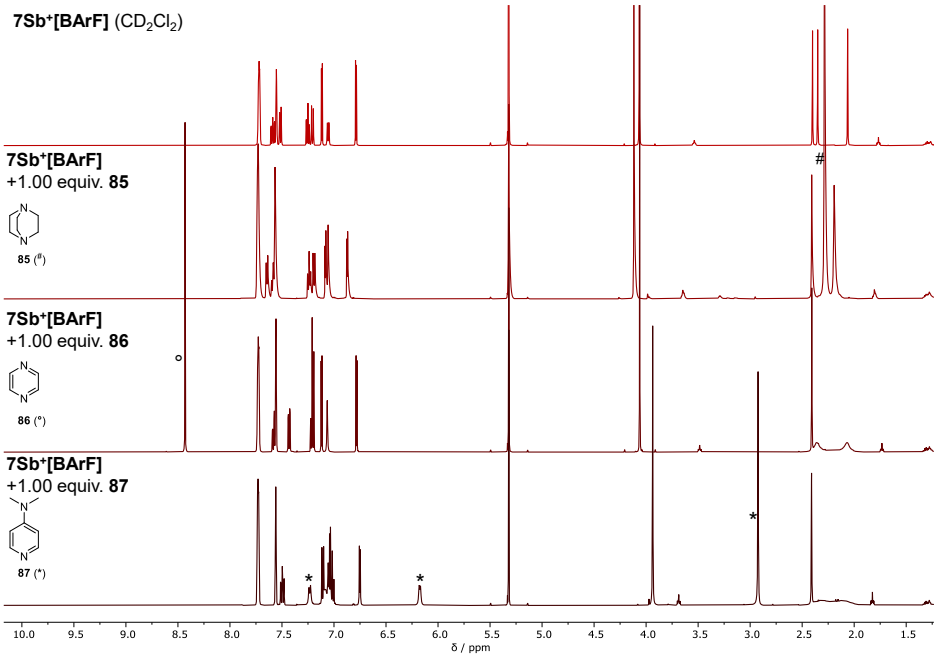


Figure 130: Stacked ^{1}H NMR spectra (500 MHz, CD_2Cl_2) of **7Sb$^+$[BArF]** (0.01 mmol) upon addition of Lewis bases **85**, **86** and **87**. Signals related to the additives are marked with corresponding signs (**85** = $^{\#}$, **86** = °, **87** = *).

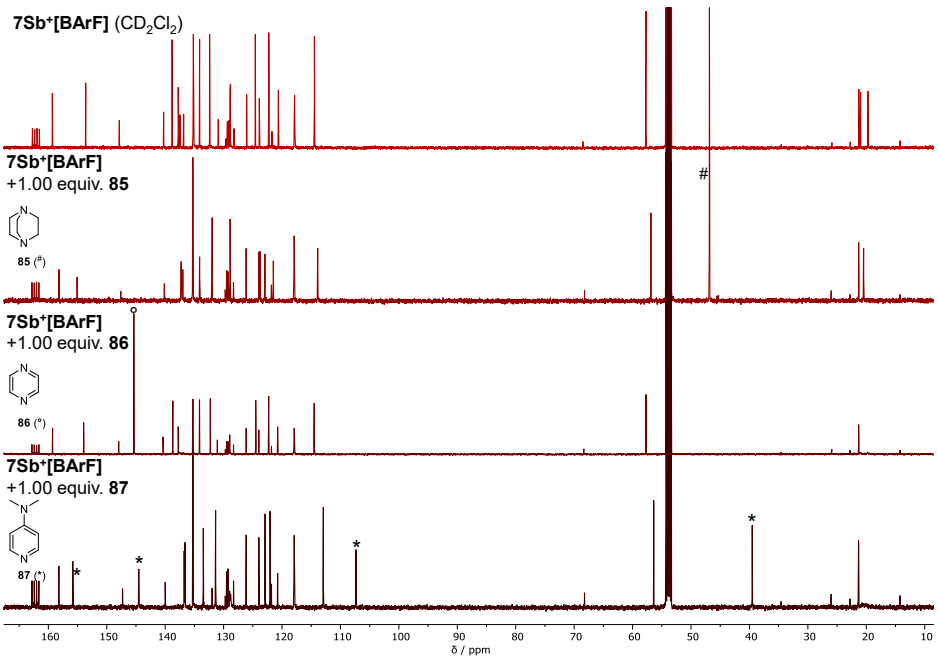


Figure 131: Stacked $^{13}C\{^{1}H\}$ NMR spectra (126 MHz, CD_2Cl_2) of **7Sb$^+$[BArF]** (0.01 mmol) upon addition of Lewis bases **85**, **86** and **87**. Signals related to the additives are marked with corresponding signs (**85** = $^{\#}$, **86** = °, **87** = *).

Due to its electrophilic nature the stibenium complex **7Sb$^+$[BArF]** was also found to readily react with a bromide source, *i.e* tetrapropylammonium bromide (TPABr), to form back **7Sb^{Br}**. Addition of 1.00 equiv. of TPABr to a CD_2Cl_2 solution of **7Sb$^+$[BArF]** resulted in an instant coulour change, which is caused by the back-formation of **7Sb^{Br}** as evidenced by ^{1}H NMR spectroscopy (Figure 132).

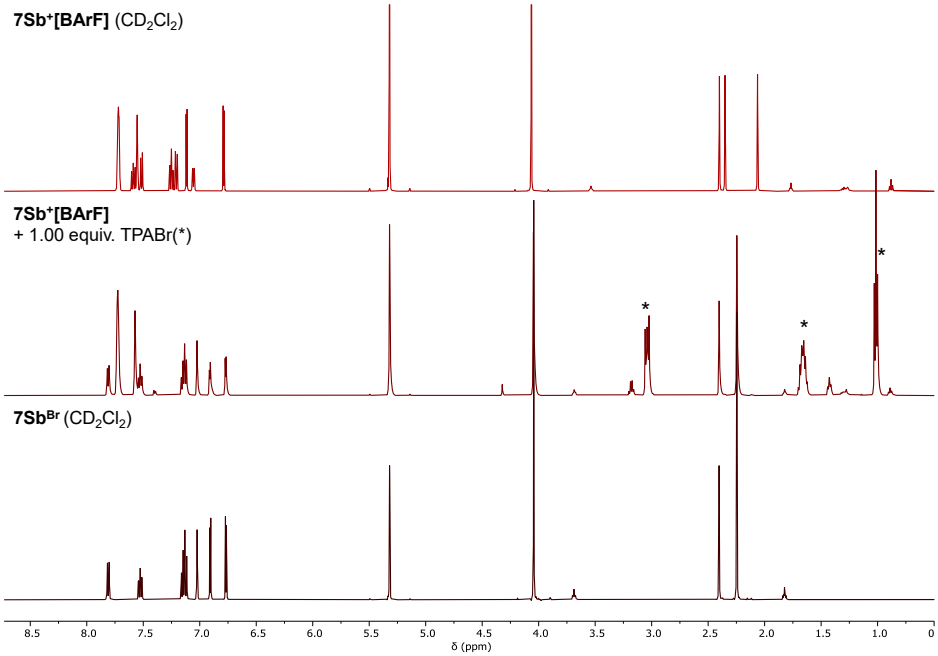


Figure 132: Stacked ^{1}H NMR spectra (500 MHz, CD_2Cl_2) of **7Sb$^+$[BArF]** (0.01 mmol, top) upon addition of TPABr (1.00 equiv., middle), and independent ^{1}H NMR spectrum of **7Sb^{Br}** (bottom). Signals related to TPABr are marked by (*).

In contrast, addition of 1.00 equiv. of tetrabutylammonium fluoride (TBAF) in THF to a CD_2Cl_2 solution of **7Sb$^+$[BArF]** caused an immediate colour change, but resulted in a much more unselective outcome based on ^{1}H NMR spectroscopy (Figure 133). This may be attributed to the lower stability of the fluoride substituted SBDIPY, which readily decomposes leading to the appearance of downfield-shifted N−H resonances at 11.6 and 10.4 ppm. Nonetheless, the reactivity of **7Sb$^+$[BArF]** should be further investigated as it presents an interesting opportunity to expand into the field of anion sensing applications.

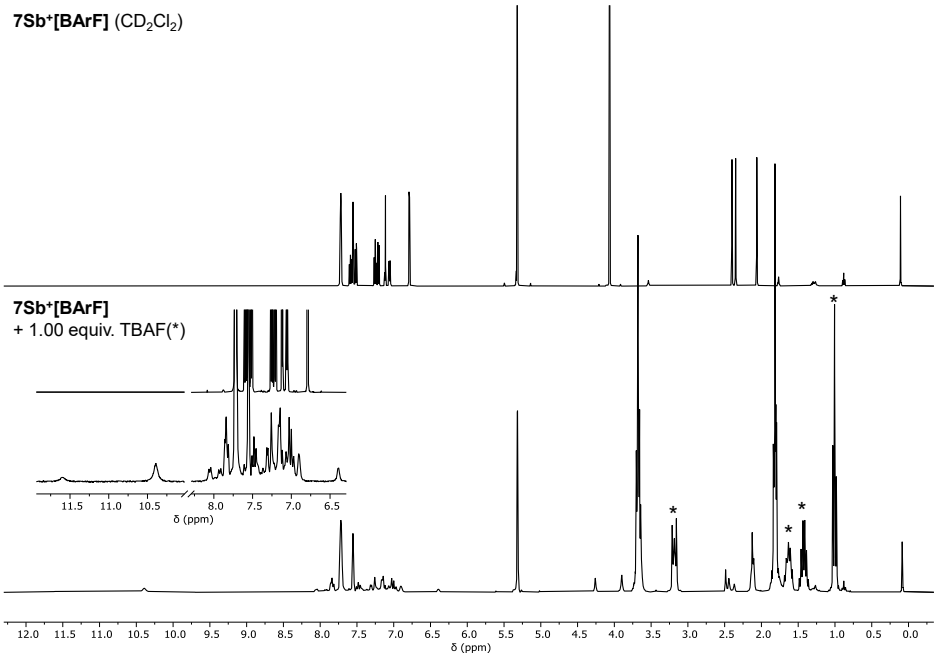


Figure 133: Stacked ^{1}H NMR spectra (500 MHz, CD_2Cl_2) of **7Sb^{+}[BArF]** (0.01 mmol, top) upon addition of TBAF (1.00 equiv., bottom). Signals related to TBAF are marked by (*).

The interaction of **7Sb^{+}[BArF]** with DMAP as a Lewis base was further examined using UV/Vis and PL spectroscopy (Figure 134). Interestingly, addition of 1.00 equiv. of DMAP resulted in a splitting of the original absorption band at λ_{abs} = 584 nm into two new maxima at 564 nm and 605 nm, which was concomitant with a significant decrease in fluorescence emission (Figure 134). Addition of excess DMAP resulted in the full conversion to a single band at λ_{abs} = 543 nm which may be associated with the proposed Lewis adduct of **7Sb^{+}[BArF]**. Moreover, it should be noted that the emission intensity in the presence of DMAP is drastically decreased compared to the original **7Sb^{+}[BArF]** sample, but reaches a level comparable to that of a circa 16 μM **7Sb^{Br}** sample, which is likely caused by coordination of DMAP.

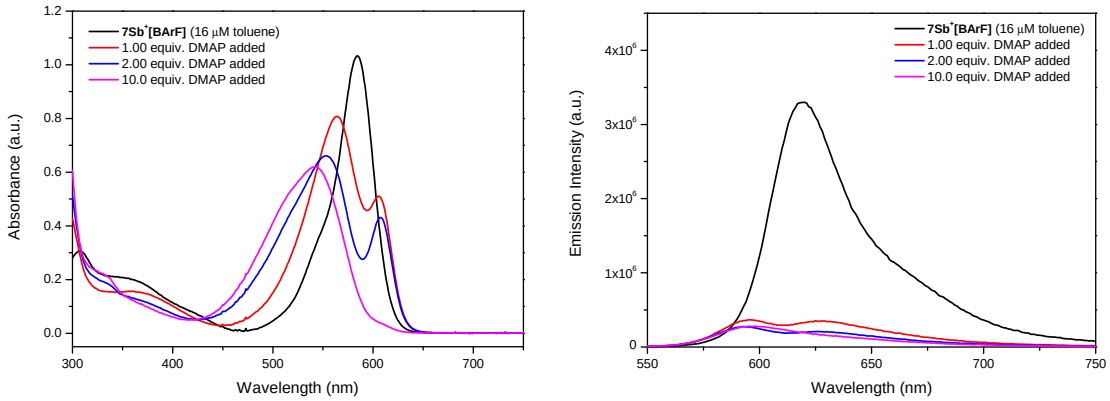
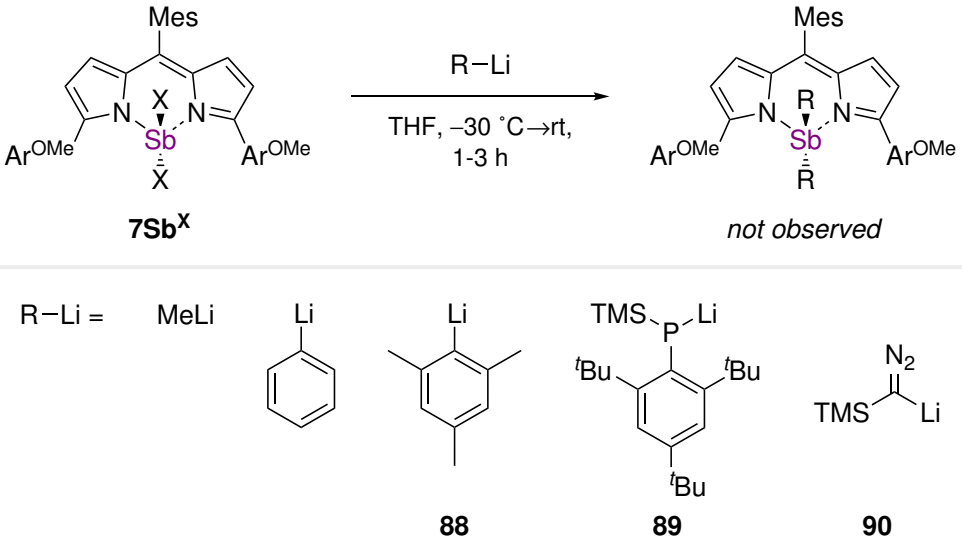


Figure 134: Spectroscopic changes upon addition of incremental amounts of 4-dimethylaminopyridine to a toluene solution of **7Sb$^+$[BArF]** (16 μM): UV/Vis spectra (left) and PL emission spectra (right).

5.3.3. Ligand exchange reactions of L7 SBDIPY complexes

Previous findings have demonstrated a considerable effect of the halido ligands on the stability and spectroscopic properties of SBDIPY chromophores. In order to obtain additional insight into the influence of the apical ligands, the exchange of halides to other viable ligands was explored as a potential method to further tune the properties of **L7** SBDIPY complexes. The substitution of halides in heavy trivalent pnictogen compounds is commonly achieved using organolithium reagents.[270,271] Accordingly, halide substitution in **7Sb^X** complexes was attempted *via* addition of various organolithium reagents at low temperature (Scheme 82).



Scheme 82: Scope of tested organolithium reagents for substitution at the antimony centre in **L7** dipyrrin complexes.

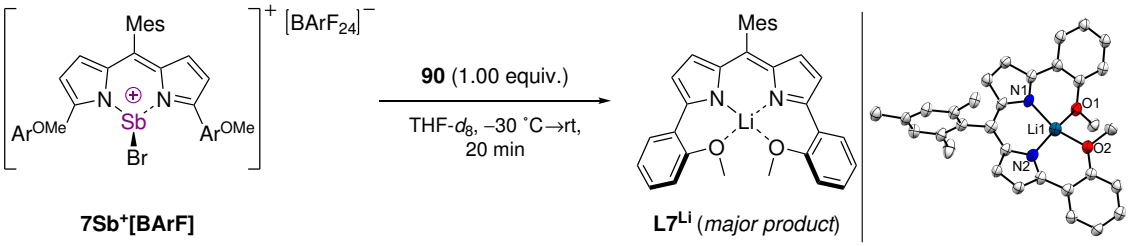
Unfortunately, for all tested organolithium reagents the formation of dipyrrinato salt **L7^{Li}** was observed as the main product by ^{1}H NMR spectroscopy (Table 17), alongside trace amounts of **L7**, possibly due to protonation of the lithium salt from solvent or neoprene NMR tube stopper. These findings strongly suggest that organolithium reagents are not suitable to achieve halide substitution on **7Sb^{X}** complexes as metallation of the dipyrrin scaffold appears to be the preferred reaction pathway, similar to the attempted reductions of **7Sb^{Br}**. However, the fate of antimony remained unclear for all tested organolithium reagents.

Table 17: Summarized reaction outcomes of **7Sb^{Br}** or **7Sb^{Cl}** (0.02 mmol) upon addition of organolithium reagents in THF.

Entry	SBDIPY complex	R−Li	Outcome[a]
e1	**7Sb^{Br}**	MeLi (2.00 equiv.)	formation of **L7^{Li}**[b]
e2	**7Sb^{Cl}**	MeLi (2.00 equiv.)	formation of **L7^{Li}**[b]
e3[c]	**7Sb^{Br}**	phenyllithium (2.00 equiv.)	formation of **L7^{Li}**[b]
e4	**7Sb^{Cl}**	**88** (2.00 equiv.)	formation of **L7^{Li}**[b]
e5	**7Sb^{Br}**	**89** (1.00 equiv.)	formation of **L7^{Li}**[b]
e6	**7Sb^{Br}**	**90** (2.00 equiv.)	formation of **L7^{Li}**[b]

[a]Major product based on ^{1}H NMR spectroscopy. [b]Verified by comparison with a 1:1 mixture of **L7** and LiHMDS in THF-d_8. [c]Conducted on 0.05 mmol scale.

Single crystals of **L7^{Li}** were obtained from reaction mixture *e1* and analyzed by X-ray crystallography, providing an additional structural proof of the reaction outcome (Scheme 83). Lastly, a more controlled approach was tested by allowing **7Sb^{+}[BArF]** to react with 1.00 equiv. **90** in THF-d_8 (Scheme 83). However, as for **7Sb^{Br}**, **L7^{Li}** was detected as the main product based on ^{1}H NMR spectroscopy.

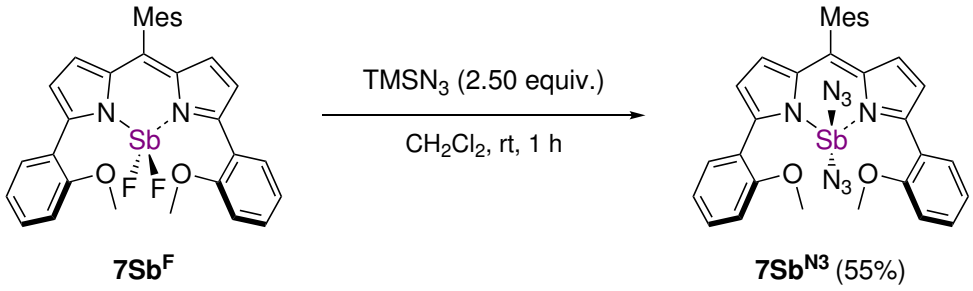


7Sb^{+}[BArF] **L7^{Li}** (*major product*)

Scheme 83: Reaction of **7Sb^{+}[BArF]** in the presence of organolithium reagent **90** (left). X-ray solid-state structure of **L7^{Li}** obtained from entry *e1* (right). Hydrogen atoms were omitted for clarity and thermal ellipsoids were set to a 30% probability level.

As organometallic reagents were found to be too reactive for halide substitution on SBDIPY chromophores due to metallation of the dipyrrin scaffold, other strategies for ligand exchange needed to be considered. Consequently, trimethylsilyl (TMS) halide

exchange of **7Sb^{F}** in the presence of a slight excess of trimethylsilyl azide ($TMSN_3$) was attempted. The addition of $TMSN_3$ (2.50 equiv.) to a CH_2Cl_2 solution of **7Sb^{F}** (1.00 equiv.) resulted in an immediate colour change change from dark magenta to dark purple, accompanied by a selective ^{1}H NMR shift, indicating a halide exchange (Scheme 84). The reaction mixture was concentrated under reduced pressure, giving a dark purple solid, which was further purified by washing with *n*-hexane to remove residual $TMSN_3$.



7Sb^{F} **7Sb^{N3}** (55%)

Scheme 84: Synthesis of **7Sb^{N3}** starting from **7Sb^{F}** .

The identity of the product was confirmed as the diazide complex **7Sb^{N3}** by IR spectroscopy, displaying a characteristic band at $\tilde{\nu}(N_3)$ = 2019 cm^{-1}, and by X-ray crystallography (Figure 135).[272]

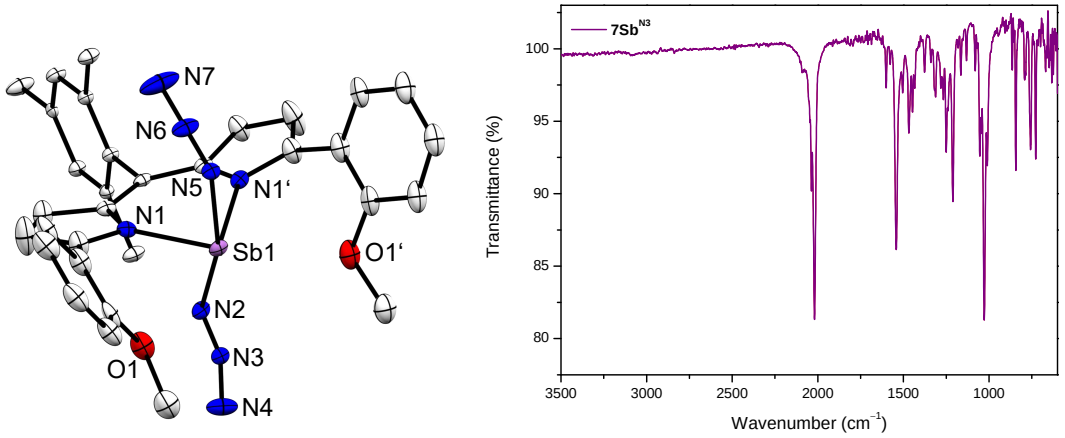
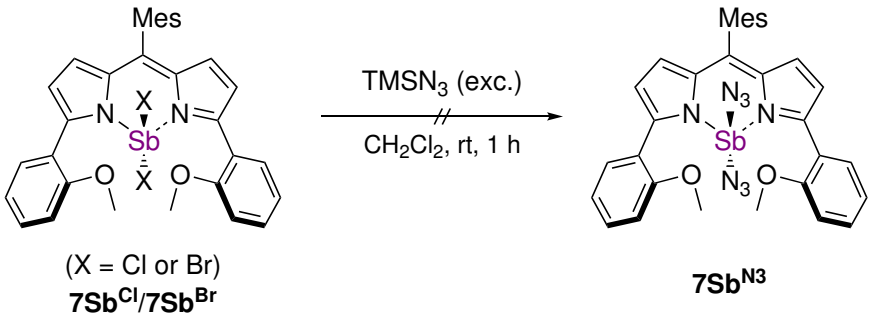


Figure 135: X-ray solid-state structures of **7Sb^{N3}** (left) and solid-state infrared spectrum of **7Sb^{N3}**. Hydrogen atoms were omitted for clarity and thermal ellipsoids were set to a 50% probability level.

Interestingly, the synthesis of **7Sb^{N3}** was not possible starting from **7Sb^{Br}** or **7Sb^{Cl}** under otherwise identical conditions (Scheme 85). Additional irradiation at 521 nm for 40 min and heating at 50 °C did not result in any changes based on ^{1}H NMR spectroscopy, suggesting an energetically disfavoured halide exchange. Moreover, no reaction of **7Sb^{Br}** towards **7Sb^{N3}** was observed in the presence of lithium azide, possibly owing to the low solubility of the lithium salt in CH_2Cl_2 .



(X = Cl or Br)
7Sb^{Cl}/7Sb^{Br}

7Sb^{N3}

Scheme 85: Unsuccessful attempts at synthesizing **7Sb^{N3}**.

Furthermore, a sample of **7Sb^{N3}** in CD_2Cl_2 appeared to be stable towards irradiation with light in the range of 270–521 nm, as well as heating at 50 °C under a slight vacuum, based on ^{1}H NMR spectroscopy. These findings underscore a considerably high stability of the azide moieties of **7Sb^{N3}** in solution. The diazide **7Sb^{N3}** displayed a considerable blue-shift versus other **7Sb^{X}** complexes, showcasing a main broad absorption band at λ_{abs} = 530 nm (Figure 136). In contrast, the emission was found to be energetically comparable to other **7Sb^{X}** complexes with a maximum at λ_{emi} = 597 nm.

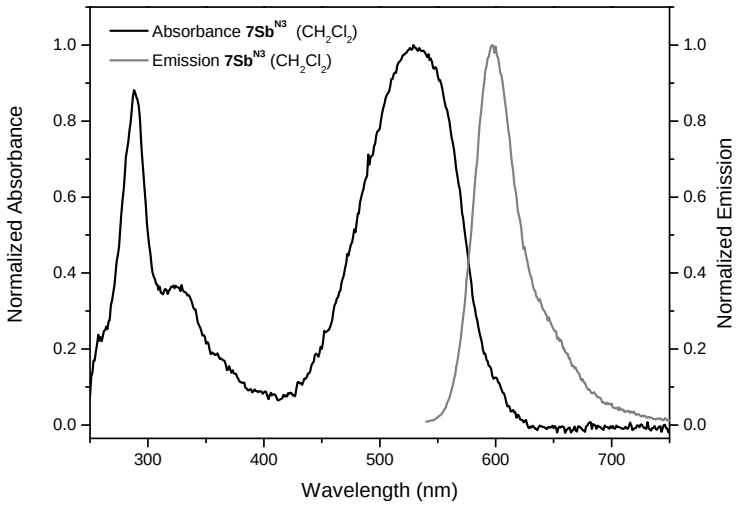
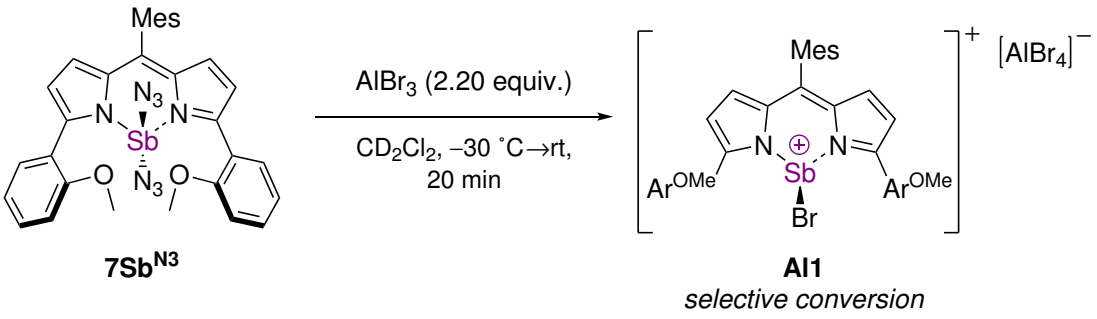


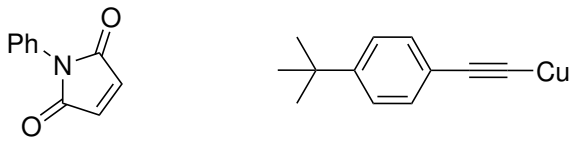
Figure 136: Normalized absorbance and PL emission spectra of **7Sb^{N3}** in CH_2Cl_2. The emission spectrum was recorded at an excitation wavelength of 520 nm.

Diazide **7Sb^{N3}** did not display 1,3-dipolar reactivity towards electron-poor phenylmaleimide (**74**), nor copper acetylide (**91**, Scheme 86). However, **7Sb^{N3}** was found to undergo ligand exchange in the presence of $AlBr_3$ to yield previously described Lewis adduct **Al1** (Scheme 86).



7Sb^{N3} **Al1**
selective conversion

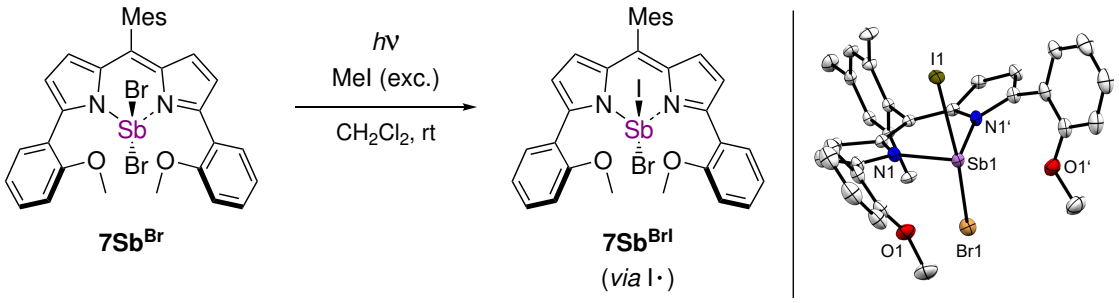
unreactive to:



74 **91**

Scheme 86: Reaction of **7Sb^{N3}** in the presence of $AlBr_3$ and unreactive substrates towards **7Sb^{N3}**.

Lastly, an unexpected possibility for halide exchange was observed for **7Sb^{Br}** in the presence of excess methyl iodide under light irradiation (Scheme 87). Upon prolonged irradiation of a **7Sb^{Br}** solution in CD_2Cl_2 with green light (521 nm, 20 h), a subtle shift of the original ^{1}H NMR spectrum was observed, alongside the appearance of a new peak at 2.65 ppm which matched the previous assignment to methyl bromide (Figure 137). Additional irradiation at higher energy light (390 nm, 4 h) caused a significant increase in the methyl bromide signal, indicating the occurrence of a halide exchange under light. X-ray solid-state structures of single crystals obtained from the reaction mixture further support this thesis, as a mixed complex **7Sb^{BrI}** was identified from the solved data (Scheme 87). As reaction kinetics appeared to be governed by irradiation wavelength, the observed reactivity may be ascribed to a radical process. Further investigation is needed to obtain a deeper understanding of the ability of SBDIPY complexes to engage in radical-based reactivity.



Scheme 87: Light-driven reaction of **7Sb^{Br}** in the presence of excess MeI (left). Slow conversion towards **7Sb^{BrI}** was observed under 521 nm green light irradiation, whereas a much faster conversion was noted using a 367 nm light source. X-ray solid-state structure of **7Sb^{BrI}** of a single crystal obtained from the reaction mixture (right). Hydrogen atoms were omitted for clarity and thermal ellipsoids were set to a 50% probability level.

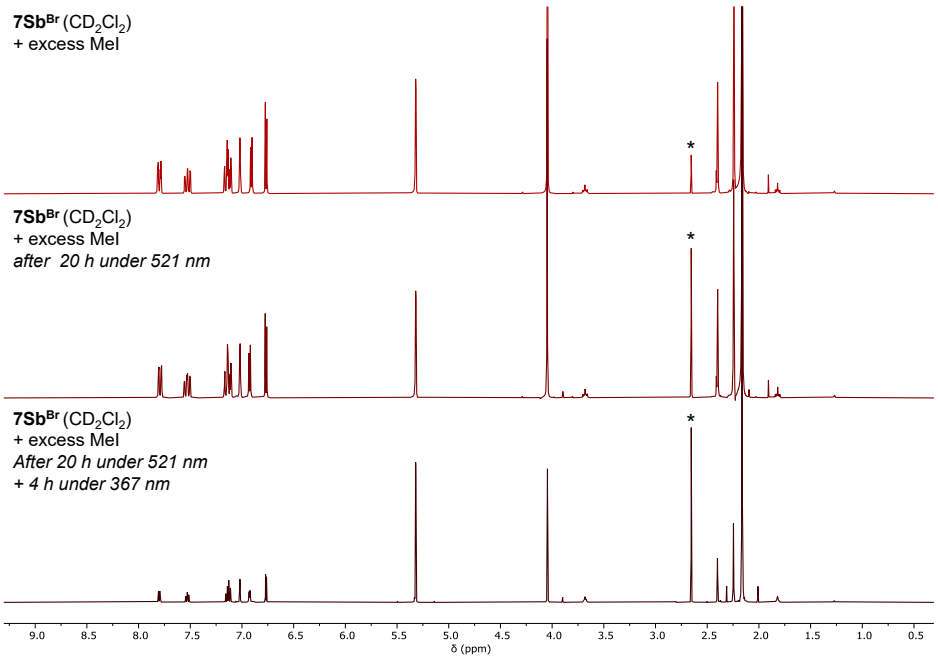


Figure 137: Stacked ^{1}H NMR spectra (CD_2Cl_2) of **7Sb^{Br}** (0.02 mmol) upon addition of an excess of MeI (0.05 mL, top, 300 MHz), upon irradiation under 521 nm light for 20 h (middle, 300 MHz) and after additional 4 h under 367 nm light (bottom, 500 MHz). Signals related to methyl bromide are marked by (*).

5.4. Conclusion and future work

The results presented in this chapter elucidated several reactivity patterns of SBDIPY chromophores. First, the reduction and oxidation of SBDIPY **7Sb^{Br}** was found to be unproductive under the tested conditions. While the compounds appeared to be unreactive towards several oxidants (**82**–**84**), treatment of **7Sb^{Br}** with reducing agents, such as sodium, resulted in sample degradation as evidenced by the formation of **L7^{Na}**. Ligand **L9** provided a more suitable platform to access low-valent antimony chemistry as treatment of **9Sb^{Cl}** yielded the corresponding Sb(I) complex **9Sb**, albeit containing 10% of an unidentified contamination which prompts further purification attempts. Nonetheless, this finding suggests that sterically shielded dipyrrins are required to access low-valent antimony chemistry, which could serve as a new platform to access photoredox catalysis akin to *N,C,N*-bismuthinidines facilitated by the pronounced chromophore properties of the dipyrrin ligand.[80]

Next, the halide lability observed for **7Sb^{Br}** enabled multiple redox-neutral reactivities that were further leveraged in the context of spectroscopic molecular sensing. The reactivity of **7Sb^{Br}** was evaluated towards a variety of Lewis acids resulting in distinct spectroscopic responses of **7Sb^{Br}** based on the properties of each additive. Systematic NMR, UV/Vis and PL spectroscopy investigations gave insight into two general sensing modes of **7Sb^{Br}**, which rely on halide abstraction and demethylation of the ligand scaffold. Moreover, the propensity of **7Sb^{Br}** to form Lewis adducts was further highlighted by a significantly higher sensitivity towards Lewis acid additives as compared to the respective BODIPY analogue **7B^{F}**. In comparison to **7Sb^{Br}**, the stibenium complex **7Sb^{+}[BArF]** displayed a considerably different reactivity pattern as it showed spectroscopic response in the presence of *N*-centred Lewis bases and halide ions, thereby providing a complementary function in the context of molecular sensing. While the decomposition of **7Sb^{Br}** in the presence of strong Lewis acids prevented the use of **7Sb^{Br}** to systematically assess effective Lewis acid strengths of additives, the high sensitivity and versatility with respect to suitable spectroscopic techniques provides a strong advantage that should be evaluated with other dipyrrin variants in order to avoid deleterious side-reactivity. Finally, the ligand exchange of halide substituents in **L7** dipyrrins was found to be challenging as substitution with organolithium reagents resulted in the formation of lithium dipyrrinato salt **L7^{Li}**. Instead, a milder approach utilizing the TMS halide exchange led to the isolation of a new diazide SBDIPY complex **7Sb^{N3}**. Treatment of **7Sb^{Br}** with MeI under irradiation with UV-LEDs led to the formation of a mixed halide SBDIPY **7Sb^{BrI}** presumably following a radical-based process.

Overall, the sensitive nature of PnDIPY chromophores can be viewed as a double-edged sword, as it restricts post-synthetic tunability but enables efficient response to chemical stimuli, making this class of chromophores viable candidates in the field of molecular sensing (Figure 138).

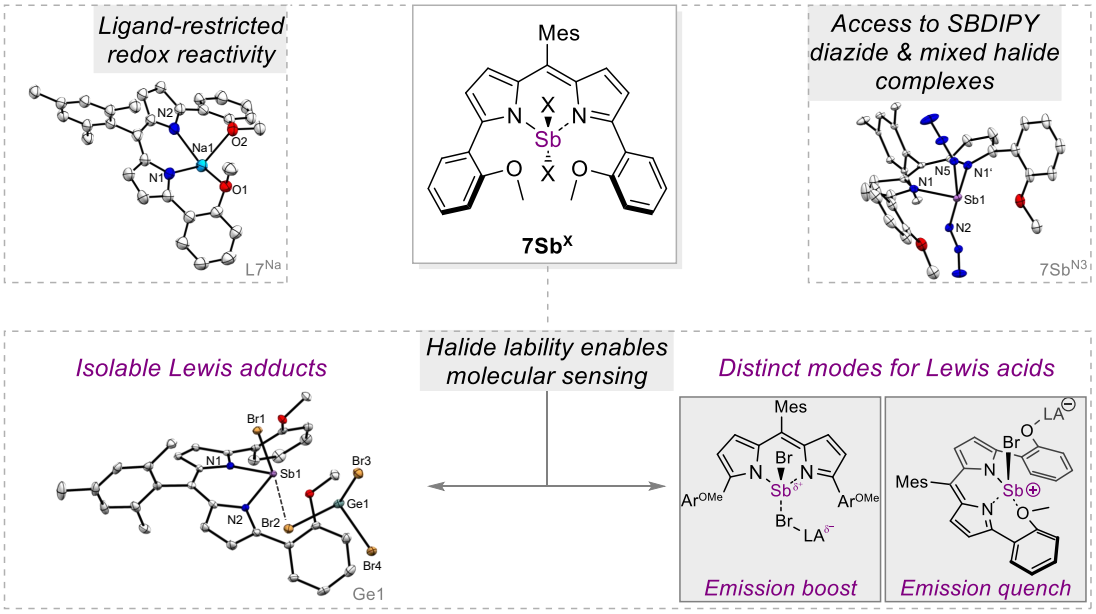


Figure 138: Overview of reactivity modes of **7Sb^{X}** complexes covered in this chapter.

6. Experimental details

Unless otherwise stated, all experiments were carried out in a glovebox (LABmaster sp, MBraun or GS MEGA 3) under an argon atmosphere or using standard Schlenk techniques.

6.1. General information

Solvents: Tetrahydrofuran, dichloromethane, *n*-pentane and acetonitrile were collected from a solvent purification system (MBraun MB-SPS7), degassed by freeze-pump-thaw cycles and stored over molecular sieves (3 Å) before use (this method was used for work within chapter 2). Otherwise, the solvents toluene, tetrahydrofuran (THF), *n*-hexane, and *n*-pentane were dried over sodium, distilled and stored over molecular sieves (3 Å) prior to use. Dichloromethane (CH_2Cl_2), acetonitrile (MeCN) and *o*-dichlorobenzene were dried over CaH_2, distilled and stored over molecular sieves (3 Å) prior to use. Hexafluoro*iso*propanol (HFIP), methanol and acetone were degassed through three freeze-pump-thaw cycles and stored over molecular sieves (3 Å) prior to use. Deuterated solvents CD_2Cl_2 and MeCN-d_3 (dried over CaH_2), THF-d_8 and C_6D_6 (dried over sodium) were distilled and stored over molecular sieves (3 Å) prior to use.
Reagents: Unless otherwise specified, all reagents were used as received from commercial suppliers (ABCR, Alfa Aesar, BLDPharm, Sigma Aldrich, Thermo Fisher Scientific, Tokyo Chemical Industry). All pnictogen halides PnX_3 were purified by sublimation under reduced pressure and stored under Ar atmosphere prior to use. Sodium tetrakis[3,5-bis(trifluoromethyl)phenyl]borate ($NaBArF_{24}$) was synthesized by S. Karnbrock (Alcarazo group Göttingen),[273] $Bi(NMe_2)_3$ was prepared by D. Meleschko.[274] Dipyrrin **L4** was independently prepared by A. Bismuto. MindBr, mesityllithium (**88**) and lithium phosphanide **89**, trispentafluorophenylborane (BCF), trispentafluorophenylalane (AlCF), $GeBr_2$·(1,4-dioxane), $GeCl_2$·(1,4-dioxane) were kindly provided by the Filippou group (Bonn) and 2-(*tert*-butylsulfonyl)iodobenzene was kindly provided by Dr. P. Brehm (Streubel group, Bonn).[275] Rhodium carbonyl chloride, Colvin's reagent **90** and KC_8 were prepared by Dr. P. Palui,[276–279] and iodobenzene dichloride was prepared by G. Pugliese.[280]

Spectroscopy: ^{1}H, ^{19}F, ^{11}B{^{1}H}and ^{13}C{^{1}H} NMR spectra were recorded in deuterated solvents at 298 K using Bruker Avance III HD 300, Bruker Avance III 400, Bruker Avance III HD 400, AV-500, Bruker Avance I 300 MHz, Bruker Avance I 400 MHz or Bruker Avance III HD Ascend 500 MHz spectrometer. ^{1}H NMR data were reported as follows: chemical shift, multiplicity (s = singlet, d = doublet, t = triplet, q = quadruplet, sept = septet, dd = doublet of doublets, dt = doublet of triplets, ddd =doublet of doublet of doublets, td = triplet of doublets and m = multiplet), coupling constant (*J*) in Hz and integration. Chemical shifts (δ) were reported with respect to the corresponding solvent residual (central) peak at 7.26 ppm for $CDCl_3$, 7.16 ppm for C_6D_6, 5.32 ppm for CD_2Cl_2, 2.50 ppm for DMSO-d_6 and 1.73 ppm for THF-d_8 for ^{1}H NMR spectroscopy. ^{13}C NMR spectra (^{1}H-broadband decoupled) were reported in ppm using the central peak of C_6D_6 (128.06 ppm), $CDCl_3$ (77.16 ppm), CD_2Cl_2 (53.84 ppm) and of THF-d_8 (25.37 ppm).

UV/Vis spectra were recorded with a JASCO V-650 or an Edinburgh Instrument FS5 spectrophotometer, and fluorescence spectra were recorded on a JASCO FP-8500 spectrofluorometer or an Edinburgh Instrument FS5 spectrophotometer using a 10×10 mm quartz sample cell sealed with a J. Young valve. For all machines the temperature of the sample holder was controlled through an external cryostat. Spectra were recorded with a dwell time of 0.150 s (UV/Vis) or 0.200 s (emission) in data intervals of 1 nm with the bandwidths set to 1.0 nm (excitation) and 2.0 nm (emission). Photoluminescence lifetime spectra were obtained using an EPL-510 picosecond pulsed laser diode. Molar absorption coefficients ϵ were determined as the slope k of linear regression analysis of the plotted absorbance maximum A against respective sample concentrations c using the following equation:

$$A = k \cdot c + b \tag{8}$$

where b denotes the y-axis intercept. The dilution series were conducted at 5 °C (chapter 2) or 15 °C (chapter 3) to avoid sample degradation throughout the measurements.

Measurements for evaluation of relative quantum yields Φ_{rel} of SBDIPY probes were conducted at 5 °C using BODIPY **1B^{F}** (Φ = 0.95) as a reference (complexes in chapter 2).[281] In these cases the quantum yields were determined by plotting the integrated emission intensities between 490 nm and 585 nm against the absorbance of differently-concentrated solutions of SBDIPY compounds in CH_2Cl_2 (maximum absorbance λ_{abs} used as an approximation due to sample instability). For all other complexes (chapter 3) relative quantum yields Φ_{rel} were determined at 25 °C using

rhodamine 101 (Φ = 0.96) as a reference.[282] The quantum yields were determined by plotting the integrated emission intensities between 550 nm and 690 nm against the absorbance at the excitation wavelength λ_{exc} = 520 nm of differently-concentrated solutions of PnDIPY compounds in CH_2Cl_2. Corresponding quantum yields Φ_{rel} were calculated using the following equation:

$$\Phi_{rel} = \frac{m}{m_{ref}} \cdot \left(\frac{n}{n_{ref}}\right)^2 \tag{9}$$

where m is the slope of the respective Pn complex, m_{ref} the slope of the reference analyte (both from linear regression analysis) and n the refractive index of the solvent (CH_2Cl_2),[283] and n_{ref} is the refractive index of the reference solvent (CH_2Cl_2 or ethanol).[283,284]

ATR-FTIR spectra were recorded in a range between 600–4000 cm^{-1} on a Shimadzu IRSpirit FTIR spectrometer with a single reflection ATR accessory (QATR-S), which was used for solid-state samples inside an Ar-filled glovebox at ambient temperatures.

Electrochemistry: Cyclic voltammetry (CV) was performed using a Palmsens4 potentiostat with all CVs conducted in a glovebox to insure a moisture and oxygen-free environment. A homogeneous system consisting of a glassy carbon working electrode, Pt wire as counter electrode and an $Ag/AgNO_3$ organic reference electrode in a one-compartment cell was employed in all measurements. Experiments were carried out in dry CH_2Cl_2 with 0.1 M tetrabutylammonium hexafluorophosphate ($TBAPF_6$) which was oven-dried beforehand. Measurements were conducted using 1 mM of analyte with a scanning range of 1.0 to -2.0 V (vs $Ag/AgNO_3$) at a sweep rate of 100 mV/s. A non-aqueous silver/silver nitrate ($Ag/AgNO_3$) reference electrode (0.01 M $AgNO_3$ in acetonitrile with 0.1 M $TBAPF_6$) was used throughout all measurements. To ensure the stability and accuracy of the reference potential, ferrocene (FcH) was used as an internal standard in separate measurements before and after each experimental series to ensure no potential drift.[ix]

LED reaction setups: LEDs used for photochemistry were manufactured by Osram Opto Semiconductors: GT CS8PM1.13, 521 nm, 148 lm, 80°or seoulviosys: Z5-CUN66A1B, 367 nm, 1.0 W, 120°. Six LEDs were mounted on a circuit board powered by a 350 mA power supply. Reactions were irradiated from a 2 cm distance while stirring and optional cooling through metal blocks mounted on top of the circuit board. For cyclic voltammetry experiments, a metal ring of 14.9 cm diameter equipped with 28 individual LEDs (Osram GT CS8PM1) was used. LEDs were mounted in the inner

[ix] CV measurements were referenced and analyzed with main contribution from M. J. McKee.

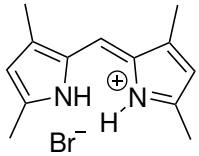
part of the ring, each separated by 16.3 mm distance.

Chemiluminescence: chemiluminescence emission was detected using a Vitl Lumini single tube luminometer.

Single crystals X-ray diffraction analysis: Depending on location of measurement (Bonn or Göttingen) two different setups were used. Data collection and refinement was performed either by Dr. C. Golz (CG) or the analytical department staff around Dr. G. Schnakenburg (GS) and indexed in the appendix. *Setup CG:* Data collection was performed on two dual source equipped Bruker D8 Venture four-circle-diffractometers from Bruker AXS GmbH. As X-ray sources microfocus IμS 2.0 Cu/Mo and microfocus IμS 3.0 Ag/Mo from Incoatec GmbH with mirror optics HELIOS and single-hole collimator from Bruker AXS GmbH were used. Photon III CE14 (Cu/Mo) and Photon III HE (Ag/Mo) from Bruker AXS GmbH were employed as detectors. For data collection the APEX4 Suite (v2022.1-1) and therein integrated programs SAINT V8.40A (Integration) und SADABS 2016/2 (Absorption correction) from Bruker AXS GmbH were used, whereas structure solution was performed with SHELXT,[285] and refinement with SHELXL-2018/3.[285] OLEX^2, Mercury and FinalCif were used for data finalization.[286–288] Sample preparation was performed with a SMZ1270 stereomicroscope from Nikon Metrology GmbH and crystals were mounted on MicroMounts or MicroLoops from MiTeGen in NVH oil. Sensitive samples were handled using the X-TEMP 2 System for picking of crystals.[289] During measurements single crystals were cooled to given temperature with a Cryostream 800 from Oxford Cryosystems.
Setup GS: The crystals were protected with Fomblin® Y under inert atmosphere before mounting on the goniometer. Data collection of was performed on a STOE IPDS-2T diffractometer using Mo-Kα (λ = 0.71073 Å, multilayer X-ray mirror optics optics ASTIX++) radiation with an image plate detector or on a BRUKER D8-VENTURE diffractometer using MoKα (λ = 0.71073 Å, HELIOS mirror optics) or CuKα (λ = 1.54178 Å) equipped with a Photon III CE14 detector. Both diffractometers were connected with low–temperature devices Cryostream 700er & 800er series (Oxford Cryosystems), for cooling at given temperatures. Intensities were measured by fine-slicing ϕ- and ω-scans, followed by correction of background, polarization and Lorentz effects. X-ray solid-state structures were solved by intrinsic phasing methods and refined using the least-squares procedure imbedded in the SHELX program suite.[285] Hydrogen atoms were placed in geometrically calculated positions and incorporated in the refinement process by using a riding model on the bound carbon atoms. Absorption corrections were carried out by the empirical method included in SADABS 2016/2 or XArea 2.4/STOE LANA 2.8.4.
Mercury and OLEX^2 were used for data finalization and visualization.[286,287]

6.2. Ligand synthesis (chapter 2)

Synthesis of L1-HBr



L1-HBr

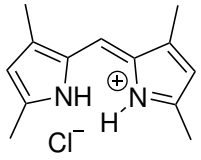
L1-HBr was prepared according to a modified literature procedure.[144] The synthesis was performed under ambient atmosphere. At room temperature, an aqueous HBr solution (48%, 4 mL) was added to a solution of 2-formyl-3,5-dimethylpyrrole (500 mg, 4.06 mmol, 1.00 equiv.) in methanol (10 mL). The reaction mixture was heated under reflux for 1 h, yielding a fine red precipitate. The precipitate was filtered off and washed with diethyl ether (3×20 mL), resulting in an amorphous red powder as the product (430 mg, 75% yield).

UV/Vis: λ_{abs} = 469 nm (CH_2Cl_2).

^{1}H NMR (300 MHz, 298 K, $CDCl_3$): δ 13.12 (br. s, 2H), 7.07 (s, 1H), 6.16 (s, 2H), 2.69 (s, 6H), 2.35 (s 6H).

NMR data were in accordance with those previously reported.[144]

Synthesis of L1-HCl



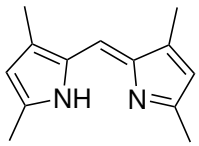
L1-HCl

L1-HCl was prepared according to a modified literature procedure.[145] The synthesis was performed under ambient atmosphere. At room temperature, 2-formyl-3,5-dimethylpyrrole (312 mg, 2.53 mmol, 1.00 equiv.) and 2,4-dimethylpyrrole (289 mg, 3.04 mmol, 1.20 equiv.) were dissolved in ethanol (6 mL). Then, an aqueous HCl solution (37%, 4 mL) was added and the reaction mixture heated to 40 °C for 1 h, resulting in the formation of a light-red precipitate. The reaction mixture was allowed to warm to room temperature and the precipitate was filtered off and washed with cold ethanol (2×5 mL) and diethyl ether (2×10 mL), giving the final product as a light-red, amorphous powder (327 mg, 99% yield).

UV/Vis: λ_{abs} = 468 nm (THF).

^{1}H NMR (400 MHz, 298 K, $CDCl_3$): δ 13.76 (br s, 2H), 7.06 (s, 1H), 6.15 (s, 2H), 2.64 (s, 6H), 2.34 (s, 6H). NMR data were in accordance with those previously reported.[145]

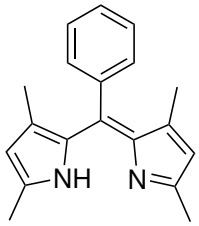
Synthesis of L1



L1

Method 1: **L1** was prepared according to a modified literature procedure.[143] A Schlenk flask was charged with **L1-HBr** (260 mg, 0.92 mmol, 1.00 equiv.) and LiH (29.3 mg, 3.69 mmol, 4.00 equiv.). The reaction was cooled to 0 °C and THF (30 mL) was slowly added, resulting in a deep red suspension. After 30 min at 0 °C, the reaction mixture was allowed to warm to room temperature and stirred for 3 h after which a yellow-orange solution was obtained. The reaction mixture was then filtered through a plug of celite® under air, using *n*-hexane to elute the product (circa 200 mL). After removal of solvents under reduced pressure, the final product was obtained as an amorphous yellow-orange solid (162 mg, 88%).
Note: This method was found to be poorly scalable for reactions above 250 mg scale.
Method 2: Under ambient conditions, **L1-HCl** (10.2 g, 43.0 mmol, 1.00 equiv.) was dissolved in THF (80 mL) and an aqueous NaOH solution (3M, 100 mL) was added. After vigorous stirring for 2 h, the solvent was removed under reduced pressure and the crude product was extracted with CH_2Cl_2 (3×40 mL). Combined organic layers were washed with water and saturated Na_2CO_3 solution and dried under reduced pressure, giving the final product as an amorphous yellow-orange solid (8.52 g, 99% yield).
UV/Vis: λ_{abs} = 432 nm (THF).
^{1}H NMR (400 MHz, 298 K, $CDCl_3$): δ 10.88 (br s, 1H), 6.70 (s, 1H), 5.96 (s, 2H), 2.34 (s, 6H), 2.23 (s, 6H).
^{1}H NMR (400 MHz, 298 K, CD_2Cl_2): δ 9.18 (br s, 1H), 6.70 (s, 1H), 5.96 (s, 2H), 2.31 (s, 6H), 2.21 (s, 6H);
^{13}C{^{1}H} NMR (101 MHz, 298 K, CD_2Cl_2): δ 153.2, 138.8, 138.0, 117.5, 116.8, 16.3, 11.5. NMR data were in accordance with those previously reported.[290]

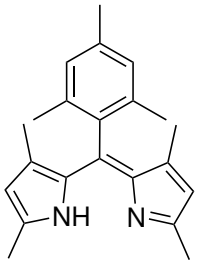
Synthesis of L2



L2

L2 was prepared according to a modified literature procedure.[291] A Schlenk flask was charged with CH_2Cl_2 (100 mL), 2,4-dimethylpyrrole (714 mg, 7.50 mmol, 2.50 equiv.) and benzaldehyde (318 mg, 3.00 mmol, 1.00 equiv.). Trifluoroacetic acid (100 µL) was added and the reaction mixture was stirred at room temperature for 4 h. Then, the reaction mixture was cooled to 0 °C and chloranil (738 mg, 3.00 mmol, 1.00 equiv.) was added in portions over the course of 5 minutes, resulting in a drastic colour change to dark red. The mixture was stirred at room temperature for 2.5 h and then filtered through a small celite® plug under air, using CH_2Cl_2 and ethyl acetate to elute the intensely coloured product. The solvents were removed under reduced pressure and the crude product was purified by column chromatography on basic aluminum oxide, using *n*-hexane with 1% NEt_3. The combined product fractions were dried under reduced pressure and washed with minimum amount of cold diethyl ether (circa 5 mL) to give the final product as an amorphous orange solid (250 mg, 30%).
UV/Vis: λ_{abs} = 443 nm (THF).
^{1}H NMR (500 MHz, 298 K, $CDCl_3$): δ 13.24 (br s, 1H), 7.47–7.38 (m, 3H), 7.34–7.28 (m, 2H), 5.90 (s, 2H), 2.35 (s, 6H), 1.31 (s, 6H).
^{13}C{^{1}H} NMR (126 MHz, 298 K, $CDCl_3$): δ 151.6, 140.5, 138.9, 138.2, 136.6, 129.4, 128.7, 128.3, 119.7, 16.1, 14.6.
NMR data were in accordance with those previously reported.[290]

Synthesis of L3



L3

L3 was prepared with help from G. Saggiotti. A Schlenk flask was charged with CH_2Cl_2 (40 mL), 2,4-dimethylpyrrole (476 mg, 5.00 mmol, 2.00 equiv.) and 2,4,6-timethylbenzaldehyde (371 mg, 2.50 mmol, 1.00 equiv.). Trifluoroacetic acid (70 μL) was added and the reaction mixture was stirred at room temperature overnight (12 h). Then, the reaction mixture was cooled to 0 °C and DDQ (568 mg, 2.50 mmol, 1.00 equiv.) was added as a solid, resulting in a drastic colour change to dark red. The mixture was stirred at room temperature for 12 h. The following work-up was performed under air. The reaction mixture was washed with saturated aqueous $NaHCO_3$ solution (3×40 mL) and the organic phase was extracted with CH_2Cl_2 (4×30 mL). The combined organic layers were dried over Na_2SO_4 and the solvent was removed under reduced pressure. The crude product was then purified by column chromatography on basic aluminum oxide, using a gradient of *n*-hexane → *n*-hexane/CH_2Cl_2(1/1) → *n*-hexane:CH_2Cl_2:EtOAc (1:1:0.1). The combined product fractions were dried under reduced pressure and washed with minimum amount of cold diethyl ether (circa 3 mL) to give the final product as an amorphous orange solid (213 mg, 27%).

UV/Vis: λ_{abs}= 443 nm (THF).

^{1}H NMR (300 MHz, 298 K, $CDCl_3$): δ 13.34 (s, 1H), 6.90 (s, 2H), 5.85 (s, 2H), 2.34 (s, 6H), 2.32 (s, 3H), 2.10 (s, 6H), 1.29 (s, 6H).

^{1}H NMR (500 MHz, 298 K, C_6D_6): δ 14.04 (s, 1H), 6.77 (s, 2H), 5.85 (s, 2H), 2.19 (s, 6H), 2.13 (s, 3H), 2.12 (s, 6H), 1.51 (s, 6H).

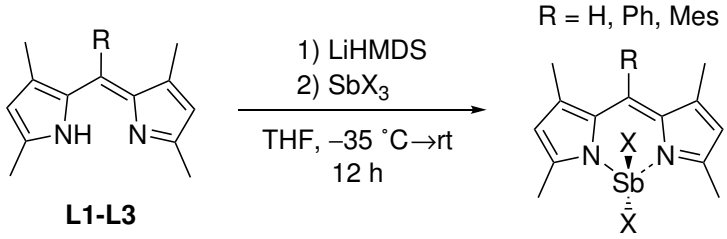
^{13}C{^{1}H} NMR (126 MHz, 298 K, C_6D_6): δ 151.0, 139.5, 137.9, 137.8, 136.4, 136.2, 135.0, 129.0, 119.7, 21.2, 19.7, 16.0, 14.0.

NMR data were in accordance with those previously reported.[292]

6.3. Synthesis of SBDIPY complexes (chapter 2)

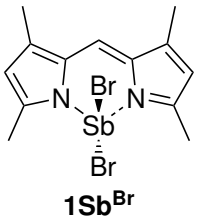
General procedure A

Complex synthesis was performed starting from a halide salt SbX_3 (see Scheme 88, where X= Br, Cl or F). A THF (0.1 M) solution of dipyrrin ligand **L1**-**L3** (1.00 equiv.) and LiHMDS (1.10 equiv.) was prepared and cooled to −35 °C. This solution was added dropwise to a precooled THF solution (0.1 M) of SbX_3 (1.15 equiv.), resulting in an immediate change in colour from orange to red. The reaction mixture was then allowed to warm to room temperature without any stirring for circa 12 h, resulting in the formation of a crystalline precipitate. The solvent was filtered off and the crude product was washed with *n*-hexane, followed by *n*-pentane until the filtrate was barely coloured. The crude product was then redissolved in CH_2Cl_2, filtered over a glass fibre filter and dried under reduced pressure, giving the SBDIPY complex as a solid.



Scheme 88: General reaction scheme for SBDIPY synthesis (X = Br, Cl and F).

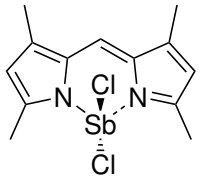
Synthesis of $1Sb^{Br}$



$1Sb^{Br}$

SBDIPY complex **$1Sb^{Br}$** was prepared following the general procedure **A** starting from **L1** (15 mg, 0.075 mmol). The product was obtained as a crystalline red solid (32 mg, 91% yield). Suitable single crystals for X-ray diffraction analysis were grown from a saturated solution of THF/*n*-hexane at room temperature. The compound is stable for months at −35 °C under an inert gas atmosphere both in solution and in solid-state.
UV/Vis: λ_{abs} = 504 nm (CH_2Cl_2). **PL**: λ_{emi} = 518 nm (CH_2Cl_2).
^{1}H NMR (500 MHz, 298 K, CD_2Cl_2): δ 7.39 (s, 1H), 6.39 (s, 2H), 2.63 (s, 6H), 2.43 (s, 6H);
^{13}C{^{1}H} NMR (126 MHz, 298 K, CD_2Cl_2): δ 157.3, 149.1, 130.2, 123.0, 120.4, 16.0, 12.4.

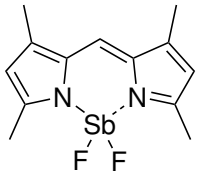
Synthesis of 1Sb^{Cl}



1Sb^{Cl}

SBDIPY complex **1Sb^{Cl}** was prepared following the general procedure **A** starting from **L1** (70 mg, 0.35 mmol). The product was obtained as a crystalline red solid (134 mg, 98% yield). Suitable single crystals for X-ray diffraction analysis were grown from a saturated solution of THF/*n*-hexane at room temperature. The compound is stable for months at −35 °C under an inert gas atmosphere both in solution and in solid-state.
UV/Vis: λ_{abs} = 501 nm (CH_2Cl_2). **PL**: λ_{emi} = 516 nm (CH_2Cl_2).
^{1}H NMR (400 MHz, 298 K, CD_2Cl_2): δ 7.38 (s, 1H), 6.37 (s, 2H), 2.67 (s, 6H), 2.42 (s, 6H);
^{13}C{^{1}H} NMR (101 MHz, 298 K, CD_2Cl_2): δ 157.1, 148.5, 130.2, 122.9, 120.0, 16.2, 12.3.

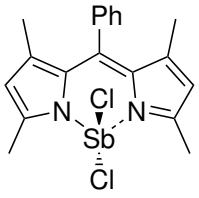
Synthesis of 1Sb^{F}



1Sb^{F}

SBDIPY complex **1Sb^{F}** was prepared following a slightly modified general procedure **A** using **L1** (16 mg, 0.080 mmol, 1.00 equiv.) and SbF_3 (14 mg, 0.080 mmol, 1.00 equiv.). The product was obtained as a crystalline red solid (27 mg, 94% yield). Best results were achieved when leaving the reaction mixture at −35 °C for several hours before warming the solution to room temperature. Suitable single crystals for X-ray diffraction analysis were grown from a saturated solution of THF/*n*-hexane at room temperature. The compound decomposed readily upon exposure to air and therefore needs to be stored at low temperatures (−35 °C) under inert conditions.
UV/Vis: λ_{abs}= 467, 496 nm (CH_2Cl_2). **PL**: λ_{emi}= 601 nm (CH_2Cl_2).
^{1}H NMR (400 MHz, 298 K, CD_2Cl_2): δ 7.19 (s, 1H), 6.21 (s, 2H), 2.60 (s, 6H), 2.33 (s, 6H);
^{19}F NMR (377 MHz, 298 K, CD_2Cl_2): δ −77.1 (s);
^{13}C{^{1}H} NMR (126 MHz, 298 K, CD_2Cl_2): δ 158.4, 145.6, 132.6, 122.4, 119.4, 16.4, 11.9.

Synthesis of 2Sb^{Cl}



2Sb^{Cl}

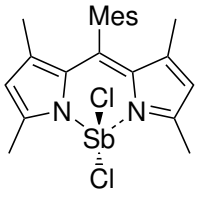
SBDIPY complex **2Sb^{Cl}** was prepared following the general procedure **A** starting from **L2** (55 mg, 0.20 mmol). The product was obtained as a crystalline orange solid (75 mg, 80% yield). Suitable single crystals for X-ray diffraction analysis were grown from a saturated solution of THF/*n*-hexane at room temperature.

UV/Vis: λ_{abs}= 501 nm (CH_2Cl_2). **PL**: λ_{emi}= 520 nm (weak, CH_2Cl_2).

^{1}H NMR (400 MHz, 298 K, CD_2Cl_2): δ 7.60–7.50 (m, 3H), 7.40–7.31 (m, 2H), 6.28 (s, 2H), 2.71 (s, 6H), 1.42 (s, 6H);

^{13}C{^{1}H} NMR (126 MHz, 298 K, CD_2Cl_2): δ 156.3, 151.1, 145.8, 136.2, 130.0, 129.9, 129.7, 128.8, 123.0, 16.4, 16.2.[x]

Synthesis of 3Sb^{Cl}



3Sb^{Cl}

SBDIPY complex **3Sb^{Cl}** was prepared following the general procedure **A** starting from **L3** (51 mg, 0.16 mmol). The product was obtained as a crystalline orange solid (55 mg, 67% yield). Suitable single crystals for X-ray diffraction analysis were grown from a saturated solution of THF/*n*-hexane at room temperature.

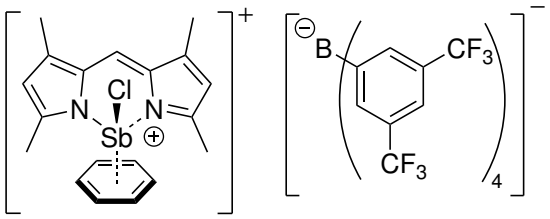
UV/Vis: λ_{abs}= 501 nm (CH_2Cl_2). **PL**: λ_{emi}= 523 nm (CH_2Cl_2).

^{1}H NMR (500 MHz, 298 K, CD_2Cl_2): δ 7.00 (s, 2H), 6.26 (s, 2H), 2.69 (s, 6H), 2.34 (s, 3H), 2.10 (s, 6H), 1.42 (s, 6H);

^{13}C{^{1}H} NMR (126 MHz, 298 K, CD_2Cl_2): δ 155.5, 149.7, 145.9, 139.8, 135.4, 132.4, 129.8, 128.8, 122.5, 21.3, 19.4, 16.0, 15.5.

[x]Data obtained by A. Bismuto

Synthesis of 1Sb$^+$[BArF]



1Sb$^+$[BArF]

A suspension of sodium tetrakis[3,5-bis(trifluoromethyl)phenyl]borate (50 mg, 0.056 mmol, 1.10 equiv.) in CH_2Cl_2 (2.0 mL) was added to a solution of **1Sb^{Cl}** (20 mg, 0.051 mmol, 1.00 equiv.) in CH_2Cl_2 (1.0 mL) at −35 °C, resulting in an instant colour change from light red to dark red. The reaction mixture was allowed to warm to room temperature and after 1 h passed through a glass fibre filter. The product was obtained as an amorphous red solid (54 mg, 87% yield) after trituration with benzene and *n*-pentane, followed by removal of solvent under reduced pressure. Suitable single crystals for X-ray diffraction analysis were grown from a saturated solution of CH_2Cl_2 and benzene at room temperature.

UV/Vis: λ_{abs}= 513 nm (CH_2Cl_2). **PL**: λ_{emi}= 518 nm (CH_2Cl_2).

^{1}H NMR (500 MHz, 298 K, CD_2Cl_2): δ 7.72 (s, 8H), 7.56 (s, 4H), 7.48 (s, 1H), 7.35 (s, 6H, C_6H_6), 6.55 (s, 2H), 2.69 (s, 6H), 2.45 (s, 6H);

^{11}B{^{1}H} NMR (161 MHz, 298 K, CD_2Cl_2): δ −6.7 (s);

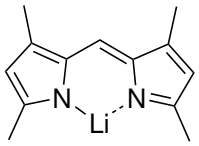
^{19}F NMR (471 MHz, 298 K, DCM): δ −62.9 (s);

^{13}C{^{1}H} NMR (126 MHz, 298 K, CD_2Cl_2): δ 162.2 (q, J_{C-B}= 50 Hz), 159.9, 153.3, 135.2, 131.2, 129.2 (q, J_{C-F}= 31 Hz), 128.7, 124.5 (q, J_{C-F}= 272 Hz), 123.8, 122.8, 117.9 (m), 16.6, 12.6.

6.4. Synthesis of alkali dipyrrinato salts (chapter 2)

alkali dipyrrinato salts were synthesized based on a literature-reported procedure and used immediately for further complex synthesis.[293]

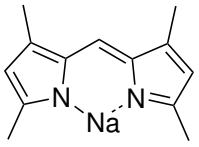
Synthesis of L1^{Li}



L1^{Li}

L1 (80 mg, 0.40 mmol, 1.00 equiv.) and LiHMDS (67 mg, 0.40 mmol, 1.00 equiv.) were separately dissolved in benzene (3.0 mL each). The LiHMDS solution was slowly added to **L1** at room temperature resulting in immediate precipitation of a dark red solid. The reaction mixture was then stirred for 2 h at room temperature and the solvent was evaporated under reduced pressure. The resulting red solid was washed with *n*-pentane (3×15 mL) and dried under reduced pressure, giving the final product as an amorphous red solid (49 mg, 59% yield).
^{1}H NMR (400 MHz, 298 K, THF-d_8): δ 6.79 (s, 1H), 5.79 (s, 2H), 2,20 (s, 6H), 2.19 (s, 6H).

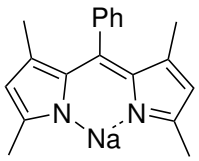
Synthesis of L1^{Na}



L1^{Na}

L1 (82 mg, 0.41 mmol, 1.00 equiv.) and NaHMDS (75 mg, 0.41 mmol, 1.00 equiv.) were separately dissolved in diethyl ether (3.5 mL each). The NaHMDS solution was slowly added to **L1** at −35 °C, resulting in immediate precipitation of a bright orange solid. The reaction mixture was then stirred for 2 h at room temperature and filtered by through glass fibre. The solid was washed with Et_2O (20 mL) and *n*-pentane (2×20 mL) and dried under reduced pressure, giving the final product as an amorphous orange solid (76 mg, 83% yield).
^{1}H NMR (400 MHz, 298 K, THF-d_8): δ 6.78 (s, 1H), 5.78 (s, 2H), 2.20 (s, 6H), 2.18 (s, 6H).

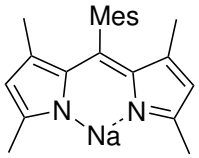
Synthesis of L2^{Na}



L2^{Na}

L2 (83 mg, 0.30 mmol, 1.00 equiv.) and NaHMDS (56 mg, 0.30 mmol, 1.02 equiv.) were separately dissolved in diethyl ether (3 mL each). The NaHMDS solution was slowly added to **L2** at −35 °C, resulting in a change in colour to red and formation of a red precipitate. The reaction mixture warmed to room temperature and left standing for 2 h before decanting off the supernatant solution. The remaining red solid was washed with *n*-pentane (3×3 mL) and dried under reduced pressure, giving the final product as an amorphous red solid (70 mg, 78% yield).
^{1}H NMR (300 MHz, 298 K, THF-d_8): δ 7.33–7.24 (m, 3H), 7.24–7.15 (m, 2H), 5.75 (s, 2H), 2.18 (s, 6H), 1.18 (s, 6H).

Synthesis of L3^{Na}



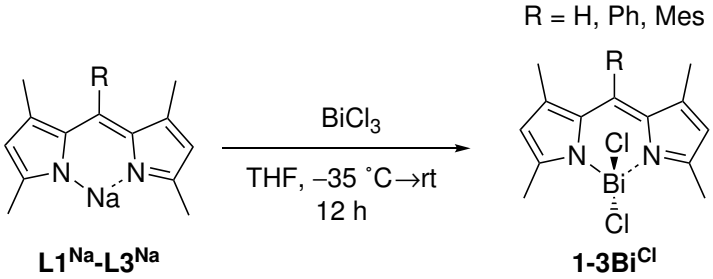
L3^{Na}

L3 (80 mg, 0.25 mmol, 1.00 equiv.) and NaHMDS (47 mg, 0.26 mmol, 1.02 equiv.) were separately dissolved in diethyl ether (3 mL each). The NaHMDS solution was slowly added to **L3** at −35 °C, resulting in a change in colour to brown and formation of a yellow precipitate. The reaction mixture warmed to room temperature and left standing for 2 h before decanting off the supernatant solution. The remaining red solid was washed with *n*-pentane (3×3 mL) and dried under reduced pressure, giving the final product as an amorphous yellow solid (53 mg, 62% yield).
^{1}H NMR (300 MHz, 298 K, THF-d_8): δ 6.81 (s, 2H), 5.68 (s, 2H), 2.27 (s, 3H) 2,18 (s, 6H), 2.02 (s, 6H), 1.17 (s, 6H).

6.5. Synthesis of BIDIPY complexes (chapter 2)

General procedure B

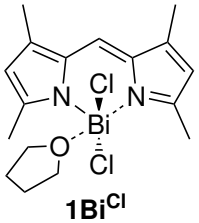
BIDIPY complexes wwere synthesized starting from $BiCl_3$ and the sodium dipyrrinato salts **L1^{Na}**-**L3^{Na}**. The respective dipyrrinato salt (1.00 equiv.) and $BiCl_3$ (1.00 equiv.) were separately suspended in THF (0.1 M) and cooled to −35 °C. Dropwise addition of ligand to $BiCl_3$ solution resulted in an immediate change in colour from orange to red. The reaction mixture was then filtered through glass fibre and allowed to warm to room temperature overnight, resulting in the formation of a crystalline precipitate. The mother liquor was removed by filtration and the product was washed with *n*-hexane and dried under reduced pressure to yield the respective BIDIPY complex as a coloured solid. BIDIPY chromophores were observed to readily decompose upon exposure to air and therefore need to be stored at low temperatures (−35 °C) under inert conditions.



L1^{Na}-L3^{Na} **1-3Bi^{Cl}**

Scheme 89: General reaction scheme for BIDIPY synthesis.

Synthesis of 1Bi^{Cl}



1Bi^{Cl}

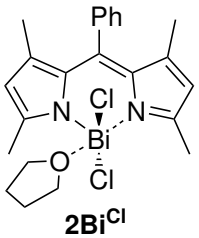
BIDIPY complex **1Bi^{Cl}** was prepared following the general procedure **B** using **L1^{Na}** (30 mg, 0.20 mmol). The product was obtained as a crystalline red solid (61 mg, 94% yield). Suitable single crystals for X-ray diffraction analysis were grown from a saturated solution of THF/*n*-hexane at room temperature. Despite prolonged drying under reduced pressure (10^{-3} mbar), THF remained coordinated to **1Bi^{Cl}**.

UV/Vis: λ_{abs}= 505 nm (CH_2Cl_2).

^{1}H NMR (500 MHz, 298 K, CD_2Cl_2): δ 7.14 (s, 1H), 6.41 (s, 2H), 3.72–3.65 (m, THF), 2.54 (s, 6H), 2.42 (s, 6H), 1.85–1.78 (m, THF);

^{13}C{^{1}H} NMR (126 MHz, 298 K, CD_2Cl_2): δ 160.2, 147.6, 132.8, 124.8, 121.2, 68.2 (THF), 26.0 (THF), 17.6, 12.2.

Synthesis of 2Bi^{Cl}



2Bi^{Cl}

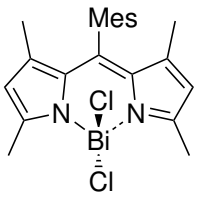
BIDIPY complex **2Bi^{Cl}** was prepared following the general procedure **B** using **L2^{Na}** (50 mg, 0.17 mmol). The product was obtained as a crystalline red solid (65 mg, 70% yield). Suitable single crystals for X-ray diffraction analysis were grown from a saturated solution of THF/*n*-hexane at room temperature. Despite prolonged drying under reduced pressure (10^{-3} mbar), THF remained coordinated to **2Bi^{Cl}**.

UV/Vis: λ_{abs}= 506 nm (CH_2Cl_2).

^{1}H NMR (500 MHz, 298 K, CD_2Cl_2): δ 7.55–7.46 (m, 3H), 7.37–7.31 (m, 2H), 6.27 (s, 2H), 3.72–3.60 (m, THF), 2.58 (s, 6H), 1.87–1.77 (m, THF), 1.47 (s, 6H);

^{13}C{^{1}H} NMR (126 MHz, 298 K, CD_2Cl_2): δ 159.9, 150.5, 147.5, 137.9, 133.5, 129.5, 129.4, 129.3, 124.4, 68.2 (THF), 25.9 (THF),17.7, 16.3.

Synthesis of 3Bi^{Cl}



3Bi^{Cl}

BIDIPY complex **3Bi^{Cl}** was prepared following the general procedure **B** using **L3^{Na}** (40 mg, 0.12 mmol). The product was obtained as a crystalline orange solid (53 mg, 80% yield). Suitable single crystals for X-ray diffraction analysis were grown from a saturated solution of THF/*n*-hexane at room temperature. Complex **3Bi^{Cl}** exhibited very poor solubility in CD_2Cl_2. Hence, the NMR data was recorded immediately after reacting **L3^{Na}** (2.5 mg, 7.3 μmol, 1.00 equiv.) and $BiCl_3$ (2.3 mg, 7.3 μmol,1.00 equiv.) in THF-d_8.

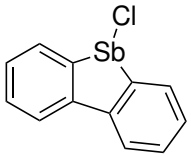
UV/Vis: λ_{abs}= 506 nm (CH_2Cl_2). **PL**: λ_{emi}= 535 nm (weak, CH_2Cl_2).

^{1}H NMR (500 MHz, 298 K, THF-d_8): δ 6.98 (s, 2H), 6.28 (s, 2H), 2.65 (s, 6H), 2.32 (s, 3H), 2.14 (s, 6H), 1.43 (s, 6H);

^{13}C{^{1}H} NMR (126 MHz, 298 K, THF-d_8): δ 158.9, 148.9, 147.7, 139.6, 137.0, 135.3, 132.6, 130.0, 123.6, 21.4, 20.3, 16.7, 15.7.

6.6. Synthesis of other reagents (chapter 2)

Synthesis of 5-chloro-5*H*-dibenzo[b,d]stibole (6)



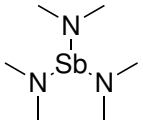
6

The reagent was prepared following a literature-reported method.[157] To a diethyl ether solution (20 mL) of 2,2'-dibromo-1,1'-biphenyl (500 mg, 1.60 mmol, 1.00 equiv.), *n*-BuLi (1.47 mL, 3.53 mmol, 2.4 M in *n*-hexane) was slowly added at −78 °C and the reaction mixture was stirred for 2 h at that temperature. Over the course of 3 h, the solution was allowed to warm to room temperature. The reaction mixture was then cooled to −78 °C again and a diethyl ether solution (5 mL) of $SbCl_3$ (442 mg, 1.76 mmol, 1.1 equiv.) was added dropwise, resulting in an immediate colour change from light yellow to brown. The mixture was gradually warmed to room temperature over 12 h. The following work-up was performed under air. The solvent was removed under reduced pressure and the residue was extracted with CH_2Cl_2 (3×50 mL) and washed with H_2O (100 mL). Combined organic layers were dried over Na_2SO_4 and dried under reduced pressure, yielding a white foam. The crude product was further purified by recrystallization from CH_2Cl_2/*n*-hexane (5:1), giving the product as an off-white crystalline solid (70 mg, 14% yield).

^{1}H NMR (300 MHz, 298 K, DMSO-d_6): δ 8.01 (d, *J* = 7.4 Hz, 2H), 7.91 (d, *J* = 7.4 Hz, 2H), 7.53–7.43 (m, 2H), 7.42–7.34 (m, 2H).

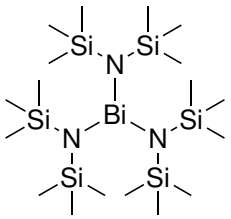
NMR data were in accordance with those previously reported.[157]

Synthesis of $Sb(NMe_2)_3$



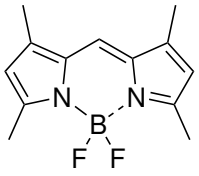
The reagent was prepared using a modified literature procedure.[156] At −74 °C, a diethyl ether solution (2.0 mL) of $SbCl_3$ (1.00 g, 4.38 mmol, 1.00 equiv.) was slowly added to a suspension of $LiNMe_2$ (671 mg, 13.2 mmol, 3.00 equiv.) in a mixture of *n*-hexane (12 mL) and diethyl ether (10 mL), resulting in a colour change from colourless to light yellow. The solution was first warmed to 0 °C and then to room temperature over the course of 1 h, yielding a grey suspension. After 1 h at room temperature, the reaction mixture was placed back into an ice bath to evaporate the solvent under reduced pressure. The resulting grey sludge was extracted with *n*-pentane (2×20 mL) through a filter cannula. The exctract was dried under reduced pressure at 0 °C, giving the final product as a light yellow oil (747 mg, 67% yield).
^{1}H NMR (400 MHz, 298 K, C_6D_6): δ 2.76 (s, 18H).
NMR data were in accordance with those previously reported.[156]

Synthesis of $Bi(HMDS)_3$



The reagent was prepared using a modified literature procedure.[294] At −35 °C, a THF solution (1.0 mL) of potassium bis(trimethylsilyl)amide (57 mg, 0.287 mmol, 3.02 equiv.) was added to a THF solution (3.0 mL) of $BiCl_3$ (30 mg, 0.095 mmol, 1.00 equiv.), resulting in a colour change from coulourless to yellow. The reaction mixture was stirred at room temperature for 4 h and the solvent was removed under reduced pressure. The crude product was then dissolved in *n*-hexane, filtered through celite®, giving the final product as an off-white amorphous solid (55 mg, 83% yield).
^{1}H NMR (400 MHz, 298 K, C_6D_6): δ 0.37 (s, 36H).
NMR data were in accordance with those previously reported.[294]

Synthesis of 1B^{F}



1B^{F}

BODIPY dye **1B^{F}** was prepared following a modified literature-reported procedure.[295] Dipyrrin **L1** (1.15 g, 5.74 mmol, 1.00 equiv.) was dissolved in toluene (50 mL) and dry triethylamine (2.07 mL, 14.9 mmol, 2.60 equiv.) was added. The reaction mixture was stirred for 15 min at room temperature and $BF_3{\cdot}OEt_2$ was slowly added, resulting in a colour change from yellow to dark orange-brown. The reaction mixture was stirred for 12 h at room temperature and then quenched by pouring into a saturated aqueous $NaHCO_3$ solution. The mixture was stirred for 30 min, followed by separation of the organic phase. The organic layer was washed with brine (2$\times$200 mL) and water (2$\times$200 mL). Subsequently, the organic phase was dried over Na_2SO_4 and concentrated under reduced pressure. The crude product was purified by column chromatography on SiO_2 using a gradient of *n*-hexane $\rightarrow$ *n*-hexane/toluene (1/3) as eluents. The target compound was obtained as a crystalline red solid (1.16 g, 81% yield).

^{1}H NMR (500 MHz, 298 K, $CDCl_3$): δ 7.03 (s, 1H), 6.04 (s, 2H), 2.53 (s, 6H), 2.24 (s, 6H);

^{13}C{^{1}H} NMR (126 MHz, 298 K, $CDCl_3$): δ 156.9, 141.3, 133.6, 120.2, 119.1, 14.8, 11.4;

^{11}B{^{1}H} NMR (160 MHz, 298 K, $CDCl_3$): δ 0.86 (t, J_{B-F} = 33.1 Hz).

^{19}F NMR (470 MHz, 298 K, $CDCl_3$): δ $-$146.5 (q, J_{B-F} = 33.0 Hz).

NMR data were in accordance with those previously reported.[295]

6.7. Spectroscopic data of PnDIPY complexes (chapter 2)

An overview of absorption maxima of **7Sb^{Cl}** in various solvents is provided in Table 18.

Table 18: UV/Vis spectroscopy solvent screening of **1Sb^{Cl}**.

Solvent	Absorption maximum λ_{abs} (nm)
Acetonitrile	497 nm
Benzene	504 nm
o-Dichlorobenzene	505 nm
Dichloromethane	501 nm
Tetrahydrofuran	500 nm

A summary of spectroscopic data of PnDIPY complexes described in Chapter 2 is provided in Table 19.

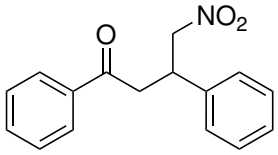
Table 19: Summary of spectroscopic data of PnDIPY complexes.

Complex	λ_{abs} (nm)	λ_{emi}[a] (nm)	Stokes shift (cm^{-1})	ϵ ($M^{-1}\cdot cm^{-1}$)	Quantum yield Φ_{rel}
1Sb^{Cl}	501	516	580	75460	0.025
1Sb^{Br}	504	518	536	67640	0.004
1Sb^{F}	496	522	1004	–[b]	–[b]
2Sb^{Cl}	501	520	729	71660	–[b]
3Sb^{Cl}	501	523	840	75280	0.011
1Sb^{+}[BArF]	513	518	188	52960	–[b]
1Bi^{Cl}	505	–[c]	–	–[b]	–[c]
2Bi^{Cl}	505	–[c]	–	–[b]	–[c]
3Bi^{Cl}	506	535	1071	–[b]	–[b]

[a] Emission recorded at excitation wavelength λ_{exc} = 460 nm. [b] not determined due to sample instability. [c] no emission observed.

6.8. Ligand synthesis (chapter 3)

Synthesis of 4-nitro-1,3-diphenylbutan-1-one (7)



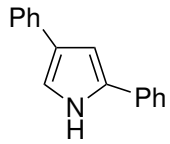
7

Compound **7** was prepared following a literature-reported method.[178] Under air, 1,3-Diphenyl-propenone (5.00 g, 24.0 mmol, 1.00 equiv.), nitromethane (5.89 g, 96.5 mmol, 4.02 equiv.) and diethylamine (5.30 g, 72.5 mmol, 3.02 equiv.) were dissolved in methanol (50.0 mL) and heated under reflux (70 °C) for 24 h. Afterwards, all volatiles were removed under reduced pressure and the resulting off-white solid was washed with *n*-hexane (3×10 mL). The target compound was obtained as an off-white solid (5.65 g, 87% yield) after drying under reduced pressure and was used without further purification.

^{1}H NMR (300 MHz, 298 K, $CDCl_3$): δ 7.96–7.87 (m, 2H), 7.62–7.53 (m, 1H), 7.50–7.43 (m, 2H), 7.37–7.27 (m, 5H), 4.88–4.79 (m, 1H), 4.74–4.65 (m, 1H), 4.29–4.18 (m, 1H), 3.57–3.35 (m, 2H).

NMR data were in accordance with those previously reported.[296]

Synthesis of 2,4-diphenyl-1*H*-pyrrole (8)



8

Compound **8** was prepared following a literature-reported method.[179] Under air, a 50 mL round bottom flask was charged with 4-nitro-1,3-diphenylbutan-1-one **7** (1.90, 7.10 mmol, 1.00 equiv.), sulfur (5.43 g, 21.2 mmol, 3.00 equiv.), morpholine (1.84 g, 21.2 mmol, 3.00 equiv.) and ammonium acetate (3.26 g, 42.3 mmol, 6.00 equiv.). The mixture was heated to 80 °C and stirred, resulting in a brown sludge. *Note: mechanical stirring was necessary as the reaction mixture was viscous*. The reaction mixture was cooled to room temperature and extracted with CH_2Cl_2, making sure to filter off residual S8. Combined organic layers were washed with water and dried over Na_2SO_4. After evaporation of solvent under reduced pressure, the crude product was subjected to column chromatography on basic aluminum oxide using a gradient of *n*-hexane + 1% NEt_3 $\rightarrow$ 25% ethyl acetate. Product fractions were collected, dried under reduced pressure and the final product was obtained as a grey crystalline solid (810 mg, 52% yield) from multiple recrystallization crops using *n*-hexane/ethyl acetate at -20 °C.

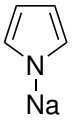
^{1}H NMR (400 MHz, 298 K, DMSO-d_6): δ 11.42 (s, 1H), 7.67 (d, J = 7.8 Hz, 2H), 7.60 (d, J = 7.7 Hz, 2H), 7.35–7.26 (m, 6H), 7.16 (t, J = 7.4 Hz, 1H), 7.11 (t, J = 7.3 Hz, 1H), 6.94 (s, 1H).

^{1}H NMR (500 MHz, 298 K, $CDCl_3$): δ 8.40 (s, 1H), 7.62–7.55 (m, 2H), 7.54–7.49 (m, 2H), 7.44–7.33 (m, 4H), 7.29–7.18 (m, 2H), 7.12 (dd, J = 2.8, 1.7 Hz, 1H), 6.85 (dd, J = 2.8, 1.7 Hz, 1H).

^{13}C{^{1}H} NMR (126 MHz, 298 K, $CDCl_3$): δ 135.7, 133.2, 132.6, 129.1, 128.8, 126.8, 126.6, 125.9, 125.3, 124.0, 115.7, 104.1.

NMR data were in accordance with those previously reported.[179]

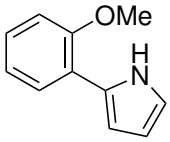
Synthesis of sodium pyrrol-1-ide (12)



12

The synthesis of sodium pyrrolide **12** was adapted from a literature-reported method.[180] A 250 mL Schlenk flask was charged with NaH (1.73 g, 72.0 mmol, 2.00 equiv.) and THF (50 mL) was added. The suspension was then cooled to 0 °C and 1*H*-pyrrole (2.42 g, 36.0 mmol, 1.00 equiv.) in THF (10 mL) was slowly added. The grey suspension was stirred for 3 h until no gas evolution was visible. The reaction mixture was filtered and the filtrate dried under reduced pressure for 2 h, giving a white solid. The solid was washed once with *n*-hexane (50 mL) and dried under reduced pressure for an extended time (circa 5 h). The product was obtained as a white amorphous solid (2.70 g, 84% yield).
^{1}H NMR (400 MHz, 298 K, THF-d_8): δ 6.79 (s, 2H), 6.03 (s, 2H).
NMR data were in good agreement with those previously reported.[297]

Synthesis of 2-(2'-methoxyphenyl)-1*H*-pyrrole (13)

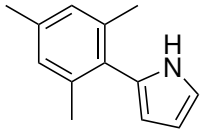


13

The synthesis of pyrrole **13** was adapted from a literature-reported method.[180] A Schlenk flask was charged with **12** (2.85 g, 32.0 mmol, 4.00 equiv.) and $ZnCl_2$ (3.27 g, 24.0 mmol, 3.00 equiv.). While cooling the mixture with an ice bath, THF (10 mL) was added, resulting in a grey suspension. Then, $Pd(OAc)_2$ (9.0 mg, 0.5 mol%), JohnPhos (11.9 mg, 0.5 mol%) and 2-chloroanisole (1.14 g, 8.00 mmol, 1.00 equiv.) were added and the reaction mixture heated to 60 °C for two days. Water (50 mL) was added to the reaction mixture and the organic phase was extracted with diethyl ether (3$\times$100 mL). Combined organic layers were dried over Na_2SO_4 and concentrated under reduced pressure. The crude product was subjected to column chromatography on SiO_2 using a slow gradient of *n*-hexane $\rightarrow$ *n*-hexane/ethyl acetate (4/1). The final product was obtained as an amorphous off-white solid (1.15 g, 83% yield). *Note: in several cases further purification through recrystallization in n-hexane/ethyl acetate at -20 °C or additional column chromatography was required to obtain analytically pure **13**.*

^{1}H NMR (400 MHz, 298 K, $CDCl_3$): δ 9.82 (br s, 1H), 7.67 (d, J = 7.7 Hz, 1H), 7.16 (t, J = 7.7 Hz, 1H), 7.03–6.94 (m, 2H), 6.87 (s, 1H), 6.65–6.60 (m, 1H), 6.32–6.25 (m, 1H), 3.97 (s, 3H).
^{13}C{^{1}H} NMR (101 MHz, 298 K, $CDCl_3$): δ 154.8, 130.0, 126.8, 126.7, 121.6, 121.3, 117.9, 111.8, 109.0, 106.2, 55.8.
NMR data were in good agreement with those previously reported.[180]

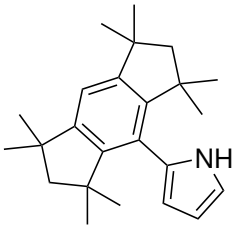
Synthesis of 2-mesitylene-1*H*-pyrrole (14)



14

The synthesis of pyrrole **14** was adapted from a literature-reported method.[180] Two screw cap vials were charged with **12** (300 mg, 3.37 mmol, 4.10 equiv.) and $ZnCl_2$ (356 mg, 2.61 mmol, 3.20 equiv.) each. THF (4 mL) was added to the solids, resulting in a grey suspension. Then, $Pd_2(dba)_3$ (1.9 mg, 0.25 mol%), JohnPhos (2.3 mg, 0.5 mol%) and mesityl bromide (163 mg, 0.82 mmol, 1.00 equiv.) were added to each vial and the reaction mixture heated to 96 °C for 50 h. Water (10 mL) was added to the reaction mixture and the organic phase was extracted with diethyl ether (3$\times$30 mL). Combined organic layers were dried over Na_2SO_4 and concentrated under reduced pressure. The crude product was subjected to column chromatography on SiO_2 using a slow gradient of *n*-hexane $\rightarrow$ *n*-hexane/ethyl acetate (95/5). The final product was obtained as an crystalline yellow solid (591 mg, 98% yield).
^{1}H NMR (400 MHz, 298 K, $CDCl_3$): δ 7.89 (s, 1H), 6.93 (s, 2H), 6.88–6.82 (m, 1H), 6.34–6.27 (m, 1H), 6.12–6.03 (m, 1H), 2.32 (s, 2H), 2.13 (s, 3H).
^{13}C{^{1}H} NMR (101 MHz, 298 K, $CDCl_3$): δ 138.7, 137.7, 130.8, 129.6, 128.2, 117.0, 108.6, 108.3, 21.2, 20.7.
NMR data were in accordance with those previously reported.[180]

Synthesis of 2-Mind-1*H*-pyrrole (15)



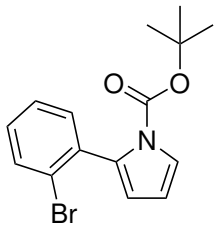
15

The synthesis of pyrrole **15** was adapted from a literature-reported method.[199] A 250 mL Schlenk flask was charged with **12** (3.70 g, 41.5 mmol, 5.00 equiv.) and dissolved in 2-methyltetrahydrofuran (23 mL). $Zn(OTf)_2$ (15.1 g, 41.5 mmol, 5.00 equiv.) was added in portions, resulting in a yellow slurry. In a separate vial, $Pd_2(dba)_3$ (380 mg, 5.00 mol%) and RuPhos (775 mg, 20.0 mol%) were dissolved in 2-methyltetrahydrofuran (2.5 mL) and heated to 60 °C for 10 minutes. The activated catalyst solution was then added to the reaction mixture, followed by the addition of MindBr (2.90 g, 8.31 mmol, 1.00 equiv.), giving a light red suspension. The reaction mixture was concentrated to circa 30% of its original volume under reduced pressure and heated at 100 °C for 72 h. After cooling to room temperature, the solvent was evaporated under reduced pressure, followed by the addition of *n*-hexane (130 mL) and water (130 mL) to the residue, stirring it for 3 h. The biphasic suspension was then filtered through a plug of celite®, followed by rinsing with *n*-hexane until the extract was practically colourless. The organic phase was washed with brine and extracted with *n*-hexane (3×100 mL) before drying the combined organic layers over Na_2SO_4. Removal of solvents under reduced pressure gave a red solid, which was further subjected to column chromatography on SiO_2 using a slow gradient of *n*-hexane → *n*-hexane/ethyl acetate (9/1). Column chromatography was repeated a second time, yielding the target compound as an off-white crystalline solid (1.68 g, 60% yield).

^{1}H NMR (500 MHz, 298 K, $CDCl_3$): δ 7.86 (s, 1H), 6.91 (s, 1H), 6.78 (td, J = 2.7, 1.5 Hz, 1H), 6.25 (dt, J = 3.4, 2.7 Hz, 1H), 6.10–6.07 (m, 1H), 1.86 (s, 4H), 1.33 (s, 6H), 1.32 (s, 6H), 1.19 (s, 6H), 0.89 (s, 6H).

^{13}C{^{1}H} NMR (126 MHz, 298 K, $CDCl_3$): δ 151.0, 149.4, 126.7, 126.6, 117.2, 115.1, 110.9, 107.8, 58.8, 44.0, 40.8, 31.7, 31.6, 31.2, 30.4.

Synthesis of *N*-Boc-2-(2'-bromophenyl)-pyrrole (18)



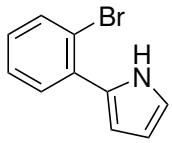
18

The synthesis of pyrrole **18** was adapted from a literature-reported method.[181] A 100 mL Schlenk flask was charged with *N*-Boc-pyrrole-2-boronic acid **16** (2.11 g, 10.0 mmol, 1.00 equiv.), $Pd(PPh_3)_2Cl_2$ (105 mg, 1.5 mol%) and K_2CO_3 (3.45 g, 25.0 mmol, 2.50 equiv.), followed by the addition 2-bromo-1-iodobenzene **17** (2.83 g, 10.0 mmol, 1.00 equiv.). A degassed mixture of DME (30.0 mL) and H_2O (4.0 mL) was added while maintaining an argon atmosphere. The reaction mixture was heated at 80 °C over the course of 18 h, resulting in a dark green suspension. After cooling to room temperature, the reaction mixture was diluted with water (50 mL) and the organic phase was extracted using CH_2Cl_2 (3×80 mL). Combined organic layers were dried over Na_2SO_4 and concentrated under reduced pressure. The crude product was subjected to flash column chromatography on SiO_2 using a gradient of *n*-hexane → *n*-hexane/CH_2Cl_2 (5/1). The target compound was obtained as a colourless oil (1.30 g, 40% yield).

^{1}H NMR (300 MHz, 298 K, DMSO-d_6): δ 7.65 (dd, *J* = 7.9, 1.3 Hz, 1H), 7.46–7.24 (m, 4H), 6.29 (t, *J* = 3.3 Hz, 1H), 6.19–6.16 (m, 1H), 1.21 (s, 9H).

NMR data were in accordance with those previously reported.[181]

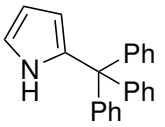
Synthesis of 2-(2'-bromophenyl)-1*H*-pyrrole (19)



19

The synthesis of pyrrole **19** was adapted from a literature-reported method.[181] Compound **18** was heated to 180 °C under constant stirring in a screw cap vial equipped with an nitrogen inlet and an outlet for 30 minutes. The target compound was obtained as a slightly pink oil (658 mg, 73% yield) without further purification.
^{1}H NMR (300 MHz, 298 K, DMSO-d_6): δ 11.12 (br s, 1H), 7.64 (dd, J = 7.9, 1.3 Hz, 1H), 7.47 (dd, J = 7.9, 1.8 Hz, 1H), 7.37 (td, J = 7.5, 1.3 Hz, 1H), 7.16–7.09 (m, 1H), 6.91–6.81 (m, 1H), 6.58-6.47 (m, 1H), 6.19–6.07 (m, 1H).
NMR data were in accordance with those previously reported.[181]

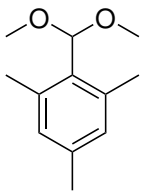
Synthesis of 2-trityl-1*H*-pyrrole (22)



22

The synthesis of pyrrole **22** was adapted from a literature-reported method.[298] In a 1 L Schlenk flask, 1*H*-pyrrole **20** (25.3 g, 377 mmol, 10.0 equiv.) was dissolved in CH_2Cl_2 (250 mL). The solution was cooled to −78 °C and $AlCl_3$ (10.0 g, 75.3 mmol, 2.00 equiv.) was added as a solid. In a separate Schlenk flask, trityl chloride **21** (10.5 g, 37.7 mmol, 1.00 equiv.) was dissolved in CH_2Cl_2 (150 mL) and slowly added to reaction mixture *via* cannula, resulting in a colour change from colourless to brown-yellow. The mixture was gradually warmed to room temperature and stirred for 4 h before quenching with sat. aqueous $NaHCO_3$ solution (200 mL). The biphasic mixture was stirred for 10 h and the organic phase was extracted with ethyl acetate (3×200 mL). Combined organic phases were dried over Na_2SO_4 and concentrated under reduced pressure. The crude product was dissolved in CH_2Cl_2 and purified by column chromatography on SiO_2 using a gradient of *n*-hexane to pure CH_2Cl_2. The product was obtained as a white amorphous solid (2.63 g, 23% yield).
^{1}H NMR (400 MHz, 298 K, $CDCl_3$): δ 7.72 (br s, 1H), 7.35–7.21 (m, 9H), 7.19–7.13 (m, 6H), 6.78–6.72 (m, 1H), 6.22–6.15 (m, 1H), 6.10–6.02 (m, 1H).
NMR data were in good agreement with those previously reported.[299]

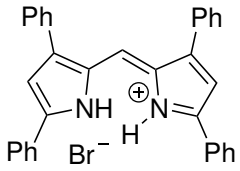
Synthesis of mesitaldehyde dimethyl acetal (24)



24

Compound **24** was synthesized according to a literature-reported procedure.[300] Camphorsulfonic acid (10 mg, 0.04 mmol) was added to a solution of trimethyl orthoformate (3.22 g, 30.4 mmol, 1.50 equiv.) and mesitaldehyde **23** (3.00 g, 20.2 mmol, 1.00 equiv.) in methanol (30.0 mL). The reaction mixture was stirred at room temperature for 12 h, followed by quenching with sat. aqueous $NaHCO_3$ solution. The organic phase was extracted with diethyl ether (3×50 mL) and combined organic layers were dried over Na_2SO_4. The solution was concentrated under reduced pressure, giving the target compound as a slightly yellow oil (3.85 g, 98% yield).
^{1}H NMR (300 MHz, 298 K, $CDCl_3$): δ 6.89 (s, 2H), 5.56 (s, 1H), 3.48 (s, 6H), 2.51 (s, 6H), 2.33 (s, 3H).

Synthesis of L5-HBr



L5-HBr

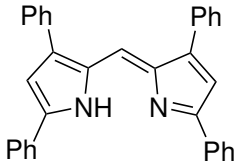
The synthesis of **L5-HBr** was adapted from a literature-reported method.[177] Under air, pyrrole **8** (300 mg, 1.37 mmol, 1.00 equiv.) was combined with aqueous HBr (48%, 3.0 mL) and formic acid (3.0 mL). The reaction mixture was heated at 110 °C for 4 h with a golden precipitate gradually forming. The reaction mixture was cooled to room temperature and the precipitate was filtered off. The solid was washed with water (250 mL) and *n*-pentane (250 mL), giving the final product as a black-golden amorphous solid (145 mg, 40% yield).

UV/Vis: λ_{abs}= 562 nm (CH_2Cl_2). **PL**: λ_{emi}= 592 nm (weak, CH_2Cl_2).

^{1}H NMR (300 MHz, 298 K, $CDCl_3$): δ 13.87 (s, 2H), 8.42 (d, *J* = 6.5 Hz, 4H), 7.63–7.48 (m, 6H), 7.46–7.29 (m, 11H), 7.03 (s, 2H).

NMR data were in good agreement with those previously reported.[177]

Synthesis of L5



L5

The synthesis of **L5** was adapted from a literature-reported method.[177] Under air, **L5-HBr** (145 mg, 0.28 mmol, 1.00 equiv.) was dissolved in CH_2Cl_2 (5.0 mL) and stirred for 10 minutes with an excess of aqueous NaOH solution (1 M) and NEt_3 (0.5 mL). The organic phase was extracted with CH_2Cl_2 (2×10 mL) and washed with water (3×50 mL) before drying over Na_2SO_4 followed by solvent evaporation under reduced pressure. The resulting solid was washed with *n*-hexane (3×10 mL) and dried under reduced pressure, giving the final product as a purple amorphous solid (126 mg, 99% yield).

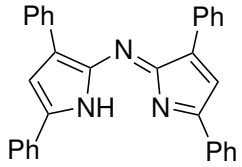
UV/Vis: λ_{abs}= 530 nm (CH_2Cl_2). **PL**: λ_{emi}= 601 nm (weak, CH_2Cl_2).

^{1}H NMR (400 MHz, 298 K, $CDCl_3$): δ 7.98 (d, *J* = 7.7 Hz, 4H), 7.57–7.48 (m, 8H), 7.48–7.30 (m, 8H), 7.24 (s, 1H), 6.97 (s, 2H). *Note: N−H signal not visible*.

^{13}C{^{1}H} NMR (101 MHz, 298 K, $CDCl_3$): δ 153.3, 144.9, 139.6, 135.0, 133.0, 129.2, 128.9, 128.9, 127.8, 126.4, 123.7, 114.7 (one signal not observed due to overlap).

NMR data were in accordance with those previously reported.[177]

Synthesis of L6



L6

The synthesis of **L6** was adapted from a literature-reported method.[178] Under air, a mixture of compound **7** (1.70 g, 6.31 mmol, 1.00 equiv.) and ammonium acetate (14.2 g, 200 mmol, exc.) were stirred while heating to 190 °C, forming a deep blue solution. The reaction mixture was heated under reflux for 2 h and diluted with water (50 mL) after cooling to room temperature. The resulting black precipitate was filtered off and washed with water (3×100 mL), followed by drying under air for 2 days. The crude compound was purified by column chromatography on basic aluminum oxide using a slow gradient of *n*-hexane + 1% NEt_3 $\rightarrow$ 40% ethyl acetate. *Note: as the product showed strong interaction with the stationary phase, remaining product was rinsed with a mixture of CH_2Cl_2 + 5% methanol. Impure product fractions were washed with cold methanol to yield analytically pure samples*. The target product was obtained as an amorphous black solid (438 mg, 31% yield).

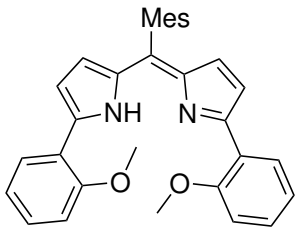
UV/Vis: λ_{abs}= 596 nm (CH_2Cl_2).

^{1}H NMR (500 MHz, 298 K, THF-d_8): δ 12.78 (br s, 1H), 8.14–8.10 (m, 4H), 8.08–8.05 (m, 4H), 7.59–7.51 (m, 4H), 7.49-7.45 (m, 2H), 7.44 (s, 2H), 7.43–7.39 (m, 4H), 7.35–7.31 (m, 2H).

^{13}C{^{1}H} NMR (126 MHz, 298 K, THF-d_8): δ 156.3, 150.6, 143.4, 134.9, 133.2, 131.0, 130.00, 129.9, 129.0, 128.7, 127.5, 116.0.

NMR data were in good agreement with those previously reported.[178]

Synthesis of L7



L7

The synthesis of **L7** was adapted from a literature-reported method.[183] To a solution of pyrrole **13** (340 mg, 1.96 mmol, 2.00 equiv.) and mesitaldehyde **23** (145 mg, 0.98 mmol, 1.00 equiv.) in CH_2Cl_2 (70 mL), TFA (23 μL, 30 mol%) was added and the reaction mixture stirred for 4 h, gradually turning to a dark red colour. Then, DDQ (223 mg, 0.98 mmol, 1.00 equiv.) was added, resulting in an immediate colour change to dark blue and the reaction mixture stirred for 12 h. The reaction mixture was quenched with sat. aqueous $NaHCO_3$ solution (200 mL) and the organic layer was extracted with CH_2Cl_2 (2×150 mL). Combined organic phases were washed with water (50 mL), dried over Na_2SO_4 and concentrated under reduced pressure. The crude product was purified by flash column chromatography on basic aluminum oxide starting with *n*-hexane as an eluent, followed by a gradient of $CH_2Cl_2 \rightarrow CH_2Cl_2$/ethyl acetate (9/1). The target compound was obtained as a dark red amorphous solid (330 mg, 71% yield). *Note: sample purity can be improved by washing with cold methanol.*

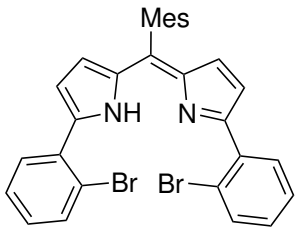
UV/Vis: λ_{abs}= 518 nm (CH_2Cl_2). **PL**: λ_{emi}= 589 nm (weak, CH_2Cl_2).

^{1}H NMR (500 MHz, 298 K, $CDCl_3$): δ 13.52 (br s, 1H), 8.08 (dd, *J* = 7.8, 1.3 Hz, 2H), 7.36–7.28 (m, 2H), 7.08–6.98 (m, 4H), 6.94 (s, 2H), 6.88 (dd, *J* = 4.3, 0.7 Hz, 2H), 6.41 (d, *J* = 4.3 Hz, 2H), 3.90 (s, 6H), 2.37 (s, 3H), 2.17 (s, 6H).

^{13}C{^{1}H} NMR (126 MHz, 298 K, $CDCl_3$): δ 157.5, 152.1, 141.0, 138.1, 137.3, 137.2, 134.3, 129.7, 129.2, 127.8, 127.2, 122.7, 121.0, 118.5, 111.7, 56.1, 21.3, 20.3.

NMR data were in accordance with those previously reported.[183]

Synthesis of L8



L8

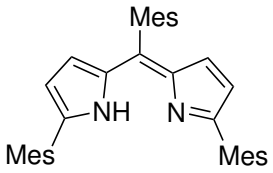
Dipyrromethene **L8** was synthesized according to a modified literature procedure.[298] Pyrrole **19** (4.70 g, 21.2 mmol, 2.00 equiv.), compound **24** (2.06 g, 10.6 mmol, 1.00 equiv.) and PPTS (532 mg, 20 mol%) were dissolved in CH_2Cl_2 (150 mL), set under partial vacuum and heated at 90 °C for 12 h and 60 °C for 20 h. After cooling to room temperature, the reaction mixture was filtered through a plug of silica under air, using CH_2Cl_2 as the eluent to afford a red filtrate. The filtrate was concentrated under reduced pressure and triturated with *n*-hexane, resulting in an orange foam upon drying. The crude product was placed in a round bottom flask, dissolved in dry CH_2Cl_2 (100 mL) and purged with argon. DDQ (2.40 g, 10.6 mmol, 1.00 equiv.) was added to the reaction mixture, resulting in an immediate colour change to dark red. After stirring at room temperature for 5 h, the mixture was concentrated under reduced pressure. The crude product was purified by flash column chromatography on basic aluminum oxide starting with *n*-hexane as an eluent, followed by CH_2Cl_2 until intensely red coloured fractions stop eluting. The target compound was obtained as a red foam (5.46 g, 90% yield).

UV/Vis: λ_{abs}= 494 nm (CH_2Cl_2). **PL**: λ_{emi}= 576 nm (weak, CH_2Cl_2).

^{1}H NMR (400 MHz, 298 K, $CDCl_3$): δ 13.37 (br s, 1H), 7.84 (dd, *J* = 8.0, 1.7 Hz, 2H), 7.67 (d, *J* = 8.0 Hz, 2H), 7.38 (t, *J* = 8.0 Hz, 2H), 7.25–7.15 (m, 2H), 6.96 (s, 2H), 6.86 (d, *J* = 4.6 Hz, 2H), 6.45 (d, *J* = 4.2 Hz, 2H), 2.38 (s, 3H), 2.19 (s, 6H).

^{13}C{^{1}H} NMR (101 MHz, 298 K, $CDCl_3$): δ 153.4, 141.5, 140.0, 137.7, 137.1, 134.4, 134.3, 133.5, 131.3, 129.6, 128.0, 127.56, 127.4, 121.3, 119.5, 21.3, 20.3.

Synthesis of L9



L9

The synthesis of **L9** was adapted from a literature-reported method.[301] To a solution of pyrrole **14** (2.75 g, 14.9 mmol, 2.00 equiv.) and compound **24** (1.44 g, 7.43 mmol, 1.00 equiv.) in CH_2Cl_2 (100 mL), PPTS (374 mg, 10 mol%) was added. The reaction mixture was set under partial vacuum and heated at 90 °C for 12 h and 60 °C for 20 h, resulting in a red solution. After cooling to room temperature, the reaction mixture was filtered through a plug of silica under air, using CH_2Cl_2 as the eluent to afford a colourless filtrate. The filtrate was concentrated under reduced pressure and triturated with *n*-hexane, resulting in a white foam upon drying. The crude product was placed in a round bottom flask, dissolved in dry CH_2Cl_2 (60 mL) and purged with argon. DDQ (1.69 g, 7.43 mmol, 1.00 equiv.) was added to the reaction mixture, resulting in an immediate colour change to dark red. After stirring at room temperature for 5 h, the mixture was concentrated under reduced pressure and filtered through a plug of basic aluminum oxide using CH_2Cl_2. Upon drying of the yellow filtrate under reduced pressure, the target compound was obtained as a yellow amorphous solid (3.02 g, 82% yield).

UV/Vis: λ_{abs}= 463 nm (CH_2Cl_2). **PL**: λ_{emi}= 562 nm (weak, CH_2Cl_2).

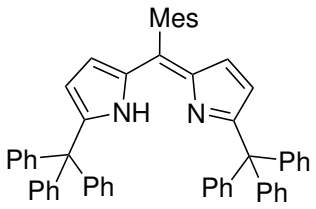
^{1}H NMR (300 MHz, 298 K, CD_2Cl_2): δ 12.47 (br s, 1H), 6.98 (s, 2H), 6.90 (s, 4H), 6.39 (d, *J* = 4.1 Hz, 2H), 6.23 (d, *J* = 4.1 Hz, 2H), 2.37 (s, 3H), 2.28 (s, 6H), 2.19 (s, 18H).

^{1}H NMR (500 MHz, 298 K, $CDCl_3$): δ 12.34 (br s, 1H), 6.96 (s, 2H), 6.91 (s, 4H), 6.41 (d, *J* = 4.1 Hz, 2H), 6.22 (d, *J* = 4.1 Hz, 2H), 2.38 (s, 3H), 2.30 (s, 6H), 2.22 (s, 12H), 2.21 (s, 6H).

^{13}C{^{1}H} NMR (126 MHz, 298 K, $CDCl_3$): δ 154.3, 140.6, 138.7, 137.8, 137.3, 137.2, 137.1, 134.0, 132.0, 128.5, 127.9, 126.9, 119.4, 21.3, 21.2, 20.8, 20.1.

NMR data were in accordance with those previously reported.[301]

Synthesis of L10



L10

The synthesis of **L10** was adapted from a literature-reported method.[301] To a solution of pyrrole **22** (1.53 g, 4.94 mmol, 2.00 equiv.) and compound **24** (1.44 g, 2.47 mmol, 1.00 equiv.) in CH_2Cl_2 (45 mL), PPTS (124 mg, 10 mol%) was added. The reaction mixture was set under partial vacuum and heated at 90 °C for 12 h and 60 °C for 20 h. After cooling to room temperature, the reaction mixture was filtered through a plug of silica under air, using CH_2Cl_2 as the eluent to afford a pale yellow filtrate. The filtrate was concentrated under reduced pressure and triturated with *n*-hexane, giving a yellow solid. The solid was placed in a round bottom flask, dissolved in dry CH_2Cl_2 (40 mL) and purged with argon. DDQ (561 mg, 2.47 mmol, 1.00 equiv.) was added to the reaction mixture, resulting in an immediate colour change to dark orange. After stirring at room temperature for 4.5 h, the mixture was concentrated under reduced pressure and filtered through a plug of basic aluminum oxide using CH_2Cl_2 as the eluent. The filtrate was concentrated under reduced pressure and triturated with acetonitrile (10 mL), giving a yellow solid. The solid was filtered off and dried under reduced pressure, affording the target compound as a yellow amorphous solid (1.40 g, 76% yield).

UV/Vis: λ_{abs}= 450 nm (CH_2Cl_2). **PL**: λ_{emi}= 527 nm (weak, CH_2Cl_2).

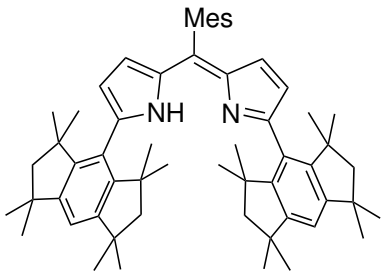
^{1}H NMR (500 MHz, 298 K, $CDCl_3$): δ 11.49 (br s, 1H), 7.14–7.02 (m, 30H), 6.86 (s, 2H), 6.13 (d, *J* = 4.2 Hz, 2H), 5.96 (d, *J* = 4.2 Hz, 2H), 2.31 (s, 3H), 2.09 (s, 6H).

^{1}H NMR (500 MHz, 298 K, CD_2Cl_2): δ 11.48 (br s, 1H), 7.19–7.05 (m, 30H), 6.92 (s, 2H), 6.15 (d, *J* = 4.2 Hz, 1H), 6.02 (d, *J* = 4.2 Hz, 2H), 2.33 (s, 3H), 2.11 (s, 6H).

^{13}C{^{1}H} NMR (126 MHz, 298 K, CD_2Cl_2): δ 161.6, 146.1, 141.0, 138.4, 137.7, 137.2, 134.3, 130.7, 128.1, 126.5, 126.1, 120.9, 62.6, 21.3, 20.1.

NMR data were in accordance with those previously reported.[298]

Synthesis of L11



L11

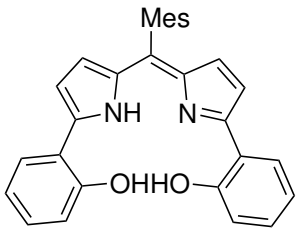
Dipyrromethene **L11** was synthesized according to a modified literature procedure.[199] Pyrrole **15** (1.03 g, 3.07 mmol, 1.90 equiv.), mesitaldehyde **23** (237 mg, 2.47 mmol, 1.00 equiv.) and PPTS (771 mg, 3.07 mmol, 1.90 equiv.) were suspended in 1,2-dichloroethane. The reaction mixture was heated at 120 °C for 72 h, resulting in a dark red solution. After cooling to room temperature, the reaction mixture was filtered through a plug of silica under air, using CH_2Cl_2 as the eluent to afford a yellow filtrate which was concentrated under reduced pressure. The oily brown residue was placed under argon and dissolved in dry CH_2Cl_2 (80 mL). At 0 °C, DDQ (918 mg, 1.84 mmol, 1.15 equiv.) was added to the reaction mixture, resulting in an immediate colour change to dark red. After stirring at room temperature for 4 h, an excess of tirethyl amine (2.1 mL, 5.0 equiv.) was added and the mixture was concentrated under reduced pressure. The crude product was purified by flash column chromatography using *n*-hexane as the eluent. Upon drying under reduced pressure, the target compound was obtained as an amorphous yellow solid . The solid was filtered off and dried under reduced pressure, affording the target compound as a yellow amorphous solid (244 mg, 20% yield).

UV/Vis: λ_{abs}= 448 nm (CH_2Cl_2). **PL**: λ_{emi}= 516 nm (weak, CH_2Cl_2).

^{1}H NMR (500 MHz, 298 K, C_6D_6): δ 12.46 (br s, 1H), 7.01 (s, 2H), 6.88 (s, 2H), 6.46 (d, *J* = 4.1 Hz, 2H), 6.28 (d, *J* = 4.1 Hz, 2H), 2.36 (s, 6H), 2.25 (s, 3H), 1.82 (s, 4H), 1.82 (s, 4H), 1.41 (s, 12H), 1.31 (s, 12H), 1.27 (s, 12H), 1.20 (s, 12H).

^{13}C{^{1}H} NMR (126 MHz, 298 K, C_6D_6): δ 153.8, 151.5, 148.1, 140.1, 139.3, 137.5, 136.9, 135.1, 129.0, 128.4, 125.9, 123.9, 117.5, 59.3, 44.3, 41.0, 32.1, 32.0, 31.5, 31.3, 21.3, 20.0.

Synthesis of L12

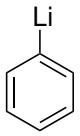


L12

The synthesis of **L12** was adapted from a literature-reported method.[183] Dipyrromethene **L7** (217 mg, 0.46 mmol, 1.00 equiv.) was dissolved in CH_2Cl_2 and BBr_3 (0.42 mL, 4.44 mmol, 9.70 equiv.) was added at 0 °C, causing an immediate change in colour from red to dark blue. The reaction mixture was allowed to warm to room temperature and stirred for 12 h. While cooling with an ice-bath, the reaction mixture was quenched with methanol under air (60 mL) and concentrated under reduced pressure. The oily residue was dissolved in methanol (35 mL), followed by the addition of conc. HCl (1.6 mL). The mixture was heated under reflux for 3 h, after which the reaction mixture was warmed to room temperature and slowly quenched with sat. aqueous $NaHCO_3$ solution (70 mL). The organic phase was extracted with ethyl acetate (3×100 mL). Combined organic layers were washed with water (20 mL) and dried over Na_2SO_4. The crude product was purified by column chromatography on SiO_2 using a slow gradient of *n*-hexane → *n*-hexane/ethyl acetate (1/1). The target compound was obtained as a burgundy amorphous solid (76 mg, 37% yield).
UV/Vis: λ_{abs}= 541 nm (CH_2Cl_2).
^{1}H NMR (400 MHz, 298 K, THF-d_8): δ 11.35 (br s, 2H), 7.76 (dd, *J* = 7.9, 1.6 Hz, 2H), 7.19 (t, *J* = 7.5 Hz, 1H), 7.02–6.95 (m, 6H), 6.88 (t, *J* = 7.5 Hz, 2H), 6.44 (br s, 1H), 2.36 (s, 3H), 2.12 (s, 6H).
^{1}H NMR (500 MHz, 298 K, $CDCl_3$): δ 7.61 (dd, *J* = 7.8, 1.5 Hz, 2H), 7.03–6.93 (m, 6H), 6.88–6.79 (m, 4H), 6.53 (d, *J* = 3.3 Hz, 2H), 2.39 (s, 3H), 2.18 (s, 6H). *Note: N−H signal not visible.*
^{13}C{^{1}H} NMR (126 MHz, 298 K, $CDCl_3$): δ 156.4, 154.3, 138.6, 138.5, 137.8, 137.3, 134.7, 130.2, 129.1, 128.0, 127.8, 120.1, 117.8, 117.2, 115.5, 21.3, 20.2.
NMR data were in good agreement with those previously reported.[183]

6.9. Chapter 3: synthesis of alkali dipyrrinato salts

Synthesis of phenyllithium

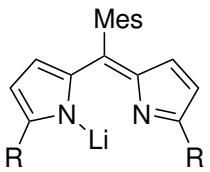


Bromobenzene (3.93 g, 25.0 mmol, 1.00 equiv.) was dissolved in a mixture consisting of *n*-hexane (70.0 mL) and Et_2O (2.0 mL). The mixture was cooled to −78 °C and an*n*-butyllithium solution in hexanes (10.0 mL, 2.50 M, 1.00 equiv.) was slowly added. Then, the reaction mixture was gradually allowed to warm to room temperature and stirred for 60 h, giving a white suspension. The solvent was removed *via* cannula filtration and the crude product was washed with *n*-pentane (2×50 mL). The target compound was obtained as a flakey white solid (965 mg, 46% yiel)

^{1}H NMR (300 MHz, 298 K, THF-d_8): δ 7.96–7.83 (m, 2H), 6.87–6.80 (m, 2H), 6.77–6.70 (m, 1H).

^{7}Li NMR (117 MHz, 298 K, THF-d_8): δ 1.49.

Synthesis of lithium dipyrrinato salts - General procedure C



R = trityl - **L10^{Li}**
Mind - **L11^{Li}**

Lithium dipyrrinato salts were prepared using a modified literature procedure.[298] Dipyrrin ligand **L** (1.00 equiv.) and phenyllithium (1.20 equiv.) were dissolved in benzene (1.5 mL per 0.1 mmol dipyrrin) and stirred at room temperature for 17 hours. Afterwards, the reaction mixture was filtered through a celite® plug, which was rinsed with additional benzene until the filtrate is no longer intensely coloured. The collected filtrate was frozen and benzene was removed by sublimation under reduced pressure, giving the lithium dipyrrinato salt as coloured powder.

Note: All lithium dipyrrinato salts were observed to be highly moisture sensitive and readily change colour in contact with ambient air, indicating decomposition.

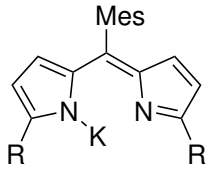
Synthesis of L10^{Li}

The compound was prepared according to general procedure **C** starting from **L10** (400 mg, 0.54 mmol, 1.00 equiv.). The product was obtained as an amorphous orange solid (400 mg, 99% yield) **^{1}H NMR** (300 MHz, 298 K, THF-d_8): δ 7.29–7.22 (m, 12H), 7.17–7.00 (m, 18H), 6.91–6.84 (m, 2H), 6.23 (d, J = 4.0 Hz, 2H), 5.82 (d, J = 4.0 Hz, 2H), 2.31 (s, 3H), 2.13 (s, 6H).
^{7}Li NMR (117 MHz, 298 K, THF-d_8): δ 0.93.

Synthesis of L11^{Li}

The compound was prepared according to general procedure **C** starting from **L11** (85 mg, 0.11 mmol, 1.00 equiv.). The product was obtained as an amorphous bright yellow-orange solid (85 mg, 99% yield).
^{1}H NMR (300 MHz, 298 K, THF-d_8): δ 6.93 (s, 2H), 6.87 (s, 2H), 6.30 (d, J = 3.8 Hz, 2H), 6.12 (d, J = 3.8 Hz, 2H), 2.36 (s, 3H), 2.22 (s, 6H), 1.88–1.76 (m, 8H), 1.29 (s, 12H), 1.23 (s, 12H), 1.12 (s, 12H), 1.05 (s, 12H).
^{7}Li NMR (117 MHz, 298 K, THF-d_8): δ 2.21.

Synthesis of potassium dipyrrinato salts - General procedure D



R =	2-methoxyphenyl	- **L7^{K}**
	2-bromophenyl	- **L8^{K}**
	mesityl	- **L9^{K}**
	trityl	- **L10^{K}**

Potassium dipyrrinato salts were prepared using a modified literature procedure.[138] Dipyrrin ligand **L** (1.00 equiv.) was suspended in toluene (0.1 M) and a slight excess of KHMDS was added as a solid at room temperature and the reaction mixture was stirred for 12 hours. *For **L7, L8** and **L10***: The coloured precipitate was collected on a filter frit and washed with a generous amount of *n*-hexane. *For **L9***: The reaction mixture was evaporated under reduced pressure and the resulting oil was triturated and washed with *n*-hexane. The potassium dipyrrinato salts were obtained as brightly coloured amorphous solids.
Note: All potassium dipyrrinato salts were observed to be highly moisture sensitive and readily change colour in contact with ambient air, indicating decomposition.

Synthesis of L7^{K}

The compound was prepared according to general procedure **D** starting from **L7** (400 mg, 0.44 mmol, 1.00 equiv.) and KHMDS (177 mg, 1.05 equiv.). The product was obtained as an amorphous dark red solid (195 mg, 90% yield).

^{1}H NMR (500 MHz, 298 K, THF-d_8): δ 7.92–7.82 (m, 2H), 7.13-7.11 (m, 2H), 7.02–6.93 (m, 4H), 6.85 (s, 2H), 6.59 (d, J = 3.9 Hz, 2H), 6.26 (s, 2H), 3.84 (s, 6H), 2.33 (s, 3H), 2.13 (s, 6H).

Synthesis of L8^{K}

The compound was prepared according to general procedure **D** starting from **L8** (100 mg, 0.17 mmol, 1.00 equiv.) and KHMDS (35 mg, 1.01 equiv.). The product was obtained as an amorphous dark red solid (79 mg, 74% yield).

^{1}H NMR (500 MHz, 298 K, THF-d_8): δ 7.86 (d, J = 7.5 Hz, 2H), 7.62 (dd, J = 8.0, 1.2 Hz, 2H), 7.31 (td, J = 7.5, 1.3 Hz, 2H), 7.11–7.04 (m, 2H), 6.90–6.86 (m, 2H), 6.71 (d, J = 3.8 Hz, 2H), 6.32 (s, 2H), 2.34 (s, 3H), 2.13 (s, 6H).

Synthesis of L9^{K}

The compound was prepared according to general procedure **D** starting from **L9** (222 mg, 0.44 mmol, 1.00 equiv.) and KHMDS (97 mg, 1.10 equiv.). The product was obtained as an amorphous red solid (195 mg, 82% yield).

^{1}H NMR (500 MHz, 298 K, C_6D_6): δ 6.78–6.77 (m, 4H), 6.77–6.76 (m, 2H), 6.63 (d, J = 4.1 Hz, 2H), 6.00 (d, J = 4.1 Hz, 2H), 2.33 (s, 12H), 2.20 (s, 3H), 2.18 (s, 6H), 2.06 (s, 6H).

Synthesis of L10^{K}

The compound was prepared according to general procedure **D** starting from **L10** (222 mg, 0.54 mmol, 1.00 equiv.) and KHMDS (117 mg, 1.10 equiv.). The product was obtained as an amorphous orange solid (254 mg, 60% yield).

^{1}H NMR (500 MHz, 298 K, C_6D_6): δ 7.48–7.41 (m, 12H), 6.96–6.83 (m, 22H), 6.42 (d, J = 3.9 Hz, 2H), 2.45 (s, 6H), 2.24 (s, 3H).

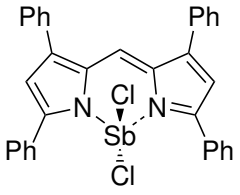
Synthesis of L11^{Na}

Dipyrrin **L11** (20 mg, 0.03 mmol, 1.00 equiv.) was dissolved in THF (3.0 mL), an excess of NaH (approximately 36 mg, 60 equiv.) was added and the reaction mixture stirred for 12 h at room temperature. The reaction mixture was filtered through a glass fibre filter and concentrated under reduced pressure, giving the target compound as an amorphous orange solid (20 mg, 99%).

^{1}H NMR (300 MHz, 298 K, THF-d_8): δ 6.93–6.90 (m, 2H), 6.87 (s, 2H), 6.28 (d, J = 3.8 Hz, 2H), 6.07 (d, J = 3.8 Hz, 2H), 2.35 (s, 3H), 2.22 (s, 6H), 1.91–1.80 (m, 8H), 1.28 (s, 12H), 1.24 (s, 12H), 1.11 (s, 12H), 1.09 (s, 12H).

6.10. Synthesis of PnDIPY complexes (chapter 3)

Synthesis of $\mathbf{5Sb^{Cl}}$



$\mathbf{5Sb^{Cl}}$

L5 (15.7 mg, 35 μmol, 1.00 equiv.) and LiHMDS (6.4 mg, 39 μmol, 1.10 equiv.) were combined in THF (0.9 mL) at −35 °C resulting in a light pink solution, which was kept at −35 °C for 30 minutes. The mixture was then added to a precooled solution of $SbCl_3$ (9.6 mg, 42 μmol, 1.20 equiv.). The reaction mixture was kept at −35 °C for 12 hours and was subsequently layered with *n*-hexane (0.5 mL) and allowed to warm to room temperature, resulting in the formation of a microcrystalline solid. The mother liquor was removed by filtration and the remaining solid was washed with cold *n*-hexane (1 mL). The solid was dissolved in CH_2Cl_2, filtered through glas fibre and dried under reduced pressure, yielding the target compound as a dark purple microcrystalline solid (15 mg, 67%).

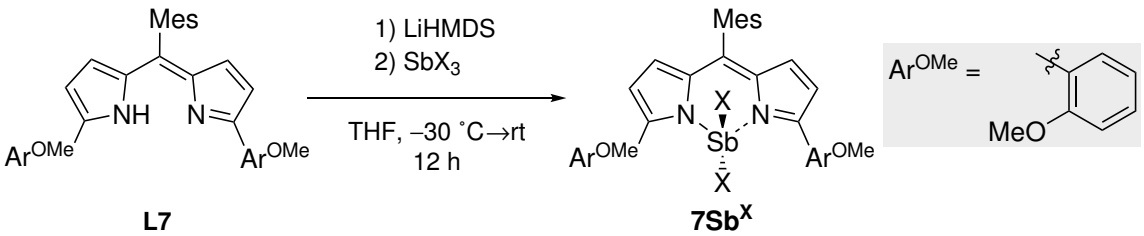
UV/Vis: λ_{abs}= 556 nm (CH_2Cl_2). **PL**: λ_{emi}= 602 nm (CH_2Cl_2).

^{1}H NMR (400 MHz, 298 K, CD_2Cl_2): δ 8.06–7.98 (m, 4H), 7.81 (s, 1H), 7.67–7.57 (m, 10H), 7.56–7.45 (m, 6H), 6.98 (s, 2H).

^{13}C{^{1}H} NMR (101 MHz, 298 K, CD_2Cl_2): δ 157.9, 151.0, 133.1, 133.0, 132.1, 131.8, 131.1, 130.7, 129.8, 129.5, 128.61, 118.7 (one signal not observed due to overlap).

Synthesis of 7Sb^{X} - General procedure E

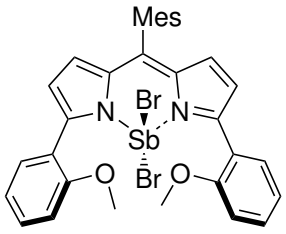
Complex synthesis was performed starting from a halide salt SbX_3 (see Scheme 90, where X= Br, Cl or F). At −30 °C, a THF solution of LiHMDS (0.2 M, 1.05 equiv.) was added to a THF solution of dipyrrin **L7** (0.2 M, 1.00 equiv.) and stirred for 30 minutes at room temperature, resulting in a colour change from red to magenta. The reaction mixture was subsequently cooled to −30 °C and added dropwise to a precooled THF solution (0.1 M) of SbX_3 (1.10 equiv.), resulting in an immediate colour change to dark magenta. The reaction mixture was then allowed to warm to room temperature without any stirring for circa 12 h, resulting in the formation of a crystalline precipitate (this process can be accelerated through addition of a small amount of *n*-hexane to the reaction mixture). The solvent was removed *via* cannula filtration and the crude product was washed with *n*-hexane, followed by *n*-pentane until the filtrate was barely coloured. The final products **7Sb^{X}** were obtained as solids after drying under reduced pressure.



L7 **7Sb^{X}**

Scheme 90: General reaction scheme for synthesis **7Sb^{X}** complexes (X = Br, Cl and F).

Synthesis of 7Sb^{Br}



7Sb^{Br}

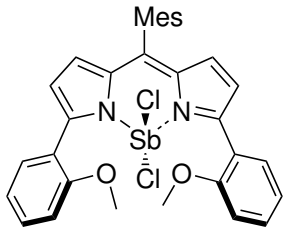
SBDIPY complex **7Sb^{Br}** was prepared following the general procedure **E** starting from **L7** (180 mg, 0.38 mmol). The product was obtained as a burgundy amorphous solid (235 mg, 82% yield). Suitable single crystals for X-ray diffraction analysis were grown from a saturated solution of THF/*n*-hexane at room temperature.

UV/Vis: λ_{abs} = 563 nm (CH_2Cl_2). **PL**: λ_{emi}= 602 nm (CH_2Cl_2).

^{1}H NMR (500 MHz, 298 K, CD_2Cl_2): δ 7.81 (dd, *J* = 7.5, 1.7 Hz, 2H), 7.53 (ddd, *J* = 8.4, 7.5, 1.7 Hz, 2H), 7.20–7.07 (m, 4H), 7.07–7.01 (m, 2H), 6.91 (d, *J* = 4.4 Hz, 2H), 6.77 (d, *J* = 4.3 Hz, 2H), 4.04 (s, 6H), 2.40 (s, 3H), 2.25 (s, 6H);

^{13}C{^{1}H} NMR (126 MHz, 298 K, CD_2Cl_2): δ 157.2, 156.5, 146.3, 139.2, 137.8, 136.2, 135.1, 133.0, 132.7, 131.3, 128.4, 122.4, 121.9, 121.8, 112.5, 56.3, 21.3, 20.5.

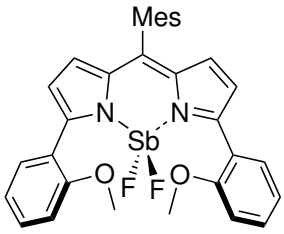
Synthesis of 7Sb^{Cl}



7Sb^{Cl}

SBDIPY complex **7Sb^{Cl}** was prepared following the general procedure **E** starting from **L7** (42 mg, 0.088 mmol). The product was obtained as a dark crystalline solid with a metallic lustre (47 mg, 80% yield). Suitable single crystals for X-ray diffraction analysis were grown from a saturated solution of THF/*n*-hexane at room temperature.
UV/Vis: λ_{abs}= 560 nm (CH_2Cl_2). **PL**: λ_{emi}= 601 nm (CH_2Cl_2).
^{1}H NMR (500 MHz, 298 K, CD_2Cl_2): δ 7.83 (dd, *J* = 7.6, 1.7 Hz, 2H), 7.55–7.48 (m, 2H), 7.19–7.10 (m, 4H), 7.03 (s, 2H), 6.87 (d, *J* = 4.4 Hz, 2H), 6.77 (d, *J* = 4.4 Hz, 2H), 4.02 (s, 6H), 2.40 (s, 3H), 2.24 (s, 6H);
^{13}C{^{1}H} NMR (126 MHz, 298 K, CD_2Cl_2): δ 156.9, 156.5, 146.1, 139.1, 137.7, 136.0, 134.6, 133.2, 132.6, 131.6, 128.4, 122.4, 121.7, 121.6, 112.5, 56.1, 21.3, 20.3.

Synthesis of 7Sb^{F}



7Sb^{F}

SBDIPY complex **7Sb^{F}** was prepared following a slightly modified procedure **E** starting from **L7** (58 mg, 0.12 mmol) but leaving the reaction mixture at −30 °C for 12 h. The product was obtained as a purple amorphous solid (69 mg, 89% yield). Suitable single crystals for X-ray diffraction analysis were grown from a saturated solution of THF/*n*-hexane at room temperature. The compound decomposed readily upon exposure to air and therefore needs to be stored at low temperatures (−30 °C) under inert conditions.

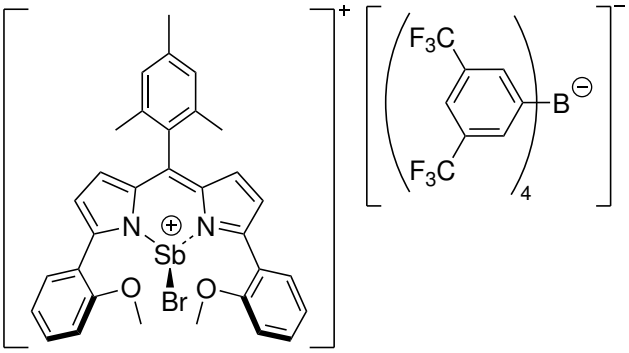
UV/Vis: λ_{abs}= 555, 601 nm (CH_2Cl_2). **PL**: λ_{emi}= 593 nm (CH_2Cl_2).

^{1}H NMR (500 MHz, 298 K, CD_2Cl_2): δ 7.62 (d, *J* = 7.6 Hz, 2H), 7.50–7.42 (m, 2H), 7.15–7.04 (m, 4H), 6.99 (s, 2H), 6.75 (d, *J* = 4.2 Hz, 2H), 6.65 (d, *J* = 4.2 Hz, 2H), 3.98 (s, 6H), 2.39 (s, 3H), 2.29–2.12 (m, 6H);

^{19}F NMR (470 MHz, 298 K, CD_2Cl_2): δ −88.1 (s);

^{13}C{^{1}H} NMR (126 MHz, 298 K, CD_2Cl_2): δ 158.3, 156.4, 145.2, 139.9, 138.4, 134.1, 132.4, 131.5, 131.3, 128.3, 128.2, 123.2, 121.7, 121.1, 112.3, 56.2, 21.3, 20.1.

Synthesis of 7Sb^{+}[BArF]



7Sb^{+}[BArF]

A suspension of sodium tetrakis[3,5-bis(trifluoromethyl)phenyl]borate (39 mg, 0.044 mmol, 1.10 equiv.) in CH_2Cl_2 (0.5 mL) was added to a solution of **7Sb^{Br}** (30 mg, 0.040 mmol, 1.00 equiv.) in CH_2Cl_2 (0.5 mL) at −30 °C, resulting in an subtle colour change from magenta to burgundy. The reaction mixture was allowed to warm to room temperature and after 1 h passed through a glass fibre filter. The product was obtained as a dark purple foam (51 mg, 83% yield) after trituration with *n*-pentane, followed by removal of solvent under reduced pressure. Suitable single crystals for X-ray diffraction analysis were grown from a saturated solution of CH_2Cl_2 and *n*-dodecane at room temperature.

UV/Vis: λ_{abs}= 577 nm (CH_2Cl_2). **PL**: λ_{emi}= 616 nm (CH_2Cl_2).

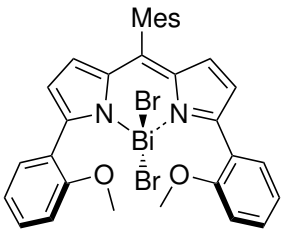
^{1}H NMR (500 MHz, 298 K, CD_2Cl_2): δ 7.75–7.69 (m, 8H), 7.59 (ddd, *J* = 8.4, 7.5, 1.7 Hz, 2H), 7.55 (s, 4H), 7.51 (dd, *J* = 7.7, 1.7 Hz, 2H), 7.25 (td, *J* = 7.6, 1.0 Hz, 2H), 7.21 (d, *J* = 8.2 Hz, 2H), 7.12 (d, *J* = 4.4 Hz, 2H), 7.06 (d, *J* = 7.1 Hz, 2H), 6.79 (d, *J* = 4.3 Hz, 2H), 4.07 (s, 6H), 2.40 (s, 3H), 2.35 (s, 3H), 2.06 (s, 3H);

^{11}B{^{1}H} NMR (161 MHz, 298 K, CD_2Cl_2): δ −6.6 (s);

^{19}F NMR (470 MHz, 298 K, DCM): δ −62.9 (s);

^{13}C{^{1}H} NMR (126 MHz, 298 K, CD_2Cl_2): δ 162.1 (q, J_{C-B}= 50 Hz), 159.3, 153.6, 147.8, 140.3, 138.8, 137.8, 137.5, 136.8, 135.2, 134.1, 132.4, 130.9, 129.2 (m), 128.9, 128.8, 125.0 (q, J_{C-F}= 272 Hz), 124.6, 122.3, 120.6, 117.9 (m), 114.5, 57.7, 21.3, 21.0, 19.7.

Synthesis of 7Bi^{Br}



7Bi^{Br}

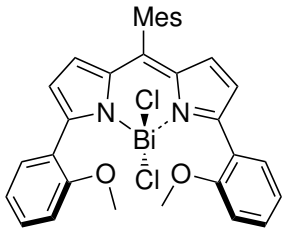
BIDIPY complex **7Bi^{Br}** was prepared starting from **L7^{K}** (171 mg, 0.33 mmol, 1.00 equiv.) and $BiBr_3$ (149 mg, 0.33 mmol, 1.00 equiv.). The two compounds were separately dissolved in THF (0.2 M) and the ligand was slowly added to the $BiBr_3$ solution at −30 °C, resulting in a subtle colour change to light purple. The reaction mixture was allowed to warm to room temperature over the course of 3 h, resulting in the formation of a crystalline precipitate. The solvent was removed *via* cannula filtration and the remaining solid was washed with *n*-hexane and dried under reduced pressure, affording **7Bi^{Br}** as a dark blue-purple crystalline solid (203 mg, 72% yield). Suitable single crystals for X-ray diffraction analysis were grown from a saturated solution of THF/*n*-hexane at room temperature.

UV/Vis: λ_{abs} = 561 nm (CH_2Cl_2). **PL**: λ_{emi}= 590 nm (CH_2Cl_2).

^{1}H NMR (500 MHz, 298 K, CD_2Cl_2): δ 7.61 (d, *J* = 7.5 Hz, 2H), 7.53–7.48 (m, 2H), 7.22–7.14 (m, 4H), 7.00 (s, 2H), 6.97 (d, *J* = 4.3 Hz, 2H), 6.88 (d, *J* = 4.3 Hz, 2H), 4.22 (s, 6H), 2.39 (s, 3H), 2.25 (s, 6H);

^{13}C{^{1}H} NMR (126 MHz, 298 K, CD_2Cl_2): δ 158.7, 155.2, 149.1, 138.8, 138.3, 137.8, 136.0, 134.2, 132.0, 131.9, 128.3, 124.0, 123.5, 121.6, 113.7, 58.2, 21.3, 20.7.

Synthesis of 7Bi^{Cl}



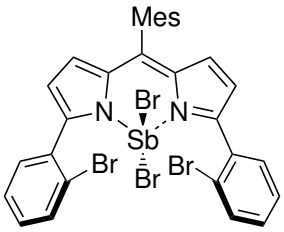
7Bi^{Cl}

BIDIPY complex **7Bi^{Cl}** was prepared starting from **L7^{K}** (200 mg, 0.39 mmol, 1.00 equiv.) and $BiCl_3$ (123 mg, 0.39 mmol, 1.00 equiv.). The two compounds were separately dissolved in THF (0.2 M) and the ligand was slowly added to the $BiBr_3$ solution at −30 °C, resulting in a subtle colour change to dark purple. The reaction mixture was allowed to warm to room temperature over the course of 12 h, resulting in the formation of a dark precipitate. The solvent was decanted and the remaining solid was washed with *n*-hexane and dried under reduced pressure, affording **7Bi^{Cl}** as a dark green amorphous solid (166 mg, 56% yield).

^{1}H NMR (400 MHz, 298 K, CD_2Cl_2): δ 7.65 (dd, J = 7.9, 1.7 Hz, 2H), 7.55–7.46 (m, 2H), 7.23–7.14 (m, 4H), 7.00 (s, 2H), 6.96 (d, J = 4.3 Hz, 2H), 6.88 (d, J = 4.3 Hz, 2H), 4.18 (s, 6H), 2.39 (s, 3H), 2.23 (s, 6H).[xi]

[xi] unfortunately, no sufficiently clean ^{13}C data was obtained for this compound.

Synthesis of 8Sb^{Br}



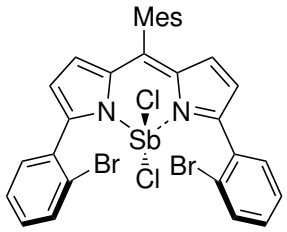
8Sb^{Br}

At −30 °C, a THF solution (0.4 M) of LiHMDS (30 mg, 0.18 mmol 1.01 equiv.) was added to a THF solution (0.4 M) of dipyrrin **L8** (100 mg, 0.17 mmol 1.00 equiv.) and stirred for 30 minutes at room temperature, resulting in a colour change from red to pink. The reaction mixture was subsequently cooled to −30 °C and added dropwise to a precooled THF solution (0.3 M) of $SbBr_3$ (64 mg, 0.18 mmol, 1.02 equiv.), resulting in an immediate colour change to dark red. The reaction mixture was layered with *n*-hexane (0.4 mL) and allowed to warm to room temperature without any stirring for 12 h, resulting in the formation of a crystalline precipitate. The solvent was removed *via* cannula filtration and the crude product was washed with *n*-hexane, followed by *n*-pentane until the filtrate was barely coloured. The target compound was obtained as a dark red crystalline solid (161 mg, 92% yield). **UV/Vis**: λ_{abs} = 535 nm (CH_2Cl_2). **PL**: λ_{emi}= 572 nm (CH_2Cl_2).

^{1}H NMR (500 MHz, 298 K, CD_2Cl_2): δ 8.26 (dd, *J* = 7.6, 1.7 Hz, 2H), 7.81 (dd, *J* = 8.1, 1.2 Hz, 2H), 7.53 (t, *J* = 7.6 Hz, 2H), 7.43 (td, *J* = 7.6, 1.7 Hz, 2H), 7.05 (s, 2H), 6.97 (d, *J* = 4.3 Hz, 2H), 6.87 (d, *J* = 4.3 Hz, 2H), 2.41 (s, 3H), 2.24 (s, 6H);

^{13}C{^{1}H} NMR (126 MHz, 298 K, CD_2Cl_2): δ 157.2, 148.7, 139.6, 137.5, 135.2, 134.9, 134.4, 133.0, 132.6, 132.3, 130.3, 128.8, 128.6, 124.6, 122.7, 21.4, 20.3.

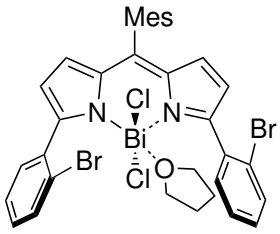
Synthesis of 8Sb^{Cl}



8Sb^{Cl}

At −30 °C, a THF solution (0.2 M) of LiHMDS (184 mg, 1.10 mmol 1.05 equiv.) was added to a THF solution (0.1 M) of dipyrrin **L8** (600 mg, 1.05 mmol 1.00 equiv.) and stirred for 30 minutes at room temperature, resulting in a colour change from red to pink. The reaction mixture was subsequently cooled to −78 °C and added dropwise to a precooled THF solution (0.1 M) of $SbCl_3$ (263 mg, 1.15 mmol, 1.10 equiv.), resulting in an immediate colour change to dark red. The reaction mixture was allowed to warm to room temperature without any stirring for 12 h. Subsequently the mixture was concentrated to circa half of the original solvent volume and *n*-hexane (5.0 mL) was added, resulting in the formation of a precipitate. After additional 2 h at room temperature, the solvent was removed *via* cannula filtration and the crude product was washed with *n*-hexane, followed by *n*-pentane until the filtrate was barely coloured. The target compound was obtained as an amorphous pink solid (646 mg, 81% yield).
UV/Vis: λ_{abs} = 532 nm (CH_2Cl_2). **PL**: λ_{emi}= 569 nm (CH_2Cl_2).
^{1}H NMR (500 MHz, 298 K, CD_2Cl_2): δ 8.16 (dd, *J* = 7.5, 1.7 Hz, 2H), 7.81 (dd, *J* = 8.0, 1.2 Hz, 2H), 7.52 (t, *J* = 7.5 Hz, 2H), 7.42 (td, *J* = 7.8, 1.7 Hz, 2H), 7.05 (s, 2H), 6.92 (d, *J* = 4.3 Hz, 2H), 6.86 (d, *J* = 4.3 Hz, 2H), 2.41 (s, 3H), 2.23 (s, 6H);
^{13}C{^{1}H} NMR (126 MHz, 298 K, CD_2Cl_2): δ 157.1, 148.6, 139.6, 137.4, 135.0, 134.8, 134.0, 132.9, 132.7, 132.4, 131.2, 128.8, 128.5, 124.6, 122.2, 21.4, 20.2.

Synthesis of 8Bi^{Cl}



8Bi^{Cl}

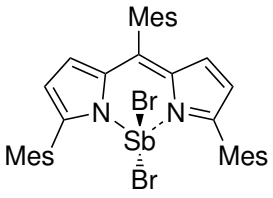
BIDIPY complex **8Bi^{Cl}** was prepared starting from **L8^{K}** (50 mg, 0.082 mmol, 1.00 equiv.) and $BiCl_3$ (26 mg, 0.082 mmol, 1.00 equiv.). The two compounds were separately dissolved in THF (0.2 M) and the ligand was slowly added to the $BiCl_3$ solution at −30 °C, resulting in a subtle colour change to dark red. The reaction mixture was allowed to warm to room temperature over the course of 3 h, resulting in the formation of a microcrystalline precipitate. The solvent was decanted and the remaining solid was washed with *n*-hexane and dried under reduced pressure, affording **8Bi^{Cl}** as a dark red microcrystalline solid (59 mg, 78% yield considering one coordinated unit of THF). Suitable single crystals for X-ray diffraction analysis were grown from a saturated solution of THF/*n*-hexane at room temperature.

UV/Vis: λ_{abs} = 537 nm (CH_2Cl_2). **PL**: λ_{emi}= 596 nm (CH_2Cl_2).

^{1}H NMR (500 MHz, 298 K, CD_2Cl_2): δ 8.08 (dd, *J* = 7.5, 1.7 Hz, 2H), 7.83 (d, *J* = 8.0 Hz, 2H), 7.54 (t, *J* = 7.5 Hz, 2H), 7.42 (td, *J* = 7.8, 1.7 Hz, 2H), 7.03 (s, 2H), 6.99 (d, *J* = 4.4 Hz, 2H), 6.94 (d, *J* = 4.4 Hz, 2H), 3.70–3.66 (m, THF), 2.41 (s, 3H), 2.23 (s, 6H), 1.86–1.77 (m, THF);

^{13}C{^{1}H} NMR (126 MHz, 298 K, CD_2Cl_2): δ 157.5, 151.3, 139.3, 137.4, 136.6, 135.6, 134.0, 133.8, 133.2, 132.8, 129.9, 129.4, 128.4, 124.6, 123.6, 68.2, 26.0, 21.4, 20.2.

Synthesis of 9Sb^{Br} [xii]



9Sb^{Br}

At −30 °C, a THF solution (0.4 M) of LiHMDS·0.75 Et_2O (93 mg, 0.41 mmol, 1.02 equiv.) was added to a THF solution (0.8 M) of dipyrrin **L9** (200 mg, 0.40 mmol 1.00 equiv.) and stirred for 1.5 hour at room temperature, resulting in a colour change from orange to red-orange. The reaction mixture was subsequently cooled to −30 °C and added dropwise to a precooled THF solution (0.4 M) of $SbBr_3$ (148 mg, 0.41 mmol, 1.02 equiv.), resulting in no apparent colour change. The reaction mixture was layered with *n*-hexane (1.0 mL) and allowed to warm to room temperature without any stirring for 12 h. Subsequently, the reaction mixture was concentrated under reduced pressure and additional *n*-hexane was added until the formation of a bright red precipitate was observed. The solvent was removed *via* cannula filtration and the crude product was washed with *n*-pentane (4×3 mL) and dried under reduced pressure, affording the target compound as an amorphous red solid (170 mg, 54% yield). *Note: due to the high solubility of **9Sb^{Br}** in non-polar solvents, extraction with benzene is recommended (see procedure for **9Sb^{Cl}**).*

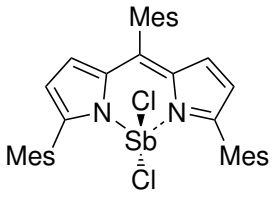
UV/Vis: λ_{abs} = 515 nm (toluene). **PL**: λ_{emi}= 550, 738 nm (toluene).

^{1}H NMR (500 MHz, 298 K, CD_2Cl_2): δ 7.06–7.02 (m, 2H), 6.98 (d, *J* = 4.2 Hz, 2H), 6.94–6.90 (m, 4H), 6.53 (d, *J* = 4.2 Hz, 2H), 2.41 (s, 3H), 2.30 (s, 6H), 2.29 (s, 12H), 2.25 (s, 6H);

^{13}C{^{1}H} NMR (126 MHz, 298 K, CD_2Cl_2): δ 160.4, 148.0, 141.5, 139.4, 139.0, 137.6, 135.7, 134.4, 132.5, 129.1, 128.5, 127.7, 121.6, 22.6, 21.4, 21.4, 20.5.

[xii] Synthesis and NMR characterization were carried out by L. Mohr during a research internship.

Synthesis of 9Sb^{Cl} [xiii]

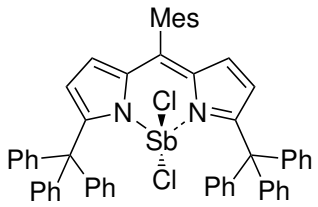


9Sb^{Cl}

At −30 °C, a THF solution (0.3 M) of LiHMDS·0.75 Et_2O (239 mg, 1.05 mmol, 1.05 equiv.) was added to a THF solution (0.3 M) of dipyrrin **L9** (500 mg, 1.00 mmol 1.00 equiv.) and stirred for 2 hours at room temperature, resulting in a colour change from orange to red-orange. The reaction mixture was subsequently cooled to −30 °C and added dropwise to a precooled THF solution (0.2 M) of $SbCl_3$ (240 mg, 1.05 mmol, 1.05 equiv.), resulting in no apparent colour change. The reaction mixture was layered with *n*-hexane (0.5 mL) and allowed to warm to room temperature without any stirring for 12 h. The reaction mixture was filtered over glas fibre and dried under reduced pressure. The crude product was extracted with benzene (15 mL) and the filtrate was concentrated under reduced pressure. The resulting solid was washed with *n*-hexane (3×4 mL) and dried under reduced pressure for several hours, giving the target compound as an amorphous orange solid (557 mg, 81% yield).
UV/Vis: λ_{abs} = 512 nm (CH_2Cl_2). **PL**: λ_{emi}= 544 nm (CH_2Cl_2).
^{1}H NMR (500 MHz, 298 K, C_6D_6): δ 6.74 (s, 2H), 6.73 (s, 4H), 6.71 (d, *J* = 4.2 Hz, 2H), 5.98 (d, *J* = 4.2 Hz, 2H), 2.44 (s, 12H), 2.25 (s, 6H), 2.18 (s, 3H), 2.06 (s, 6H);
^{13}C{^{1}H} NMR (126 MHz, 298 K, C_6D_6): δ 159.8, 147.2, 140.7, 139.1, 138.6, 137.5, 134.4, 133.8, 133.2, 128.9, 128.6, 128.3, 120.3, 22.2, 21.2, 21.2, 20.2.

[xiii] Synthesis and NMR characterization were carried out by L. Mohr during a research internship.

Synthesis of 10Sb^{Cl} [xiv]



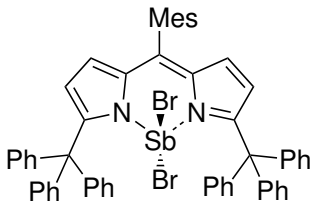
10Sb^{Cl}

At −30 °C, a THF solution (0.2 M) of LiHMDS (11 mg, 0.068 mmol 1.02 equiv.) was added to a THF solution (0.2 M) of dipyrrin **L10** (50 mg, 0.067 mmol 1.00 equiv.) and stirred for 20 minutes at room temperature. The reaction mixture was subsequently cooled to −30 °C and added dropwise to a precooled THF solution (0.2 M) of $SbCl_3$ (16 mg, 0.070 mmol, 1.04 equiv.), resulting in no apparent colour change. The reaction mixture was allowed to warm to room temperature without any stirring for 12 h. Subsequent layering with *n*-hexane (0.5 mL) led to the formation of a crystalline orange precipitate. The reaction mixture was filtered over glas fibre and the residue was dried under reduced pressure, giving the crude product as an orange solid (circa 15 mg, 24% yield).

^{1}H NMR (400 MHz, 298 K, CD_2Cl_2): δ 7.35–7.29 (m, 18H), 7.28–7.22 (m, 12H), 6.97–6.92 (m, 2H), 6.60 (d, J = 4.5 Hz, 2H), 6.24 (d, J = 4.5 Hz, 2H), 2.35 (s, 3H), 2.17 (s, 6H).

[xiv] The compound was only isolated in a small quantity and scalability of the provided procedure was found to be limited. A successful alternative method is given for **10Sb^{Br}** and **10Bi^{Br}**.

Synthesis of 10Sb^{Br}



10Sb^{Br}

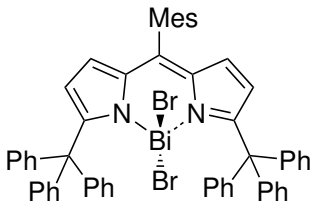
SBDIPY complex **10Sb^{Br}** was prepared starting from **L10^{K}** (50 mg, 0.064 mmol, 1.00 equiv.) and $SbBr_3$ (23 mg, 0.064 mmol, 1.00 equiv.). The two compounds were separately dissolved in THF and the ligand (0.1 M) was added to the $SbBr_3$ solution (0.2 M) at −30 °C, resulting in a colour change from red-orange to dark red. The reaction mixture was layered with *n*-hexane (0.2 mL) and allowed to warm to room temperature over the course of 4 h, resulting in the formation of a microcrystalline precipitate. The solvent was decanted and the remaining solid was washed with *n*-hexane (5 mL) and dried under reduced pressure, affording **10Sb^{Br}** as a red microcrystalline solid (49 mg, 75% yield).

UV/Vis: λ_{abs} = 523 nm (CH_2Cl_2). **PL**: λ_{emi}= 545 nm (CH_2Cl_2).

^{1}H NMR (500 MHz, 298 K, CD_2Cl_2): δ 7.39–7.36 (m, 12H), 7.35–7.31 (m, 6H), 7.28–7.24 (m, 12H), 6.97–6.93 (m, 2H), 6.64 (d, *J* = 4.5 Hz, 2H), 6.19 (d, *J* = 4.5 Hz, 2H), 2.35 (s, 3H), 2.20 (s, 6H);

^{13}C{^{1}H} NMR (126 MHz, 298 K, CD_2Cl_2): δ 167.1, 146.0, 143.7, 138.9, 137.6, 135.2, 133.5, 133.4, 132.6, 128.7, 128.7, 128.2, 125.4, 63.8, 21.3, 20.3.

Synthesis of 10Bi^{Br}



10Bi^{Br}

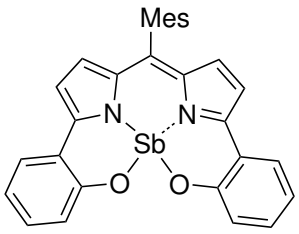
BIBDIPY complex **10Bi^{Br}** was prepared starting from **L10^{K}** (50 mg, 0.064 mmol, 1.00 equiv.) and $BiBr_3$ (29 mg, 0.064 mmol, 1.00 equiv.). The two compounds were separately dissolved in THF and the ligand (0.1 M) was added to the $BiBr_3$ solution (0.2 M) at −30 °C, resulting in a colour change from red-orange to dark red. The reaction mixture was layered with *n*-hexane (0.2 mL) and allowed to warm to room temperature over the course of 4 h, resulting in the formation of a a precipitate. The solvent was decanted and the remaining solid was washed with *n*-hexane (5 mL) and dried under reduced pressure, affording **10Sb^{Br}** as a red amorphous solid (51 mg, 72% yield).

UV/Vis: λ_{abs} = 525 nm (CH_2Cl_2). **PL**: λ_{emi}= 544 nm (weak, CH_2Cl_2).

^{1}H NMR (500 MHz, 298 K, CD_2Cl_2): δ 7.40–7.34 (m, 18H), 7.33–7.27 (m, 12H), 6.94 (s, 2H), 6.61 (d, *J* = 4.5 Hz, 2H), 6.33 (d, *J* = 4.5 Hz, 2H), 2.35 (s, 3H), 2.19 (s, 6H);

^{13}C{^{1}H} NMR (126 MHz, 298 K, CD_2Cl_2): δ 168.4, 148.4, 143.9, 138.5, 137.5, 136.5, 134.8, 133.3, 132.5, 128.9, 128.7, 128.1, 126.6, 63.8, 21.3, 20.2.

Synthesis of 12Sb



12Sb

At −35 °C, a THF solution (0.3 M) of LiHMDS (23 mg, 0.14 mmol 3.10 equiv.) was added to a THF solution (0.1 M) of dipyrrin **L12** (20 mg, 0.045 mmol 1.00 equiv.) and stirred for 20 minutes at room temperature, resulting in a colour change from magenta to blue. The reaction mixture was subsequently cooled to −35 °C and slowly added to a precooled THF solution (0.1 M) of $SbCl_3$ (11 mg, 0.050 mmol, 1.10 equiv.), resulting in an immediate colour change to light blue. The reaction mixture was kept at −35 °C and subsequently concentrated under reduced pressure. The crude product was washed with *n*-hexane (2×1 mL), dissolved in CH_2Cl_2 and dried under reduced pressure, giving the target compound as an amorphous black solid (13 mg, 51% yield).

Note 1: washing with n-hexane is not recommended as the product appeared to be partially soluble.

Note 2: The compound was obtained containing an unknown Si-related impurity.

Note 3: The compound was also prepared on NMR-scale in THF-d_8, using NaH (5.00 equiv.) as a base. No Si-related impurity was present following this method.

UV/Vis: λ_{abs} = 658 nm (CH_2Cl_2). **PL**: λ_{emi}= 697 nm (CH_2Cl_2).

^{1}H NMR (500 MHz, 298 K, CD_2Cl_2): δ 7.55 (dd, *J* = 8.1, 1.7 Hz, 2H), 7.30–7.23 (m, 2H), 7.02 (d, *J* = 8.1 Hz, 1H), 6.98 (s, 2H), 6.90–6.80 (m, 4H), 6.57 (d, *J* = 4.4 Hz, 2H), 2.37 (s, 3H), 2.22 (s, 3H), 2.12 (s, 3H);

^{13}C{^{1}H} NMR (126 MHz, 298 K, CD_2Cl_2): δ 159.7, 159.3, 141.2, 139.3, 138.7, 137.2, 137.0, 133.0, 132.7, 132.4, 128.5, 128.3, 128.1, 122.7, 120.5, 119.6, 117.0, 21.3, 20.4, 19.9.

6.11. Spectroscopic data of PnDIPY complexes (chapter 3)

An overview of absorption maxima of **7Sb^{Br}** in various solvents is provided in Table 20.

Table 20: UV/Vis spectroscopy solvent screening of **7Sb^{Br}**.

Solvent	Absorption maximum λ_{abs} (nm)
Acetonitrile	516 nm
Acetone	563 nm
Dichloromethane	563 nm
Tetrahydrofuran	563 nm
Toluene	558 nm

A summary of spectroscopic data of PnDIPY complexes described in Chapter 3 is provided in Table 21. Aggregation effects were noted for **L7** SBDIPYs at concentrations above 1 μM as absorption and excitation spectra showed discrepancies. While the absorption maxima were vitually unaffected by sample concentrations, emission maxima displayed subtle shifts (both values are reported below).

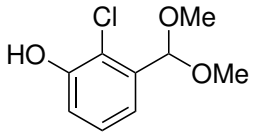
Table 21: Compilation of spectroscopic data of PnDIPY complexes (n.d. = not determined).

Complex	λ_{abs} (nm)	λ_{emi} (nm)	Stokes shift (cm^{-1})	ϵ ($M^{-1}\cdot cm^{-1}$)	Quantum yield Φ_{rel}
5Sb^{Cl}	556	602[a]	1374	n.d.	n.d.
7Sb^{Br}	563	597 (602)[a,b]	1012	62790	0.05
7Sb^{Cl}	560	597 (601)[a,b]	1107	75120	0.37
7Sb^{F}	555, 601	597 (593)[a,b]	1296	_[c]	_[c]
7Sb^{+}[BArF]	577	608 (616)[a,b]	884	54860	0.26
7Bi^{Br}	561	590[a]	876	84610	0.005
8Sb^{Br}	535	572[d]	1209	n.d.	n.d.
8Sb^{Cl}	532	569[d]	1222	n.d.	n.d.
8Bi^{Cl}	537	596[d]	1843	n.d.	n.d.
9Sb^{Br}[e]	550	596, 738[f]	5867	n.d.	n.d.
9Sb^{Cl}[e]	511	541[f]	1085	n.d.	n.d.
10Sb^{Br}	523	545[g]	772	n.d.	n.d.
10Bi^{Br}	525	544[g]	665	n.d.	n.d.
12Sb	658	697[h]	850	n.d.	n.d.

[a] λ_{exc} = 520 nm. [b] Refers to emission maximum of a 16 μM sample. [c] Not determined due to sample instability. [d] λ_{exc} = 500 nm. [e] recorded in toluene. [f] λ_{exc} = 515 nm. [g] λ_{exc} = 510 nm. [h] λ_{exc} = 570 nm.

6.12. Reagent synthesis (chapter 4)

Synthesis of 2-chloro-3-(dimethoxymethyl)phenol (26)



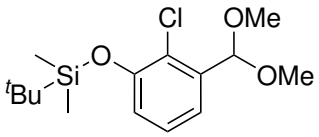
26

Compound **26** was prepared according to a literature-reported procedure.[204] Under ambient air, 2-chloro-3-hydroxybenzaldehyde (**25**, 3.18 g, 20.3 mmol, 1.00 equiv.) was dissolved in methanol (40 mL) at room temperature and trimethyl orthoformate (3.56 mL, 32.5 mmol, 1.60 equiv.) and tetrabutylammonium tribromide (490 mg, 5 mol%) were added to give a yellow solution. The mixture was stirred for 6 h at room temperature. Upon completion, the reaction mixture was diluted with ethyl acetate (150 mL) and the organic layer was washed with 0.01 M aqueous $NaHCO_3$ solution (2×100 mL). The organic phase was then dried over Na_2SO_4 and concentrated under reduced pressure, and purified by column chromatography on SiO_2 using *n*-hexane/ethyl acetate (8/2). Compound **26** was obtained as a colourless oil (3.71 g, 90% yield) after drying under reduced pressure. The compound contained trace amounts of starting material and was used as such for the next step without additional purification.

^{1}H NMR (300 MHz, 298 K, $CDCl_3$): δ 7.22–7.14 (m, 2H), 7.06–6.96 (m, 1H), 5.58 (s, 1H), 3.37 (s, 6H).

NMR data were in accordance with those previously reported.[204]

Synthesis of compound 27

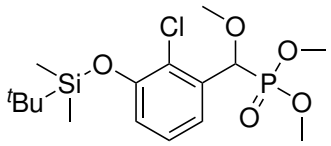


27

Compound **27** was prepared according to a literature-reported procedure.[204] Under ambient air, phenol **26** (2.20 g, 10.9 mmol, 1.00 equiv.) and imidazole (1.48 g, 21.7 mmol, 2.00 equiv.) were dissolved in CH_2Cl_2 (14 mL) and *tert*-butyldimethylsilyl chloride (1.96 g, 13.0 mmol, 1.20 equiv.) while stirring at room temperature, resulting in the formation of a white precipitate. The mixture was stirred for 2 h at room temperature whereupon the precipitate was filtered off and the mixture was concentrated under reduced pressure. The crude product was purified by column chromatography on SiO_2 using *n*-hexane/ethyl acetate (95/5) giving the target compound **27** in a mixture with the deprotected acetal as a colourless oil (3.00 g, 87% yield) after drying under reduced pressure. The compound was used for the next step without additional purification.

^{1}H NMR (300 MHz, 298 K, $CDCl_3$): δ 7.23 (d, J = 7.9 Hz, 1H), 7.14 (t, J = 8.0 Hz, 1H), 6.88 (dd, J = 8.0, 1.6 Hz, 1H), 5.63 (s, 1H), 3.37 (s, 6H), 1.03 (s, 9H), 0.22 (s, 6H).
NMR data were in accordance with those previously reported.[204]

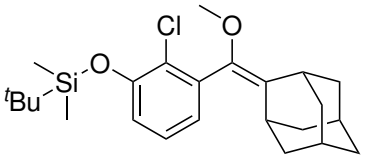
Synthesis of compound 28



28

Compound **28** was prepared according to a literature-reported procedure.[204] The mixture obtained for compound **27** (3.00 g, 9.5 mmol, 1.00 equiv.) and trimethyl phosphite (1.46 mL, 12.4 mmol, 1.31 equiv.) were dissolved in CH_2Cl_2 (25 mL). The reaction mixture was cooled to 0 °C and $TiCl_4$ (1.25 mL, 11.3 mmol, 1.20 equiv.) was added dropwise resulting in an orange-yellow reaction mixture. After 2 h at 0 °C, the reaction mixture was poured into a cold sat. $NaHCO_3$ solution (120 mL) at 0 °C and stirred for 10 minutes. The mixture was diluted with CH_2Cl_2 (100 mL) and the organic layer was extracted. The organic phase was dried over Na_2SO_4 and concentrated under reduced pressure. The resulting colourless oil was subjected to column chromatography on SiO_2 using *n*-hexane/ethyl acetate (4/6), yielding the target product as a colourless oil (3.10 g, 83% yield) after drying under reduced pressure.
^{1}H NMR (300 MHz, 298 K, $CDCl_3$): δ 7.33–7.23 (m, 1H, *overlap with $CDCl_3$*), 7.19 (t, *J* = 7.9 Hz, 1H), 6.88 (d, *J* = 7.9 Hz, 1H), 5.20 (d, *J* = 15.7 Hz, 1H), 3.79 (d, *J* = 10.6 Hz, 3H), 3.65 (d, *J* = 10.5 Hz, 3H), 3.36 (s, 3H), 1.03 (s, 9H), 0.23 (s, 6H).
NMR data were in accordance with those previously reported.[204]

Synthesis of compound 29

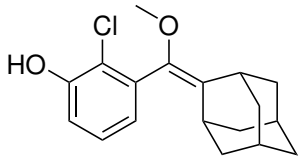


29

Compound **29** was prepared according to a literature-reported procedure.[204] Under an argon atmosphere, phosphonate **28** (3.35 g, 8.5 mmol, 1.00 equiv.) was dissolved in anhydrous THF (20 mL) and cooled to −78 °C. At this temperature, a solution of lithium diisopropylamide (2.0 M in THF, 10.2 mmol, 1.20 equiv.) was slowly added and the reaction mixture was stirred for 20 minutes. At −78 °C, a THF solution (20 mL) of adamantan-2-one (1.91 mL, 12.7 mmol, 1.50 equiv.) was added dropwise to the reaction mixture, resulting in a colour change from red to orange. The reaction mixture was stirred at −78 °C for 15 minutes and then allowed to warm to room temperature over the course of 12 h. The reaction mixture was diluted with ethyl acetate (150 mL) and the organic layer was washed with brine. The organic phase was extracted, dried over Na_2SO_4 and concentrated under reduced pressure. The crude product was subjected to column chromatography on SiO_2 using *n*-hexane/ethyl acetate (95/5), giving the target product as a white solid (1.99 g, 56% yield) after drying under reduced pressure.

^{1}H NMR (300 MHz, 298 K, $CDCl_3$): δ 7.13–7.05 (m, 1H), 6.97–6.82 (m, 2H), 3.31 (s, 3H), 3.27 (br s, 1H), 2.05 (s, 1H), 2.00–1.56 (m, 12H), 1.04 (s, 9H), 0.23 (s, 6H).
NMR data were in decent agreement with those previously reported.[204]

Synthesis of compound 30



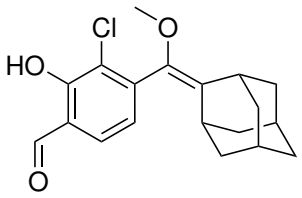
30

Compound **30** was prepared according to a literature-reported procedure.[204] Under ambient air, compound **29** (1.99 g, 5.0 mmol, 1.00 equiv.) was dissolved in THF (20 mL) and tetrabutylammonium fluoride (1.0 M, 5.5 mmol 1.10 equiv.) was added. The reaction mixture was stirred at room temperature for 4 h, resulting in a colour change from colourless to light yellow. The reaction mixture was diluted with ethyl acetate (100 mL) and washed with 1 M HCl (100 mL) to and brine (100 mL). The organic phase was extracted, dried over Na_2SO_4 and concentrated under reduced pressure. The crude product was subjected to column chromatography on SiO_2 using *n*-hexane/ethyl acetate (85/15), giving the target compound as a white solid (1.32 g, 86% yield) after drying under reduced pressure.

^{1}H NMR (400 MHz, 298 K, $CDCl_3$): δ 7.16 (t, J = 7.8 Hz, 1H), 7.00 (d, J = 7.9 Hz, 1H), 6.83 (d, J = 7.5 Hz, 1H), 5.69 (s, 1H), 3.31 (s, 3H), 3.28 (br s, 1H), 2.11 (s, 1H), 2.01–1.66 (m, 12H).

NMR data were in accordance with those previously reported.[204]

Synthesis of compound 31



31

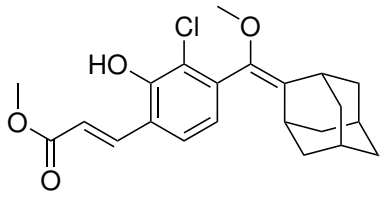
Compound **31** was prepared according to a modified literature-reported procedure.[205] Under ambient air, two 8 mL screw cap vials were charged with compound **30** (600 mg, 2.0 mmol, 1.00 equiv.), anhydrous $MgCl_2$ (412 mg, 4.3 mmol, 2.20 equiv.), triethylamine (600 μL, 4.3 mmol, 2.20 equiv.), paraformaldehyde (477 mg, 15.7 mmol, 8.00 equiv) and acetonitrile (4.0 mL). The mixture was briefly sonicated and heated at 94 °C for 24 h. After cooling to room temperature, the reaction mixture was diluted with CH_2Cl_2 (120 mL) and washed with 0.5 M aqueous HCl (60 mL). The organic phase was washed with brine (100 mL), extracted and dried over Na_2SO_4 before evaporating the solvent under reduced pressure. The crude product was subjected to column chromatography on SiO_2 using *n*-hexane/ethyl acetate (95/5), giving the target compound as a slightly yellow solid (680 mg, 52% yield) after drying under reduced pressure.

^{1}H NMR (500 MHz, 298 K, $CDCl_3$): δ 11.62 (s, 1H), 9.90 (s, 1H), 7.48 (d, *J* = 7.9 Hz, 1H), 6.98 (d, *J* = 7.9 Hz, 1H), 3.33 (s, 3H), 3.28 (br s, 1H), 2.07 (s, 1H), 1.99–1.59 (m, 12H);

^{13}C{^{1}H} NMR (126 MHz, 298 K, $CDCl_3$): δ 195.8, 157.7, 143.7, 139.0, 133.5, 131.0, 123.1, 123.0, 120.5, 57.7, 39.4, 39.2, 38.7, 38.6, 37.1, 33.1, 29.9, 28.4, 28.3.

NMR data were in decent agreement with those previously reported.[205]

Synthesis of compound 32



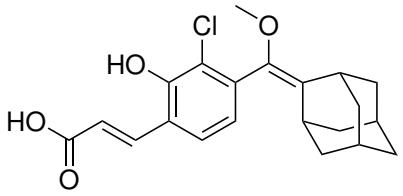
32

Compound **32** was prepared according to a literature-reported procedure.[206] Under ambient air, compound **31** (165 mg, 0.50 mmol, 1.00 equiv.) and methyl (triphenylphosphoranylidene)acetate (182 mg, 0.54 mmol, 1.10 quiv.) were dissolved in CH_2Cl_2 and stirred at room temperature for 30 minutes. The reaction mixture was then diluted with ethyl acetate and washed with 0.5 M aqueous HCl (50 mL), followed by brine (50 mL). The organic phase was dried over Na_2SO_4 and concentrated under reduced pressure. The crude product was subjected to column chromatography on SiO_2 using a *n*-hexane/ethyl acetate (60/40). After drying under reduced pressure, the target compound was obtained as a white solid (155 mg, 90% yield).

^{1}H NMR (300 MHz, 298 K, $CDCl_3$): δ 7.94 (d, *J* = 16.1 Hz, 1H), 7.37 (d, *J* = 8.0 Hz, 1H), 6.86 (d, *J* = 8.0 Hz, 1H), 6.61 (d, *J* = 16.1 Hz, 1H), 6.30 (s, 1H), 3.81 (s, 3H), 3.31 (s, 3H), 3.27 (br s, 1H), 2.12 (s, 1H), 2.00–1.63 (m, 12H);

^{13}C{^{1}H} NMR (126 MHz, 298 K, $CDCl_3$): δ 167.8, 150.7, 139.5, 139.3, 136.7, 133.0, 126.9, 123.8, 122.1, 121.6, 119.9, 57.4, 51.9, 39.2, 38.9, 37.2, 33.0, 29.9, 28.4. (*Note*: 3 signals not visible due to overlap) NMR data were in decent agreement with those previously reported.[206]

Synthesis of compound 33



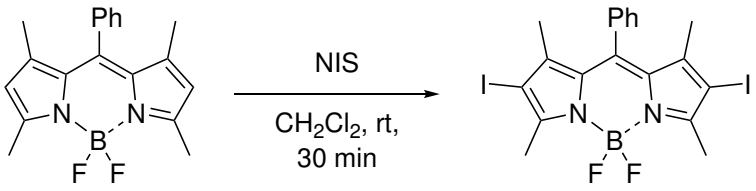
33

Compound **33** was prepared according to a literature-reported procedure.[203] Under ambient air, compound **32** (180 mg, 0.46 mmol, 1.00 equiv.) and NaOH (39 mg, 0.97 mmol, 2.10 quiv.) were dissolved in amixture of THF (3.5 mL) and H_2O (1.0 mL). The reaction mixture stirred at 60 °C for 4 h, going from a yellow solution to a bright fluorecent green colour. The reaction mixture was diluted with ethyl acetate (50 mL) and washed with 0.5 M aqueous HCl (50 mL), followed by water (50 mL). The organic phase was extracted with ethyl acetate (50 mL) and combined organic layers were dried over Na_2SO_4 and concentrated under reduced pressure. The crude product was subjected to column chromatography on SiO_2 using a slow gradient of *n*-hexane $\rightarrow$ *n*-hexane/ethyl acetate (85/15). After drying under reduced pressure, the target compound was obtained as a pale yellow solid (180 mg, 93% yield).

^{1}H NMR (500 MHz, 298 K, CD_3OD): δ 8.00 (d, *J* = 16.1 Hz, 1H), 7.49 (d, *J* = 8.0 Hz, 1H), 6.83 (d, *J* = 8.0 Hz, 1H), 6.59 (d, *J* = 16.1 Hz, 1H), 3.29 (s, 3H), 3.24 (br s, 1H), 2.08 (s, 1H), 2.00–1.71 (m, 12H);

^{13}C{^{1}H} NMR (126 MHz, 298 K, CD_3OD): δ 170.7, 153.5, 141.4, 141.0, 138.1, 132.5, 127.3, 124.5, 124.3, 123.4, 120.5, 57.3, 40.1, 40.0, 39.7, 39.6, 38.2, 34.3, 31.0, 29.9, 29.7. NMR data were in decent agreement with those previously reported, albeit displaying a slightly larger chemical shift as compared to literature.[203] The identity of the compound was verified with independently synthesized material provided by O. Green.

Synthesis of BDP-I



2B^F **BDP-I**

BODIPY dye **BDP-I** was prepared according to a modified literature-reported procedure.[302] BODIPY dye **2B^F** [xv] (34 mg, 0.10 mmol, 1.00 equiv.) was dissolved in anyhdrous CH_2Cl_2 (3.0 mL) and *N*-iodosuccinimide (NIS, 94 mg, 0.42 mmol, 4.00 equiv.) was added and the reaction mixture was stirred at room temperature for 30 minutes. Upon completion, the solution was washed with saturated aqueous $Na_2S_2O_3$ solution (3×10 mL) and the organic phase was extracted with ethyl acetate (3×10 mL). Combined organic layers were dried over Na_2SO_4 and concentrated under reduced pressure. The crude product was purified by flash colum chromatography on SiO_2 using CH_2Cl_2/*n*-hexane (1/1) as the eluent system. The target compound **BDP-I** was obtained as red crystalline solid (49 mg, 81% yield).

^{1}H NMR (500 MHz, 298 K, $CDCl_3$): δ 7.57–7.48 (m, 3H), 7.27–7.23 (m, 2H, *overlap with $CDCl_3$*), 2.65 (s, 6H), 1.39 (s, 6H);

^{13}C{^{1}H} NMR (126 MHz, 298 K, $CDCl_3$): δ 157.0, 145.5, 141.6, 134.9, 131.5, 129.7, 129.6, 128.0, 85.8, 17.0, 16.2;

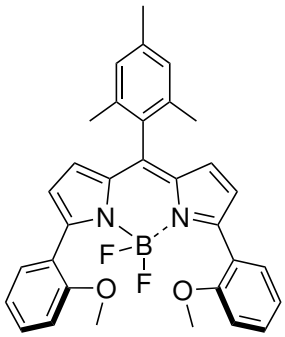
^{11}B{^{1}H} NMR (160 MHz, 298 K, $CDCl_3$): δ 0.56 (t, J_{B-F} = 32.6 Hz).

^{19}F NMR (470 MHz, 298 K, $CDCl_3$): δ −145.8 (q, J_{B-F} = 32.3 Hz).

NMR data were in good agreement with those previously reported.[302]

[xv] this compound was independently synthesized by Y. Song during a research internship.

Synthesis of 7B^F



7B^F

BODIPY dye **7B^F** was prepared according to a literature-reported procedure.[182] Dipyrrin **L7** (137 mg, 0.29 mmol, 1.00 equiv) and *N*-ethyldiisopropylamine (0.6 mL, 3.6 mmol, 12.6 equiv.) were dissolved in toluene (60 mL). While vigorously stirring, boron trifluoride-diethyletherate (0.6 mL, 5.0 mmol, 17.4 equiv.) was added and the reaction mixture was heated at 80 °C for 17 h, resulting in a gradual colour change from red to dark magenta. Upon cooling to room temperature, chloroform (100 mL) was added and the organic phase was washed with water (3×80 mL) and brine (100 mL). The organic phase was dried over Na_2SO_4 and concentrated under reduced pressure giving a dark purple oil. The crude product was subjected to column chromatography on SiO_2 using a gradient of *n*-hexane → *n*-hexane/chloroform (1/1) → chloroform. The target compound was obtained as a dark magenta amorphous solid (79 mg, 52% yield).

^{1}H NMR (500 MHz, 298 K, $CDCl_3$): δ 7.81 (dd, *J* = 7.7, 1.7 Hz, 2H), 7.33 (ddd, *J* = 8.4, 7.4, 1.7 Hz, 2H), 7.00 (td, *J* = 7.7, 1.1 Hz, 2H), 6.98–6.98 (m, 2H), 6.91 (dd, *J* = 8.4, 1.0 Hz, 2H), 6.60 (d, *J* = 4.1 Hz, 2H), 6.54 (d, *J* = 4.1 Hz, 2H), 3.78 (s, 6H), 2.38 (s, 3H), 2.24 (s, 6H);

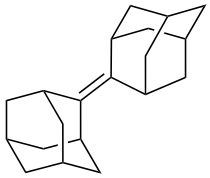
^{13}C{^{1}H} NMR (126 MHz, 298 K, $CDCl_3$): δ 157.8, 155.3, 143.1, 138.5, 137.1, 135.8, 132.2, 130.8, 130.7, 128.2, 128.2, 122.4, 122.4, 120.4, 111.1, 55.9, 21.3, 20.4;

^{11}B{^{1}H} NMR (160 MHz, 298 K, $CDCl_3$): δ 1.16 (t, J_{B-F} = 31.4 Hz).

^{19}F NMR (470 MHz, 298 K, $CDCl_3$): δ −138.5 (q, J_{B-F} = 31.2 Hz).

NMR data were in good agreement with those previously reported.[182]

Synthesis of adamantylideneadamanatane (38)



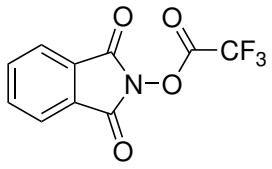
38

Adamantylideneadamanatane (**38**) was prepared according to a literature-reported procedure.[303] At 0 °C, $TiCl_4$ (1.57 mL, 14.3 mmol, 1.07 equiv.) was added to anhydrous THF (40 mL) giving a yellow slurry. Subsequently, Zn dust (1.86 g, 28.5 mmol, 2.14 equiv.) was added, followed by the addition of adamantan-2-one (2.00 g, 13.3 mmol, 1.00 equiv.) in THF (35 mL), affording a grey suspension. The reaction mixture was heated under reflux for 20 h and at 60 °C for additional 12 h. Upon cooling to room temperature, the reaction mixture was quenched with 10% aqueous K_2CO_3 (30 mL). The mixture was roughly filtered and the organic phase was extracted with diethyl ether (3×100 mL). Combined organic phases were dried over Na_2SO_4 and concentrated under reduced pressure giving a white solid. The crude product was subjected to column chromatography on SiO_2 using *n*-hexane, giving the target compound as a white crystalline solid (1.37 g, 77% yield) after drying under reduced pressure.

^{1}H NMR (500 MHz, 298 K, $CDCl_3$): δ 2.91 (s, 4H), 1.96–1.90 (m, 4H), 1.88–1.82 (m, 12H), 1.72–1.65 (m, 8H).

^{13}C{^{1}H} NMR (126 MHz, 298 K, $CDCl_3$): δ 133.37, 39.83, 37.56, 32.12, 28.78. NMR data were in good agreement with those previously reported.[304]

Synthesis of *N*-(trifluoromethyl)acyloxyphthalimide (76)



76

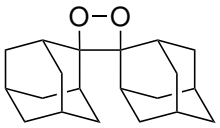
N-(trifluoromethyl)acyloxyphthalimide (**76**) was prepared according to a literature-reported procedure.[305] A 50 mL Schlenk flask was charged with *N*-Hydroxyphthalimide (1.50 g, 9.20 mmol, 1.00 equiv.), acetonitrile (9.0 mL) and trifluoroacetic anhydride (2.56 mL, 18.4 mmol, 2.00 equiv.) resulting in a clear solution. The reaction mixture was stirred at room temperature for 5.5 h, whereupon the mixture was concentrated under reduced pressure to afford the crude product as a white amorphous solid. The target compound was obtained after extended drying under reduced pressure (approximately 5 h) as a white amorphous solid (1.76 g, 74% yield).
^{1}H NMR (500 MHz, 298 K, C_6D_6): δ 7.16–7.07 (m, 2H), 6.75–6.67 (m, 2H);
^{19}F{^{1}H} NMR (471 MHz, 298 K, C_6D_6): δ −72.5 (s).
NMR data were in good agreement with those previously reported.[305]

6.13. Photocatalytic oxygenation reactions (chapter 4)

Photochemical oxidation reactions: general procedure F

A Schlenk tube equipped with a magnetic stirring bar was charged with photocatalyst **7Sb^{Br}**, starting material (1.00 equiv.) and solvent (0.1 M). Subsequently, the reaction mixture was frozen in liquid nitrogen, degassed one time and set under an oxygen atmosphere (circa 1.2 bar). The Schlenk tube was then placed in an LED reactor (Figure 82) and irradiated with 521 nm light for 12 h at 10°C.

Synthesis of adamantylideneadamantane-1,2-dioxetane (39)



39

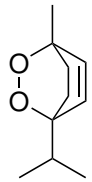
Dioxetane **39** was synthesized following the general procedure **F** starting from **38** (201 mg, 0.75 mmol, 1.00 equiv.) and **7Sb^{Br}** (0.5 mol%) in CH_2Cl_2 (7.5 mL). The product was purified by column chromatography on SiO_2 using a gradient of *n*-hexane $\rightarrow$ *n*-hexane/ethyl acetate (9/1). Dioxetane **39** was obtained as an off-white crystalline solid (185 mg, 82% yield) after drying under reduced pressure.

^{1}H NMR (500 MHz, 298 K, $CDCl_3$): δ 2.63 (s, 4H), 2.02–1.69 (m, 20H), 1.60–1.54 (m, 4H);

^{13}C{^{1}H} NMR (126 MHz, 298 K, $CDCl_3$): δ 95.9, 37.4, 34.8, 33.0, 32.0, 26.9, 26.7.

NMR data were in good agreement with those previously reported.[304]

Synthesis of ascaridole (39)



41

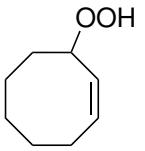
Endoperoxide **41** was synthesized following the general procedure **F** starting from α-terpinene (49 µL, 0.30 mmol, 1.00 equiv.) and **7Sb^{Br}** (0.25 mol%) in CH_2Cl_2 (3.0 mL). The product was purified by column chromatography on SiO_2 using a gradient of *n*-hexane $\rightarrow$ *n*-hexane/ethyl acetate (7/3). Ascaridrole (**41**) was obtained as a light pink oil (41 mg, 80% yield) after briefly drying under reduced pressure.

^{1}H NMR (500 MHz, 298 K, $CDCl_3$): δ 6.49 (d, *J* = 8.5 Hz, 1H), 6.41 (d, *J* = 8.5 Hz, 1H), 2.07–1.97 (m, 2H), 1.91 (sept, *J* = 6.8 Hz, 1H), 1.53–1.49 (m, 2H), 1.37 (s, 3H), 1.00 (s, 3H), 0.98 (s, 3H);

^{13}C{^{1}H} NMR (126 MHz, 298 K, $CDCl_3$): δ 136.5, 133.2, 79.9, 74.5, 32.2, 29.6, 25.7, 21.5, 17.4, 17.3.

NMR data were in good agreement with those previously reported.[306]

Synthesis of cyclooct-1-en-3-yl hydroperoxide (43)



43

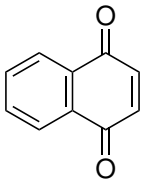
compound was not isolated

Hyroperoxide **43** was synthesized following the general procedure **F** starting from cyclooctene (39 µL, 0.30 mmol, 1.00 equiv.) and **7Sb^{Br}** (0.08 mol%) in CH_2Cl_2 (3.0 mL). Upon completion, the crude mixture was evaporated under reduced pressure and analyzed by ^{1}H NMR spectroscopy, which indicated a quantitative conversion of starting material to **43**.

^{1}H NMR (500 MHz, 298 K, $CDCl_3$): δ 8.09 br (s, 1H), 5.79–5.56 (m, 2H), 4.99–4.90 (m, 1H), 2.25–2.06 (m, 2H), 1.99–1.88 (m, 1H), 1.72–1.27 (m, 7H).

NMR data were in good agreement with those previously reported.[307]

Synthesis of naphthalene-1,4-dione (45)



45

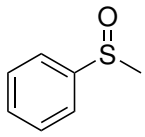
Quinone **45** was synthesized following the general procedure **F** starting from 1-naphthol (50 mg, 0.35 mmol, 1.00 equiv.) and **7Sb^{Br}** (5.0 mol%) in CH_2Cl_2 (3.5 mL). The product was purified by column chromatography on SiO_2 using a gradient of CH_2Cl_2 $\rightarrow$ CH_2Cl_2/acetone (9/1). Compound **45** was obtained as a yellow-brown crystalline solid (55 mg, 99% yield) after drying under reduced pressure.

^{1}H NMR (500 MHz, 298 K, $CDCl_3$): δ 8.07–8.01 (m, 2H), 7.75–7.70 (m, 2H), 6.95 (s, 2H);

^{13}C{^{1}H} NMR (126 MHz, 298 K, $CDCl_3$): δ 185.1, 138.7, 134.0, 131.9, 126.5.

NMR data were in good agreement with those previously reported.[308]

Synthesis of methyl phenyl sulfoxide (56a)



56a

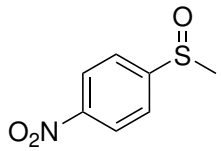
Sulfoxide **56a** was synthesized following the general procedure **F** starting from thioanisole (37 mg, 0.30 mmol, 1.00 equiv.) and **7Sb^{Br}** (1.0 mol%) in HFIP (3.0 mL). The product was purified by column chromatography on SiO_2 using a gradient of CH_2Cl_2 $\rightarrow$ CH_2Cl_2/acetone (9/1). Sulfoxide **56a** was obtained as a light pink oil (42 mg, 99% yield) after drying under reduced pressure.

^{1}H NMR (500 MHz, 298 K, $CDCl_3$): δ 7.65–7.58 (m, 2H), 7.53–7.43 (m, 3H), 2.69 (s, 3H);

^{13}C{^{1}H} NMR (126 MHz, 298 K, $CDCl_3$): δ 145.6, 131.1, 129.4, 123.5, 43.9.

NMR data were in good agreement with those previously reported.[309]

Synthesis of 1-(methylsulfinyl)-4-nitrobenzene (56b)



56b

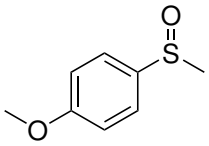
Sulfoxide **56b** was synthesized following the general procedure **F** starting from 4-nitrothioanisole (51 mg, 0.30 mmol, 1.00 equiv.) and **7Sb^{Br}** (5.0 mol%) in HFIP (3.0 mL). The product was purified by column chromatography on SiO_2 using a gradient of $CH_2Cl_2 \rightarrow CH_2Cl_2$/acetone (7/3). Sulfoxide **56b** was obtained as a brown crystalline solid (55 mg, 99% yield) after drying under reduced pressure.

^{1}H NMR (500 MHz, 298 K, $CDCl_3$): δ 8.39–8.31 (m, 2H), 7.85–7.78 (m, 2H), 2.77 (s, 3H);

^{13}C{^{1}H} NMR (126 MHz, 298 K, $CDCl_3$): δ 153.3, 149.5, 124.7, 124.5, 43.9.

NMR data were in good agreement with those previously reported.[309]

Synthesis of 1-methoxy-4-(methylsulfinyl)benzene



56c

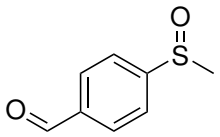
Sulfoxide **56c** was synthesized following the general procedure **F** starting from 4-methoxythioanisole (46 mg, 0.30 mmol, 1.00 equiv.) and **7Sb^{Br}** (1.0 mol%) in HFIP (3.0 mL). The product was purified by column chromatography on SiO_2 using a gradient of $CH_2Cl_2 \rightarrow CH_2Cl_2$/acetone (9/1). Sulfoxide **56c** was obtained as a light pink oil (37 mg, 78% yield) after drying under reduced pressure.

^{1}H NMR (500 MHz, 298 K, $CDCl_3$): δ 7.58–7.50 (m, 2H), 7.01–6.95 (m, 2H), 3.80 (s, 3H), 2.64 (s, 3H);

^{13}C{^{1}H} NMR (126 MHz, 298 K, $CDCl_3$): δ 162.0, 136.7, 125.5, 114.9, 55.5, 44.0.

NMR data were in good agreement with those previously reported.[310]

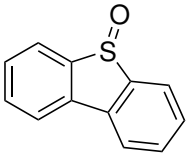
Synthesis of 4-(methylsulfinyl)benzaldehyde (56d)



56d

Sulfoxide **56d** was synthesized following the general procedure **F** starting from 4-(methylthio)benzaldehyde (46 mg, 0.30 mmol, 1.00 equiv.) and **7Sb^{Br}** (1.0 mol%) in HFIP (3.0 mL). The product was purified by column chromatography on SiO_2 using a gradient of CH_2Cl_2 → CH_2Cl_2/acetone (9/1). Sulfoxide **56d** was obtained as a white amorphous solid (37 mg, 72% yield) after drying under reduced pressure.
^{1}H NMR (500 MHz, 298 K, $CDCl_3$): δ 10.04 (s, 1H), 8.04 – 7.96 (m, 2H), 7.81 – 7.75 (m, 2H), 2.74 (s, 3H);
^{13}C{^{1}H} NMR (126 MHz, 298 K, $CDCl_3$): δ 191.1, 152.6, 138.2, 130.4, 124.2, 43.8.
NMR data were in good agreement with those previously reported.[309]

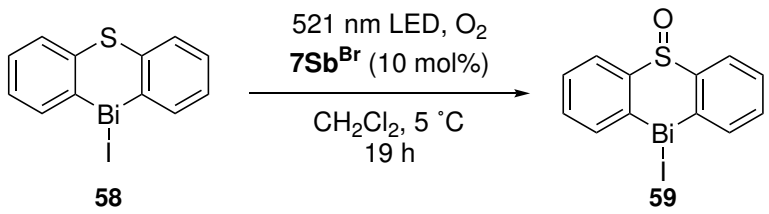
Synthesis of Dibenzo[b,d]thiophene 5-oxide (57)



57

Sulfoxide **57** was synthesized following the general procedure **F** starting from dibenzothiophene (55 mg, 0.30 mmol, 1.00 equiv.) and **7Sb^{Br}** (5.0 mol%) in HFIP (3.0 mL). The product was purified by column chromatography on SiO_2 using a gradient of CH_2Cl_2 → CH_2Cl_2/acetone (9/1). Sulfoxide **57** was obtained as a white crystalline solid (21 mg, 35% yield) after drying under reduced pressure.
^{1}H NMR (500 MHz, 298 K, $CDCl_3$): δ 7.99 (dt, *J* = 7.7, 0.9 Hz, 2H), 7.81 (dt, *J* = 7.7, 0.9 Hz, 2H), 7.60 (td, *J* = 7.6, 1.1 Hz, 2H), 7.50 (td, *J* = 7.5, 1.1 Hz, 2H);
^{13}C{^{1}H} NMR (126 MHz, 298 K, $CDCl_3$): δ 145.4, 137.2, 132.7, 129.7, 127.7, 122.0.
NMR data were in good agreement with those previously reported.[311]

Synthesis of 10-iodophenothiabismine 5-monoxide (59)



58 **59**

Sulfoxide **59** was synthesized following a modified general procedure **F** starting from 10-iodophenothiabismine (104 mg, 0.20 mmol, 1.00 equiv.) and **7Sb^{Br}** (10 mol%) in CH_2Cl_2 (2.0 mL). The reaction was performed at 5 °C with an irradiation time of 19 h. The product was purified by column chromatography on SiO_2 using a gradient of *n*-hexane/ethyl acetate (2/1) $\rightarrow$ *n*-hexane/ethyl acetate (1/1). Sulfoxide **59** was obtained as a pale yellow crystalline solid (91 mg, 85% yield) after drying under reduced pressure. [xvi]

^{1}H NMR (500 MHz, 298 K, DMSO-d_6): δ 8.85–8.80 (m, 2H), 8.32 (d, J = 7.2 Hz, 2H), 7.55–7.42 (m, 4H);

^{13}C{^{1}H} NMR (126 MHz, 298 K, DMSO-d_6): δ 151.7, 144.3, 133.0, 127.4, 126.8.

Photooxidation of benzylamines

Due to instability of imines **63**, **65** and **67** on silica gel, the product yields of the photocatalysed oxidation were determined by ^{1}H NMR spectroscopy using 1,3,5-trimethoxybenzene (20 mol%) as an internal standard. NMR yields of the oxidation products are summarized in Table 22. The crude ^{1}H NMR spectra are provided in Figures 139-141.

Table 22: Summary of benzylamine oxidation using **7Sb^{Br}** as catalyst. All reactions were performed using 0.2 mmol of amine starting material in CH_2Cl_2 (2.0 mL).

Entry	Product	Catalyst loading	NMR yield[a]
e1	*N*-Benzylidenebenzylamine (**63**)	1.0 mol%	99
e2	*N*-Isopropyl-1-phenylmethanimine (**65**)	5.0 mol%	70
e3	3,4-Dihydroisoquinoline (**67**)	10 mol%	47

[a]Determined by ^{1}H NMR spectroscopy comparing relative intergrals of 1,3,5-trimethoxybenzene (s, 6.12 ppm) and imine C−H of corresponding oxidation product.

[xvi]Starting material synthesized by G. Pugliese. Purification of crude product carried out by G. Pugliese.

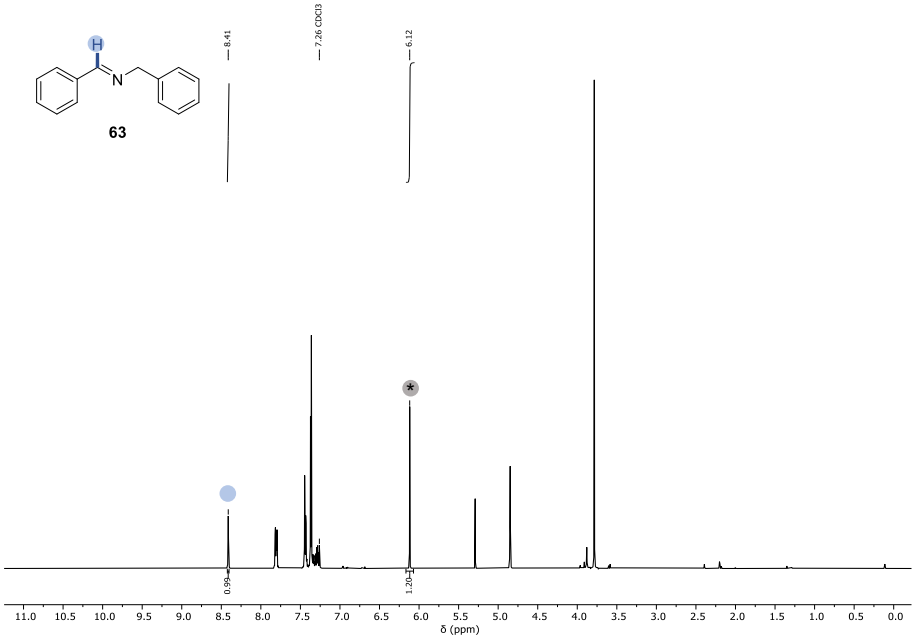


Figure 139: Crude ^{1}H NMR (400 MHz) spectrum of photoxidation mixture *e1* of benzylamine (**62**) in $CDCl_3$. Imine C−H resonance is marked by colour, whereas aromatic C−H resonance of internal standard is marked by (*).

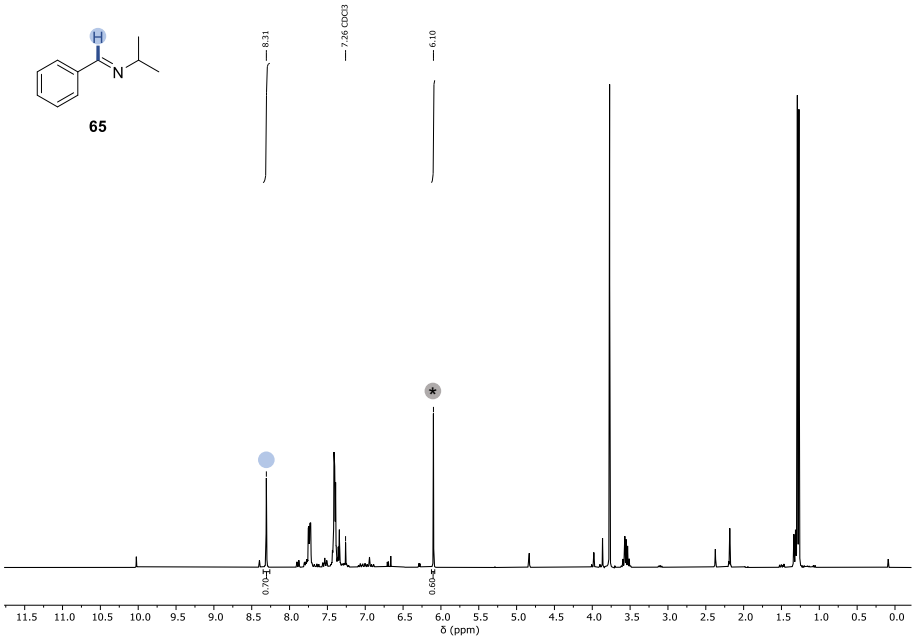


Figure 140: Crude ^{1}H NMR (300 MHz) spectrum of photoxidation mixture *e2* of *N*-isopropylbenzylamine (**64**) in $CDCl_3$. Imine C−H resonance is marked by colour, whereas aromatic C−H resonance of internal standard is marked by (*).

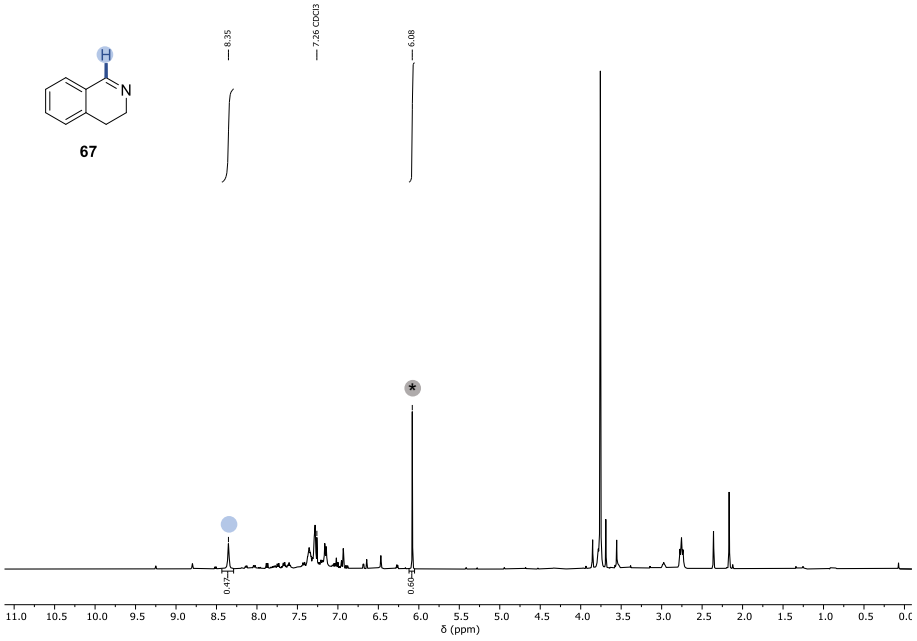
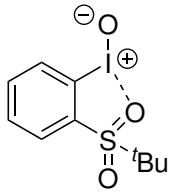


Figure 141: Crude ^{1}H NMR (400 MHz) spectrum of photoxidation mixture *e3* of 1,2,3,4-tetrahydroisoquinoline (**66**) in $CDCl_3$. Imine C−H resonance is marked by colour, whereas aromatic C−H resonance of internal standard is marked by (*).

6.14. Syntheses (chapter 5)

Synthesis of 2-(*tert*-butylsulfonyl)iodosylbenzene (84)

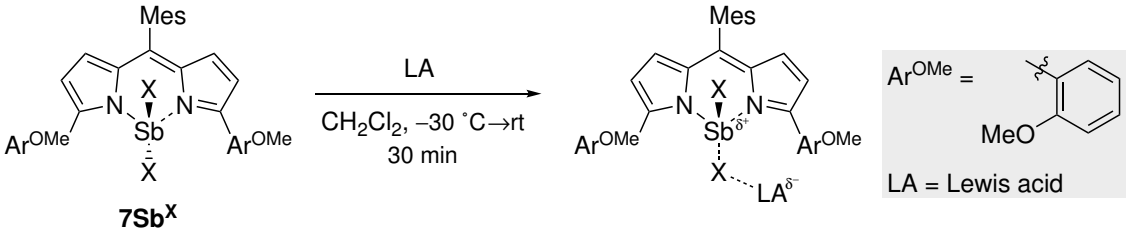


84

2-(*tert*-butylsulfonyl)iodosylbenzene (**84**) was prepared according to a literature-reported procedure and under ambient conditions.[275] 2-(tert-butylsulfonyl)iodobenzene (300 mg, 0.93 mmol, 1.00 equiv.) was suspended in a mixture of CCl_4 (1.0 mL) and conc. HCl (0.7 mL) and cooled to 0 °C. While vigorously stirring, $KClO_3$ (170 mg, 1.39 mmol, 1.50 equiv.) was added portion-wise over the course of 15 minutes. The reaction mixture was then stirred at 0 °C for 3 h, resulting in the formation of a yellow precipitate. The pale yellow powder was filtered off and washed with HCl (0.1 M, 10 mL) at 0 °C, followed by water (25 mL). The obtained solid was transferred into a 10 mL round-bottom flask and aqueous NaOH solution (5 M, 1.5 mL) was slowly added at 0 °C. The reaction mixture was stirred for 30 minutes at 0 °C, followed by addition of water (2 mL) and further stirring at room temperature for 16 h. The resulting precipitate was filtered off and washed with water (30 mL) and diethyl ether (30 mL) at 0 °C. The target compound was obtained as an amorphous yellow solid (135 mg, 42% yield) after drying under reduced pressure containing approximately 10% of an unknown impurity.

^{1}H NMR (300 MHz, 298 K, $CDCl_3$): δ 8.14–8.04 (m, 1H), 7.92–7.81 (m, 2H), 7.68–7.60 (m, 1H), 1.42 (s, 9H). NMR data were in good agreement with those previously reported.[275]

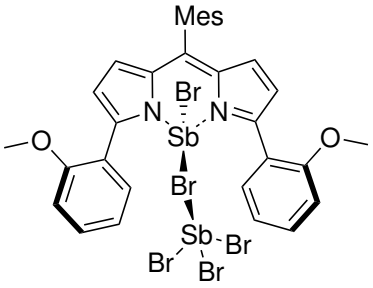
Synthesis of SBDIPY Lewis adducts: general procedure G



7Sb^{X}

Lewis adducts of SBDIPY complexes were synthesized starting from **7Sb^{X}** (X = Cl, Br). Respective SBDIPY **7Sb^{X}** (0.4 M, 1.00 equiv.) was dissolved in CH_2Cl_2 and cooled to −30 °C, followed by addition of the Lewis acid, LA (1.00 equiv.) as a solid. The reaction mixture was allowed to warm to room temperature and stirred for 30 min, whereupon the solvent was evaporated under reduced pressure. The crude product was washed with *n*-hexane (2×5 mL) and dried under reduced pressure, affording the product as an amorphous solid.

Synthesis of Lewis adduct Sb1



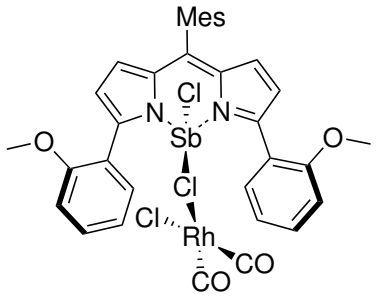
Sb1

Lewis adduct **Sb1** was synthesized according to the general procedure **G** starting from **7Sb^{Br}** (19 mg, 0.025 mmol) and $SbBr_3$ (9 mg, 0.025 mmol). The target compound was obtained as a dark blue amorphous solid (27 mg, 97% yield). Suitable single crystals for X-ray diffraction analysis were grown by slow evaporation from a saturated CD_2Cl_2 solution.

^{1}H NMR (500 MHz, 298 K, CD_2Cl_2): δ 7.75 (dd, *J* = 7.6, 1.7 Hz, 2H), 7.58–7.53 (m, 2H), 7.20–7.14 (m, 4H), 7.02 (s, 2H), 6.93 (d, *J* = 4.3 Hz, 2H), 6.77 (d, J = 4.4 Hz, 2H), 4.08 (s, 6H), 2.40 (s, 3H), 2.24 (s, 6H);

^{13}C{^{1}H} NMR (126 MHz, 298 K, CD_2Cl_2): δ 157.7, 156.1, 146.5, 139.3, 137.7, 136.5, 135.7, 133.0, 132.8, 131.7, 128.5, 122.9, 121.9, 121.9, 112.8, 56.5, 21.3, 20.6.

Synthesis of Lewis adduct Rh1



Rh1

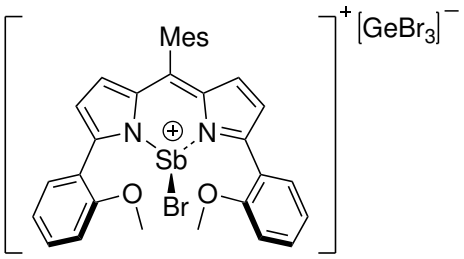
Lewis adduct **Rh1** was synthesized according to the general procedure **G** starting from **7Sb^{Cl}** (100 mg, 0.15 mmol) and $[RhCl(CO)_2]_2$ (59 mg, 0.15 mmol). The target compound was obtained as a dark purple amorphous solid (83 mg, 64% yield). Suitable single crystals for X-ray diffraction analysis were grown by slow evaporation from a saturated CH_2Cl_2 solution layered with *n*-dodecane.

^{1}H NMR (500 MHz, 298 K, CD_2Cl_2): δ 7.63 (dd, J = 7.7, 1.7 Hz, 2H), 7.57–7.51 (m, 2H), 7.22–7.17 (m, 4H), 7.02 (s, 2H), 6.91 (d, J = 4.4 Hz, 2H), 6.72 (d, J = 4.3 Hz, 2H), 4.17 (s, 6H), 2.40 (s, 3H), 2.22 (s, 6H);

^{13}C{^{1}H} NMR (126 MHz, 298 K, CD_2Cl_2): δ 180.1 (d, J_{Rh-C} = 74.3 Hz), 158.6, 155.1, 146.3, 139.2, 137.6, 136.7, 136.1, 132.8, 132.7, 132.2, 128.5, 123.0, 121.8, 121.3, 113.2, 55.9, 21.3, 20.3.

IR (ATR, neat) $\tilde{\nu}$ = 2705, 2004, 1804, 1544, 1476, 1444, 1297, 1257, 1205, 1058, 1025, 840, 797, 748 cm^{-1}

Synthesis of Lewis adduct Ge1



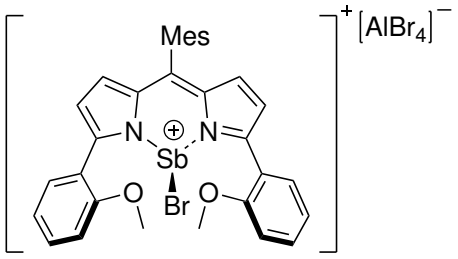
Ge1

Lewis adduct **Ge1** was synthesized according to the general procedure **G** starting from **7Sb^{Br}** (100 mg, 0.13 mmol) and $GeBr_2$·(1,4-dioxane) (41 mg, 0.13 mmol). The target compound was obtained as a black amorphous solid (88 mg, 76% yield). Suitable single crystals for X-ray diffraction analysis were grown by slow evaporation from a saturated CD_2Cl_2 solution layered with *n*-dodecane.

^{1}H NMR (500 MHz, 298 K, CD_2Cl_2): δ 7.74–7.68 (m, 2H), 7.55 (m, 2H), 7.22–7.15 (m, 4H), 7.04–7.01 (m, 2H), 6.95 (d, *J* = 4.3 Hz, 2H), 6.77 (d, *J* = 4.3 Hz, 2H), 4.10 (s, 6H), 2.40 (s, 3H), 2.24 (s, 6H);

^{13}C{^{1}H} NMR (126 MHz, 298 K, CD_2Cl_2): δ 158.2, 155.6, 146.5, 139.4, 137.7, 136.8, 136.2, 133.0, 132.6, 131.8, 128.5, 123.1, 121.9, 121.6, 113.1, 56.6, 21.3, 20.6.

Synthesis of Lewis adduct Al1



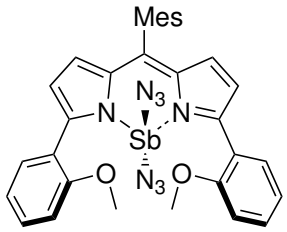
Al1

Lewis adduct **Al1** was synthesized according to the general procedure **G** starting from **7Sb^{Br}** (100 mg, 0.13 mmol) and $AlBr_4$ (34 mg, 0.13 mmol). The target compound was obtained as a dark blue amorphous solid (110 mg, 92% yield). Suitable single crystals for X-ray diffraction analysis were grown by slow evaporation from a saturated CH_2Cl_2 solution layered with *n*-dodecane.

^{1}H NMR (500 MHz, 298 K, CD_2Cl_2): δ 7.62–7.58 (m, 4H), 7.26–7.22 (m, 4H), 7.07–7.02 (m, 4H), 6.79 (d, J = 4.3 Hz, 2H), 4.11 (s, 6H), 2.41 (s, 3H), 2.23 (s, 6H);

^{13}C{^{1}H} NMR (126 MHz, 298 K, CD_2Cl_2): δ 159.0, 154.4, 147.1, 139.8, 137.6, 137.4, 137.3, 133.8, 132.2, 131.7, 128.7, 123.9, 122.1, 120.9, 114.0, 57.4, 21.3, 20.5.

Synthesis of 7Sb^{N3}



7Sb^{N3}

A 50 mL Schlenk tube was charged with **7Sb^{F}** (150 mg, 0.24 mmol, 1.00 equiv.) and CH_2Cl_2 (3.0 mL) was added. While vigorously stirring at room temperature, trimethylsilyl azide (79 μL, 0.59 mmol, 2.50 equiv.) was added, resulting in a subtle colour change from magenta to dark purple. After stirring for 1 h at room temperature the volatiles were evaporated under reduced pressure. The crude product was washed with *n*-hexane (3×7 mL) and dried again under reduced pressure to give the target compound as a dark purple amorphous solid (89 mg, 55% yield).
UV/Vis: λ_{abs} = 530 nm (CH_2Cl_2). **PL**: λ_{emi}= 597 nm (CH_2Cl_2).
^{1}H NMR (500 MHz, 298 K, CD_2Cl_2): δ 7.67 (d, *J* = 7.2 Hz, 2H), 7.51 (t, *J* = 7.8 Hz, 2H), 7.16 (t, J = 7.5 Hz, 2H), 7.12 (d, *J* = 8.5 Hz, 2H), 7.03 (s, 2H), 6.82 (d, *J* = 4.0 Hz, 2H), 6.73 (d, *J* = 4.1 Hz, 2H), 3.99 (s, 6H), 2.40 (s, 3H), 2.26 (s, 6H);
^{13}C{^{1}H} NMR (126 MHz, 298 K, CD_2Cl_2): δ 158.0, 155.9, 146.2, 139.0, 137.6, 134.0, 133.2, 132.4, 131.7, 128.4, 122.4, 121.8, 120.8, 112.4, 55.9, 21.3, 19.8 (*Note*: one signal not visible due to overlap).
IR (ATR, neat) $\tilde{\nu}$ = 2019, 1601, 1541, 1468, 1312, 1250, 1212, 1028, 844, 792, 757, 727 cm^{-1}

References

[1] B. N. Nunes, C. L. de Barros, D. W. Bahnemann, A. O. T. Patrocinio in *Springer Handbook of Inorganic Photochemistry*, (Eds.: D. Bahnemann, A. O. T. Patrocinio), Springer International Publishing, **2022**, pp. 3–25, DOI 10.1007/978-3-030-63713-2_1.

[2] S. E. Braslavsky, “Glossary of terms used in photochemistry, (IUPAC Recommendations 2006)”, *Pure and Applied Chemistry* **2007**, *79*, 293–465, DOI 10.1351/pac200779030293.

[3] B. Valeur, M. N. Berberan-Santos in *Molecular Fluorescence*, John Wiley & Sons, Ltd, **2012**, Chapter 1, pp. 1–30, DOI 10.1002/9783527650002.ch1.

[4] J. R. Lakowicz in *Principles of Fluorescence Spectroscopy*, Springer US, **2006**, pp. 1–26, DOI 10.1007/978-0-387-46312-4_1.

[5] International Union of Pure and Applied Chemistry (IUPAC), fluorophore, IUPAC Compendium of Chemical Terminology (the "Gold Book"), **2025**, DOI 10.1351/goldbook.FT07380.

[6] B. Valeur, M. N. Berberan-Santos in *Molecular Fluorescence*, John Wiley & Sons, Ltd, **2012**, Chapter 3, pp. 53–74, DOI 10.1002/9783527650002.ch3.

[7] S. Dutta, J. E. Erchinger, F. Strieth-Kalthoff, R. Kleinmans, F. Glorius, “Energy transfer photocatalysis: exciting modes of reactivity”, *Chemical Society Reviews* **2024**, *53*, 1068–1089, DOI 10.1039/d3cs00190c.

[8] N. A. Romero, D. A. Nicewicz, “Organic Photoredox Catalysis”, *Chemical Reviews* **2016**, *116*, 10075–10166, DOI 10.1021/acs.chemrev.6b00057.

[9] S. K. Lower, M. A. El-Sayed, “The Triplet State and Molecular Electronic Processes in Organic Molecules”, *Chemical Reviews* **1966**, *66*, 199–241, DOI 10.1021/cr60240a004.

[10] International Union of Pure and Applied Chemistry (IUPAC), heavy atom effect, IUPAC Compendium of Chemical Terminology (the "Gold Book"), **2025**, DOI 10.1351/goldbook.H02756.

[11] S. Arunkumar, D. Ghosh, G. R. Kumar, “Heavy main group element containing organometallic phosphorescent materials”, *Results in Chemistry* **2022**, *4*, 100399, DOI 10.1016/j.rechem.2022.100399.

[12] Y. Wu, Z. Zhao, S. Jiao, T. Song, C. Du, B. Fan, Y. Pang, H. Yuan, H. Ou, “Recent advances in organic phosphorescent materials for bioimaging”, *Biomedical Technology* **2025**, *11*, 100098, DOI 10.1016/j.bmt.2025.100098.

[13] J. P. Green, J. A. Wells, A. Orthaber, “Heavier pnictogens–treasures for optical electronic and reactivity tuning”, *Dalton Transactions* **2019**, *48*, 4460–4466, DOI 10.1039/C9DT00574A.

[14] S. M. Parke, E. Hupf, G. K. Matharu, I. de Aguiar, L. Xu, H. Yu, M. P. Boone, G. L. C. de Souza, R. McDonald, M. J. Ferguson, G. He, A. Brown, E. Rivard, “Aerobic Solid State Red Phosphorescence from Benzobismole Monomers and Patternable Self-Assembled Block Copolymers”, *Angewandte Chemie International Edition* **2018**, *57*, 14841–14846, DOI 10.1002/anie.201809357.

[15] T. Matsumoto, K. Tanaka, Y. Chujo, “Synthesis and Optical Properties of Stable Gallafluorene Derivatives: Investigation of Their Emission via Triplet States”, *Journal of the American Chemical Society* **2013**, *135*, 4211–4214, DOI 10.1021/ja400287y.

[16] C. Yao, Q. Cui, J. Peng, X. Xu, R. Liu, J. Wang, Y. Tian, L. Li, “Solution processed blue phosphorescent organic light emitting diodes using a Ge-based small molecular host”, *Journal of Materials Chemistry C* **2015**, *3*, 5017–5025, DOI 10.1039/C5TC00612K.

[17] G. He, W. Torres Delgado, D. J. Schatz, C. Merten, A. Mohammadpour, L. Mayr, M. J. Ferguson, R. McDonald, A. Brown, K. Shankar, et al., “Coaxing solid-state phosphorescence from tellurophenes”, *Angewandte Chemie International Edition* **2014**, *53*, 4587–4591, DOI 10.1002/anie.201307373.

[18] Y. Kang, D. Song, H. Schmider, S. Wang, “Novel Blue Phosphorescent Group 15 Compounds MR_3 (M = P, Sb, Bi; R = *p*-(N-7-Azaindolyl)phenyl)”, *Organometallics* **2002**, *21*, 2413–2421, DOI 10.1021/om020220g.

[19] J. Ohshita, S. Matsui, R. Yamamoto, T. Mizumo, Y. Ooyama, Y. Harima, T. Murafuji, K. Tao, Y. Kuramochi, T. Kaikoh, H. Higashimura, “Synthesis of Dithienobismoles as Novel Phosphorescence Materials”, *Organometallics* **2010**, *29*, 3239–3241, DOI 10.1021/om100560n.

[20] W. Ma, L. Xu, S. Zhang, G. Li, T. Ma, B. Rao, M. Zhang, G. He, “Phosphorescent Bismoviologens for Electrophosphorochromism and Visible Light-Induced Cross-Dehydrogenative Coupling”, *Journal of the American Chemical Society* **2021**, *143*, 1590–1597, DOI 10.1021/jacs.0c12015.

[21] K. L. Deuter, B. Schneider, K. Jellinek, R. F. Winter, “Pnicturesque Luminescence: The Photophysical and Emissive Properties of Dipyridine Pyrrolide Group 15 Diiodide Complexes”, *Zeitschrift für anorganische und allgemeine Chemie* **2025**, *651*, e202500102, DOI 10.1002/zaac.202500102.

[22] K. L. Deuter, D. J. Balaba, M. Linseis, R. F. Winter, “Room-temperature near-infrared phosphorescence of a bismuthinidene N,C,N pincer complex”, *Chemical Communications* **2025**, *61*, 3548–3551, DOI 10.1039/D5CC00127G.

[23] International Union of Pure and Applied Chemistry (IUPAC), photocatalysis, IUPAC Compendium of Chemical Terminology (the "Gold Book"), **2025**, DOI 10.1351/goldbook.P04580.

[24] F. Strieth-Kalthoff, M. J. James, M. Teders, L. Pitzer, F. Glorius, “Energy transfer catalysis mediated by visible light: principles, applications, directions”, *Chemical Society Reviews* **2018**, *47*, 7190–7202, DOI 10.1039/C8CS00054A.

[25] International Union of Pure and Applied Chemistry (IUPAC), photosensitization, IUPAC Compendium of Chemical Terminology (the "Gold Book"), **2025**, DOI 10.1351/goldbook.P04652.

[26] International Union of Pure and Applied Chemistry (IUPAC), energy transfer, IUPAC Compendium of Chemical Terminology (the "Gold Book"), **2025**, DOI 10.1351/goldbook.E02116.

[27] T. Förster, “Zwischenmolekulare Energiewanderung und Fluoreszenz”, *Annalen der Physik* **1948**, *437*, 55–75, DOI 10.1002/andp.19484370105.

[28] A. Kaur, P. Kaur, S. Ahuja, “Förster resonance energy transfer (FRET) and applications thereof”, *Analytical Methods* **2020**, *12*, 5532–5550, DOI 10.1039/D0AY01961E.

[29] D. L. Dexter, “A theory of sensitized luminescence in solids”, *The Journal of Chemical Physics* **1953**, *21*, 836–850, DOI 10.1063/1.1699044.

[30] B. Valeur, M. N. Berberan-Santo in *Molecular Fluorescence*, John Wiley & Sons, Ltd, **2012**, Chapter 8, pp. 213–261, DOI 10.1002/9783527650002.ch8.

[31] International Union of Pure and Applied Chemistry (IUPAC), spin conservation rule, IUPAC Compendium of Chemical Terminology (the "Gold Book"), **2025**, DOI 10.1351/goldbook.S05862.

[32] R. A. Marcus, “Electron transfer reactions in chemistry. Theory and experiment”, *Reviews of Modern Physics* **1993**, *65*, 599–610, DOI 10.1103/RevModPhys.65.599.

[33] F. Strieth-Kalthoff, F. Glorius, “Triplet Energy Transfer Photocatalysis: Unlocking the Next Level”, *Chem* **2020**, *6*, 1888–1903, DOI 10.1016/j.chempr.2020.07.010.

[34] N. F. Nikitas, P. L. Gkizis, C. G. Kokotos, “Thioxanthone: a powerful photocatalyst for organic reactions”, *Organic & Biomolecular Chemistry* **2021**, *19*, 5237–5253, DOI 10.1039/D1OB00221J.

[35] M. C. DeRosa, R. J. Crutchley, “Photosensitized singlet oxygen and its applications”, *Coordination Chemistry Reviews* **2002**, *233-234*, 351–371, DOI 10.1016/S0010-8545(02)00034-6.

[36] Z. Lu, T. P. Yoon, “Visible Light Photocatalysis of [2+2] Styrene Cycloadditions by Energy Transfer”, *Angewandte Chemie International Edition* **2012**, *51*, 10329–10332, DOI 10.1002/anie.201204835.

[37] J. Ma, S. Chen, P. Bellotti, R. Guo, F. Schäfer, A. Heusler, X. Zhang, C. Daniliuc, M. K. Brown, K. N. Houk, et al., “Photochemical intermolecular dearomative cycloaddition of bicyclic azaarenes with alkenes”, *Science* **2021**, *371*, 1338–1345, DOI 10.1126/science.abg072.

[38] E. Brachet, T. Ghosh, I. Ghosh, B. König, “Visible light C–H amidation of heteroarenes with benzoyl azides”, *Chemical science* **2015**, *6*, 987–992, DOI 10.1039/C4SC02365J.

[39] H. Kautsky, H. de Bruijn, “Die Aufklärung der Photoluminescenztilgung fluorescierender Systeme durch Sauerstoff: Die Bildung aktiver, diffusionsfähiger Sauerstoffmoleküle durch Sensibilisierung”, *Naturwissenschaften* **1931**, *19*, 1043–1043, DOI 10.1007/BF01516190.

[40] C. S. Foote, S. Wexler, “Singlet oxygen. A probable intermediate in photosensitized autoxidations”, *Journal of the American Chemical Society* **1964**, *86*, 3880–3881, DOI 10.1021/ja01072a061.

[41] E. J. Corey, W. C. Taylor, “A Study of the Peroxidation of Organic Compounds by Externally Generated Singlet Oxygen Molecules”, *Journal of the American Chemical Society* **1964**, *86*, 3881–3882, DOI 10.1021/ja01072a062.

[42] E. L. Clennan, A. Pace, “Advances in singlet oxygen chemistry”, *Tetrahedron* **2005**, *61*, 6665–6691, DOI 10.1016/j.tet.2005.04.017.

[43] F. Wilkinson, W. P. Helman, A. B. Ross, “Quantum yields for the photosensitized formation of the lowest electronically excited singlet state of molecular oxygen in solution”, *Journal of physical and chemical reference data* **1993**, *22*, 113–262, DOI 10.1063/1.555934.

[44] M. Hayyan, M. A. Hashim, I. M. AlNashef, “Superoxide Ion: Generation and Chemical Implications”, *Chemical Reviews* **2016**, *116*, 3029–3085, DOI 10.1021/acs.chemrev.5b00407.

[45] R. Schmidt, “Photosensitized generation of singlet oxygen”, *Photochemistry and photobiology* **2006**, *82*, 1161–1177, DOI 10.1562/2006-03-03-IR-833.

[46] Y. Cai, T. Chai, W. Nguyen, J. Liu, E. Xiao, X. Ran, Y. Ran, D. Du, W. Chen, X. Chen, “Phototherapy in cancer treatment: strategies and challenges”, *Signal Transduction and Targeted Therapy* **2025**, *10*, 115, DOI 10.1038/s41392-025-02140-y.

[47] N. Hoffmann, “Photochemical Reactions as Key Steps in Organic Synthesis”, *Chemical Reviews* **2008**, *108*, 1052–1103, DOI 10.1021/cr0680336.

[48] A. A. Ghogare, A. Greer, “Using Singlet Oxygen to Synthesize Natural Products and Drugs”, *Chemical Reviews* **2016**, *116*, 9994–10034, DOI 10.1021/acs.chemrev.5b00726.

[49] E. L. Clennan, “New mechanistic and synthetic aspects of singlet oxygen chemistry”, *Tetrahedron* **2000**, *56*, 9151–9179, DOI 10.1016/S0040-4020(00)00794-8.

[50] D. G. Ho, R. Gao, J. Celaje, H.-Y. Chung, M. Selke, “Phosphadioxirane: A peroxide from an ortho-substituted arylphosphine and singlet dioxygen”, *Science* **2003**, *302*, 259–262, DOI 10.1126/science.1089145.

[51] A. Toutchkine, E. L. Clennan, “The reactions of singlet oxygen with β-chlorosulfides. The role of hydroperoxy sulfonium ylides in the oxidative destruction of chemical warfare simulants”, *Tetrahedron letters* **1999**, *40*, 6519–6522, DOI 10.1016/S0040-4039(99)01304-0.

[52] M. Selke, C. S. Foote, “Reactions of organometallic complexes with singlet oxygen. Photooxidation of Vaska’s complex”, *Journal of the American Chemical Society* **1993**, *115*, 1166–1167, DOI 10.1021/ja00056a061.

[53] F. Lévesque, P. H. Seeberger, “Continuous-Flow Synthesis of the Anti-Malaria Drug Artemisinin”, *Angewandte Chemie International Edition* **2012**, *51*, 1706–1709, DOI 10.1002/anie.201107446.

[54] S. Ito, M. Gon, K. Tanaka, “Effects of Heavy p-Block Elements on Photophysical Properties of π-Conjugated Complexes and Organoelement Compounds”, *European Journal of Inorganic Chemistry* **2024**, *27*, e202400180, DOI 10.1002/ejic.202400180.

[55] Z. Liu, X. Lin, H. Wang, P. Zhang, “Structure-property relationships of main-group element phthalocyanines in photo/sono-driven cancer therapy”, *Coordination Chemistry Reviews* **2025**, *544*, 216969, DOI 10.1016/j.ccr.2025.216969.

[56] V. Caliskanyürek, S. Eulberg, O. Lange, M. Bröring, S. Tschierlei, “Sb(v) dihalide corroles: efficient singlet oxygen photosensitisers”, *Chemical Communications* **2024**, *60*, 4096–4099, DOI 10.1039/D4CC00675E.

[57] S. Mondal, T. Pain, M. Villa, S. Angeloni, A. Tarai, P. Ceroni, S. Kar, “Synthesis, Characterization, and Singlet Oxygen Sensitization by Antimony (III/V) Corrole Complexes”, *European Journal of Inorganic Chemistry* **2023**, *26*, e202300283, DOI 10.1002/ejic.202300283.

[58] L. M. Reith, M. Stiftinger, U. Monkowius, G. Knör, W. Schoefberger, “Synthesis and Characterization of a Stable Bismuth(III) A_3–Corrole”, *Inorganic Chemistry* **2011**, *50*, 6788–6797, DOI 10.1021/ic200840m.

[59] T. Shiragami, J. Matsumoto, H. Inoue, M. Yasuda, “Antimony porphyrin complexes as visible-light driven photocatalyst”, *Journal of Photochemistry and Photobiology C: Photochemistry Reviews* **2005**, *6*, 227–248, DOI 10.1016/j.jphotochemrev.2005.12.001.

[60] T. Hirayama, A. Mukaimine, K. Nishigaki, H. Tsuboi, S. Hirosawa, K. Okuda, M. Ebihara, H. Nagasawa, “Bismuth-rhodamine: a new red light-excitable photosensitizer”, *Dalton Transactions* **2017**, *46*, 15991–15995, DOI 10.1039/C7DT03194G.

[61] C. K. Prier, D. A. Rankic, D. W. MacMillan, “Visible light photoredox catalysis with transition metal complexes: applications in organic synthesis”, *Chemical reviews* **2013**, *113*, 5322–5363, DOI 10.1021/cr300503r.

[62] J. M. Narayanam, C. R. Stephenson, “Visible light photoredox catalysis: applications in organic synthesis”, *Chemical Society Reviews* **2011**, *40*, 102–113, DOI 10.1039/B913880N.

[63] J. Mateos, F. Rigodanza, A. Vega-Peñaloza, A. Sartorel, M. Natali, T. Bortolato, G. Pelosi, X. Companyó, M. Bonchio, L. Dell’Amico, “Naphthochromenones: Organic Bimodal Photocatalysts Engaging in Both Oxidative and Reductive Quenching Processes”, *Angewandte Chemie International Edition* **2020**, *59*, 1302–1312, DOI 10.1002/anie.201912455.

[64] S. Fukuzumi, S. Mochizuki, T. Tanaka, “Photocatalytic reduction of phenacyl halides by 9,10-dihydro-10-methylacridine: control between the reductive and oxidative quenching pathways of tris(bipyridine)ruthenium complex utilizing an acid catalysis”, *The Journal of Physical Chemistry* **1990**, *94*, 722–726, DOI 10.1021/j100365a039.

[65] E. H. Discekici, N. J. Treat, S. O. Poelma, K. M. Mattson, Z. M. Hudson, Y. Luo, C. J. Hawker, J. R. de Alaniz, “A highly reducing metal-free photoredox catalyst: design and application in radical dehalogenations”, *Chemical Communications* **2015**, *51*, 11705–11708, DOI 10.1039/C5CC04677G.

[66] A. Vogler, A. Paukner, H. Kunkely, “Photochemistry of coordination compounds of the main group metals”, *Coordination Chemistry Reviews* **1990**, *97*, 285–297, DOI 10.1016/0010-8545(90)80096-C.

[67] H. Inoue, M. Sumitani, A. Sekita, M. Hida, “Photochemical epoxidation of alkenes by visible light in a redox system involving tetraphenylporphyrinantimony(V) and water”, *Journal of the Chemical Society Chemical Communications* **1987**, 1681–1682, DOI 10.1039/C39870001681.

[68] H. Inoue, T. Okamoto, Y. Kameo, M. Sumitani, A. Fujiwara, D. Ishibashi, M. Hida, “Photochemical epoxidation of cyclohexene sensitized by tetraphenylporphyrinatoantimony(V) in the presence of water acting both as an electron and an oxygen donor”, *Journal of the Chemical Society Perkin Transactions 1* **1994**, 105–111, DOI 10.1039/P19940000105.

[69] S. Takagi, T. Okamoto, T. Shiragami, H. Inoue, “Photochemical Electron Transfer from Hydroxide Ion to the Excited Triplet State of Tetraphenylporphyrinatoantimony(V) upon Visible Light Irradiation in Aqueous Acetonitrile.”, *Chemistry Letters* **1993**, 793–796, DOI 10.1246/cl.1993.793.

[70] H. Inoue, T. Okamoto, M. Komiyama, M. Hida, “Photochemical epoxidation of alkene by visible light in a redox system involving metalloporphyrins and water”, *Journal of Photochemistry and Photobiology A: Chemistry* **1992**, *65*, 221–227, DOI 10.1016/1010-6030(92)85047-X.

[71] T. Shiragami, K. Kubomura, D. Ishibashi, H. Inoue, “Efficient photochemical oxygenation of cyclohexene with water as an oxygen donor sensitized by dimethoxy-coordinated tetraphenylporphyrinatoantimony(V)”, *Journal of the American Chemical Society* **1996**, *118*, 6311–6312, DOI 10.1021/ja960020u.

[72] G. Knör, A. Vogler, S. Roffia, F. Paolucci, V. Balzani, “Switchable photoreduction pathways of antimony(V) tetraphenylporphyrin. A potential multielectron transfer photosensitizer”, *Chemical Communications* **1996**, 1643–1644, DOI 10.1039/CC9960001643.

[73] G. Knör, “Bionic catalyst design: A photochemical approach to artificial enzyme function”, *ChemBioChem* **2001**, *2*, 593–596, DOI 10.1002/1439-7633(20010803)2:7/8<593::AID-CBIC593>3.0.CO;2-1.

[74] C. M. Lemon, S. J. Hwang, A. G. Maher, D. C. Powers, D. G. Nocera, "Halogen Photoelimination from Sb^{V} Dihalide Corroles", *Inorganic Chemistry* **2018**, *57*, 5333–5342, DOI 10.1021/acs.inorgchem.8b00314.

[75] L. Capaldo, M. Ertl, M. Fagnoni, G. Knör, D. Ravelli, "Antimony–Oxo Porphyrins as Photocatalysts for Redox-Neutral C–H to C–C Bond Conversion", *ACS Catalysis* **2020**, *10*, 9057–9064, DOI 10.1021/acscatal.0c02250.

[76] H. W. Moon, J. Cornella, "Bismuth Redox Catalysis: An Emerging Main-Group Platform for Organic Synthesis", *ACS Catalysis* **2022**, *12*, 1382–1393, DOI 10.1021/acscatal.1c04897.

[77] D. Birnthaler, R. Narobe, E. Lopez-Berguno, C. Haag, B. König, "Synthetic Application of Bismuth LMCT Photocatalysis in Radical Coupling Reactions", *ACS Catalysis* **2023**, *13*, 1125–1132, DOI 10.1021/acscatal.2c05631.

[78] M. Mato, D. Spinnato, M. Leutzsch, H. W. Moon, E. J. Reijerse, J. Cornella, "Bismuth radical catalysis in the activation and coupling of redox-active electrophiles", *Nature Chemistry* **2023**, *15*, 1138–1145, DOI 10.1038/s41557-023-01229-7.

[79] S. Ni, D. Spinnato, J. Cornella, "Reductive Cyclopropanation through Bismuth Photocatalysis", *Journal of the American Chemical Society* **2024**, *146*, 22140–22144, DOI 10.1021/jacs.4c07262.

[80] A. Stamoulis, M. Mato, P. C. Bruzzese, M. Leutzsch, A. Cadranel, M. Gil-Sepulcre, F. Neese, J. Cornella, "Red-Light-Active *N,C,N*-Pincer Bismuthinidene: Excited State Dynamics and Mechanism of Oxidative Addition into Aryl Iodides", *Journal of the American Chemical Society* **2025**, *147*, 6037–6048, DOI 10.1021/jacs.4c16815.

[81] M. Mato, A. Stamoulis, P. Cleto Bruzzese, J. Cornella, "Activation and C–C Coupling of Aryl Iodides via Bismuth Photocatalysis", *Angewandte Chemie International Edition* **2025**, *64*, e202418367, DOI 10.1002/anie.202418367.

[82] S. Ni, A. Stamoulis, V. A. Béland, J. Cornella, "Bismuth-photocatalysed Heck-type coupling with alkyl and aryl electrophiles", *Nature Catalysis* **2025**, *8*, 1–9, DOI 10.1038/s41929-025-01438-y.

[83] T. Tsuruta, D. Spinnato, H. W. Moon, M. Leutzsch, J. Cornella, "Bi-Catalyzed Trifluoromethylation of $C(sp^2)$–H Bonds under Light", *Journal of the American Chemical Society* **2023**, *145*, 25538–25544, DOI 10.1021/jacs.3c10333.

[84] T. E. Wood, A. Thompson, “Advances in the Chemistry of Dipyrrins and Their Complexes”, *Chemical Reviews* **2007**, *107*, 1831–1861, DOI 10.1021/cr050052c.

[85] O. Piloty, J. Stock, E. Dormann, “Zur Konstitution des Blutfarbstoffs; Dipyrrylmethan-Derivate mit Farbstoff-Charakter”, *Berichte der deutschen chemischen Gesellschaft* **1914**, *47*, 400–406, DOI 10.1002/cber.19140470163.

[86] R. S. Singh, R. P. Paitandi, R. K. Gupta, D. S. Pandey, “Recent developments in metal dipyrrin complexes: Design, synthesis, and applications”, *Coordination Chemistry Reviews* **2020**, *414*, 213269, DOI 10.1016/j.ccr.2020.213269.

[87] G. P. Moss, “Nomenclature of tetrapyrroles (Recommendations 1986)”, *Pure and Applied Chemistry* **1987**, *59*, 779–832, DOI 10.1351/pac198759060779.

[88] A. Al-Sheikh-Ali, K. S. Cameron, T. S. Cameron, K. N. Robertson, A. Thompson, “Highly Diastereoselective Templated Complexation of Dipyrromethenes”, *Organic Letters* **2005**, *7*, 4773–4775, DOI 10.1021/ol052044o.

[89] J. A. van Koeveringe, J. Lugtenburg, “Novel pyrromethenes. 1-Oxygen and 1-sulfur analogues; evidence for photochemical Z-E isomerization”, *Recueil des Travaux Chimiques des Pays-Bas* **1977**, *96*, 55–57, DOI 10.1002/recl.19770960209.

[90] C.-H. Lee, J. S. Lindsey, “One-flask synthesis of meso-substituted dipyrromethanes and their application in the synthesis of trans-substituted porphyrin building blocks”, *Tetrahedron* **1994**, *50*, 11427–11440, DOI 10.1016/S0040-4020(01)89282-6.

[91] A. Loudet, K. Burgess, “BODIPY Dyes and Their Derivatives: Syntheses and Spectroscopic Properties”, *Chemical Reviews* **2007**, *107*, 4891–4932, DOI 10.1021/cr078381n.

[92] A. Treibs, F.-H. Kreuzer, “Difluorboryl-Komplexe von Di- und Tripyrrylmethenen”, *Justus Liebigs Annalen der Chemie* **1968**, *718*, 208–223, DOI 10.1002/jlac.19687180119.

[93] G. Ulrich, R. Ziessel, A. Harriman, “The Chemistry of Fluorescent Bodipy Dyes: Versatility Unsurpassed”, *Angewandte Chemie International Edition* **2008**, *47*, 1184–1201, DOI 0.1002/anie.200702070.

[94] N. Boens, V. Leen, W. Dehaen, “Fluorescent indicators based on BODIPY”, *Chemical Society Reviews* **2012**, *41*, 1130–1172, DOI 10.1039/C1CS15132K.

[95] A. P. Felgueiras, Z. A. Arnaut, J. F. Cebola, G. M. Martins, F. M. Rodrigues, V. S. Bagnato, K. T. de Oliveira, M. J. Calvete, M. M. Pereira, "Unlocking BODIPY Dye Synthetic Methodologies with ^{1}H-NMR Monitoring and Continuous Flow Techniques", *Dyes and Pigments* **2025**, 113075, DOI 10.1016/j.dyepig.2025.113075.

[96] M. Shah, K. Thangaraj, M.-L. Soong, L. T. Wolford, J. H. Boyer, I. R. Politzer, T. G. Pavlopoulos, "Pyrromethene-BF_2 complexes as laser dyes:1.", *Heteroatom Chemistry* **1990**, *1*, 389–399, DOI 10.1002/hc.520010507.

[97] C. Goze, G. Ulrich, L. J. Mallon, B. D. Allen, A. Harriman, R. Ziessel, "Synthesis and Photophysical Properties of Borondipyrromethene Dyes Bearing Aryl Substituents at the Boron Center", *Journal of the American Chemical Society* **2006**, *128*, 10231–10239, DOI 10.1021/ja062405a.

[98] C. Goze, G. Ulrich, R. Ziessel, "Unusual Fluorescent Monomeric and Dimeric Dialkynyl Dipyrromethene-Borane Complexes", *Organic Letters* **2006**, *8*, 4445–4448, DOI 10.1021/ol061601j.

[99] C. Thivierge, R. Bandichhor, K. Burgess, "Spectral Dispersion and Water Solubilization of BODIPY Dyes via Palladium-Catalyzed C–H Functionalization", *Organic Letters* **2007**, *9*, 2135–2138, DOI 10.1021/ol0706197.

[100] L. Huang, X. Yu, W. Wu, J. Zhao, "Styryl Bodipy-C_{60} Dyads as Efficient Heavy-Atom-Free Organic Triplet Photosensitizers", *Organic Letters* **2012**, *14*, 2594–2597, DOI 10.1021/ol3008843.

[101] H. Sunahara, Y. Urano, H. Kojima, T. Nagano, "Design and Synthesis of a Library of BODIPY-Based Environmental Polarity Sensors Utilizing Photoinduced Electron-Transfer-Controlled Fluorescence ON/OFF Switching", *Journal of the American Chemical Society* **2007**, *129*, 5597–5604, DOI 10.1021/ja068551y.

[102] T. Werner, C. Huber, S. Heinl, M. Kollmannsberger, J. Daub, O. S. Wolfbeis, "Novel optical pH-sensor based on a boradiaza-indacene derivative", *Fresenius' journal of analytical chemistry* **1997**, *359*, 150–154, DOI 10.1007/s002160050552.

[103] M. Kollmannsberger, T. Gareis, S. Heinl, J. Daub, J. Breu, "Electrogenerated Chemiluminescence and Proton-Dependent Switching of Fluorescence: Functionalized Difluoroboradiaza-s-indacenes", *Angewandte Chemie International Edition* **1997**, *36*, 1333–1335, DOI 10.1002/anie.199713331.

[104] H. W. Mbatia, D. P. Kennedy, C. E. Camire, C. D. Incarvito, S. C. Burdette, “Buffering Heavy Metal Ions with Photoactive CrownCast Cages”, *European Journal of Inorganic Chemistry* **2010**, *2010*, 5069–5078, DOI 10.1002/ejic.201000673.

[105] Z. Ekmekci, M. D. Yilmaz, E. U. Akkaya, “A Monostyryl-boradiazaindacene (BODIPY) Derivative as Colorimetric and Fluorescent Probe for Cyanide Ions”, *Organic Letters* **2008**, *10*, 461–464, DOI 10.1021/ol702823u.

[106] O. Green, P. Finkelstein, M. A. Rivero-Crespo, M. D. R. Lutz, M. K. Bogdos, M. Burger, J.-C. Leroux, B. Morandi, “Activity-Based Approach for Selective Molecular CO_2 Sensing”, *Journal of the American Chemical Society* **2022**, *144*, 8717–8724, DOI 10.1021/jacs.2c02361.

[107] E. Bassan, A. Gualandi, P. G. Cozzi, P. Ceroni, “Design of BODIPY dyes as triplet photosensitizers: electronic properties tailored for solar energy conversion, photoredox catalysis and photodynamic therapy”, *Chemical Science* **2021**, *12*, 6607–6628, DOI 10.1039/D1SC00732G.

[108] D. Wang, X. Wang, S. Zhou, P. Gu, X. Zhu, C. Wang, Q. Zhang, “Evolution of BODIPY as triplet photosensitizers from homogeneous to heterogeneous: The strategies of functionalization to various forms and their recent applications”, *Coordination Chemistry Reviews* **2023**, *482*, 215074, DOI 10.1016/j.ccr.2023.215074.

[109] M. A. Filatov, “Heavy-atom-free BODIPY photosensitizers with intersystem crossing mediated by intramolecular photoinduced electron transfer”, *Organic & Biomolecular Chemistry* **2020**, *18*, 10–27, DOI 10.1039/C9OB02170A.

[110] J. Zhao, W. Wu, J. Sun, S. Guo, “Triplet photosensitizers: from molecular design to applications”, *Chemical Society Reviews* **2013**, *42*, 5323–5351, DOI 10.1039/C3CS35531D.

[111] P. Irmler, R. F. Winter, “σ-Pt-BODIPY Complexes with Platinum Attachment to Carbon Atoms C2 or C3: Spectroscopic, Structural, and (Spectro)Electrochemical Studies and Photocatalysis”, *Organometallics* **2018**, *37*, 235–253, DOI 10.1021/acs.organomet.7b00806.

[112] P. De Bonfils, L. Péault, P. Nun, V. Coeffard, “State of the Art of Bodipy-Based Photocatalysts in Organic Synthesis”, *European Journal of Organic Chemistry* **2021**, *2021*, 1809–1824, DOI 10.1002/ejoc.202001446.

[113] L. Huang, J. Zhao, S. Guo, C. Zhang, J. Ma, "Bodipy derivatives as organic triplet photosensitizers for aerobic photoorganocatalytic oxidative coupling of amines and photooxidation of dihydroxylnaphthalenes", *The Journal of Organic Chemistry* **2013**, *78*, 5627–5637, DOI 10.1021/jo400769u.

[114] L. Huang, J. Zhao, "Iodo-Bodipys as visible-light-absorbing dual-functional photoredox catalysts for preparation of highly functionalized organic compounds by formation of C–C bonds via reductive and oxidative quenching catalytic mechanisms", *RSC advances* **2013**, *3*, 23377–23388, DOI 10.1039/C3RA43299H.

[115] Y.-Q. Zou, L.-Q. Lu, L. Fu, N.-J. Chang, J. Rong, J.-R. Chen, W.-J. Xiao, "Visible-Light-Induced Oxidation/[3+2] Cycloaddition/Oxidative Aromatization Sequence: A Photocatalytic Strategy To Construct Pyrrolo[2,1-*a*]isoquinolines", *Angewandte Chemie International Edition* **2011**, *50*, 7171–7175, DOI 10.1002/anie.201102306.

[116] I. S. Schomberg-Sanchez, W. A. Janusz, C. M. Lemon, "Beyond BODIPY: dipyrrin complexes of P-block elements", *Journal of Coordination Chemistry* **2025**, *78*, 2449–2502, DOI 10.1080/00958972.2025.2539945.

[117] S. A. Baudron, "Dipyrrin based metal complexes: reactivity and catalysis", *Dalton Transactions* **2020**, *49*, 6161–6175, DOI 10.1039/D0DT00884B.

[118] V. S. Thoi, J. R. Stork, D. Magde, S. M. Cohen, "Luminescent Dipyrrinato Complexes of Trivalent Group 13 Metal Ions", *Inorganic Chemistry* **2006**, *45*, 10688–10697, DOI 10.1021/ic061581h.

[119] C. S. Gutsche, S. Graefe, B. Gitter, K. J. Flanagan, M. O. Senge, N. Kulak, A. Wiehe, "Pre-/post-functionalization in dipyrrin metal complexes–antitumor and antibacterial activity of their glycosylated derivatives", *Dalton Transactions* **2018**, *47*, 12373–12384, DOI 10.1039/C8DT03059F.

[120] W. Wan, M. S. Silva, C. D. McMillen, S. E. Creager, R. C. Smith, "Highly Luminescent Heavier Main Group Analogues of Boron-Dipyrromethene", *Journal of the American Chemical Society* **2019**, *141*, 8703–8707, DOI 10.1021/jacs.9b03235.

[121] L. Erlemeier, M. J. Müller, G. Stuhrmann, T. Dunaj, G. Werncke, S. Chatterjee, C. von Hänisch, "Easy access to strongly fluorescent higher homologues of BODIPY", *Dalton Transactions* **2024**, *53*, 887–893, DOI 10.1039/D3DT03323F.

[122] L. Erlemeier, R.-M. Richter, T. Dunaj, M. J. Müller, S. Chatterjee, C. von Hänisch, “Higher BODIPY Homologues–Synthesis, Reactivity, and Photoluminescence Investigations”, *Chemistry - A European Journal* **2025**, *31*, e202404764, DOI 10.1002/chem.202404764.

[123] T. Richter, S. Thum, T. Vilpas, O. P. E. Townrow, L. Klerner, J. Langer, S. Harder, “Dipyrromethene as a Ligand for the Stabilization of Low-Valent Gallium Complexes”, *Organometallics* **2024**, *43*, 1377–1385, DOI 10.1021/acs.organomet.4c00164.

[124] T. Richter, S. Thum, O. P. Townrow, J. Langer, M. Wiesinger, S. Harder, “Selectivity control in the reactivity of dipyrromethene gallium (I) complexes”, *Journal of Organometallic Chemistry* **2024**, *1021*, 123356, DOI 10.1016/j.jorganchem.2024.123356.

[125] H. Kim, A. Burghart, M. B. Welch, J. Reibenspies, K. Burgess, “Synthesis and spectroscopic properties of a new 4-bora-3a, 4a-diaza-s-indacene (BODIPY®) dye”, *Chemical Communications* **1999**, 1889–1890, DOI 10.1039/A905739K.

[126] A. Sumiyoshi, Y. Chiba, R. Matsuoka, T. Noda, T. Nabeshima, “Efficient luminescent properties and cation recognition ability of heavy group 13 element complexes of N_2O_2- and N_2O_4-type dipyrrins”, *Dalton Transactions* **2019**, *48*, 13169–13175, DOI 10.1039/C9DT02403D.

[127] M. Saikawa, T. Noda, R. Matsuoka, T. Nakamura, T. Nabeshima, “Heterodinuclear Group 13 Element Complexes of N_4O_6-Type Dipyrrin with an Unsymmetrical Twisted Structure”, *European Journal of Inorganic Chemistry* **2019**, *2019*, 766–769, DOI 10.1002/ejic.201801062.

[128] A. Godard, L. A. Galán, J. Rouillon, S. Al Shehimy, W. Tajani, C. Cave, R. Malacea-Kabbara, Y. Rousselin, P. Le Gendre, A. Fihey, M. Bendellaa, B. Busser, L. Sancey, B. Le Guennic, C. Bucher, O. Maury, C. Goze, E. Bodio, “Al(III) and Ga(III) Bisphenolate Azadipyrromethene-Based “N_2O_2” Complexes as Efficient NIR-Fluorophores”, *Inorganic Chemistry* **2023**, *62*, 5067–5080, DOI 10.1021/acs.inorgchem.2c03918.

[129] C. K. Jha, S. Karwasara, S. Nagendran, “Can Low-Valent Germanium Chemistry Be Practiced Under Ambient Conditions? A Tale of a Water-Stable Yet Reactive Germylene Monochloride Complex”, *Chemistry - A European Journal* **2014**, *20*, 10240–10244, DOI 10.1002/chem.201403598.

[130] P. Mahawar, M. K. Wasson, M. K. Sharma, C. K. Jha, G. Mukherjee, P. Vivekanandan, S. Nagendran, "A Prelude to Biogermylene Chemistry", *Angewandte Chemie International Edition* **2020**, *59*, 21377–21381, DOI 10.1002/anie.202004551.

[131] P. Shukla, J. Nath Acharyya, P. Mahawar, H. Kumar, P. Chandra Joshi, V. Kumar Singh, G. Vijaya Prakash, S. Nagendran, "Germylenes Exhibiting Solid-State Emissions that Extend to NIR", *Chemistry – A European Journal* **2023**, *29*, e202301486, DOI 10.1002/chem.202301486.

[132] P. C. Joshi, P. Shukla, V. Singh, V. K. Singh, A. Garg, H. Gaur, P. Mahawar, H. Kumar, S. Nagendran, "Bis(Dipyrrinate) Based Bis(Germylenes): Synthesis, Reactivity, and UV-Vis Spectroscopic Analysis", *Chemistry – A European Journal* **2025**, *31*, e202500214, DOI 10.1002/chem.202500214.

[133] H. Kumar, P. Mahawar, P. Dua, V. K. Singh, P. Shukla, P. C. Joshi, G. Rajaraman, S. Nagendran, "Low-valent Main-group Catalysis under Ambient Conditions using a Germylene Cation", *Chemistry – An Asian Journal* **2025**, *20*, e202400692, DOI 10.1002/asia.202400692.

[134] Y. Dai, M. Bao, W. Wang, Z. Xie, C. Liu, Y. Su, "Crystalline Germanium-Dipyrromethene Radicals: from a Delocalized Neutral to a Localized Cation", *Chinese Journal of Chemistry* **2022**, *40*, 2387–2392, DOI 10.1002/cjoc.202200431.

[135] Q. Bao, Y. Dai, C. Liu, X. Liu, J. Xiao, D. Xu, Y. Su, "Isolable Dipyrromethene-Based Heavier Group 14 and 15 Element Complexes", *European Journal of Inorganic Chemistry* **2024**, *27*, e202300643, DOI 10.1002/ejic.202300643.

[136] M. Yamamura, M. Albrecht, M. Albrecht, Y. Nishimura, T. Arai, T. Nabeshima, "Red/Near-Infrared Luminescence Tuning of Group-14 Element Complexes of Dipyrrins Based on a Central Atom", *Inorganic Chemistry* **2014**, *53*, 1355–1360, DOI 10.1021/ic402116j.

[137] X.-D. Jiang, J. Zhao, D. Xi, H. Yu, J. Guan, S. Li, C.-L. Sun, L.-J. Xiao, "A New Water-Soluble Phosphorus-Dipyrromethene and Phosphorus-Azadipyrromethene Dye: PODIPY/aza-PODIPY", *Chemistry – A European Journal* **2015**, *21*, 6079–6082, DOI 10.1002/chem.201406535.

[138] C. Liu, Y. Dai, Q. Han, C. Liu, Y. Su, "Crystalline heaviest pnictogen-dipyrromethenes: isolation, characterization, and reactivity", *Chemical Communications* **2023**, *59*, 2161–2164, DOI 10.1039/D2CC05736K.

[139] T. Agou, S. Kuroiwa, H. Fukumoto, T. Nabeshima, “Synthesis and optical properties of antimony(V) complexes of a trianionic N_2O_2-type tetradentate dipyrrin ligand”, *Chemical Communications* **2024**, *60*, 4557–4560, DOI 10.1039/D4CC00630E.

[140] T. Agou, S. Kuroiwa, R. Moriyama, T. Kuroda, K. Kubo, H. Fukumoto, M. Morita, R. Inoue, T. Nabeshima, “Synthesis and structural characterization of Sb(III) and Bi(III) complexes with an N_2O_2-type tetradentate dipyrrin ligand”, *Chemical Communications* **2025**, *61*, 7141–7144, DOI 10.1039/D5CC01037C.

[141] A. Korzun, S. Crespi, C. Golz, A. Bismuto, “Replacing the BO in BODIPY: unlocking the path to SBDIPY and BIDIPY chromophores”, *Chemical Science* **2023**, *14*, 6579–6584, DOI 10.1039/D3SC01493B.

[142] E. N. Nuraneeva, G. B. Guseva, E. V. Antina, R. T. Kuznetsova, M. B. Berezin, A. I. V’yugin, “Synthesis, spectral luminescent properties, and photostability of monoiodo- and dibromo-substituted BF_2-dipyrrinates”, *Russian Journal of General Chemistry* **2016**, *86*, 840–847, DOI 10.1134/S1070363216040149.

[143] J. Cipot-Wechsler, A. A.-S. Ali, E. E. Chapman, T. S. Cameron, A. Thompson, “Synthesis and Reactivity of a Dipyrrinatolithium Complex”, *Inorganic Chemistry* **2007**, *46*, 10947–10949, DOI 10.1021/ic701369h.

[144] S. L. Yutanova, M. B. Berezin, A. S. Semeikin, E. V. Antina, G. B. Guseva, A. I. V’yugin, “Thermal oxidative degradation of the functionally substituted 2,2′-dipyrrolylmethenes hydrobromides and difluoroborates”, *Russian Journal of General Chemistry* **2013**, *83*, 545–551, DOI 10.1134/S1070363213030237.

[145] J. L. Sessler, L. R. Eller, W.-S. Cho, S. Nicolaou, A. Aguilar, J. T. Lee, V. M. Lynch, D. J. Magda, “Synthesis, Anion-Binding Properties, and In Vitro Anticancer Activity of Prodigiosin Analogues”, *Angewandte Chemie International Edition* **2005**, *44*, 5989–5992, DOI 10.1002/anie.200501740.

[146] A. A.-S. Ali, J. Cipot-Wechsler, S. M. Crawford, O. Selim, R. L. Stoddard, T. S. Cameron, A. Thompson, “The first series of alkali dipyrrinato complexes”, *Canadian Journal of Chemistry* **2010**, *88*, 725–735, DOI 10.1139/V09-180.

[147] R. Bandichhor, C. Thivierge, N. S. P. Bhuvanesh, K. Burgess, “4,4-Difluoro-1,3,5,7-tetramethyl-4-bora-3a,4a-diaza-*s*-indacene”, *Acta Crystallographica Section E* **2006**, *62*, o4310–o4311, DOI 10.1107/S1600536806032235.

[148] S. Grimme, A. Hansen, S. Ehlert, J.-M. Mewes, "r^{2}SCAN-3c: "A Swiss army knife" composite electronic-structure method", *The Journal of Chemical Physics* **2021**, *154*, 064103, DOI 10.1063/5.0040021.

[149] R. Sharma, A. Ghosh, B. Wolfram, M. Bröring, M. Ravikanth, "Synthesis and characterization of hexa-coordinated Sn(iv) complexes of meso-aryl dipyrrins", *Dalton Transactions* **2013**, *42*, 5627–5630, DOI 10.1039/C3DT00031A.

[150] S. Kusaka, R. Sakamoto, H. Nishihara, "Luminescent Heteroleptic Tris(dipyrrinato)indium(III) Complexes", *Inorganic Chemistry* **2014**, *53*, 3275–3277, DOI 10.1021/ic500326u.

[151] A. T. Mohammed, U. Müller, "Tetraphenylphosphonium-octabromodiantimonat, $(PPh_4)_2$ $[Sb_2Br_8]$. Synthese und Kristallstruktur", *Zeitschrift für Naturforschung B* **1985**, *40*, 562–564, DOI 10.1515/znb-1985-0423.

[152] P. Pyykkö, M. Atsumi, "Molecular Single-Bond Covalent Radii for Elements 1–118", *Chemistry – A European Journal* **2009**, *15*, 186–197, DOI 10.1002/chem.200800987.

[153] M. Mantina, A. C. Chamberlin, R. Valero, C. J. Cramer, D. G. Truhlar, "Consistent van der Waals Radii for the Whole Main Group", *The Journal of Physical Chemistry A* **2009**, *113*, 5806–5812, DOI 10.1021/jp8111556.

[154] M. B. Kindervater, K. M. Marczenko, U. Werner-Zwanziger, S. S. Chitnis, "A Redox-Confused Bismuth(I/III) Triamide with a T-Shaped Planar Ground State", *Angewandte Chemie International Edition* **2019**, *58*, 7850–7855, DOI 10.1002/anie.201903354.

[155] K. M. Marczenko, J. A. Zurakowski, M. B. Kindervater, S. Jee, T. Hynes, N. Roberts, S. Park, U. Werner-Zwanziger, M. Lumsden, D. N. Langelaan, S. S. Chitnis, "Periodicity in Structure, Bonding, and Reactivity for p-Block Complexes of a Geometry Constraining Triamide Ligand", *Chemistry – A European Journal* **2019**, *25*, 16414–16424, DOI 10.1002/chem.201904361.

[156] H. Schumann, "Synthese und spektroskopische charakterisierung von cyclopentadienyleisen-komplexen mit P-N-Liganden des Typs $(C_6H_5)_{3-n}P(NR_2)_n$ (n = 0–3; R = CH_3, C_2H_5)", *Journal of Organometallic Chemistry* **1986**, *299*, 169–178, DOI 10.1016/0022-328X(86)82012-5.

[157] D. Zhang, L. Le, R. Qiu, W.-Y. Wong, N. Kambe, "Nickel- and Palladium-Catalyzed Cross-Coupling Reactions of Organostibines with Organoboronic Acids", *Angewandte Chemie International Edition* **2021**, *60*, 3104–3114, DOI 10.1002/anie.202011491.

[158] T. Storr, P. Verma, Y. Shimazaki, E. C. Wasinger, T. D. P. Stack, “Ligand Radical Localization in a Nonsymmetric One-Electron Oxidized NiII Bis-phenoxide Complex”, *Chemistry – A European Journal* **2010**, *16*, 8980–8983, DOI 10.1002/chem.201001401.

[159] S. Zhang, W. Huang, Y. Zhu, J. Wang, F. Cao, Q. Zhang, E. Zhao, Z. He, “Robust organic radical cations with near-unity absorption across solar spectrum”, *Nature Communications* **2025**, *16*, 7320, DOI 10.1038/s41467-025-62581-5.

[160] M. Ates, H. J. Breunig, A. Soltani-Neshan, M. Tegeler, “Synthese von Mesitylstibanen / Synthesis of Mesitylstibanes”, *Zeitschrift für Naturforschung B* **1986**, *41*, 321–326, DOI 10.1515/znb-1986-0305.

[161] S. Chibani, B. Le Guennic, A. Charaf-Eddin, A. D. Laurent, D. Jacquemin, “Revisiting the optical signatures of BODIPY with ab initio tools”, *Chemical Science* **2013**, *4*, 1950–1963, DOI 10.1039/C3SC22265A.

[162] International Union of Pure and Applied Chemistry (IUPAC), Beer–Lambert law, IUPAC Compendium of Chemical Terminology (the "Gold Book"), **2025**, DOI 10.1351/goldbook.B00626.

[163] P. Atkins, J. de Paula, *Atkins' Physical Chemistry*, 8th ed., Oxford University Press, Oxford, **2010**, pp. 791–822.

[164] B. Valeur, M. N. Berberan-Santo in *Molecular Fluorescence*, John Wiley & Sons, Ltd, **2012**, Chapter 4, pp. 75–107, DOI 10.1002/9783527650002.ch4.

[165] A. Orte, E. Debroye, M. J. Ruedas-Rama, E. Garcia-Fernandez, D. Robinson, L. Crovetto, E. M. Talavera, J. M. Alvarez-Pez, V. Leen, B. Verbelen, L. Cunha Dias de Rezende, W. Dehaen, J. Hofkens, M. Van der Auweraer, N. Boens, “Effect of the substitution position (2, 3 or 8) on the spectroscopic and photophysical properties of BODIPY dyes with a phenyl, styryl or phenylethynyl group”, *RSC Adv.* **2016**, *6*, 102899–102913, DOI 10.1039/C6RA22340K.

[166] M. Rahm, R. Hoffmann, N. W. Ashcroft, “Atomic and Ionic Radii of Elements 1–96”, *Chemistry – A European Journal* **2016**, *22*, 14625–14632, DOI 10.1002/chem.201602949.

[167] D. H. Barton, N. Y. Bhatnagar, J.-P. Finet, W. B. Motherwell, “Pentavalent organobismuth reagents. Part VI. Comparative migratory aptitudes of aryl groups in the arylation of phenols and enols by pentavalent bismuth reagents”, *Tetrahedron* **1986**, *42*, 3111–3122, DOI 10.1016/S0040-4020(01)87378-6.

[168] H. Suzuki, T. Ikegami in *Science of Synthesis*, *Vol. 4*, Thieme, **2002**, pp. 77–116, DOI 10.1055/sos-SD-004-00134.

[169] A. Schier, J. M. Wallis, G. Müller, H. Schmidbaur, "$[C_6H_3(CH_3)_3][BiCl_3]$ and $[C_6(CH_3)_6]$ $[BiCl_3]_2$, Arene Complexes of Bismuth with Half-Sandwich and "Inverted" Sandwich Structures", *Angewandte Chemie International Edition* **1986**, *25*, 757–759, DOI 10.1002/anie.198607571.

[170] J. E. Walley, L. S. Warring, E. Kertész, G. Wang, D. A. Dickie, Z. Benkő, R. J. J. Gilliard, "Indirect Access to Carbene Adducts of Bismuth- and Antimony-Substituted Phosphaketene and Their Unusual Thermal Transformation to Dipnictines and $[(NHC)_2OCP][OCP]$", *Inorganic Chemistry* **2021**, *60*, 4733–4743, DOI 10.1021/acs.inorgchem.0c03683.

[171] H. Kuhn, A. Docker, P. D. Beer, "Anion Recognition with Antimony(III) and Bismuth(III) Triaryl-Based Pnictogen Bonding Receptors", *Chemistry – A European Journal* **2022**, *28*, e202201838, DOI 10.1002/chem.202201838.

[172] S. Chibani, A. D. Laurent, B. Le Guennic, D. Jacquemin, "Improving the Accuracy of Excited-State Simulations of BODIPY and Aza-BODIPY Dyes with a Joint SOS-CIS(D) and TD-DFT Approach", *Journal of Chemical Theory and Computation* **2014**, *10*, 4574–4582, DOI 10.1021/ct500655k.

[173] F. Neese, F. Wennmohs, U. Becker, C. Riplinger, "The ORCA quantum chemistry program package", *The Journal of chemical physics* **2020**, *152*, DOI 10.1063/5.0004608.

[174] A. Korzun, M. J. McKee, H. Neugebauer, O. Green, G. Schnakenburg, S. Grimme, N. Kornienko, A. Bismuto, "Antimony and Bismuth Complexes as Visible Light Photosensitizers in Catalytic Oxidation Reactions", *Inorganic Chemistry* **2025**, *64*, 15667–15679, DOI 10.1021/acs.inorgchem.5c02152.

[175] A. Y. Kritskaya, M. B. Berezin, E. V. Antina, A. I. Vyugin, "Effect of aryl-, halogen-, and ms-aza-substitution on the luminescent properties and photostability of difluoroborates of 2, 2′-dipyrrometenes", *Journal of Fluorescence* **2019**, *29*, 911–920, DOI 10.1007/s10895-019-02403-2.

[176] Y. Ge, D. F. O'Shea, "Azadipyrromethenes: from traditional dye chemistry to leading edge applications", *Chemical Society Reviews* **2016**, *45*, 3846–3864, DOI 10.1039/C6CS00200E.

[177] R. M. Diaz-Rodriguez, K. N. Robertson, A. Thompson, "Classifying donor strengths of dipyrrinato/aza-dipyrrinato ligands", *Dalton Transactions* **2019**, *48*, 7546–7550, DOI 10.1039/C9DT01148J.

[178] N. A. Dudina, M. B. Berezin, A. S. Semeikin, E. V. Antina, “Difluoroborates of phenyl-substituted aza-dipyrromethenes: preparation, spectral properties, and stability in solution”, *Russian Journal of General Chemistry* **2015**, *85*, 2739–2742, DOI 10.1134/S1070363215120130.

[179] M. Adib, N. Ayashi, F. Heidari, P. Mirzaei, “Reaction between 4-Nitro-1,3-diarylbutan-1-ones and ammonium acetate in the Presence of Morpholine and Sulfur: an efficient synthesis of 2,4-Diarylpyrroles”, *Synlett* **2016**, *27*, 1738–1742, DOI 10.1055/s-0035-1561852.

[180] R. D. Rieth, N. P. Mankad, E. Calimano, J. P. Sadighi, “Palladium-Catalyzed Cross-Coupling of Pyrrole Anions with Aryl Chlorides, Bromides, and Iodides”, *Organic Letters* **2004**, *6*, 3981–3983, DOI 10.1021/ol048367m.

[181] S. Sugiura, W. Matsuda, W. Zhang, S. Seki, N. Yasuda, H. Maeda, “Ion-Pairing Assemblies Comprising Anion Complexes of π-Extended Anion-Responsive Molecules”, *The Journal of Organic Chemistry* **2019**, *84*, 8886–8898, DOI 10.1021/acs.joc.9b00754.

[182] N. Sakamoto, C. Ikeda, M. Yamamura, T. Nabeshima, “α-Bridged BODIPY oligomers with switchable near-IR photoproperties by external-stimuli-induced foldamer formation and disruption”, *Chemical Communications* **2012**, *48*, 4818–4820, DOI 10.1039/C2CC17513D.

[183] C. Ikeda, S. Ueda, T. Nabeshima, “Aluminium complexes of N_2O_2-type dipyrrins: the first hetero-multinuclear complexes of metallo-dipyrrins with high fluorescence quantum yields”, *Chemical Communications* **2009**, 2544–2546, DOI 10.1039/B820141B.

[184] K. Nakano, K. Kobayashi, K. Nozaki, “Tetravalent Metal Complexes as a New Family of Catalysts for Copolymerization of Epoxides with Carbon Dioxide”, *Journal of the American Chemical Society* **2011**, *133*, 10720–10723, DOI 10.1021/ja203382q.

[185] N. P. van Leest, W. Stroek, M. A. Siegler, J. I. van der Vlugt, B. de Bruin, “Ligand-Mediated Spin-State Changes in a Cobalt-Dipyrrin-Bisphenol Complex”, *Inorganic Chemistry* **2020**, *59*, 12903–12912, DOI 10.1021/acs.inorgchem.0c01979.

[186] K. E. Thomas, N. Desbois, J. Conradie, S. J. Teat, C. P. Gros, A. Ghosh, “Gold dipyrrin-bisphenolates: a combined experimental and DFT study of metal–ligand interactions”, *RSC Advances* **2019**, *10*, 533–540, DOI 10.1039/C9RA09228E.

[187] M. Yamamura, H. Takizawa, Y. Gobo, T. Nabeshima, “Stable neutral radicals of planar N_2O_2-type dipyrrin platinum complexes: hybrid radicals of the delocalized organic π-orbital and platinum d-orbital”, *Dalton Transactions* **2016**, *45*, 6834–6838, DOI 10.1039/C5DT05039A.

[188] P. C. P. Teeuwen, Z. Melissari, M. O. Senge, R. M. Williams, “Metal Coordination Effects on the Photophysics of Dipyrrinato Photosensitizers”, *Molecules* **2022**, *27*, DOI 10.3390/molecules27206967.

[189] N. Sakamoto, C. Ikeda, M. Yamamura, T. Nabeshima, “Structural Interconversion and Regulation of Optical Properties of Stable Hypercoordinate Dipyrrin-Silicon Complexes”, *Journal of the American Chemical Society* **2011**, *133*, 4726–4729, DOI 10.1021/ja2001924.

[190] C. A. Stewart, J. C. Calabrese, A. J. I. Arduengo, “Synthesis and structure of the first 20-Bi-9 system: a discrete nine-coordinate 20-electron bismuth”, *Journal of the American Chemical Society* **1985**, *107*, 3397–3398, DOI 10.1021/ja00297a084.

[191] N. K. Karmakar, S. Pandey, R. K. Pandey, S. S. Shukla, “Solvatochromism: a tool for solvent discretion for UV-Vis spectroscopic studies”, *Applied Spectroscopy Reviews* **2021**, *56*, 513–529, DOI 10.1080/05704928.2020.1838918.

[192] J.-Y. Shin, D. Dolphin, B. O. Patrick, “Protonated Dipyrromethenes and Tetrahalozinc Anions as Synthons in the Solid State”, *Crystal Growth & Design* **2004**, *4*, 659–661, DOI 10.1021/cg049979g.

[193] L. Erlemeier, R.-M. Richter, T. Dunaj, M. J. Müller, S. Chatterjee, C. von Hänisch, “Higher BODIPY Homologues–Synthesis, Reactivity, and Photoluminescence Investigations”, *Chemistry – A European Journal* **2025**, *31*, e202404764, DOI 10.1002/chem.202404764.

[194] M. Geppert, K. Jellinek, M. Linseis, M. Bodensteiner, J. Geppert, M. M. Unterlass, R. F. Winter, “Dual Fluorescence and Phosphorescence Emissions from Dye-Modified (*NCN*)-Bismuth Pincer Thiolate Complexes”, *Inorganic Chemistry* **2024**, *63*, 14876–14888, DOI 10.1021/acs.inorgchem.4c01023.

[195] W.-L. Jia, Q.-D. Liu, R. Wang, S. Wang, “Novel Phosphorescent Cyclometalated Organotin(IV) and Organolead(IV) Complexes of 2,6-Bis(2‘-indolyl)pyridine and 2,6-Bis[2‘-(7-azaindolyl)]pyridine”, *Organometallics* **2003**, *22*, 4070–4078, DOI 10.1021/om030404a.

[196] D. Maeda, H. Shimakoshi, M. Abe, Y. Hisaeda, “Syntheses and Photophysical Behavior of Porphyrin Isomer Sn(IV) Complexes”, *Inorganic Chemistry* **2009**, *48*, 9853–9860, DOI 10.1021/ic901401t.

[197] A. S. Gowda, T. S. Lee, M. C. Rosko, J. L. Petersen, F. N. Castellano, C. Milsmann, “Long-Lived Photoluminescence of Molecular Group 14 Compounds through Thermally Activated Delayed Fluorescence”, *Inorganic Chemistry* **2022**, *61*, 7338–7348, DOI 10.1021/acs.inorgchem.2c00182.

[198] F. Geist, A. Jackel, R. F. Winter, “Ligand Based Dual Fluorescence and Phosphorescence Emission from BODIPY Platinum Complexes and Its Application to Ratiometric Singlet Oxygen Detection”, *Inorganic Chemistry* **2015**, *54*, 10946–10957, DOI 10.1021/acs.inorgchem.5b01969.

[199] K. M. Carsch, I. M. DiMucci, D. A. Iovan, A. Li, S.-L. Zheng, C. J. Titus, S. J. Lee, K. D. Irwin, D. Nordlund, K. M. Lancaster, T. A. Betley, “Synthesis of a copper-supported triplet nitrene complex pertinent to copper-catalyzed amination”, *Science* **2019**, *365*, 1138–1143, DOI 10.1126/science.aax4423.

[200] T. D. Goddard, C. C. Huang, E. C. Meng, E. F. Pettersen, G. S. Couch, J. H. Morris, T. E. Ferrin, “UCSF ChimeraX: Meeting modern challenges in visualization and analysis”, *Protein science* **2018**, *27*, 14–25, DOI 10.1002/pro.3235.

[201] C. Schweitzer, R. Schmidt, “Physical Mechanisms of Generation and Deactivation of Singlet Oxygen”, *Chemical Reviews* **2003**, *103*, 1685–1758, DOI 10.1021/cr010371d.

[202] I. E. Kochevar, R. W. Redmond in *Singlet Oxygen, UV-A, and Ozone*, [2] Methods in Enzymology, Academic Press, **2000**, pp. 20–28, DOI 10.1016/S0076-6879(00)19004-4.

[203] N. Hananya, O. Green, R. Blau, R. Satchi-Fainaro, D. Shabat, “A Highly Efficient Chemiluminescence Probe for the Detection of Singlet Oxygen in Living Cells”, *Angewandte Chemie International Edition* **2017**, *56*, 11793–11796, DOI 10.1002/anie.201705803.

[204] N. Hananya, A. Eldar Boock, C. R. Bauer, R. Satchi-Fainaro, D. Shabat, “Remarkable enhancement of chemiluminescent signal by dioxetane–fluorophore conjugates: turn-on chemiluminescence probes with color modulation for sensing and imaging”, *Journal of the American Chemical Society* **2016**, *138*, 13438–13446, DOI 10.1021/jacs.6b09173.

[205] K. J. Bruemmer, O. Green, T. A. Su, D. Shabat, C. J. Chang, “Chemiluminescent probes for activity-based sensing of formaldehyde released from folate degradation in living mice”, *Angewandte Chemie International Edition* **2018**, *57*, 7508–7512, DOI 10.1002/anie.201802143.

[206] S. Son, M. Won, O. Green, N. Hananya, A. Sharma, Y. Jeon, J. H. Kwak, J. L. Sessler, D. Shabat, J. S. Kim, “Chemiluminescent Probe for the In Vitro and In Vivo Imaging of Cancers Over-Expressing NQO1”, *Angewandte Chemie International Edition* **2019**, *58*, 1739–1743, DOI 10.1002/anie.201813032.

[207] L. Gou, C. N. Coretsopoulos, A. B. Scranton, “Measurement of the dissolved oxygen concentration in acrylate monomers with a novel photochemical method”, *Journal of Polymer Science Part A: Polymer Chemistry* **2004**, *42*, 1285–1292, DOI 10.1002/pola.11083.

[208] A. Sheehan, T. Mikulchyk, C. S. De Castro, S. Karuthedath, W. Althobaiti, M. Dvoracek, H. J. Byrne, F. Laquai, I. Naydenova, M. A. Filatov, et al., “Diethoxycarbonyl-BODIPYs as heavy-atom-free photosensitizers for holographic recording in cellulose acetate photopolymer”, *Journal of Materials Chemistry C* **2023**, *11*, 15084–15096, DOI 10.1039/D3TC02640J.

[209] A. A. Buglak, A. Charisiadis, A. Sheehan, C. J. Kingsbury, M. O. Senge, M. A. Filatov, “Quantitative Structure-Property Relationship Modelling for the Prediction of Singlet Oxygen Generation by Heavy-Atom-Free BODIPY Photosensitizers”, *Chemistry - A European Journal* **2021**, *27*, 9934–9947, DOI 10.1002/chem.202100922.

[210] R. W. Redmond, J. N. Gamlin, “A compilation of singlet oxygen yields from biologically relevant molecules”, *Photochemistry and photobiology* **1999**, *70*, 391–475, DOI 10.1111/j.1751-1097.1999.tb08240.x.

[211] T. L. Figueiredo, R. A. Johnstone, A. M. S. Sørensen, D. Burget, P. Jacques, “Determination of Fluorescence Yields, Singlet Lifetimes and Singlet Oxygen Yields of Water-Insoluble Porphyrins and Metalloporphyrins in Organic Solvents and in Aqueous Media”, *Photochemistry and photobiology* **1999**, *69*, 517–528, DOI 10.1111/j.1751-1097.1999.tb03322.x.

[212] R. H. Young, R. L. Martin, “Mechanism of quenching of singlet oxygen by amines”, *Journal of the American Chemical Society* **1972**, *94*, 5183–5185, DOI 10.1021/ja00770a006.

[213] Y. Tomimori, T. Okujima, T. Yano, S. Mori, N. Ono, H. Yamada, H. Uno, “Synthesis of π-expanded O-chelated boron–dipyrromethene as an NIR dye”, *Tetrahedron* **2011**, *67*, 3187–3193, DOI 10.1016/j.tet.2011.03.016.

[214] K. Liu, R. A. Lalancette, F. Jakle, “B–N Lewis pair functionalization of anthracene: structural dynamics, optoelectronic properties, and O_2 sensitization”, *Journal of the American Chemical Society* **2017**, *139*, 18170–18173, DOI 10.1021/jacs.7b11062.

[215] F. H. Quina, G. T. M. Silva, “The photophysics of photosensitization: A brief overview”, *Journal of Photochemistry and Photobiology* **2021**, *7*, 100042, DOI 10.1016/j.jpap.2021.100042.

[216] N. Mardirossian, M. Head-Gordon, “ωB97X-V: A 10-Parameter, Range-Separated Hybrid, Generalized Gradient Approximation Density Functional with Nonlocal Correlation, Designed by a Survival-of-the-Fittest Strategy”, *Physical Chemistry Chemical Physics* **2014**, *16*, 9904–9924, DOI 10.1039/C3CP54374A.

[217] M. Müller, A. Hansen, S. Grimme, “ωB97X-3c: A Composite Range-Separated Hybrid DFT Method with a Molecule-Optimized Polarized Valence Double-ζ Basis Set”, *Journal of Chemical Physics* **2023**, *158*, 014103, DOI 10.1063/5.0133026.

[218] E. Caldeweyher, S. Ehlert, A. Hansen, H. Neugebauer, S. Spicher, C. Bannwarth, S. Grimme, “A Generally Applicable Atomic-Charge Dependent London Dispersion Correction”, *Journal of Chemical Physics* **2019**, *150*, 154122, DOI 10.1063/1.5090222.

[219] F. Weigend, R. Ahlrichs, “Balanced Basis Sets of Split Valence, Triple Zeta Valence and Quadruple Zeta Valence Quality for H to Rn: Design and Assessment of Accuracy”, *Physical Chemistry Chemical Physics* **2005**, *7*, 3297–3305, DOI 10.1039/B508541A.

[220] J. G. Brandenburg, C. Bannwarth, A. Hansen, S. Grimme, “B97-3c: A Revised Low-Cost Variant of the B97-D Density Functional Method”, *Journal of Chemical Physics* **2018**, *148*, 064104, DOI 10.1063/1.5012601.

[221] A. V. Marenich, C. J. Cramer, D. G. Truhlar, “Universal Solvation Model Based on Solute Electron Density and on a Continuum Model of the Solvent Defined by the Bulk Dielectric Constant and Atomic Surface Tensions”, *Journal of Physical Chemistry B* **2009**, *113*, 6378–6396, DOI 10.1021/jp810292n.

[222] F. Neese, “Software Update: The ORCA Program System—Version 5.0”, *WIREs Computational Molecular Science* **2022**, *12*, e1606, DOI 10.1002/wcms.1606.

[223] F. Neese, “The SHARK Integral Generation and Digestion System”, *Journal of Computational Chemistry* **2023**, *44*, 381–396, DOI 10.1002/jcc.26942.

[224] B. Helmich-Paris, B. de Souza, F. Neese, R. Izsák, "An Improved Chain of Spheres for Exchange Algorithm", *Journal of Chemical Physics* **2021**, *155*, 104109, DOI 10.1063/5.0058766.

[225] A. T. B. Gilbert, N. A. Besley, P. M. W. Gill, "Self-Consistent Field Calculations of Excited States Using the Maximum Overlap Method", *Journal of Physical Chemistry A* **2008**, *112*, 13164–13171, DOI 10.1021/jp801738f.

[226] T. Froitzheim, L. Kunze, S. Grimme, J. M. Herbert, J.-M. Mewes, "Benchmarking Charge-Transfer Excited States in TADF Emitters: △DFT Outperforms TD-DFT for Emission Energies", *The Journal of Physical Chemistry A* **2024**, *128*, 6324–6335, DOI 10.1021/acs.jpca.4c03273.

[227] M. Golfmann, L. Glagow, A. Giakoumidakis, C. Golz, J. C. Walker, "Organophotocatalytic [2+2] Cycloaddition of Electron-Deficient Styrenes", *Chemistry - A European Journal* **2023**, *29*, e202202373, DOI 10.1002/chem.202202373.

[228] M. L. Graziano, M. R. Lesce, R. Scarpati, "Photosensitized oxidation of furans. Part 4. Influence of the substituents on the behaviour of the endo-peroxides of furans", *J. Chem. Soc., Perkin Trans. 1* **1982**, 2007–2012, DOI 10.1039/P19820002007.

[229] M. Prein, W. Adam, "The Schenck Ene Reaction: Diastereoselective Oxyfunctionalization with Singlet Oxygen in Synthetic Applications", *Angewandte Chemie International Edition* **1996**, *35*, 477–494, DOI 10.1002/anie.199604771.

[230] G. Ohloff in *Organic Synthesis*, (Eds.: A. Bruylants, L. Ghosez, H. Viehe), Butterworth-Heinemann, **1975**, pp. 481–502, DOI 10.1016/B978-0-408-70725-1.50014-8.

[231] B. Clark, B. Jones, G. Iacobucci, "Characterization of the hydroperoxides derived from singlet oxygen oxidation of (+)-limonene", *Tetrahedron* **1981**, *37*, 405–409, DOI 10.1016/0040-4020(81)85078-8.

[232] J. A. Celaje, D. Zhang, A. M. Guerrero, M. Selke, "Chemistry of trans-Resveratrol with Singlet Oxygen: [2+2] Addition, [4+2] Addition, and Formation of the Phytoalexin Moracin M", *Org. Lett.* **2011**, *13*, 4846–4849, DOI 10.1021/ol201922u.

[233] R. H. Young, R. L. Martin, D. Feriozi, B. D., R. Kayser, "ON THE MECHANISM OF QUENCHING OF SINGLET OXYGEN BY AMINES-III. EVIDENCE FOR A CHARGE-TRANSFER-LIKE COMPLEX", *Photochemistry and Photobiology* **1973**, *17*, 233–244, DOI 10.1111/j.1751-1097.1973.tb06352.x.

[234] F. Jensen, A. Greer, E. L. Clennan, “Reaction of Organic Sulfides with Singlet Oxygen. A Revised Mechanism”, *Journal of the American Chemical Society* **1998**, *120*, 4439–4449, DOI 10.1021/ja973782d.

[235] S. M. Bonesi, A. Albini, “Effect of Protic Cosolvents on the Photooxygenation of Diethyl Sulfide”, *The Journal of Organic Chemistry* **2000**, *65*, 4532–4536, DOI 10.1021/jo000069p.

[236] M. Forchetta, F. Sabuzi, L. Stella, V. Conte, P. Galloni, “KuQuinone as a Highly Stable and Reusable Organic Photocatalyst in Selective Oxidation of Thioethers to Sulfoxides”, *The Journal of Organic Chemistry* **2022**, *87*, 14016–14025, DOI 10.1021/acs.joc.2c01648.

[237] J. G. Riess, “Oxygen Carriers (“Blood Substitutes”): Raison d’Etre, Chemistry, and Some Physiology: Blut ist ein ganz besondrer Saft”, *Chemical Reviews* **2001**, *101*, 2797–2920, DOI 10.1021/cr970143c.

[238] M. Matsumoto, Y. Kitano, H. Kobayashi, H. Ikawa, “Singlet oxygenation of 1-aminomethyl-1-tert-butyl-2-methoxy-2-(3-methoxy-phenyl)ethylenes: Marked effect of allylic nitrogen on the reaction pathways and chemoselectivity”, *Tetrahedron Letters* **1996**, *37*, 8191–8194, DOI 10.1016/0040-4039(96)01858-8.

[239] G. Jiang, J. Chen, J.-S. Huang, C.-M. Che, “Highly Efficient Oxidation of Amines to Imines by Singlet Oxygen and Its Application in Ugi-Type Reactions”, *Organic Letters* **2009**, *11*, 4568–4571, DOI 10.1021/ol9018166.

[240] R. Kumar, E. H. Gleißner, E. G. V. Tiu, Y. Yamakoshi, “C70 as a Photocatalyst for Oxidation of Secondary Benzylamines to Imines”, *Organic Letters* **2016**, *18*, 184–187, DOI 10.1021/acs.orglett.5b03194.

[241] A. Berlicka, B. König, “Porphycene-mediated photooxidation of benzylamines by visible light”, *Photochemical & Photobiological Sciences* **2010**, *9*, 1359–1366, DOI 10.1039/c0pp00192a.

[242] F. Su, S. C. Mathew, L. Möhlmann, M. Antonietti, X. Wang, S. Blechert, “Aerobic oxidative coupling of amines by carbon nitride photocatalysis with visible light”, *Angewandte Chemie International Edition* **2011**, *123*, 683–686, DOI 10 .1002/anie.201004365.

[243] J. H. Park, K. C. Ko, E. Kim, N. Park, J. H. Ko, D. H. Ryu, T. K. Ahn, J. Y. Lee, S. U. Son, “Photocatalysis by Phenothiazine Dyes: Visible-Light-Driven Oxidative Coupling of Primary Amines at Ambient Temperature”, *Organic Letters* **2012**, *14*, 5502–5505, DOI 10.1021/ol302584y.

[244] D. B. Ushakov, M. B. Plutschack, K. Gilmore, P. H. Seeberger, “Factors Influencing the Regioselectivity of the Oxidation of Asymmetric Secondary Amines with Singlet Oxygen”, *Chemistry – A European Journal* **2015**, *21*, 6528–6534, DOI 10.1002/chem.201500121.

[245] T. Bortolato, S. Cuadros, G. Simionato, L. Dell’Amico, “The advent and development of organophotoredox catalysis”, *Chemical Communications* **2022**, *58*, 1263–1283, DOI 10.1039/D1CC05850A.

[246] L. Chu, C. Ohta, Z. Zuo, D. W. MacMillan, “Carboxylic acids as a traceless activation group for conjugate additions: a three-step synthesis of (±)-pregabalin”, *Journal of the American Chemical Society* **2014**, *136*, 10886–10889, DOI 10.1021/ja505964r.

[247] A. Joshi-Pangu, F. Lévesque, H. G. Roth, S. F. Oliver, L.-C. Campeau, D. Nicewicz, D. A. DiRocco, “Acridinium-Based Photocatalysts: A Sustainable Option in Photoredox Catalysis”, *The Journal of Organic Chemistry* **2016**, *81*, 7244–7249, DOI 10.1021/acs.joc.6b01240.

[248] E. Speckmeier, T. G. Fischer, K. Zeitler, “A toolbox approach to construct broadly applicable metal-free catalysts for photoredox chemistry: deliberate tuning of redox potentials and importance of halogens in donor–acceptor cyanoarenes”, *Journal of the American Chemical Society* **2018**, *140*, 15353–15365, DOI 10.1021/jacs.8b08933.

[249] Z. Liang, S. Xu, W. Tian, R. Zhang, “Eosin Y-catalyzed visible-light-mediated aerobic oxidative cyclization of N,N-dimethylanilines with maleimides”, *Beilstein Journal of Organic Chemistry* **2015**, *11*, 425–430, DOI 10.3762/bjoc.11.48.

[250] X. Ju, D. Li, W. Li, W. Yu, F. Bian, “The reaction of tertiary anilines with maleimides under visible light redox catalysis”, *Advanced Synthesis & Catalysis* **2012**, *354*, 3561–3567, DOI 10.1002/adsc.201200608.

[251] C. B. Tripathi, T. Ohtani, M. T. Corbett, T. Ooi, “Photoredox ketone catalysis for the direct C–H imidation and acyloxylation of arenes”, *Chemical Science* **2017**, *8*, 5622–5627, DOI 10.1039/C7SC01700F.

[252] D. Kalyani, K. B. McMurtrey, S. R. Neufeldt, M. S. Sanford, “Room-Temperature C-H Arylation: Merger of Pd-Catalyzed C–H Functionalization and Visible-Light Photocatalysis”, *Journal of the American Chemical Society* **2011**, *133*, 18566–18569, DOI 10.1021/ja208068w.

[253] A. Korzun, P. C. Brehm, G. Schnakenburg, A. Bismuto, “SBDIPY Chromophores as Multitools for Molecular Sensing”, *Organometallics* **2026**, *45*, 81–89, DOI 10.1021/acs.organomet.5c00408.

[254] U. Mayer, V. Gutmann, W. Gerger, “The acceptor number—A quantitative empirical parameter for the electrophilic properties of solvents”, *Monatshefte für Chemie* **1975**, *106*, 1235–1257, DOI 10.1007/BF00913599.

[255] V. Gutmann, “Solvent effects on the reactivities of organometallic compounds”, *Coordination Chemistry Reviews* **1976**, *18*, 225–255, DOI 10.1016/S0010-8545(00)82045-7.

[256] M. A. Beckett, G. C. Strickland, J. R. Holland, K. S. Varma, “A convenient n.m.r. method for the measurement of Lewis acidity at boron centres: correlation of reaction rates of Lewis acid initiated epoxide polymerizations with Lewis acidity”, *Polymer* **1996**, *37*, 4629–4631, DOI 10.1016/0032-3861(96)00323-0.

[257] P. Erdmann, L. Greb, “What Distinguishes the Strength and the Effect of a Lewis Acid: Analysis of the Gutmann–Beckett Method”, *Angewandte Chemie International Edition* **2022**, *61*, e202114550, DOI 10.1002/anie.202114550.

[258] J. R. Gaffen, J. N. Bentley, L. C. Torres, C. Chu, T. Baumgartner, C. B. Caputo, “A Simple and Effective Method of Determining Lewis Acidity by Using Fluorescence”, *Chem* **2019**, *5*, 1567–1583, DOI 10.1016/j.chempr.2019.03.022.

[259] J. N. Bentley, S. A. Elgadi, J. R. Gaffen, P. Demay-Drouhard, T. Baumgartner, C. B. Caputo, “Fluorescent Lewis Adducts: A Practical Guide to Relative Lewis Acidity”, *Organometallics* **2020**, *39*, 3645–3655, DOI 10.1021/acs.organomet.0c00389.

[260] C. R. Wade, I.-S. Ke, F. P. Gabbaï, “Sensing of aqueous fluoride anions by cationic stibine-palladium complexes.”, *Angewandte Chemie (International ed. in English)* **2011**, *51*, 478–481, DOI 10.1002/anie.201106242.

[261] I.-S. Ke, M. Myahkostupov, F. N. Castellano, F. P. Gabbaï, “Stibonium ions for the fluorescence turn-on sensing of F^- in drinking water at parts per million concentrations”, *Journal of the American Chemical Society* **2012**, *134*, 15309–15311, DOI 10.1021/ja308194w.

[262] M. Hirai, F. P. Gabbaï, “Lewis acidic stiborafluorenes for the fluorescence turn-on sensing of fluoride in drinking water at ppm concentrations”, *Chemical Science* **2014**, *5*, 1886–1893, DOI 10.1039/C4SC00343H.

[263] T. Chu, G. I. Nikonov, “Oxidative Addition and Reductive Elimination at Main-Group Element Centers”, *Chemical Reviews* **2018**, *118*, 3608–3680, DOI 10.1021/acs.chemrev.7b00572.

[264] H. Haldar, C. B. Yildiz, M. Majumdar, “Coordination Chemistry of the Antimony(III) and Bismuth(III) Cations using Bis(α-iminopyridine) as Ligand”, *Chem PlusChem* **2023**, *88*, e202300211, DOI 10.1002/cplu.202300211.

[265] R. J. Mayer, N. Hampel, A. R. Ofial, “Lewis Acidic Boranes, Lewis Bases, and Equilibrium Constants: A Reliable Scaffold for a Quantitative Lewis Acidity/Basicity Scale”, *Chemistry – A European Journal* **2021**, *27*, 4070–4080, DOI https://doi.org/10.1002/chem.202003916.

[266] B. F. G. Johnson, J. Lewis, P. W. Robinson, J. R. Miller, “The infrared spectra of metal carbonyl compounds. Part III. Exchange studies on tetracarbonylrhodium complexes of the type $Rh_2(CO)_4X_2$(X = Cl, Br, I, SEt, or SPh)”, *Journal of the Chemical Society A: Inorganic Physical Theoretical* **1969**, 2693–2695, DOI 10.1039/J19690002693.

[267] N. Boens, V. Leen, W. Dehaen, “Fluorescent indicators based on BODIPY”, *Chemical Society Reviews* **2012**, *41*, 1130–1172, DOI 10.1039/C1CS15132K.

[268] P. Erdmann, M. Schmitt, L. M. Sigmund, F. Krämer, F. Breher, L. Greb, “How to Deal with Charge in the Ranking of Lewis Acidity: Critical Evaluation of an Extensive Set of Cationic Lewis Acids”, *Angewandte Chemie International Edition* **2024**, *63*, e202403356, DOI 10.1002/anie.202403356.

[269] V. Barone, M. Cossi, “Quantum Calculation of Molecular Energies and Energy Gradients in Solution by a Conductor Solvent Model”, *The Journal of Physical Chemistry A* **1998**, *102*, 1995–2001, DOI 10.1021/jp9716997.

[270] I. Vránová, R. Jambor, A. Růžička, R. Jirásko, L. Dostál, “Reactivity of N,C,N-Chelated Antimony(III) and Bismuth(III) Chlorides with Lithium Reagents: Addition vs Substitution”, *Organometallics* **2015**, *34*, 534–541, DOI 10.1021/om5011879.

[271] A. Gagnon, J. Dansereau, A. Le Roch, “Organobismuth reagents: synthesis, properties and applications in organic synthesis”, *Synthesis* **2017**, *49*, 1707–1745, DOI 10.1055/s-0036-1589482.

[272] E. Lieber, C. N. R. Rao, T. S. Chao, C. W. W. Hoffman, “Infrared Spectra of Organic Azides”, *Analytical Chemistry* **1957**, *29*, 916–918, DOI 10.1021/ac60126a016.

[273] N. A. Yakelis, R. G. Bergman, “Safe Preparation and Purification of Sodium Tetrakis[(3,5-trifluoromethyl)phenyl]borate ($NaBArF_{24}$): Reliable and Sensitive Analysis of Water in Solutions of Fluorinated Tetraarylborates”, *Organometallics* **2005**, *24*, 3579–3581, DOI 10.1021/om0501428.

[274] C. J. Carmalt, N. A. Compton, R. J. Errington, G. A. Fisher, I. Moenandar, N. C. Norman, K. H. Whitmire, “Homoleptic bismuth amides”, *Inorganic syntheses* **1996**, *31*, 98–101, DOI 10.1002/9780470132623.ch15.

[275] A. D. Cardenal, A. Maity, W.-Y. Gao, R. Ashirov, S.-M. Hyun, D. C. Powers, “Iodosylbenzene Coordination Chemistry Relevant to Metal–Organic Framework Catalysis”, *Inorganic Chemistry* **2019**, *58*, 10543–10553, DOI 10.1021/acs.inorgchem.9b01191.

[276] J. A. McCleverty, G. Wilkinson, L. G. Lipson, M. L. Maddox, H. D. Kaesz in *Inorganic Syntheses*, John Wiley & Sons, Ltd, **1966**, pp. 211–214, DOI 10.1002/9780470132395.ch56.

[277] Z.-J. Lv, K. A. Eisenlohr, R. Naumann, T. Reuter, H. Verplancke, S. Demeshko, R. Herbst-Irmer, K. Heinze, M. C. Holthausen, S. Schneider, “Triplet carbenes with transition-metal substituents”, *Nature Chemistry* **2024**, *16*, 1788–1793, DOI 10.1038/s41557-024-01597-8.

[278] K. Fredenhagen, G. Cadenbach, “Die bindung von kalium durch kohlenstoff”, *Zeitschrift für anorganische und allgemeine Chemie* **1926**, *158*, 249–263, DOI 10.1002/zaac.19542770307.

[279] W. Rüdorff, E. Schulze, “Über Alkaligraphitverbindungen”, *Zeitschrift für anorganische und allgemeine Chemie* **1954**, *277*, 156–171, DOI 10.1002/zaac.19542770307.

[280] J. Tang, Y. Liu, B. Qiu, Z. Zhang, X. Zhang, “$PhI(OAc)_2$-Promoted Site-Selective C–H Chlorination of (Hetero)arenes with *p*-Toluenesulfonyl Chloride”, *Organic Letters* **2024**, *26*, 8708–8712, DOI 10.1021/acs.orglett.4c03017.

[281] L. Cunha Dias de Rezende, M. Menezes Vaidergorn, J. C. Biazzotto Moraes, F. da Silva Emery, “Synthesis, photophysical properties and solvatochromism of meso-substituted tetramethyl BODIPY dyes”, *Journal of fluorescence* **2014**, *24*, 257–266, DOI 10.1007/s10895-013-1293-8.

[282] R. F. Kubin, A. N. Fletcher, “Fluorescence quantum yields of some rhodamine dyes”, *Journal of Luminescence* **1982**, *27*, 455–462, DOI 10.1016/0022-2313(82)90045-X.

[283] J. E. Bertie, Z. Lan, R. N. Jones, Y. Apelblat, "Infrared intensities of liquids XVIII: Accurate optical constants and molar absorption coefficients between 6500 and 800 cm^{-1} of dichloromethane at 25 °C, from spectra recorded in several laboratories", *Applied spectroscopy* **1995**, *49*, 840–851, DOI 10.1366/000370295396443.

[284] J. Ortega, "Densities and refractive indices of pure alcohols as a function of temperature", *Journal of Chemical & Engineering Data* **1982**, *27*, 312–317, DOI 10.1021/je00029a024.

[285] G. M. Sheldrick, "A short history of *SHELX*", *Acta Crystallographica Section A* **2008**, *64*, 112–122, DOI 10.1107/S0108767307043930.

[286] O. V. Dolomanov, L. J. Bourhis, R. J. Gildea, J. A. K. Howard, H. Puschmann, "*OLEX2*: a complete structure solution, refinement and analysis program", *Journal of Applied Crystallography* **2009**, *42*, 339–341, DOI 10.1107/S0021889808042726.

[287] C. F. Macrae, I. Sovago, S. J. Cottrell, P. T. A. Galek, P. McCabe, E. Pidcock, M. Platings, G. P. Shields, J. S. Stevens, M. Towler, P. A. Wood, "*Mercury 4.0*: from visualization to analysis, design and prediction", *Journal of Applied Crystallography* **2020**, *53*, 226–235, DOI 10.1107/S1600576719014092.

[288] D. Kratzert, *FinalCif*, *V113*, https://dkratzert.de/finalcif.html.

[289] T. Kottke, D. Stalke, "Crystal handling at low temperatures", *Journal of Applied Crystallography* **1993**, *26*, 615–619, DOI 10.1107/S0021889893002018.

[290] X. Liu, H. Nan, W. Sun, Q. Zhang, M. Zhan, L. Zou, Z. Xie, X. Li, C. Lu, Y. Cheng, "Synthesis and characterisation of neutral mononuclear cuprous complexes based on dipyrrin derivatives and phosphine mixed-ligands", *Dalton Transactions* **2012**, *41*, 10199–10210, DOI 10.1039/C2DT30618B.

[291] J. Karges, O. Blacque, H. Chao, G. Gasser, "Polymeric Bis(dipyrrinato) Zinc(II) Nanoparticles as Selective Imaging Probes for Lysosomes of Cancer Cells", *Inorganic Chemistry* **2019**, *58*, 12422–12432, DOI 10.1021/acs.inorgchem.9b02019.

[292] R. Tabone, D. Feser, E. D. Lemma, U. Schepers, C. Bizzarri, "Intriguing Heteroleptic Zn^{II} bis(dipyrrinato) Emitters in the Far-Red Region With Large Pseudo-Stokes Shift for Bioimaging", *Frontiers in Chemistry* **2021**, *9*, DOI 10.3389/fchem.2021.754420.

[293] A. A.-S. Ali, J. Cipot-Wechsler, S. M. Crawford, O. Selim, R. L. Stoddard, T. S. Cameron, A. Thompson, “The first series of alkali dipyrrinato complexes”, *Canadian Journal of Chemistry* **2010**, *88*, 725–735, DOI 10.1139/V09-180.

[294] M. Vehkamäki, T. Hatanpää, M. Ritala, M. Leskelä, “Bismuth precursors for atomic layer deposition of bismuth-containing oxide films”, *Journal of Materials Chemistry* **2004**, *14*, 3191–3197, DOI 10.1039/b405891g.

[295] M. Sekiya, K. Umezawa, A. Sato, D. Citterio, K. Suzuki, “A novel luciferin-based bright chemiluminescent probe for the detection of reactive oxygen species”, *Chemical communications* **2009**, 3047–3049, DOI 10.1039/B903751A.

[296] A. Gorman, J. Killoran, C. O’Shea, T. Kenna, W. M. Gallagher, D. F. O’Shea, “In Vitro Demonstration of the Heavy-Atom Effect for Photodynamic Therapy”, *Journal of the American Chemical Society* **2004**, *126*, 10619–10631, DOI 10.1021/ja047649e.

[297] I. Heldt, U. Behrens, “Strukturen der Alkalimetallsalze aromatischer, heterocyclischer Amide: Synthese und Struktur von Kronenether-Addukten der Alkalimetall-Pyrrolide”, *Zeitschrift für anorganische und allgemeine Chemie* **2005**, *631*, 749–758, DOI 10.1002/zaac.200400449.

[298] Y. Baek, E. T. Hennessy, T. A. Betley, “Direct manipulation of metal imido geometry: Key principles to enhance C–H amination efficacy”, *Journal of the American Chemical Society* **2019**, *141*, 16944–16953, DOI 10.1021/jacs.9b09015.

[299] J. A. McCubbin, O. V. Krokhin, “Organocatalyzed Friedel–Crafts arylation of benzylic alcohols”, *Tetrahedron Letters* **2010**, *51*, 2447–2449, DOI 10.1016/j.tetlet.2010.02.151.

[300] N. Ji, H. O’Dowd, B. M. Rosen, A. G. Myers, “Enantioselective synthesis of N1999A2”, *Journal of the American Chemical Society* **2006**, *128*, 14825–14827, DOI 10.1021/ja0662467.

[301] E. R. King, T. A. Betley, “C–H bond amination from a ferrous dipyrromethene complex”, *Inorganic chemistry* **2009**, *48*, 2361–2363, DOI 10.1021/ic900219b.

[302] Z. Mahmood, K. Xu, B. Küçüköz, X. Cui, J. Zhao, Z. Wang, A. Karatay, H. G. Yaglioglu, M. Hayvali, A. Elmali, “DiiodoBodipy-Perylenebisimide Dyad/Triad: Preparation and Study of the Intramolecular and Intermolecular Electron/Energy Transfer”, *The Journal of Organic Chemistry* **2015**, *80*, 3036–3049, DOI 10.1021/jo502899p.

[303] D. Lenoir, “The application of low-valent titanium reagents in organic synthesis”, *Synthesis* **1989**, *1989*, 883–897, DOI 10.1055/s-1989-27424.

[304] Y. Kabe, T. Takata, K. Ueno, W. Ando, “Stereochemical studies of dioxetane formation with hindered olefins”, *Journal of the American Chemical Society* **1984**, *106*, 8174–8180, DOI 10.1021/ja00338a028.

[305] L. J. Allen, P. J. Cabrera, M. Lee, M. S. Sanford, “N-Acyloxyphthalimides as Nitrogen Radical Precursors in the Visible Light Photocatalyzed Room Temperature C–H Amination of Arenes and Heteroarenes”, *Journal of the American Chemical Society* **2014**, *136*, 5607–5610, DOI 10.1021/ja501906x.

[306] F. Lévesque, P. H. Seeberger, “Highly Efficient Continuous Flow Reactions Using Singlet Oxygen as a “Green” Reagent”, *Organic Letters* **2011**, *13*, 5008–5011, DOI 10.1021/ol2017643.

[307] T. Kuga, Y. Sasano, Y. Iwabuchi, “IBX as a catalyst for dehydration of hydroperoxides: green entry to α, β-unsaturated ketones via oxygenative allylic transposition”, *Chemical Communications* **2018**, *54*, 798–801, DOI 10.1039/C7CC08957K.

[308] M. M. Hossain, S.-G. Shyu, “Biphasic copper-catalyzed C–H bond activation of arylalkanes to ketones with tert-butyl hydroperoxide in water at room temperature”, *Tetrahedron* **2016**, *72*, 4252–4257, DOI 10.1016/j.tet.2016.05.066.

[309] F. Silva, A. Baker, J. Stansall, W. Michalska, M. S. Yusubov, M. Graz, R. Saunders, G. J. Evans, T. Wirth, “Selective oxidation of sulfides in flow chemistry”, *European Journal of Organic Chemistry* **2018**, *2018*, 2134–2137, DOI 10.1002/ejoc.201800339.

[310] Y. Imada, I. Tonomura, N. Komiya, T. Naota, “Aerobic oxidation of sulfides with a vitamin b2-derived organocatalyst”, *Synlett* **2013**, *24*, 1679–1682, DOI 10.1055/s-0033-1339276.

[311] M. H. Aukland, M. Šiaučiulis, A. West, G. J. Perry, D. J. Procter, “Metal-free photoredox-catalysed formal C–H/C–H coupling of arenes enabled by interrupted Pummerer activation”, *Nature Catalysis* **2020**, *3*, 163–169, DOI 10.1038/s41929-019-0415-3.

I. Compound abbreviations

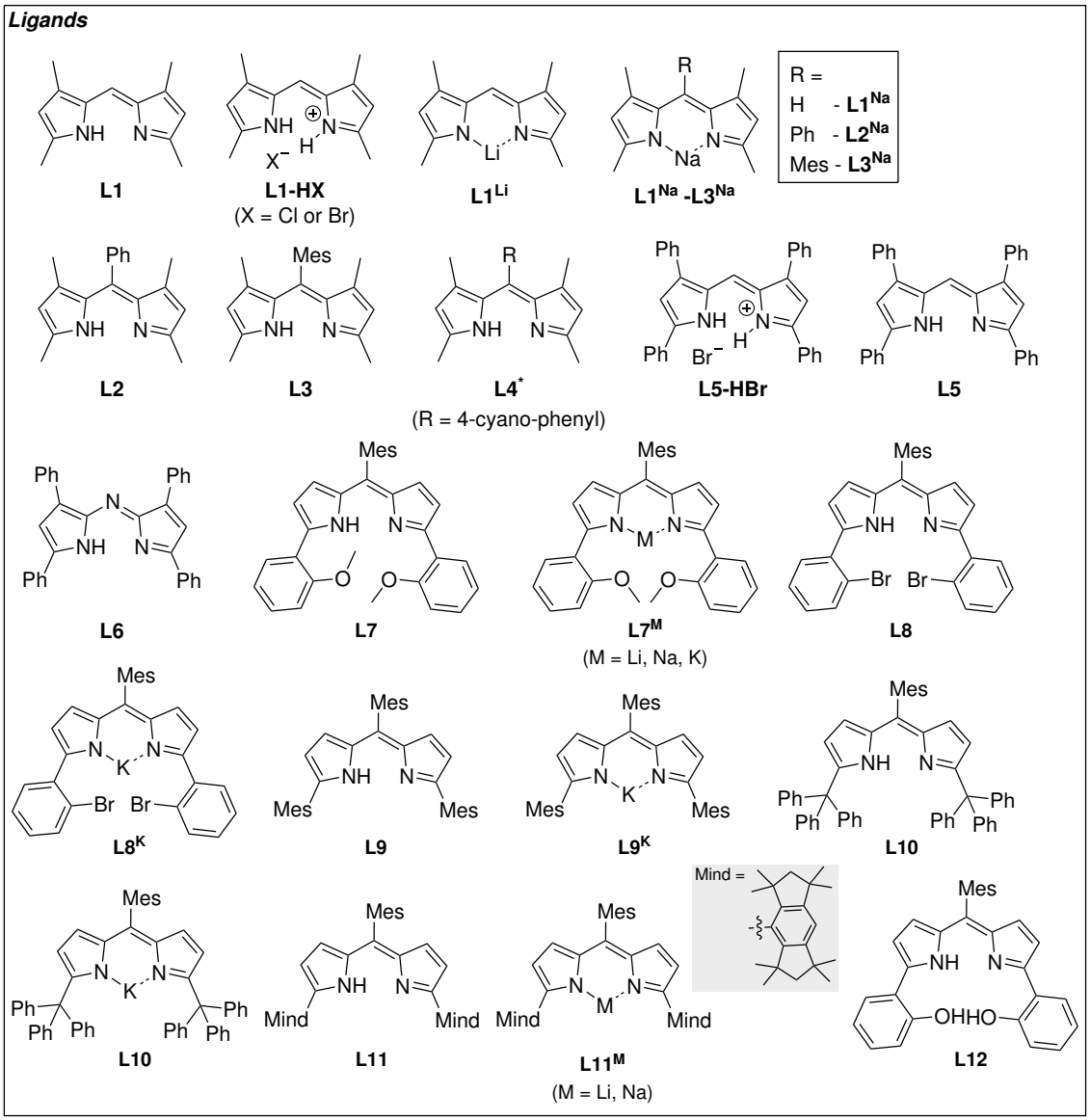


Figure 142: Abbreviations of ligands used within this work. *__L4__ was independently synthesized by A. Bismuto.

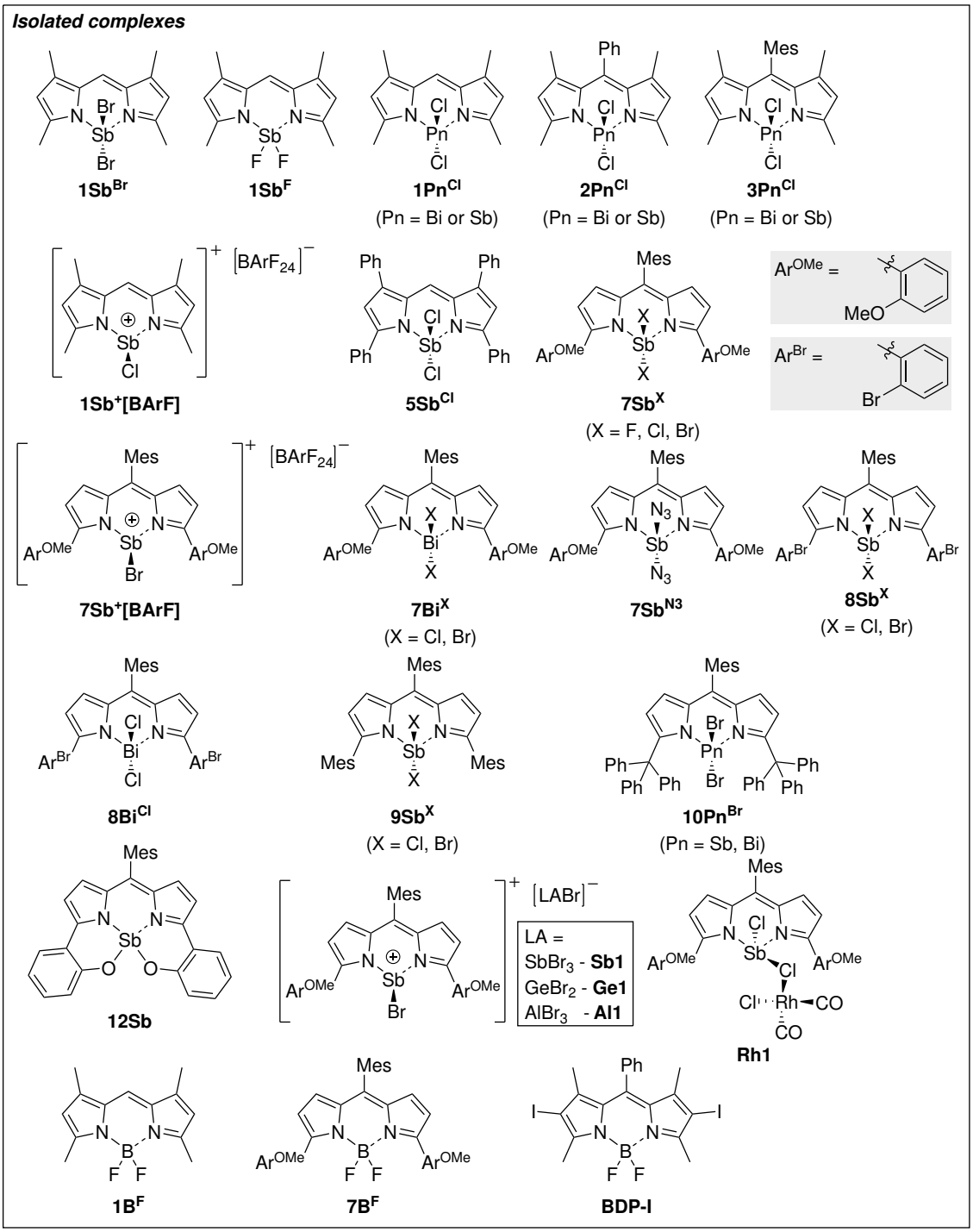


Figure 143: Abbreviations of isolated complexes within this work.

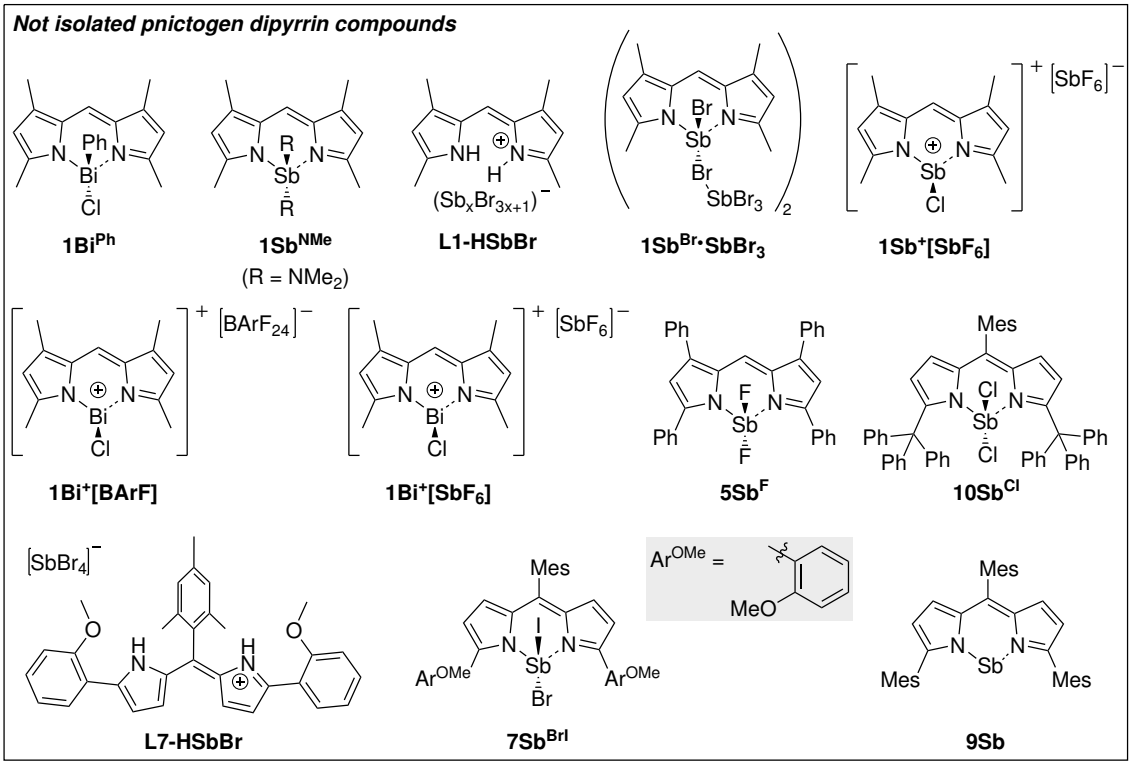


Figure 144: Abbreviations of non-isolated pnictogen dipyrrin compounds within this work.

II. Appendix: Publications

The work presented in this dissertation was partially published in the following articles:

1. **Korzun, A.**; Brehm, P. C.; Schnakenburg, G.; Bismuto, A.* SBDIPY Chromophores as Multitools for Molecular Sensing. *Organometallics* **2026**, *45*, 81–89, doi.org/10.1021/acs.organomet.5c00408.

2. **Korzun, A.**; McKee, M. J.; Neugebauer, H.; Green, O.; Schnakenburg, G.; Grimme, S; Kornienko, N; Bismuto, A.* Antimony and Bismuth Complexes as Visible Light Photosensitizers in Catalytic Oxidation Reactions. *Inorg. Chem.* **2025**, *64*, 15667–15679, doi.org/10.1021/acs.inorgchem.5c02152.

3. **Korzun, A.**; Crespi, S.; Golz, C.; Bismuto, A.* Replacing the BO in BODIPY: unlocking the path to SBDIPY and BIDIPY chromophores. *Chem. Sci.* **2023**, *14*, 6579–6584, doi.org/10.1039/D3SC01493B.

III. Appendix: NMR spectra

Chapter 2

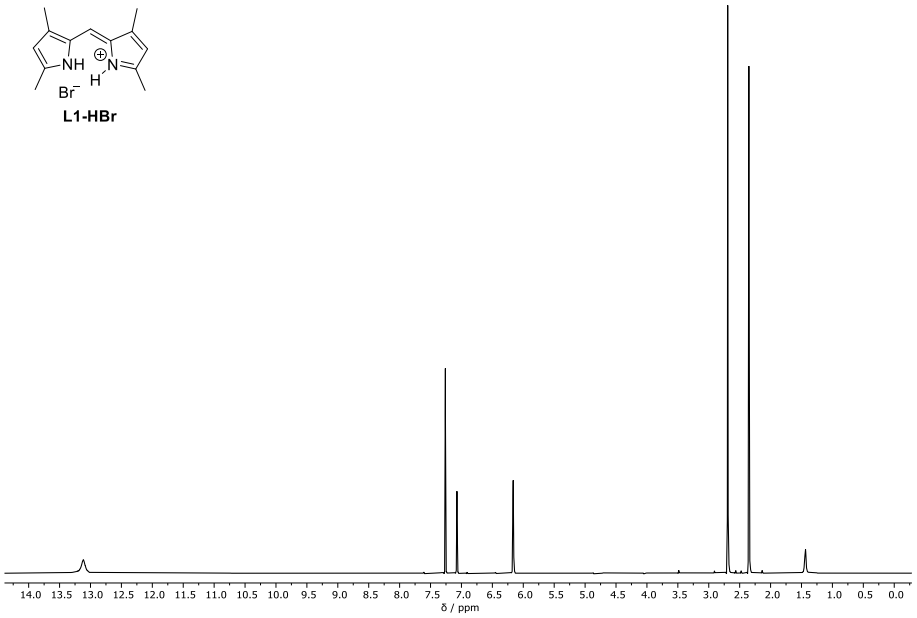


Figure 145: ^{1}H NMR (300 MHz) spectrum of **L1-HBr** in $CDCl_3$.

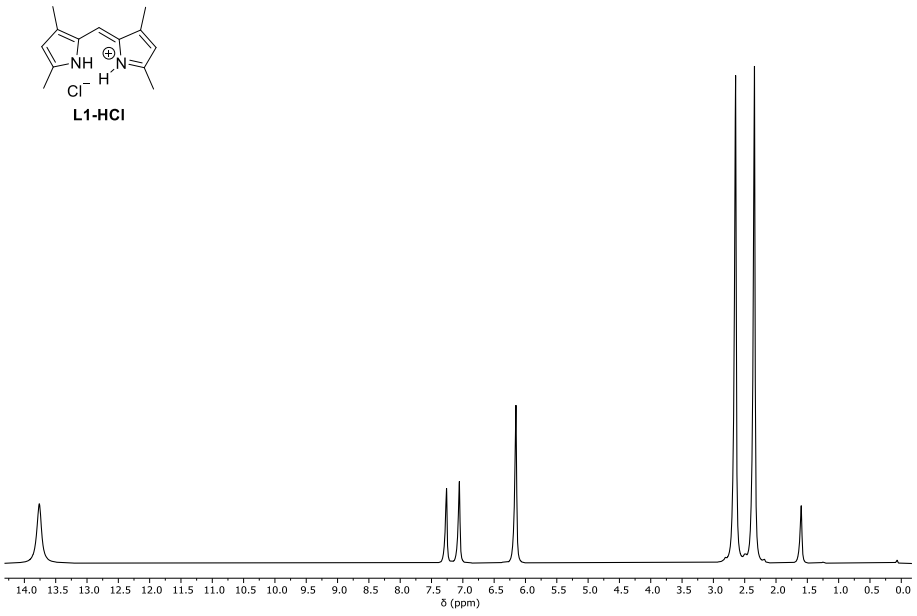


Figure 146: ^{1}H NMR (400 MHz) spectrum of **L1-HCl** in $CDCl_3$.

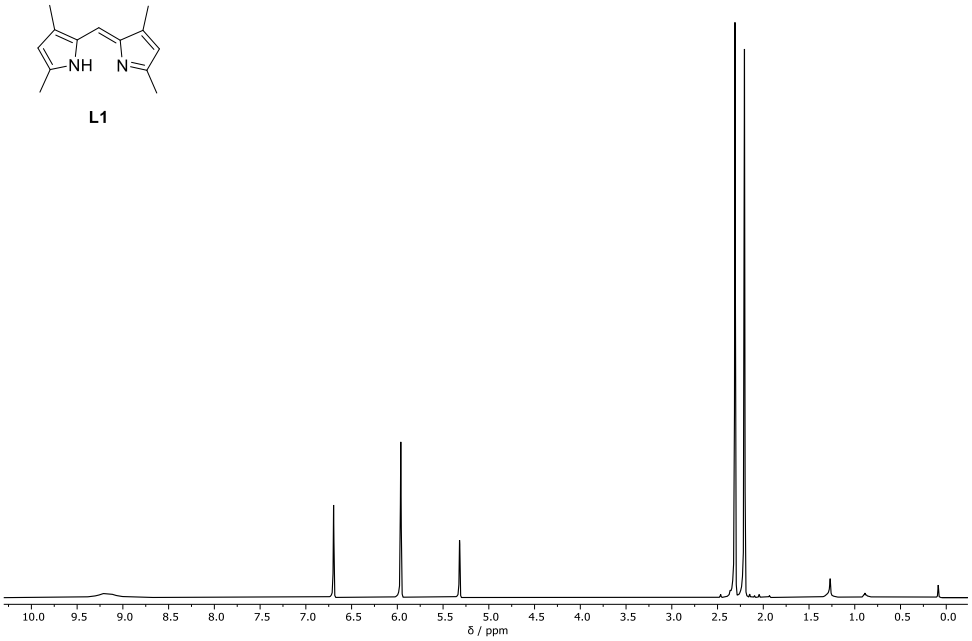


Figure 147: ^{1}H NMR (400 MHz) spectrum of **L1** in CD_2Cl_2.

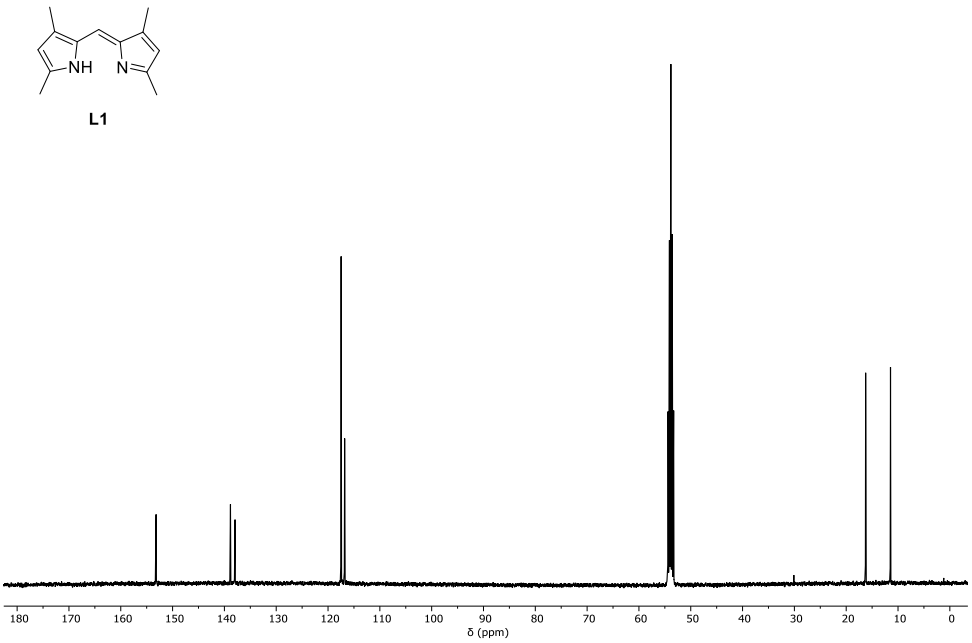


Figure 148: $^{13}C\{^{1}H\}$ NMR (101 MHz) spectrum of **L1** in CD_2Cl_2.

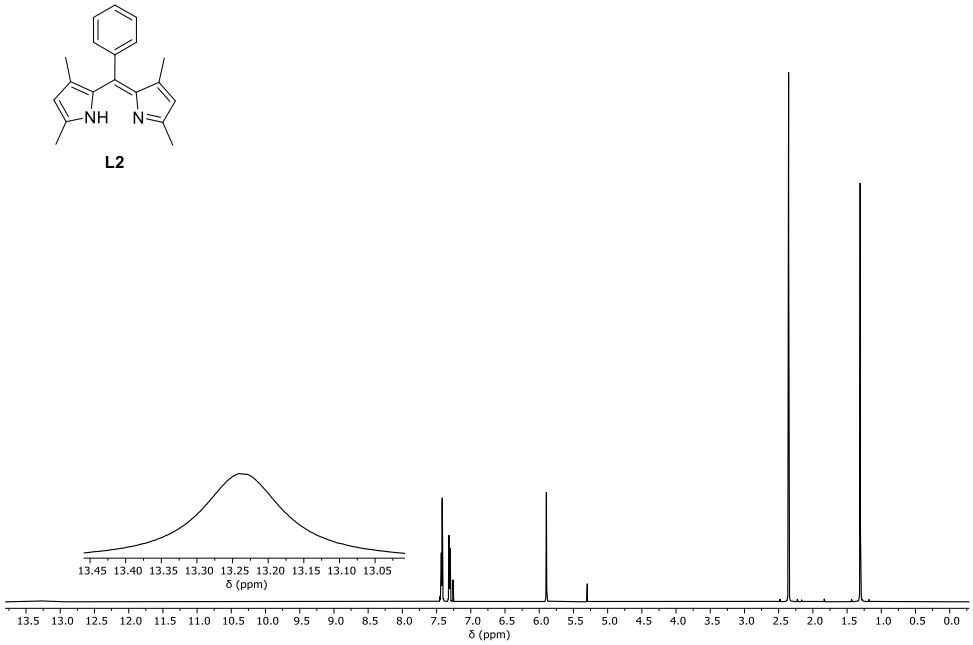


Figure 149: ^{1}H NMR (500 MHz) spectrum of **L2** in $CDCl_3$.

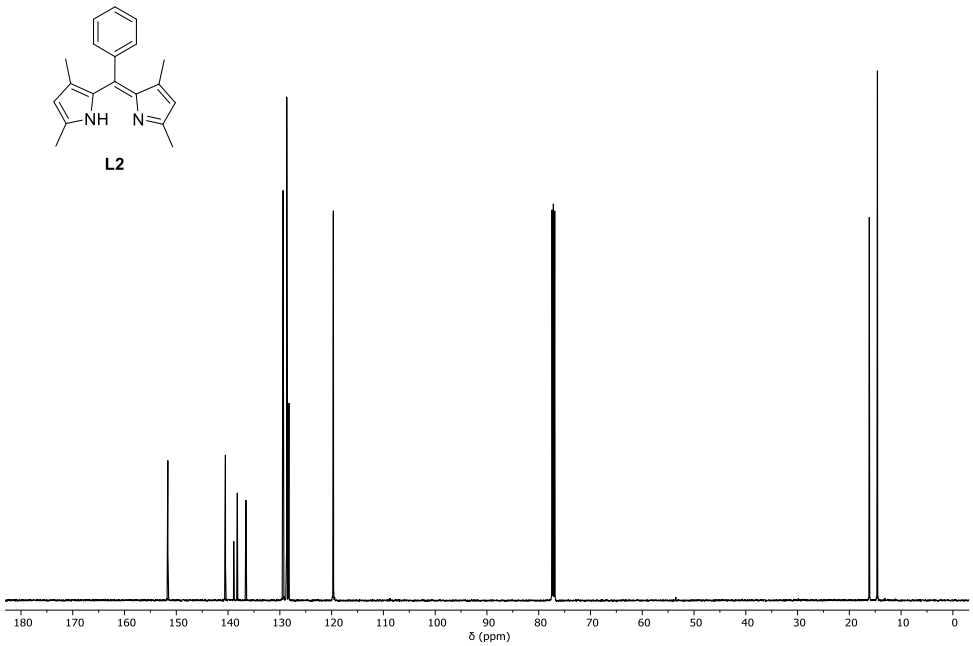


Figure 150: $^{13}C\{^{1}H\}$ NMR (126 MHz) spectrum of **L2** in $CDCl_3$.

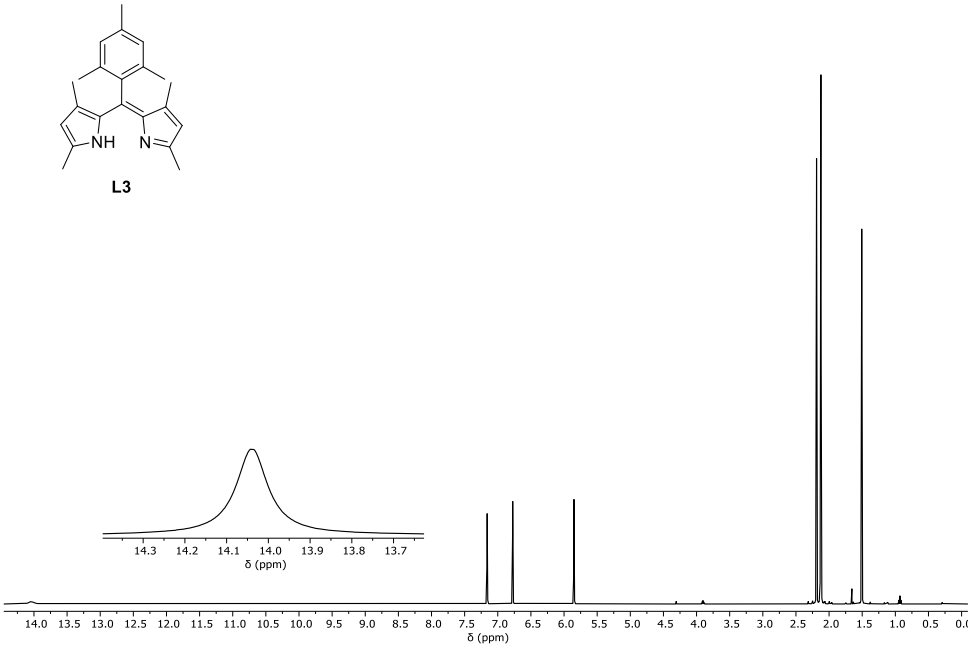


Figure 151: ^{1}H NMR (500 MHz) spectrum of **L3** in C_6D_6.

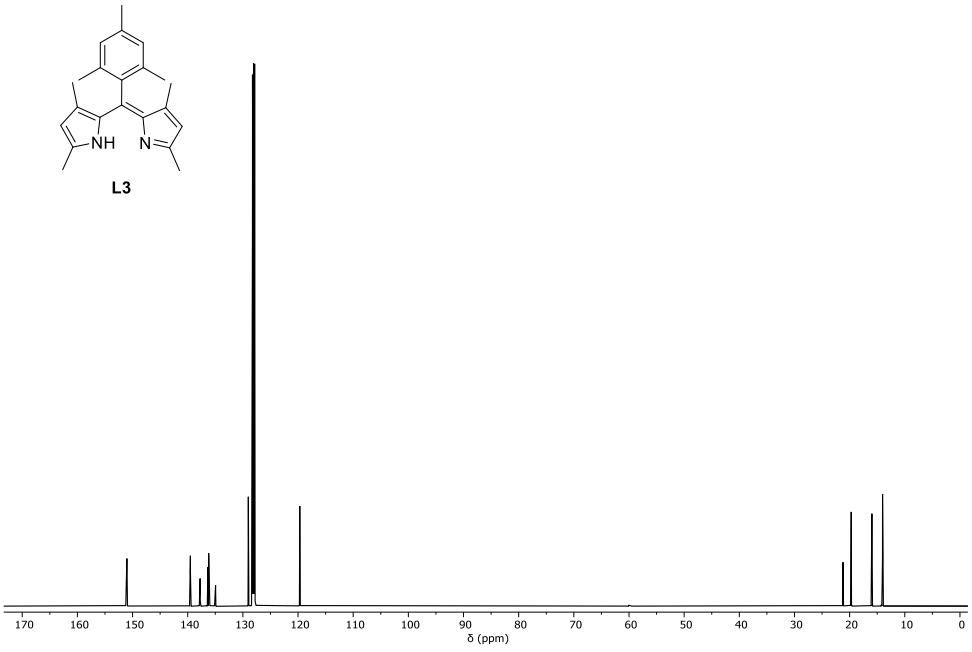


Figure 152: $^{13}C\{^{1}H\}$ NMR (126 MHz) spectrum of **L3** in C_6D_6.

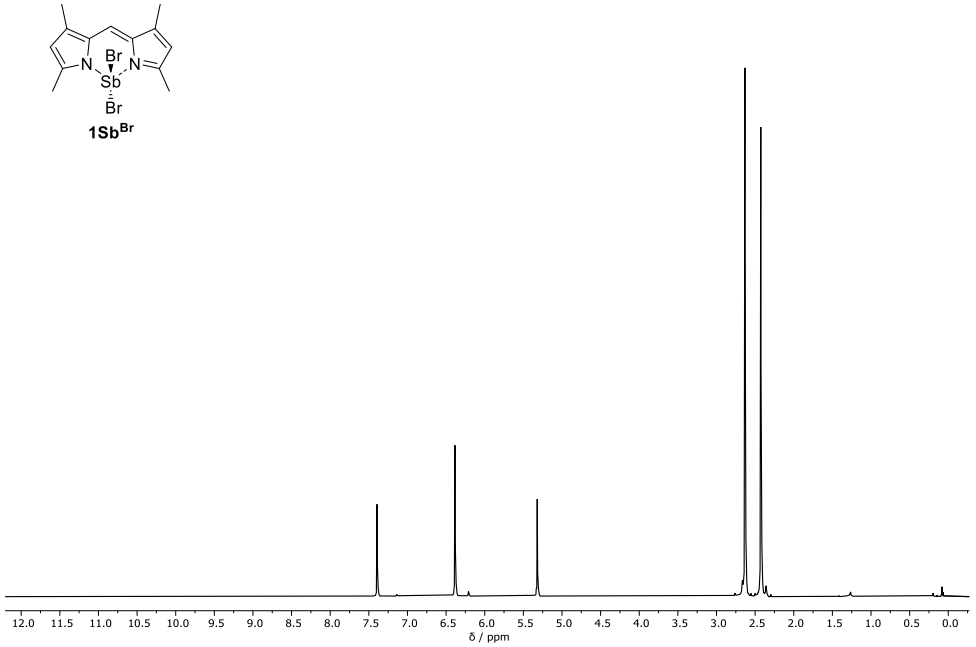


Figure 153: ^{1}H NMR (500 MHz) spectrum of **1Sb^{Br}** in CD_2Cl_2.

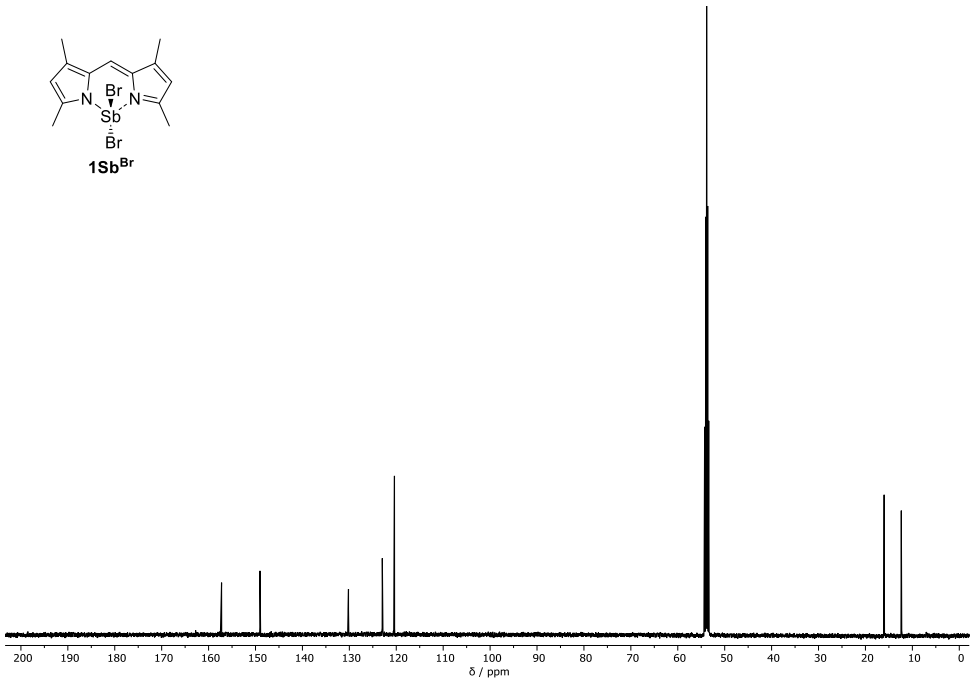


Figure 154: ^{13}C{^{1}H} NMR (126 MHz) spectrum of **1Sb^{Br}** in CD_2Cl_2.

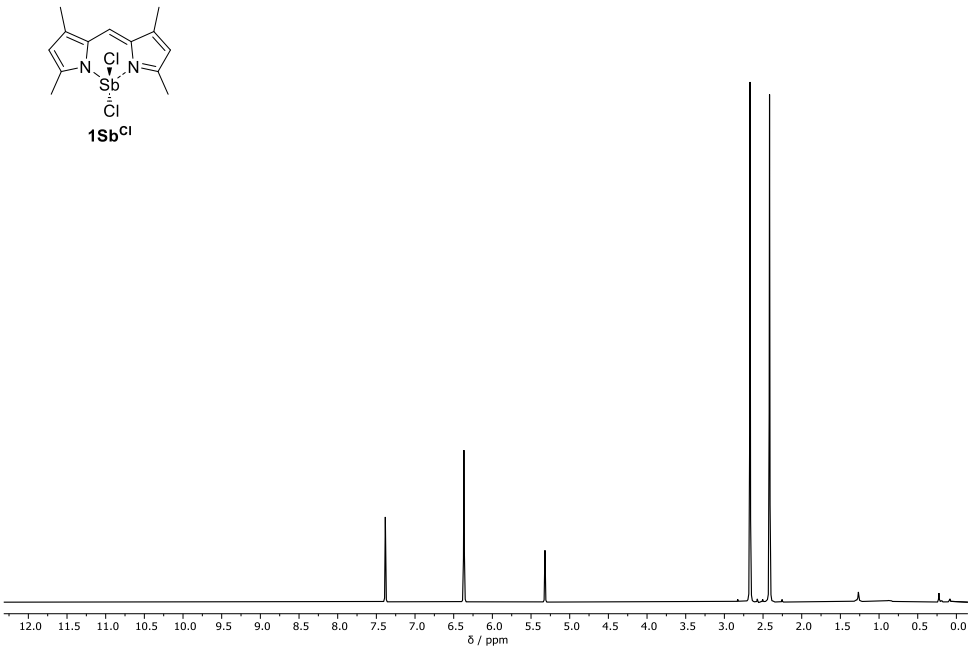


Figure 155: ^{1}H NMR (400 MHz) spectrum of **1Sb^{Cl}** in CD_2Cl_2.

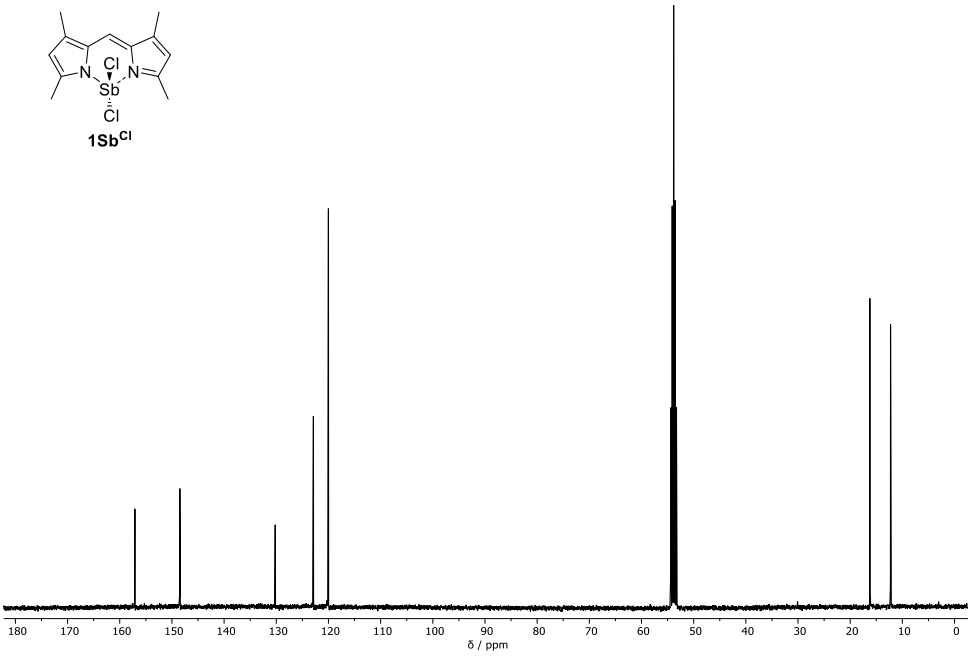


Figure 156: $^{13}C\{^{1}H\}$ NMR (101 MHz) spectrum of **1Sb^{Cl}** in CD_2Cl_2.

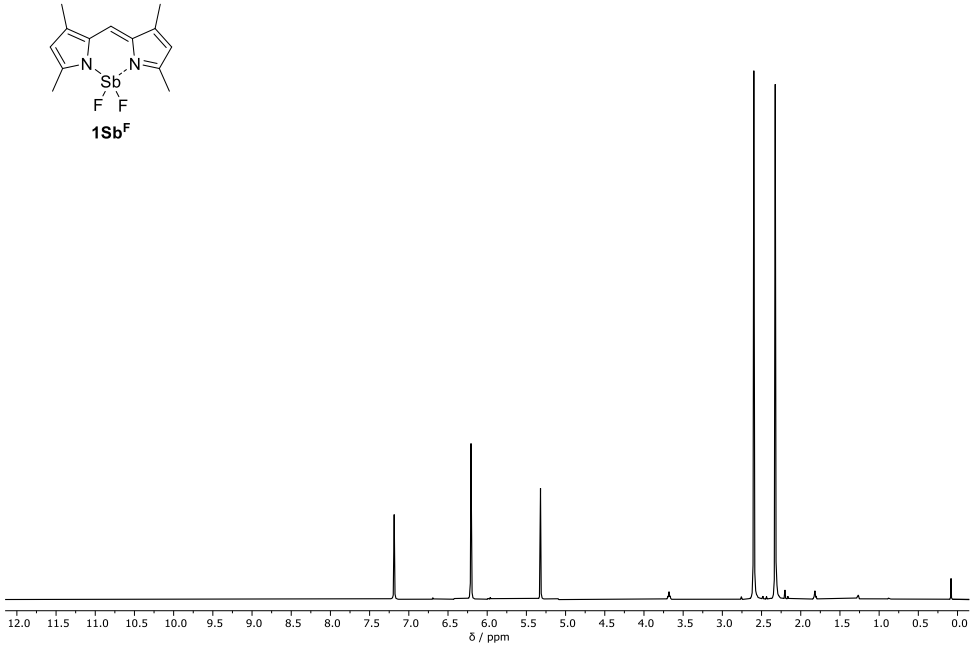


Figure 157: ^{1}H NMR (400 MHz) spectrum of **1Sb^{F}** in CD_2Cl_2.

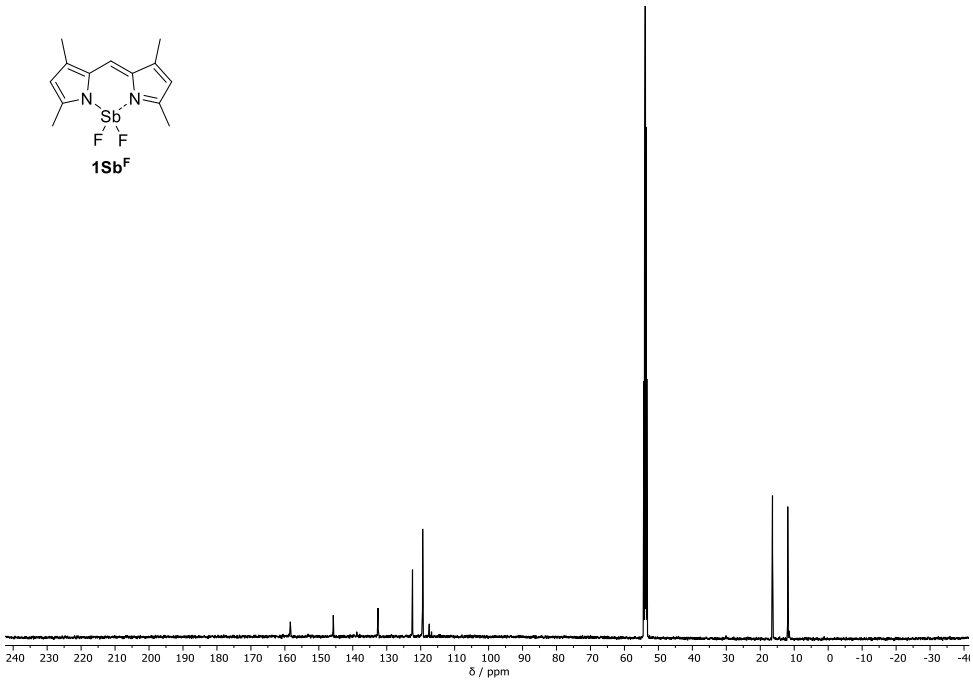


Figure 158: $^{13}C\{^{1}H\}$ NMR (126 MHz) spectrum of **1Sb^{F}** in CD_2Cl_2.

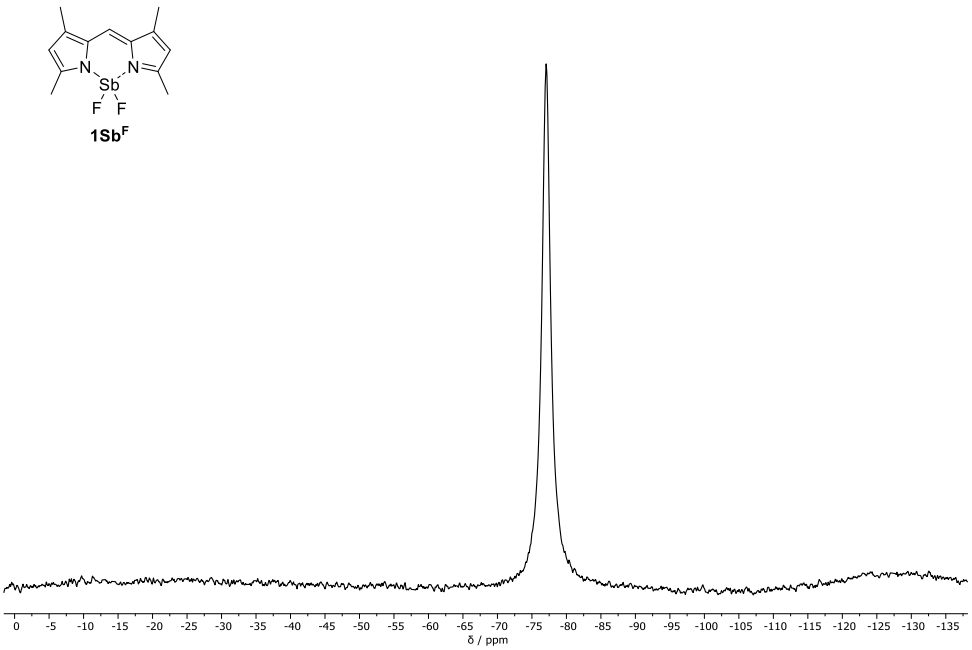


Figure 159: ^{19}F NMR (377 MHz) spectrum of **1Sb^{F}** in CD_2Cl_2.

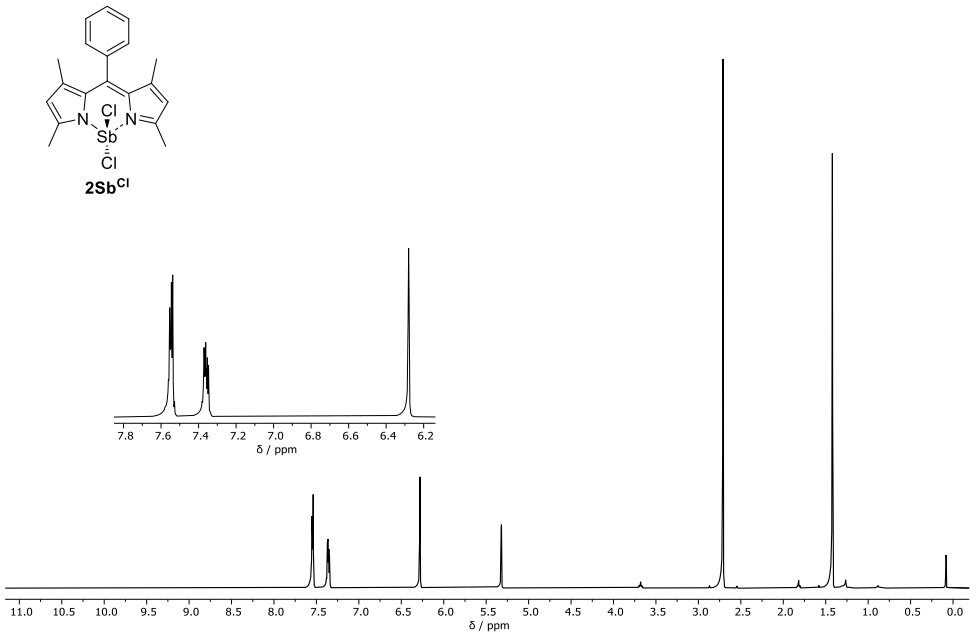


Figure 160: ^{1}H NMR (400 MHz) spectrum of **2Sb^{Cl}** in CD_2Cl_2.

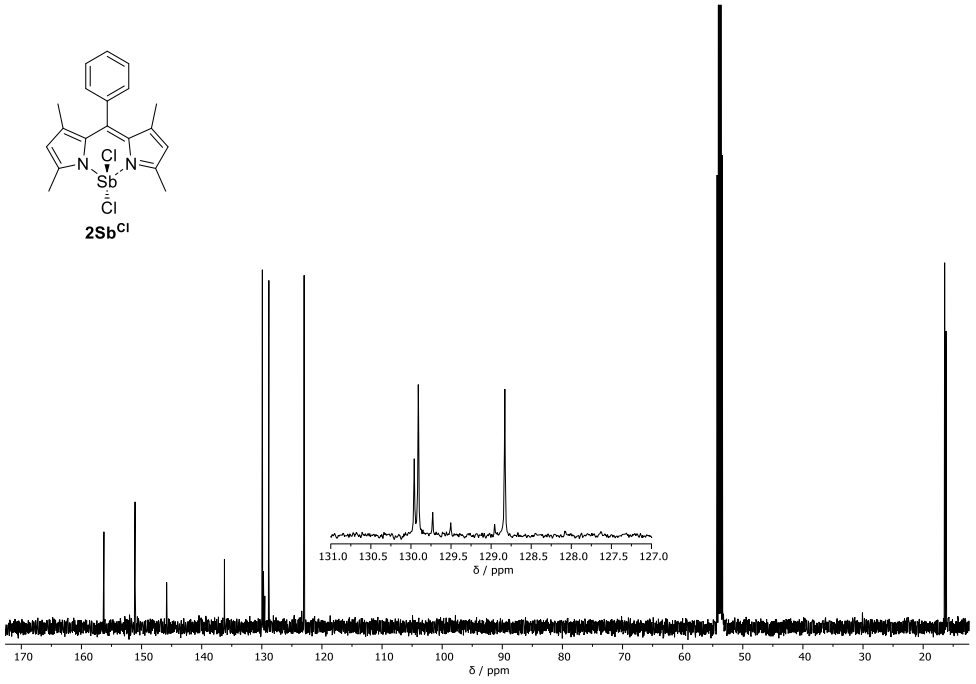


Figure 161: $^{13}C\{^{1}H\}$ NMR (126 MHz) spectrum of **2Sb^{Cl}** in CD_2Cl_2 (*recorded by A. Bismuto*).

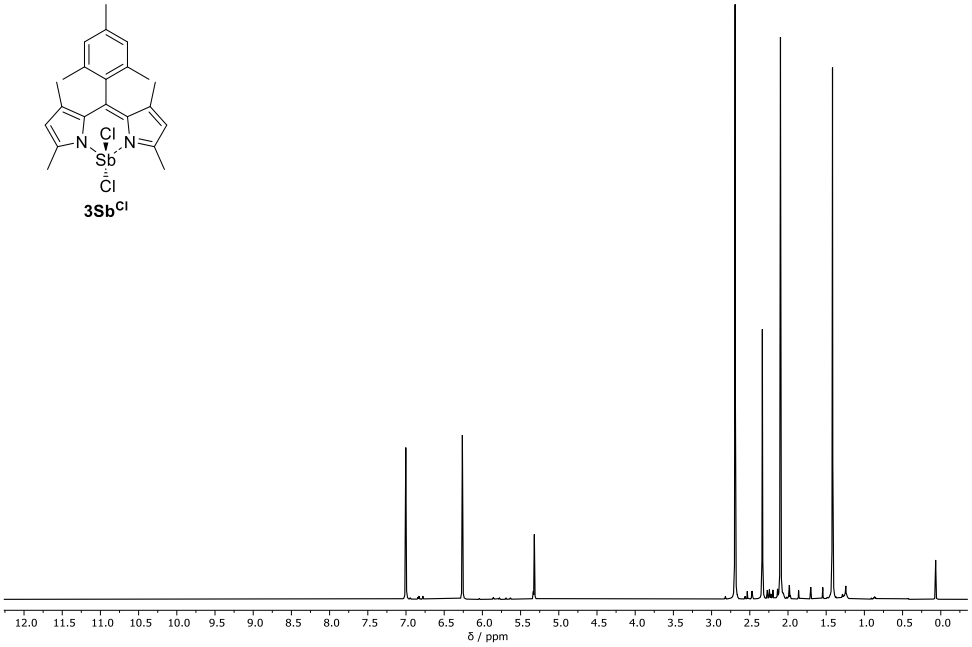


Figure 162: ^{1}H NMR (400 MHz) spectrum of **3Sb^{Cl}** in CD_2Cl_2.

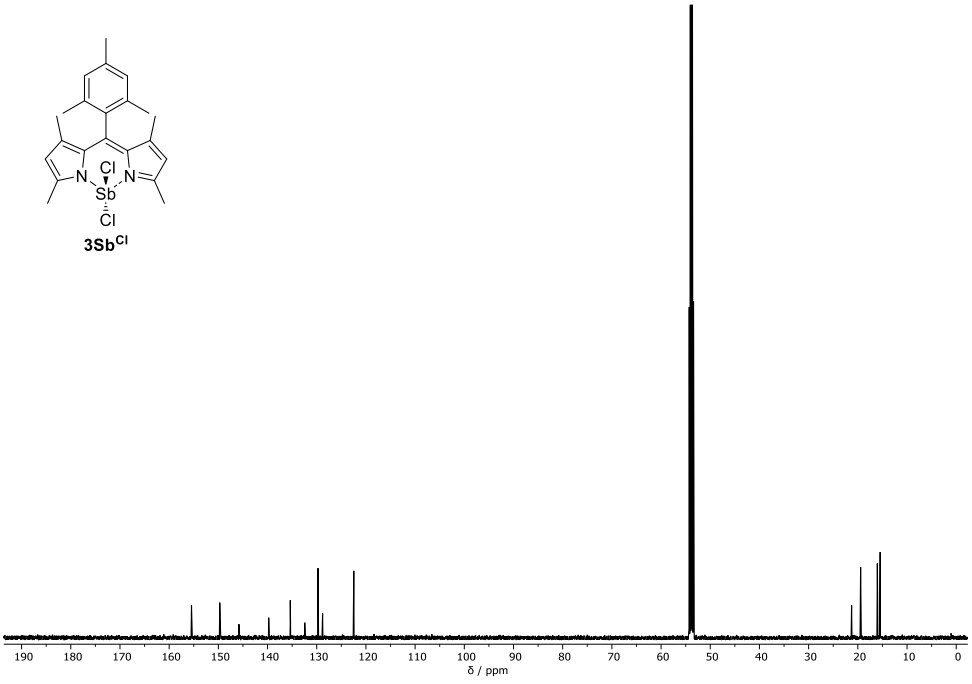


Figure 163: $^{13}C\{^{1}H\}$ NMR (126 MHz) spectrum of **3Sb^{Cl}** in CD_2Cl_2.

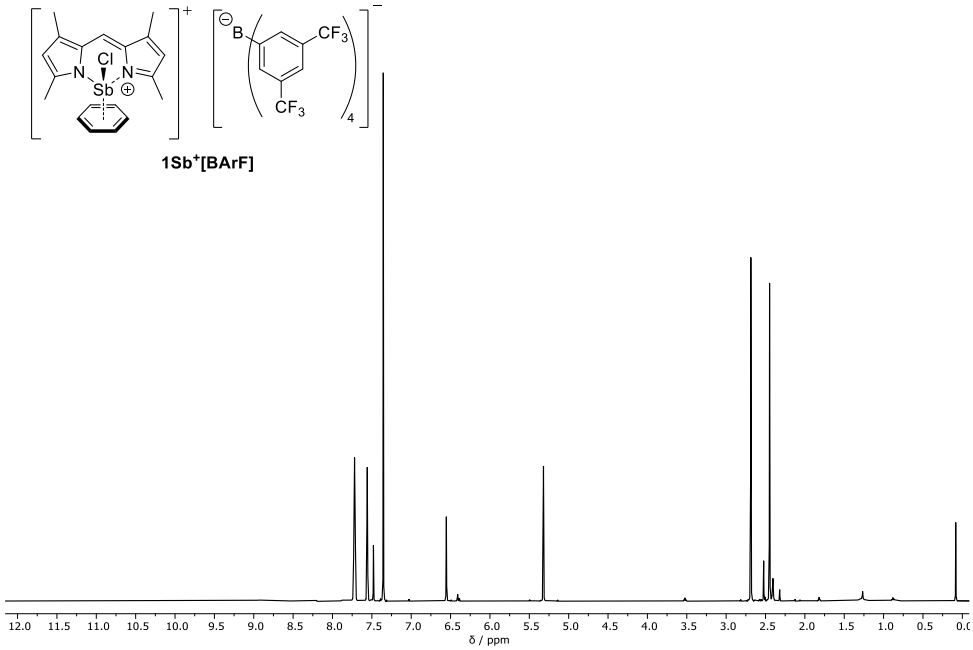


Figure 164: ^{1}H NMR (500 MHz) spectrum of **1Sb^{+}[BArF]** in CD_2Cl_2.

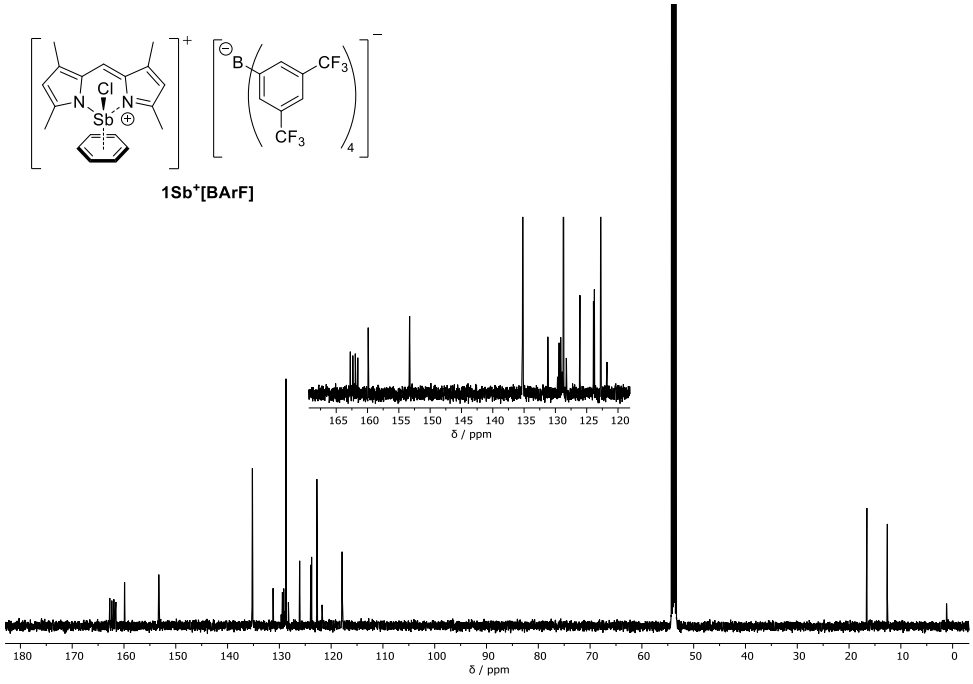


Figure 165: ^{1}H NMR (126 MHz) spectrum of **1Sb^{+}[BArF]** in CD_2Cl_2.

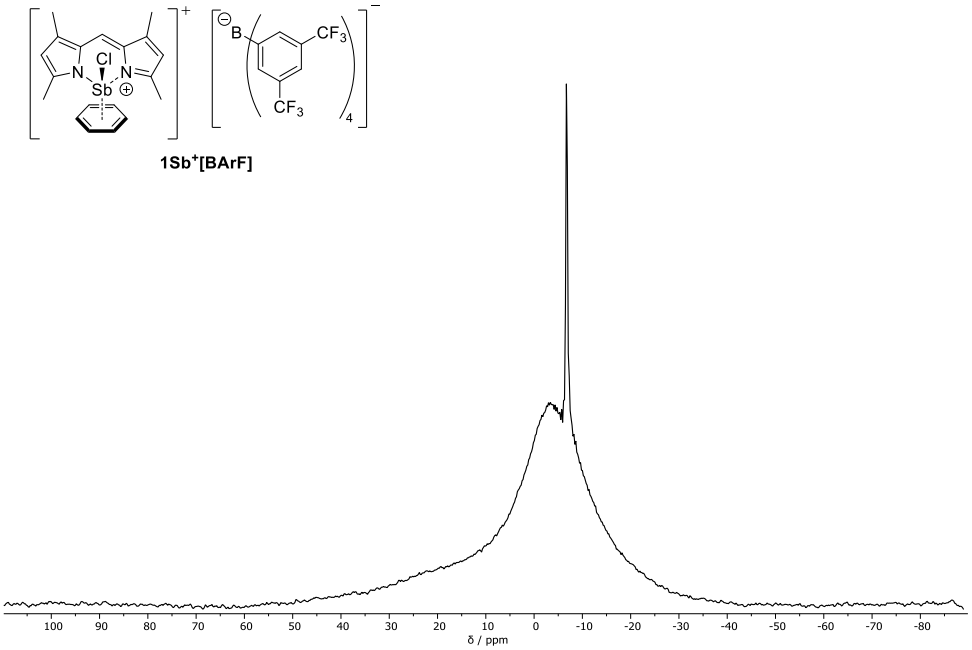


Figure 166: $^{11}B\{^{1}H\}$ NMR (161 MHz) spectrum of **1Sb⁺[BArF]** in CD_2Cl_2.

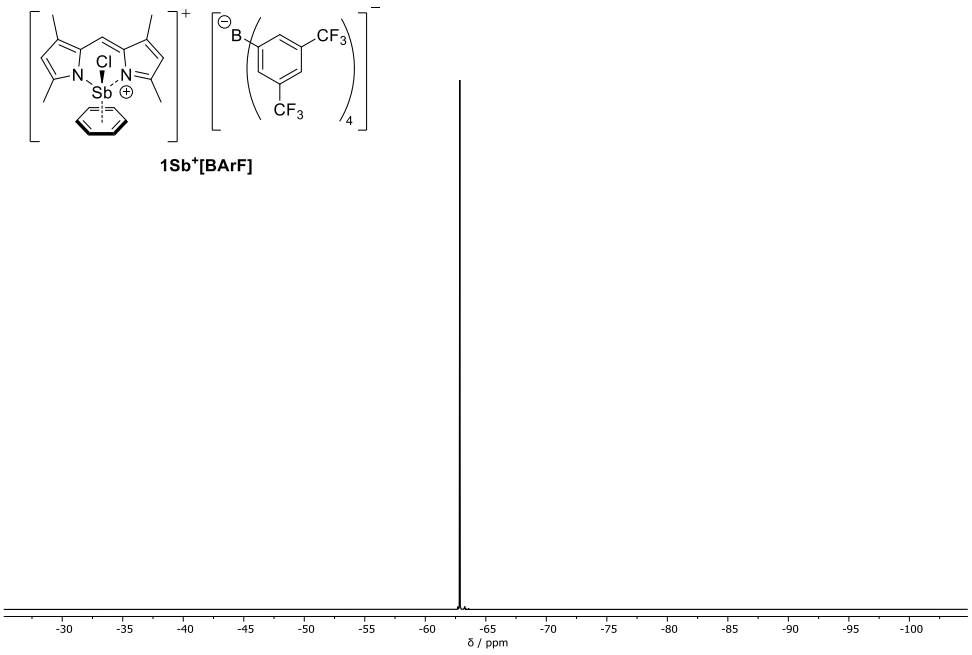


Figure 167: ^{19}F NMR (471 MHz) spectrum of **1Sb⁺[BArF]** in CD_2Cl_2.

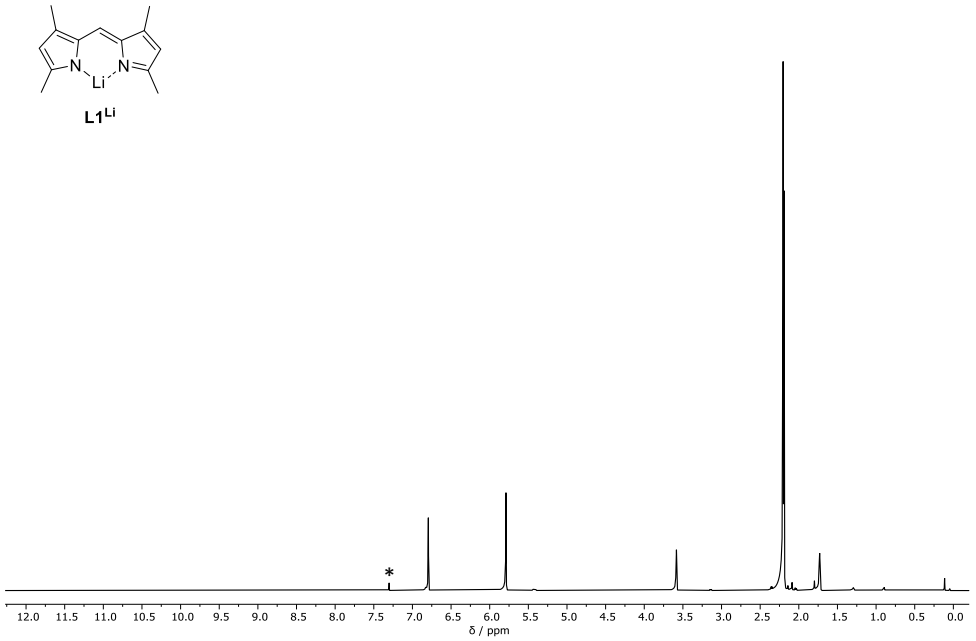


Figure 168: ^{1}H NMR (400 MHz) spectrum of **L1^{Li}** in THF-d_8. The sign (*) marks benzene.

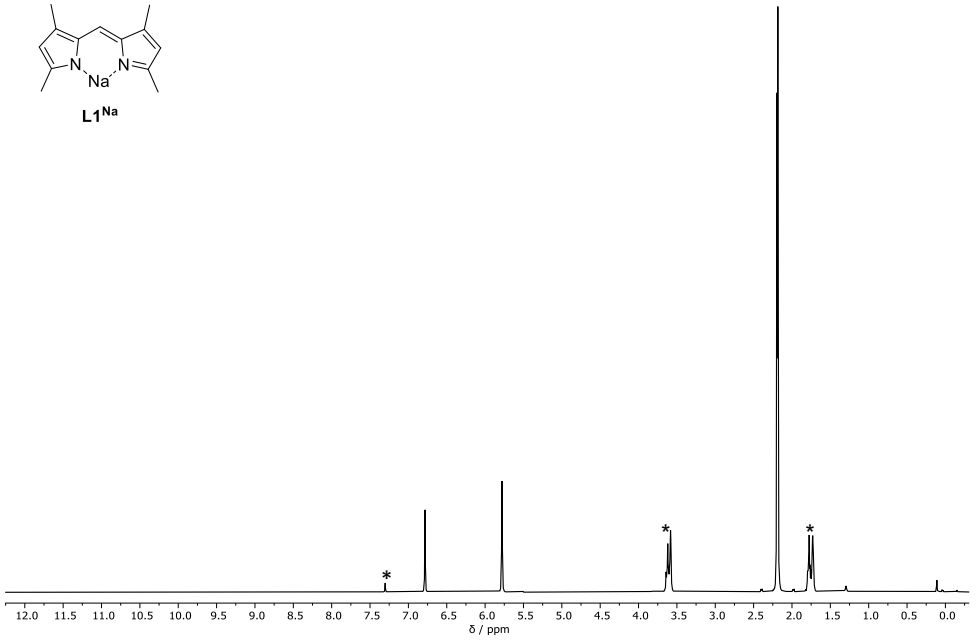


Figure 169: ^{1}H NMR (400 MHz) spectrum of **L1^{Na}** in THF-d_8. The sign (*) marks THF and (*) marks benzene.

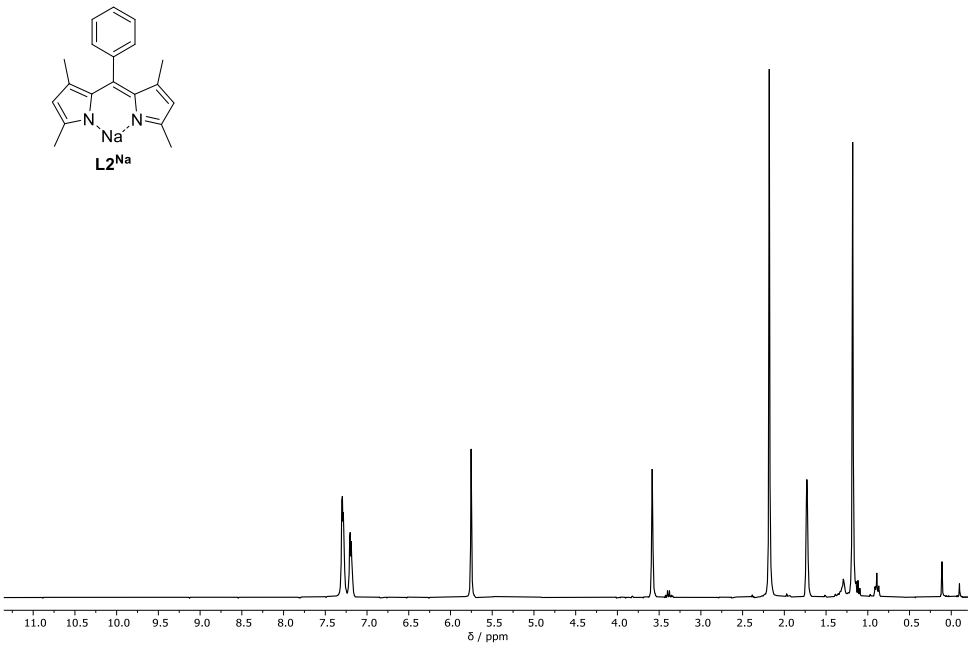


Figure 170: ^{1}H NMR (300 MHz) spectrum of **L2^{Na}** in THF-d_8.

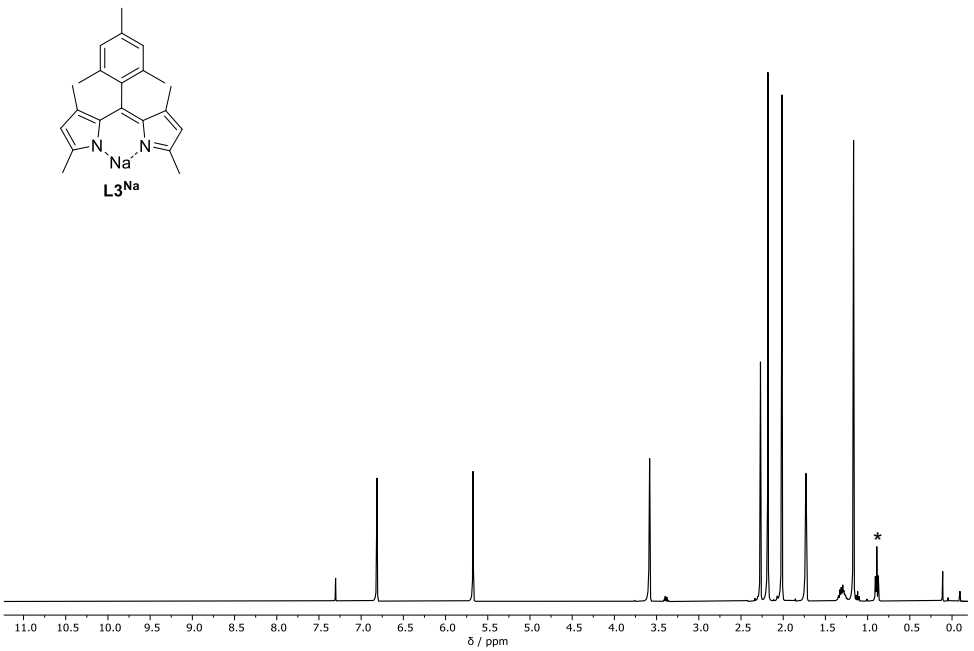


Figure 171: ^{1}H NMR (300 MHz) spectrum of **L3^{Na}** in THF-d_8. The sign (*) marks *n*-pentane.

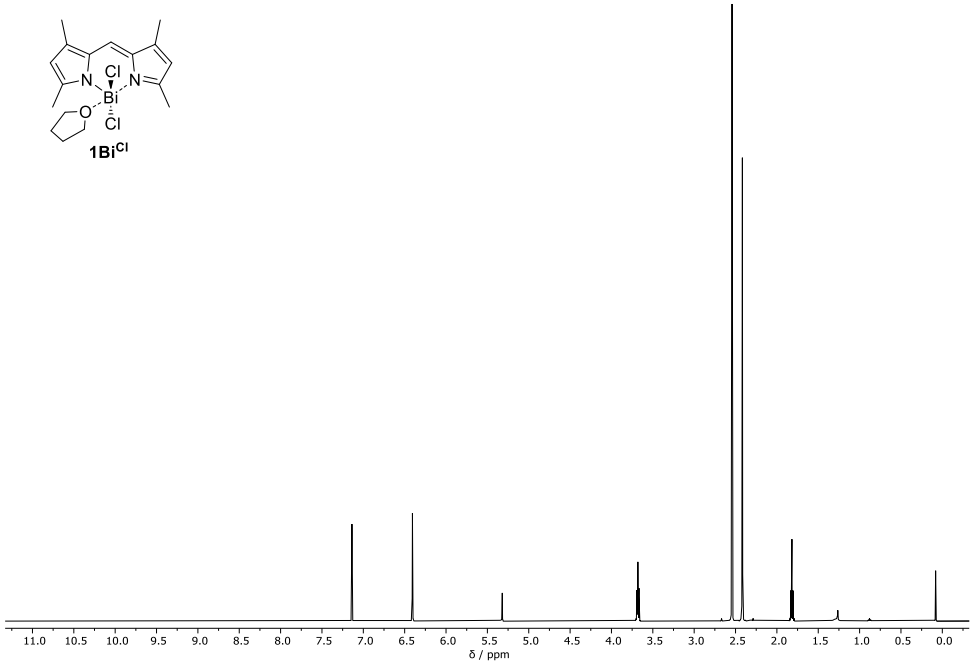


Figure 172: ^{1}H NMR (500 MHz) spectrum of **1Bi^{Cl}** in CD_2Cl_2.

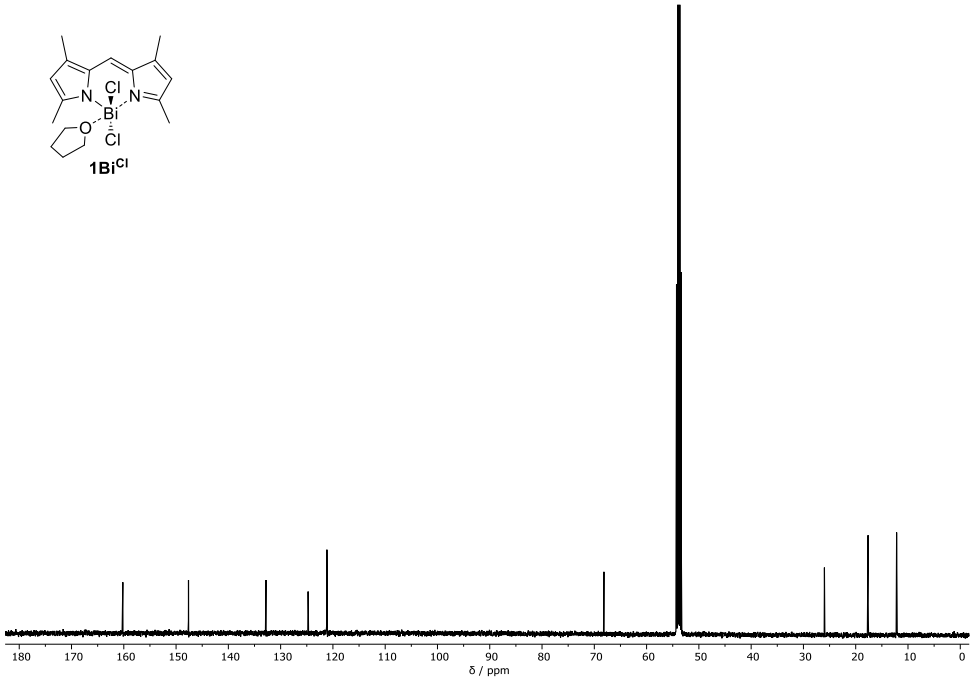


Figure 173: ^{13}C{^{1}H} NMR (126 MHz) spectrum of **1Bi^{Cl}** in CD_2Cl_2.

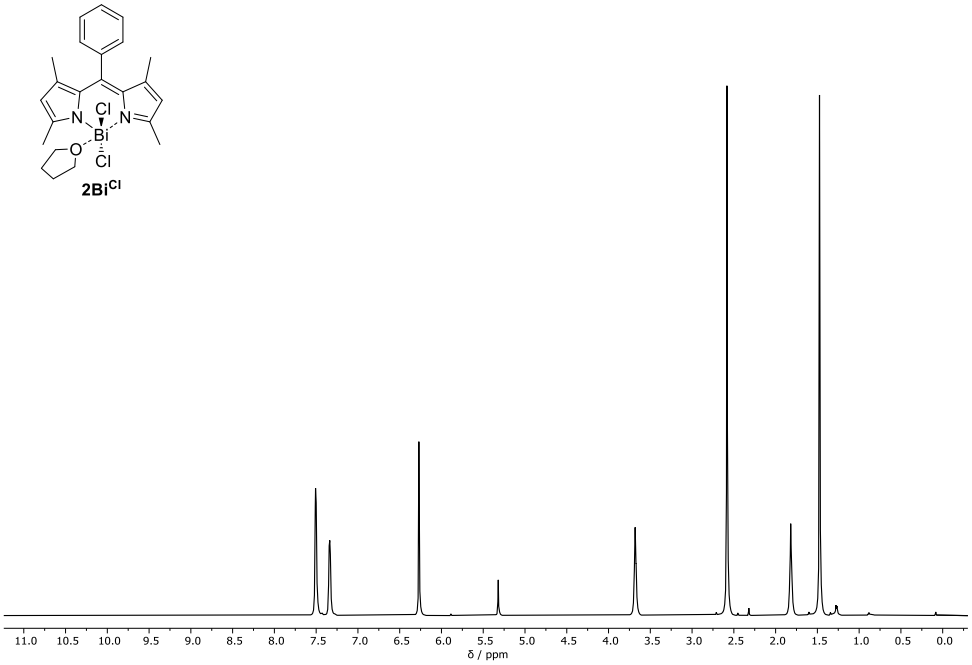


Figure 174: ^{1}H NMR (500 MHz) spectrum of **2Bi^{Cl}** in CD_2Cl_2.

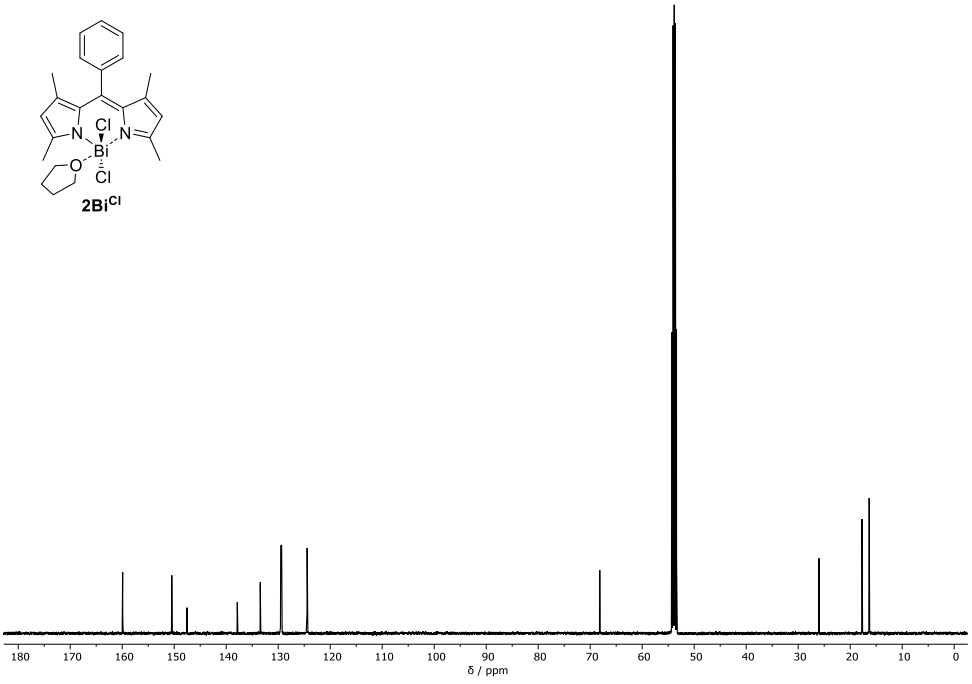


Figure 175: $^{13}C\{^{1}H\}$ NMR (126 MHz) spectrum of **2Bi^{Cl}** in CD_2Cl_2.

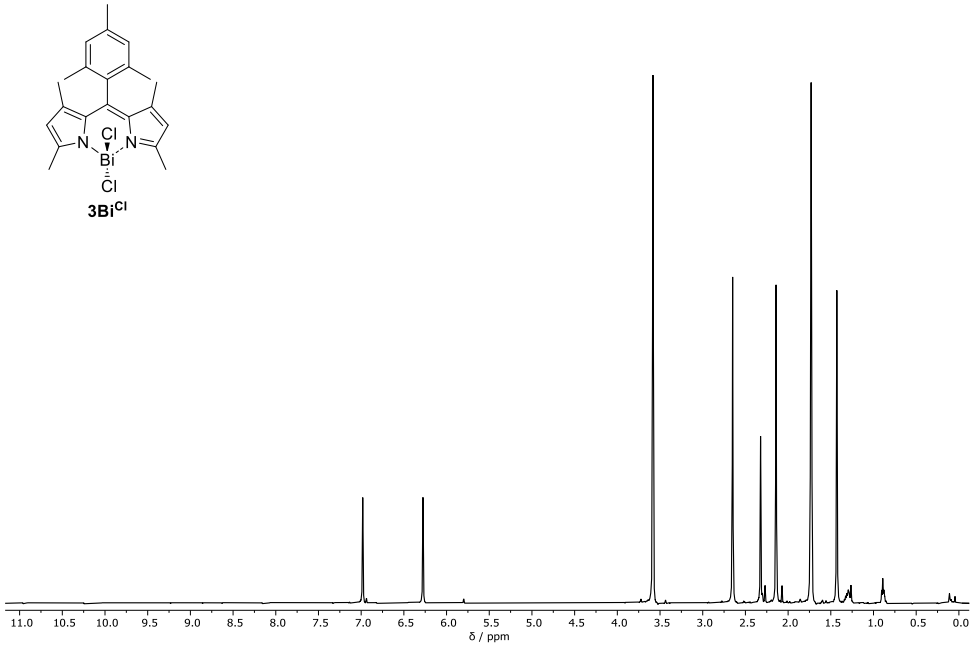


Figure 176: ^{1}H NMR (500 MHz) spectrum of **3Bi^{Cl}** in THF-d_8.

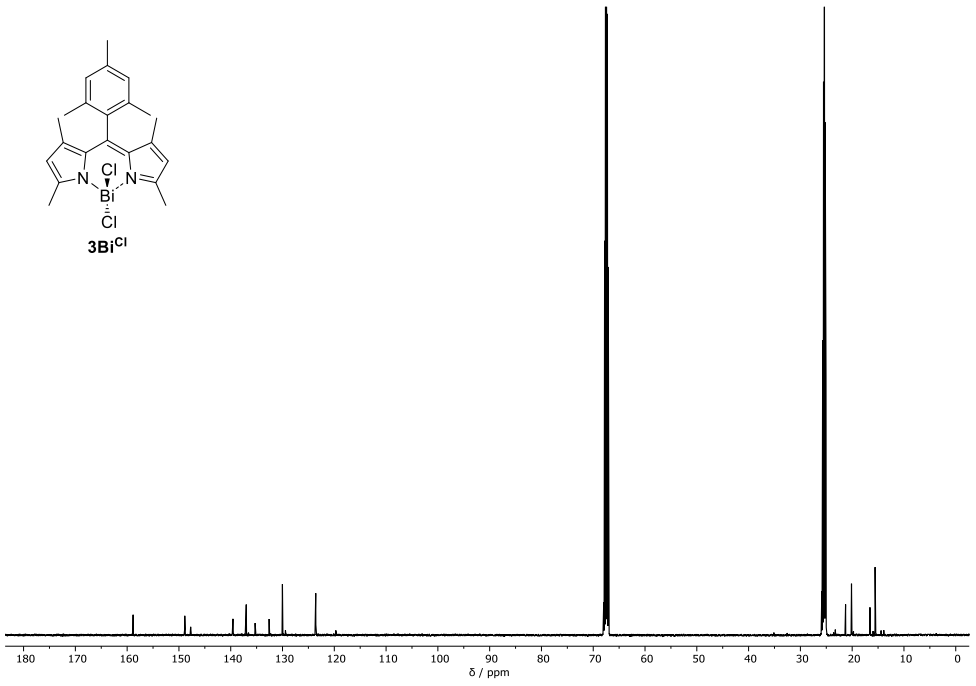


Figure 177: ^{13}C{^{1}H} NMR (126 MHz) spectrum of **3Bi^{Cl}** in THF-d_8.

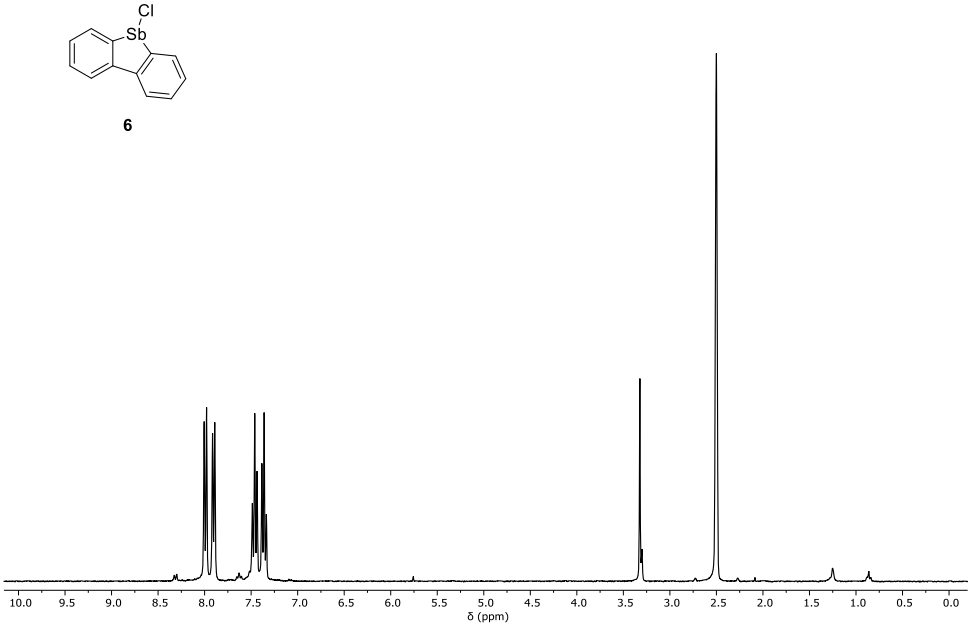


Figure 178: ^{1}H NMR (300 MHz) spectrum of **6** in DMSO-d_6.

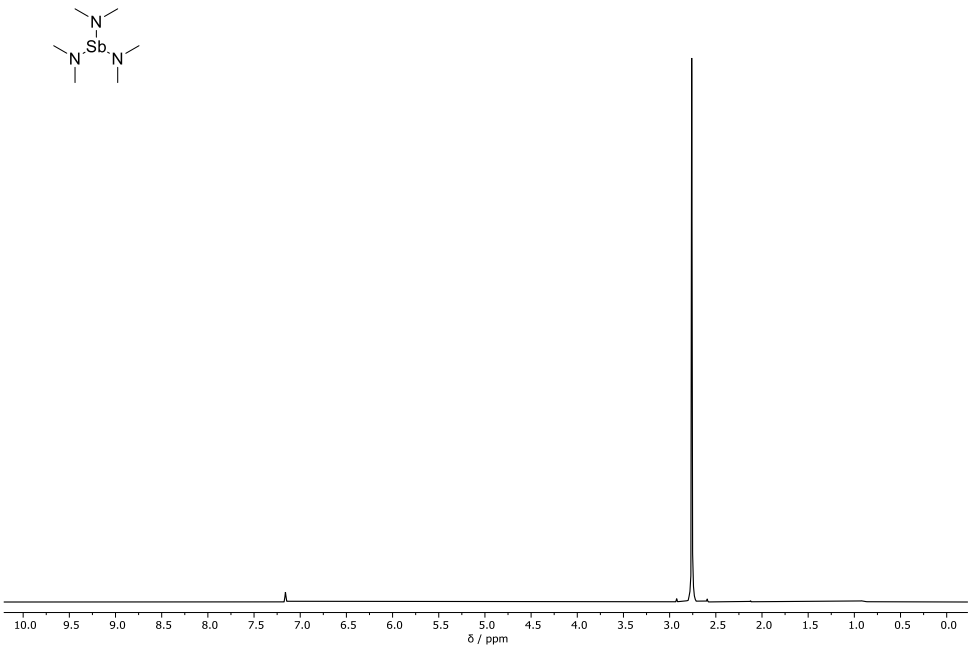


Figure 179: ^{1}H NMR (400 MHz) spectrum of $Sb(NMe_2)_3$ in C_6D_6.

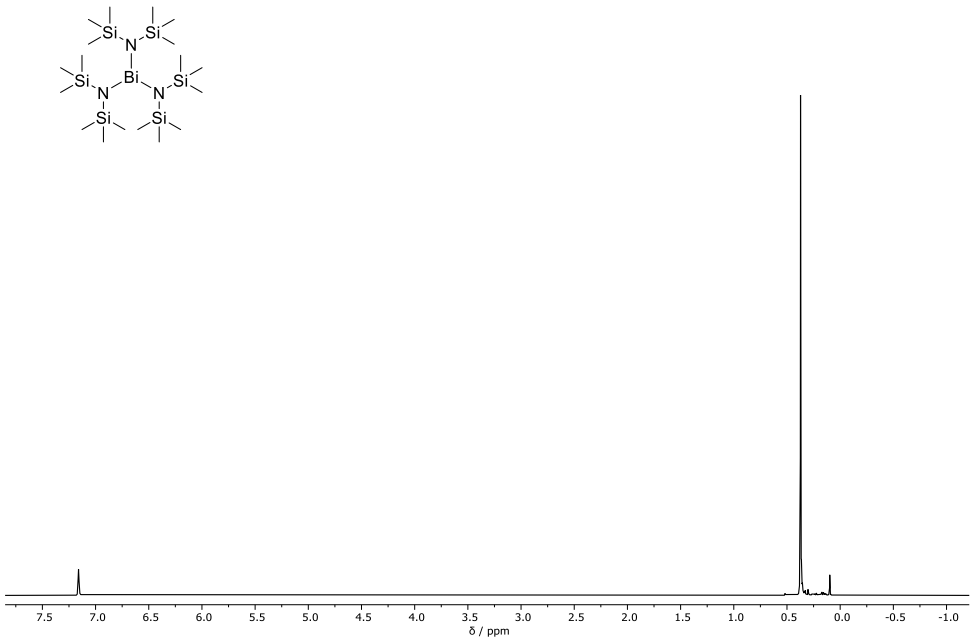
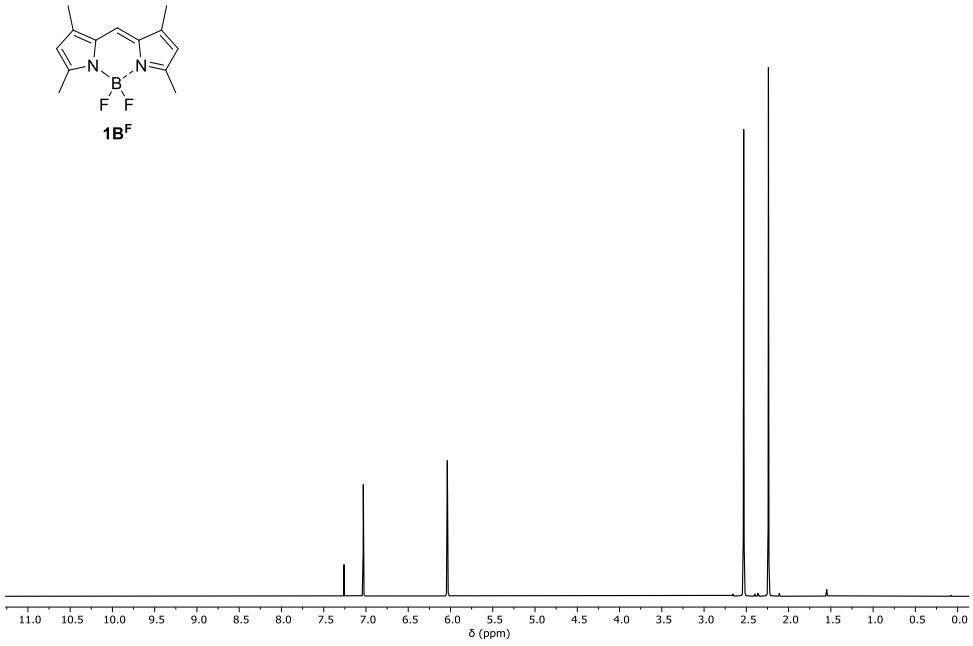
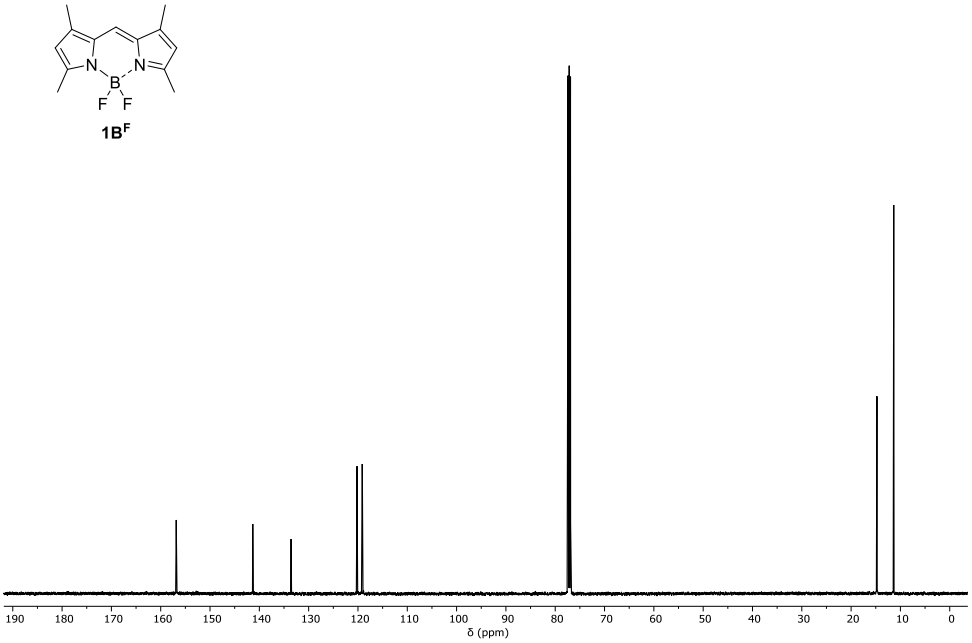


Figure 180: ^{1}H NMR (400 MHz) spectrum of $Bi(HMDS)_3$ in C_6D_6.



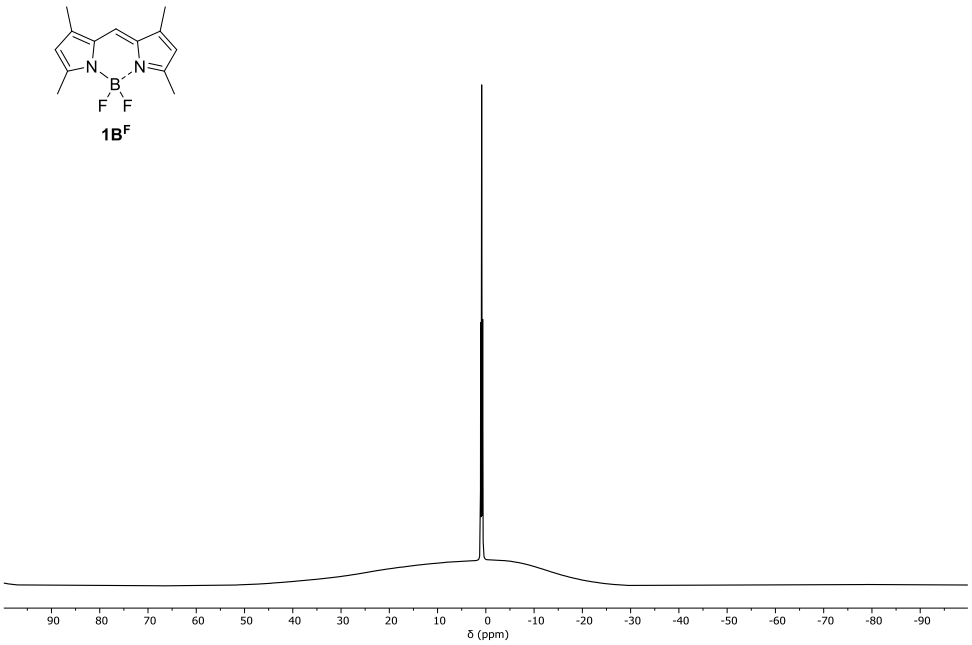
1B^{F}

Figure 181: ^{1}H NMR (500 MHz) spectrum of **1B^{F}** in $CDCl_3$.



1B^{F}

Figure 182: $^{13}C\{^{1}H\}$ NMR (126 MHz) spectrum of **1B^{F}** in $CDCl_3$.



1B^{F}

Figure 183: $^{11}B\{^{1}H\}$ NMR (160 MHz) spectrum of **1B^{F}** in $CDCl_3$.

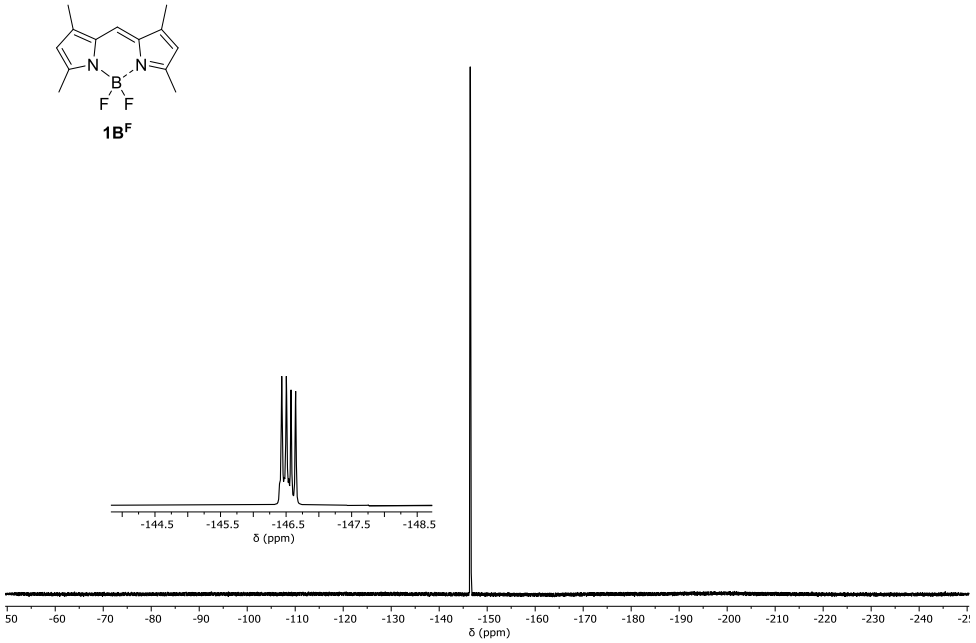


Figure 184: ^{19}F NMR (470 MHz) spectrum of **1B^F** in $CDCl_3$.

Chapter 3

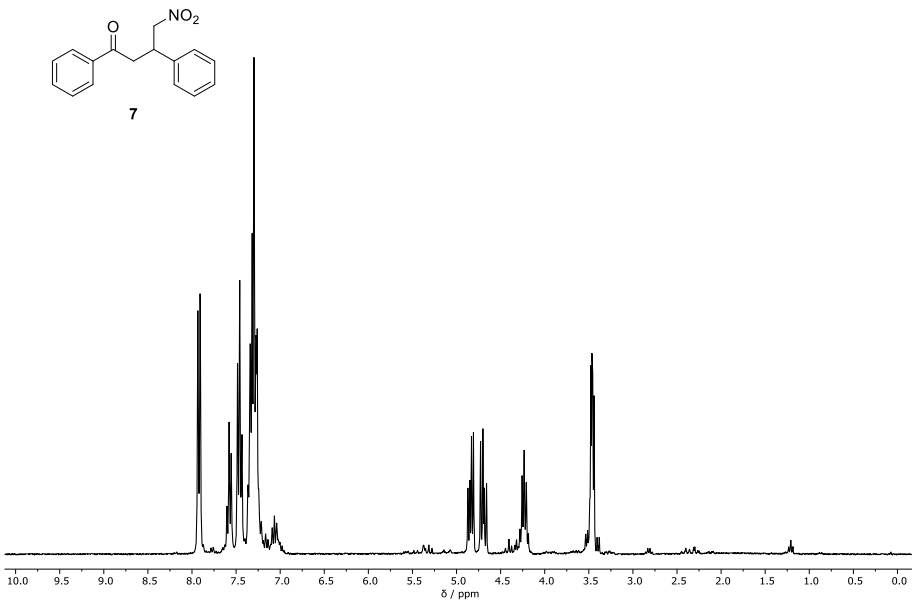


Figure 185: ^1H NMR (300 MHz) spectrum of **7** in $CDCl_3$.

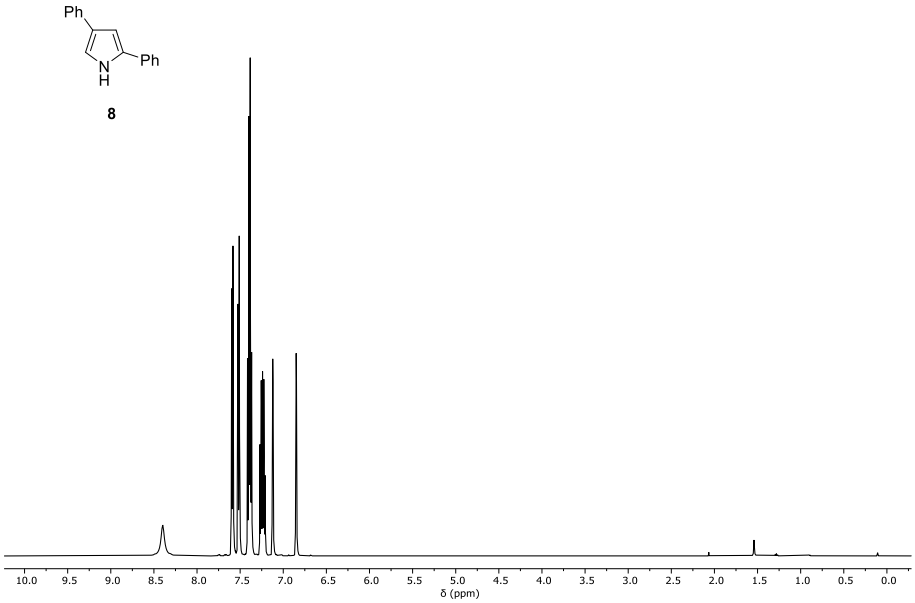


Figure 186: ^{1}H NMR (500 MHz) spectrum of **8** in $CDCl_3$.

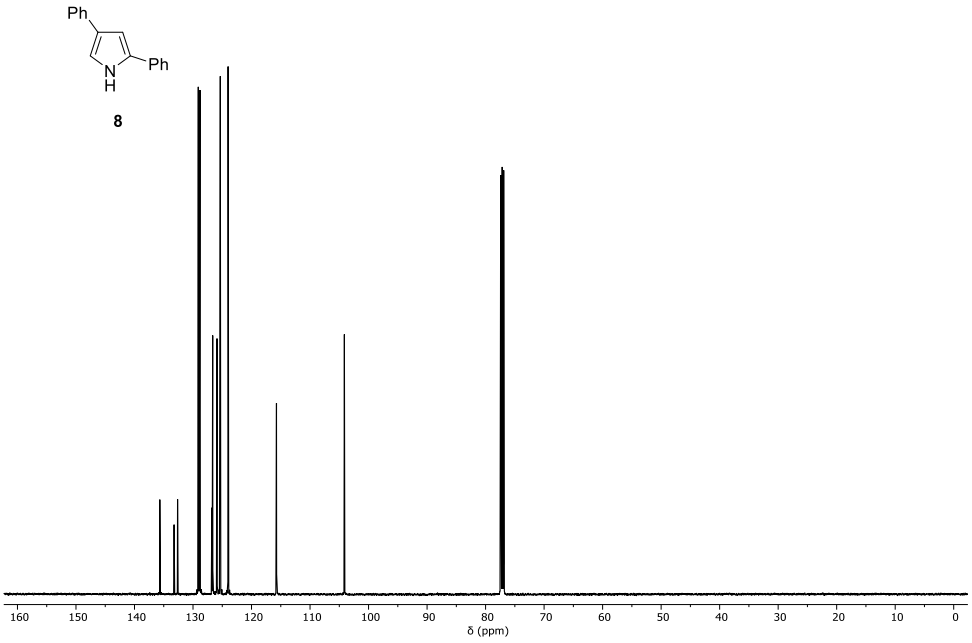


Figure 187: $^{13}C\{^{1}H\}$ NMR (126 MHz) spectrum of **8** in $CDCl_3$.

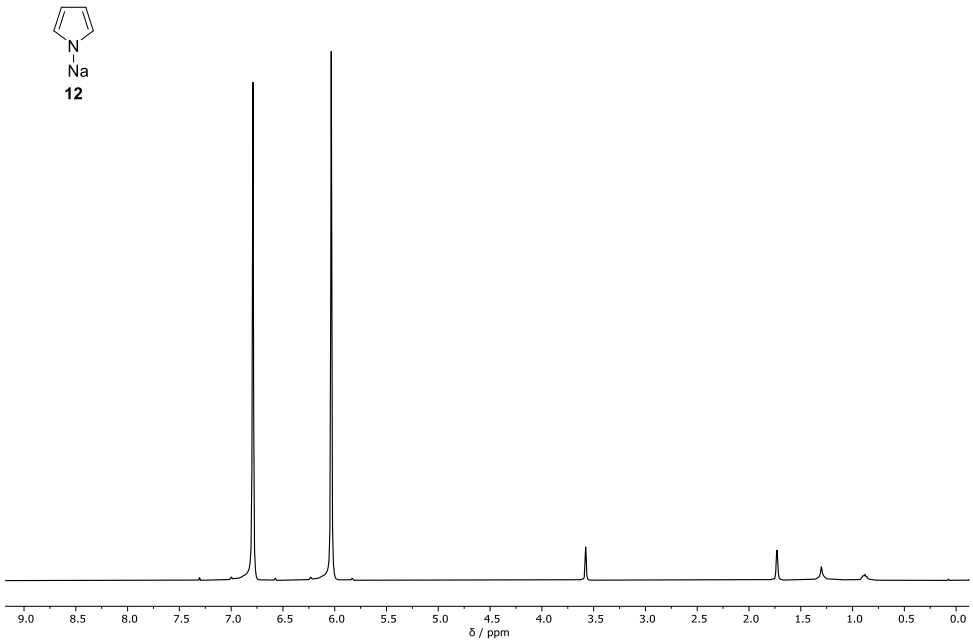


Figure 188: ^{1}H NMR (400 MHz) spectrum of **12** in THF-d_8.

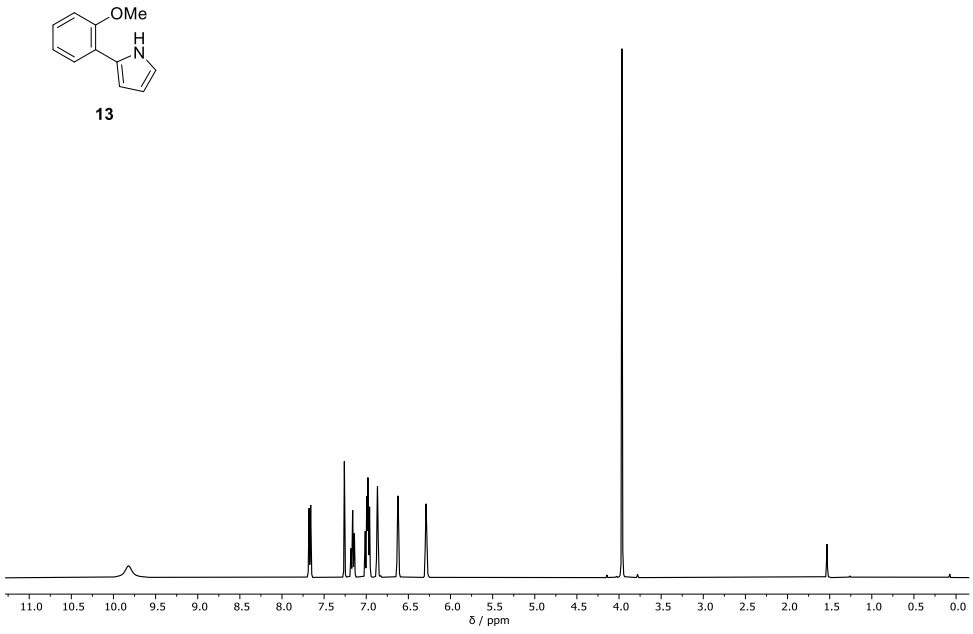


Figure 189: ^{1}H NMR (400 MHz) spectrum of **13** in $CDCl_3$.

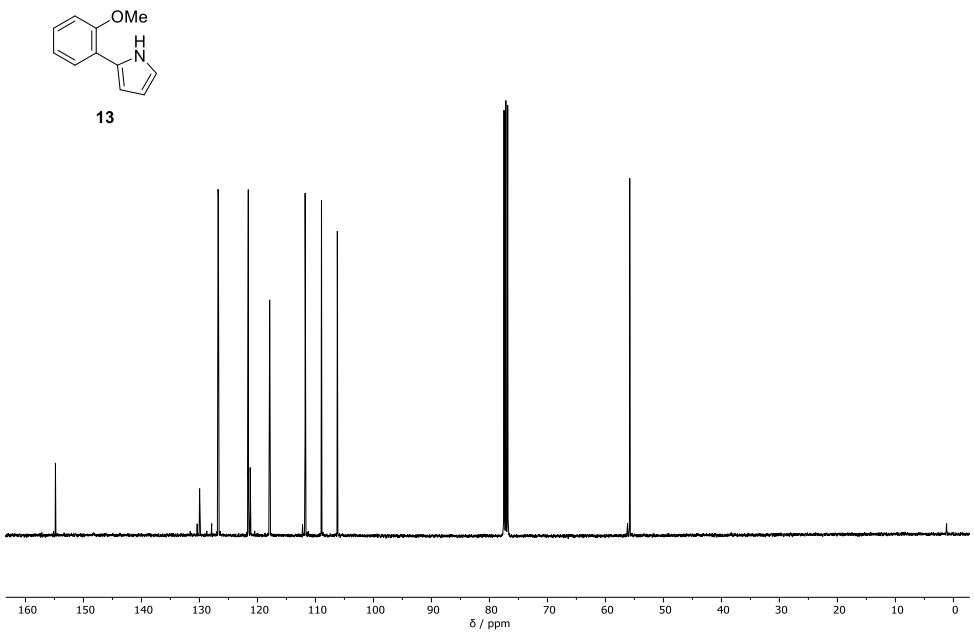


Figure 190: $^{13}C\{^{1}H\}$ NMR (101 MHz) spectrum of **13** in $CDCl_3$.

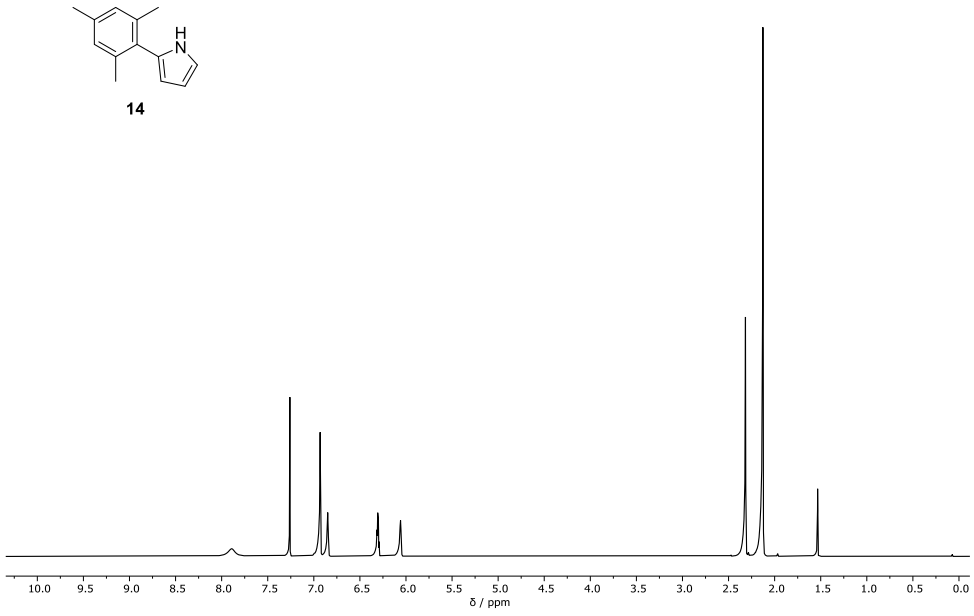


Figure 191: ^{1}H NMR (400 MHz) spectrum of **14** in $CDCl_3$.

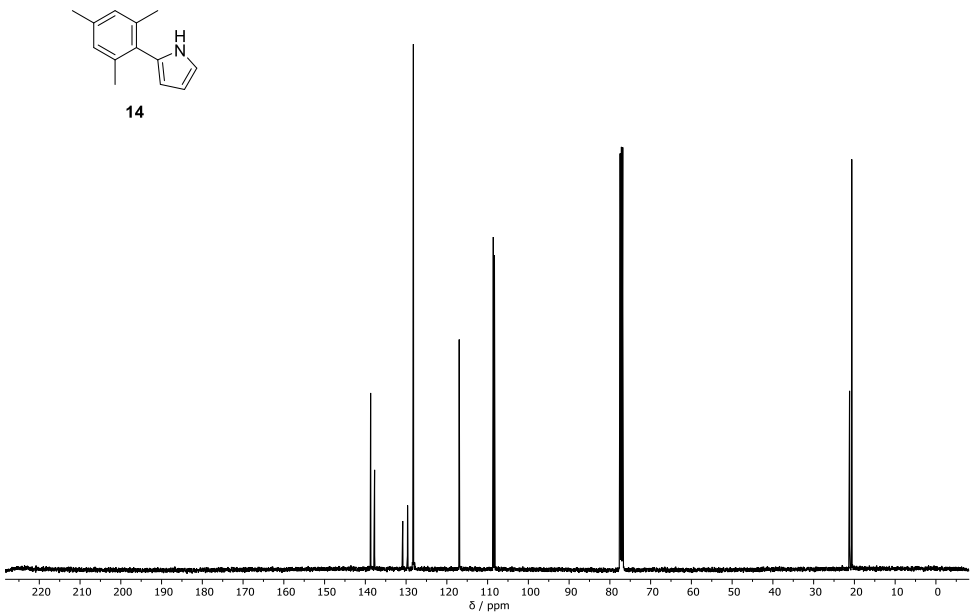


Figure 192: $^{13}C\{^{1}H\}$ NMR (101 MHz) spectrum of **14** in $CDCl_3$.

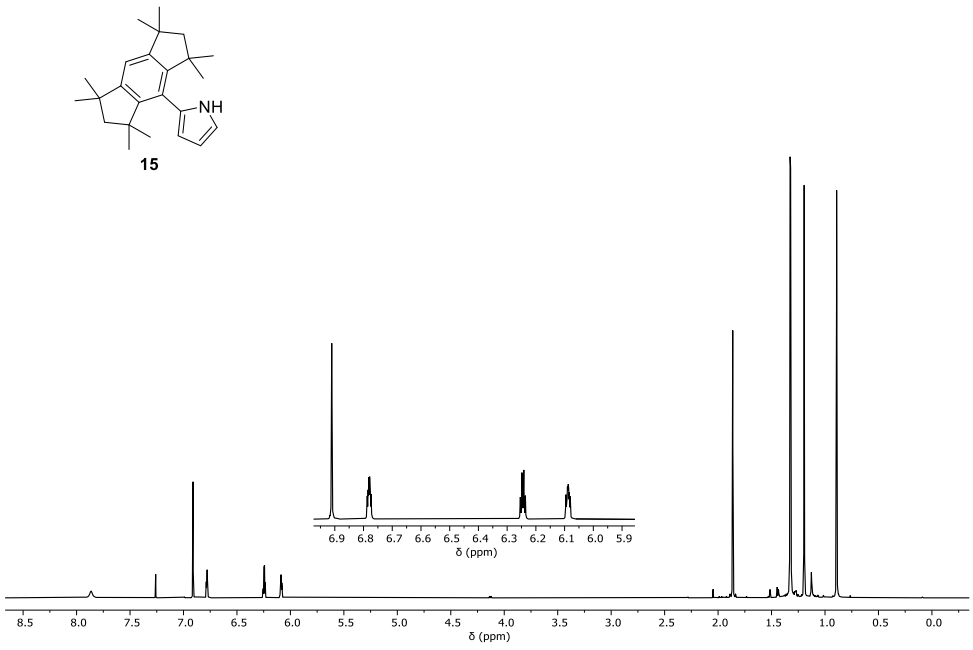


Figure 193: ^{1}H NMR (500 MHz) spectrum of **15** in $CDCl_3$.

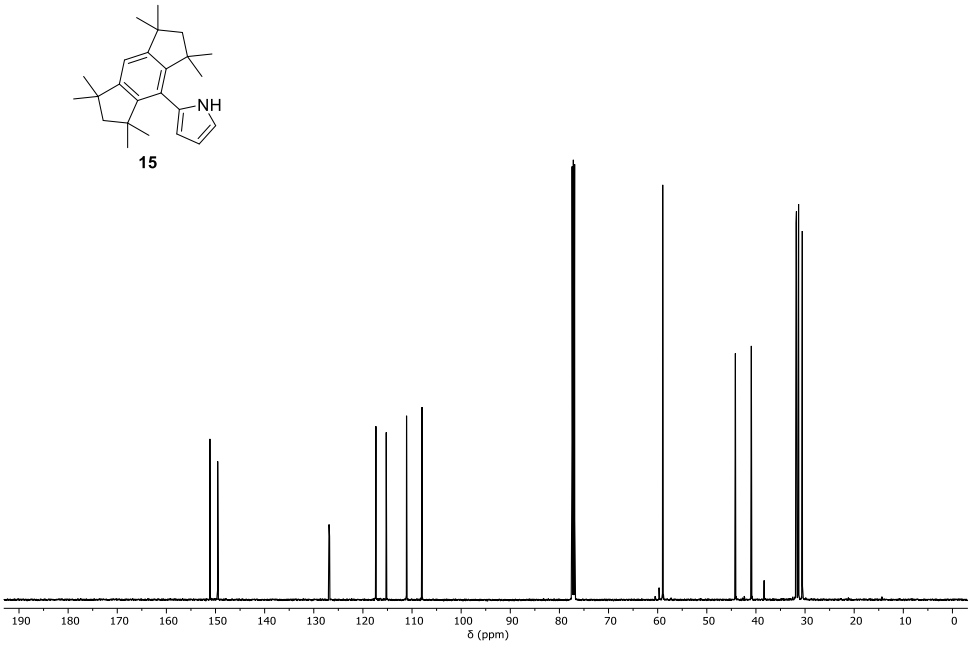


Figure 194: $^{13}C\{^{1}H\}$ NMR (126 MHz) spectrum of **15** in $CDCl_3$.

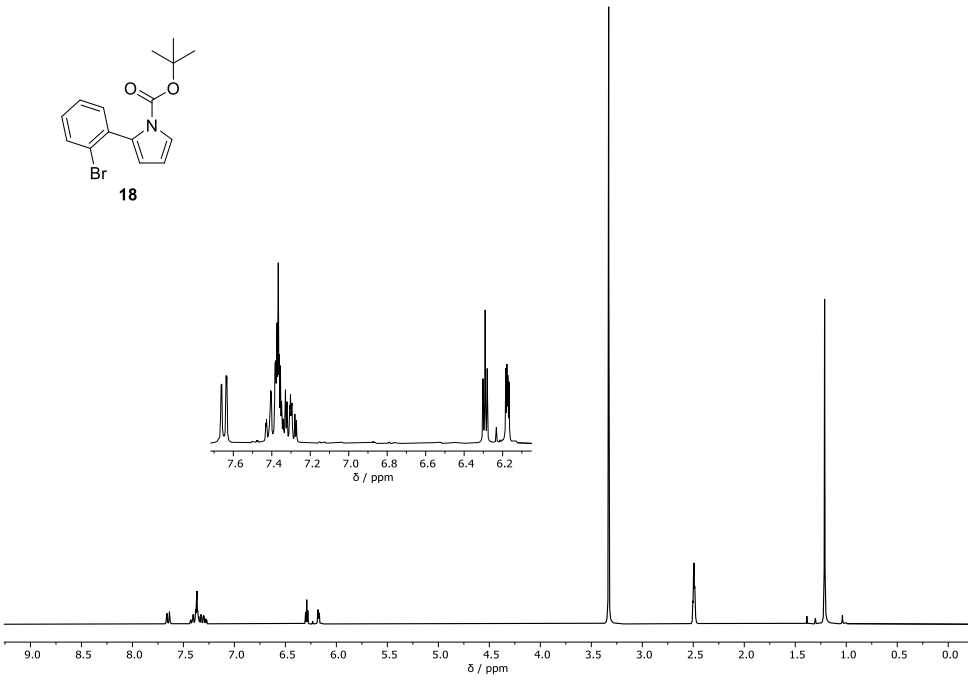


Figure 195: ^{1}H NMR (500 MHz) spectrum of **18** in DMSO-d_6.

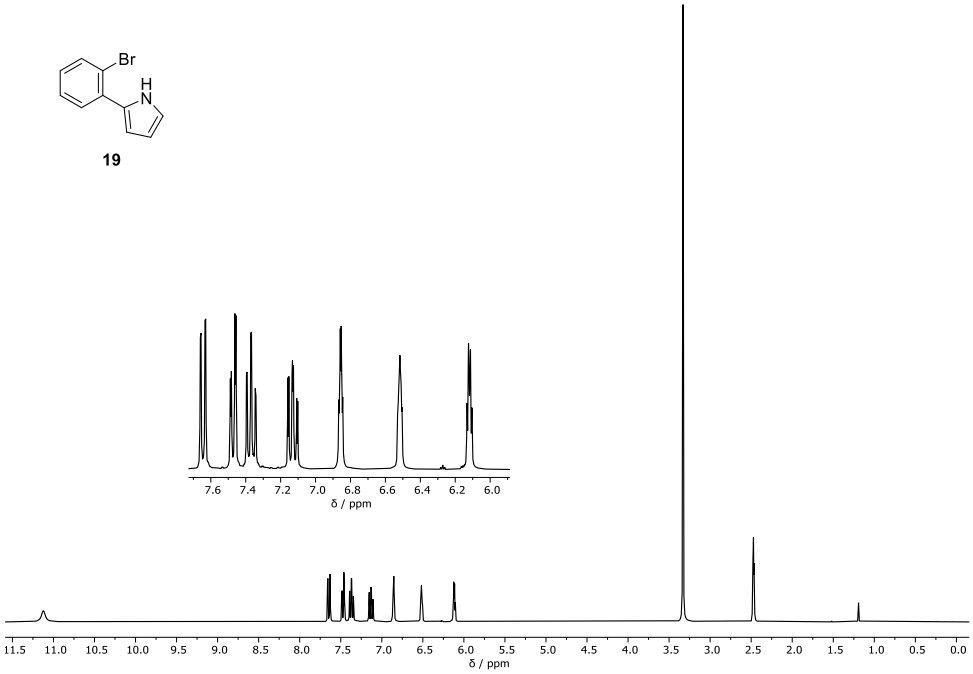


Figure 196: ^{1}H NMR (300 MHz) spectrum of **19** in DMSO-d_6.

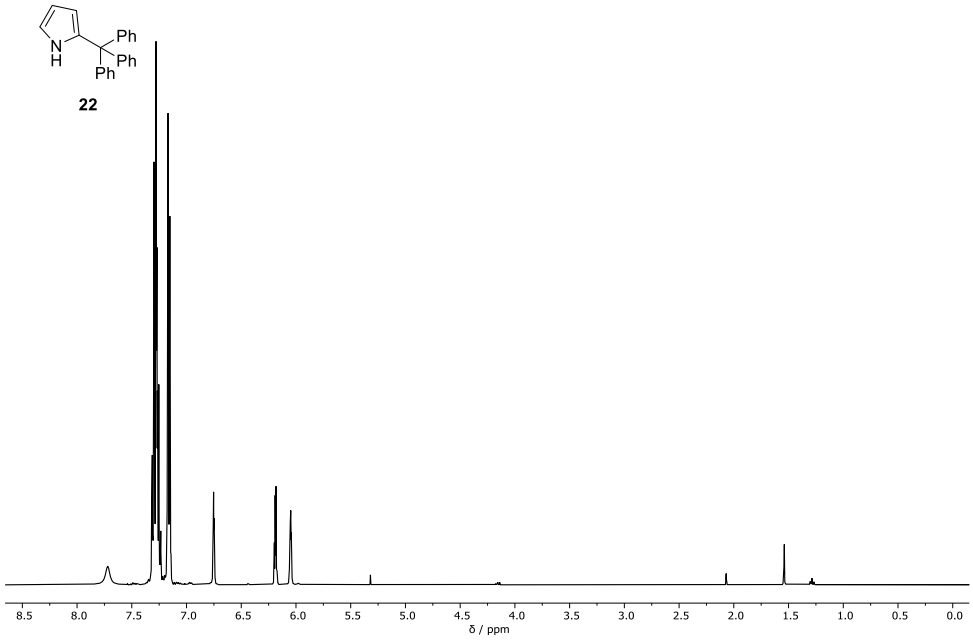


Figure 197: ^{1}H NMR (400 MHz) spectrum of **22** in $CDCl_3$.

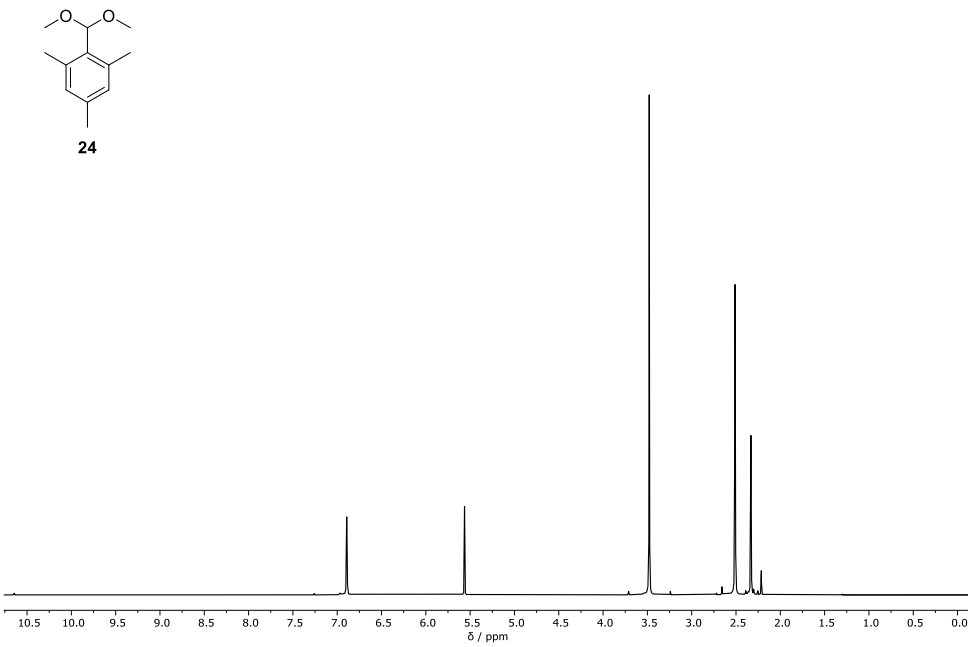


Figure 198: ^{1}H NMR (300 MHz) spectrum of **24** in $CDCl_3$.

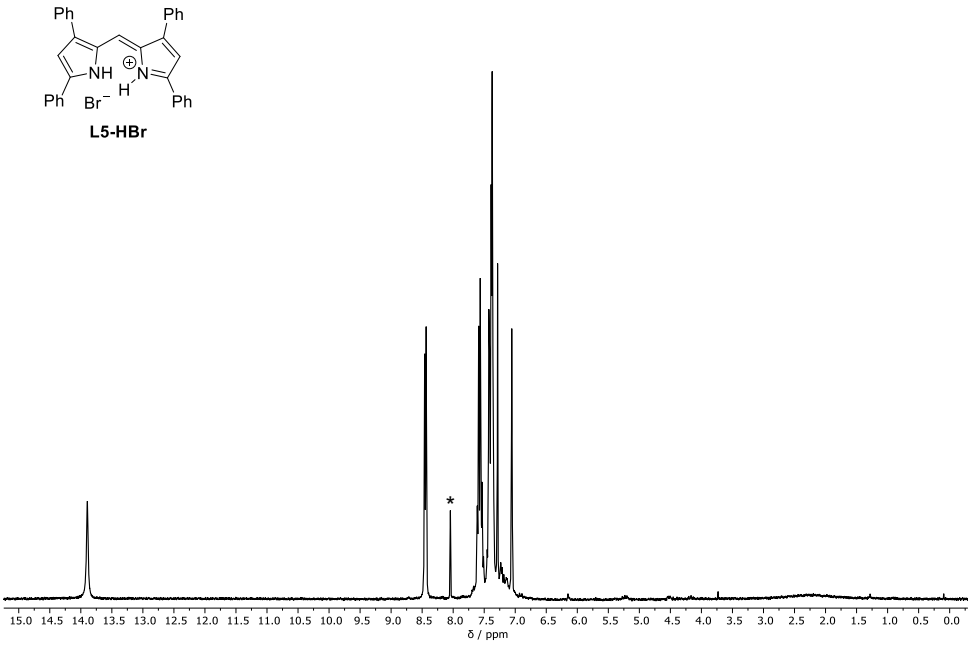


Figure 199: ^{1}H NMR (300 MHz) spectrum of **L5-HBr** in $CDCl_3$. The sign (*) marks formic acid.

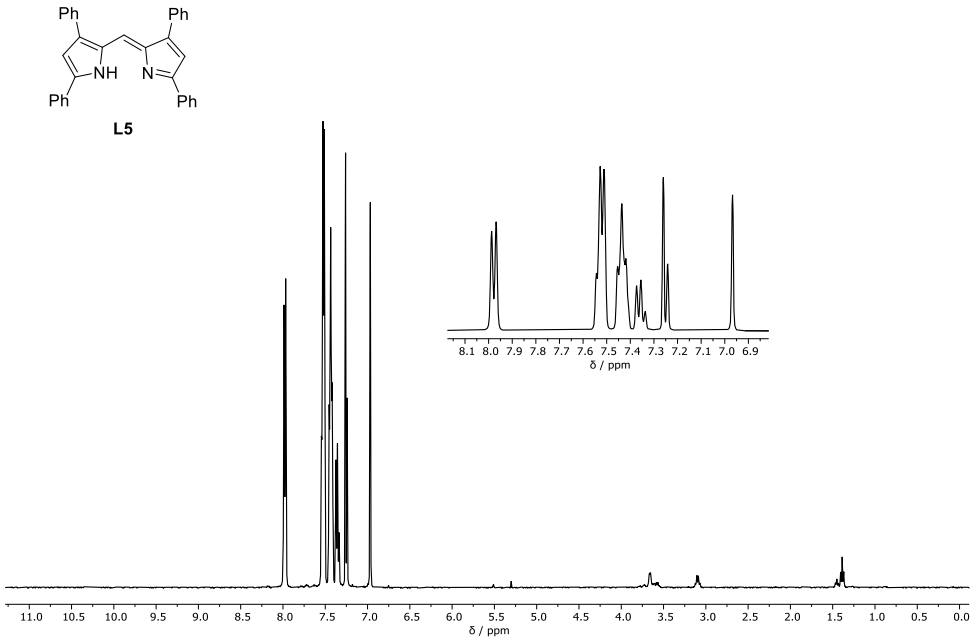


Figure 200: ^{1}H NMR (400 MHz) spectrum of **L5** in $CDCl_3$.

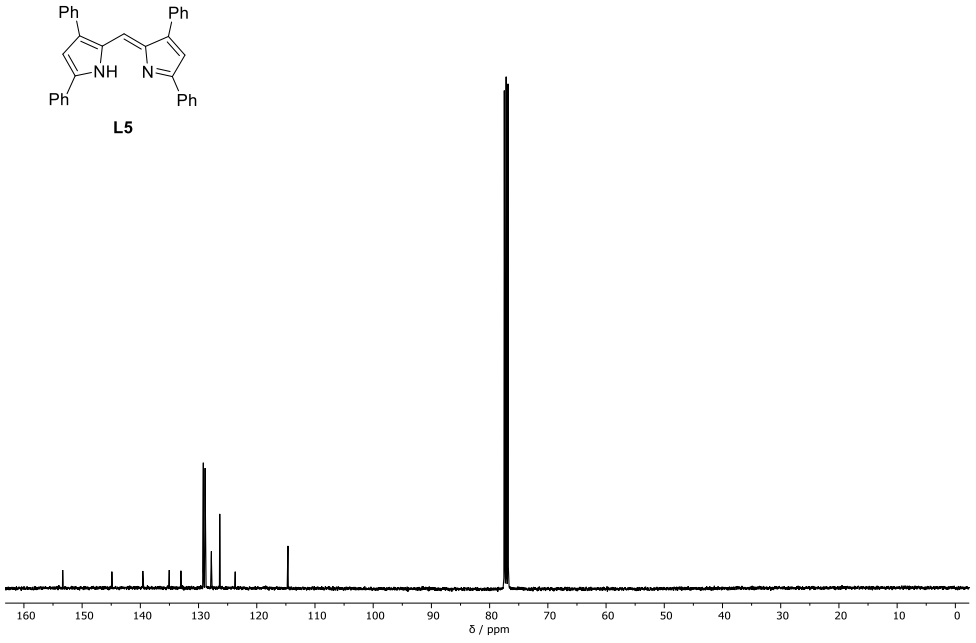


Figure 201: $^{13}C\{^{1}H\}$ NMR (101 MHz) spectrum of **L5** in $CDCl_3$.

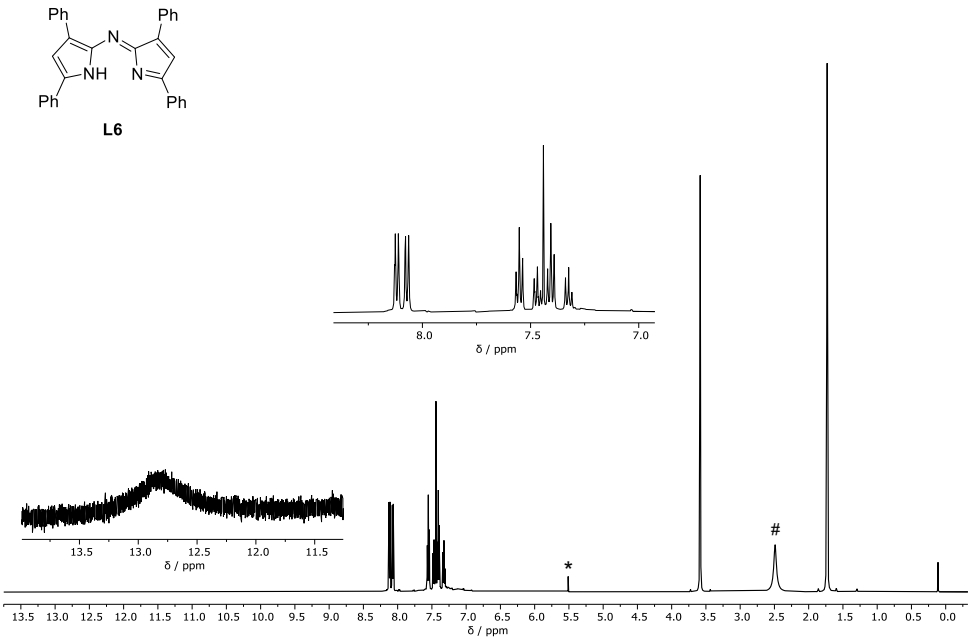


Figure 202: ^{1}H NMR (500 MHz) spectrum of **L6** in THF-d_8. The sign (*) marks CH_2Cl_2 and ($^{\#}$) marks water.

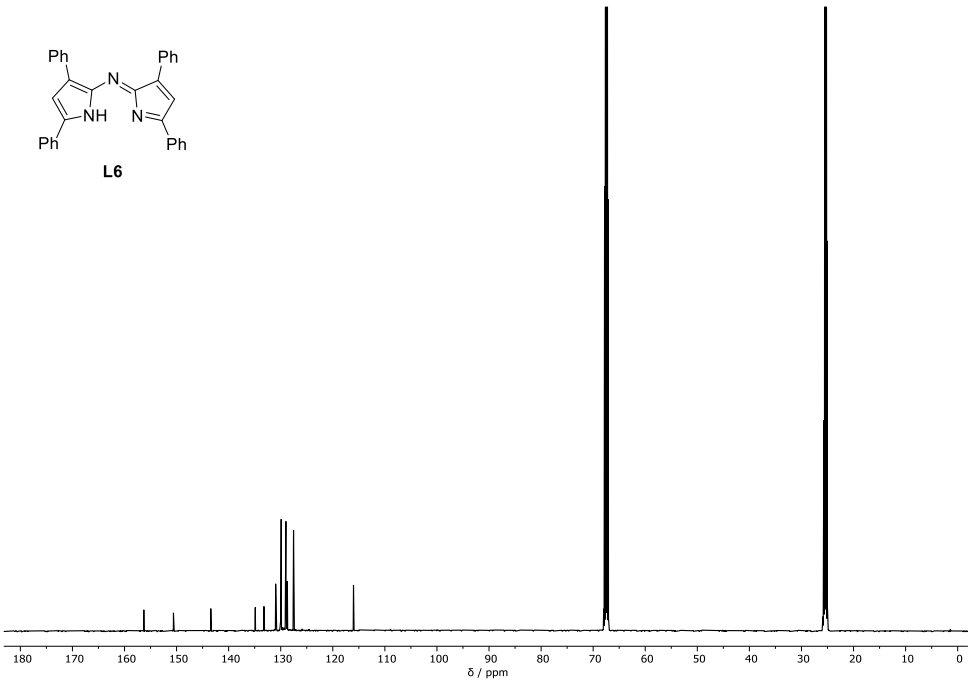


Figure 203: ^{13}C{^{1}H} NMR (126 MHz) spectrum of **L6** in THF-d_8.

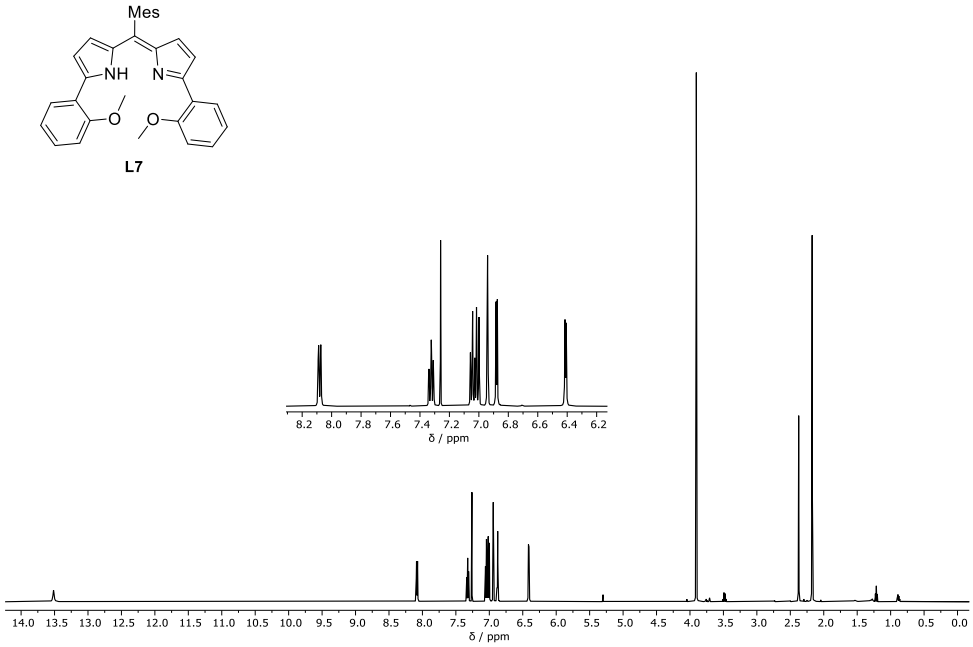


Figure 204: ^{1}H NMR (500 MHz) spectrum of **L7** in $CDCl_3$.

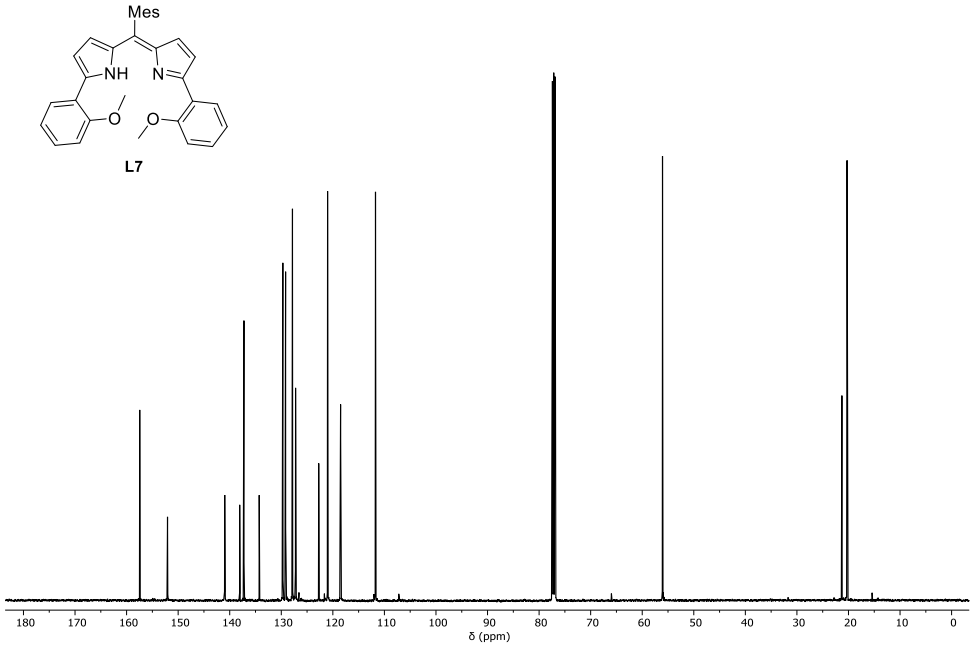


Figure 205: $^{13}C\{^{1}H\}$ NMR (126 MHz) spectrum of **L7** in $CDCl_3$.

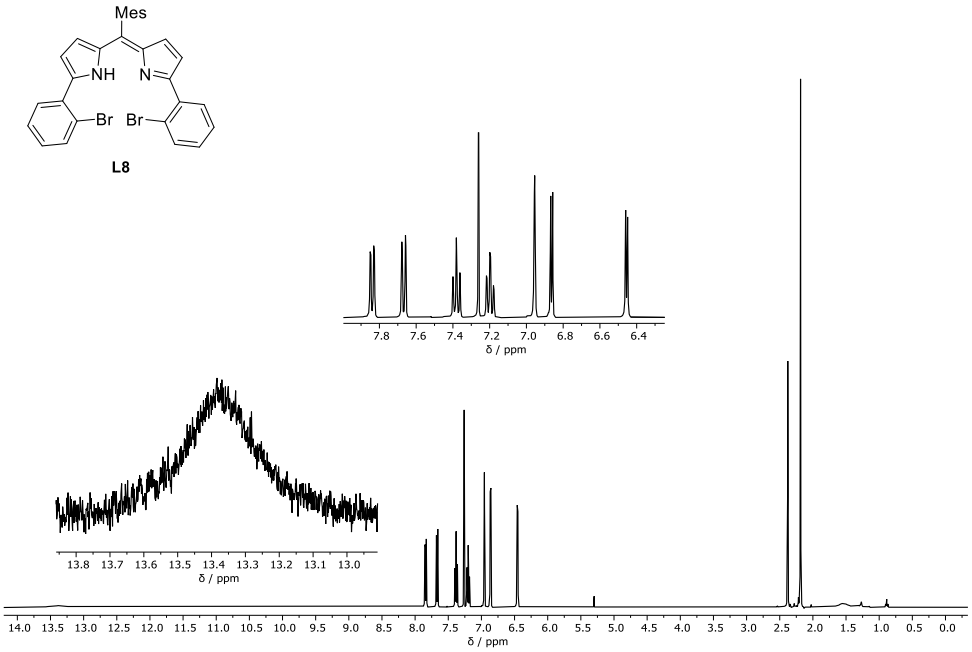


Figure 206: ^{1}H NMR (400 MHz) spectrum of **L8** in $CDCl_3$.

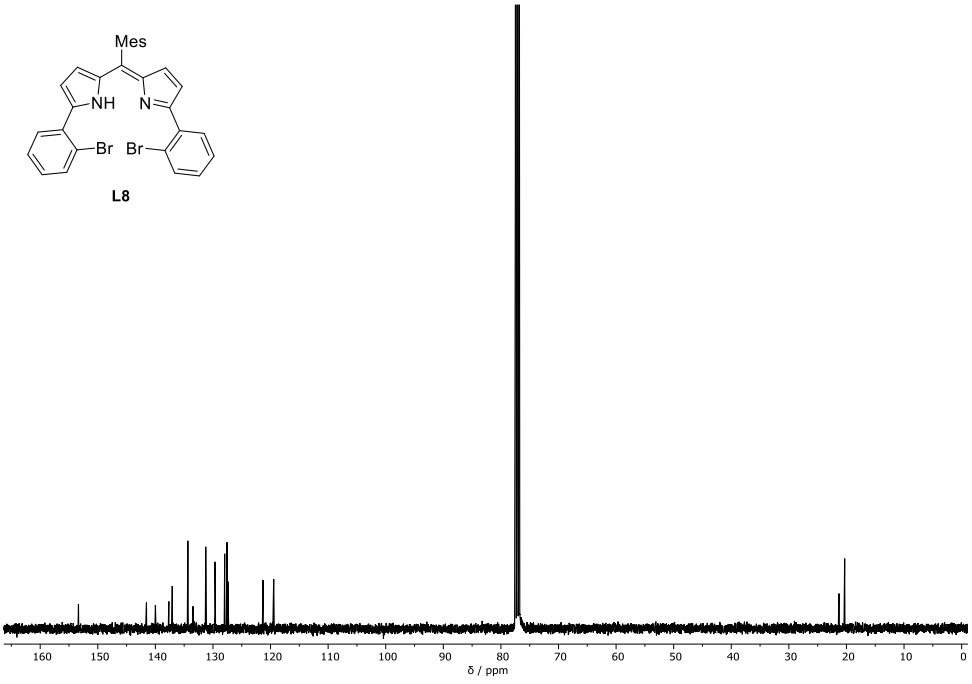


Figure 207: $^{13}C\{^{1}H\}$ NMR (101 MHz) spectrum of **L8** in $CDCl_3$.

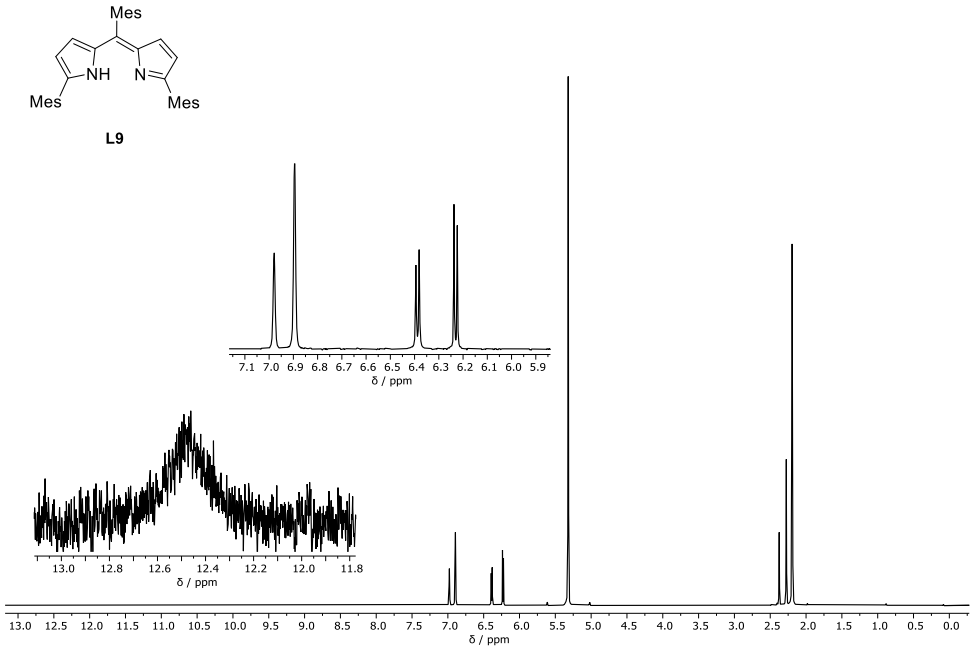


Figure 208: ^{1}H NMR (300 MHz) spectrum of **L9** in CD_2Cl_2.

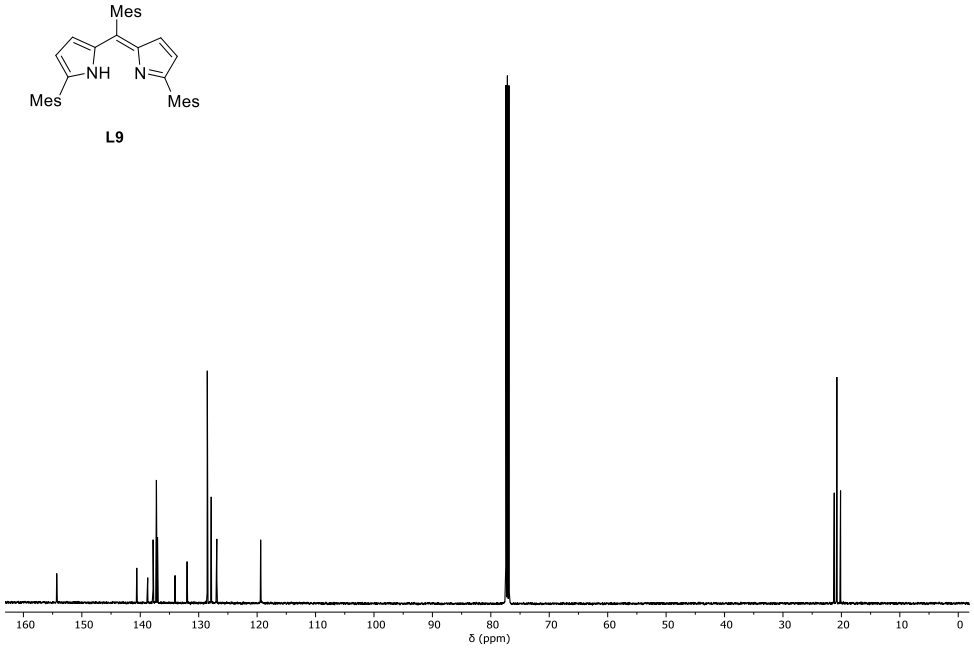


Figure 209: $^{13}C\{^{1}H\}$ NMR (126 MHz) spectrum of **L9** in $CDCl_3$.

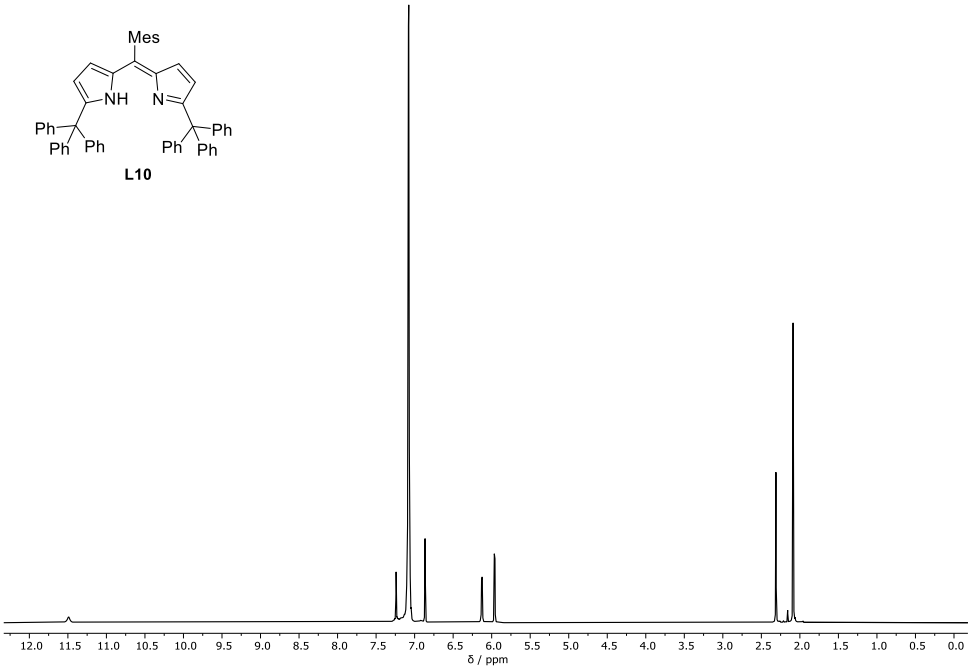


Figure 210: ^{1}H NMR (500 MHz) spectrum of **L10** in $CDCl_3$.

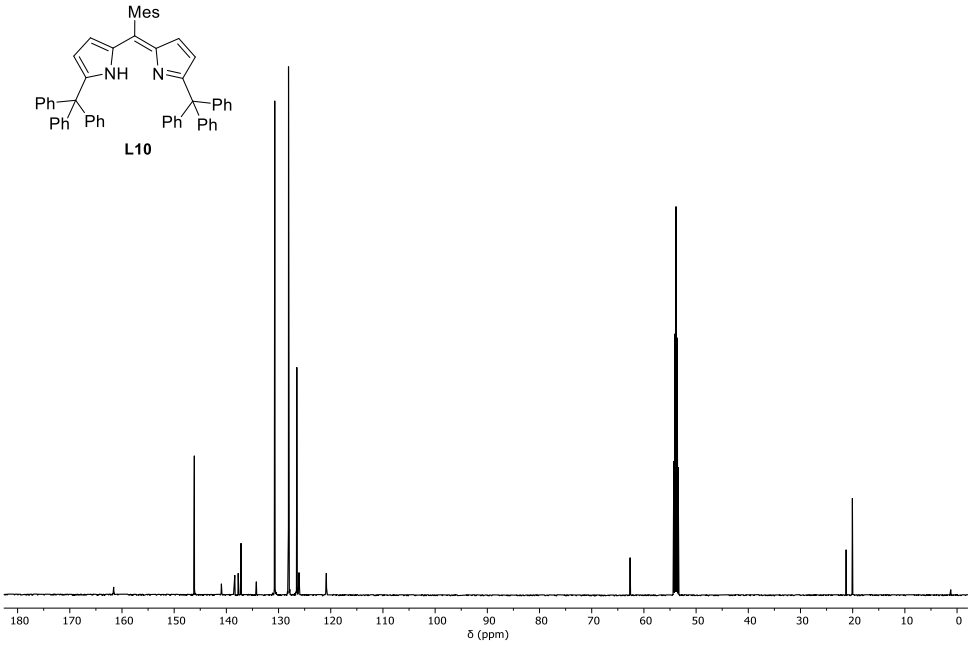


Figure 211: $^{13}C\{^{1}H\}$ NMR (126 MHz) spectrum of **L10** in CD_2Cl_2.

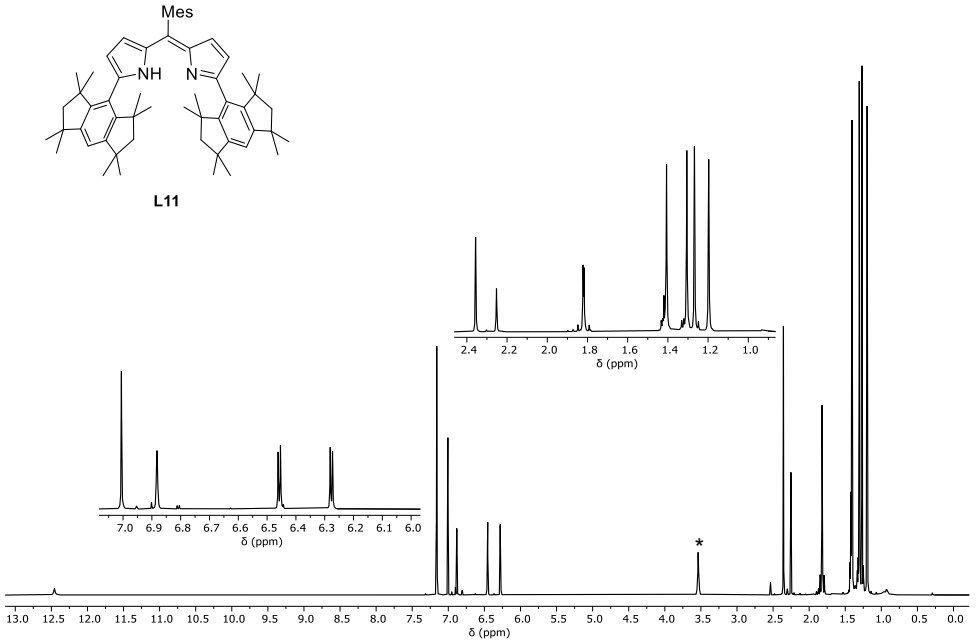


Figure 212: ^{1}H NMR (500 MHz) spectrum of **L11** in C_6D_6. The sign (*) marks THF.

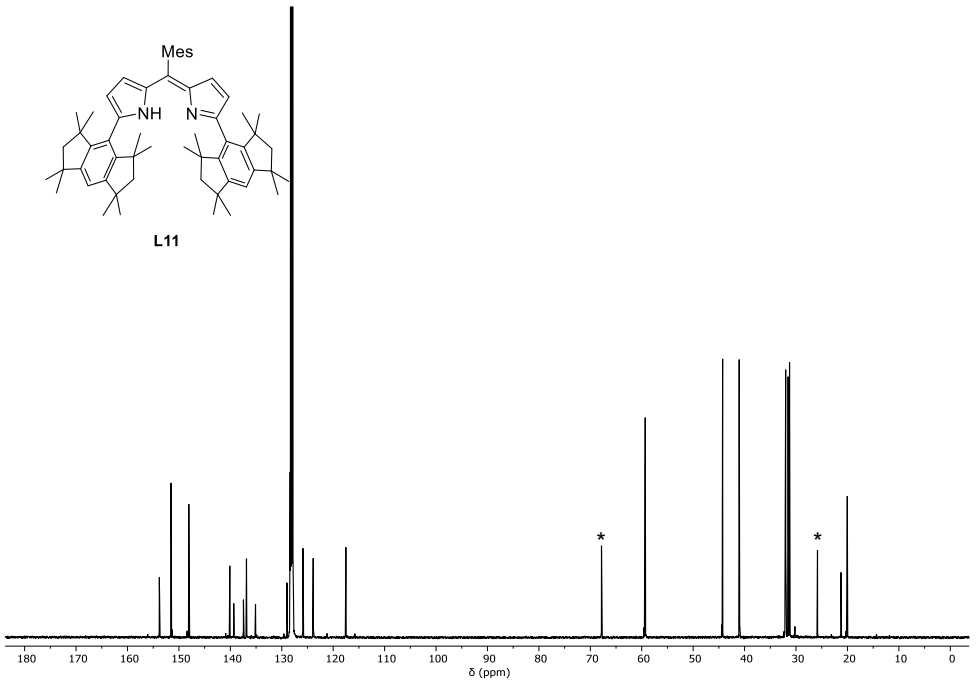


Figure 213: ^{13}C{^{1}H} NMR (126 MHz) spectrum of **L11** in C_6D_6. The sign (*) marks THF.

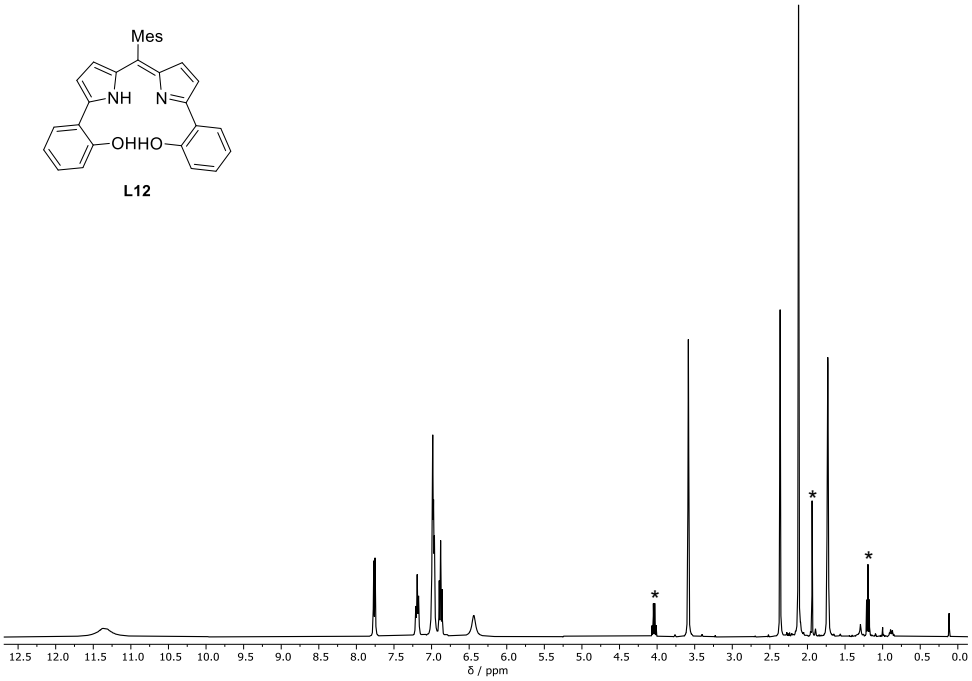


Figure 214: ^{1}H NMR (400 MHz) spectrum of **L12** in THF-d_8. The sign (*) marks ethyl acetate.

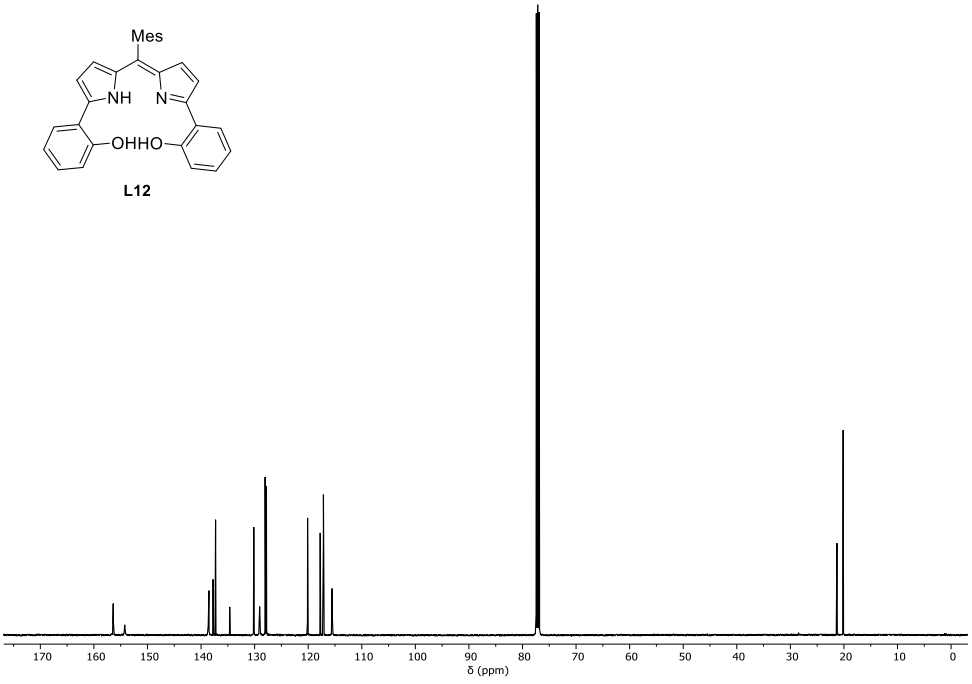


Figure 215: ^{13}C{^{1}H} NMR (126 MHz) spectrum of **L12** in $CDCl_3$.

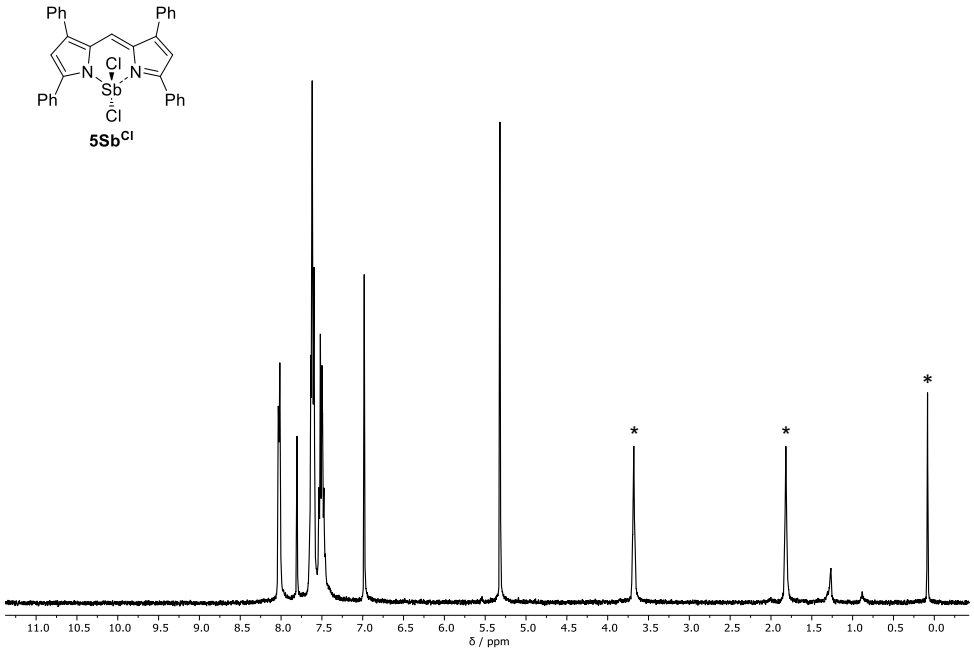


Figure 216: ^{1}H NMR (400 MHz) spectrum of **5Sb^{Cl}** in CD_2Cl_2. The sign (*) marks THF and (*) marks silicone grease.

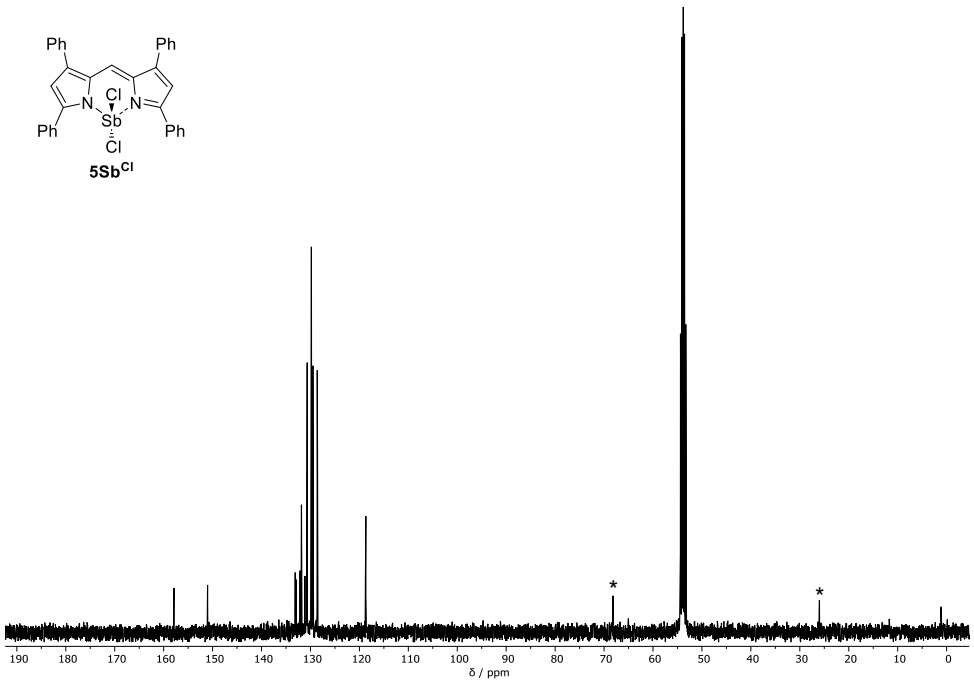


Figure 217: ^{13}C{^{1}H} NMR (126 MHz) spectrum of **5Sb^{Cl}** in CD_2Cl_2. The sign (*) marks THF.

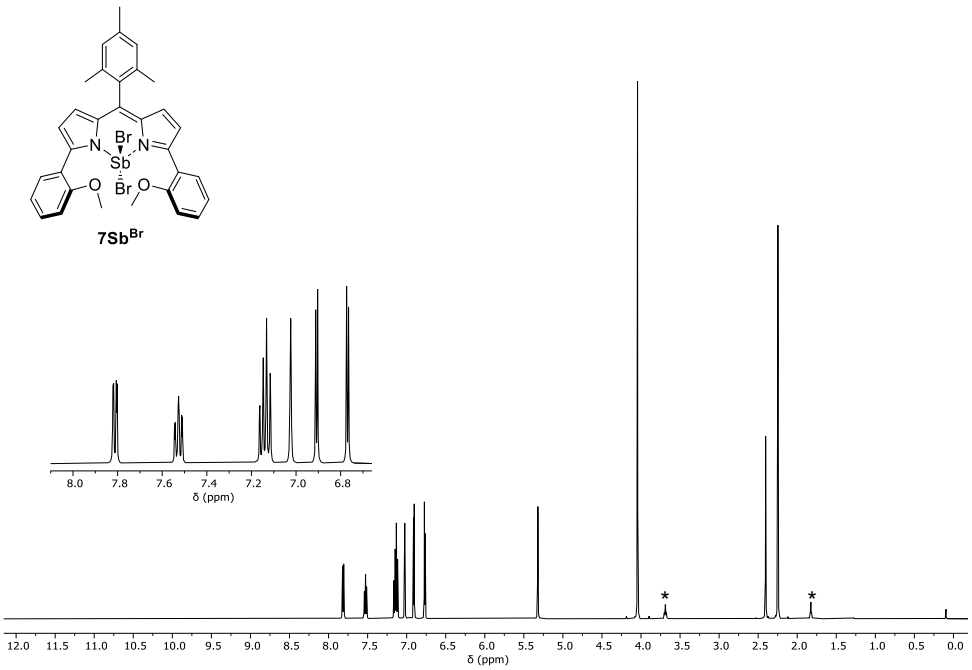


Figure 218: ^{1}H NMR (500 MHz) spectrum of **7Sb^{Br}** in CD_2Cl_2. The sign (*) marks THF.

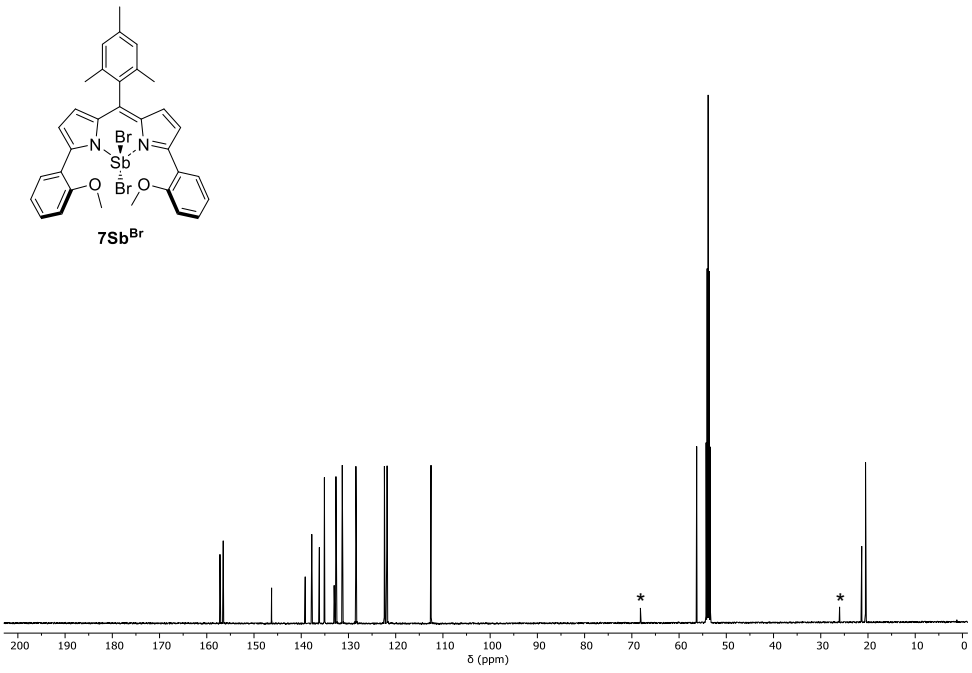


Figure 219: $^{13}C\{^{1}H\}$ NMR (126 MHz) spectrum of **7Sb^{Br}** in CD_2Cl_2. The sign (*) marks THF.

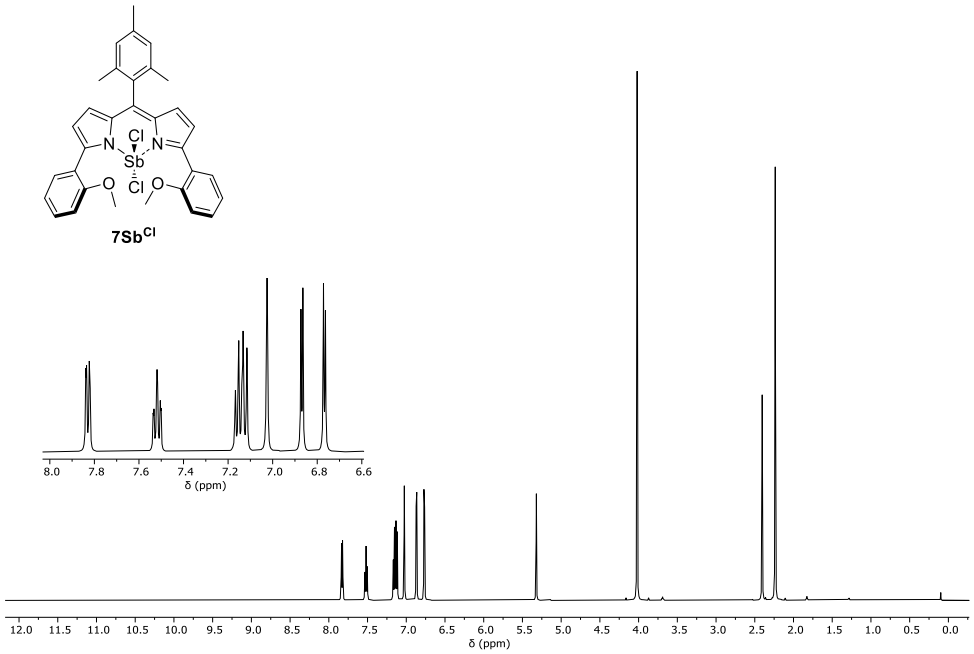


Figure 220: ^{1}H NMR (500 MHz) spectrum of **7Sb^{Cl}** in CD_2Cl_2.

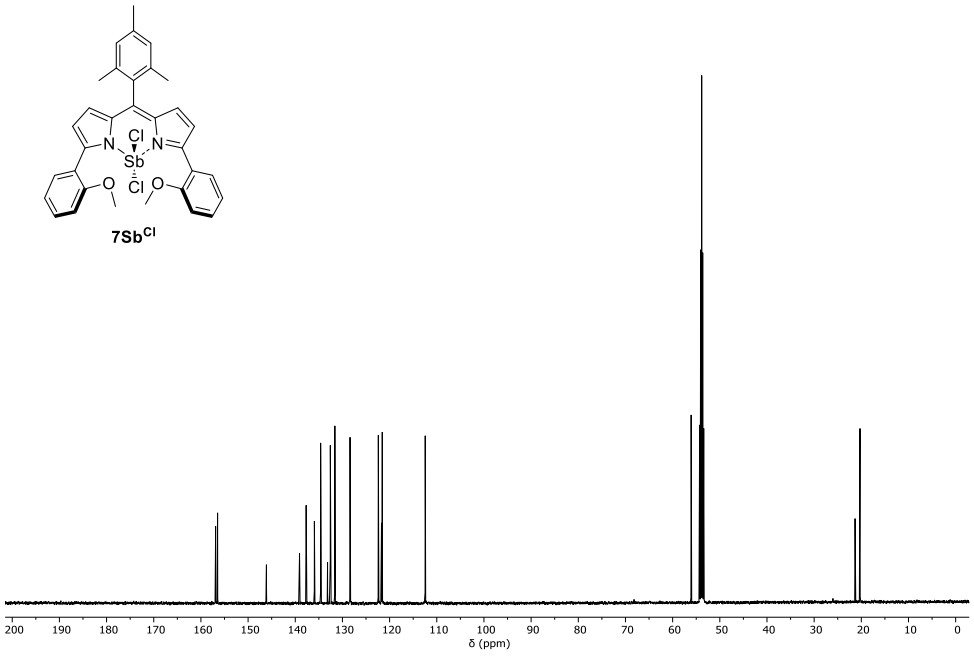


Figure 221: ^{13}C{^{1}H} NMR (126 MHz) spectrum of **7Sb^{Cl}** in CD_2Cl_2.

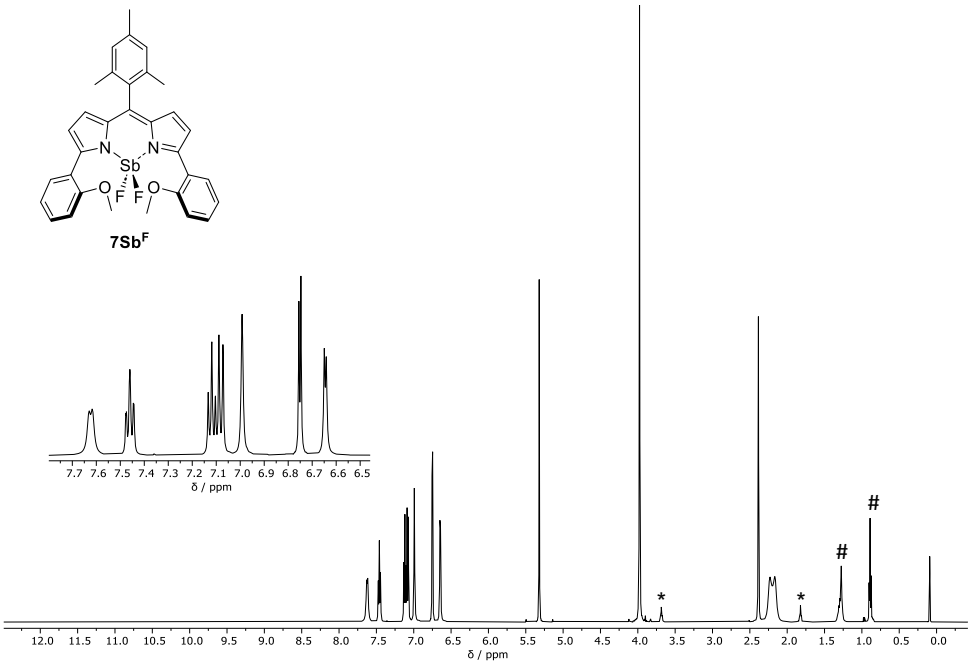


Figure 222: ^{1}H NMR (500 MHz) spectrum of **7Sb^{F}** in CD_2Cl_2. The sign (*) marks THF and (#) marks *n*-hexane.

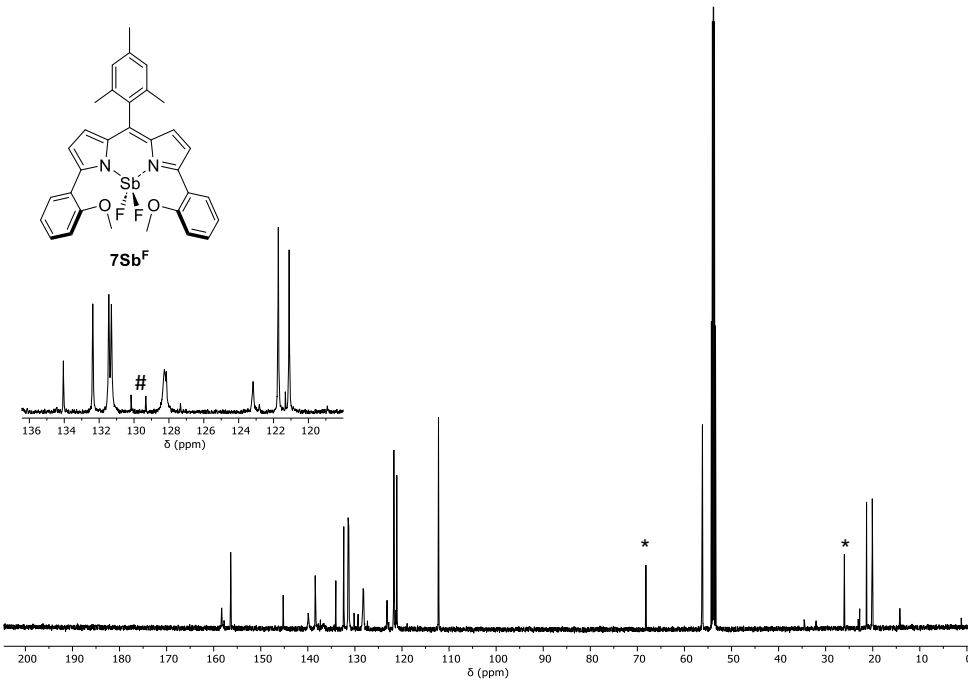


Figure 223: ^{13}C{^{1}H} NMR (126 MHz) spectrum of **7Sb^{F}** in CD_2Cl_2.

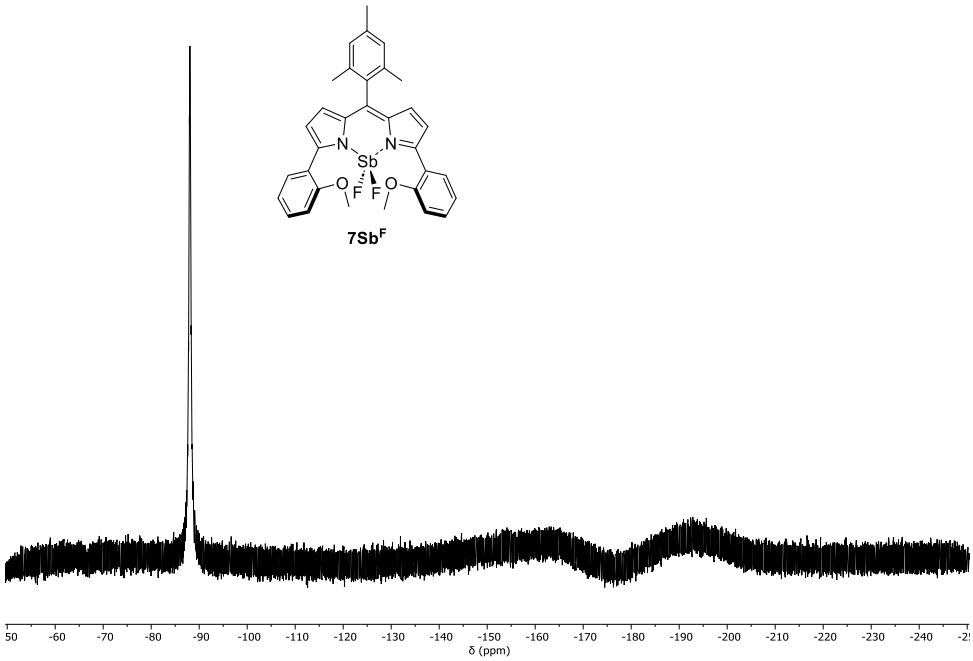


Figure 224: ^{19}F NMR (470 MHz) spectrum of **7Sb^F** in CD_2Cl_2.

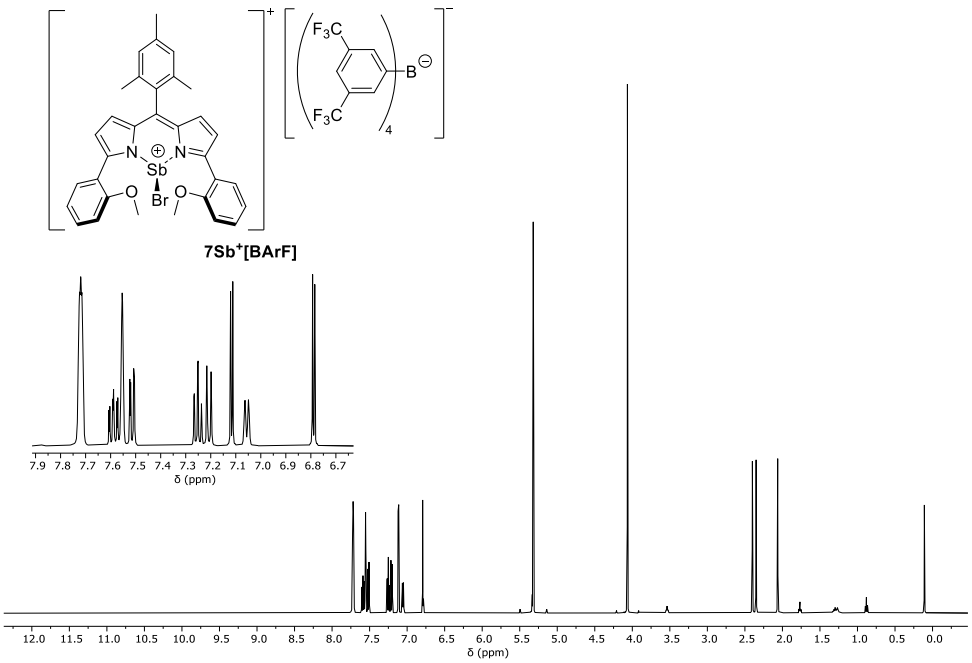


Figure 225: ^{1}H NMR (500 MHz) spectrum of **7Sb^{+}[BArF]** in CD_2Cl_2.

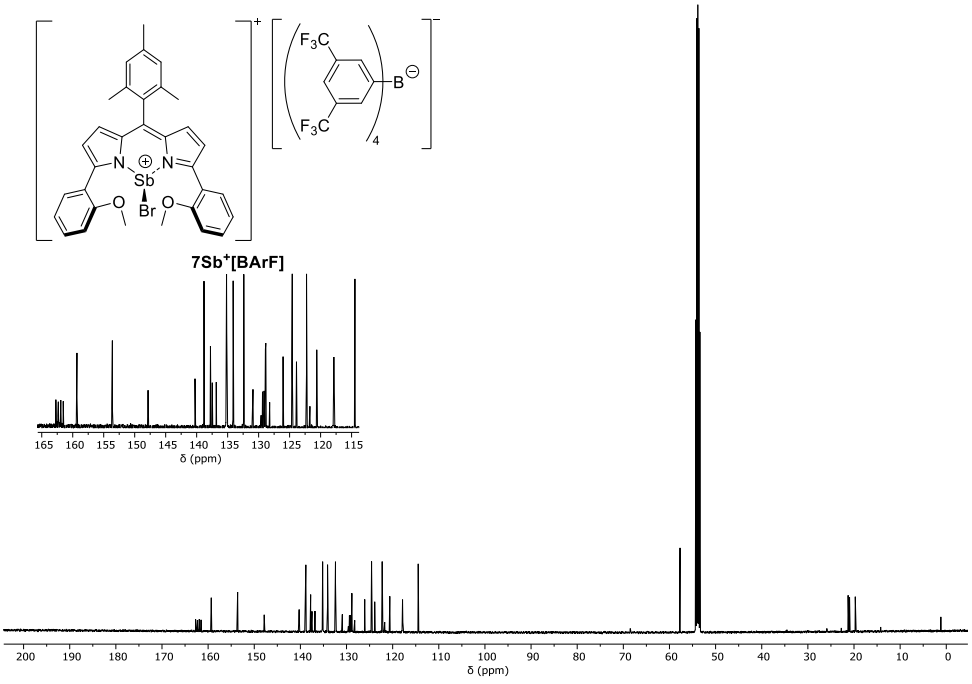


Figure 226: $^{13}C\{^{1}H\}$ NMR (126 MHz) spectrum of **7Sb^{+}[BArF]** in CD_2Cl_2.

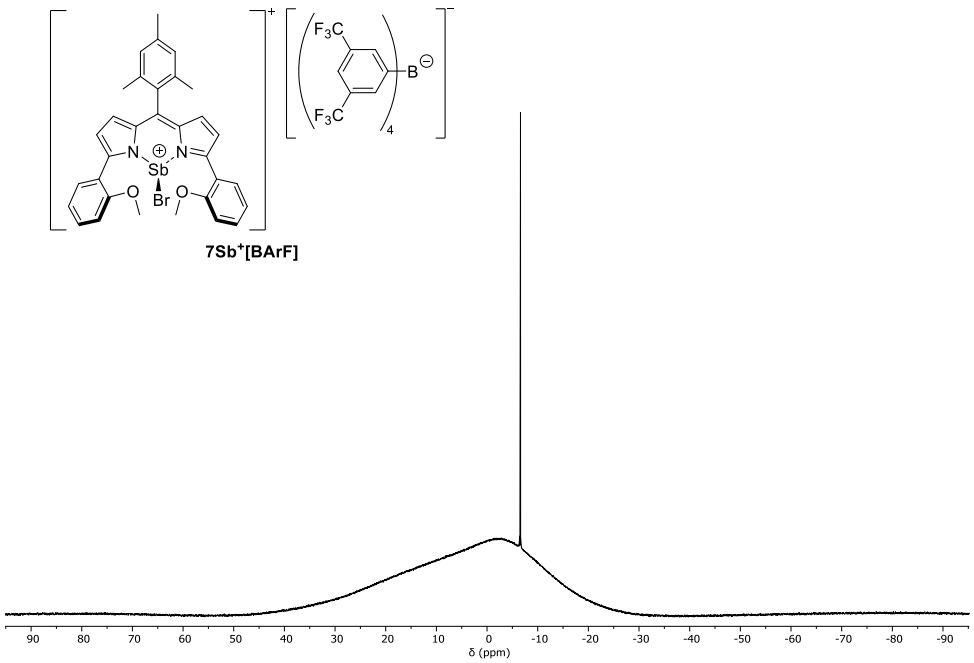


Figure 227: $^{11}B\{^{1}H\}$ NMR (161 MHz) spectrum of **7Sb⁺[BArF]** in CD_2Cl_2.

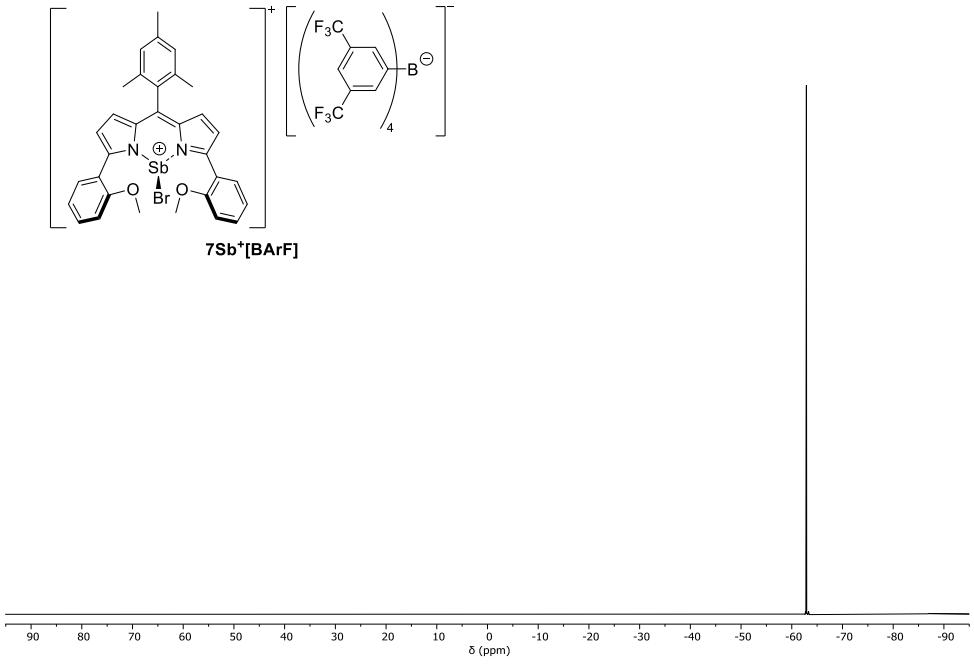


Figure 228: ^{19}F NMR (470 MHz) spectrum of **7Sb⁺[BArF]** in CD_2Cl_2.

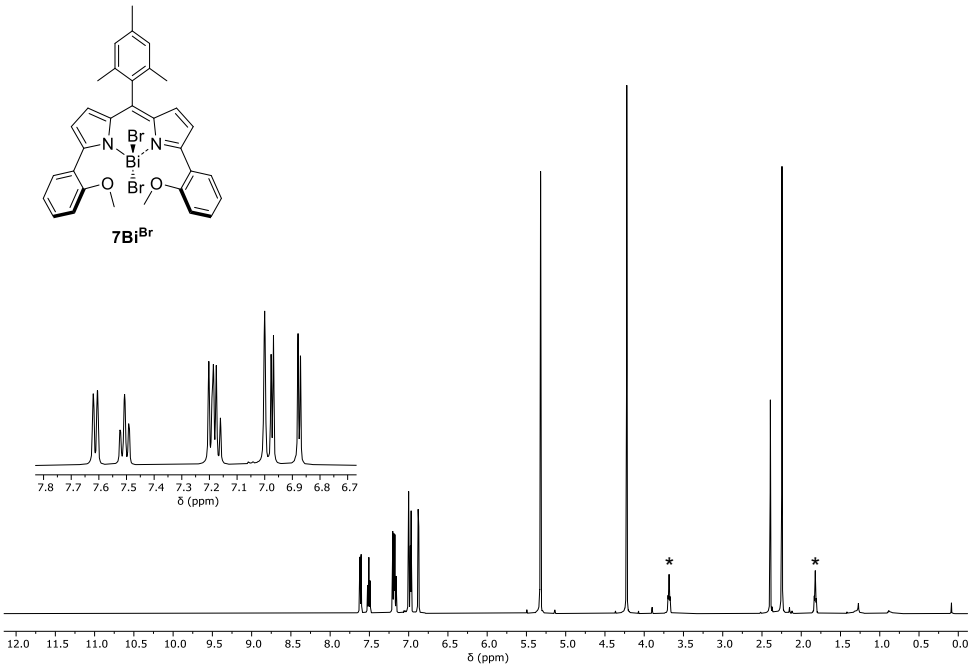


Figure 229: ^{1}H NMR (500 MHz) spectrum of **7Bi^{Br}** in CD_2Cl_2. The sign (*) marks THF.

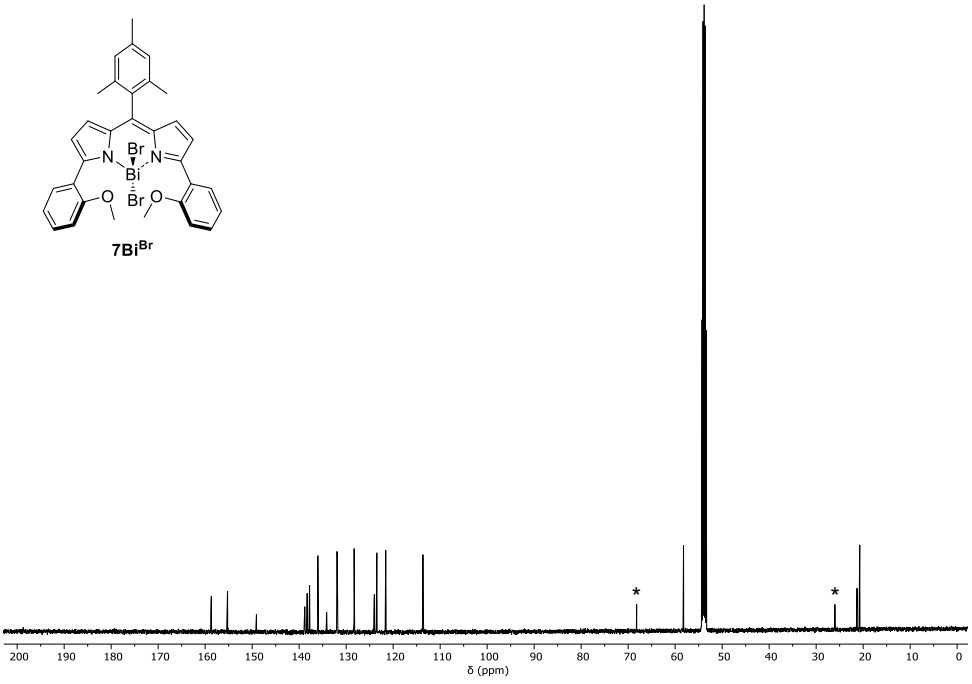


Figure 230: $^{13}C\{^{1}H\}$ NMR (126 MHz) spectrum of **7Bi^{Br}** in CD_2Cl_2. The sign (*) marks THF.

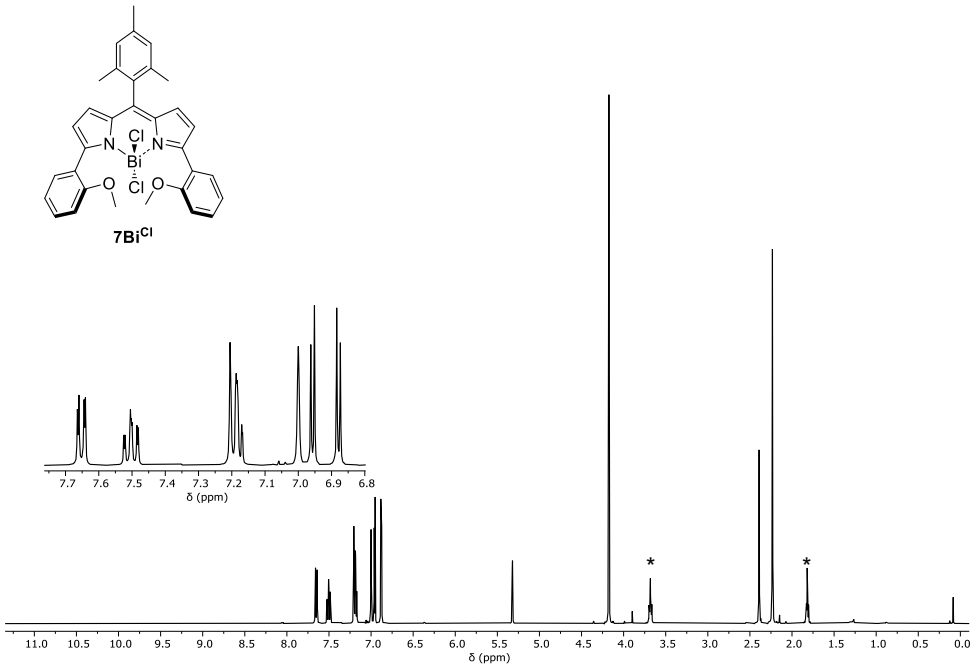


Figure 231: ^{1}H NMR (400 MHz) spectrum of **7Bi^{Cl}** in CD_2Cl_2. The sign (*) marks THF.

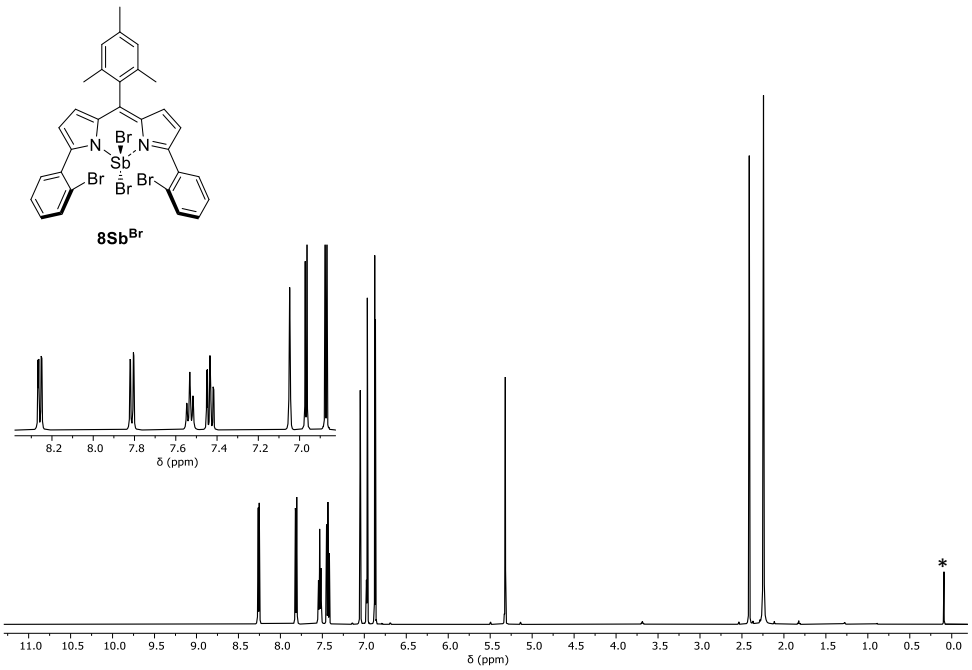


Figure 232: ^{1}H NMR (500 MHz) spectrum of **8Sb^{Br}** in CD_2Cl_2. The sign (*) marks silicone grease.

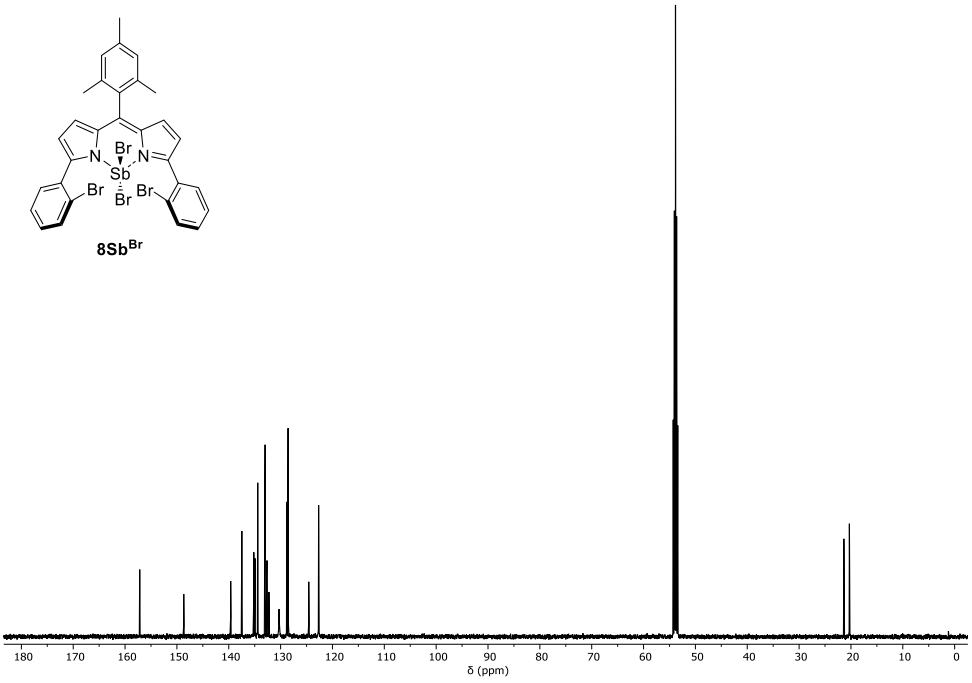


Figure 233: $^{13}C\{^{1}H\}$ NMR (126 MHz) spectrum of **8Sb^{Br}** in CD_2Cl_2.

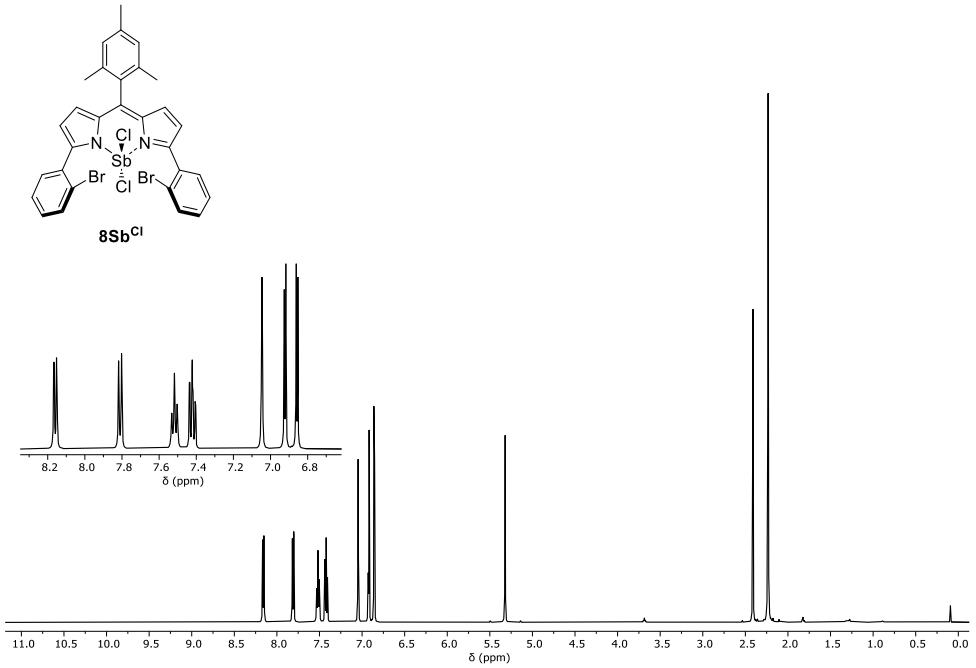


Figure 234: ^{1}H NMR (500 MHz) spectrum of **8Sb^{Cl}** in CD_2Cl_2.

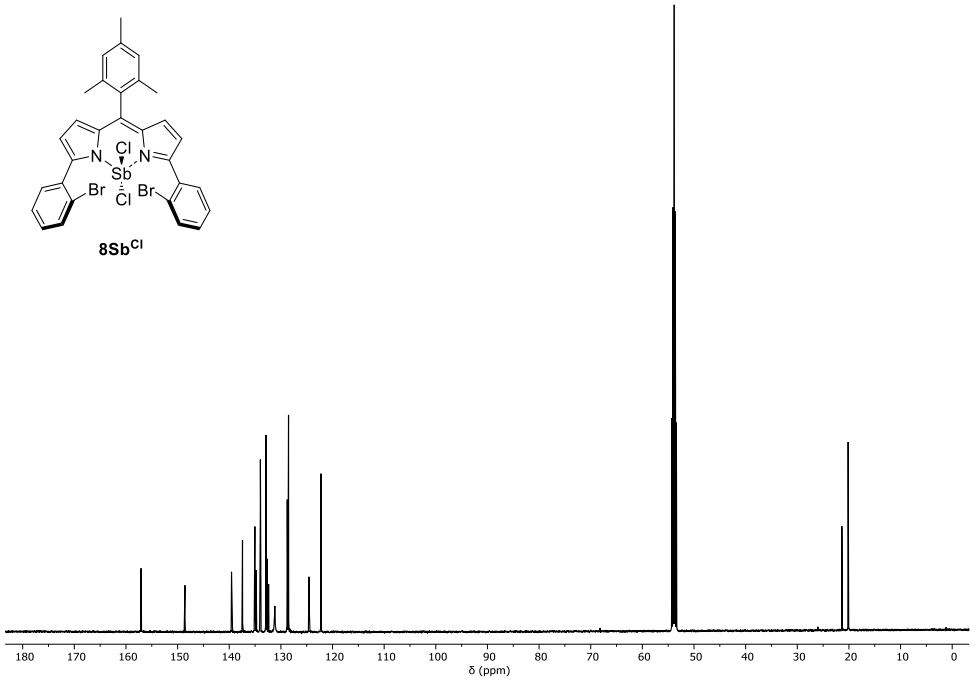


Figure 235: $^{13}C\{^{1}H\}$ NMR (126 MHz) spectrum of **8Sb^{Cl}** in CD_2Cl_2.

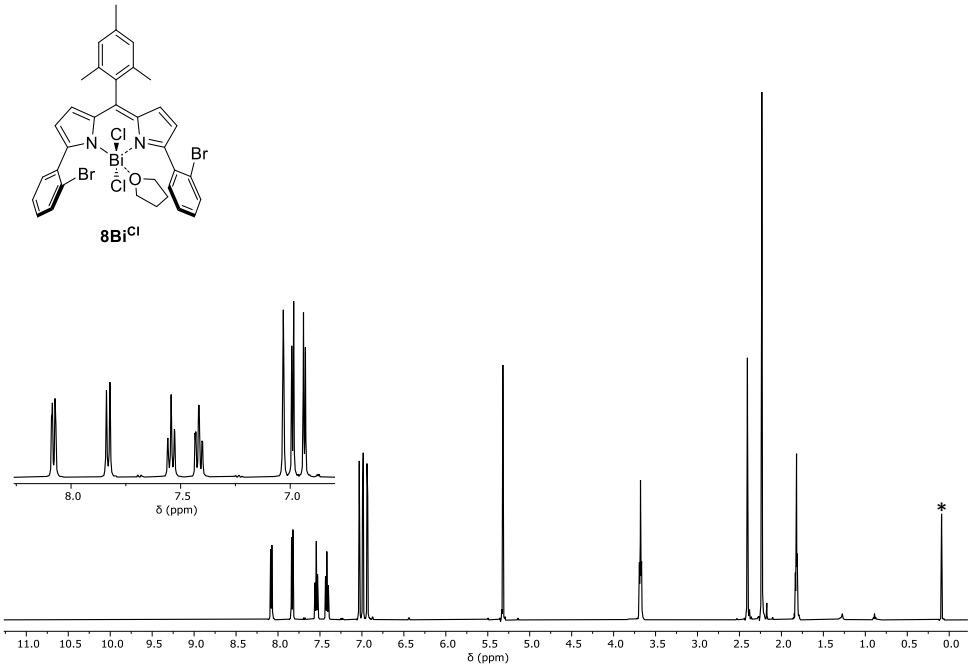


Figure 236: ^{1}H NMR (500 MHz) spectrum of **8Bi^{Cl}** in CD_2Cl_2. The sign (⋆) marks THF and (*) marks silicone grease.

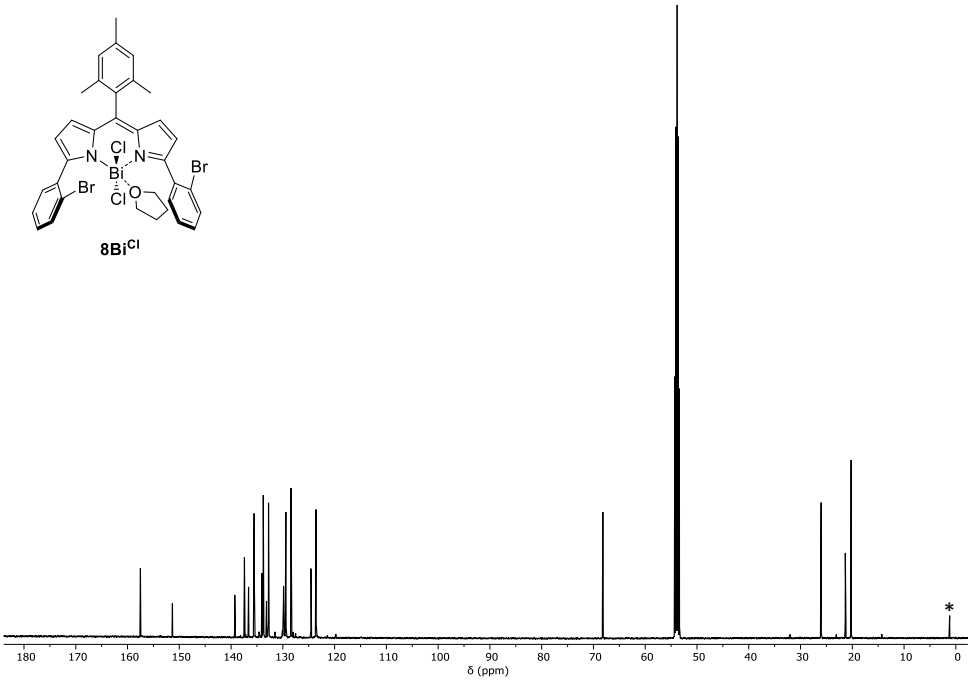


Figure 237: $^{13}C\{^{1}H\}$ NMR (126 MHz) spectrum of **8Bi^{Cl}** in CD_2Cl_2. The sign (⋆) marks THF and (*) marks silicone grease.

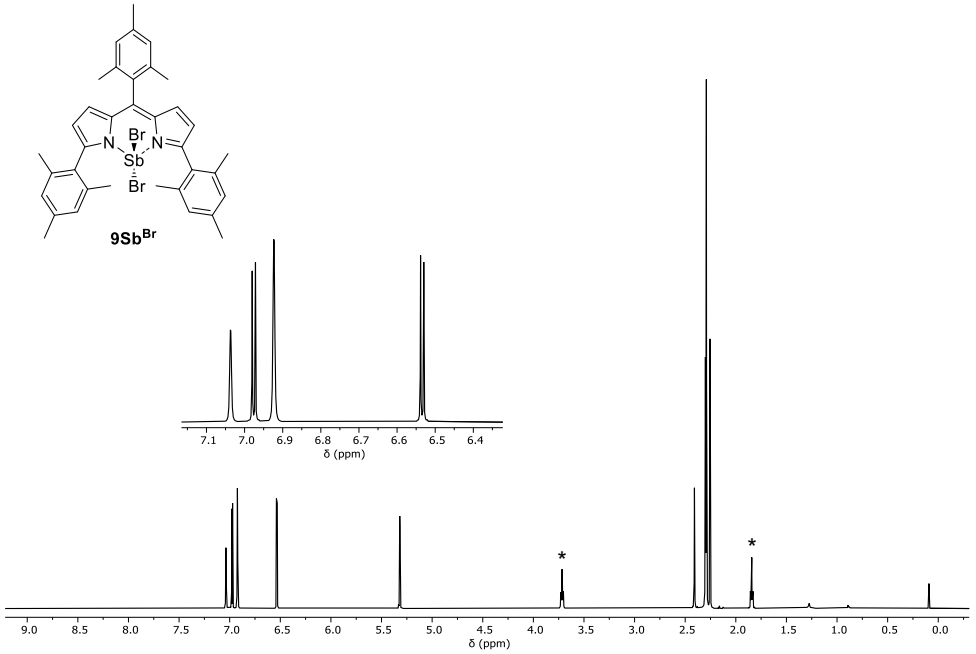


Figure 238: ^{1}H NMR (500 MHz) spectrum of **9Sb^{Br}** in CD_2Cl_2. The sign (*) marks THF. *Spectrum recorded by L. Mohr*.

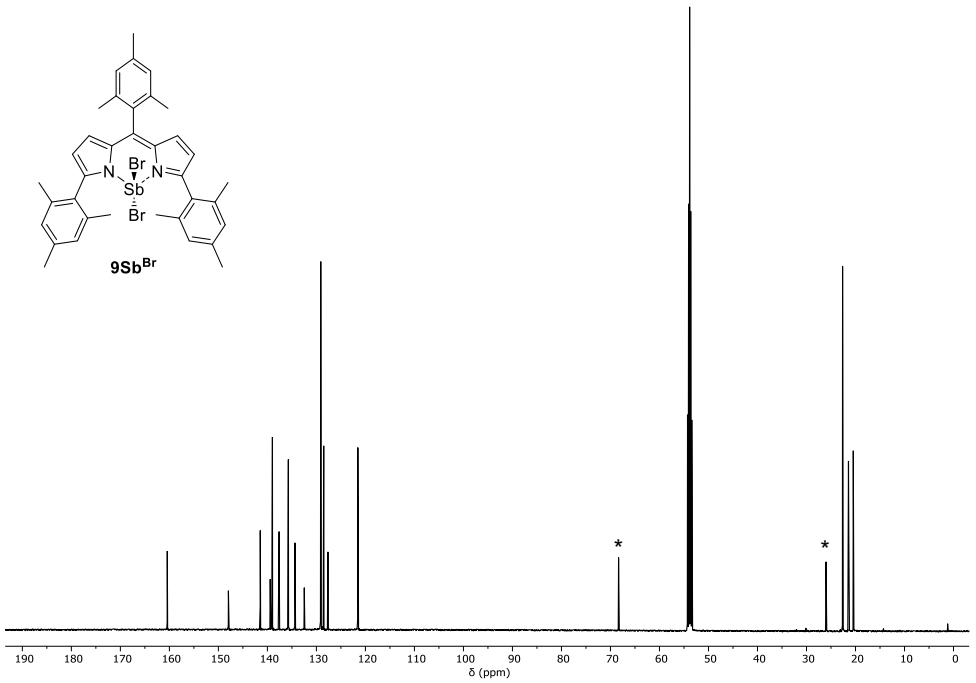


Figure 239: ^{13}C{^{1}H} NMR (126 MHz) spectrum of **9Sb^{Br}** in CD_2Cl_2. The sign (*) marks THF. *Spectrum recorded by L. Mohr*.

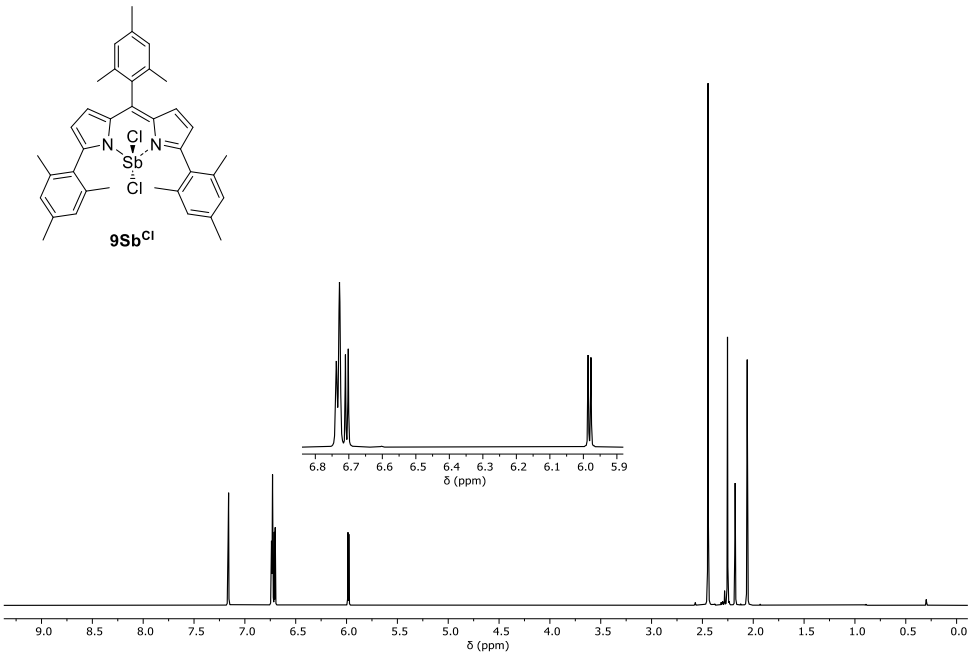


Figure 240: ^{1}H NMR (500 MHz) spectrum of **9Sb^{Cl}** in C_6D_6. *Spectrum recorded by L. Mohr.*

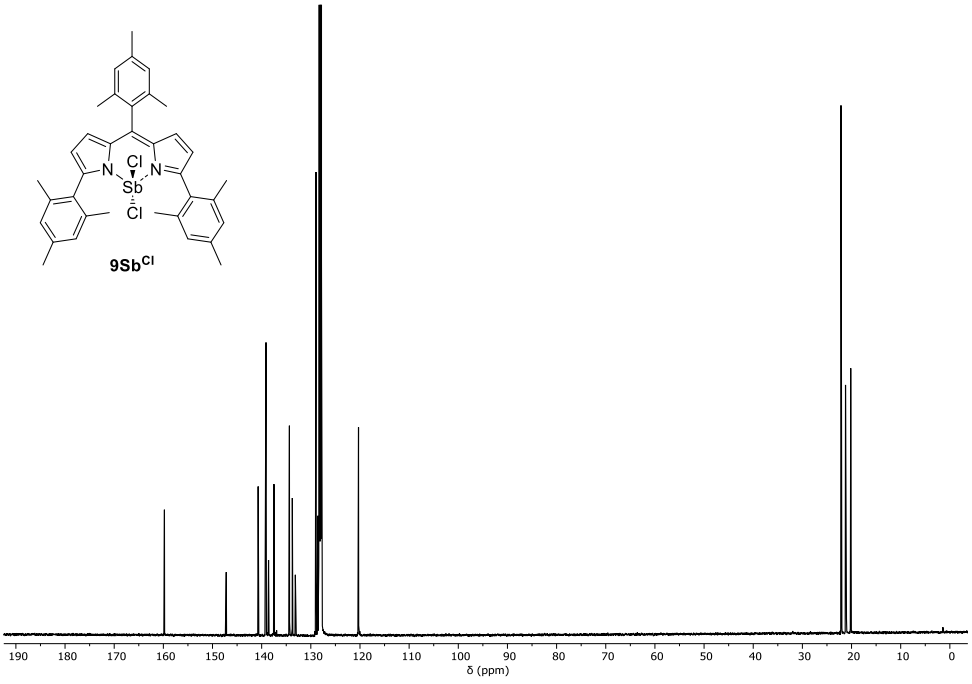


Figure 241: $^{13}C\{^{1}H\}$ NMR (126 MHz) spectrum of **9Sb^{Cl}** in C_6D_6. *Spectrum recorded by L. Mohr.*

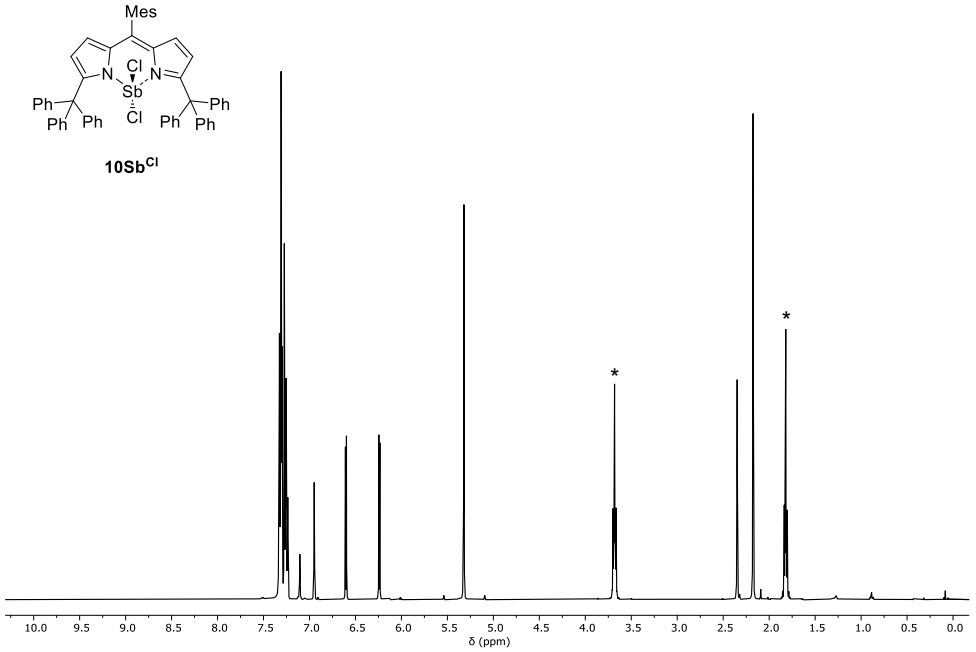


Figure 242: ^{1}H NMR (400 MHz) spectrum of **10Sb^{Cl}** in CD_2Cl_2.The sign (*) marks THF.

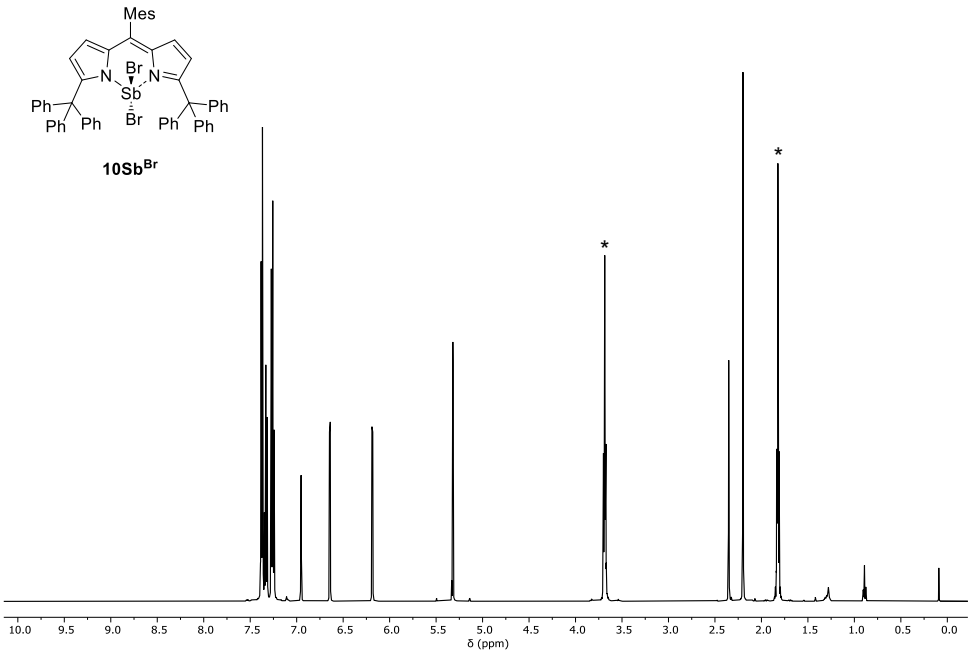


Figure 243: ^{1}H NMR (500 MHz) spectrum of **10Sb^{Br}** in CD_2Cl_2. The sign (*) marks THF.

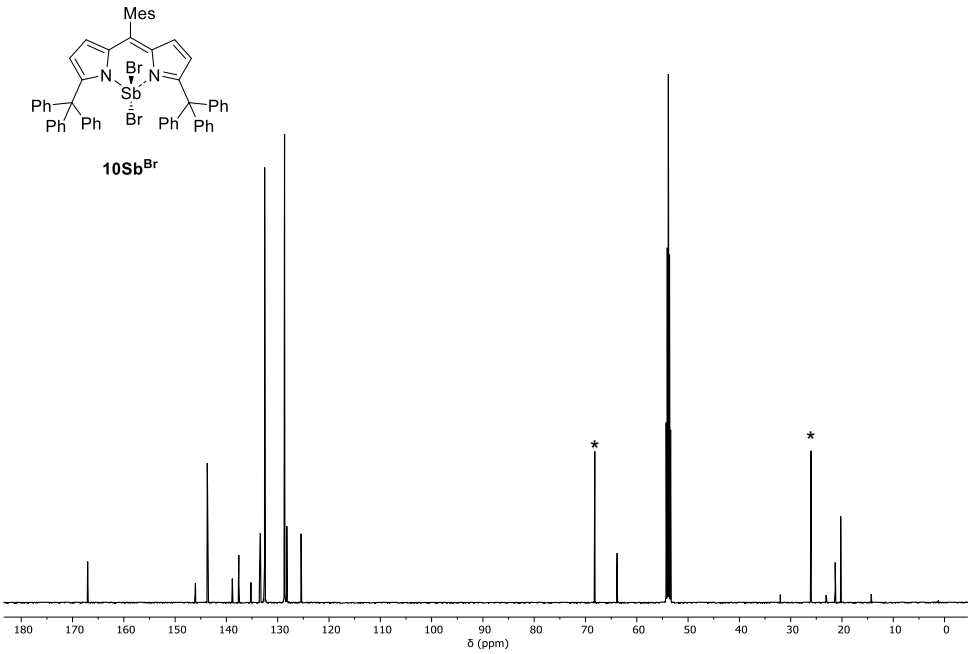


Figure 244: ^{13}C{^{1}H} NMR (126 MHz) spectrum of **10Sb^{Br}** in CD_2Cl_2. The sign (*) marks THF.

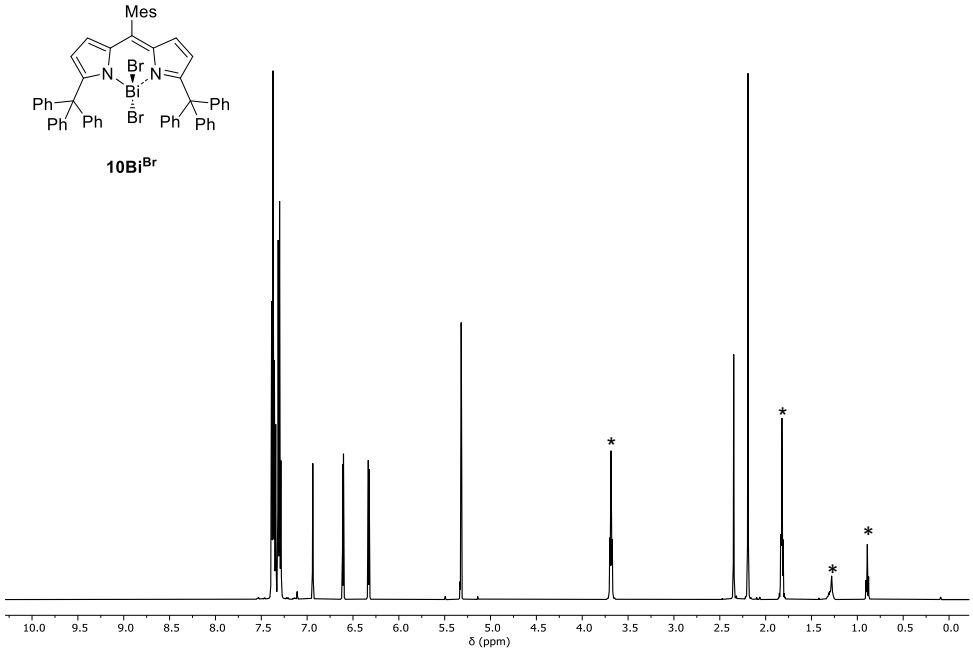


Figure 245: ^{1}H NMR (500 MHz) spectrum of **10Bi^{Br}** in CD_2Cl_2. The sign (*) marks THF, whereas (*) marks *n*-hexane.

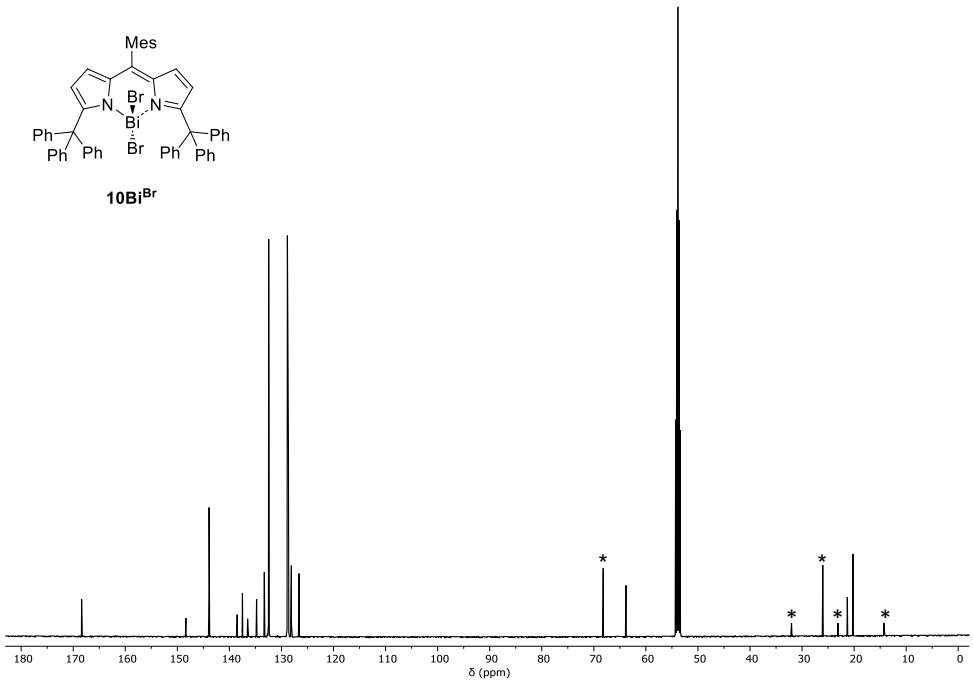


Figure 246: ^{13}C{^{1}H} NMR (126 MHz) spectrum of **10Bi^{Br}** in CD_2Cl_2. The sign (*) marks THF, whereas (*) marks *n*-hexane.

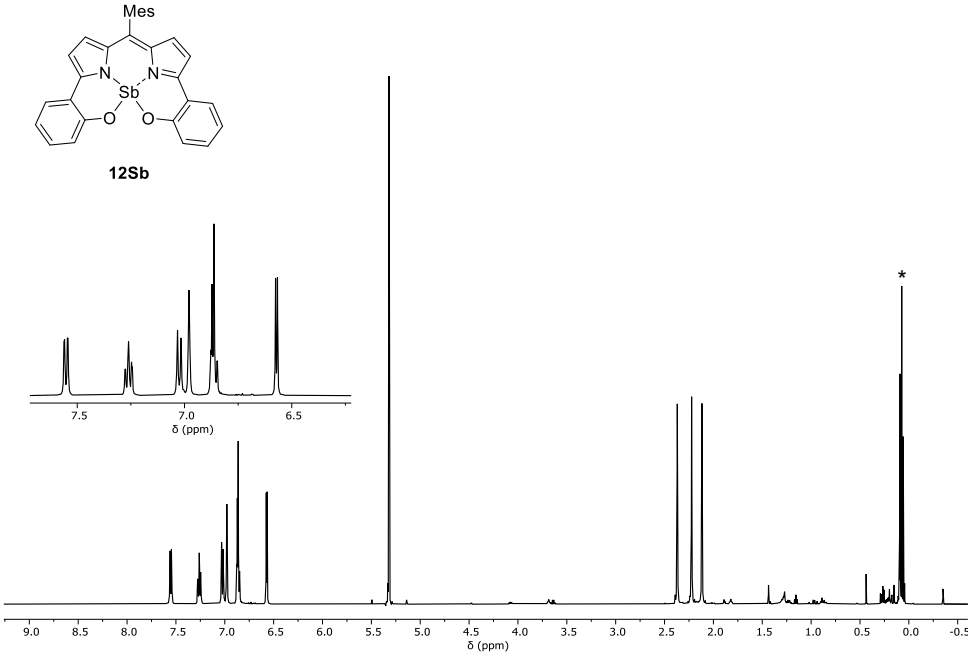


Figure 247: ^{1}H NMR (500 MHz) spectrum of **12Sb** in CD_2Cl_2. The sign (*) marks unknown silicon-related impurities.

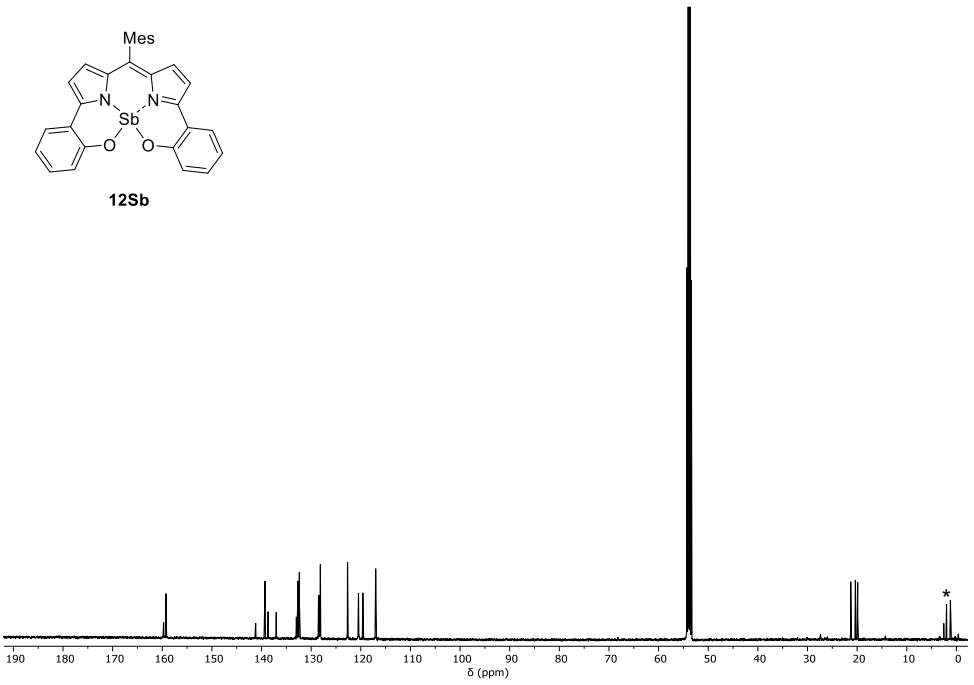


Figure 248: $^{13}C\{^{1}H\}$ NMR (126 MHz) spectrum of **12Sb** in CD_2Cl_2. The sign (*) marks unknown silicon-related impurities.

Chapter 4

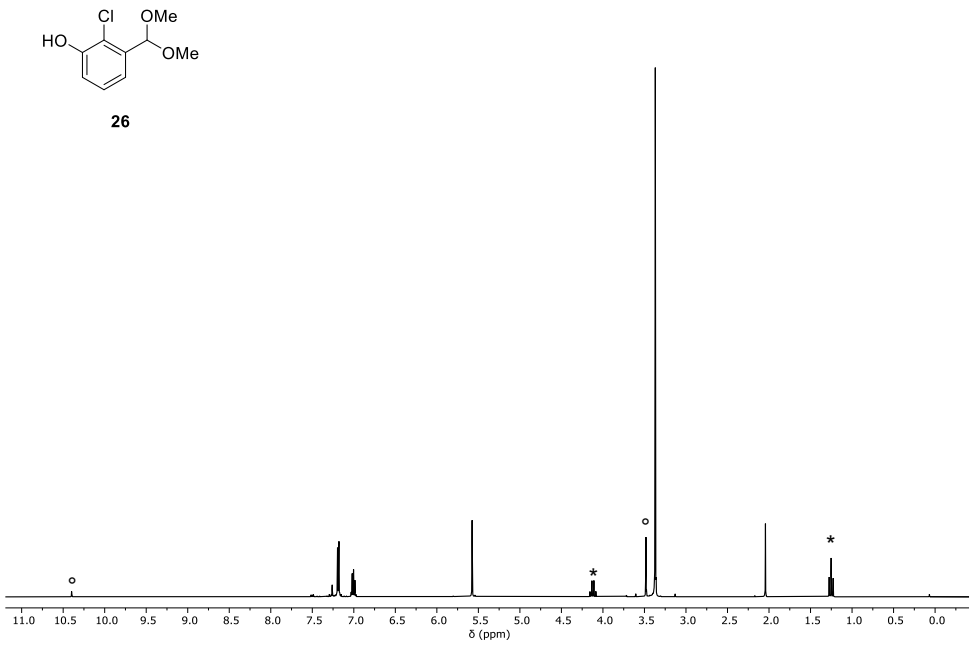


Figure 249: ^{1}H NMR (300 MHz) spectrum of **26** in $CDCl_3$. Starting material is marked by (°), whereas (*) marks ethyl acetate.

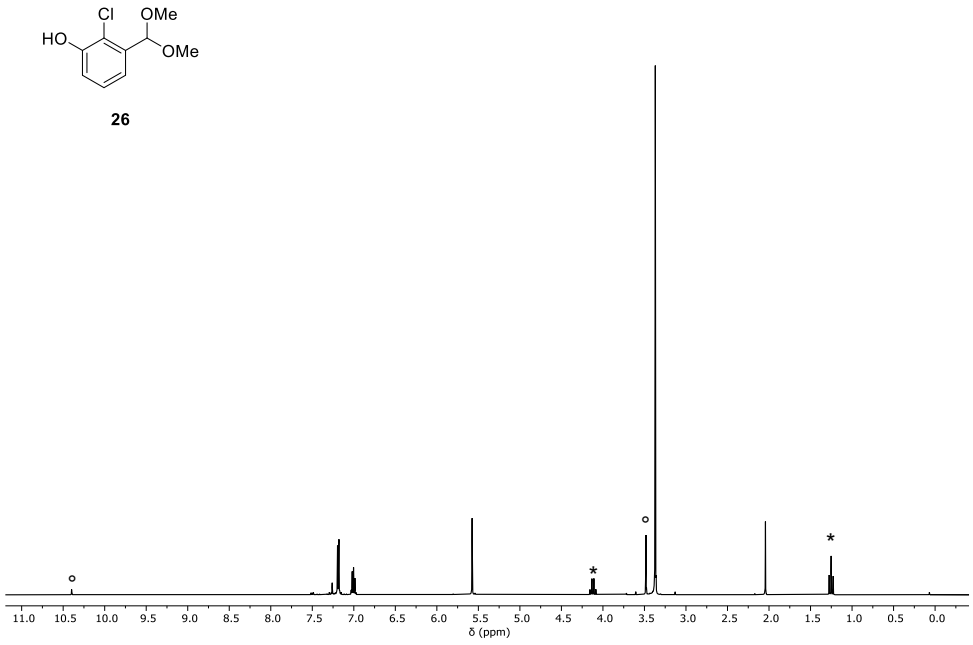


Figure 250: ^{1}H NMR (300 MHz) spectrum of **27** and sideproduct (°) in $CDCl_3$.

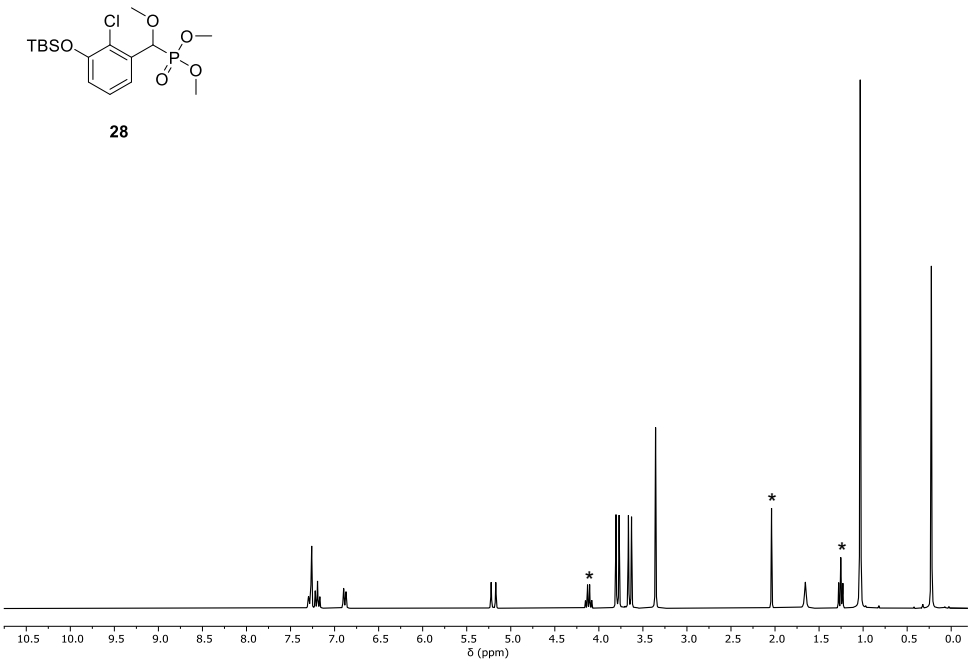


Figure 251: ^{1}H NMR (300 MHz) spectrum of **28** in $CDCl_3$. The sign (*) marks ethyl acetate.

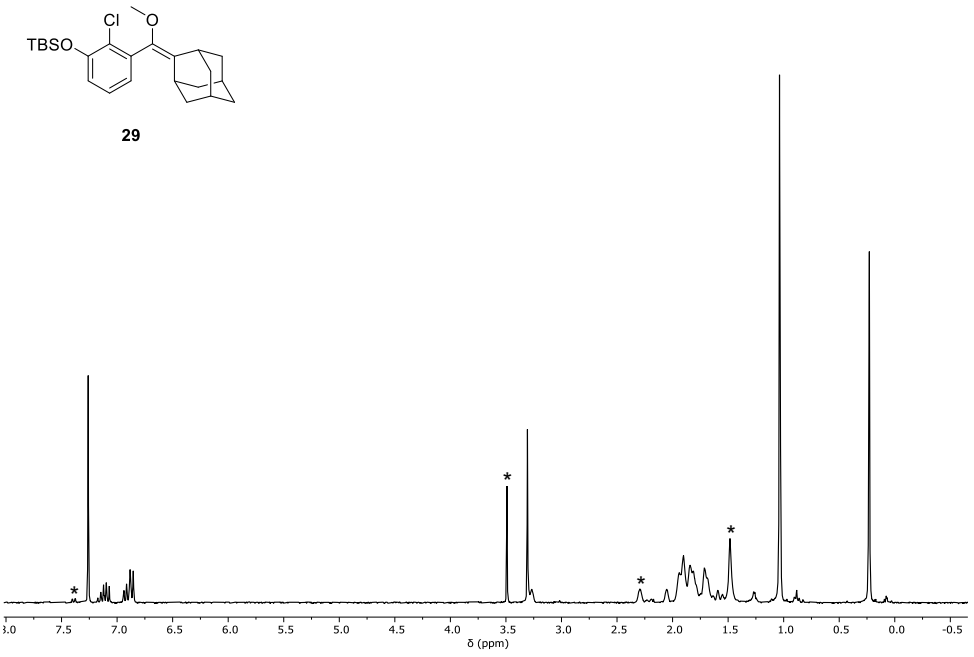


Figure 252: ^{1}H NMR (300 MHz) spectrum of **29** in $CDCl_3$. The sign (*) marks an unkown impurity.

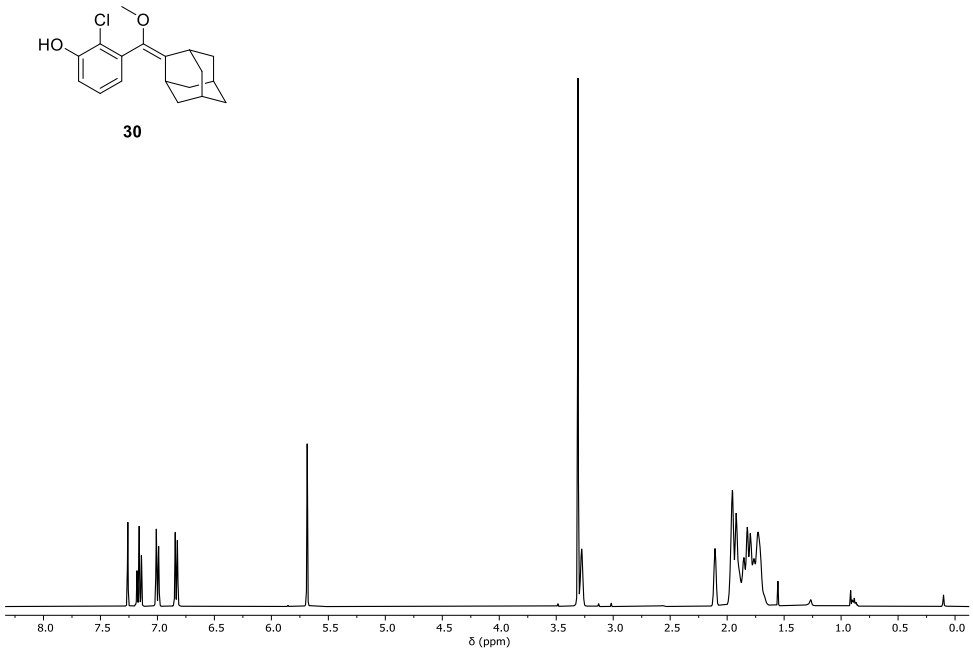


Figure 253: ^{1}H NMR (400 MHz) spectrum of **30** in $CDCl_3$.

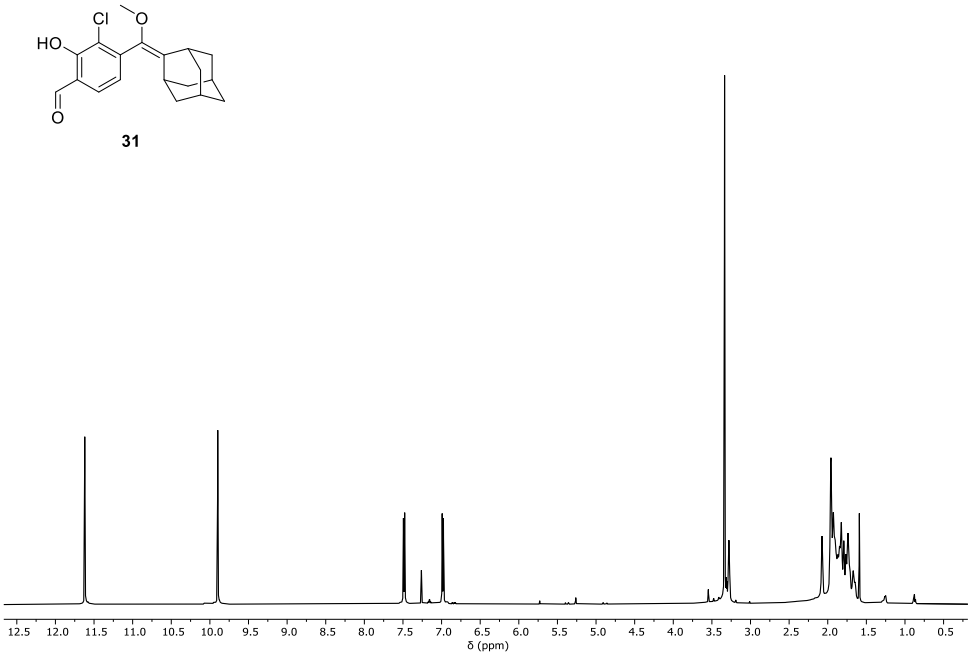


Figure 254: ^{1}H NMR (500 MHz) spectrum of **31** in $CDCl_3$.

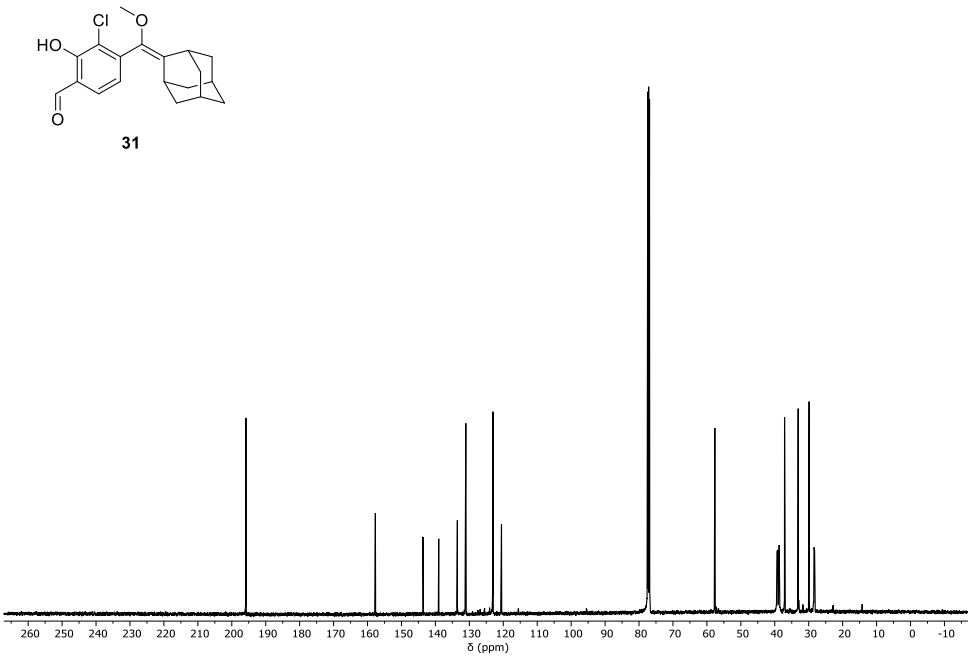


Figure 255: $^{13}C\{^{1}H\}$ NMR (126 MHz) spectrum of **30** in $CDCl_3$.

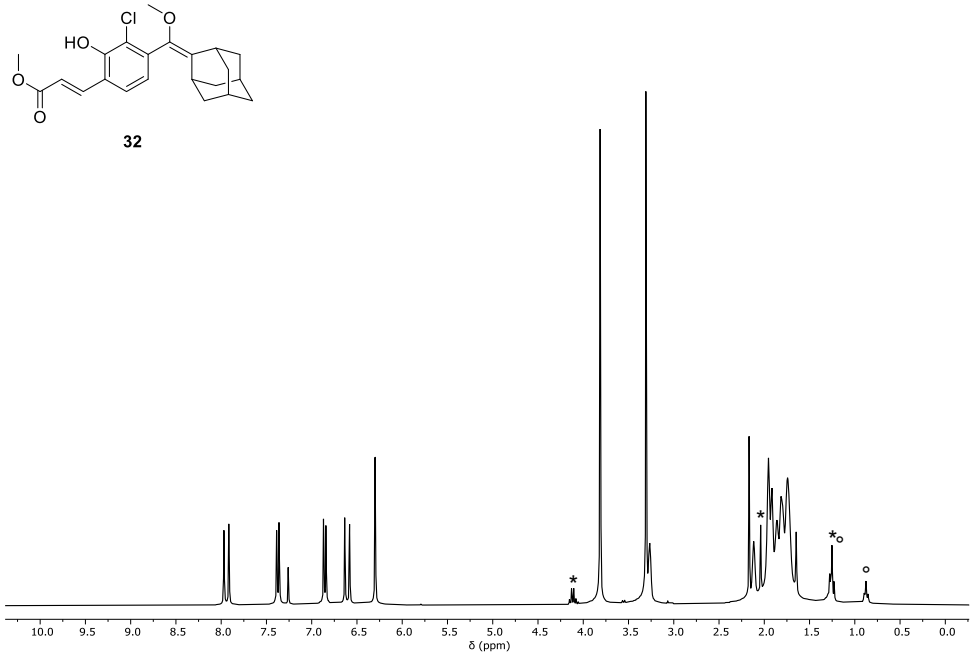


Figure 256: ^{1}H NMR (300 MHz) spectrum of **32** in $CDCl_3$. The sign (*) marks ethyl acetate, whereas *n*-hexane is marked by (°).

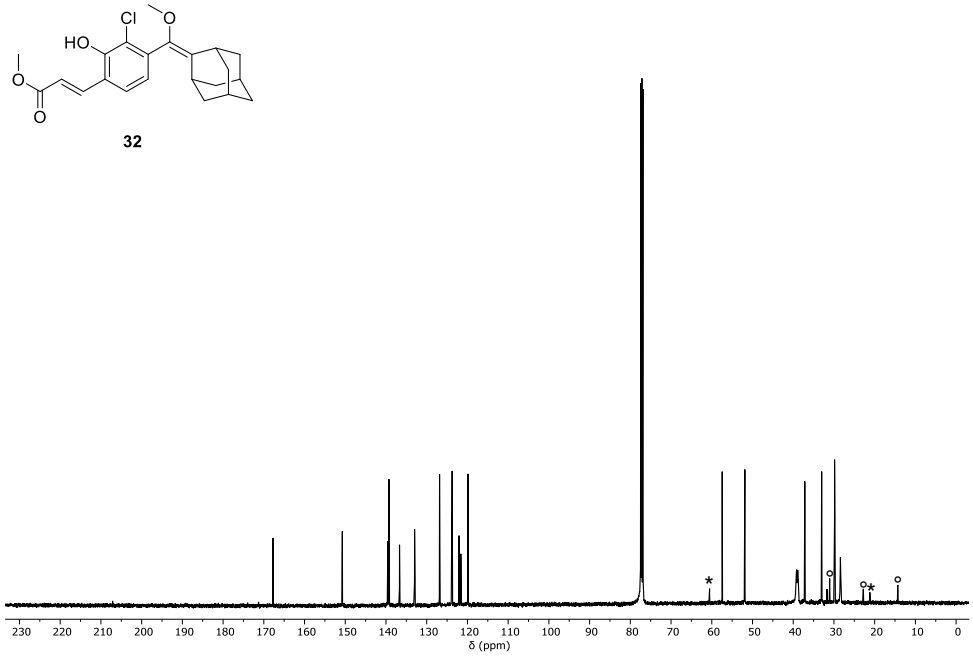


Figure 257: ^{13}C{^{1}H} NMR (126 MHz) spectrum of **32** in $CDCl_3$. The sign (*) marks ethyl acetate, whereas *n*-hexane is marked by (°).

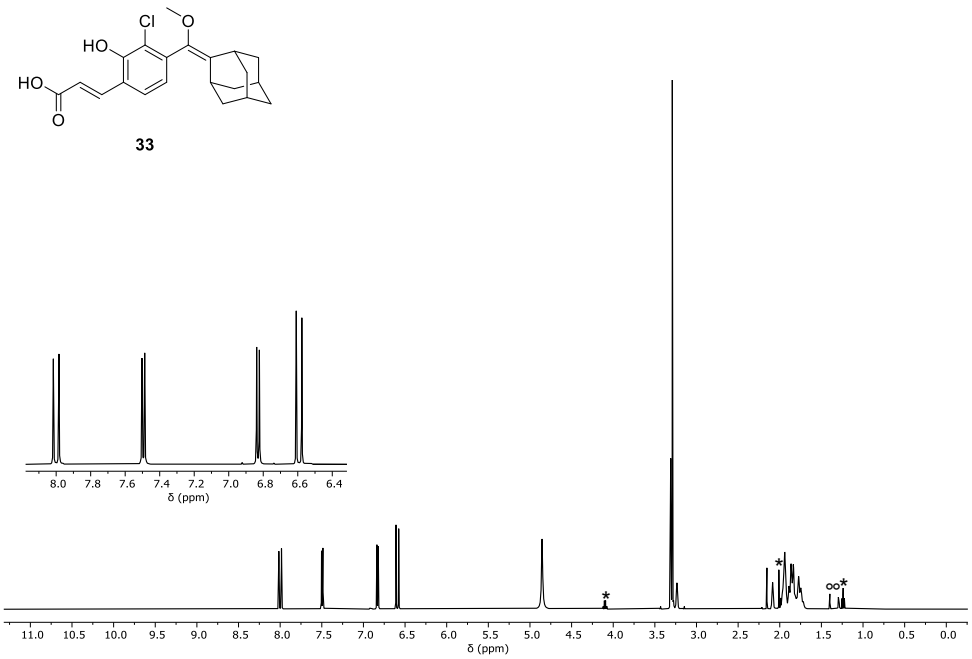


Figure 258: ^{1}H NMR (500 MHz) spectrum of **33** in CD_3OD. The sign (*) marks ethyl acetate, whereas *n*-hexane is marked by (°).

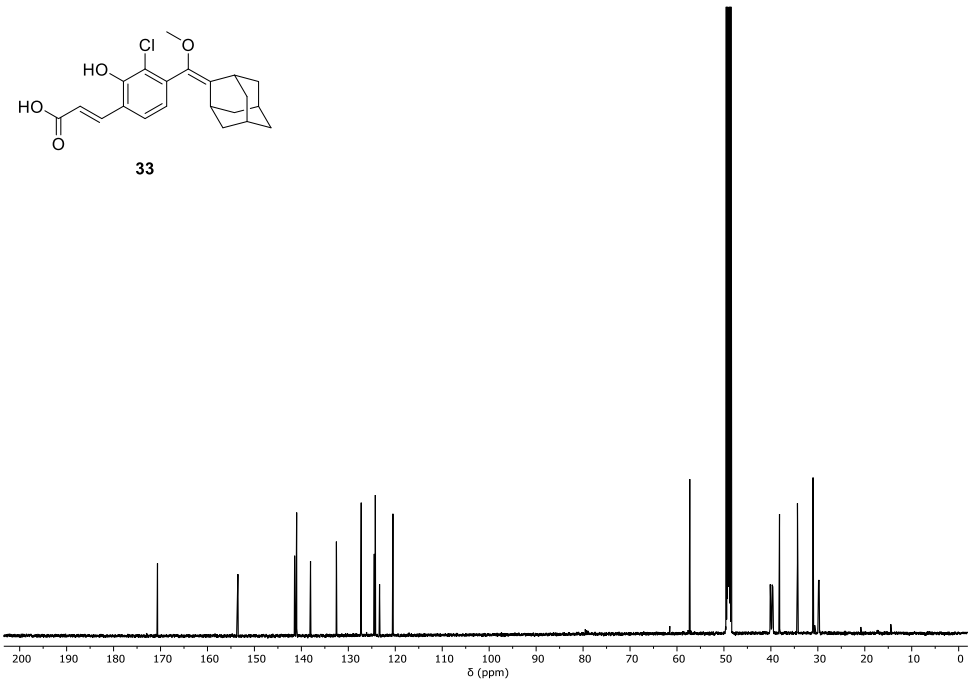


Figure 259: $^{13}C\{^{1}H\}$ NMR (126 MHz) spectrum of **33** in CD_3OD.

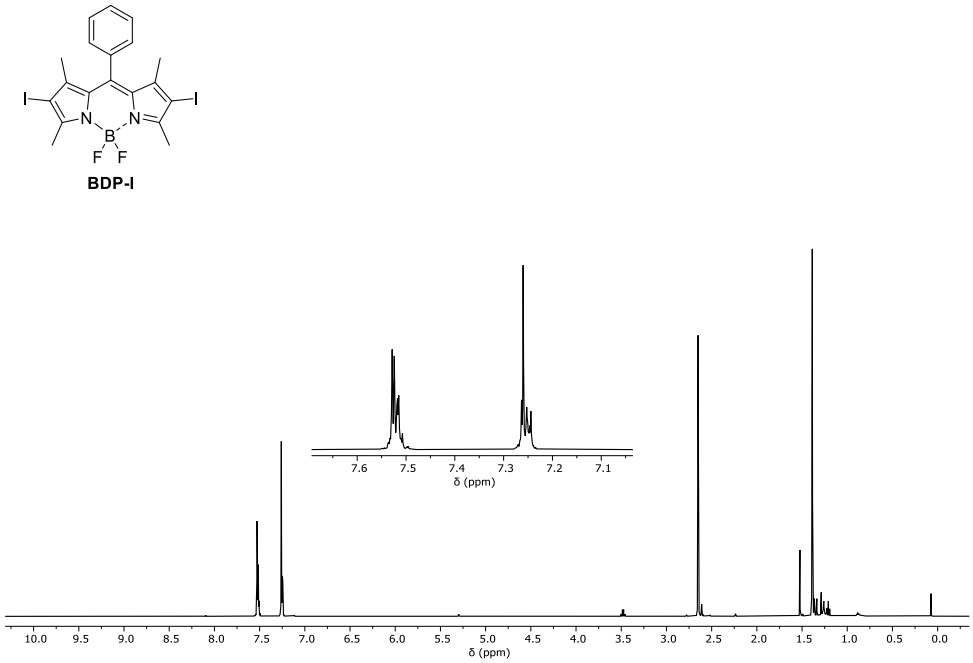


Figure 260: ^{1}H NMR (500 MHz) spectrum of **BDP-I** in $CDCl_3$.

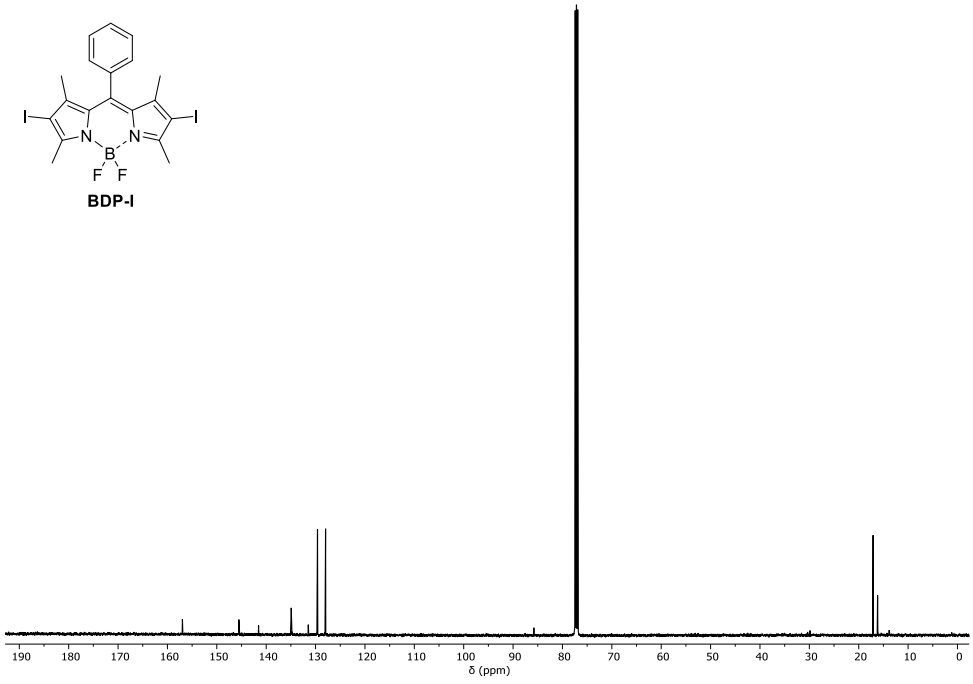


Figure 261: $^{13}C\{^{1}H\}$ NMR (126 MHz) spectrum of **BDP-I** in $CDCl_3$.

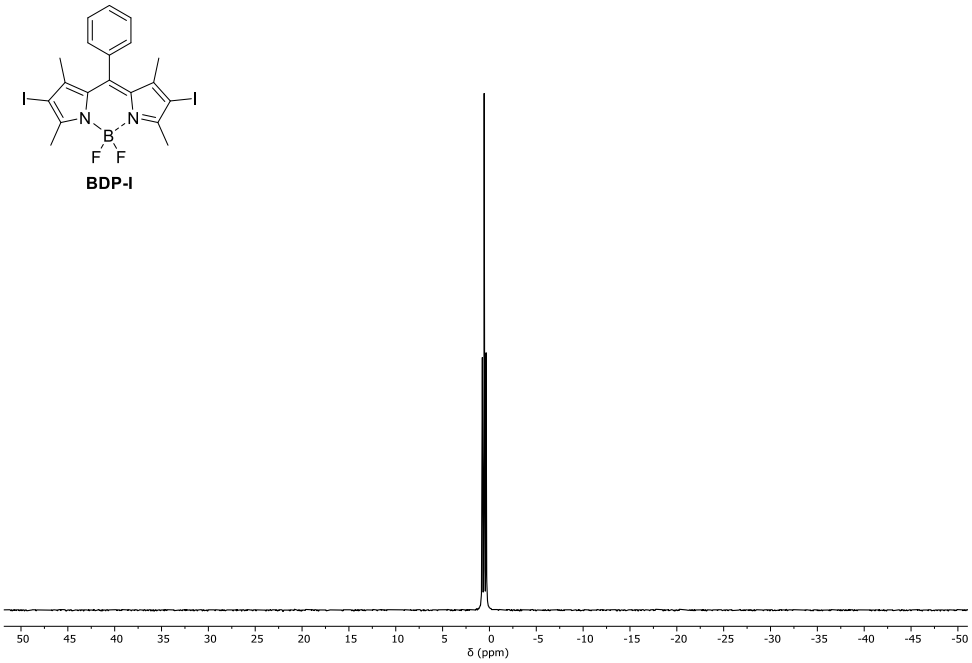


Figure 262: $^{11}B\{^{1}H\}$ NMR (160 MHz) spectrum of **BDP-I** in $CDCl_3$.

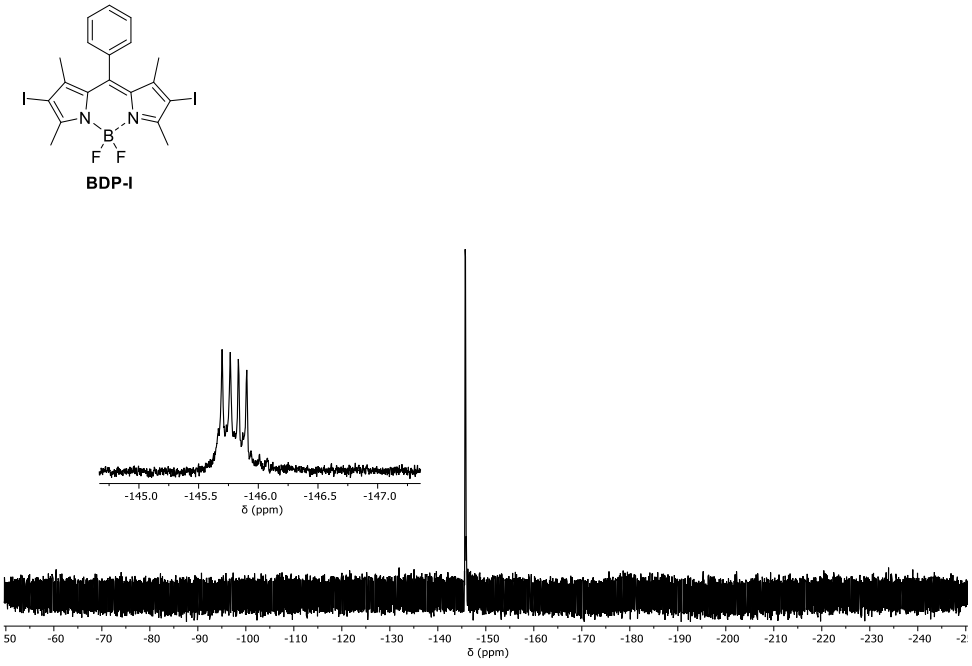


Figure 263: ^{19}F NMR (470 MHz) spectrum of **BDP-I** in $CDCl_3$.

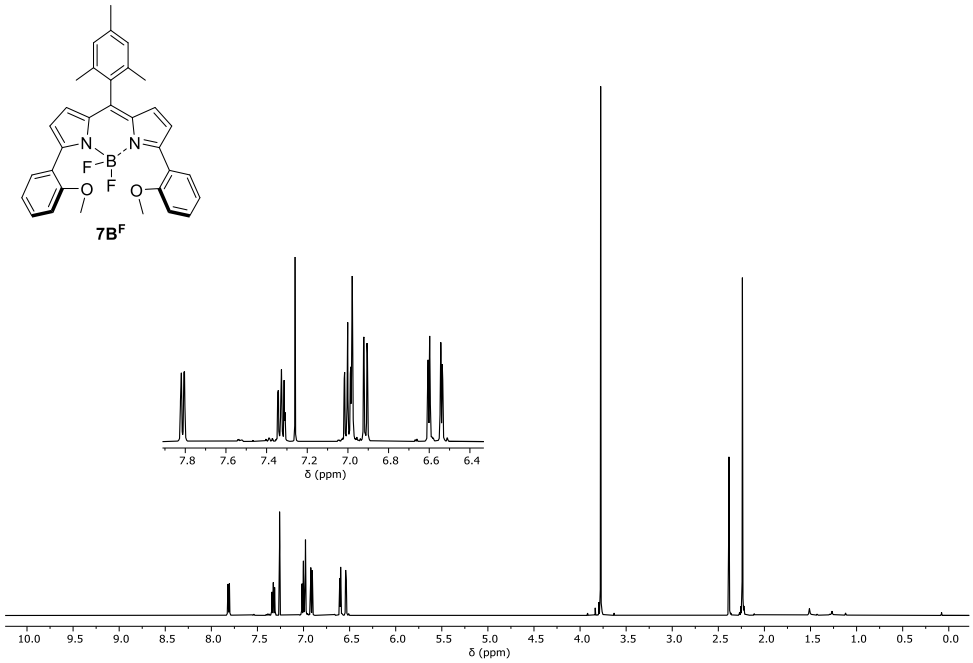


Figure 264: ^{1}H NMR (500 MHz) spectrum of **7B^{F}** in $CDCl_3$.

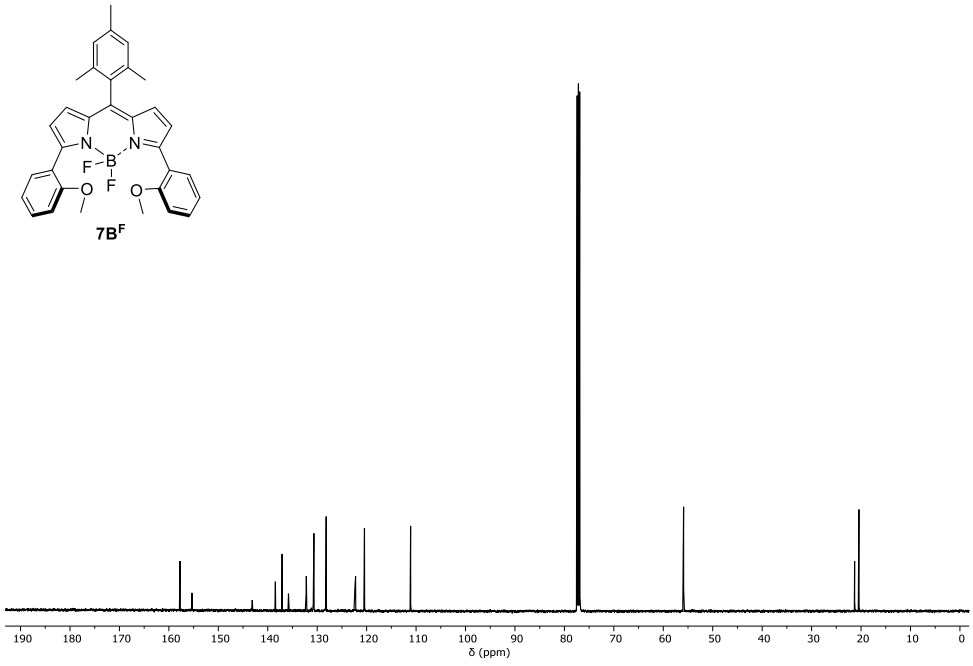


Figure 265: $^{13}C\{^{1}H\}$ NMR (126 MHz) spectrum of **7B^{F}** in $CDCl_3$.

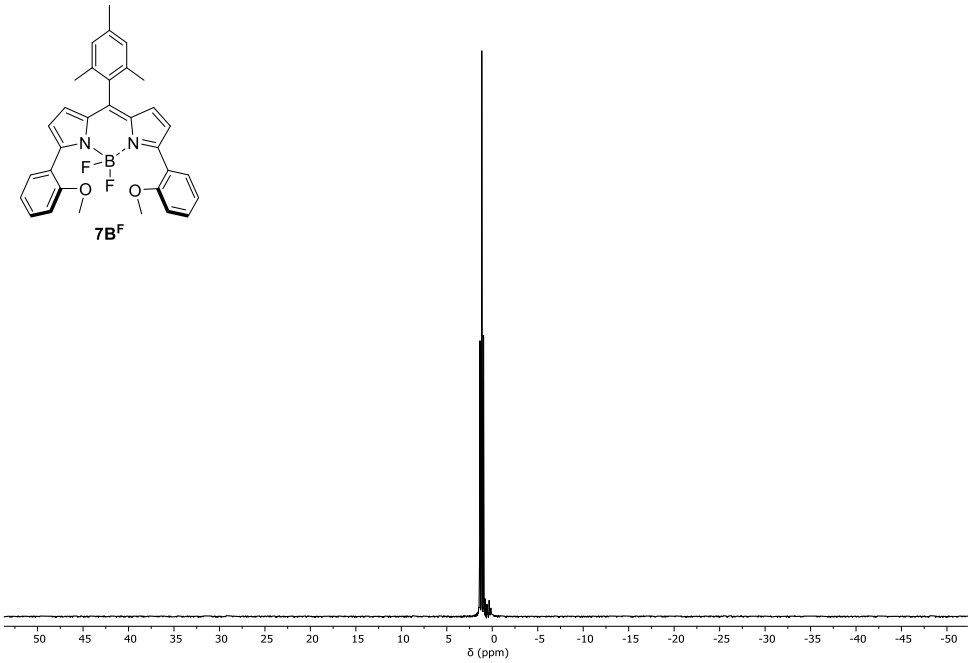


Figure 266: $^{11}B\{^{1}H\}$ NMR (160 MHz) spectrum of **7B^{F}** in $CDCl_3$.

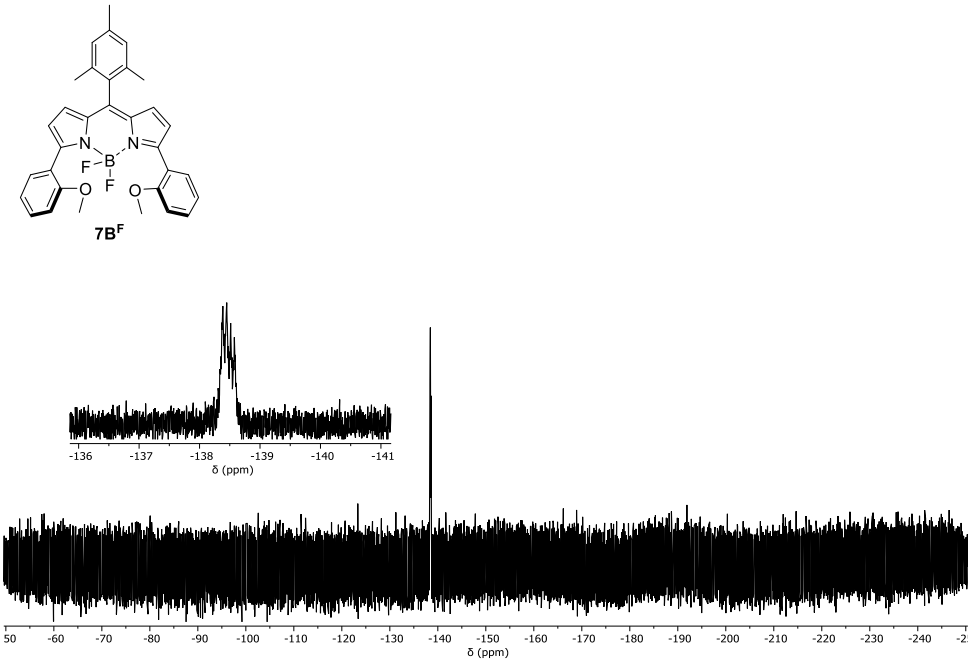


Figure 267: ^{19}F NMR (470 MHz) spectrum of **7B^{F}** in $CDCl_3$.

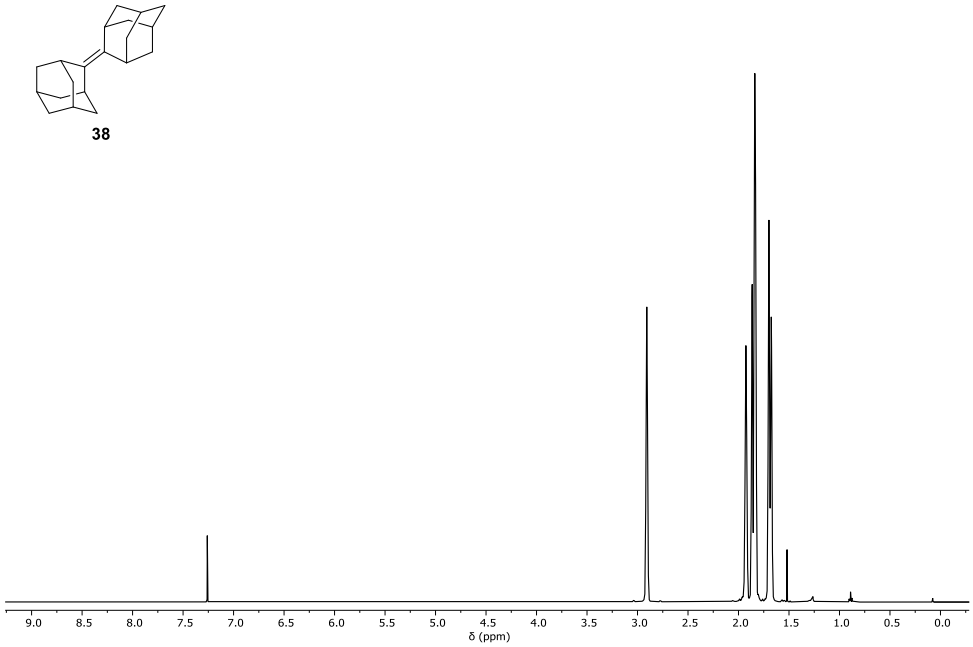


Figure 268: ^{1}H NMR (500 MHz) spectrum of compound **38** in $CDCl_3$.

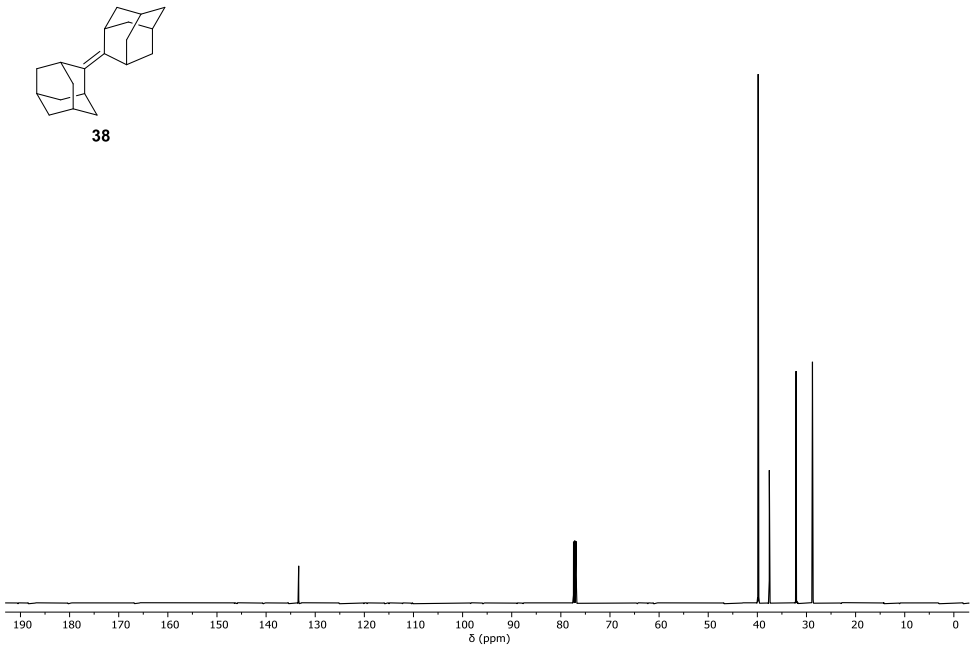


Figure 269: ^{1}H NMR (126 MHz) spectrum of compound **38** in $CDCl_3$.

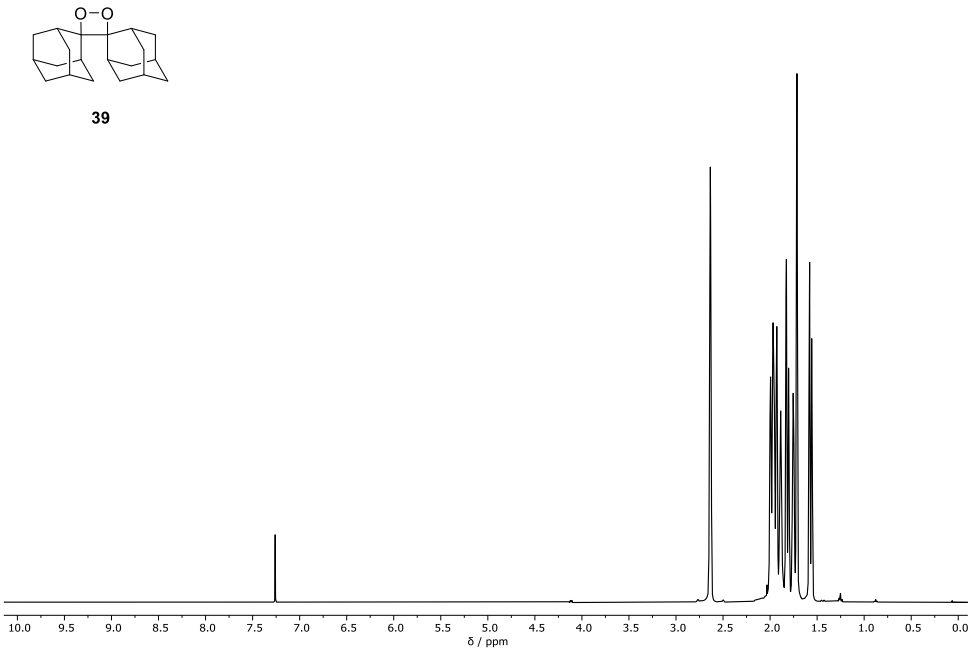


Figure 270: ^{1}H NMR (500 MHz) spectrum of compound **39** in $CDCl_3$.

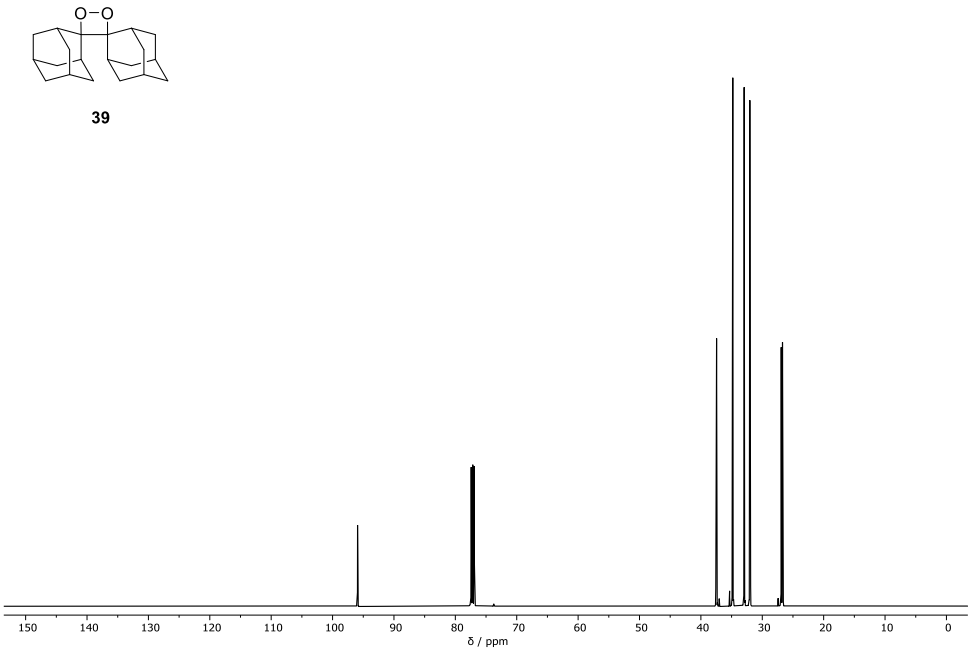


Figure 271: $^{13}C\{^{1}H\}$ NMR (126 MHz) spectrum of compound **39** in $CDCl_3$.

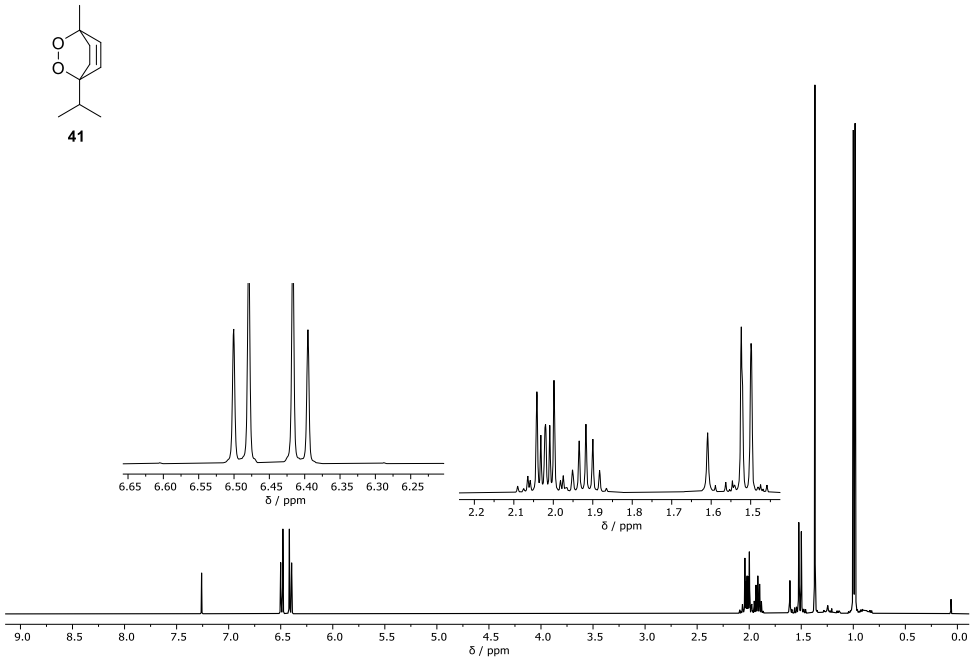


Figure 272: ^{1}H NMR (500 MHz) spectrum of compound **41** in $CDCl_3$.

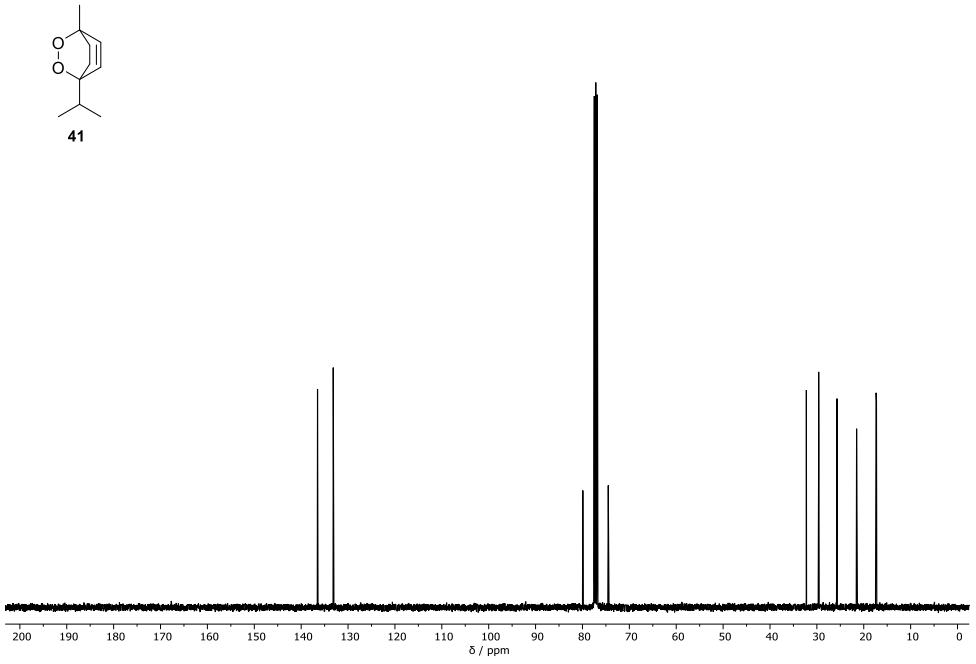


Figure 273: $^{13}C\{^{1}H\}$ NMR (126 MHz) spectrum of compound **41** in $CDCl_3$.

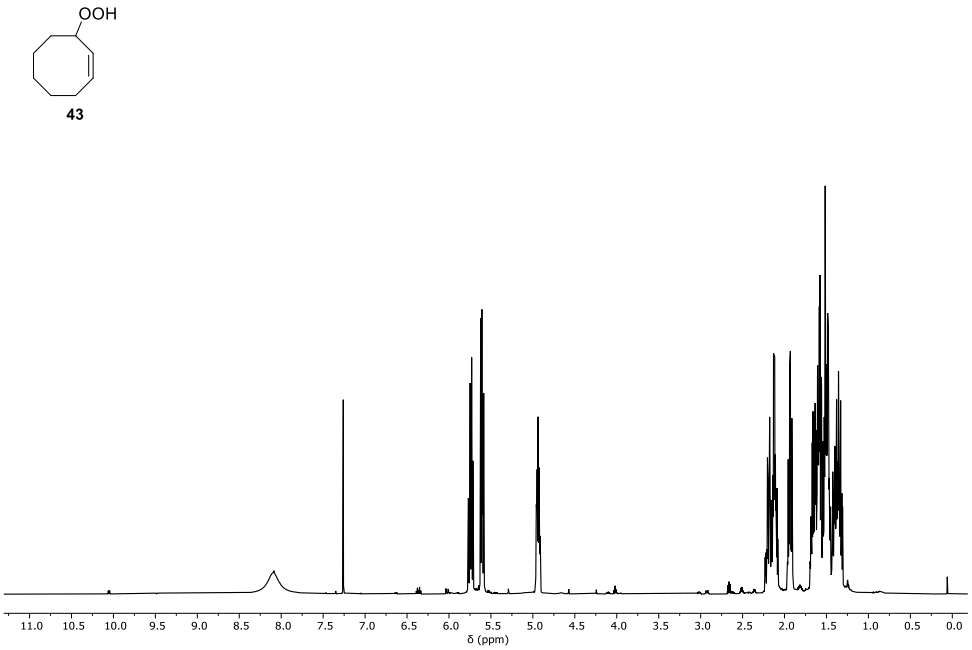


Figure 274: Crude ^{1}H NMR (500 MHz) spectrum of compound **43** in $CDCl_3$.

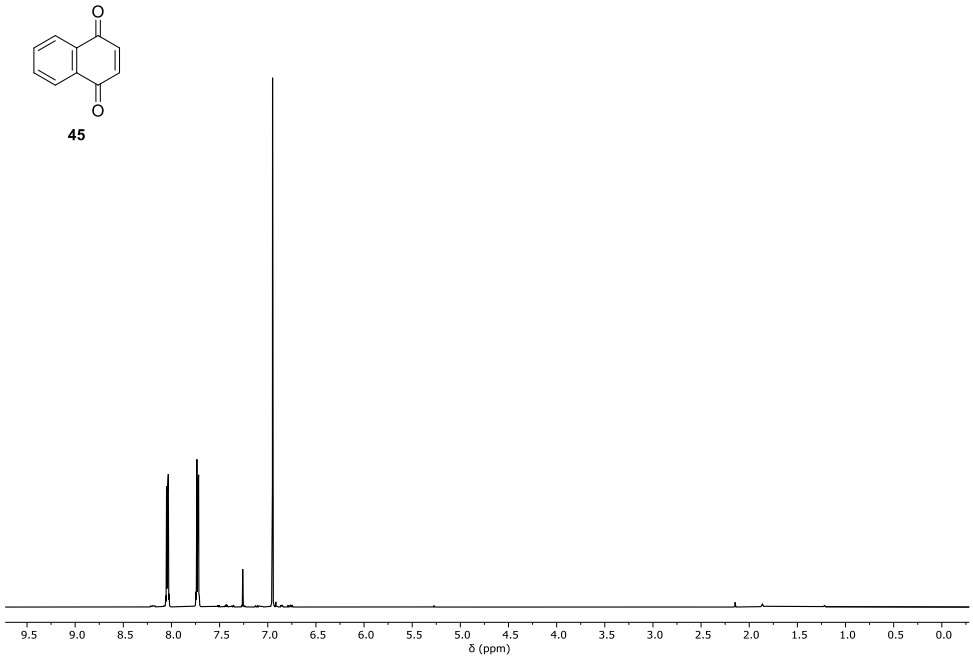


Figure 275: ^{1}H NMR (500 MHz) spectrum of compound **45** in $CDCl_3$.

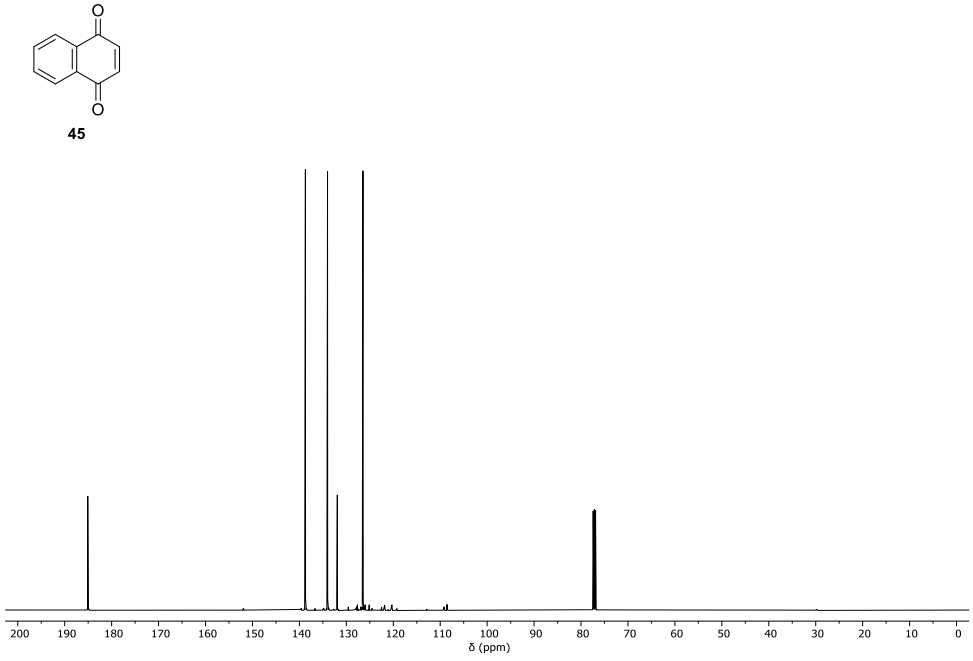


Figure 276: $^{13}C\{^{1}H\}$ NMR (126 MHz) spectrum of compound **45** in $CDCl_3$.

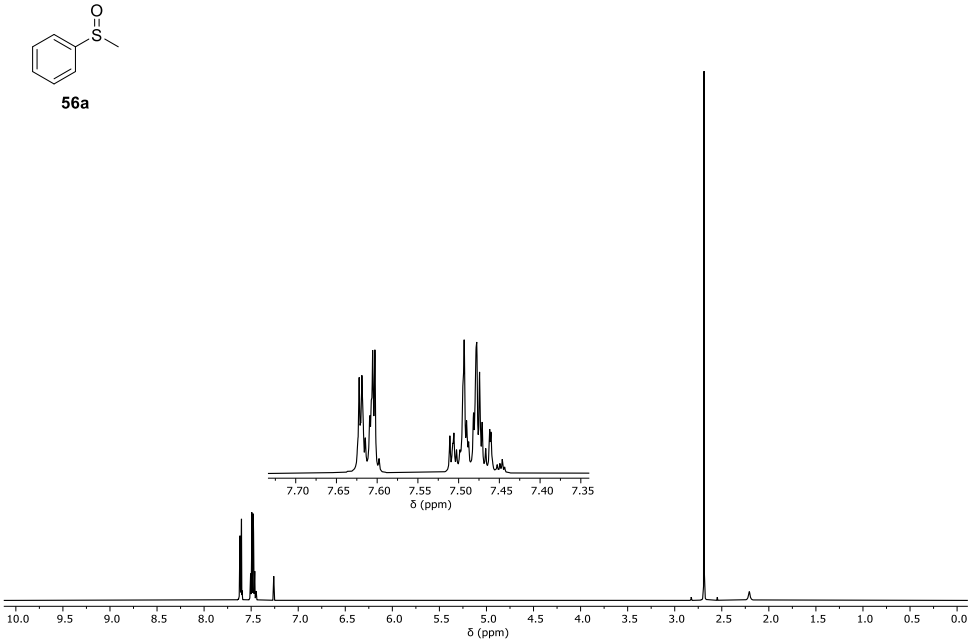


Figure 277: ^{1}H NMR (500 MHz) spectrum of compound **56a** in $CDCl_3$.

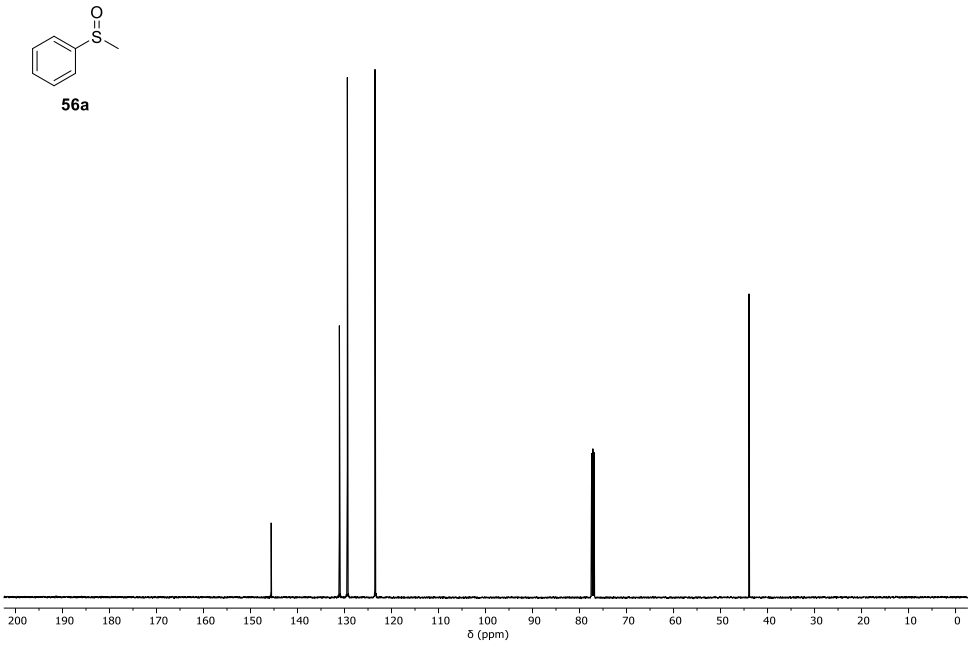


Figure 278: $^{13}C\{^{1}H\}$ NMR (126 MHz) spectrum of compound **56a** in $CDCl_3$.

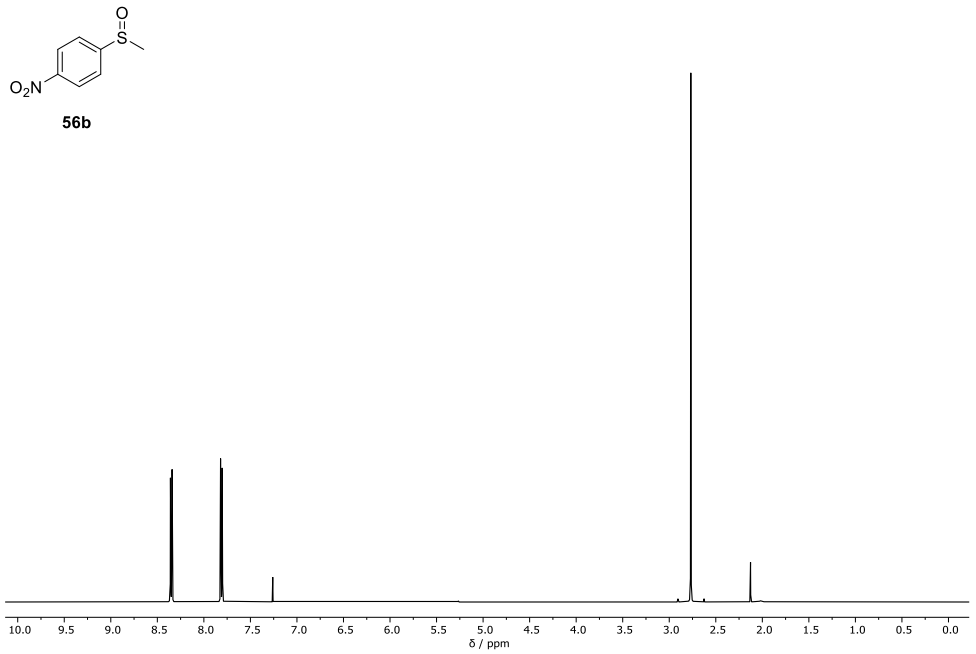


Figure 279: ^{1}H NMR (500 MHz) spectrum of compound **56b** in $CDCl_3$.

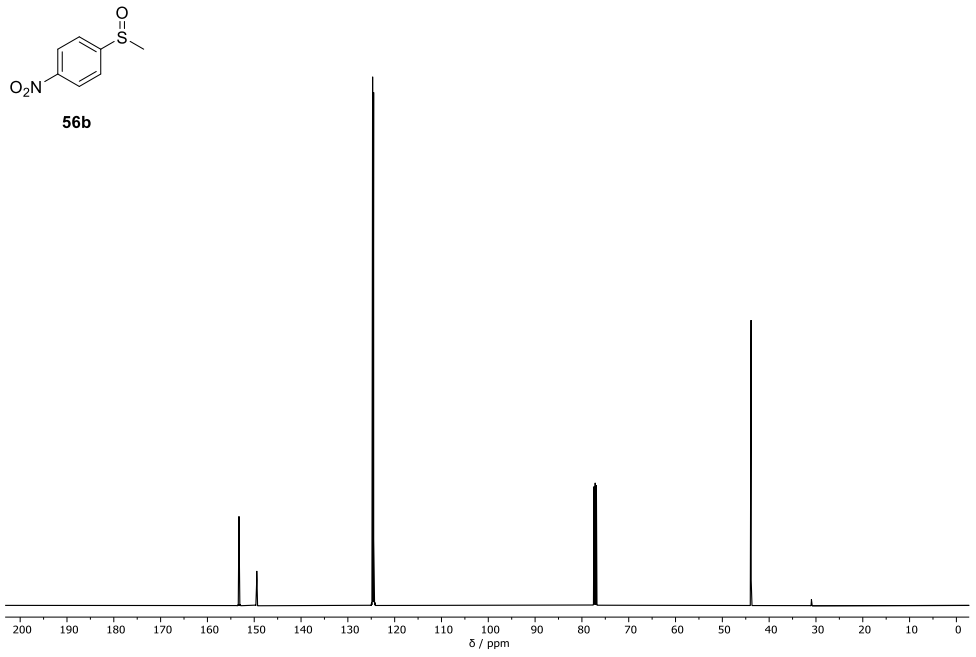


Figure 280: $^{13}C\{^{1}H\}$ NMR (126 MHz) spectrum of compound **56b** in $CDCl_3$.

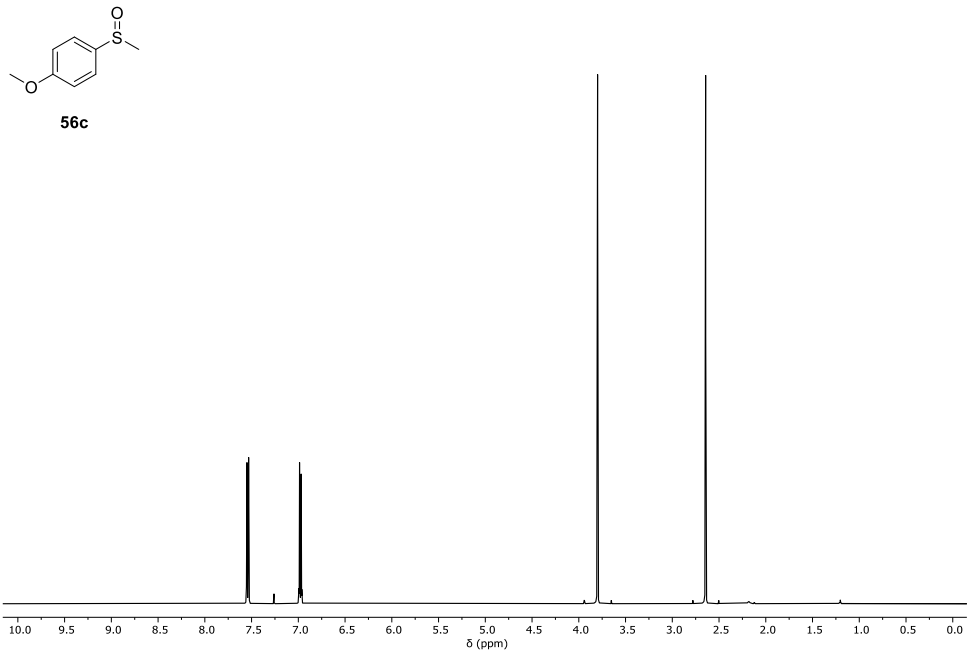


Figure 281: ^{1}H NMR (500 MHz) spectrum of compound **56c** in $CDCl_3$.

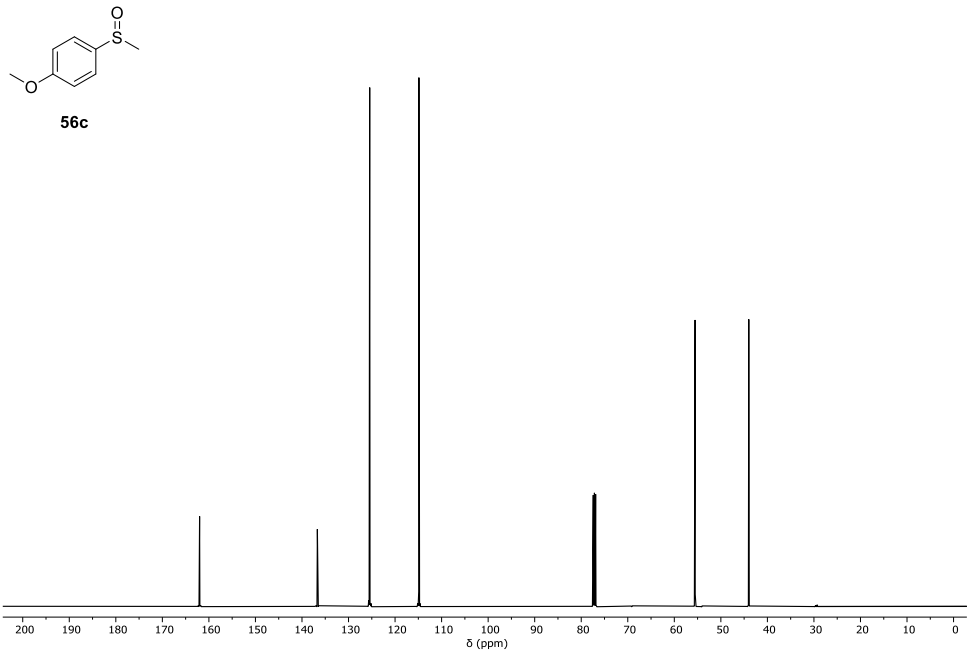


Figure 282: $^{13}C\{^{1}H\}$ NMR (126 MHz) spectrum of compound **56c** in $CDCl_3$.

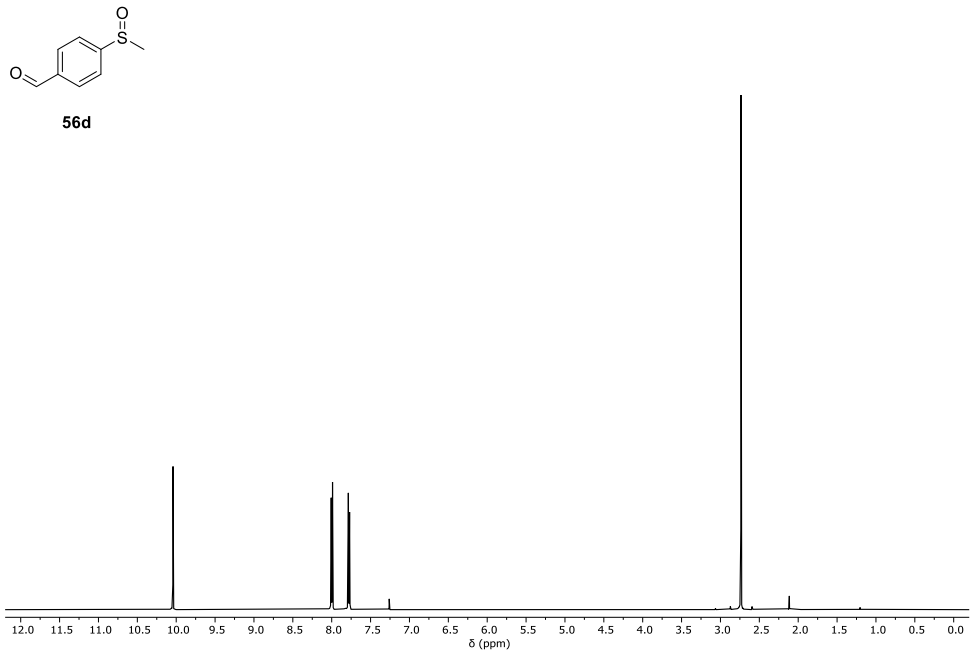


Figure 283: ^{1}H NMR (500 MHz) spectrum of compound **56d** in $CDCl_3$.

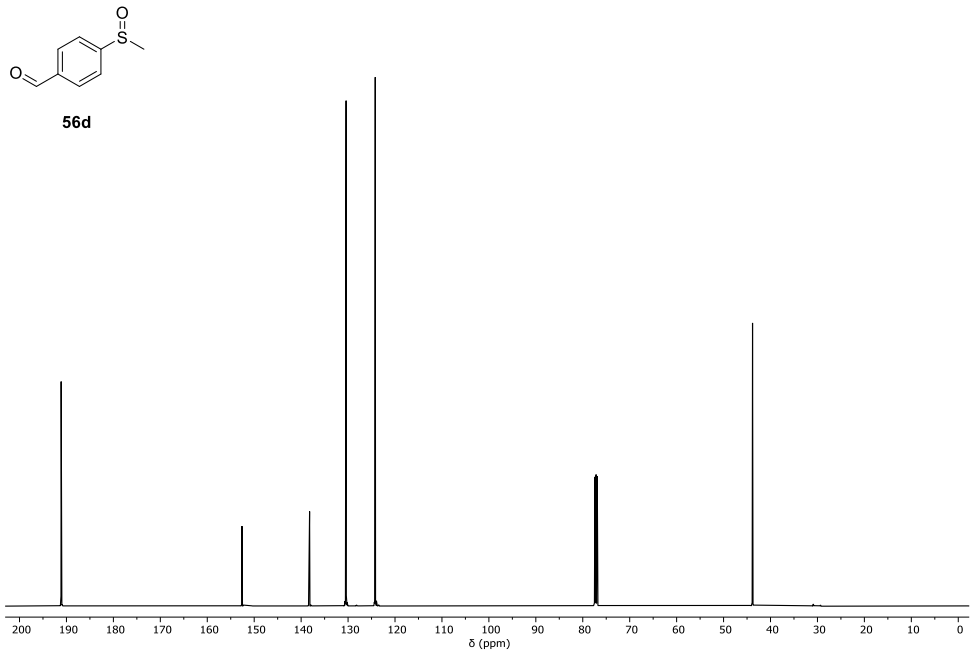


Figure 284: $^{13}C\{^{1}H\}$ NMR (126 MHz) spectrum of compound **56d** in $CDCl_3$.

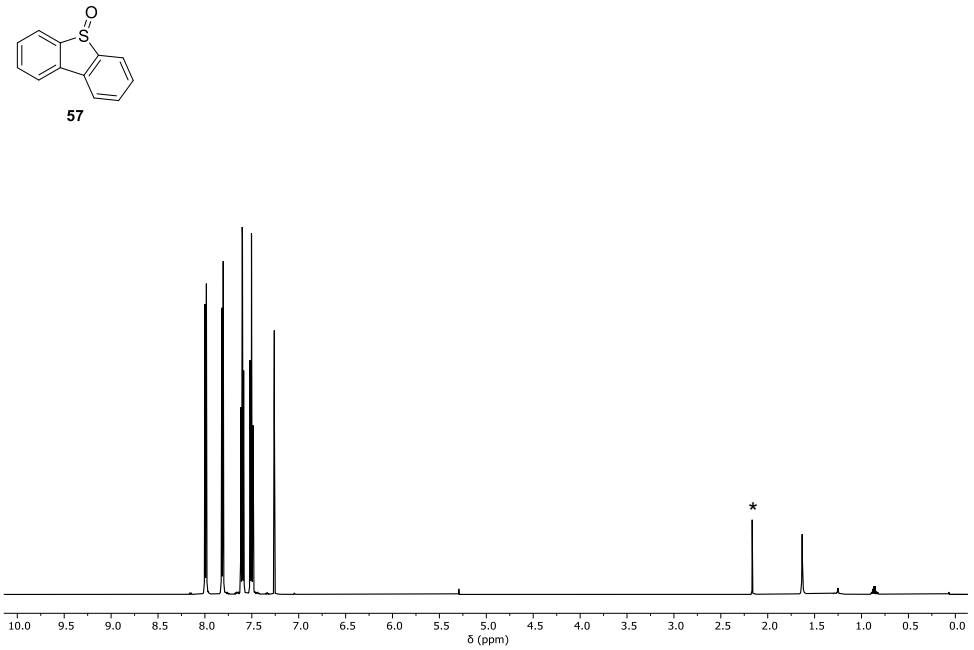


Figure 285: ^{1}H NMR (500 MHz) spectrum of compound **57** in $CDCl_3$. The sign (*) marks acetone.

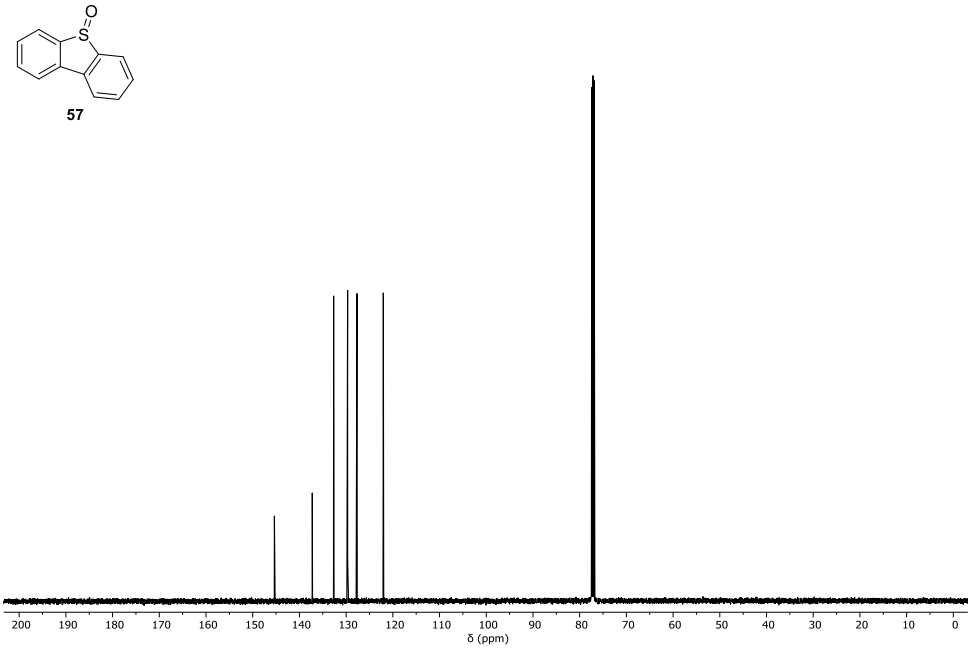


Figure 286: $^{13}C\{^{1}H\}$ NMR (126 MHz) spectrum of compound **57** in $CDCl_3$.

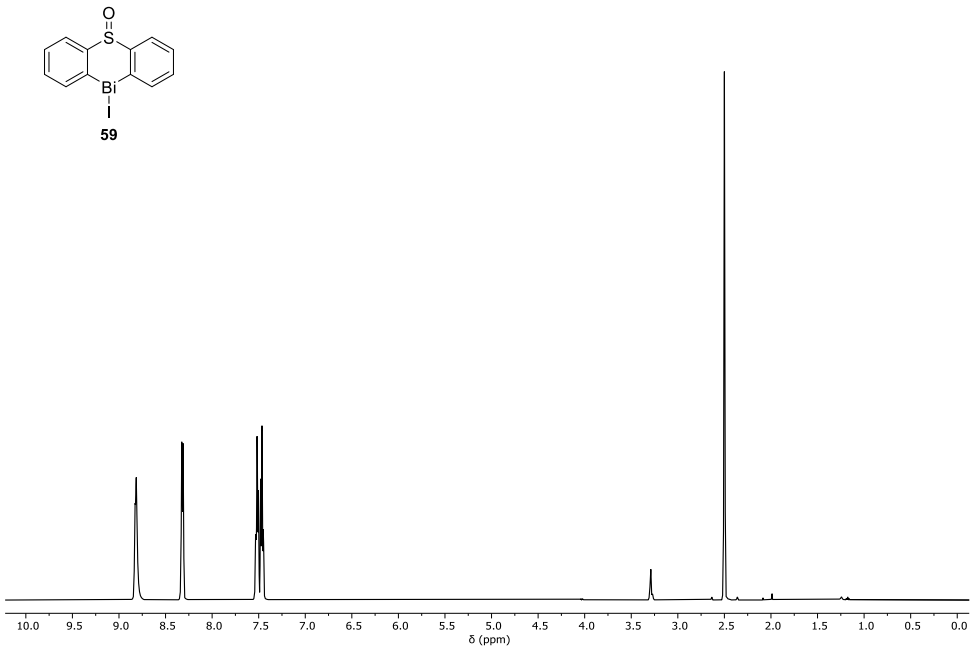


Figure 287: ^{1}H NMR (500 MHz) spectrum of compound **59** in DMSO-d_6.

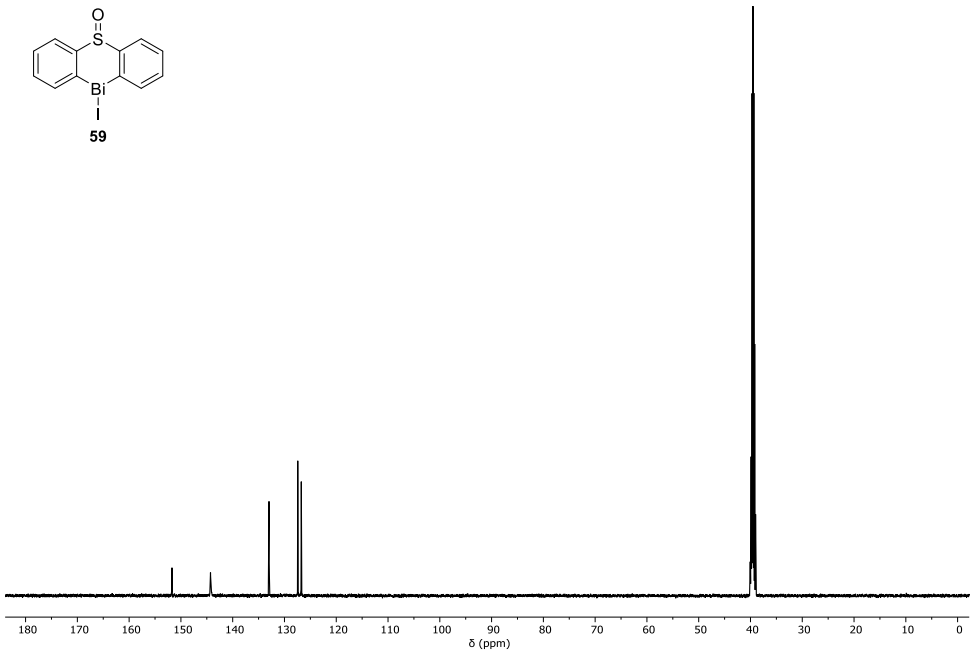
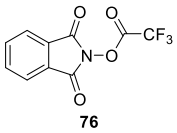


Figure 288: ^{13}C{^{1}H} NMR (126 MHz) spectrum of compound **59** in DMSO-d_6.



76

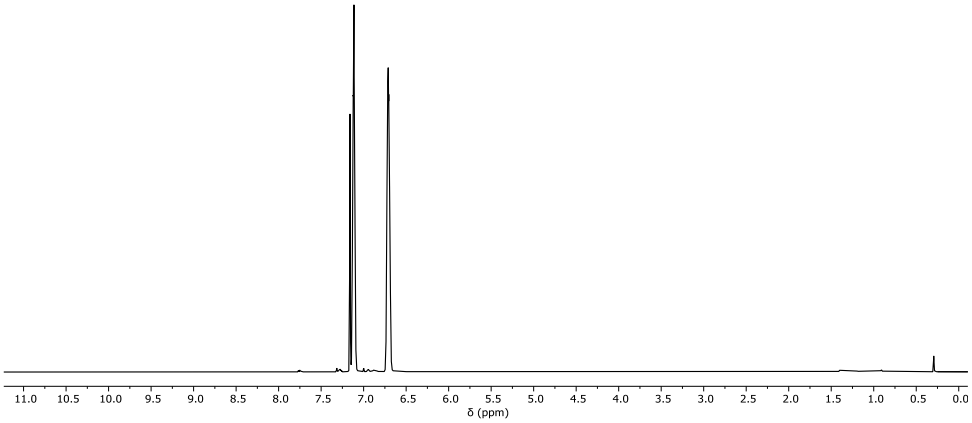
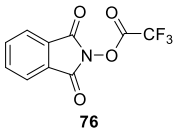


Figure 289: ^{1}H NMR (500 MHz) spectrum of compound **76** in C_6D_6.



76

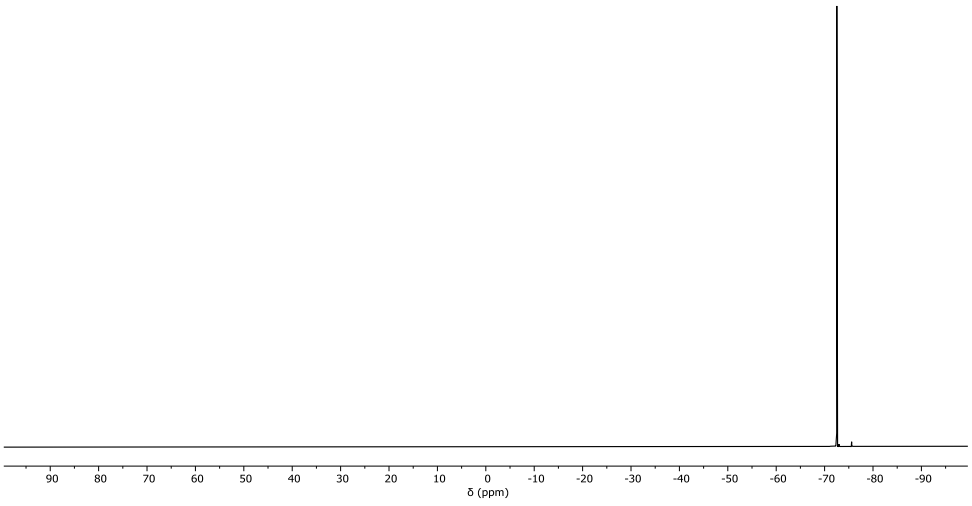


Figure 290: ^{19}F NMR (471 MHz) spectrum of compound **76** in C_6D_6.

Chapter 5

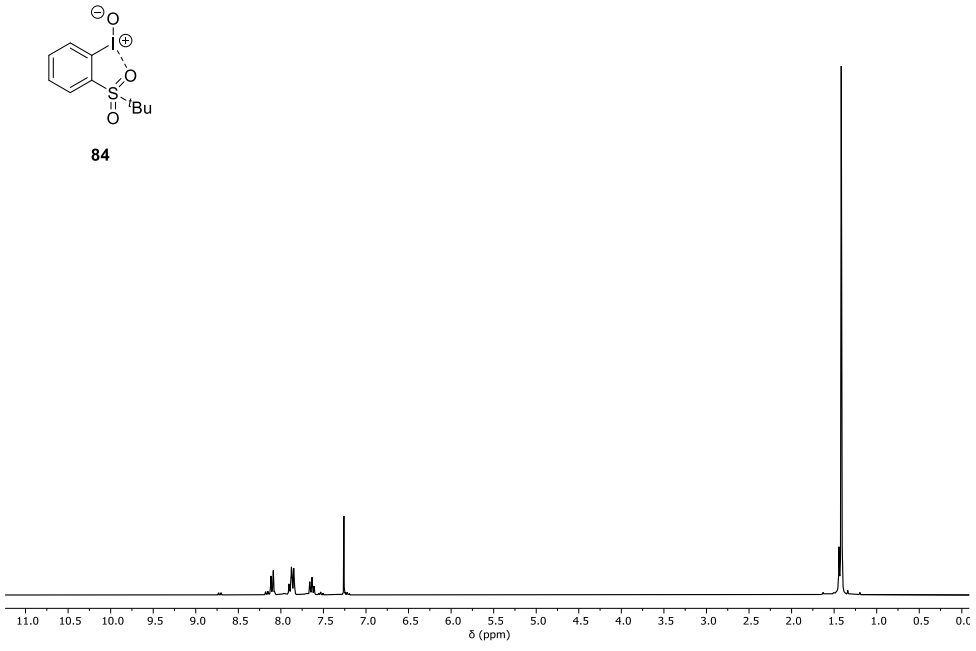


Figure 291: ^{1}H NMR (300 MHz) spectrum of **84** in $CDCl_3$.

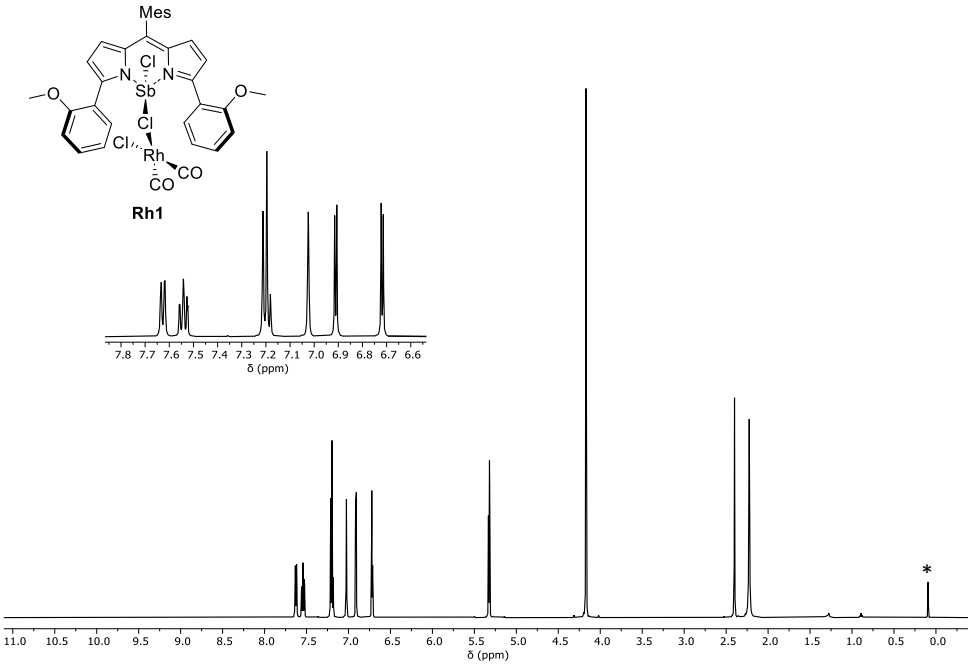


Figure 292: ^{1}H NMR (500 MHz) spectrum of compound **Rh1** in CD_2Cl_2. The sign (*) marks silicone grease.

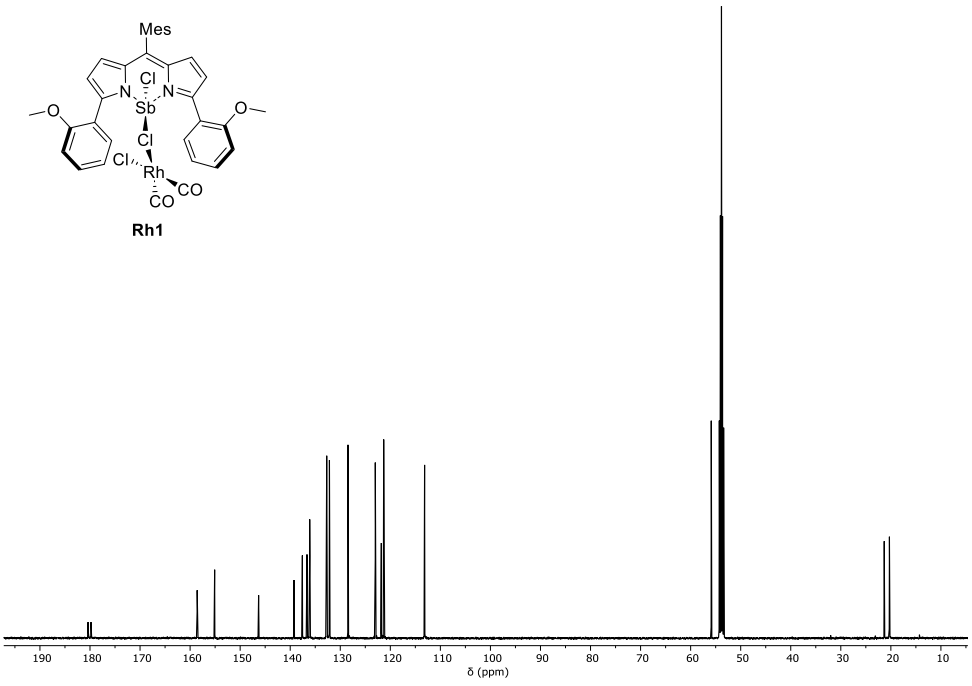


Figure 293: $^{13}C\{^{1}H\}$ NMR (126 MHz) spectrum of compound **Rh1** in CD_2Cl_2.

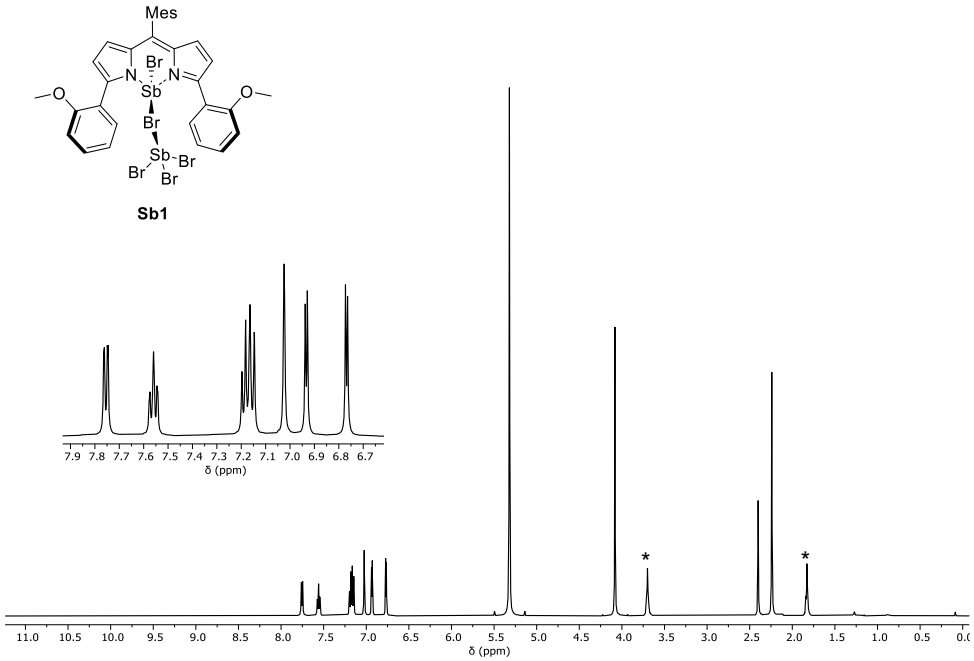


Figure 294: ^{1}H NMR (500 MHz) spectrum of compound **Sb1** in CD_2Cl_2. The sign (*) marks THF.

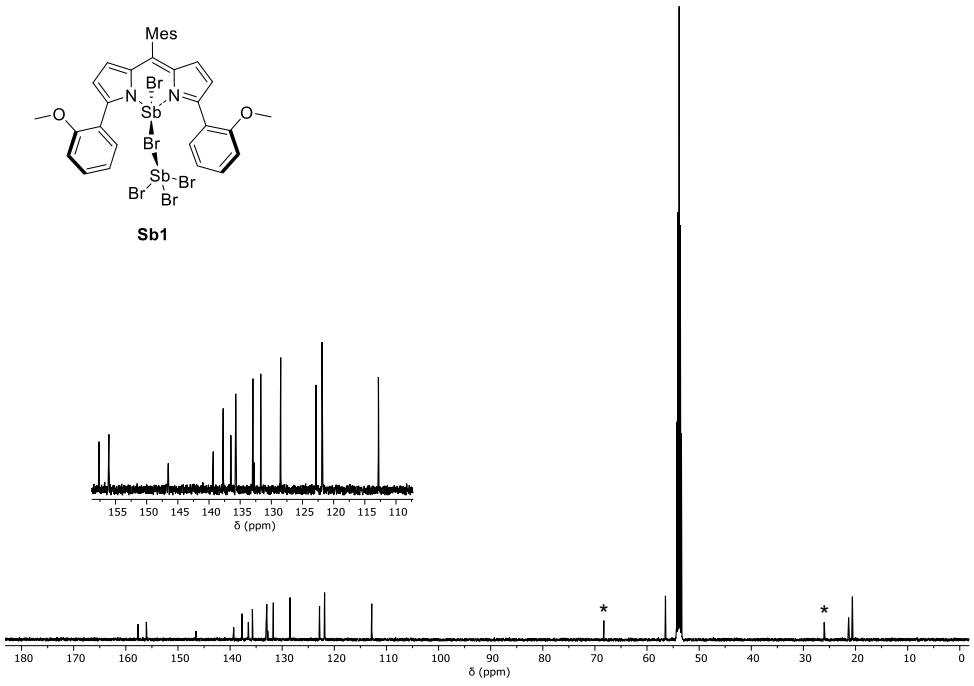


Figure 295: $^{13}C\{^{1}H\}$ NMR (126 MHz) spectrum of compound **Sb1** in CD_2Cl_2. The sign (*) marks THF.

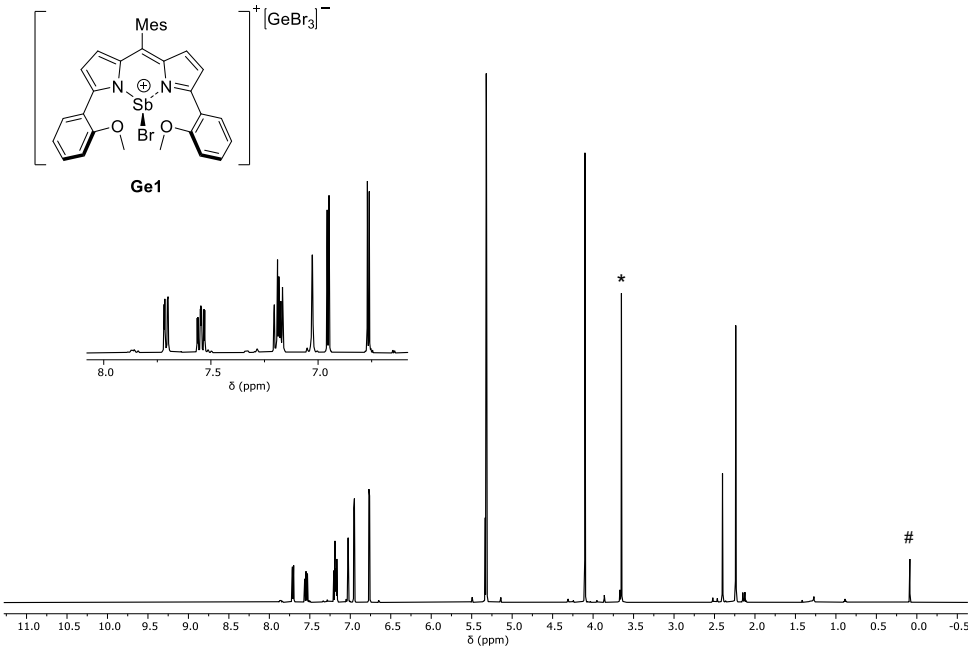


Figure 296: ^{1}H NMR (500 MHz) spectrum of compound **Ge1** in CD_2Cl_2. The sign (*) marks 1,4-dioxane and (#) marks silicone grease.

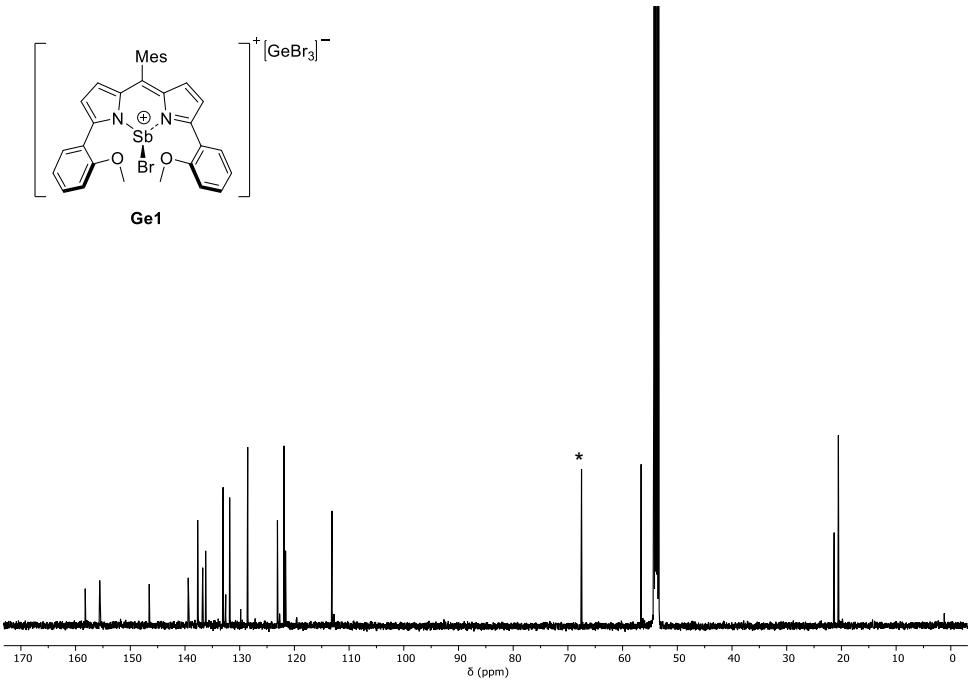


Figure 297: $^{13}C\{^{1}H\}$ NMR (126 MHz) spectrum of compound **Ge1** in CD_2Cl_2. The sign (*) marks 1,4-dioxane.

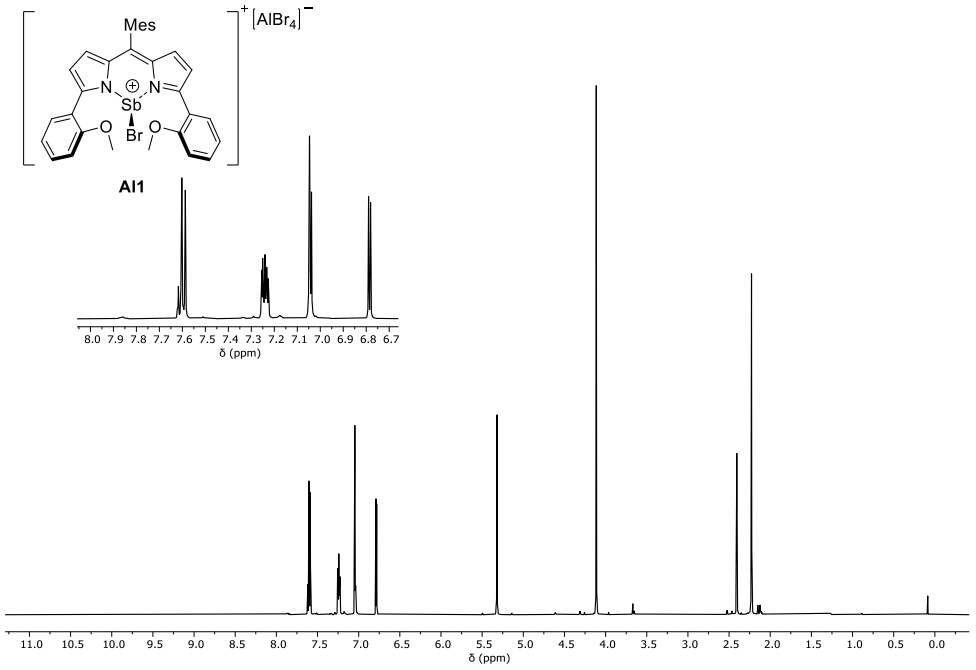


Figure 298: ^{1}H NMR (500 MHz) spectrum of compound **Al1** in CD_2Cl_2.

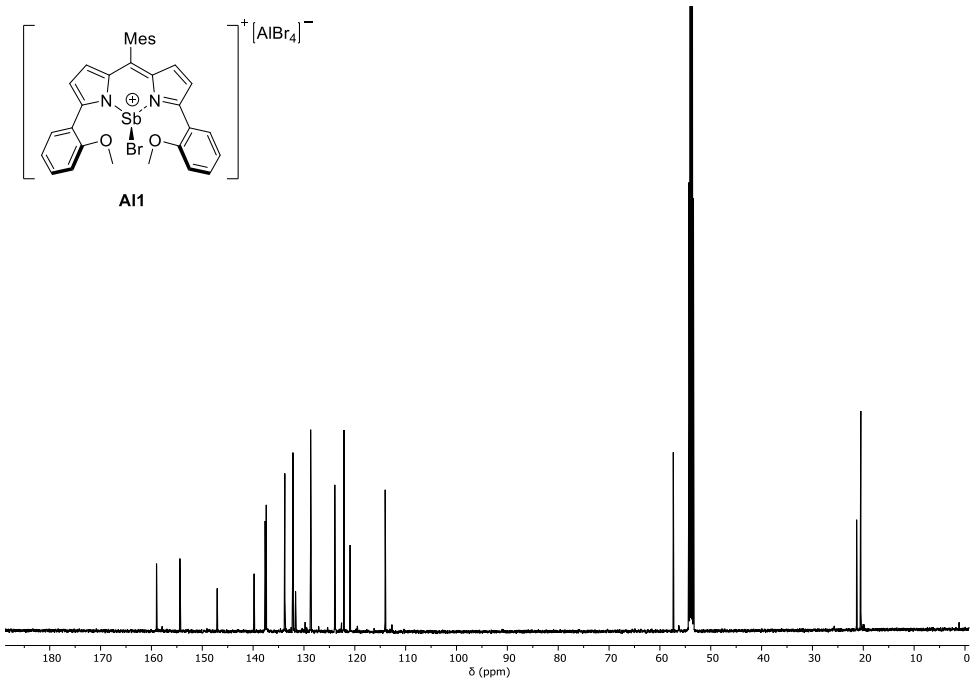


Figure 299: $^{13}C\{^{1}H\}$ NMR (126 MHz) spectrum of compound **Al1** in CD_2Cl_2.

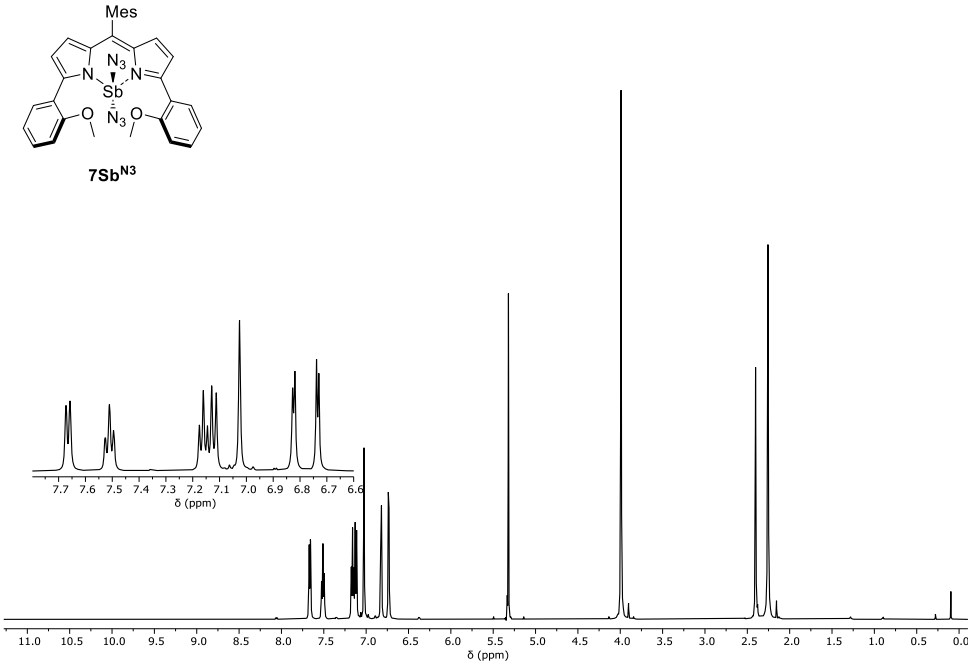


Figure 300: ^{1}H NMR (500 MHz) spectrum of compound **7Sb^{N3}** in CD_2Cl_2.

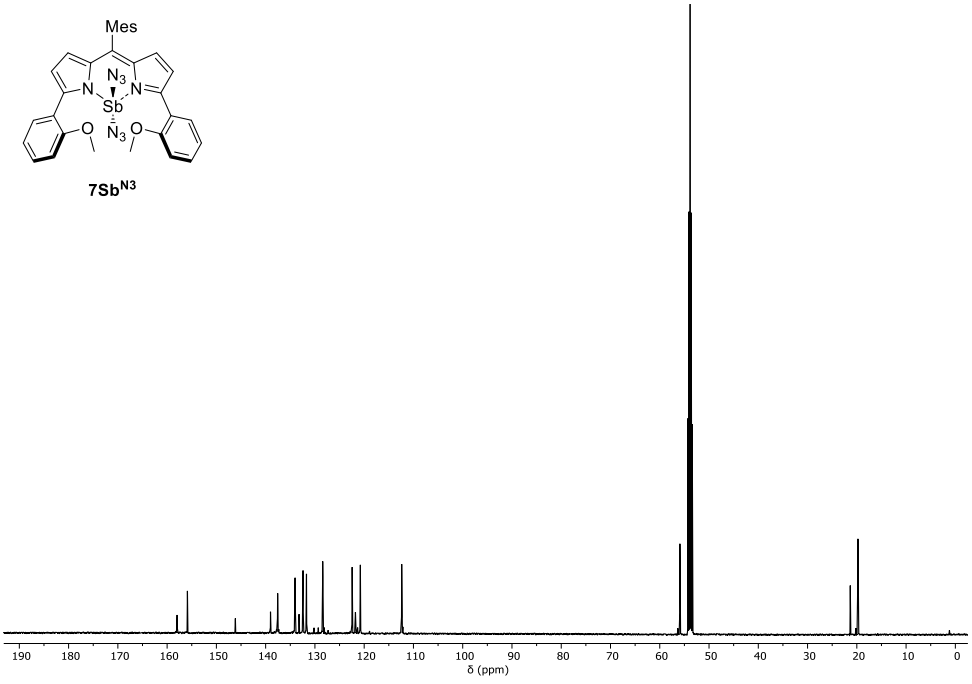


Figure 301: $^{13}C\{^{1}H\}$ NMR (126 MHz) spectrum of compound **7Sb^{N3}** in CD_2Cl_2.

Lewis acid additive screening with 7Sb^{Br}

The reactivity of **7Sb^{Br}** towards a series of different Lewis acid additives was evaluated by using ^{1}H and ^{13}C{^{1}H} NMR spectroscopy. All reactions were conducted at room temperature using 0.020 mmol of **7Sb^{Br}** in CD_2Cl_2 (0.50 mL). Resulting NMR spectra are shown upon stepwise increase of respective Lewis acids equivalents.

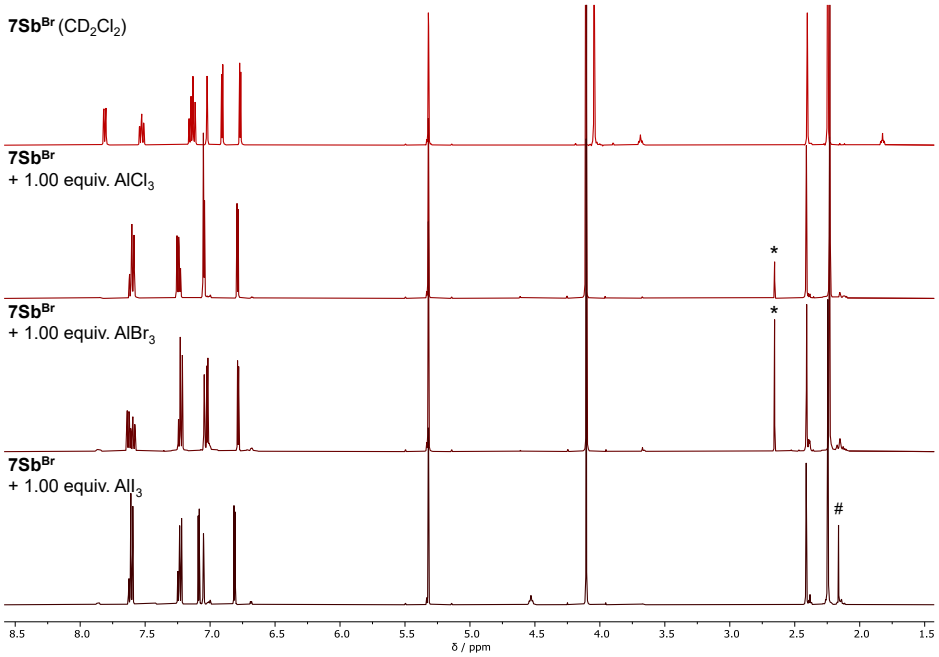


Figure 302: Stacked ^{1}H NMR spectra (500 MHz, CD_2Cl_2) of **7Sb^{Br}** (0.02 mmol) upon addition of 1.00 equiv. of AlX_3 (X = Cl, Br or I). Bromomethane is marked by (*), whereas iodomethane is marked by (#).

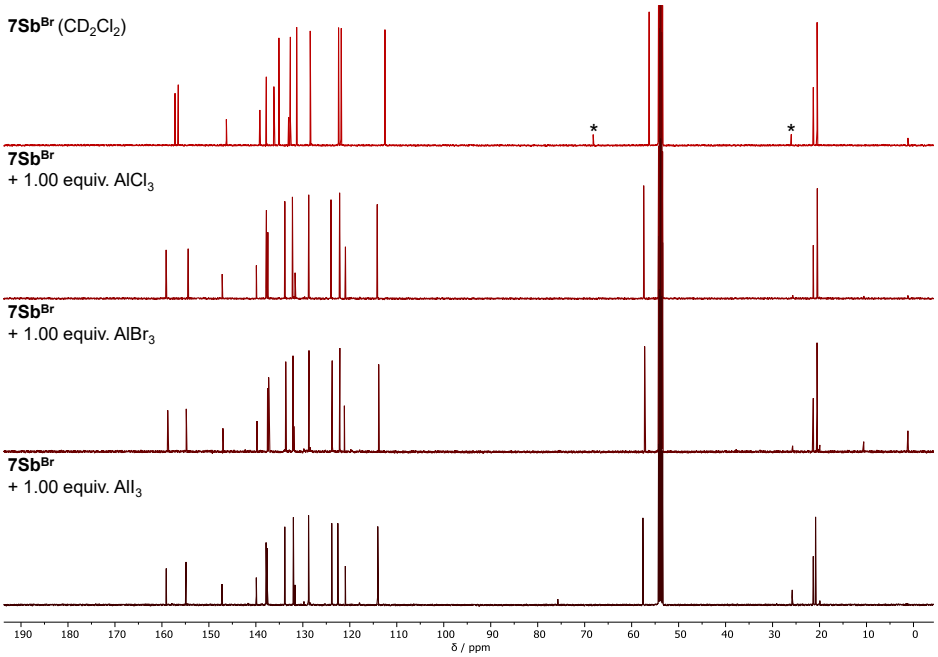


Figure 303: Stacked $^{13}C\{^{1}H\}$ NMR spectra (126 MHz, CD_2Cl_2) of **7Sb^{Br}** (0.02 mmol) upon addition of 1.00 equiv. of AlX_3 (X = Cl, Br or I). The sign (*) marks THF.

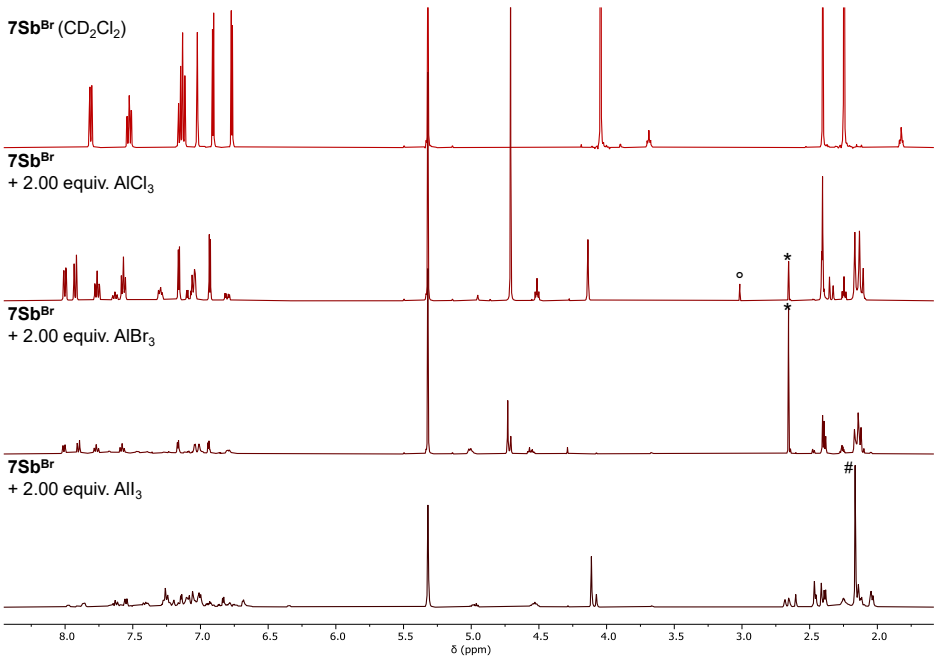


Figure 304: Stacked ^{1}H NMR spectra (500 MHz, CD_2Cl_2) of **7Sb^{Br}** (0.02 mmol) upon addition of 2.00 equiv. of AlX_3 (X = Cl, Br or I). The sign (°) marks CH_3Cl, (*) marks CH_3Br and (#) marks CH_3I.

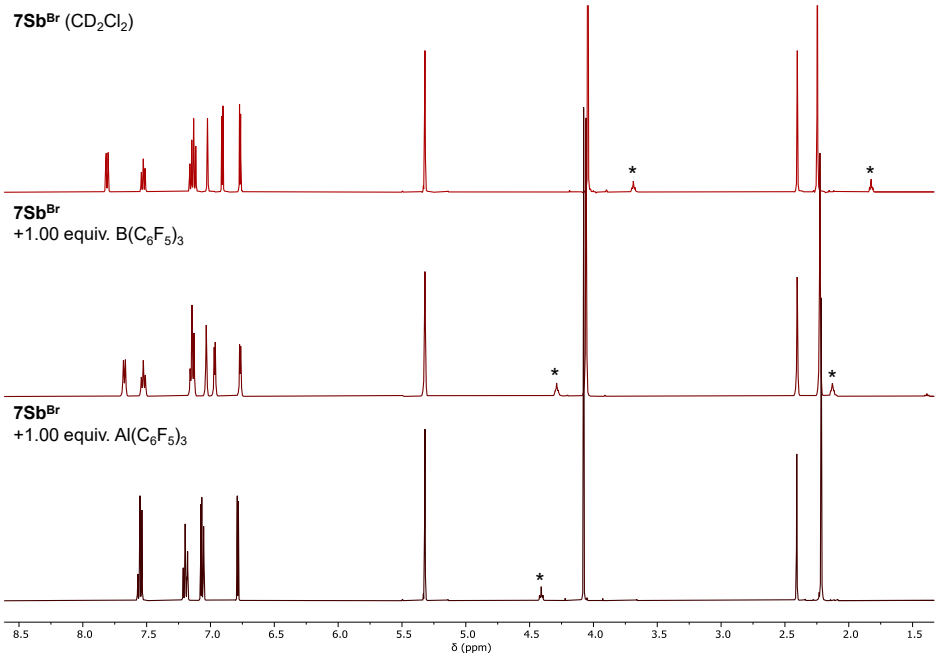


Figure 305: Stacked ^{1}H NMR spectra (500 MHz, CD_2Cl_2) of **7Sb^{Br}** (0.02 mmol) upon addition of 1.00 equiv. of BCF (middle) and 1.00 equiv. of AlCF (bottom). THF is marked by the sign (*).

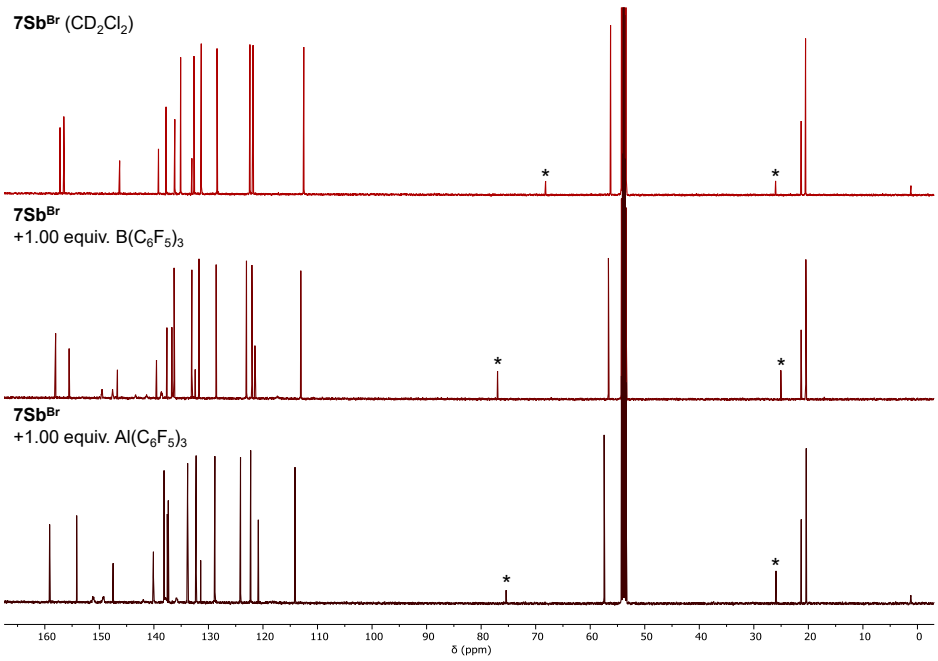


Figure 306: Stacked $^{13}C\{^{1}H\}$ NMR spectra (126 MHz, CD_2Cl_2) of **7Sb^{Br}** (0.02 mmol) upon addition of 1.00 equiv. of BCF (middle) and 1.00 equiv. of AlCF (bottom). THF is marked by the sign (*).

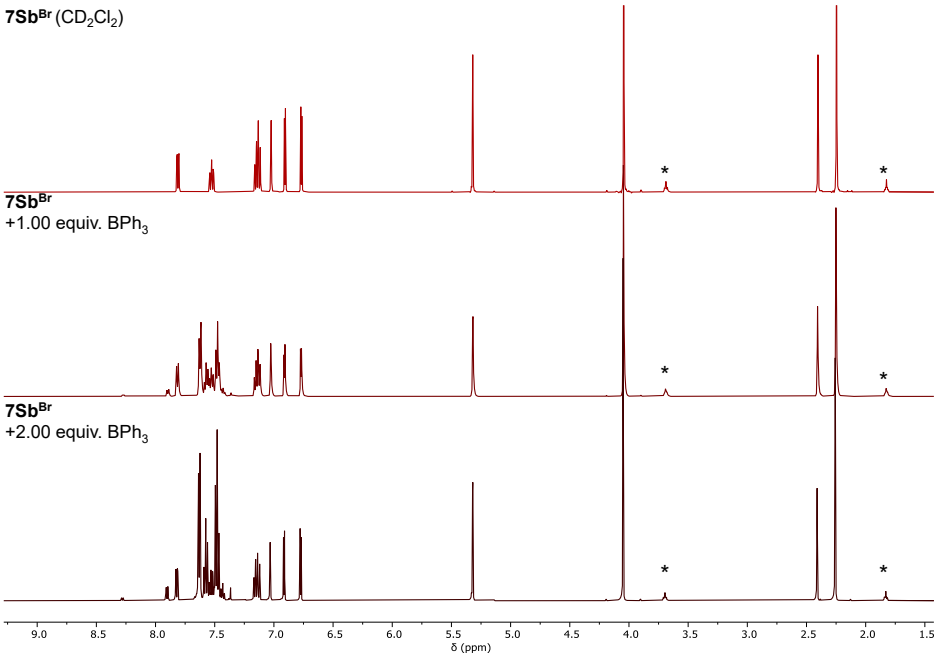


Figure 307: Stacked ^{1}H NMR spectra (500 MHz, CD_2Cl_2) of **7Sb^{Br}** (0.02 mmol) upon addition of 1.00 equiv. of BPh_3 (middle) and 2.00 equiv. of BPh_3 (bottom). THF is marked by the sign (*).

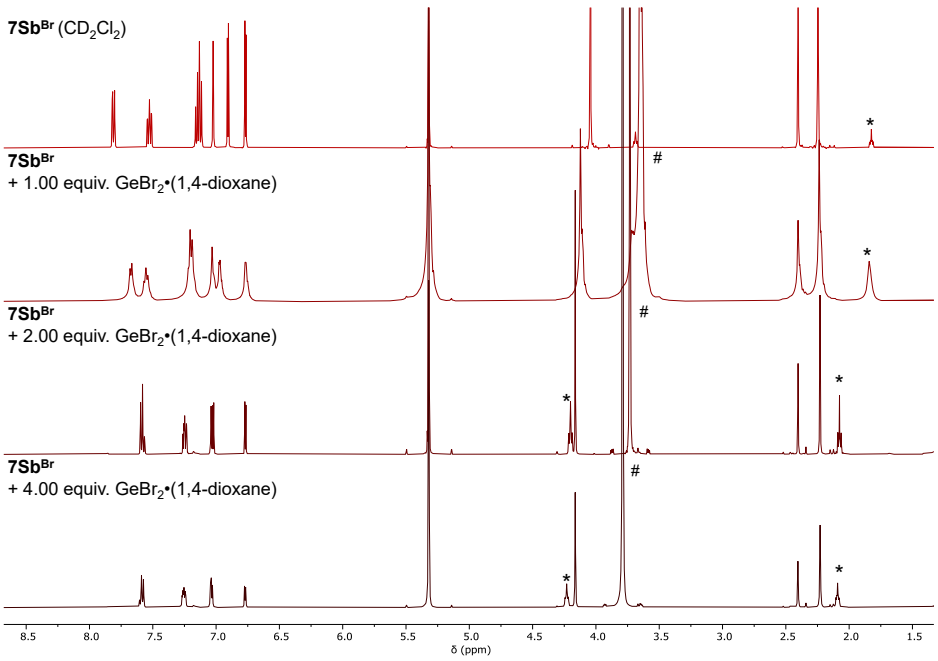


Figure 308: Stacked ^{1}H NMR spectra (500 MHz, CD_2Cl_2) of **7Sb^{Br}** (0.02 mmol) upon addition of 1.00 equiv., 2.00 equiv. and 4.00 equiv. of $GeBr_2$·(1,4-dioxane) (top to bottom). THF is marked by the sign (*) and 1,4-dioxane by ($^{\#}$).

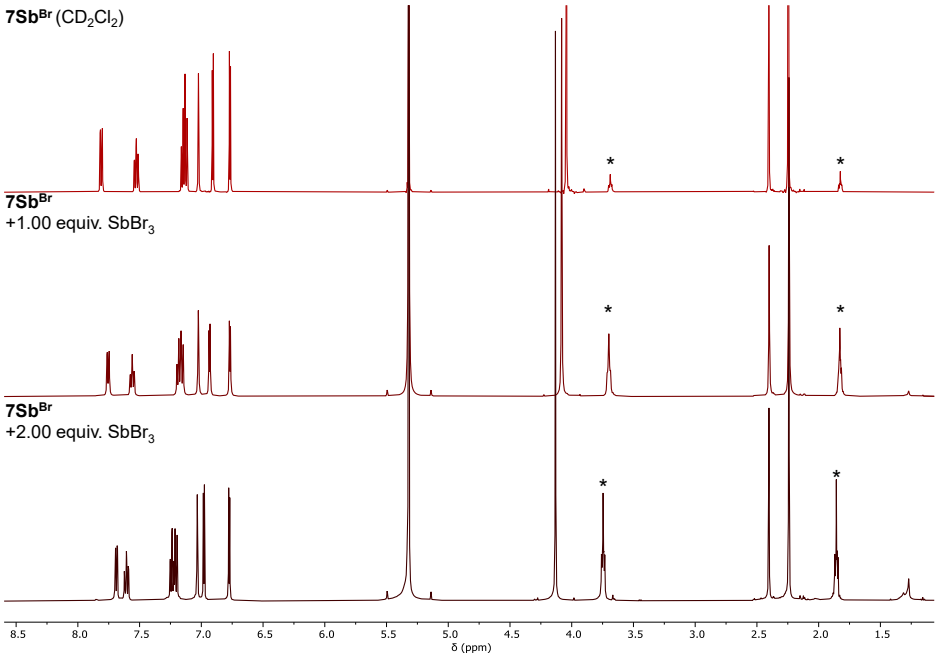


Figure 309: Stacked ^{1}H NMR spectra (500 MHz, CD_2Cl_2) of **7Sb^{Br}** (0.02 mmol) upon addition of 1.00 equiv. of $SbBr_3$ (middle) and 2.00 equiv. of $SbBr_3$ (bottom). THF is marked by the sign (*).

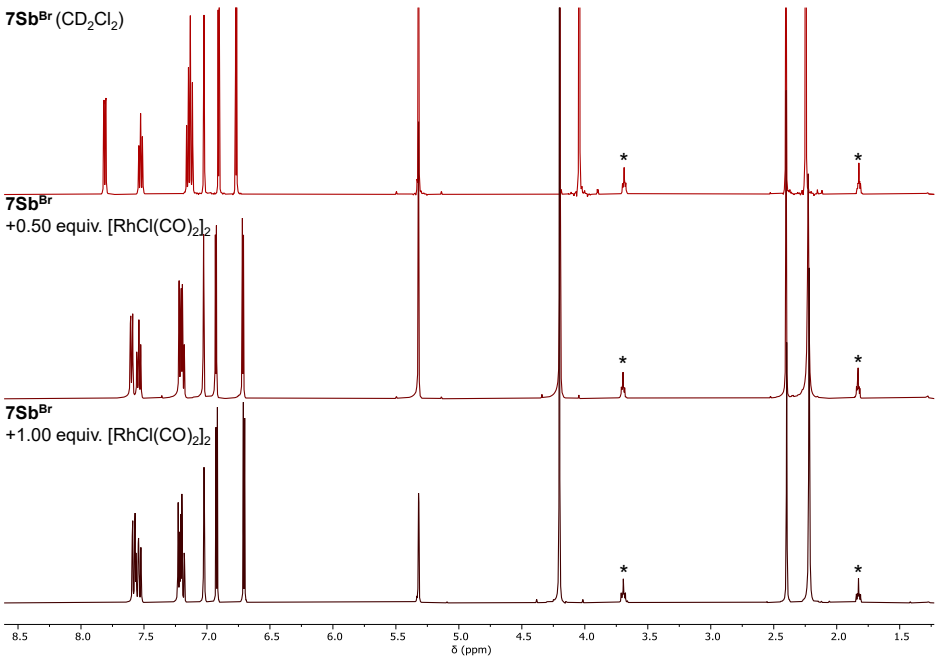


Figure 310: Stacked ^{1}H NMR spectra (500 MHz, CD_2Cl_2) of **7Sb^{Br}** (0.02 mmol) upon addition of 0.50 equiv. of $[RhCl(CO)_2]_2$ (middle) and 1.00 equiv. of $[RhCl(CO)_2]_2$ (bottom). The sign (*) marks THF.

IV. Appendix: Spectroscopic data

Chapter 2: Evaluation of solvents

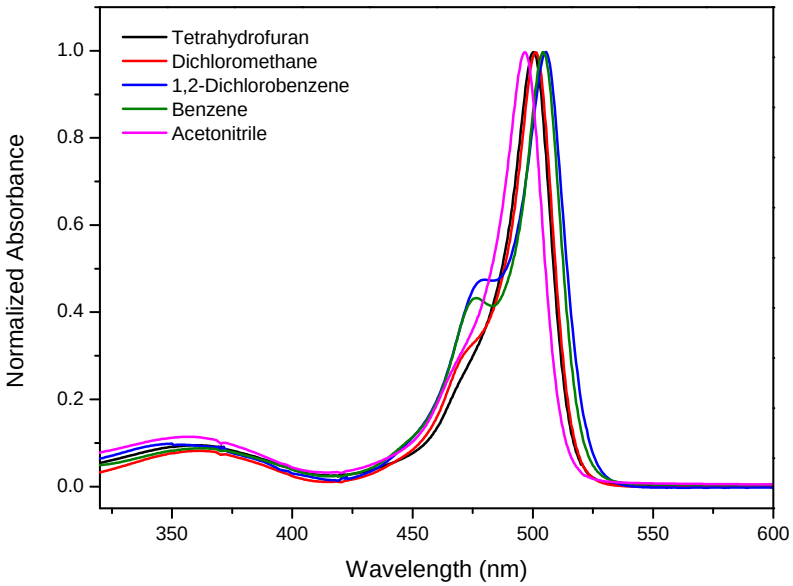


Figure 311: Normalized UV/Vis absorption spectra of **1Sb^{Cl}** in various solvents at 25 °C.

Chapter 2: Absorbance and PL emission profiles of PnDIPY complexes

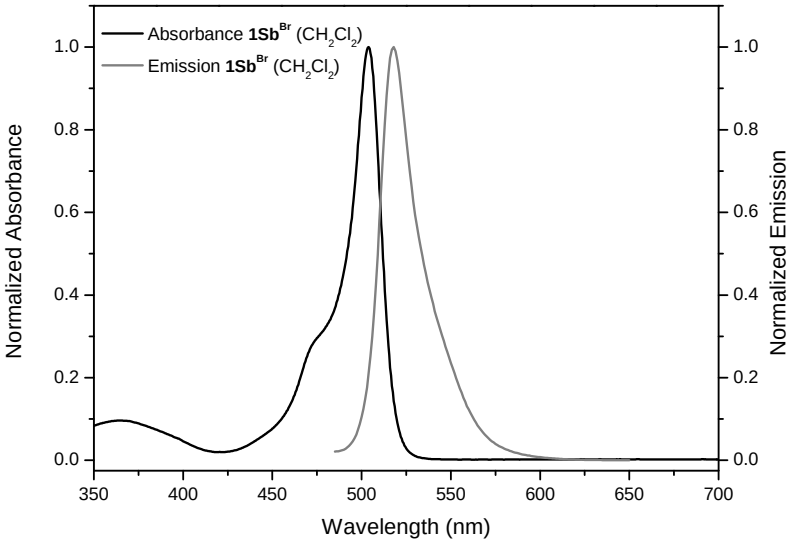


Figure 312: Normalized absorbance and emission spectra of **1Sb^{Br}** in CH_2Cl_2 at 5 °C.

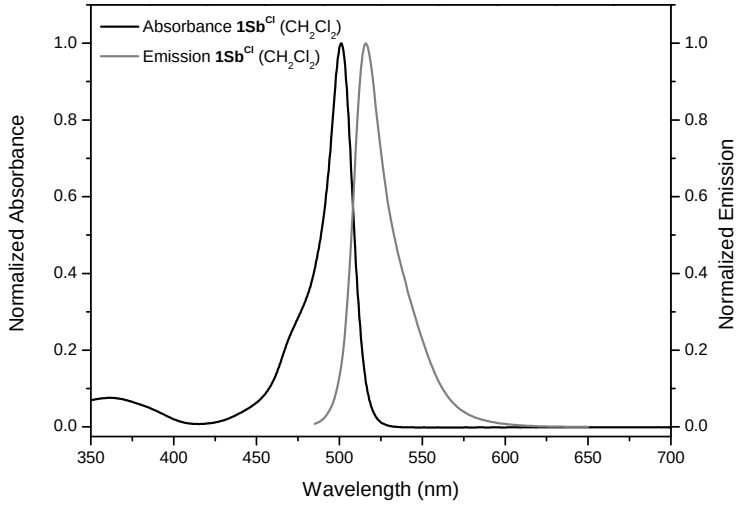


Figure 313: Normalized absorbance and PL emission spectra of **1Sb^{Cl}** in CH_2Cl_2 at 5 °C.

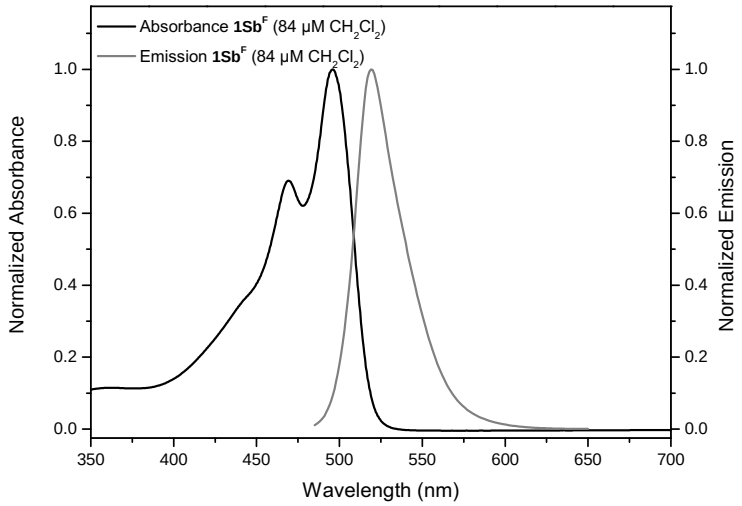


Figure 314: Normalized absorbance and PL emission spectra of **1Sb^{F}** in CH_2Cl_2 at −10 °C and increased concentration (84 µM).

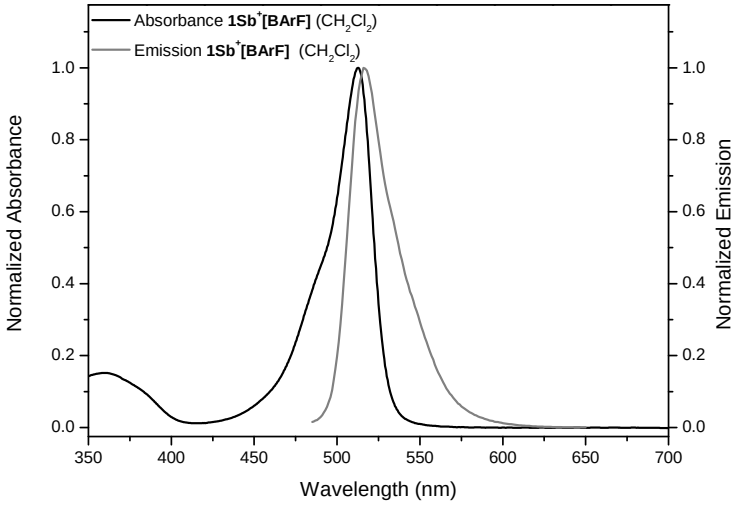


Figure 315: Normalized absorbance and PL emission spectra of **1Sb$^+$[BArF]** in CH_2Cl_2 at 5 °C.

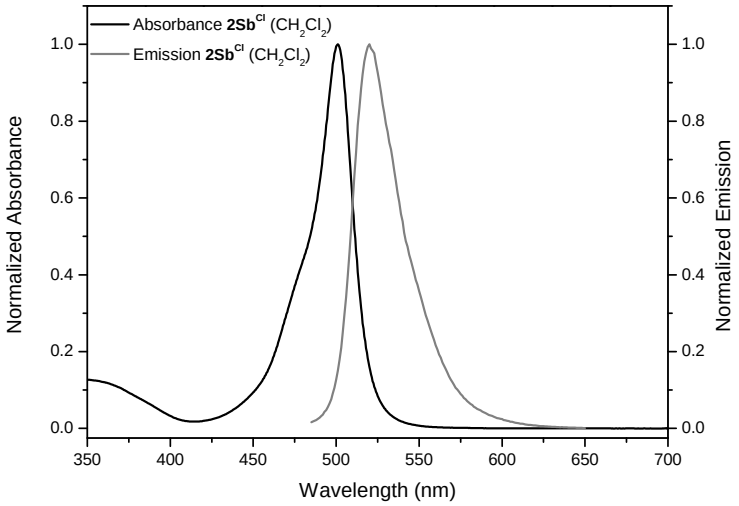


Figure 316: Normalized absorbance and PL emission spectra of **2Sb^{Cl}** in CH_2Cl_2 at 5 °C.

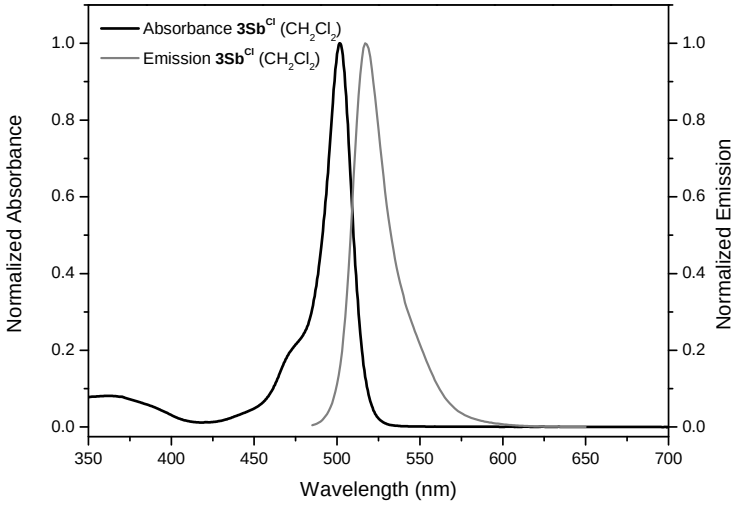


Figure 317: Normalized absorbance and PL emission spectra of **3Sb^{Cl}** in CH_2Cl_2 at 5 °C.

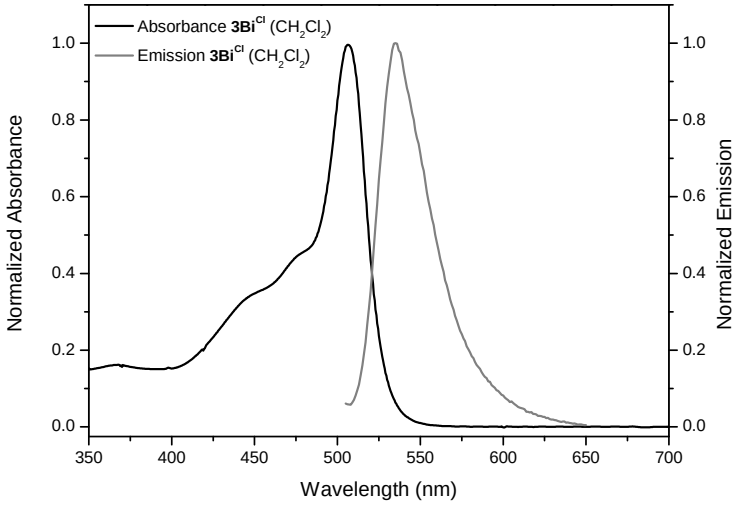


Figure 318: Normalized absorbance and PL emission spectra of **3Bi^{Cl}** in CH_2Cl_2 at 5 °C.

Chapter 2: Dilution series for estimation of molar absorption coefficients ϵ and quantum yields

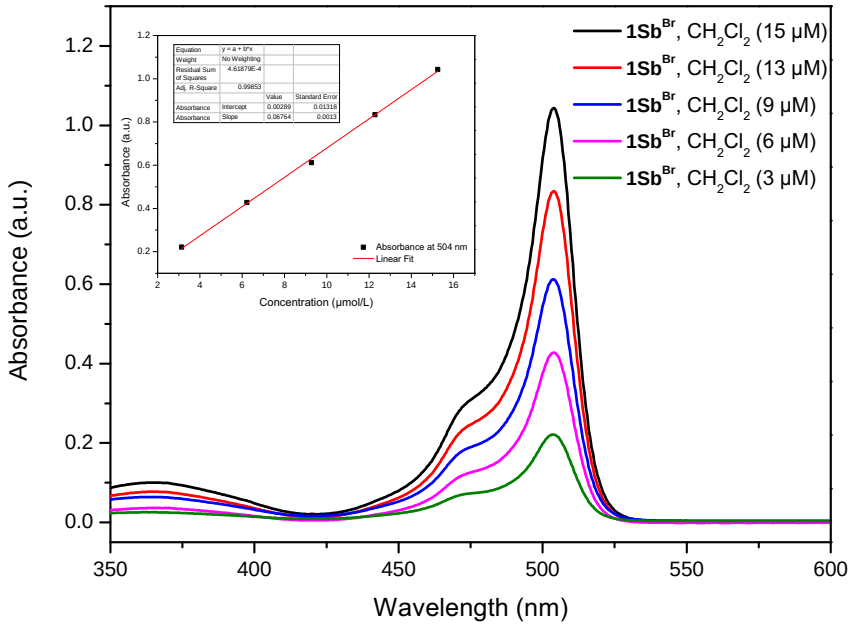


Figure 319: UV/Vis dilution series of **1Sb^{Br}** in CH_2Cl_2 at 5 °C and linear regression analysis of absorbance (λ_{abs} =504 nm) plotted against respective sample concentration.

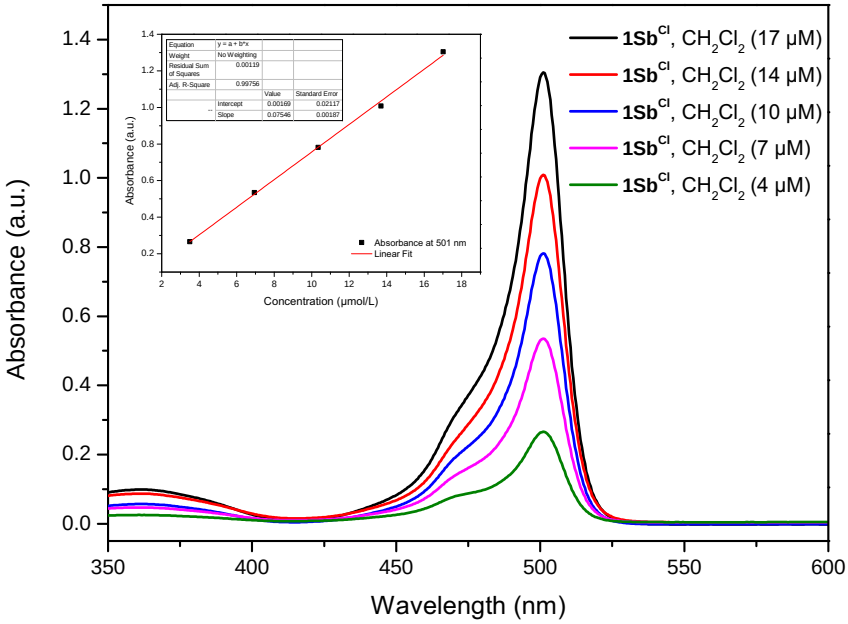


Figure 320: UV/Vis dilution series of **1Sb^{Cl}** in CH_2Cl_2 at 5 °C and linear regression analysis of absorbance (λ_{abs} =501 nm) plotted against respective sample concentration.

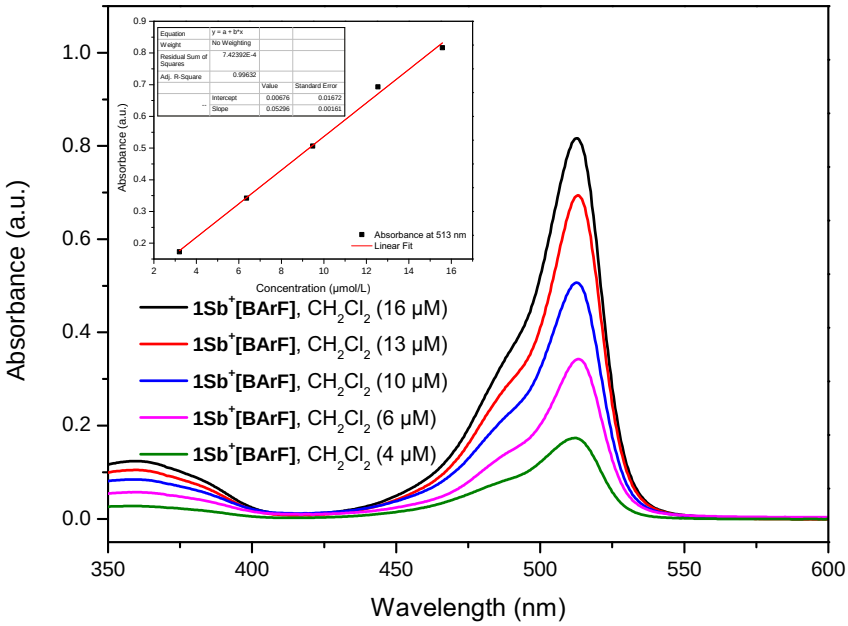


Figure 321: UV/Vis dilution series of **1Sb$^+$[BArF]** in CH_2Cl_2 at 5 °C and linear regression analysis of absorbance (λ_{abs} =513 nm) plotted against respective sample concentration.

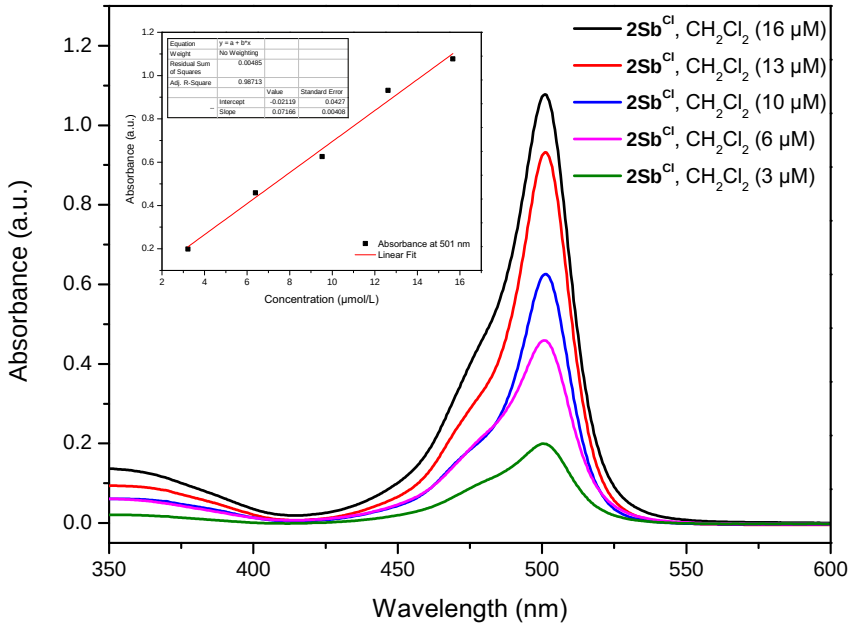


Figure 322: UV/Vis dilution series of **2Sb^{Cl}** in CH_2Cl_2 at 5 °C and linear regression analysis of absorbance (λ_{abs} =501 nm) plotted against respective sample concentration.

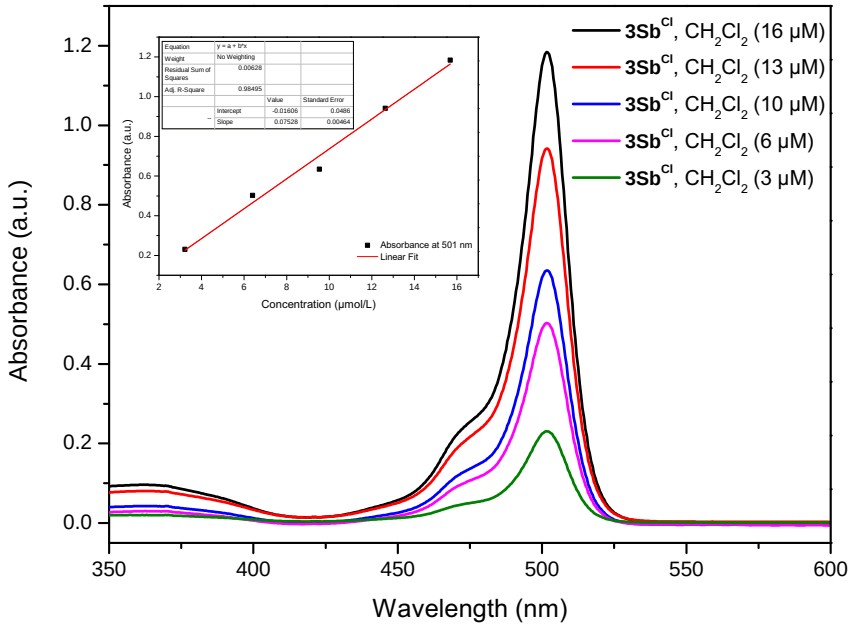


Figure 323: UV/Vis dilution series of **3Sb^{Cl}** in CH_2Cl_2 at 5 °C and linear regression analysis of absorbance (λ_{abs} =501 nm) plotted against respective sample concentration.

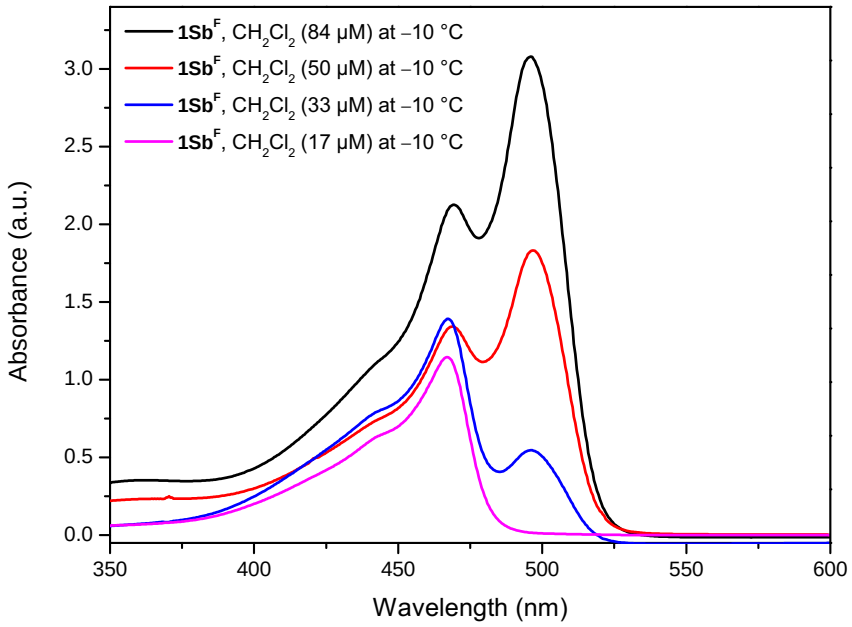


Figure 324: UV/Vis dilution series of **3Sb^{Cl}** in CH_2Cl_2 at −10 °C.

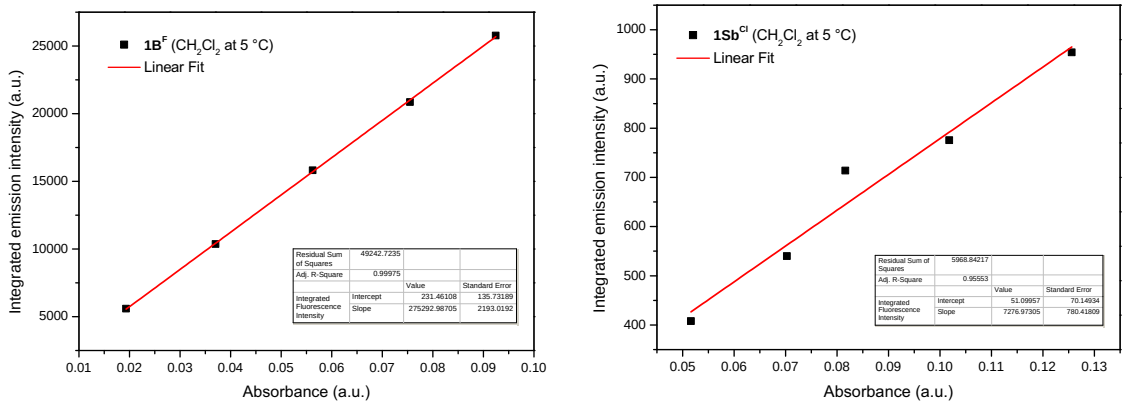


Figure 325: Integrated emission intensities of **1B^{F}** (left) and **1Sb^{Cl}** (right) dilution series in CH_2Cl_2 at 5 °C against maximum absorbance.

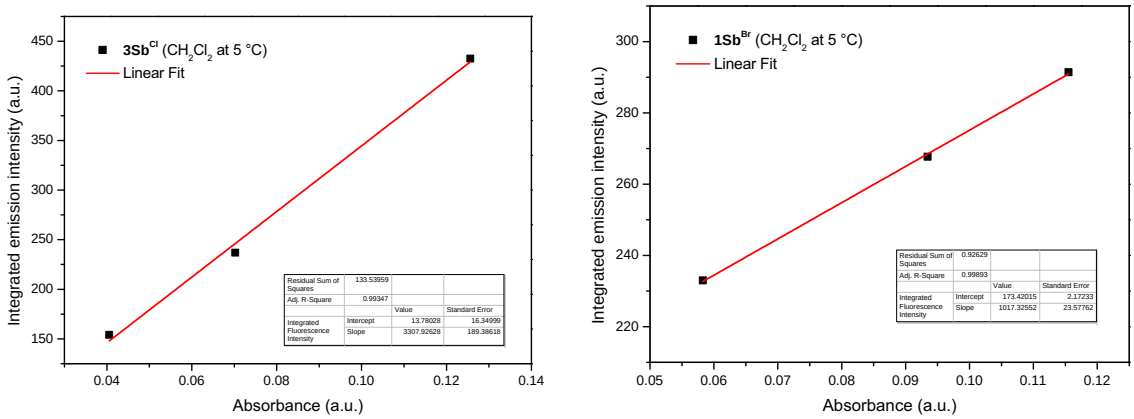


Figure 326: Integrated emission intensities of **3Sb^{Cl}** (left) and **1Sb^{Br}** (right) dilution series in CH_2Cl_2 at 5 °C against maximum absorbance.

Chapter 2: Complex stability assessment

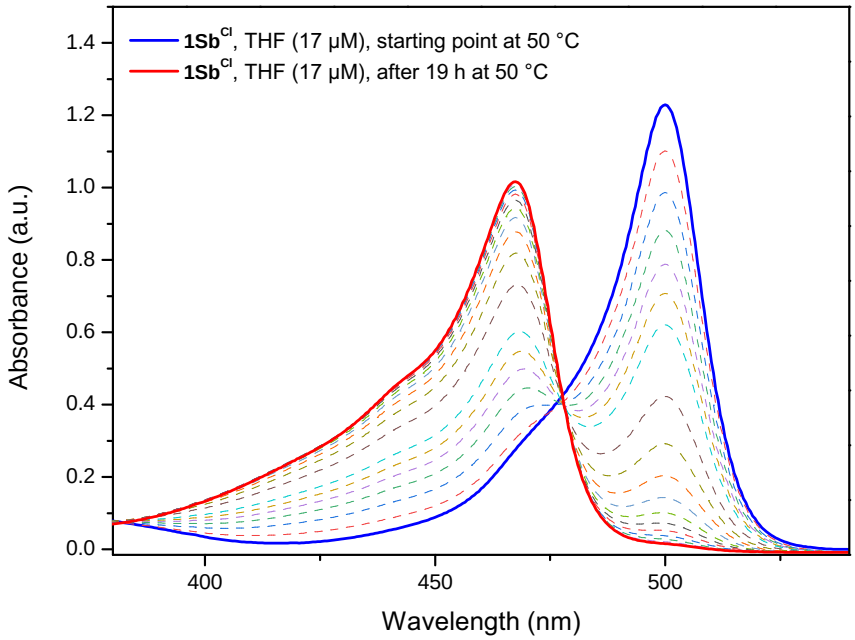


Figure 327: Time-resolved UV/Vis spectra of **1Sb^{Cl}** (17 µM) recorded at 50 °C in THF over the course of 19 h.

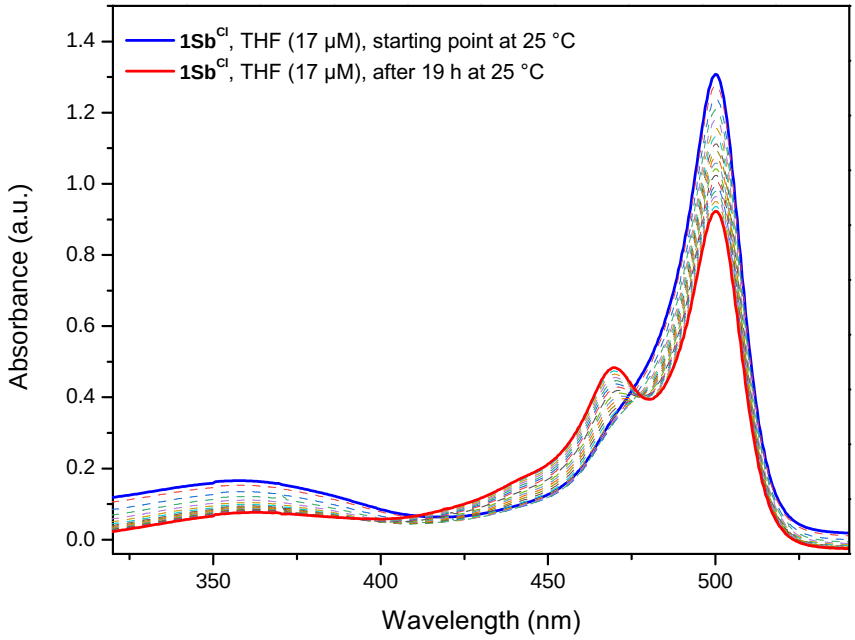


Figure 328: Time-resolved UV/Vis spectra of **1Sb^{Cl}** (17 µM) recorded at 25 °C in THF over the course of 19 h.

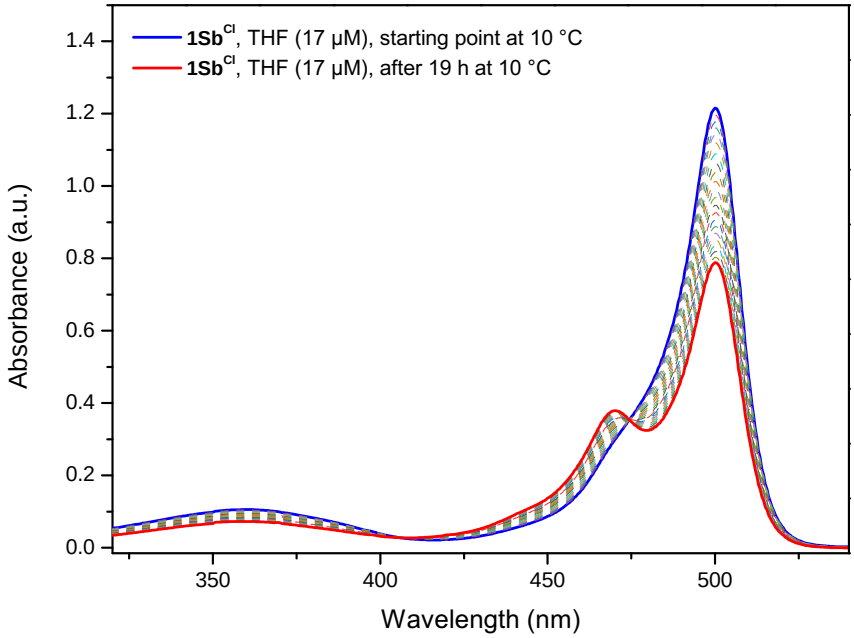


Figure 329: Time-resolved UV/Vis spectra of **1Sb^{Cl}** (17 µM) recorded at 10 °C in THF over the course of 19 h.

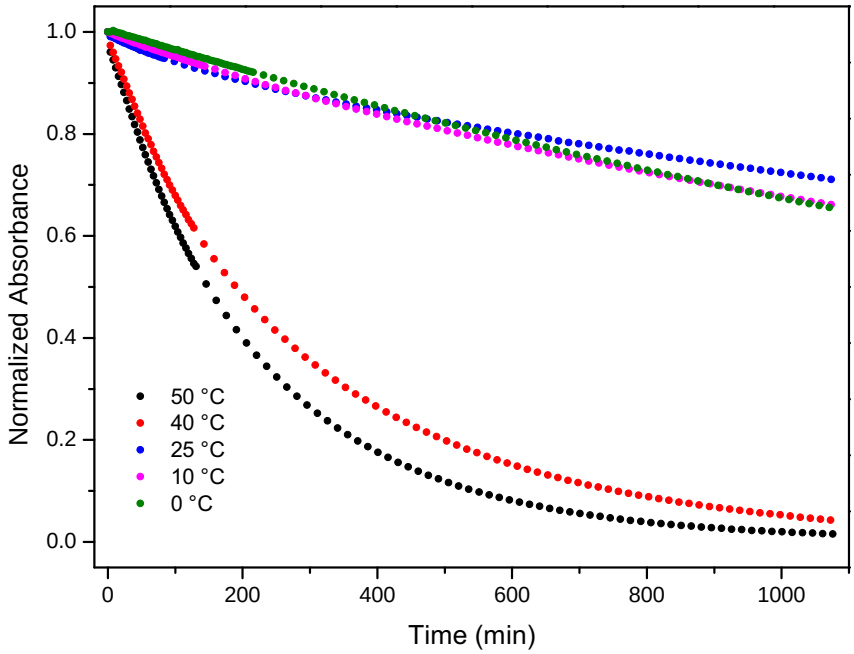


Figure 330: Temperature depended decay of absorption maximum of **1Sb^{Cl}** (17 µM) in THF against time.

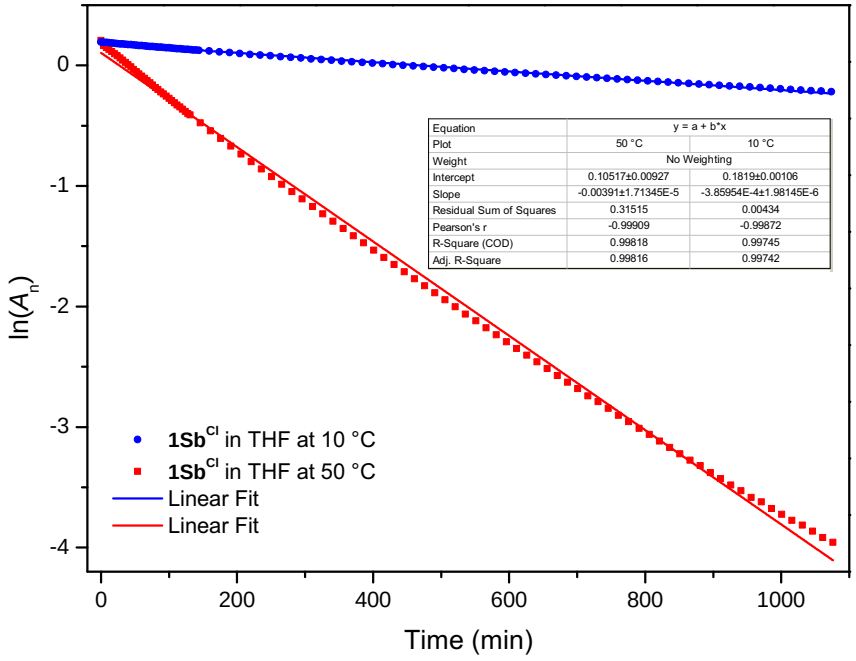


Figure 331: Kinetic analysis plot of ln(A) of **1Sb^{Cl}** (17 μM) in THF against time.

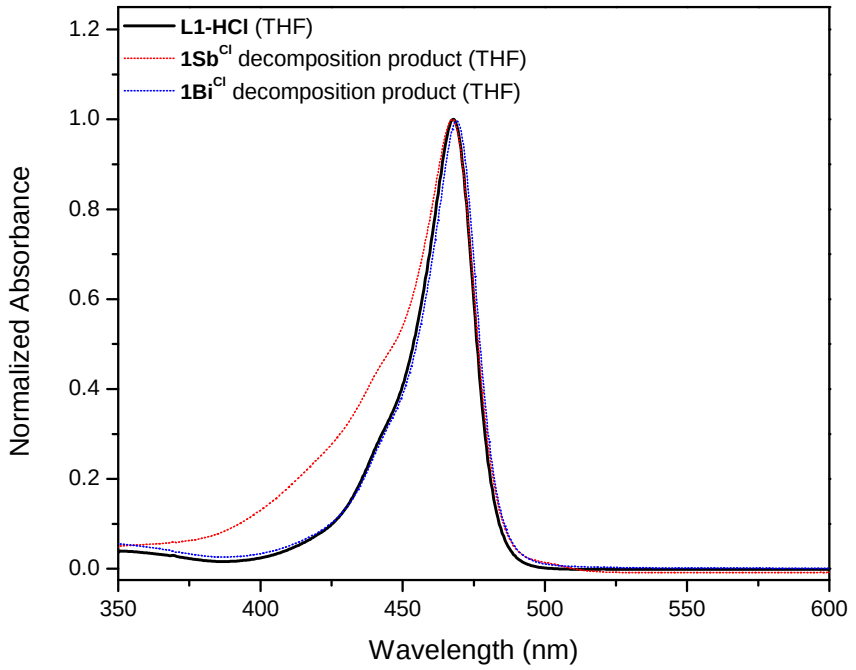


Figure 332: Comparison of absorption spectra of **1Sb^{Cl}** and **1Bi^{Cl}** decomposition bands with **L1-HCl** in THF.

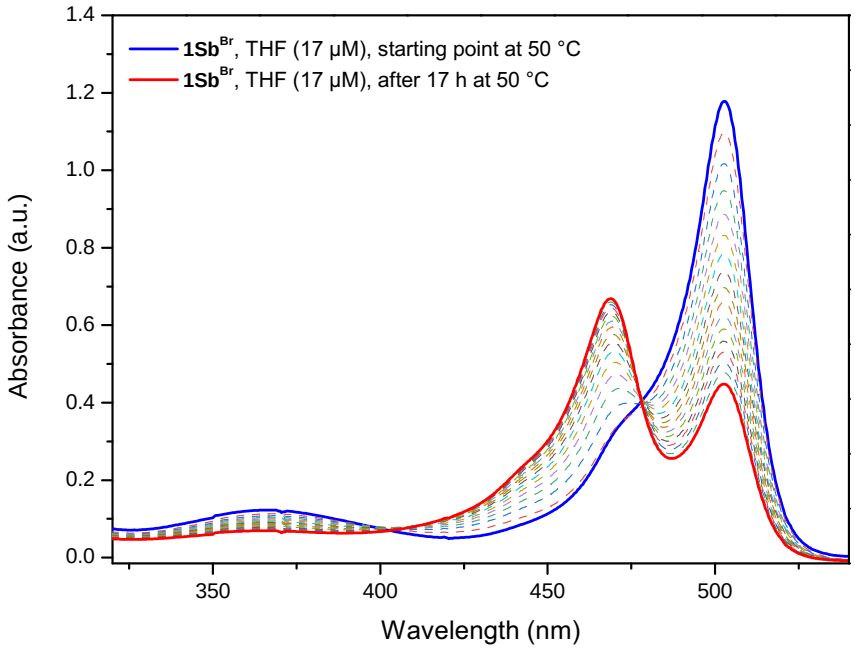


Figure 333: Time-resolved UV/Vis spectra of **1Sb^{Br}** (17 µM) recorded at 50 °C in THF over the course of 17 h.

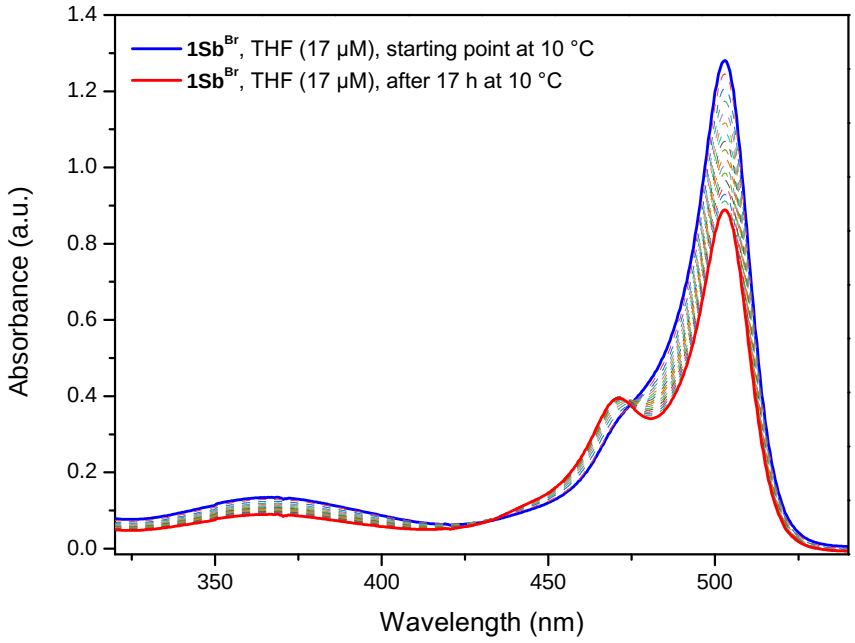


Figure 334: Time-resolved UV/Vis spectra of **1Sb^{Br}** (17 µM) recorded at 10 °C in THF over the course of 17 h.

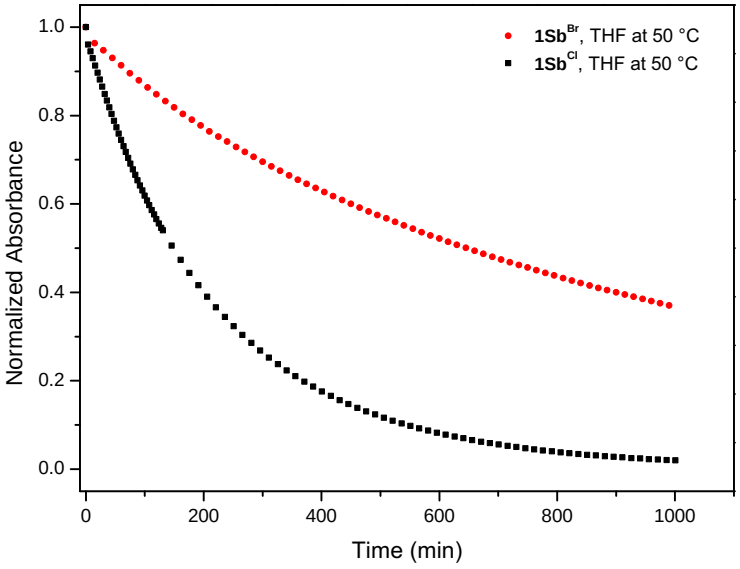


Figure 335: Comparison of absorption maxima decay of **1Sb^{Cl}** and **1Sb^{Br}** (both 17 μM) in THF at 50 °C against time.

Chapter 3: Absorbance and PL emission profiles of PnDIPY complexes

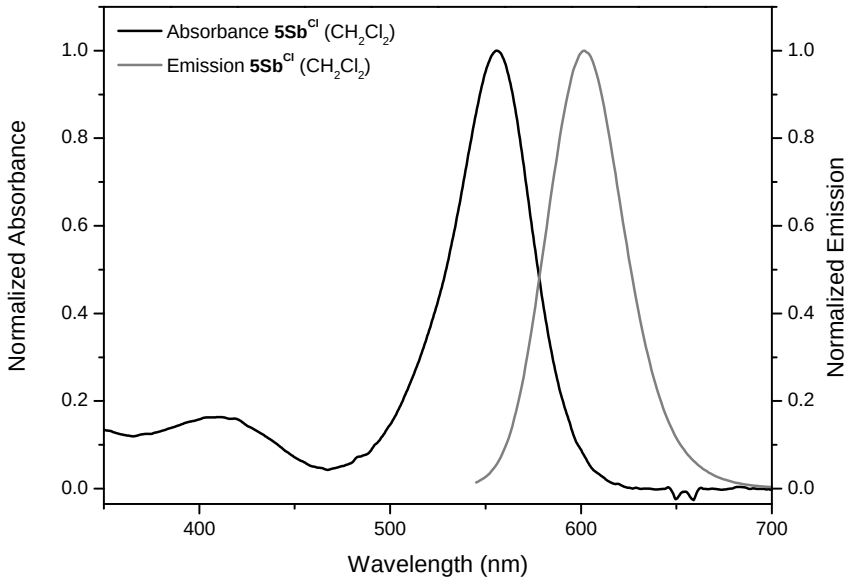


Figure 336: Normalized absorbance and PL emission spectra of **5Sb^{Cl}** in CH_2Cl_2 at 25 °C. Emission was recorded at an excitation wavelength of λ_{exc} = 520 nm.

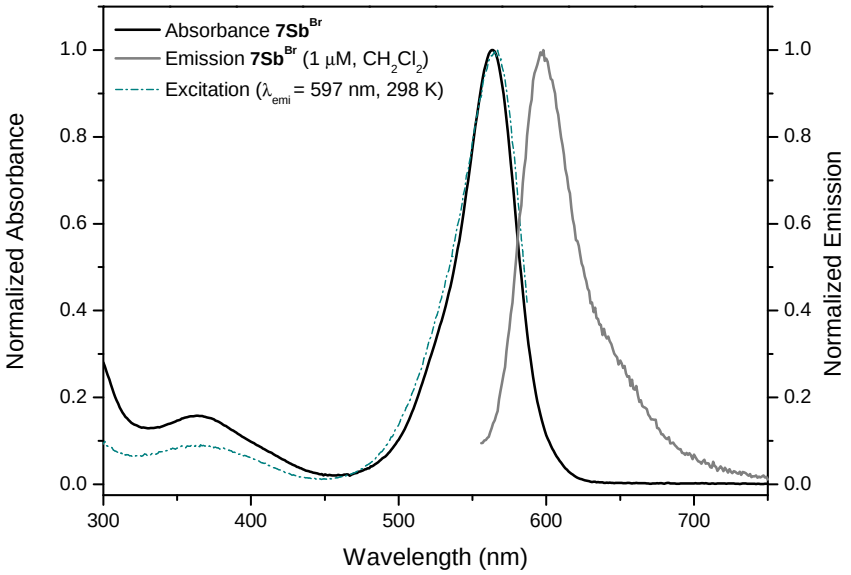


Figure 337: Normalized absorbance and PL emission (λ_{exc} = 520 nm) spectra of **7Sb^{Br}** in CH_2Cl_2 at 25 °C. The normalized excitation spectrum (dashed line) is shown for λ_{emi} = 597 nm (recorded at 25 °C in CH_2Cl_2).

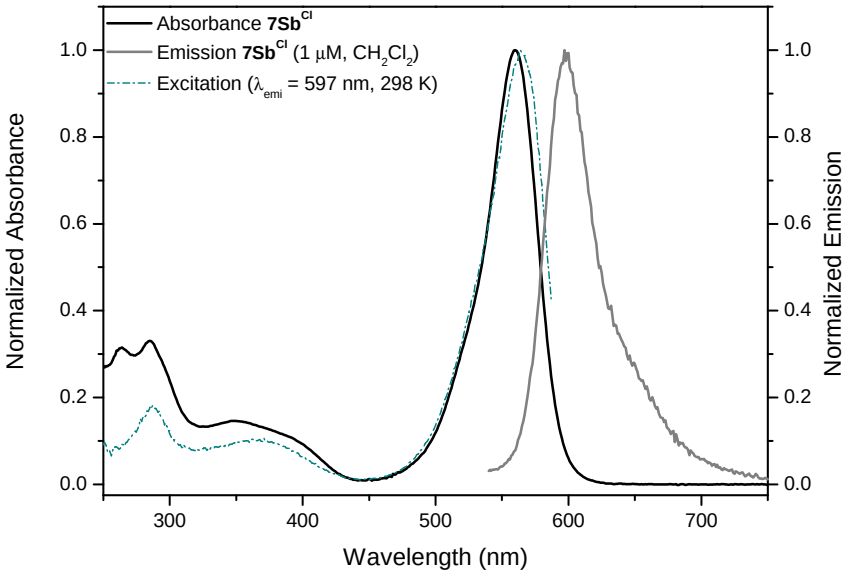


Figure 338: Normalized absorbance and PL emission (λ_{exc} = 520 nm) spectra of **7Sb^{Cl}** in CH_2Cl_2 at 25 °C. The normalized excitation spectrum (dashed line) is shown for λ_{emi} = 597 nm (recorded at 25 °C in CH_2Cl_2).

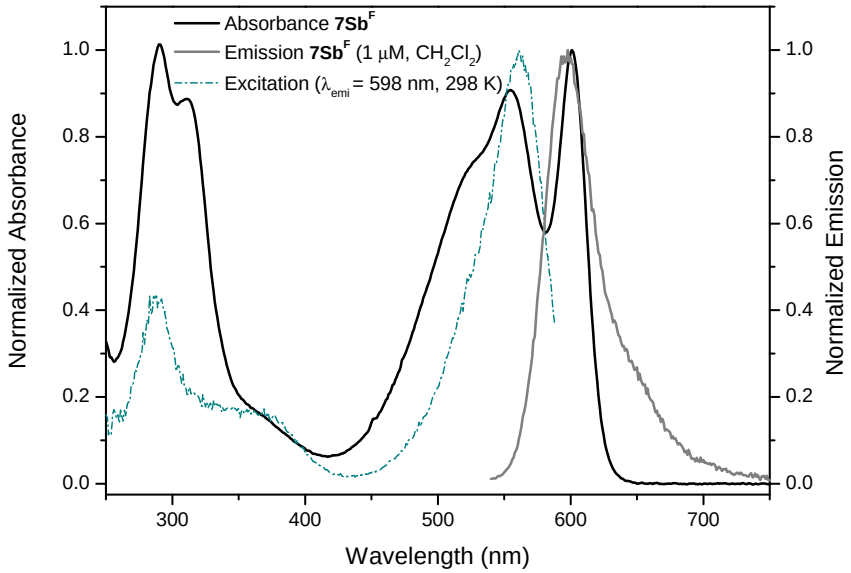


Figure 339: Normalized absorbance and PL emission (λ_{exc} = 520 nm) spectra of **7Sb^{Cl}** in CH_2Cl_2 at 25 °C. The normalized excitation spectrum (dashed line) is shown for λ_{emi} = 598 nm (recorded at 25 °C in CH_2Cl_2).

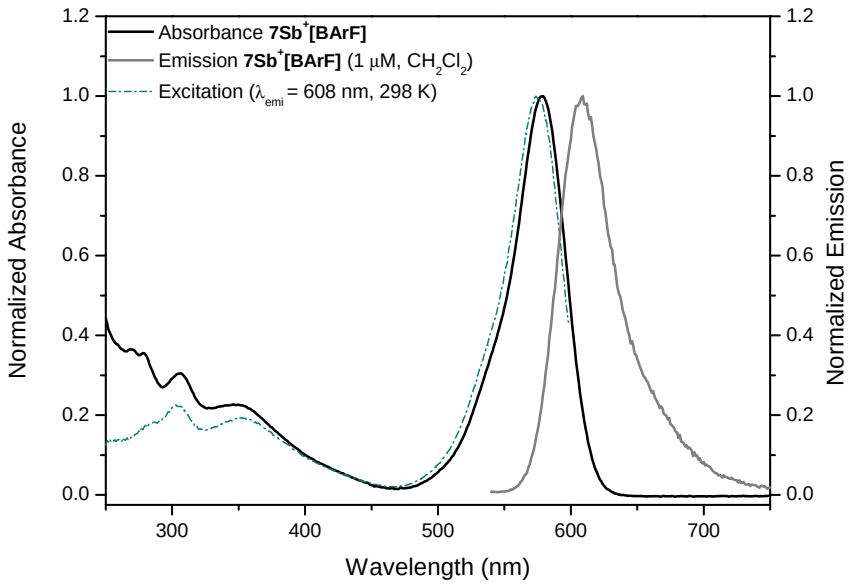


Figure 340: Normalized absorbance and PL emission (λ_{exc} = 520 nm) spectra of **7Sb$^+$[BArF]** in CH_2Cl_2 at 25 °C. The normalized excitation spectrum (dashed line) is shown for λ_{emi} = 608 nm (recorded at 25 °C in CH_2Cl_2).

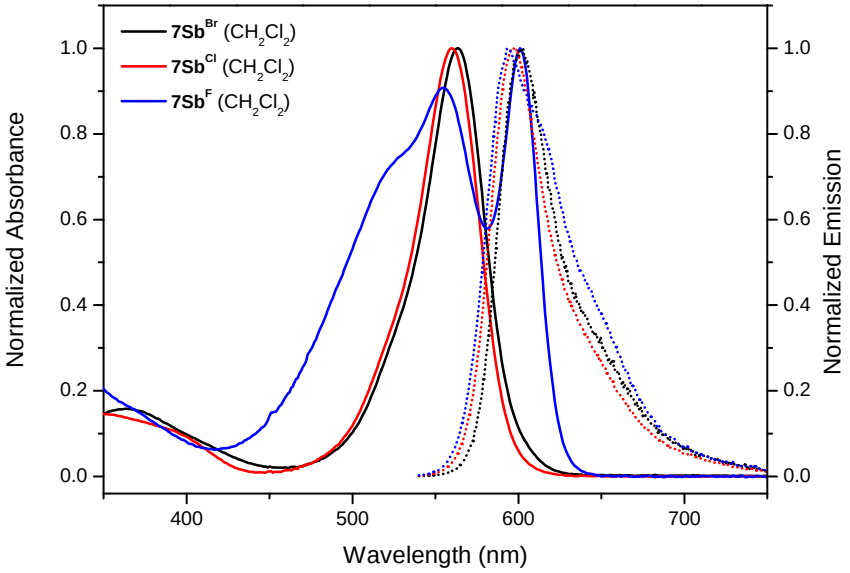


Figure 341: Overview of normalized absorbance and PL emission (λ_{exc} = 520 nm) spectra of **L7** SBDIPY complexes in CH_2Cl_2 at 25 °C.

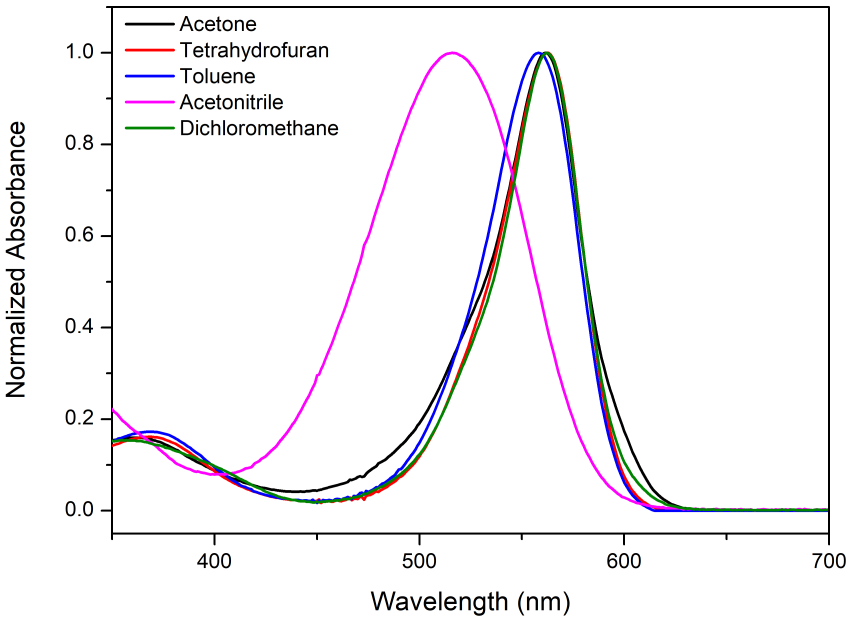


Figure 342: Overview of normalized absorbance spectra of **7Sb^{Br}** in different solvents at 15 °C.

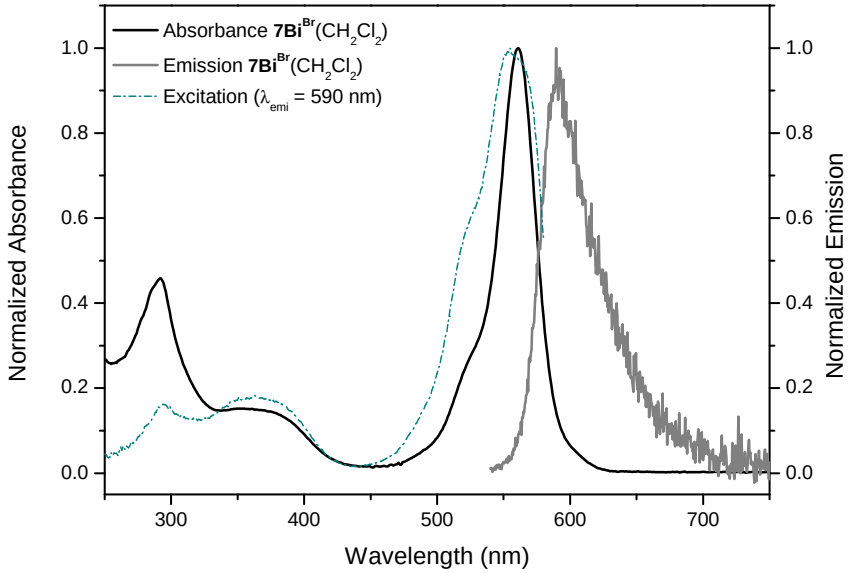


Figure 343: Normalized absorbance and PL emission (λ_{exc} = 520 nm) spectra of **7Bi^{Br}** in CH_2Cl_2 at 25 °C. The normalized excitation spectrum (dashed line) is shown for λ_{emi} = 590 nm (recorded at 25 °C in CH_2Cl_2).

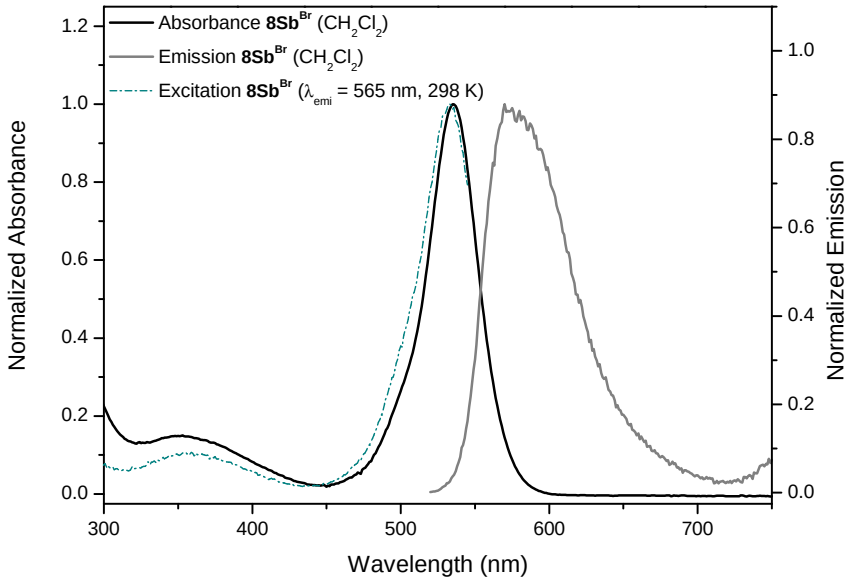


Figure 344: Normalized absorbance and PL emission (λ_{exc} = 500 nm) spectra of **8Sb^{Br}** in CH_2Cl_2 at 25 °C. The normalized excitation spectrum (dashed line) is shown for λ_{emi} = 565 nm (recorded at 25 °C in CH_2Cl_2).

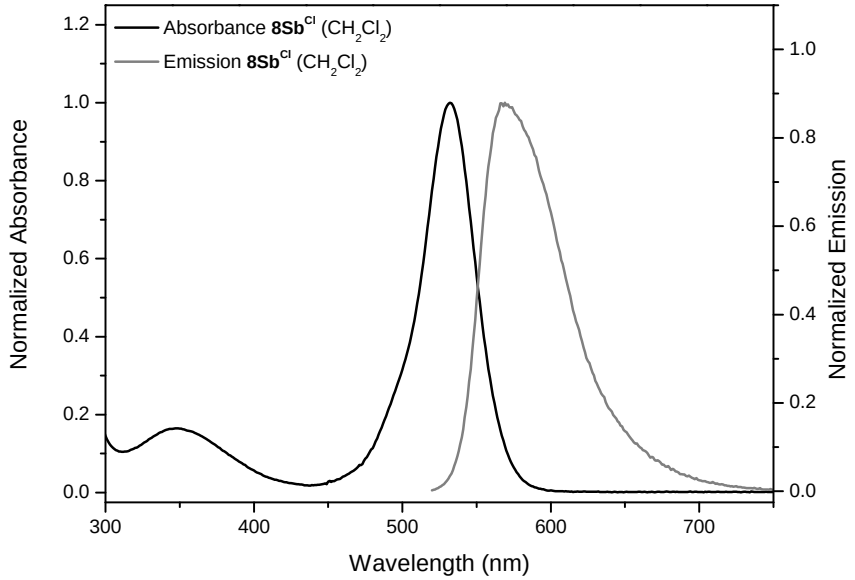


Figure 345: Normalized absorbance and PL emission (λ_{exc} = 500 nm) spectra of **8Sb^{Cl}** in CH_2Cl_2 at 25 °C.

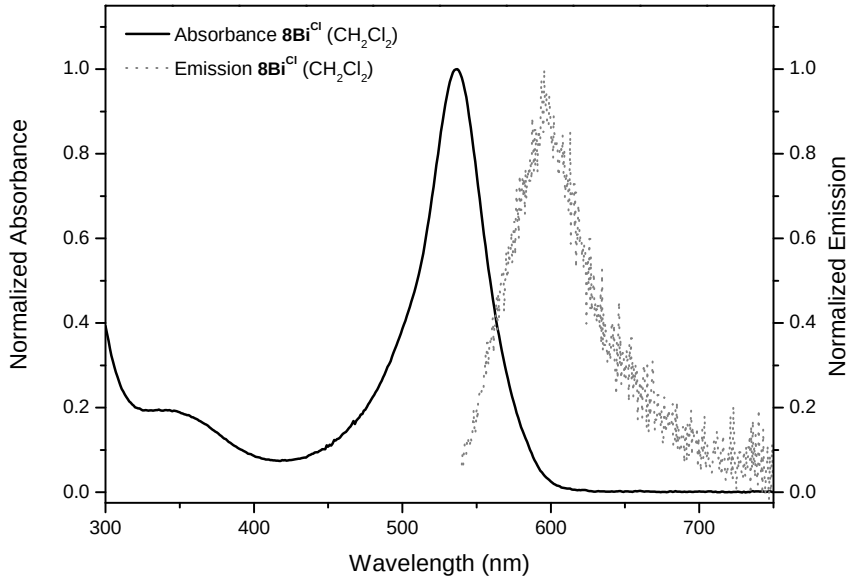


Figure 346: Normalized absorbance and PL emission (λ_{exc} = 500 nm) spectra of **8Bi^{Cl}** in CH_2Cl_2 at 25 °C.

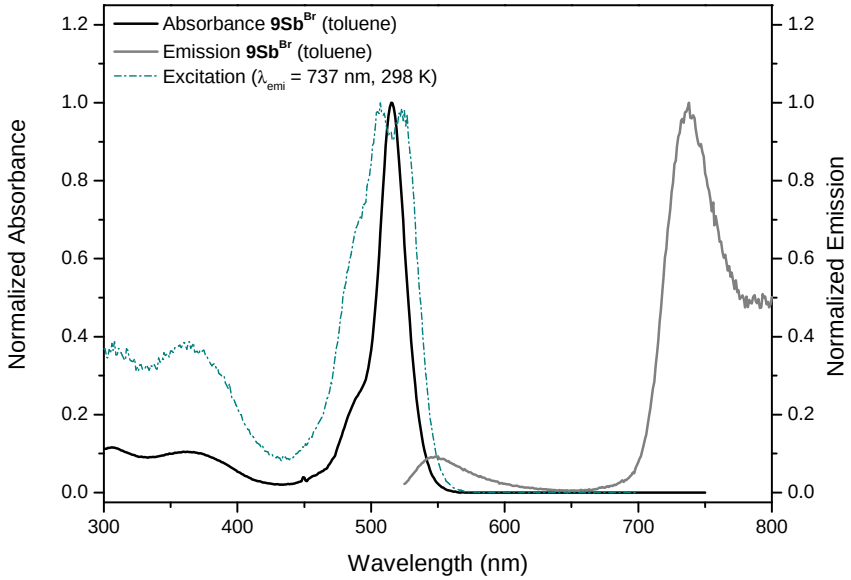


Figure 347: Normalized absorbance and PL emission (λ_{exc} = 515 nm) spectra of **9Sb^{Br}** in toluene at 25 °C. The normalized excitation spectrum (dashed line) is shown for λ_{emi} = 737 nm (recorded at 25 °C in toluene).

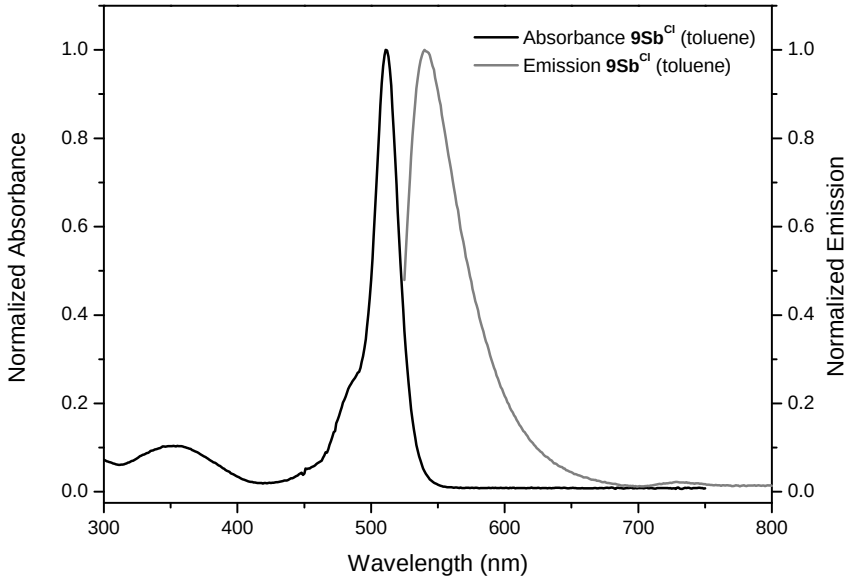


Figure 348: Normalized absorbance and PL emission (λ_{exc} = 510 nm) spectra of **9Sb^{Cl}** in toluene at 25 °C.

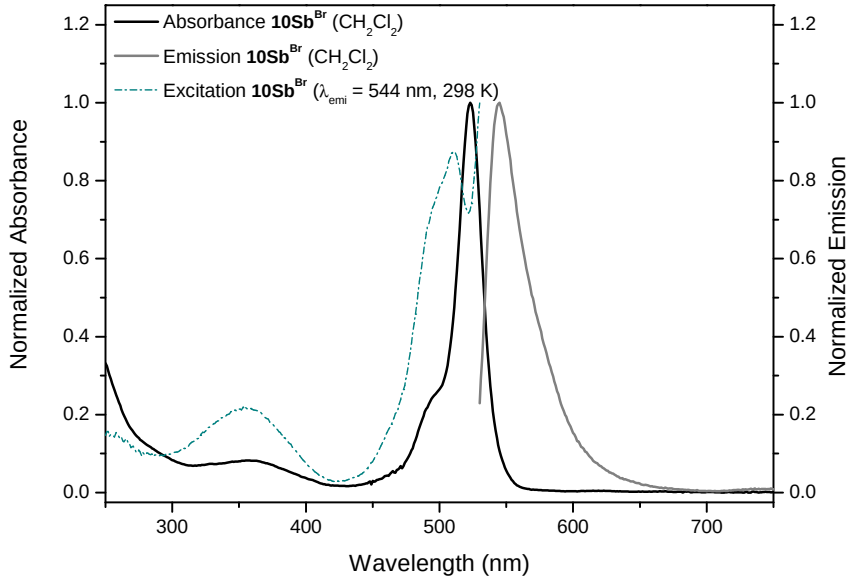


Figure 349: Normalized absorbance and PL emission (λ_{exc} = 510 nm) spectra of **10Sb^{Br}** in CH_2Cl_2 at 25 °C. The normalized excitation spectrum (dashed line) is shown for λ_{emi} = 544 nm (recorded at 25 °C in CH_2Cl_2).

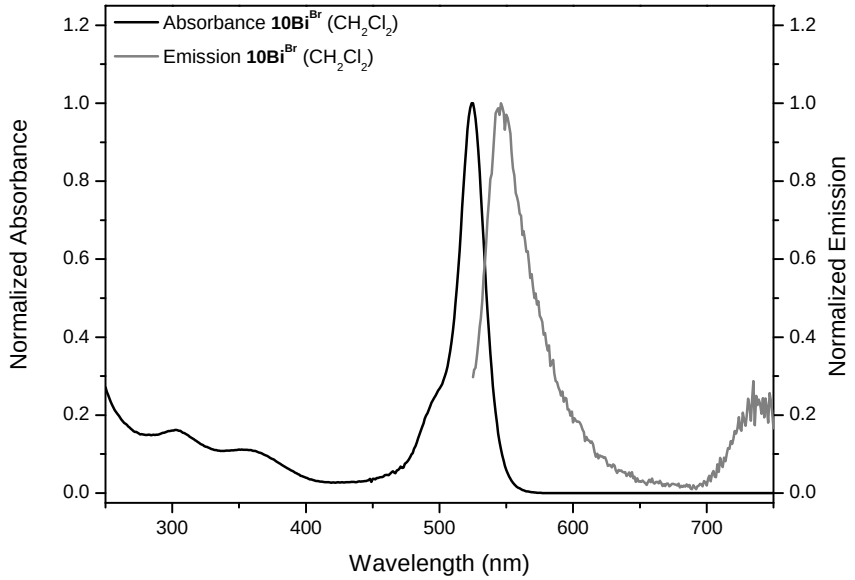


Figure 350: Normalized absorbance and PL emission (λ_{exc} = 510 nm) spectra of **10Sb^{Br}** in CH_2Cl_2 at 25 °C. Photoluminescence was recorded using an emission bandwidth of 5.0 nm.

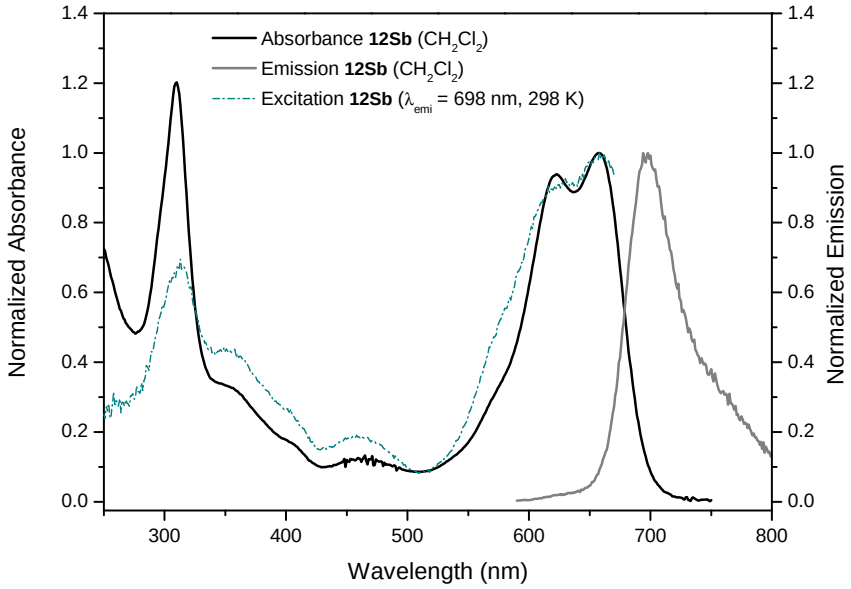


Figure 351: Normalized absorbance and PL emission (λ_{exc} = 570 nm) spectra of **12Sb** in CH_2Cl_2 at 25 °C. The normalized excitation spectrum (dashed line) is shown for λ_{emi} = 698 nm (recorded at 25 °C in CH_2Cl_2).

Chapter 3: Dilution series for estimation of molar absorption coefficients ϵ and quantum yields

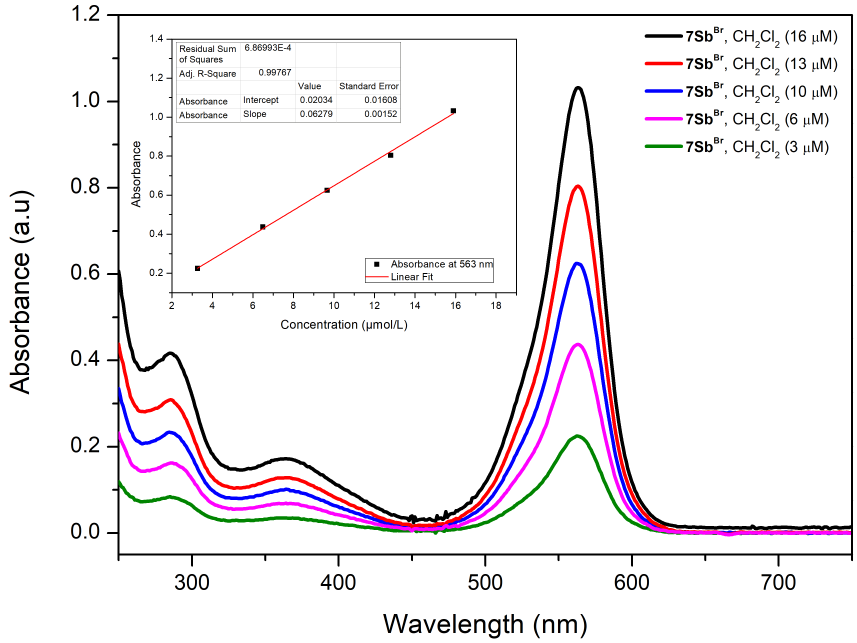


Figure 352: UV/Vis dilution series of **7Sb^{Br}** in CH_2Cl_2 at 15 °C and linear regression analysis of absorbance ($\lambda_{abs} = 563$ nm) plotted against respective sample concentration.

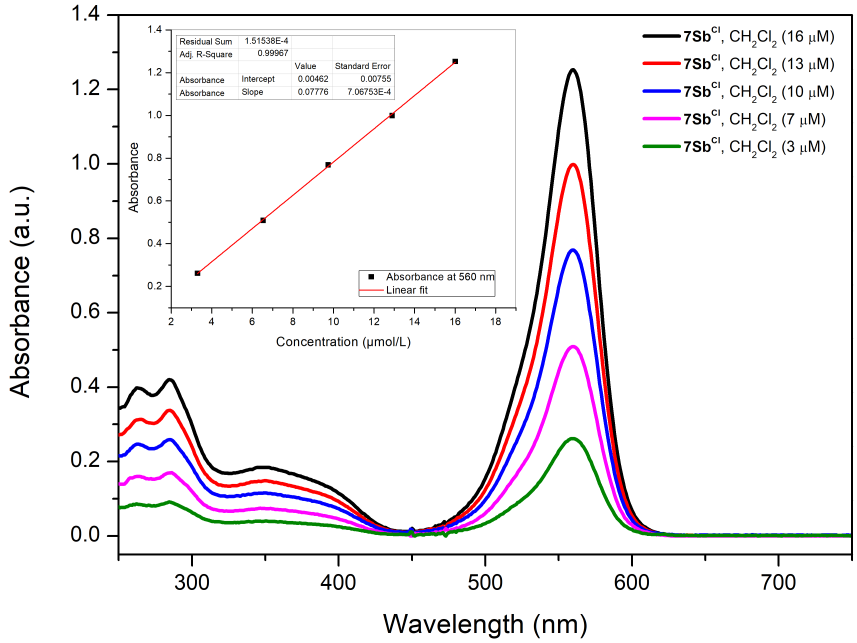


Figure 353: UV/Vis dilution series of **7Sb^{Cl}** in CH_2Cl_2 at 15 °C and linear regression analysis of absorbance ($\lambda_{abs} = 560$ nm) plotted against respective sample concentration.

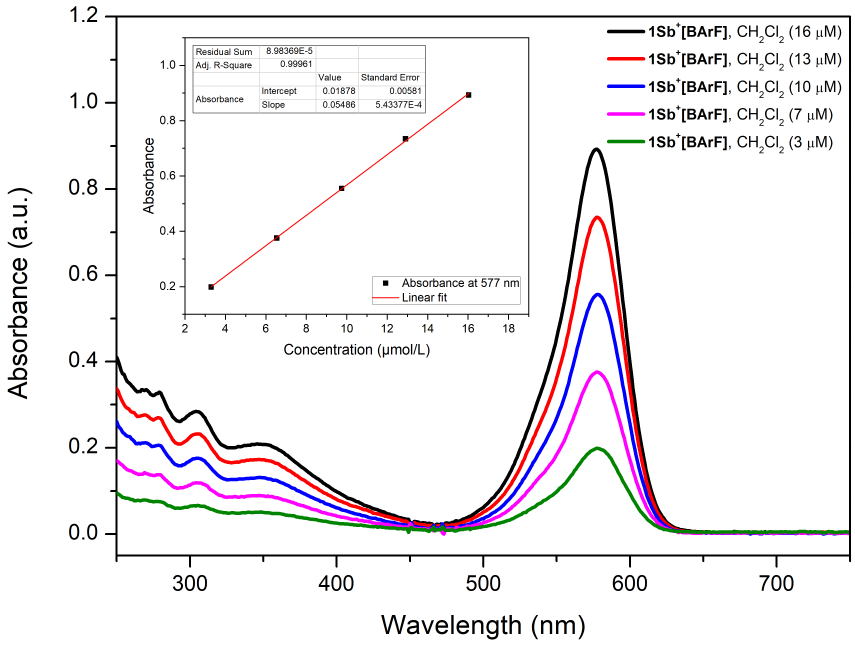


Figure 354: UV/Vis dilution series of **7Sb$^+$[BArF]** in CH_2Cl_2 at 15 °C and linear regression analysis of absorbance (λ_{abs} = 577 nm) plotted against respective sample concentration.

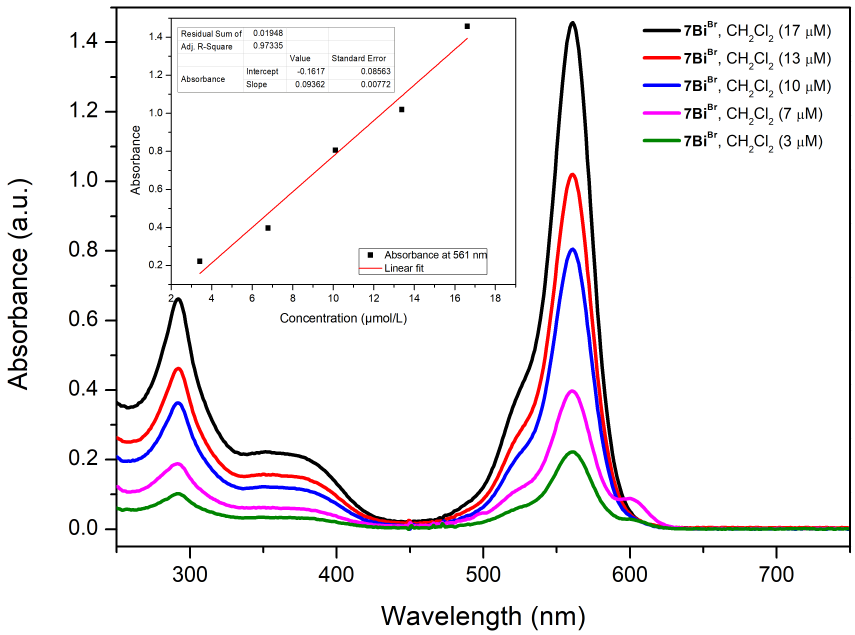


Figure 355: UV/Vis dilution series of **7Bi^{Br}** in CH_2Cl_2 at 15 °C and linear regression analysis of absorbance (λ_{abs} = 561 nm) plotted against respective sample concentration.

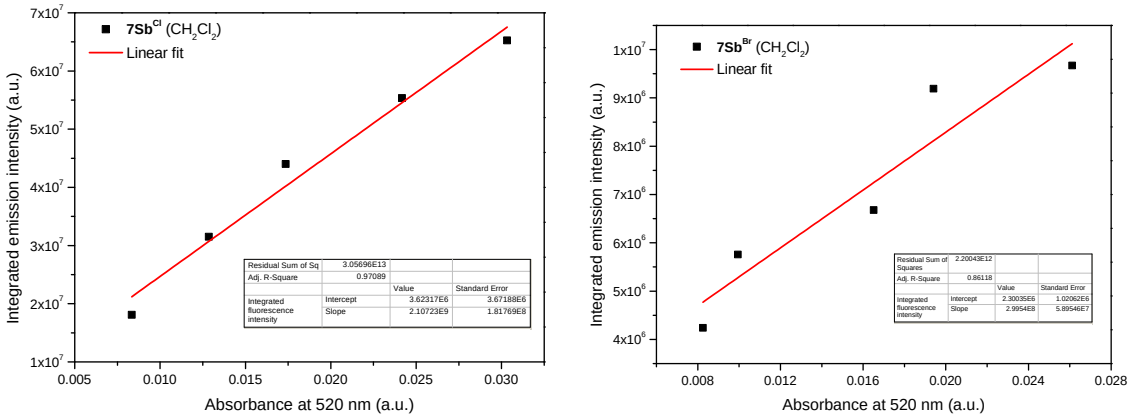


Figure 356: Integrated emission intensities of **7Sb^{Cl}** (left) and **7Sb^{Br}** (right) dilution series in CH_2Cl_2 at 25 °C against absorbance at 520 nm.

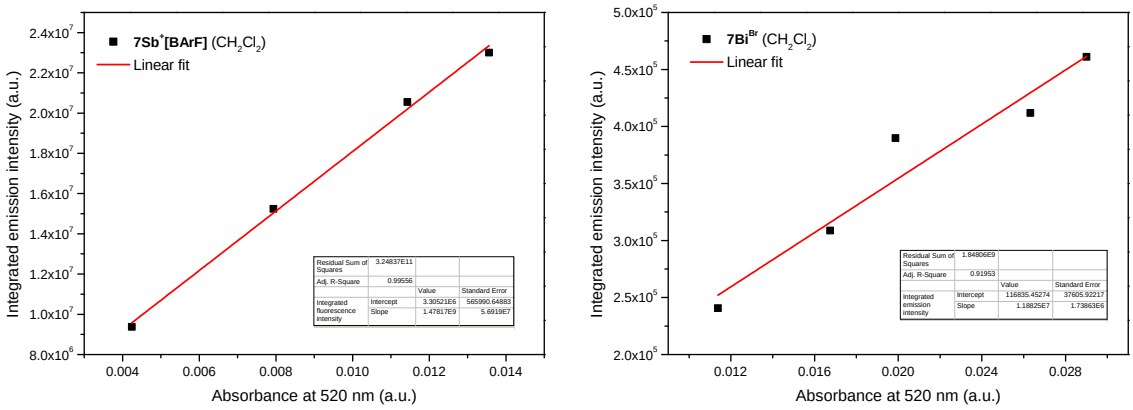


Figure 357: Integrated emission intensities of **7Sb$^+$[BArF]** (left) and **7Bi^{Br}** (right) dilution series in CH_2Cl_2 at 25 °C against absorbance at 520 nm.

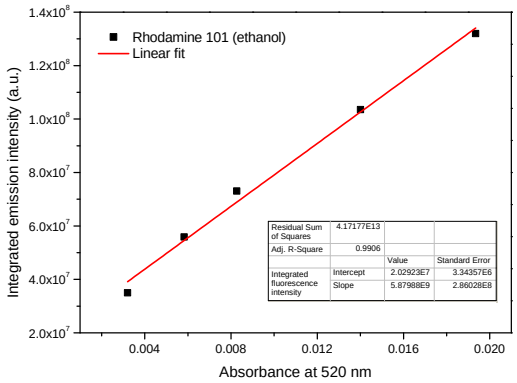


Figure 358: Integrated emission intensities of rhodamine 101 dilution series in ethanol at 25 °C against absorbance at 520 nm.

Chapter 3: Complex stability assessment

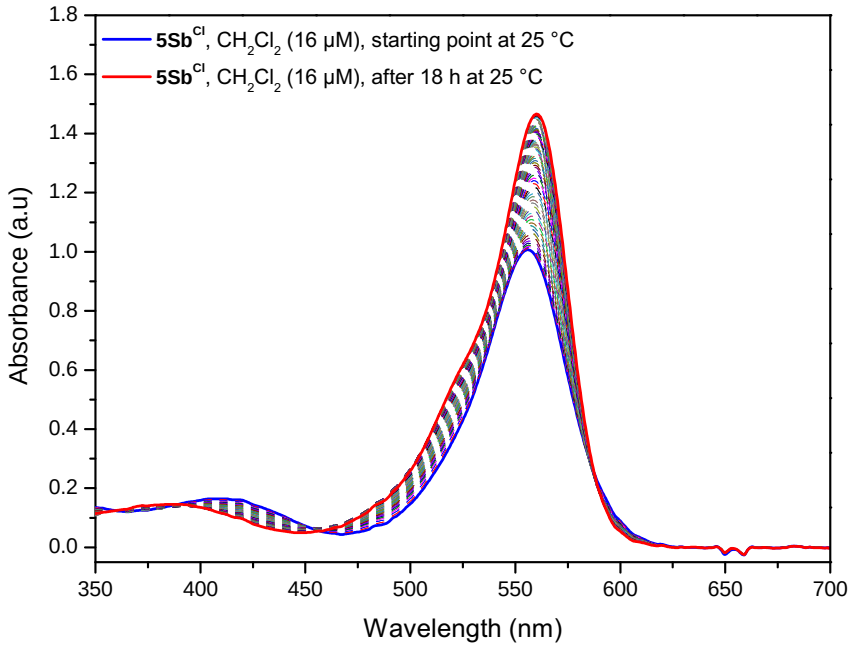


Figure 359: Time-resolved UV/Vis spectra of **5Sb^{Cl}** (16 µM) recorded at 25 °C in CH_2Cl_2 over the course of 18 h.

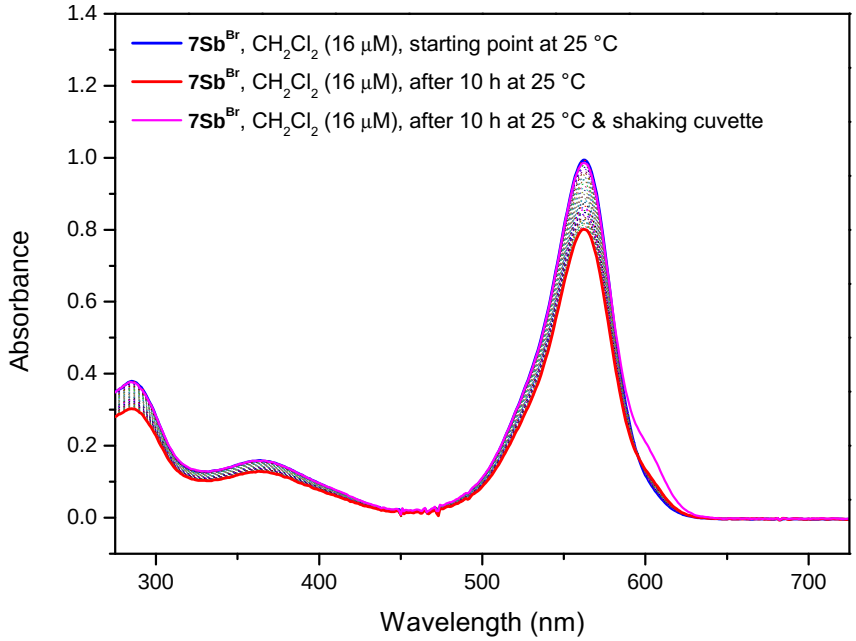


Figure 360: Time-resolved UV/Vis spectra of **7Sb^{Br}** (16 µM) recorded at 25 °C in CH_2Cl_2 over the course of 10 h.

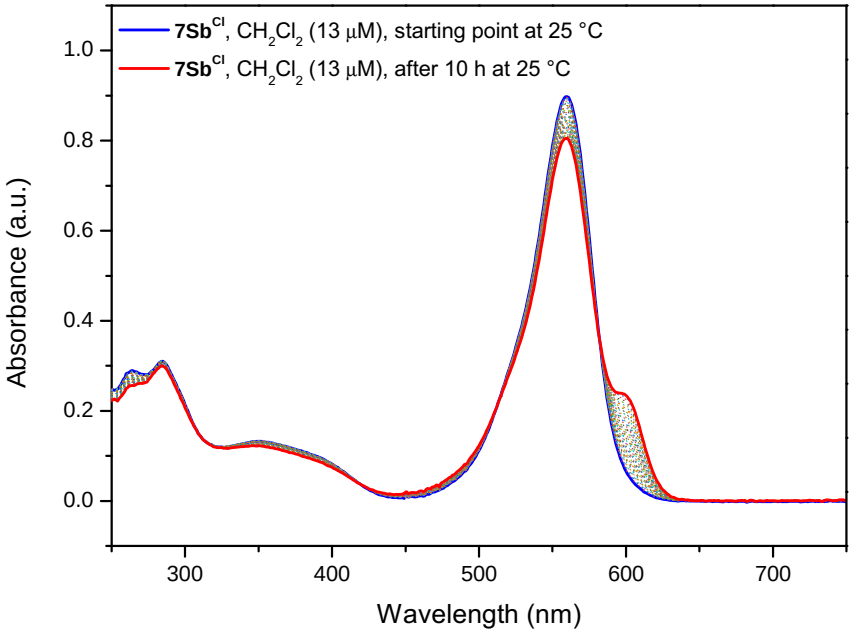


Figure 361: Time-resolved UV/Vis spectra of **7Sb^{Cl}** (13 μM) recorded at 25 °C in CH_2Cl_2 over the course of 10 h.

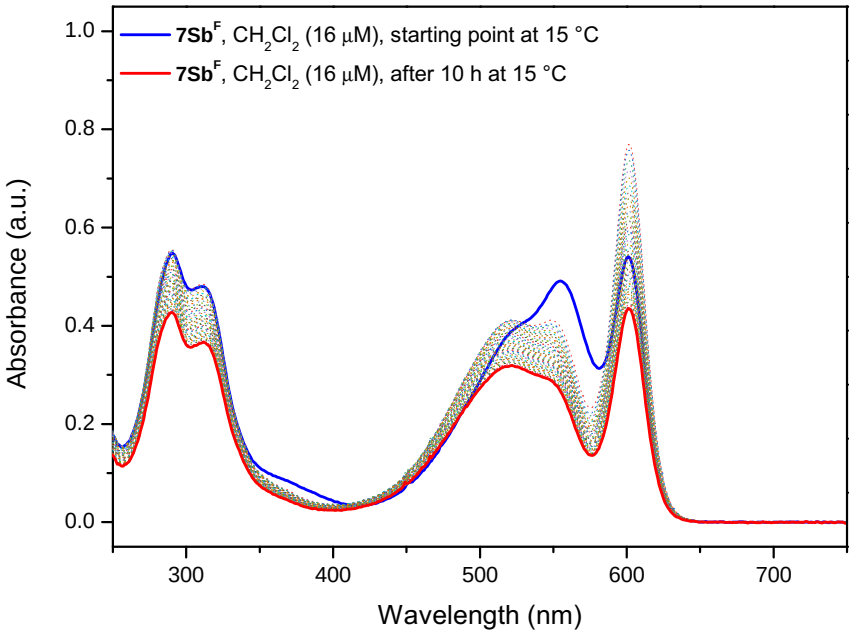


Figure 362: Time-resolved UV/Vis spectra of **7Sb^{F}** (16 μM) recorded at 15 °C in CH_2Cl_2 over the course of 10 h.

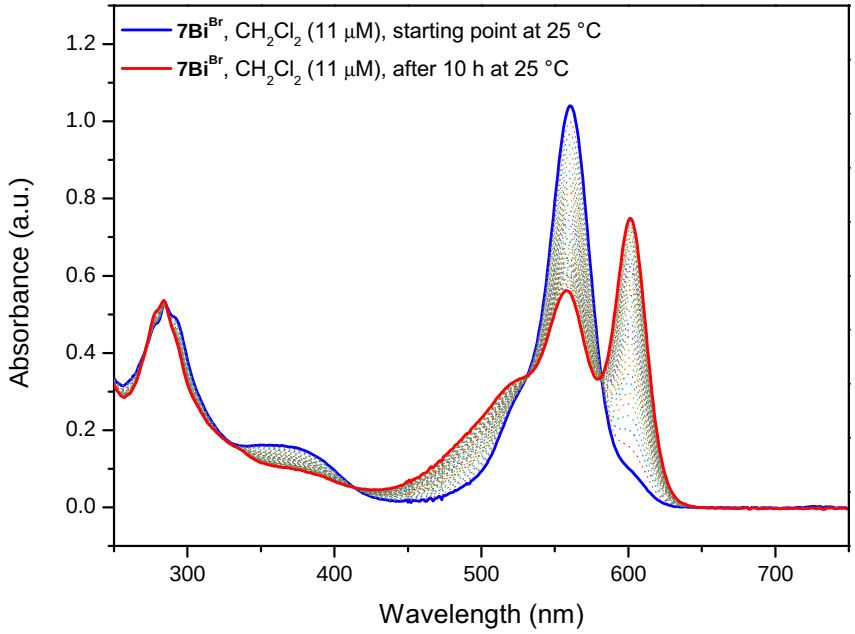


Figure 363: Time-resolved UV/Vis spectra of **7Bi^{Br}** (11 µM) recorded at 25 °C in CH_2Cl_2 over the course of 10 h.

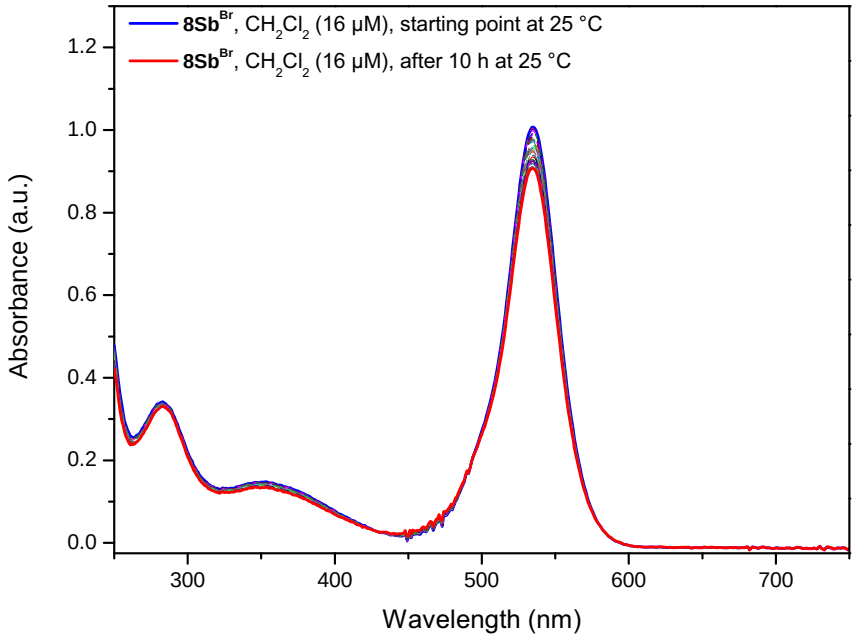


Figure 364: Time-resolved UV/Vis spectra of **8Sb^{Br}** (16 µM) recorded at 25 °C in CH_2Cl_2 over the course of 10 h.

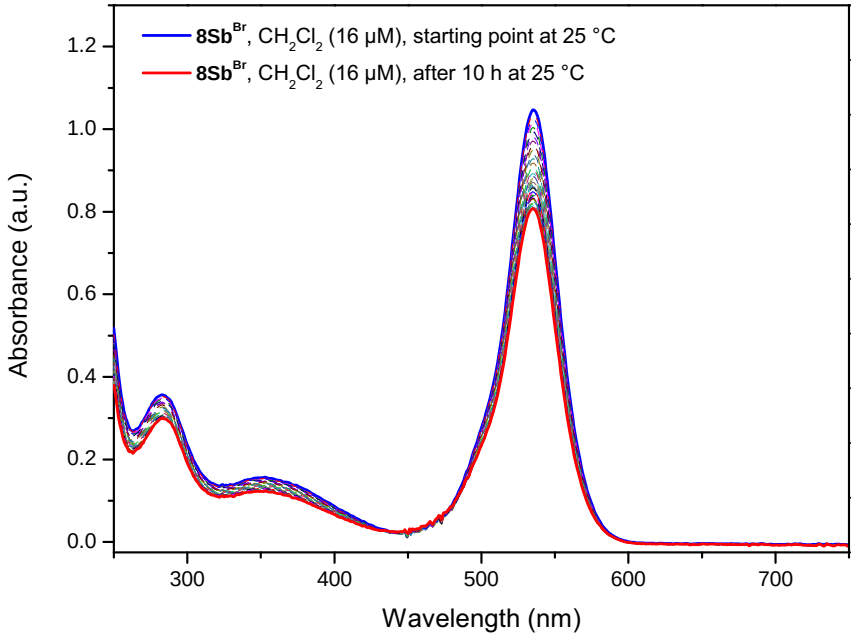


Figure 365: Time-resolved UV/Vis spectra of **8Sb^{Br}** (16 µM) recorded at 15 °C in CH_2Cl_2 over the course of 10 h.

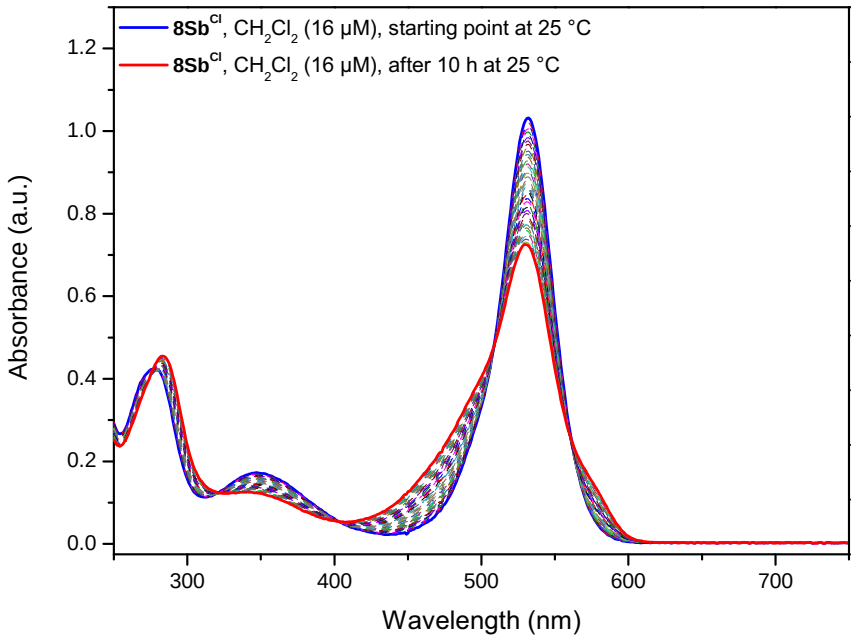


Figure 366: Time-resolved UV/Vis spectra of **8Sb^{Cl}** (16 µM) recorded at 25 °C in CH_2Cl_2 over the course of 10 h.

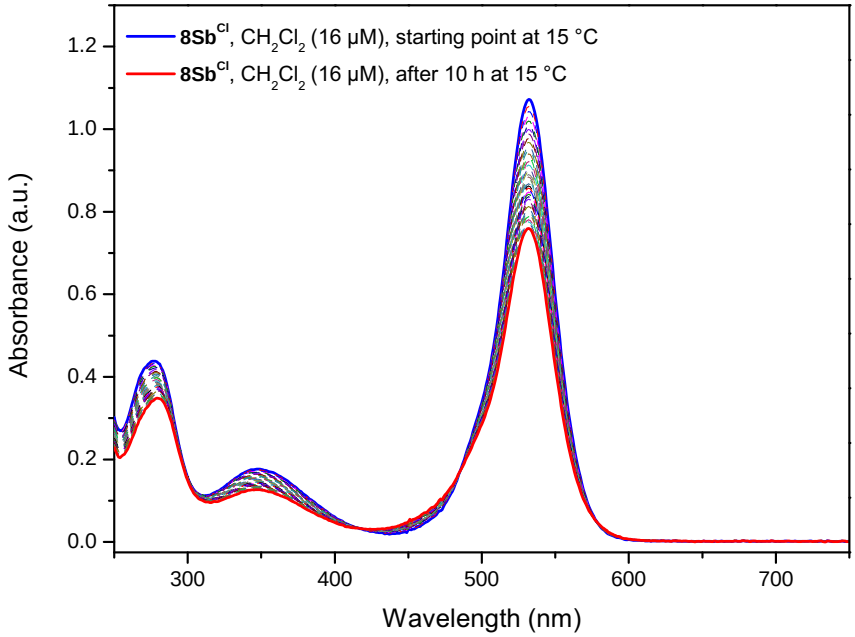


Figure 367: Time-resolved UV/Vis spectra of **8Sb^{Cl}** (16 µM) recorded at 15 °C in CH_2Cl_2 over the course of 10 h.

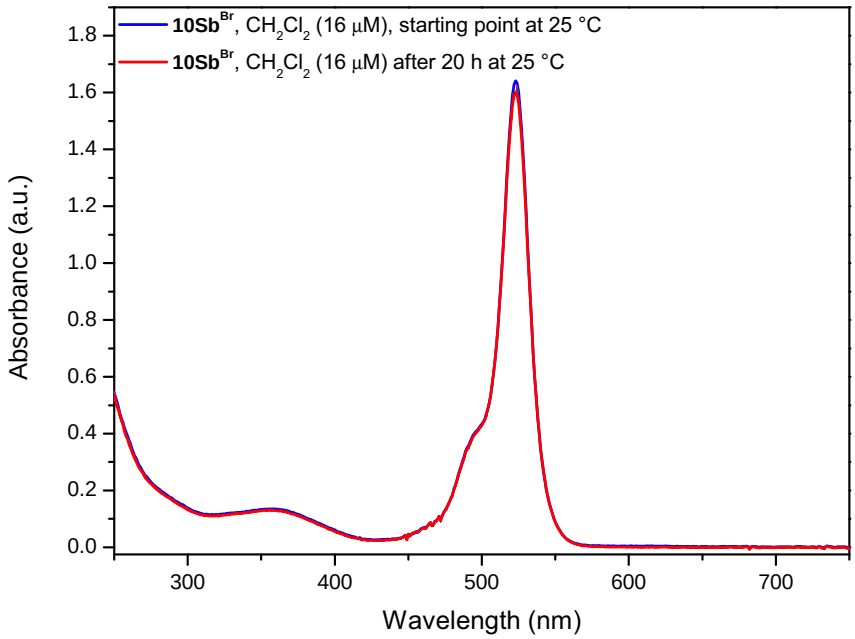


Figure 368: Time-resolved UV/Vis spectra of **10Sb^{Br}** (16 µM) recorded at 25 °C in CH_2Cl_2 over the course of 20 h.

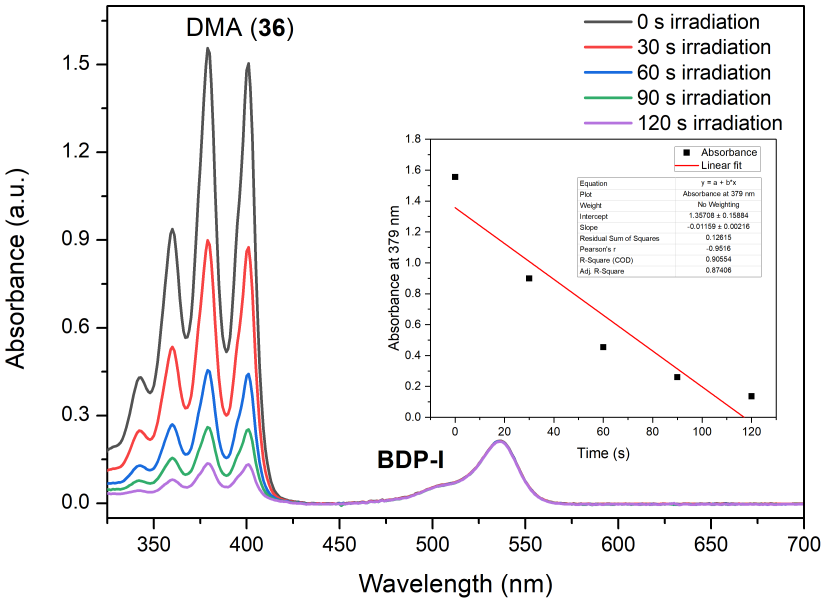


Figure 369: UV/Vis spectra and linear regression analysis of absorbance decrease at 379 nm of 9,10-dimethylanthracene (DMA, **36**) in the presence of **BDP-I** after given irradiation times in toluene at room temperature and under ambient air.

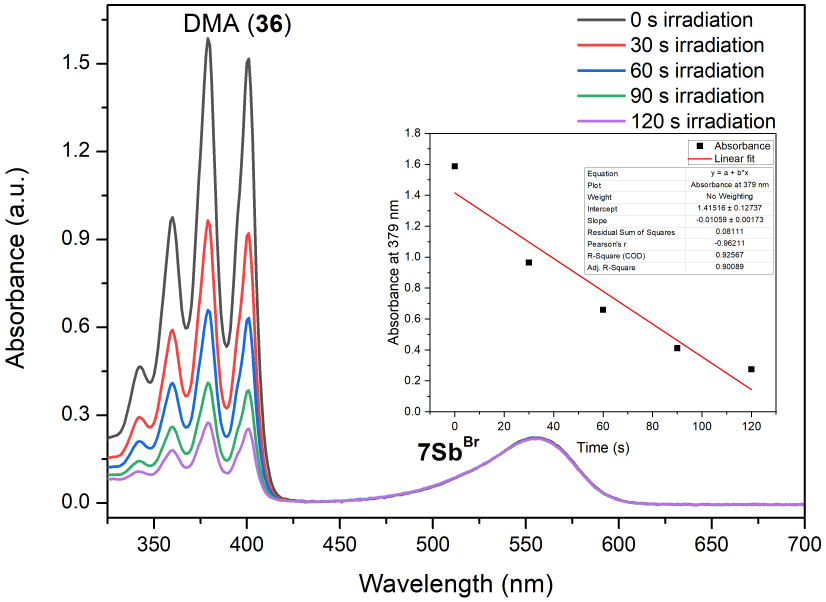


Figure 370: UV/Vis spectra and linear regression analysis of absorbance decrease at 379 nm of 9,10-dimethylanthracene (DMA, **36**) in the presence of **7Sb^{Br}** after given irradiation times in toluene at room temperature and under ambient air.

Chapter 5: Spectroscopic data and titration studies of SBDIPY complexes

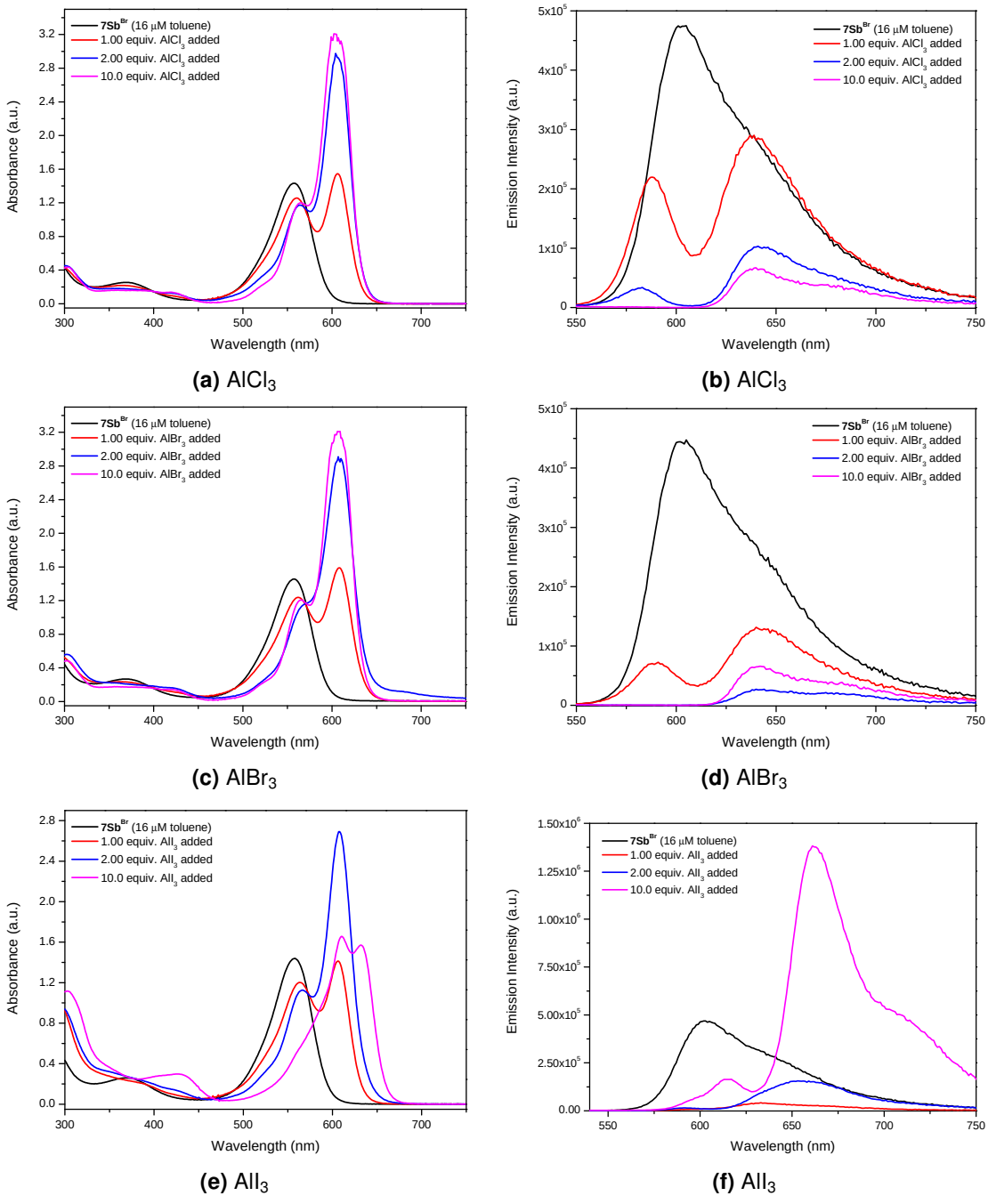


Figure 371: UV/Vis (left) and PL emission spectra (right) upon addition of increasing amounts of $AlCl_3$ (a and b), $AlBr_3$ (c and d) or AlI_3 (e and f) to toluene solutions of **7Sb^{Br}** (16 μM).

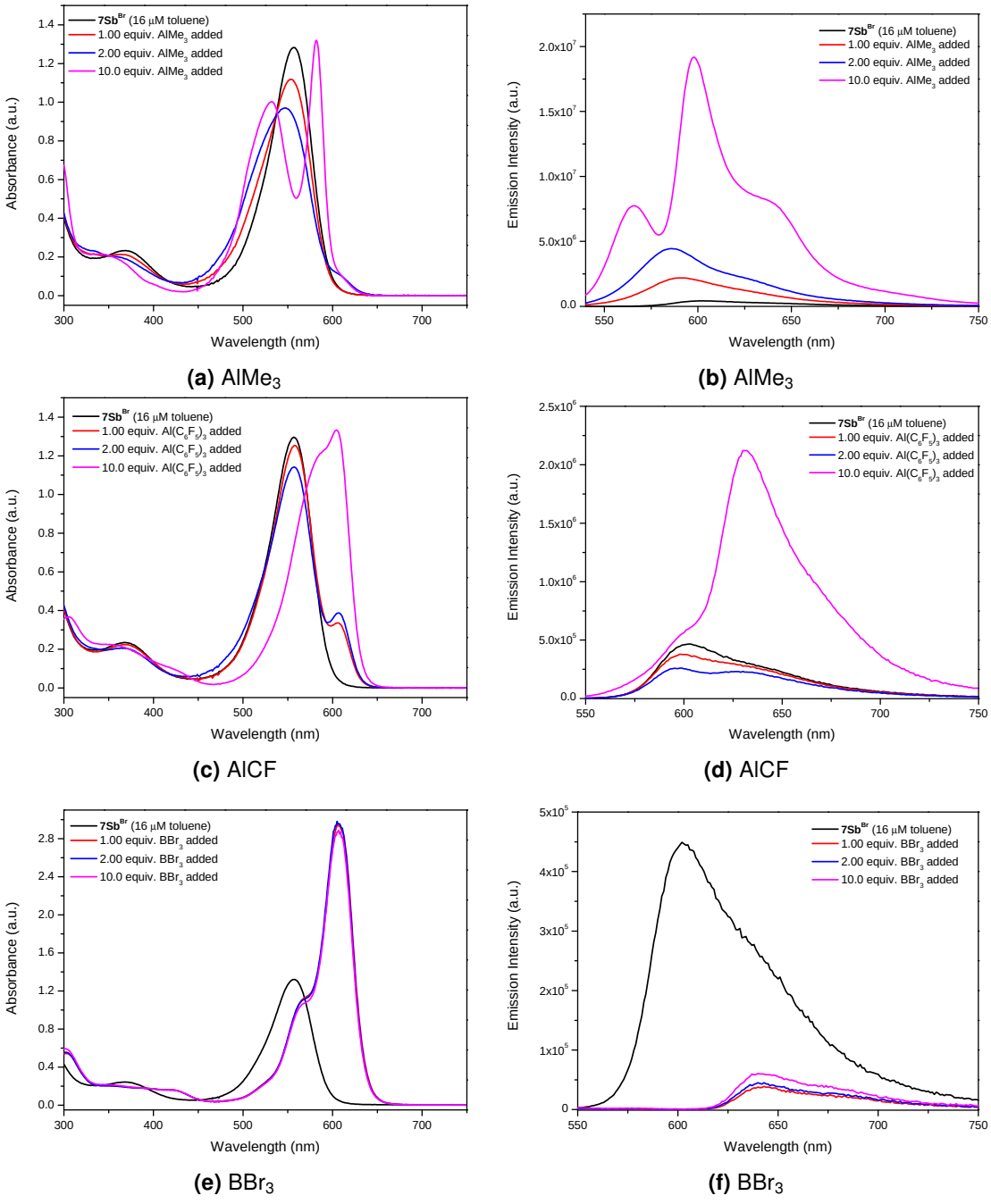


Figure 372: UV/Vis (left) and PL emission spectra (right) upon addition of increasing amounts of $AlMe_3$ (a and b), AlCF (c and d) or BBr_3 (e and f) to toluene solutions of **7Sb^{Br}** (16 μM).

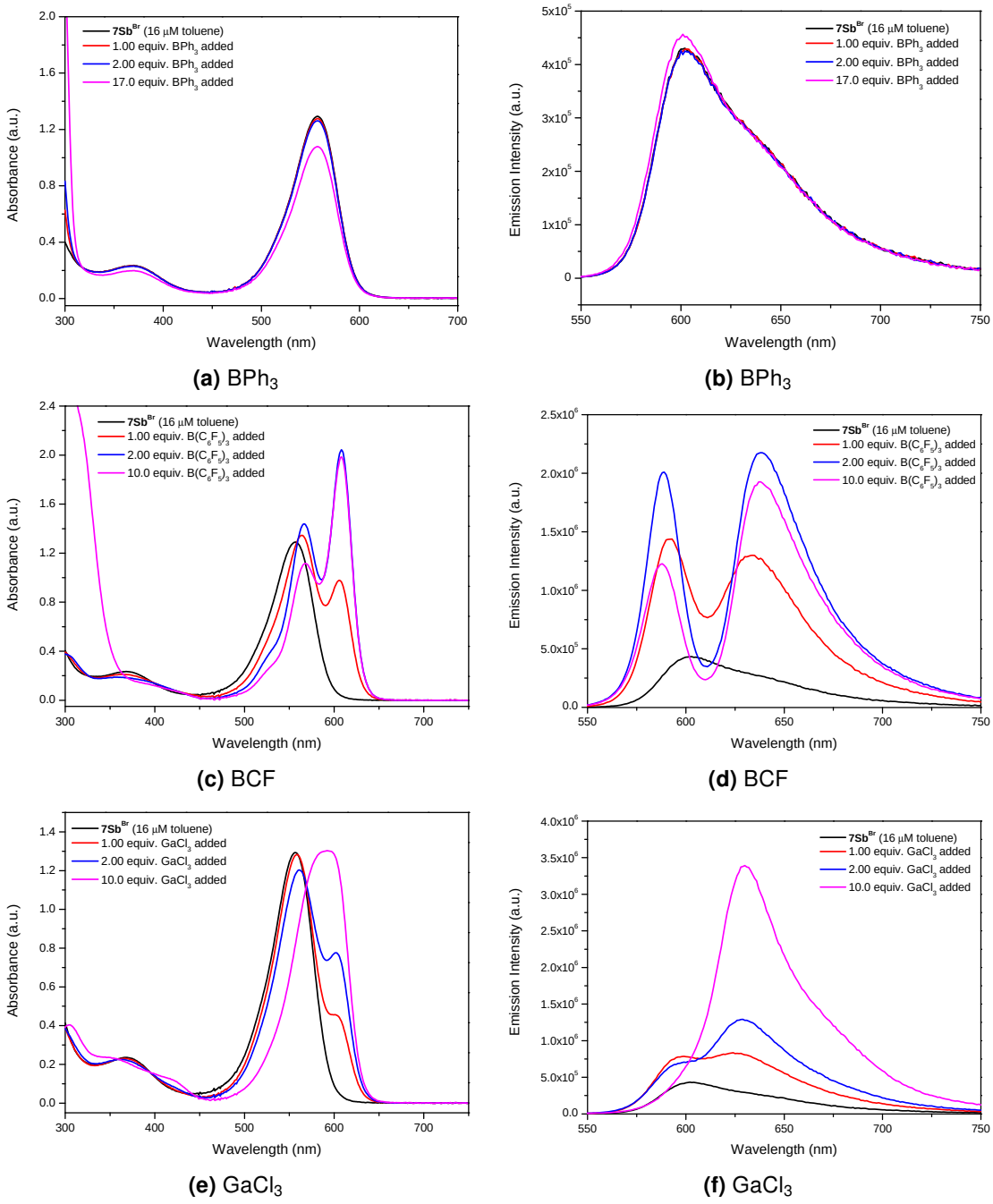
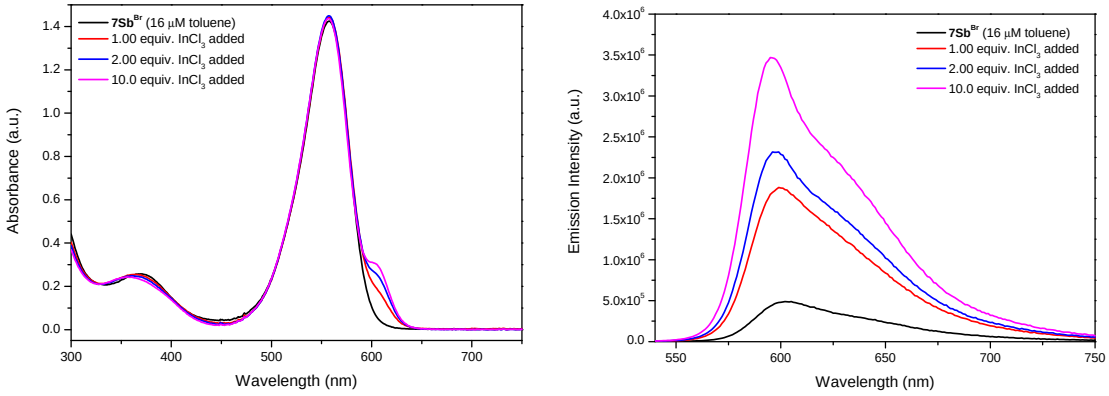
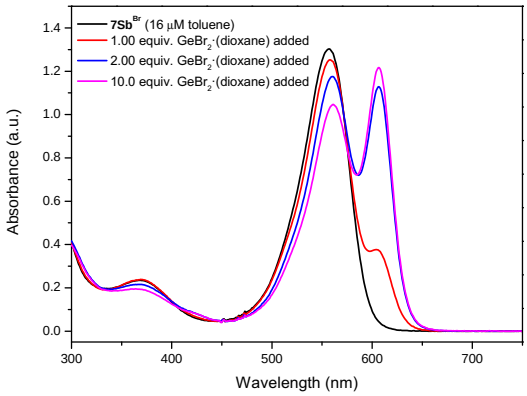


Figure 373: UV/Vis (left) and PL emission spectra (right) upon addition of increasing amounts of BPh_3 (a and b), BCF (c and d) or $GaCl_3$ (e and f) to toluene solutions of **7Sb^{Br}** (16 μM).

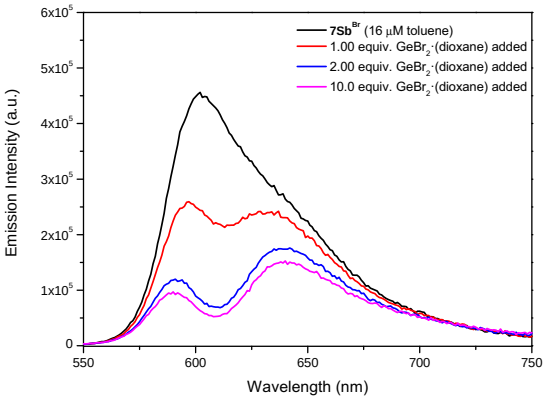


(a) $InCl_3$

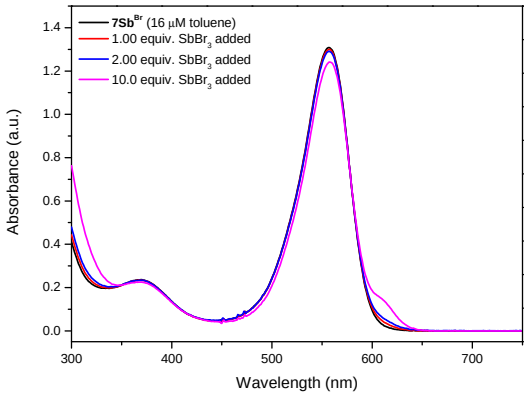
(b) $InCl_3$



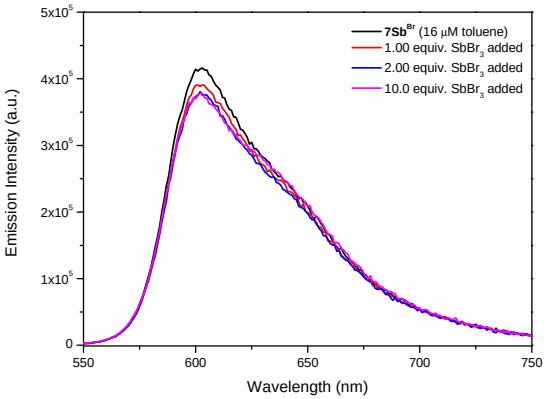
(c) $GeBr_2$·(1,4-dioxane)



(d) $GeBr_2$·(1,4-dioxane)



(e) $SbBr_3$



(f) $SbBr_3$

Figure 374: UV/Vis (left) and PL emission spectra (right) upon addition of increasing amounts of $InCl_3$ (a and b), $GeBr_2$·(1,4-dioxane) (c and d) or $SbBr_3$ (e and f) to toluene solutions of **7Sb^{Br}** (16 μM).

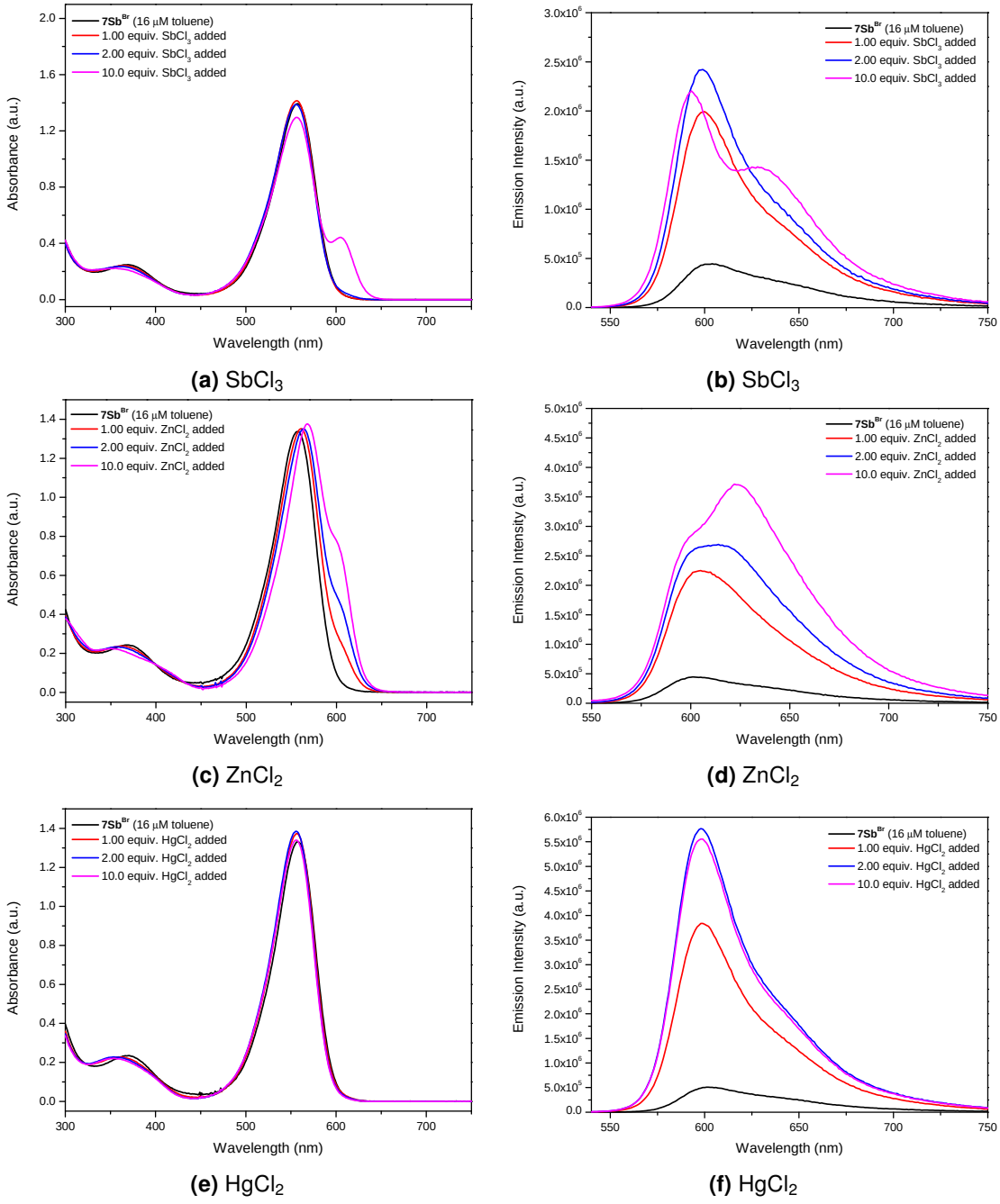
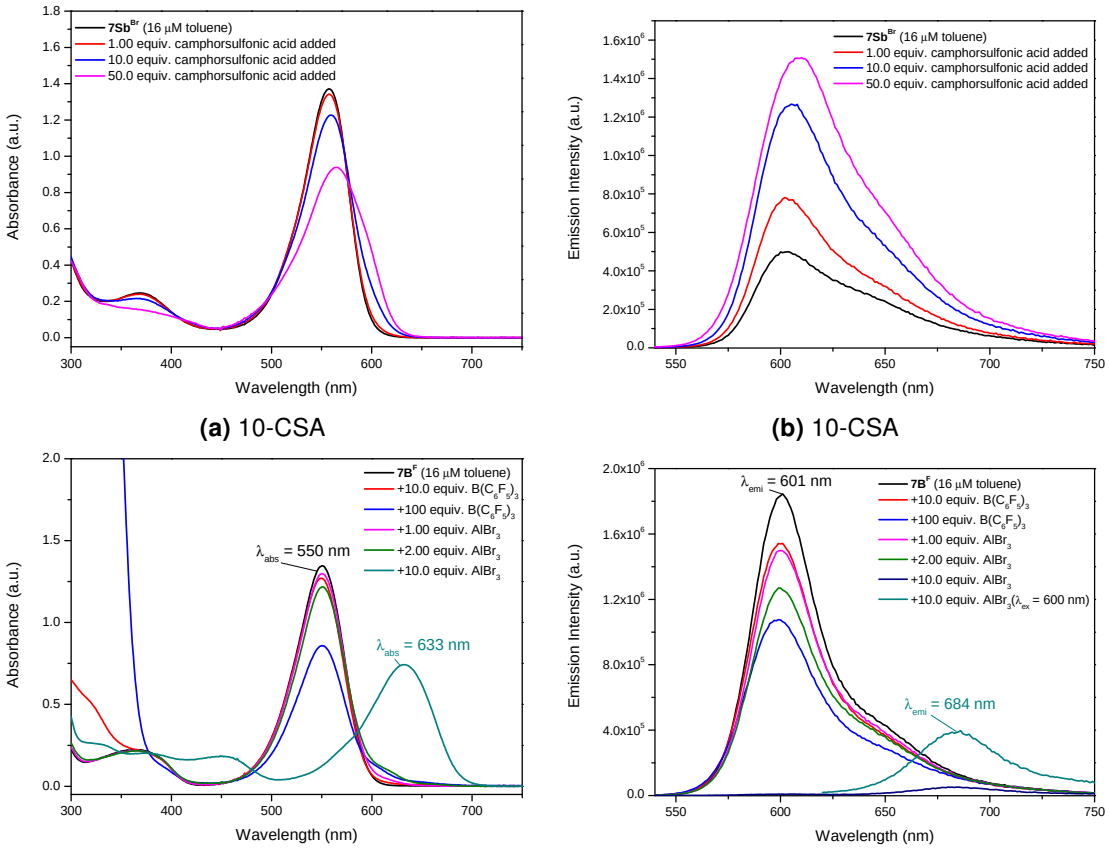


Figure 375: UV/Vis (left) and PL emission spectra (right) upon addition of increasing amounts of $SbCl_3$ (a and b), $ZnCl_2$ (c and d) or $HgCl_2$ (e and f) to toluene solutions of **7Sb^{Br}** (16 μM).



(a) 10-CSA **(b)** 10-CSA

(c) Comparison with **7B^{F}** **(d)** Comparison with **7B^{F}**

Figure 376: UV/Vis (left) and PL emission spectra (right) upon addition of increasing amounts of 10-CSA (a and b) to a toluene solution of **7Sb^{Br}** (16 μM). Spectra upon addition of increasing amounts of BCF or $AlBr_3$ (c and d) to a toluene solution of **7B^{F}** (16 μM).

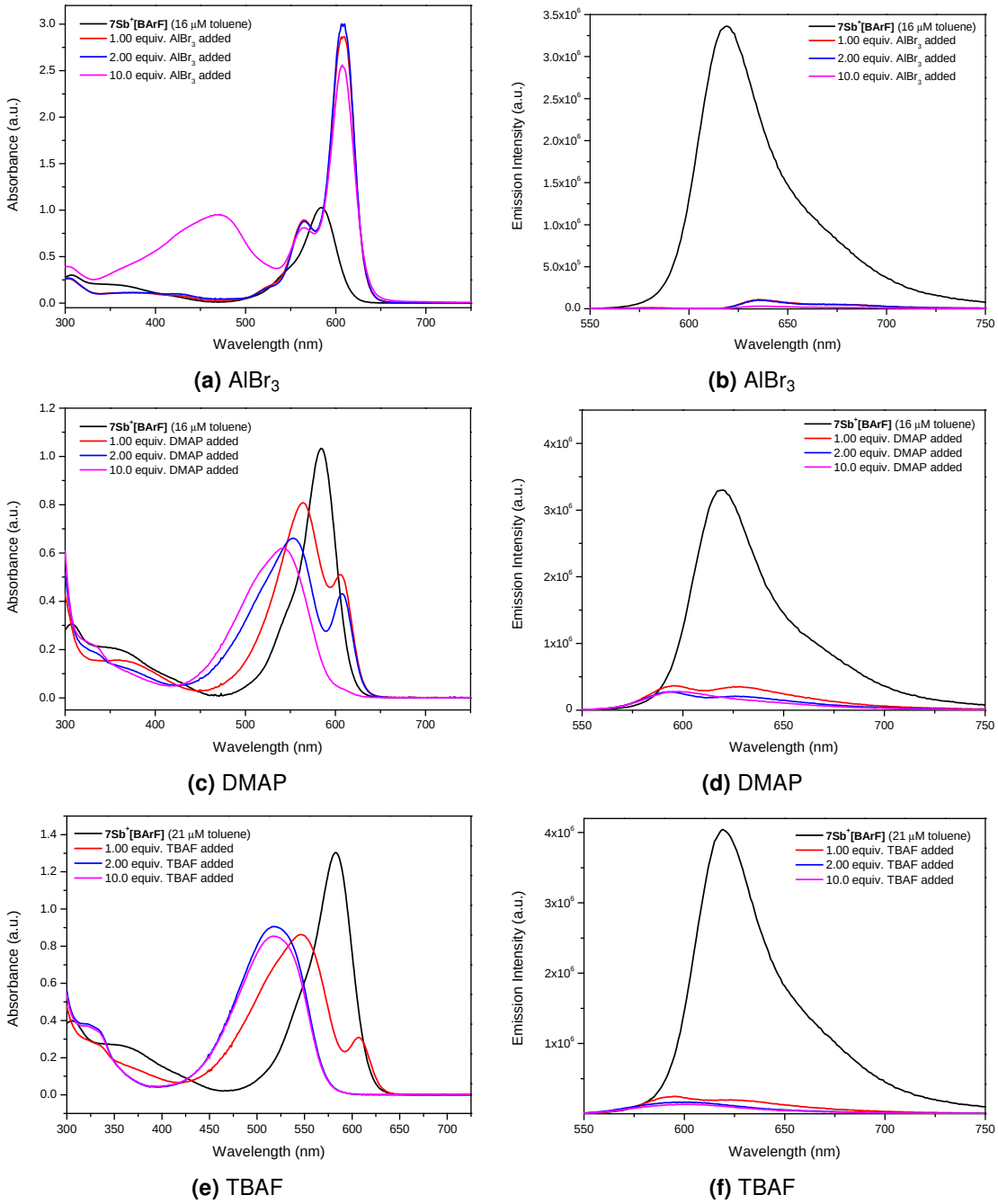


Figure 377: UV/Vis (left) and PL emission spectra (right) upon addition of increasing amounts of $AlBr_3$ (a and b), 4-dimethylaminopyridine (c and d) or tetrabutylammonium fluoride (e and f) to toluene solutions of **7Sb$^+$[BArF]** (16 μM or 21 μM).

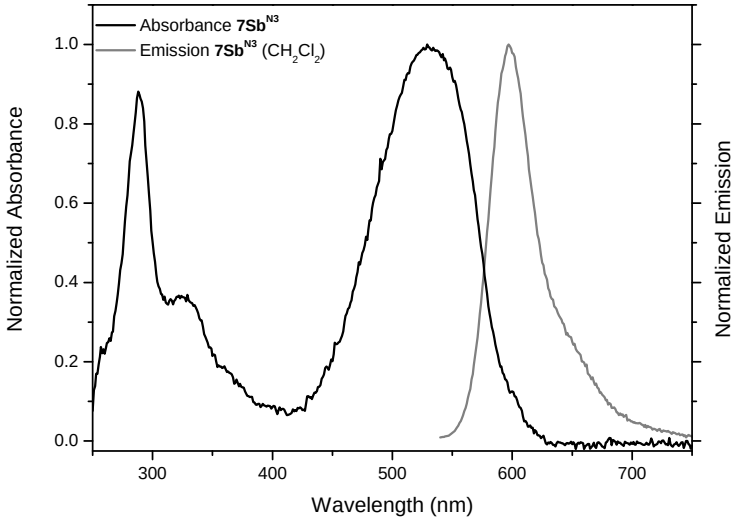


Figure 378: Normalized absorbance and PL emission (λ_{exc} = 520 nm) spectra of **7Sb^{N3}** in CH_2Cl_2 at 25 °C.

V. Appendix: Electrochemical data

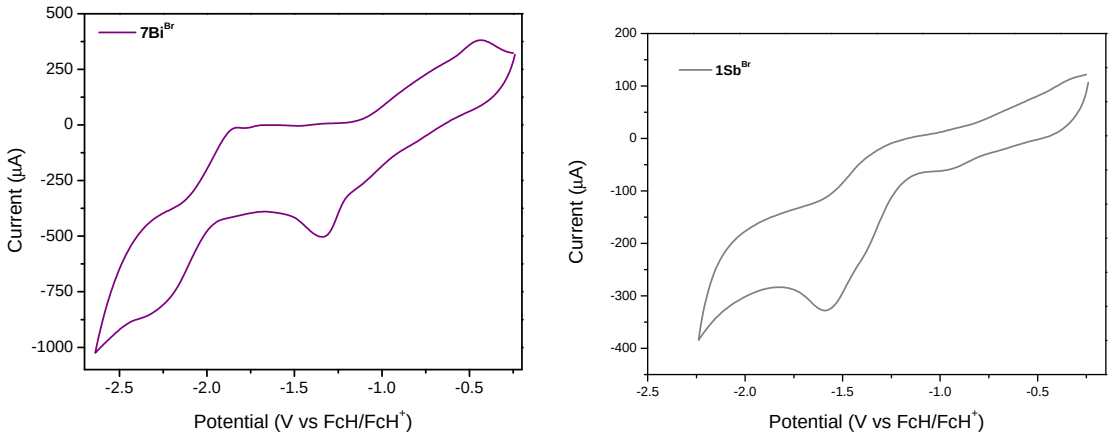


Figure 379: Cyclic voltammograms of **7Bi^{Br}** (left) and **1Sb^{Br}** (right). All measurements were conducted at a 1 mM analyte concentration in a CH_2Cl_2 solution of $TBAPF_6$ (0.1 M) using a scan rate of 100 mV/s.

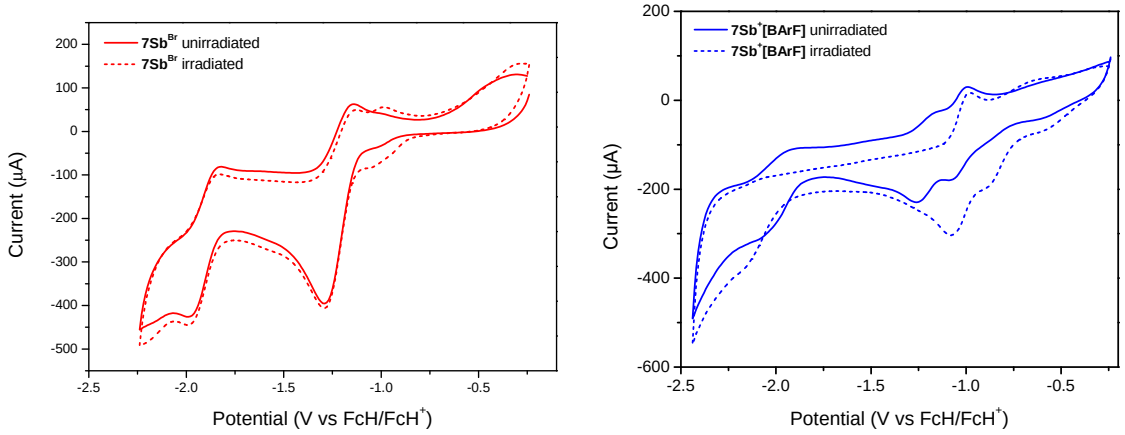


Figure 380: Cyclic voltammograms of **7Sb^{Br}** (left) and **7Sb^{+}[BArF]** (right) with (dashed line) and without (solid line) irradiation with a 521 nm LED reactor. All measurements were conducted at a 1 mM analyte concentration in a CH_2Cl_2 solution of $TBAPF_6$ (0.1 M) using a scan rate of 100 mV/s.

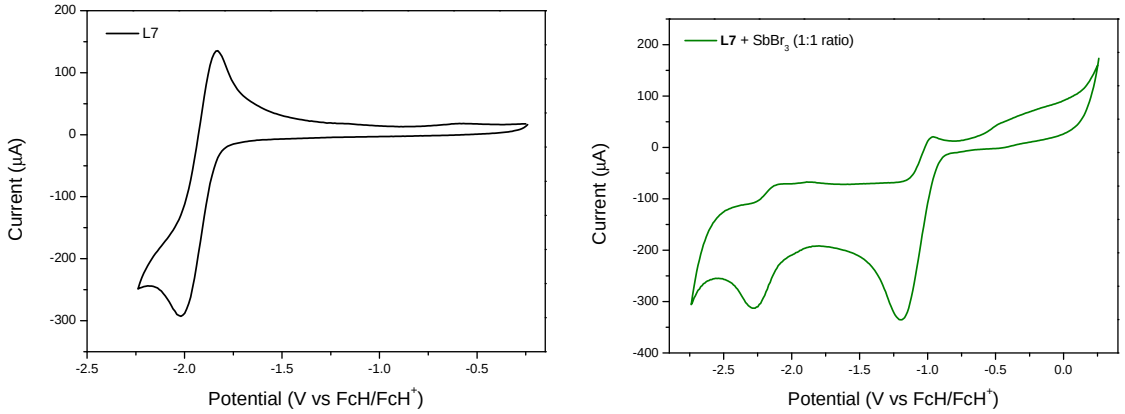


Figure 381: Cyclic voltammograms of **L7** (left) and a 1:1 mixture of **L7** and $SbBr_3$ (right). All measurements were conducted at a 1 mM analyte concentration in a CH_2Cl_2 solution of $TBAPF_6$ (0.1 M) using a scan rate of 100 mV/s.

VI. Appendix: X-ray crystallographic data

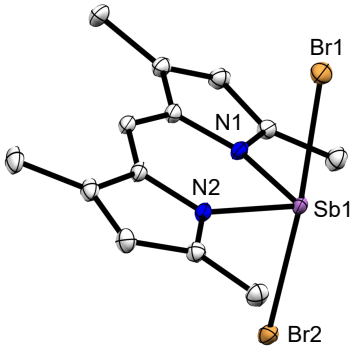


Figure 382: X-ray solid-state structure of **1Sb^{Br}** with thermal ellipsoids were set to a 50% probability level. Hydrogen atoms were omitted for clarity. Bromine atoms are shown in orange, carbon atoms in grey, nitrogens in blue and antimony in dark magenta. Hydrogen atoms were omitted for clarity. Selected bond lengths [Å] Sb1−Br1 2.7464(2), Sb1−Br2 2.7193(3), Sb1−N2 2.0822(17), Sb1−N1 2.0850(17) and bond angles [°] Br2−Sb1−Br1 175.197(7), N2−Sb1−Br1 90.75(5), N2−Sb1−Br2 87.00(5), N1−Sb1−N2 86.39(7).

Table 23: Crystallographic data and structure refinement of **1Sb^{Br}** (Figure 382).

Empirical formula	$C_{13}H_{15}Br_2N_2Sb$	Index ranges	$-27 \leq h \leq 27$
Formula weight	480.84		$-18 \leq k \leq 17$
Temperature (K)	100.00		$-17 \leq l \leq 11$
Crystal system	monoclinic	Reflections collected	49573
Space group (number)	Cc (9)	Independent reflections	5708
a (Å)	17.2704(8)		R_{int} = 0.0238
b (Å)	12.0396(6)		R_{sigma} = 0.0131
c (Å)	7.6022(3)	Completeness to	
α (°)	90	Θ = 25.242°	100.0%
β (°)	108.934(2)	Data / Restraints / Parameters	5708/2/168
γ (°)	90	Goodness-of-fit on F^2	1.033
Volume (Å^3)	1495.19(12)	Final R indices	R_1 = 0.0137
Z	4	[I$\geq 2\sigma$(I)]	wR_2 = 0.0330
ρ_{calc} (gcm^{-3})	2.136	Final R indices	R_1 = 0.0141
μ (mm^{-1})	7.175	[all data]	wR_2 = 0.0332
F(000)	912	Largest peak/hole [eÅ^{-3}]	0.31/−0.45
Crystal size (mm^3)	0.394×0.209×0.02	Flack X parameter	0.164(4)
Crystal colour	yellow	Internal ID (crystallographer)	1724 (CG)
Crystal shape	plate	CCDC number	**2241583**
Radiation	MoK_α (λ = 0.71073 Å)		
2Θ range (°)	4.20 to 68.17 (0.63 Å)		

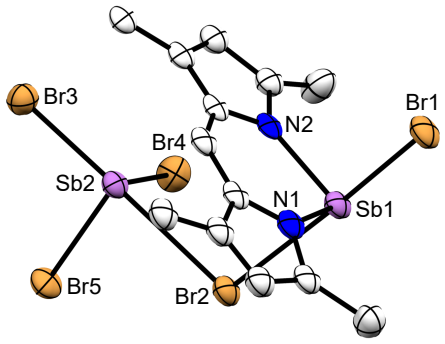


Figure 383: X-ray solid-state structure of **1Sb·SbBr$_3$**. Thermal ellipsoids were set to a 50% probability level. Hydrogen atoms were omitted for clarity. Bromine atoms are shown in orange, carbon atoms in grey, nitrogen in blue and antimony in dark magenta. Selected bond lengths [Å] Sb1−Br1 2.546(3), Sb1−Br2 3.019(3), Sb1−N1 2.10(3), Sb1−N2 2.09(2), Sb2−Br3 2.559(4), Sb2−Br4 2.565(4), Sb2−Br5 2.504(4) and bond angles [°] Br1−Sb1−Br2 174.00(13), N1−Sb1−Br1 90.4(6), N1−Sb1−Br2 83.8(6), N2−Sb1−N1 86.7(10), Br3−Sb2−Br4 95.56(13), Br3−Sb2−Br4 93.93(13), Br5−Sb2−Br4 93.37(13).

Table 24: Crystallographic data and structure refinement of **1Sb·SbBr$_3$** (Figure 383).

Empirical formula	$C_{13}H_{15}Br_5N_2Sb_2$		
Formula weight	842.32	2Θ range (°)	4.83 to 51.998
Temperature (K)	102	Completeness to Θ	99.9%
Crystal system	triclinic	Index ranges	$-14 \leq h \leq 14$
Space group (number)	P-1		$-14 \leq k \leq 14$
a (Å)	11.6718(16)		$0 \leq l \leq 19$
b (Å)	11.8853(14)		
c (Å)	15.5460(18)	Reflections collected	8401
α (°)	83.332(4)	Independent reflections	8401
β (°)	79.146(4)		R_{int} = ?
γ (°)	86.567(4)		R_{sigma} = 0.2232
Volume (Å^3)	2102.1(5)	Data / Restraints / Parameters	8401/342/406
Z	4	Goodness-of-fit on F^2	1.048
ρ_{calc} (gcm^{-3})	2.662	Final R indices	R_1 = 0.1018
μ (mm^{-1})	12.071	[I$\geq 2\sigma$(I)]	wR_2= 0.2233
F(000)	1536	Final R indices	R_1 = 0.2207
Crystal size (mm^3)	0.04×0.02×0.02	[all data]	wR_2 = 0.2913
Crystal habitus	clear dark red plank	Largest peak/hole [eÅ^{-3}]	3.38/−1.94
Absorption correction	multi-scan	Internal ID (crystallographer)	8558f (GS)
Tmin; Tmax	0.5071; 0.7458		
Radiation	MoK_α (λ=0.71073 Å)	device type	Bruker D8 Venture

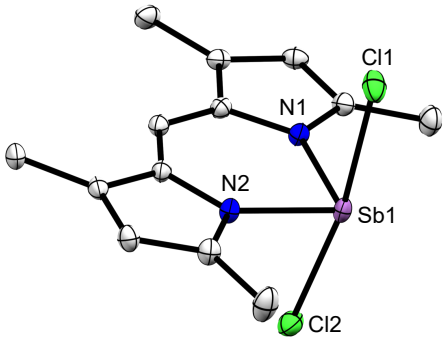


Figure 384: X-ray solid-state structure of **1Sb^{Cl}** with thermal ellipsoids were set to a 50% probability level. Hydrogen atoms were omitted for clarity. Chlorine atoms are shown in green, carbon atoms in grey, nitrogen in blue and antimony in dark magenta. Hydrogen atoms were omitted for clarity. Selected bond lengths [Å] Sb1−Cl1 2.5887(3), Sb1−Cl2 2.5298(3), Sb1−N2 2.0788(8), Sb1−N1 2.0860(8) and bond angles [°] Cl2−Sb1−Cl1 170.663(9), N2−Sb1−Cl1 85.70(2), N2−Sb1−Cl2 86.46(2), N1−Sb1−N2 88.20(3).

Table 25: Crystallographic data and structure refinement of **1Sb^{Cl}** (Figure 385).

Empirical formula	$C_{13}H_{15}Cl_2N_2Sb$	Index ranges	$-17 \leq h \leq 17$
Formula weight	391.92		$-16 \leq k \leq 16$
Temperature (K)	100.00		$-22 \leq l \leq 22$
Crystal system	monoclinic	Reflections collected	67080
Space group (number)	$P2_1/c$ (14)	Independent reflections	6547
a (Å)	10.7292(5)		R_{int} = 0.0193
b (Å)	9.9358(6)		R_{sigma} = 0.0101
c (Å)	13.9550(7)	Completeness to	
α (°)	90	Θ = 25.242°	99.9%
β (°)	91.646(2)	Data / Restraints / Parameters	6547/4/168
γ (°)	90	Goodness-of-fit on F^2	1.094
Volume (Å^3)	1487.03(14)	Final R indices	R_1 = 0.0151
Z	4	[I$\geq 2\sigma$(I)]	wR_2= 0.0368
ρ_{calc} (gcm^{-3})	1.751	Final R indices	R_1 = 0.0176
μ (mm^{-1})	2.199	[all data]	wR_2 = 0.0379
F(000)	768	Largest peak/hole [eÅ^{-3}]	0.54/−0.40
Crystal size (mm^3)	0.149×0.119×0.111		
Crystal colour	red	Internal ID (crystallographer)	1555 (CG)
Crystal shape	block	CCDC number	**2241590**
Radiation	MoK_α (λ = 0.71073 Å)		
2Θ range (°)	3.80 to 71.19 (0.61 Å)		

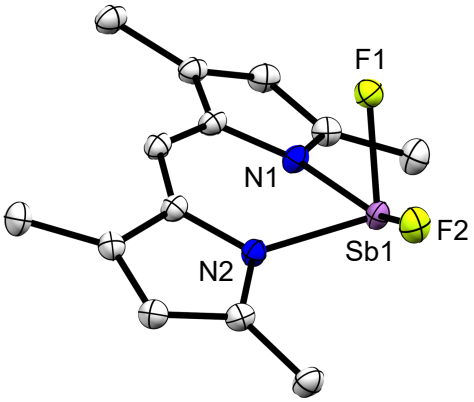


Figure 385: X-ray solid-state structure of **1Sb^{F}** with thermal ellipsoids were set to a 50% probability level. Hydrogen atoms were omitted for clarity. Fluorine atoms are shown in lime green, carbon atoms in grey, nitrogen in blue and antimony in dark magenta. Hydrogen atoms were omitted for clarity.

Table 26: Selected bond lengths and angles for **1Sb^{F}** (Figure 385). Uncertainties are displayed as standard deviation in parentheses.

Bond	Length (Å)	Bonds	Angle (°)
Sb1−F1	1.9411(11)	F1−Sb1−F1'	170.663(9)
Sb1−F1'	2.8619(11)	F1−Sb1−F2	85.70(2)
Sb1−F2	1.9943(11)	F1−Sb1−N1	86.46(2)
Sb1−N1	2.2488(15)	F1−Sb1−N2	88.20(3)
Sb1−N2	2.0975(15)	F2−Sb1−N1	153.01(5)
		F2−Sb1−N2	85.30(5)
		N2−Sb1−N1	81.10(6)

Table 27: Crystallographic data and structure refinement of **1Sb^{F}** (Figure 385).

Empirical formula	$C_{13}H_{15}F_2N_2Sb$	Index ranges	$-11 \leq h \leq 11$
Formula weight	359.02		$-12 \leq k \leq 12$
Temperature (K)	100.00		$-13 \leq l \leq 13$
Crystal system	triclinic	Reflections collected	18096
Space group (number)	$P\bar{1}$ (2)	Independent reflections	3824
a (Å)	8.0025(9)		R_{int} = 0.0297
b (Å)	8.9517(8)		R_{sigma} = 0.0235
c (Å)	9.5870(10)	Completeness to	
α (°)	68.099(4)	Θ = 25.242°	100.0%
β (°)	79.046(4)	Data / Restraints / Parameters	3824/0/167
γ (°)	82.806(3)	Goodness-of-fit on F^2	1.081
Volume (Å^3)	624.49(11)	Final R indices	R_1 = 0.0194
Z	2	[I$\geq 2\sigma$(I)]	wR_2= 0.0446
ρ_{calc} (gcm^{-3})	1.909	Final R indices	R_1 = 0.0225
μ (mm^{-1})	2.217	[all data]	wR_2 = 0.0460
F(000)	352	Largest peak/hole [eÅ^{-3}]	0.63/$-$0.37
Crystal size (mm^3)	0.096$\times$0.079$\times$0.028		
Crystal colour	red	Internal ID (crystallographer)	1730 (CG)
Crystal shape	block	CCDC number	**2241582**
Radiation	MoK_α (λ = 0.71073 Å)		
2Θ range (°)	4.64 to 61.05 (0.70 Å)		

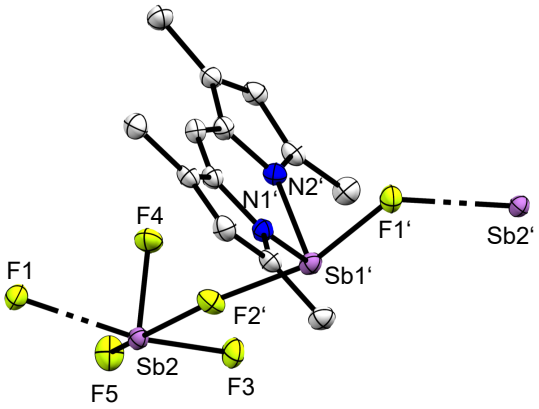


Figure 386: X-ray solid-state structure of SbF_3-adduct of **1Sb^{F}** with thermal ellipsoids were set to a 50% probability level. Hydrogen atoms were omitted for clarity. Fluorine atoms are shown in lime green, carbon atoms in grey, nitrogen in blue and antimony in dark magenta. Hydrogen atoms were omitted for clarity.

Table 28: Selected bond lengths and angles for SbF_3-adduct of **1Sb^F** (Figure 386). Uncertainties are displayed as standard deviation in parentheses.

Bond	Length (Å)	Bonds	Angle (°)
Sb1'−F1'	2.098(2)	F2'−Sb1'−F'1	160.35(7)
Sb1'−F2'	2.067(2)	F2'−Sb1'−N1'	84.67(10)
Sb1'−N1'	2.068(3)	N2'−Sb1'−F2'	81.80(10)
Sb1'−N2'	2.061(3)	N2'−Sb1'−N1'	89.28(10)
Sb2−F1	2.455(3)	F1−Sb2−F2'	116.21(6)
Sb2−F2'	2.467(3)	F3−Sb2−F1	157.92(7)
Sb2−F3	1.945(2)	F3−Sb2−F2	77.34(8)
Sb2−F4	1.914(3)	F4−Sb2−F1	77.68(7)
Sb2−F5	1.935(3)	Sb1'−F1'−Sb2'	132.09(8)

Table 29: Crystallographic data and structure refinement of SbF_3-adduct of **1Sb^F** (Figure 386).

Empirical formula	$C_{13}H_{15}F_5N_2Sb_2$	Index ranges	$-15 \leq h \leq 16$
Formula weight	537.77		$-14 \leq k \leq 14$
Temperature (K)	100.00		$-18 \leq l \leq 19$
Crystal system	monoclinic	Reflections collected	27595
Space group (number)	$P2_1/n$ (14)	Independent reflections	4257
a (Å)	11.474(11)		R_{int} = 0.0333
b (Å)	10.537(10)		R_{sigma} = 0.0223
c (Å)	13.353(13)	Completeness to	
α (°)	90	Θ = 25.242°	100.0%
β (°)	104.31(3)	Data / Restraints / Parameters	4257/0/203
γ (°)	90	Goodness-of-fit on F^2	1.042
Volume (Å^3)	1564(3)	Final R indices	R_1 = 0.0231
Z	4	[I$\geq 2\sigma$(I)]	wR_2= 0.0507
ρ_{calc} (gcm^{-3})	2.283	Final R indices	R_1 = 0.0280
μ (mm^{-1})	3.502	[all data]	wR_2 = 0.0535
F(000)	1016	Largest peak/hole [eÅ^{-3}]	0.89/−0.96
Crystal size (mm^3)	0.161×0.106×0.02		
Crystal colour	orange	Internal ID (crystallographer)	1782 (CG)
Crystal shape	plate		
Radiation	MoK_α (λ=0.71073 Å)		
2Θ range (°)	4.20 to 60.99 (0.70 Å)		

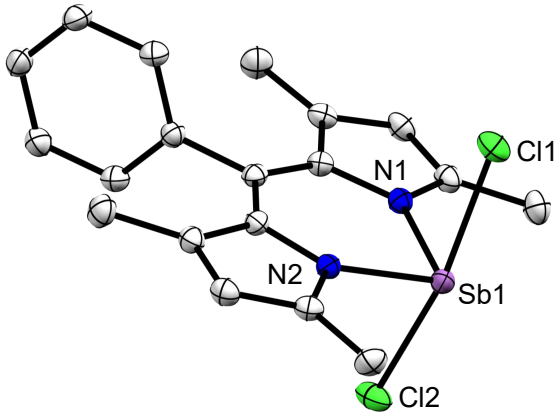


Figure 387: X-ray solid-state structure of **2Sb^{Cl}** with thermal ellipsoids were set to a 50% probability level. Hydrogen atoms were omitted for clarity. Chlorine atoms are shown in green, carbon atoms in grey, nitrogen in blue and antimony in dark magenta. Hydrogen atoms were omitted for clarity. Selected bond lengths [Å] Sb1−Cl1 2.5826(5), Sb1−Cl2 2.5197(5), Sb1−N1 2.0626(14), Sb1−N2 2.0589(14) and bond angles [°] Cl2−Sb1−Cl1 170.113(17), N2−Sb1−Cl1 88.29(4), N2−Sb1−Cl2 86.80(4), N2−Sb1−N1 88.02(5).

Table 30: Crystallographic data and structure refinement of **2Sb^{Cl}** (Figure 387).

Empirical formula	$C_{19}H_{19}Cl_2N_2Sb$	Index ranges	$-17 \leq$ h ≤ 17
Formula weight	468.01		$-11 \leq$ k ≤ 9
Temperature (K)	100.00		$-27 \leq$ l ≤ 27
Crystal system	monoclinic	Reflections collected	45683
Space group (number)	$P2_1/n$ (14)	Independent reflections	5660
a (Å)	12.4279(6)		R_{int} = 0.0310
b (Å)	7.8441(4)		R_{sigma} = 0.0188
c (Å)	19.0889(10)	Completeness to	
α (°)	90	Θ = 25.242°	100.0%
β (°)	96.771(2)	Data / Restraints / Parameters	5660/0/221
γ (°)	90	Goodness-of-fit on F^2	1.063
Volume (Å^3)	1847.92(16)	Final R indices	R_1 = 0.0224
Z	4	[I$\geq 2\sigma$(I)]	wR_2= 0.0461
ρ_{calc} (gcm^{-3})	1.682	Final R indices	R_1 = 0.0288
μ (mm^{-1})	1.785	[all data]	wR_2 = 0.0487
F(000)	928	Largest peak/hole [eÅ^{-3}]	0.49/−0.53
Crystal size (mm^3)	0.183×0.09×0.034		
Crystal colour	orange	Internal ID (crystallographer)	1507 (CG)
Crystal shape	plate	CCDC number	**2241588**
Radiation	MoK_α (λ = 0.71073 Å)		
2Θ range (°)	4.15 to 61.12 (0.70 Å)		

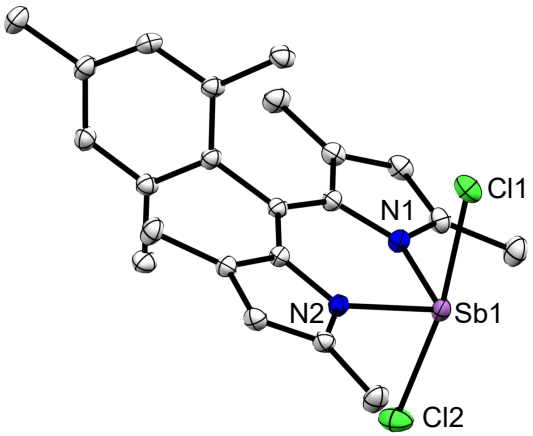


Figure 388: X-ray solid-state structure of **3Sb^{Cl}** with thermal ellipsoids were set to a 50% probability level. Hydrogen atoms were omitted for clarity. Chlorine atoms are shown in green, carbon atoms in grey, nitrogen in blue and antimony in dark magenta. Hydrogen atoms were omitted for clarity. Selected bond lengths [Å] Sb1−Cl1 2.5738(4), Sb1−Cl2 2.5369(5), Sb1−N2 2.0547(12), Sb1−N1 2.0632(12) and bond angles [°] Cl2−Sb1−Cl1 171.088(14), N2−Sb1−Cl1 85.28(3), N2−Sb1−Cl2 88.68(3), N2−Sb1−N1 87.37(5).

Table 31: Crystallographic data and structure refinement of **3Sb^{Cl}** (Figure 388).

Empirical formula	$C_{22}H_{25}Cl_2N_2Sb$	Index ranges	$-10 \leq h \leq 10$
Formula weight	510.09		$-15 \leq k \leq 15$
Temperature (K)	100.00		$-19 \leq l \leq 19$
Crystal system	triclinic	Reflections collected	65221
Space group (number)	$P\bar{1}$ (2)	Independent reflections	6011
a (Å)	7.7567(9)		R_{int} = 0.0322
b (Å)	11.3335(15)		R_{sigma} = 0.0144
c (Å)	13.6924(17)	Completeness to	
α (°)	65.998(3)	Θ = 25.242°	99.9%
β (°)	80.920(3)	Data / Restraints / Parameters	6011/0/252
γ (°)	76.814(3)	Goodness-of-fit on F^2	1.078
Volume (Å^3)	1067.8(2)	Final R indices	R_1 = 0.0178
Z	2	[I$\geq 2\sigma$(I)]	wR_2= 0.0446
ρ_{calc} (gcm^{-3})	1.587	Final R indices	R_1 = 0.0196
μ (mm^{-1})	1.552	[all data]	wR_2 = 0.0455
F(000)	512	Largest peak/hole [eÅ^{-3}]	0.68/−0.42
Crystal size (mm^3)	0.078×0.077×0.048		
Crystal colour	orange	Internal ID (crystallographer)	1569 (CG)
Crystal shape	plate	CCDC number	**2241584**
Radiation	MoK_α (λ = 0.71073 Å)		
2Θ range (°)	4.07 to 59.31 (0.72 Å)		

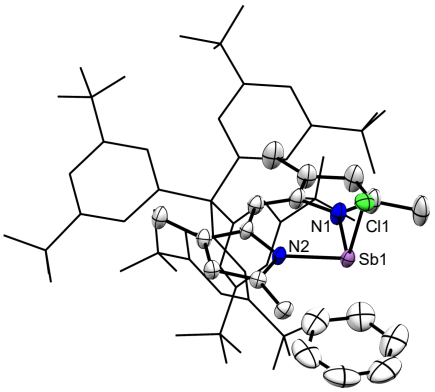


Figure 389: X-ray solid-state structure of **1Sb$^+$[BArF]** with thermal ellipsoids were set to a 50% probability level. Hydrogen atoms were omitted for clarity. The chlorine atom is shown in green, carbon atoms in grey, nitrogen in blue and antimony in dark magenta. Hydrogen atoms and non-coordinating benzene were omitted for clarity. Tetrakis[3,5-bis(trifluoromethyl)phenyl]borate anion is shown in wire-frame style (disorder of CF_3 groups omitted for clarity). Selected bond lengths [Å] Sb1−Cl1 2.3684(9), Sb1−N1 2.057(2), Sb1−N2 2.056(2) and bond angles [°] N1−Sb1−Cl1 95.25(9), N2−Sb1−Cl1 94.04(7), N2−Sb1−N1 87.51(10).

Table 32: Crystallographic data and structure refinement of **1Sb$^+$[BArF]** (Figure 389).

Empirical formula	$C_{54}H_{36}BClF_{24}N_2Sb$	Index ranges	$-15 \leq h \leq 16$
Formula weight	1336.86		$-16 \leq k \leq 16$
Temperature (K)	100.00		$-24 \leq l \leq 24$
Crystal system	triclinic	Reflections collected	84600
Space group (number)	$P\bar{1}$ (2)	Independent reflections	13335
a (Å)	12.379(4)		R_{int} = 0.0577
b (Å)	12.587(4)		R_{sigma} = 0.0402
c (Å)	18.983(6)	Completeness to	
α (°)	79.607(7)	Θ = 25.242°	99.9%
β (°)	75.288(7)	Data / Restraints / Parameters	13335/161/947
γ (°)	80.032(7)	Goodness-of-fit on F^2	1.068
Volume (Å^3)	2788.7(14)	Final R indices	R_1 = 0.0445
Z	2	[I$\geq 2\sigma$(I)]	wR_2= 0.1123
ρ_{calc} (gcm^{-3})	1.592	Final R indices	R_1 = 0.0569
μ (mm^{-1})	0.661	[all data]	wR_2 = 0.1195
F(000)	1326	Largest peak/hole [eÅ^{-3}]	0.68/−0.42
Crystal size (mm^3)	0.135×0.114×0.043		
Crystal colour	orange	Internal ID (crystallographer)	1708 (CG)
Crystal shape	plate	CCDC number	**2241589**
Radiation	MoK_α (λ = 0.71073 Å)		
2Θ range (°)	4.26 to 55.92 (0.76 Å)		

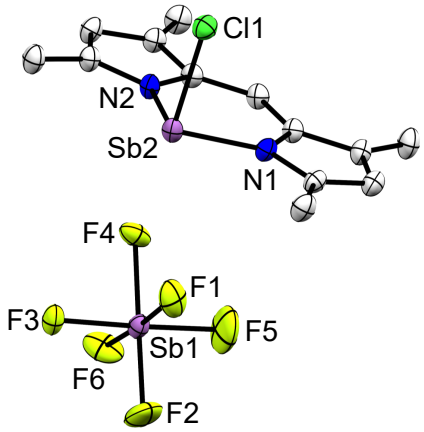


Figure 390: X-ray solid-state structure of **1Sb$^+$[SbF$_6$]** with thermal ellipsoids were set to a 50% probability level. Hydrogen atoms were omitted for clarity. The chlorine atom is shown in green, flourine atoms in lime green, carbon atoms in grey, nitrogen in blue and antimony in dark magenta. Hydrogen atoms and molecule disorder in SbF_6^- anion omitted for clarity. Selected bond lengths [Å] Sb2−Cl1 2.3542(6), Sb2−N1 2.0623(18), Sb2−N2 2.0625(17) and bond angles [°] N1−Sb2−Cl1 93.48(5), N2−Sb2−Cl1 92.15(5), N2−Sb2−N1 87.61(7).

Table 33: Crystallographic data and structure refinement of **1Sb$^+$[SbF$_6$]** (Figure 390).

Empirical formula	$C_{13}H_{15}ClF_6N_2Sb_2$	Index ranges	$-12 \leq$ h ≤ 11
Formula weight	592.22		$-30 \leq$ k ≤ 30
Temperature (K)	100.00		$-13 \leq$ l ≤ 13
Crystal system	monoclinic	Reflections collected	23313
Space group (number)	$P2_1/c$ (14)	Independent reflections	4992
a (Å)	8.6449(8)		R_{int} = 0.0278
b (Å)	21.870(2)		R_{sigma} = 0.0205
c (Å)	9.9182(8)	Completeness to	
α (°)	90	Θ = 25.242°	100.0%
β (°)	108.697(2)	Data / Restraints / Parameters	4992/78/285
γ (°)	90	Goodness-of-fit on F^2	1.131
Volume (Å^3)	1776.2(3)	Final R indices	R_1 = 0.0205
Z	4	[I$\geq 2\sigma$(I)]	wR_2= 0.0487
ρ_{calc} (gcm^{-3})	2.215	Final R indices	R_1 = 0.0219
μ (mm^{-1})	3.248	[all data]	wR_2 = 0.0494
F(000)	1120	Largest peak/hole [eÅ^{-3}]	0.58/−0.55
Crystal size (mm^3)	0.152×0.077×0.05		
Crystal colour	orange	Internal ID (crystallographer)	1780 (CG)
Crystal shape	block		
Radiation	MoK_α (λ = 0.71073 Å)		
2Θ range (°)	4.72 to 59.22 (0.72 Å)		

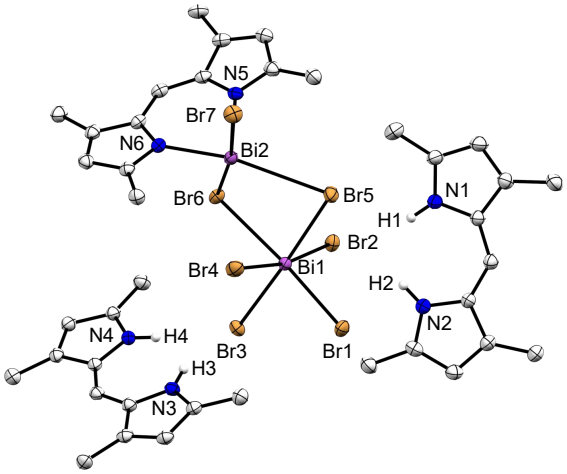


Figure 391: X-ray solid-state structure of BIDIPY *decomposition product 1* with thermal ellipsoids were set to a 50% probability level. Non-nitrogen-bound hydrogen atoms were omitted for clarity. Bromine atoms are shown in orange, carbon atoms in grey, nitrogen in blue and bismuth in dark magenta. Non-nitrogen bound hydrogen atoms and CH_2Cl_2 were omitted for clarity.

Table 34: Selected bond lengths and angles for BIDIPY *decomposition product 1* (Figure 391). Uncertainties are displayed as standard deviation in parentheses.

Bond	Length (Å)	Bonds	Angle (°)
Bi1–Br1	2.7233(4)	Br7–Bi2–Br6	170.968(14)
Bi1–Br2	2.8593(4)	N5–Bi2–N6	83.07(13)
Bi1–Br3	2.9153(4)	Br1–Bi1–Br6	175.757(14)
Bi1–Br4	2.8705(5)	Br2–Bi1–Br3	86.311(13)
Bi1–Br5	2.7918(5)	Br2–Bi1–Br4	170.434(14)
Bi1–Br6	3.0034(4)	Br7–Bi2–Br4	110.841(13)
Bi2–Br4	3.4030(5)	Br7–Bi2–Br5	109.784(14)
Bi2–Br5	3.3136(5)	N5–Bi2–Br5	97.36(9)
Bi2–Br6	2.9787(4)	N5–Bi2–Br6	84.93(9)
Bi2–Br7	2.7196(5)	Bi1–Br4–Bi2	81.053(11)
Bi2–N5	2.233(3)	Bi1–Br5–Bi2	83.819(12)
Bi2–N6	2.235(3)	Bi2–Br6–Bi1	86.439(11)

Table 35: Crystallographic data and structure refinement of BIDIPY *decomposition product 1* (Figure 391).

Empirical formula	$C_{40}H_{51}Bi_2Br_7Cl_2N_6$	Index ranges	$-16 \leq h \leq 16$
Formula weight	1664.09		$-17 \leq k \leq 17$
Temperature (K)	100.00		$-29 \leq l \leq 29$
Crystal system	triclinic	Reflections collected	32797
Space group (number)	$P\bar{1}$ (2)	Independent reflections	32797
a (Å)	11.5304(3)		R_{int} = 0.0449
b (Å)	11.7325(4)		R_{sigma} = 0.0375
c (Å)	19.9360(6)	Completeness to	
α (°)	101.2890(10)	Θ = 25.242°	99.9%
β (°)	100.1570(10)	Data / Restraints / Parameters	32797/0/527
γ (°)	102.6830(10)	Goodness-of-fit on F^2	1.035
Volume (Å^3)	2511.52(13)	Final R indices	R_1 = 0.0329
Z	2	[I$\geq 2\sigma$(I)]	wR_2= 0.0645
ρ_{calc} (gcm^{-3})	2.200	Final R indices	R_1 = 0.0456
μ (mm^{-1})	12.707	[all data]	wR_2 = 0.0689
F(000)	1556	Largest peak/hole [eÅ^{-3}]	3.34/−1.41
Crystal size (mm^3)	0.156×0.086×0.08		
Crystal colour	red	Internal ID (crystallographer)	1688 (CG)
Crystal shape	block		
Radiation	MoK_α (λ = 0.71073 Å)		
2Θ range (°)	4.28 to 63.15 (0.68 Å)		

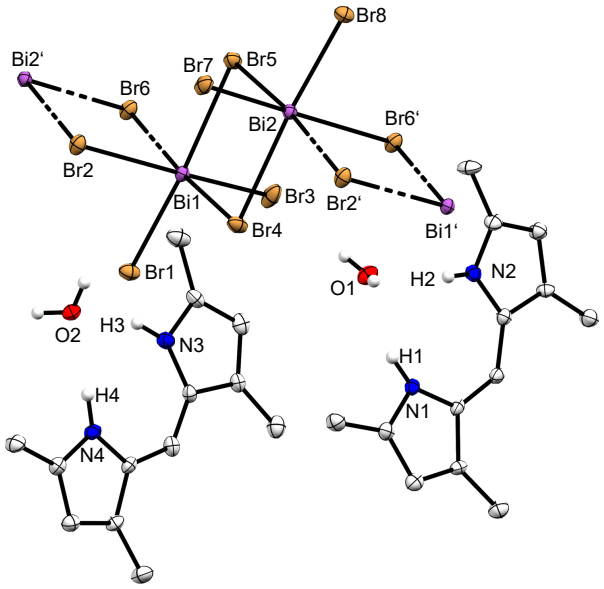


Figure 392: X-ray solid-state structure of BIDIPY *decomposition product 2* with thermal ellipsoids were set to a 50% probability level. Non-nitrogen-bound hydrogen atoms were omitted for clarity. Bromine atoms are shown in orange, carbon atoms in grey, nitrogen in blue, oxygen in red and bismuth in dark magenta. Non-nitrogen or oxygen bound hydrogen atoms were omitted for clarity.

Table 36: Selected bond lengths and angles for BIDIPY *decomposition product 2* (Figure 392). Uncertainties are displayed as standard deviation in parentheses.

Bond	Length (Å)	Bonds	Angle (°)
Bi1–Br1	2.6930(6)	Br1–Bi1–Br2	87.276(19)
Bi1–Br2	2.9933(6)	Br1–Bi1–Br3	91.71(2)
Bi1–Br3	2.7390(6)	Br1–Bi1–Br4	92.640(19)
Bi1–Br4	2.8195(6)	Br3–Bi1–Br2	173.550(19)
Bi1–Br5	3.1246(6)	Br3–Bi1–Br4	93.35(2)
Bi1–Br6	2.9079(6)	Br3–Bi1–Br5	96.18(2)
Bi2–Br2'	2.9134(6)	Br2–Bi2–Br4	89.718(17)
Bi2–Br4	3.1341(6)	Br2–Bi2–Br6'	85.565(16)
Bi2–Br5	2.8330(6)	Br5–Bi2–Br2	173.040(18)
Bi2–Br6'	2.9929(6)	Bi2–Br2–Bi1	94.321(17)
Bi2–Br7	2.7274(6)	Bi1–Br4–Bi2	96.508(18)
Bi2–Br8	2.6768(6)	Bi2–Br5–Bi1	96.442(17)

Table 37: Crystallographic data and structure refinement of BIDIPY *decomposition product 2* (Figure 392).

Empirical formula	$C_{26}H_{40}Bi_2Br_8N_4O_6$	Index ranges	$-10 \leq h \leq 10$
Formula weight	1497.86		$-24 \leq k \leq 24$
Temperature (K)	100.00		$-45 \leq l \leq 45$
Crystal system	monoclinic	Reflections collected	111049
Space group (number)	$P2_1/n$ (14)	Independent reflections	11966
a (Å)	7.3733(6)		R_{int} = 0.0408
b (Å)	16.8154(13)		R_{sigma} = 0.0195
c (Å)	31.553(2)	Completeness to	
α (°)	90	Θ = 25.242°	99.9%
β (°)	91.586(3)	Data / Restraints / Parameters	11966/9/418
γ (°)	90	Goodness-of-fit on F^2	1.261
Volume (Å^3)	3910.6(5)	Final R indices	R_1 = 0.0413
Z	4	[I$\geq 2\sigma$(I)]	wR_2= 0.0756
ρ_{calc} (gcm^{-3})	2.544	Final R indices	R_1 = 0.0455
μ (mm^{-1})	17.191	[all data]	wR_2 = 0.0769
F(000)	2744	Largest peak/hole [eÅ^{-3}]	1.29/−3.47
Crystal size (mm^3)	0.183×0.139×0.026		
Crystal colour	orange	Internal ID (crystallographer)	1768_2 (CG)
Crystal shape	plate		
Radiation	MoK_α (λ = 0.71073 Å)		
2Θ range (°)	4.57 to 61.08 (0.70 Å)		

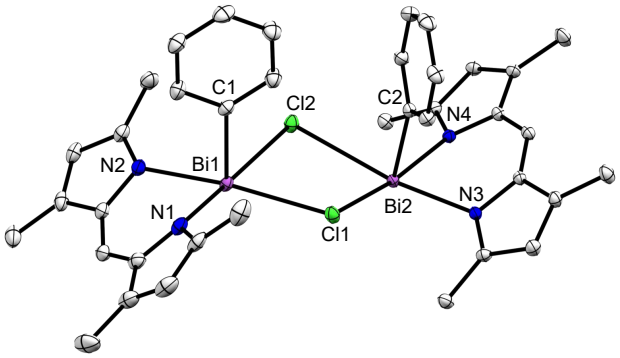


Figure 393: X-ray solid-state structure of **1Bi^{Ph}** with thermal ellipsoids were set to a 50% probability level. Hydrogen atoms were omitted for clarity. Chlorine atoms are shown in green, carbon atoms in grey, nitrogen in blue and bismuth in dark magenta.

Table 38: Selected bond lengths and angles for **1Bi^{Ph}** (Figure 393). Uncertainties are displayed as standard deviation in parentheses.

Bond	Length (Å)	Bonds	Angle (°)
Bi1–Cl1	2.8916(5)	Cl1–Bi1–Cl2	82.140(13)
Bi1–Cl2	2.9662(5)	N1–Bi1–Cl1	95.42(4)
Bi1–N1	2.3098(17)	N1–Bi1–Cl2	174.94(5)
Bi1–N2	2.3179(16)	N1–Bi1–N2	79.91(6)
Bi1–C1	2.232(2)	N2–Bi1–Cl1	174.26(4)
Bi2–Cl1	2.9241(5)	N2–Bi1–Cl2	102.77(4)
Bi2–Cl2	2.9441(5)	C1–Bi1–Cl1	92.83(5)
Bi2–N3	2.3027(15)	C1–Bi1–N1	89.50(7)
Bi2–N4	2.3196(15)	C2–Bi2–Cl1	80.34(5)
Bi2–C2	2.2452(18)	C2–Bi2–N3	85.96(6)

Table 39: Crystallographic data and structure refinement of **1Bi^{Ph}** (Figure 393).

Empirical formula	$C_{38}H_{40}Bi_2Cl_2N_4$	Index ranges	$-16 \leq h \leq 16$
Formula weight	1041.6		$-12 \leq k \leq 17$
Temperature (K)	100.00		$-22 \leq l \leq 22$
Crystal system	triclinic	Reflections collected	101472
Space group (number)	$P\bar{1}$ (2)	Independent reflections	12092
a (Å)	11.3168(11)		R_{int} = 0.0346
b (Å)	11.9555(8)		R_{sigma} = 0.0190
c (Å)	15.0269(16)	Completeness to	
α (°)	72.178(3)	Θ = 25.242°	100.0%
β (°)	69.013(3)	Data / Restraints / Parameters	12092/0/423
γ (°)	85.649(3)	Goodness-of-fit on F^2	1.048
Volume (Å^3)	1805.8(3)	Final R indices	R_1 = 0.0164
Z	2	[I$\geq 2\sigma$(I)]	wR_2= 0.0314
ρ_{calc} (gcm^{-3})	1.916	Final R indices	R_1 = 0.0219
μ (mm^{-1})	9.912	[all data]	wR_2 = 0.0330
F(000)	992	Largest peak/hole [eÅ^{-3}]	0.64/$-$0.68
Crystal size (mm^3)	0.079$\times$0.054$\times$0.046		
Crystal colour	orange	Internal ID (crystallographer)	1779 (CG)
Crystal shape	block		
Radiation	MoK_α (λ = 0.71073 Å)		
2Θ range (°)	3.86 to 63.22 (0.68 Å)		

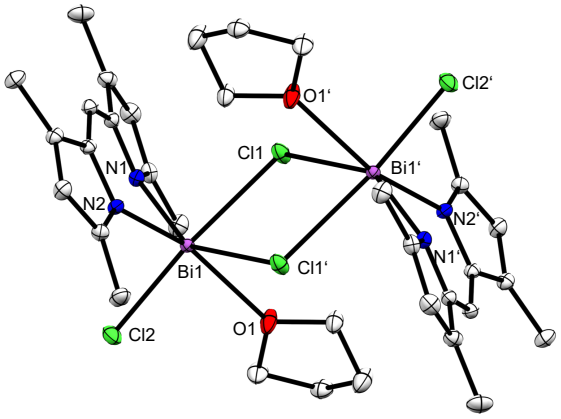


Figure 394: Symmetric unit depiction of X-ray solid-state structure of **1Bi^{Cl}** (THF adduct) with thermal ellipsoids were set to a 50% probability level. Hydrogen atoms were omitted for clarity. Chlorine atoms are shown in green, carbon atoms in grey, nitrogen in blue, oxygen atoms in red and bismuth in dark magenta. Selected bond lengths [Å] Bi1–Cl1' 3.0460(6), Bi1–Cl1 2.8258(5), Bi1–Cl2 2.5799(5), Bi1–O1 2.7622(15), Bi1–N1 2.2687(16), Bi1–N2 2.2554(16) and bond angles [°] Cl1–Bi1–Cl1' 76.917(15), Cl2–Bi1–Cl1' 170.113(17), Cl2–Bi1–Cl1 153.417(16), Cl2–Bi1–O1 120.423(17), N2–Bi1–Cl1 77.90(4), N1–Bi1–N2 81.52(6).

Table 40: Crystallographic data and structure refinement of **1Bi^{Cl}** (THF adduct) (Figure 394).

Empirical formula	$C_{34}H_{46}Bi_2Cl_4N_4O_2$	Index ranges	$-13 \leq h \leq 13$
Formula weight	1102.51		$-14 \leq k \leq 14$
Temperature (K)	100.00		$-35 \leq l \leq 35$
Crystal system	monoclinic	Reflections collected	46052
Space group (number)	$P2_1/c$ (14)	Independent reflections	6909
a (Å)	8.7403(9)		R_{int} = 0.0337
b (Å)	9.2435(6)		R_{sigma} = 0.0241
c (Å)	22.984(3)	Completeness to	
α (°)	90	Θ = 25.242°	100.0%
β (°)	95.441(4)	Data / Restraints / Parameters	6909/0/212
γ (°)	90	Goodness-of-fit on F^2	1.044
Volume (Å^3)	1848.5(3)	Final R indices	R_1 = 0.0187
Z	2	[I$\geq 2\sigma$(I)]	wR_2= 0.0324
ρ_{calc} (gcm^{-3})	1.981	Final R indices	R_1 = 0.0262
μ (mm^{-1})	9.832	[all data]	wR_2 = 0.0348
F(000)	1056	Largest peak/hole [eÅ^{-3}]	1.10/−0.95
Crystal size (mm^3)	0.156×0.074×0.034		
Crystal colour	orange	Internal ID (crystallographer)	1749 (CG)
Crystal shape	block	CCDC number	**2241585**
Radiation	MoK_α (λ = 0.71073 Å)		
2Θ range (°)	4.68 to 67.51 (0.64 Å)		

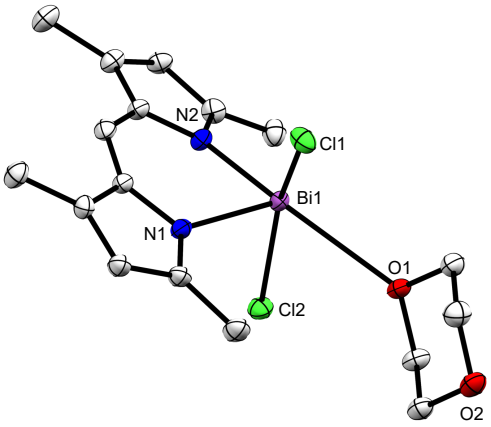


Figure 395: X-ray solid-state structure of **1Bi^{Cl}** (1,4-dioxane adduct) with thermal ellipsoids were set to a 50% probability level. Hydrogen atoms were omitted for clarity. Chlorine atoms are shown in green, carbon atoms in grey, nitrogen in blue, oxygen atoms in red and bismuth in dark magenta. Selected bond lengths [Å] Bi1–Cl1' 3.0034(14), Bi1–Cl1 2.8298(14), Bi1–Cl2 2.6008(13), Bi1–O1 2.877(4), Bi1–N1 2.242(5), Bi1–N2 2.244(5) and bond angles [°] Cl1–Bi1–Cl1' 75.14(4), Cl2–Bi1–Cl1 152.77(4), Cl2–Bi1–Cl1' 126.78(4), N1–Bi1–Cl1 112.76(12), N1–Bi1–N2 81.72(18).

Table 41: Crystallographic data and structure refinement of **1Bi^{Cl}** (1,4-dioxane adduct) (Figure 395).

Empirical formula	$C_{17}H_{23}BiCl_2N_2O_2$	Index ranges	$-12 \leq h \leq 12$
Formula weight	567.25		$0 \leq k \leq 14$
Temperature (K)	100.00		$0 \leq l \leq 35$
Crystal system	monoclinic	Reflections collected	6667
Space group (number)	$P2_1/c$ (14)	Independent reflections	6667
a (Å)	8.6878(5)		R_{int} = 0.0644
b (Å)	10.1050(5)		R_{sigma} = 0.0279
c (Å)	21.6417(12)	Completeness to	
α (°)	90	Θ = 25.242°	99.8%
β (°)	94.444(2)	Data / Restraints / Parameters	6667/0/223
γ (°)	90	Goodness-of-fit on F^2	1.115
Volume (Å^3)	1894.22(18)	Final R indices	R_1 = 0.0270
Z	4	[I$\geq 2\sigma$(I)]	wR_2= 0.0797
ρ_{calc} (gcm^{-3})	1.989	Final R indices	R_1 = 0.0286
μ (mm^{-1})	9.602	[all data]	wR_2 = 0.0807
F(000)	1088	Largest peak/hole [eÅ^{-3}]	1.36/$-$1.08
Crystal size (mm^3)	0.142$\times$0.138$\times$0.081		
Crystal colour	red	Internal ID (crystallographer)	1817 (CG)
Crystal shape	block		
Radiation	MoK_α (λ = 0.71073 Å)		
2Θ range (°)	4.45 to 59.24 (0.72 Å)		

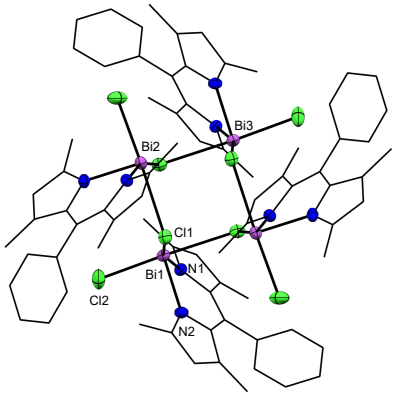


Figure 396: X-ray solid-state structure of **2Bi^{Cl}** with thermal ellipsoids were set to a 50% probability level. Hydrogen atoms were omitted for clarity. Chlorine atoms are shown in green, carbon atoms in grey, nitrogen in blue, oxygen atoms in red and bismuth in dark magenta. Ligand hydrocarbon scaffold is depicted as wireframe for clarity. Selected bond lengths [Å] Bi1−Bi3 4.90388(19), Bi1−Bi2 4.66489(15), Bi1−Cl1 2.8401(6), Bi1−Cl2 2.5703(7), Bi1−N1 2.2178(18), Bi1−N2 2.2042(18) and bond angles [°] Bi2−Bi1−Bi3 58.290(1), Cl1−Bi1−Bi3 40.661(11), Cl2−Bi1−Bi3 140.112(18), Cl2−Bi1−Cl1 170.80(2), N2−Bi1−N1 80.21(7), N1−Bi1−Cl1 80.49(5).

Table 42: Crystallographic data and structure refinement of **2Bi^{Cl}** (Figure 396).

Empirical formula	$C_{19}H_{19}BiCl_2N_2$	Index ranges	$-33 \leq h \leq 33$
Formula weight	555.24		$-33 \leq k \leq 33$
Temperature (K)	100.00		$-20 \leq l \leq 20$
Crystal system	tetragonal	Reflections collected	112176
Space group (number)	$I4_1/a$ (88)	Independent reflections	6239
a (Å)	22.9835(6)		R_{int} = 0.0366
b (Å)	22.9835(6)		R_{sigma} = 0.0126
c (Å)	14.1686(4)	Completeness to	
α (°)	90	Θ = 25.242°	99.9%
β (°)	90	Data / Restraints / Parameters	6239/0/221
γ (°)	90	Goodness-of-fit on F^2	1.049
Volume (Å^3)	7484.4(4)	Final R indices	R_1 = 0.0187
Z	16	[I$\geq 2\sigma$(I)]	wR_2= 0.0438
ρ_{calc} (gcm^{-3})	1.971	Final R indices	R_1 = 0.0221
μ (mm^{-1})	9.711	[all data]	wR_2 = 0.0452
F(000)	4224	Largest peak/hole [eÅ^{-3}]	1.64/−0.87
Crystal size (mm^3)	0.289×0.114×0.056		
Crystal colour	dark green	Internal ID (crystallographer)	1768 (CG)
Crystal shape	block	CCDC number	**2241586**
Radiation	MoK_α (λ=0.71073 Å)		
2Θ range (°)	4.07 to 56.18 (0.75 Å)		

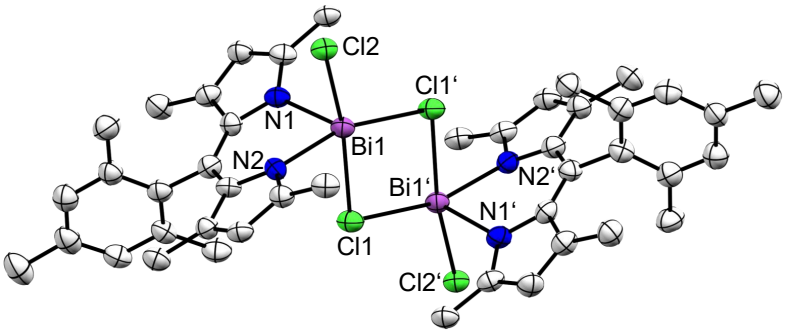


Figure 397: X-ray solid-state structure of **3Bi^{Cl}** with thermal ellipsoids were set to a 50% probability level. Hydrogen atoms were omitted for clarity. Chlorine atoms are shown in green, carbon atoms in grey, nitrogen in blue, oxygen atoms in red and bismuth in dark magenta. Full asymmetric unit (Z' = 2). Selected bond lengths [Å] Bi1−Cl1 2.692(2), Bi1−Cl2 2.687(2), Bi1−N1 2.223(7), Bi1−N2 2.218(7) and bond angles [°] Cl2−Bi1−Cl1 165.31(6), N1−Bi1−Cl1 86.98(19), N1−Bi1−Cl2 79.72(19), N2−Bi1−Cl1 87.6(2), N2−Bi1−Cl2 96.3(2), N2−Bi1−N1 80.6(3).

Table 43: Crystallographic data and structure refinement of **3Bi^{Cl}** (Figure 397).

Empirical formula	$C_{22}H_{25}BiCl_2N_2$	Index ranges	$-10 \leq h \leq 10$
Formula weight	597.32		$0 \leq k \leq 21$
Temperature (K)	100.00		$0 \leq l \leq 49$
Crystal system	monoclinic	Reflections collected	11478
Space group (number)	$P2_1/n$ (14)	Independent reflections	11478
a (Å)	7.7393(7)		R_{int} = ?
b (Å)	15.609(2)		R_{sigma} = 0.0299
c (Å)	36.440(5)	Completeness to	
α (°)	90	Θ = 25.242°	99.4%
β (°)	93.984(3)	Data / Restraints / Parameters	11478/0/502
γ (°)	90	Goodness-of-fit on F^2	1.064
Volume (Å^3)	4391.5(10)	Final R indices	R_1 = 0.0464
Z	8	[I$\geq 2\sigma$(I)]	wR_2= 0.1047
ρ_{calc} (gcm^{-3})	1.807	Final R indices	R_1 = 0.0519
μ (mm^{-1})	8.282	[all data]	wR_2 = 0.1090
F(000)	2304	Largest peak/hole [eÅ^{-3}]	1.91/−3.56
Crystal size (mm^3)	0.186×0.081×0.021		
Crystal colour	yellow	Internal ID (crystallographer)	1852 (CG)
Crystal shape	plate	CCDC number	**2241587**
Radiation	MoK_α (λ=0.71073 Å)		
2Θ range (°)	4.26 to 57.45 (0.74 Å)		

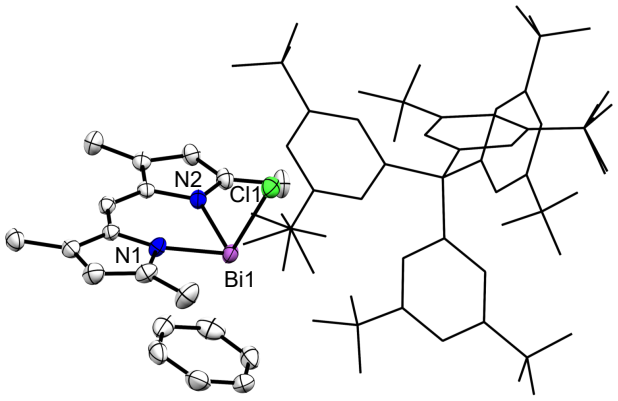


Figure 398: X-ray solid-state structure of **1Bi$^+$[BArF]** with thermal ellipsoids were set to a 50% probability level. Hydrogen atoms were omitted for clarity. Chlorine atoms are shown in green, carbon atoms in grey, nitrogen in blue, oxygen atoms in red and bismuth in dark magenta. Tetrakis[3,5-bis(trifluoromethyl)phenyl]borate depicted in wireframe-style for clarity. Selected bond lengths [Å] Bi1−Cl1 2.4773(8), Bi1−N1 2.166(2), Bi1−N2 2.168(3) and bond angles [°] N1−Bi1−Cl1 92.87(7), N1−Bi1−N2 84.78(9), N2−Bi1−Cl1 94.48(7).

Table 44: Crystallographic data and structure refinement of **1Bi$^+$[BArF]** (Figure 398).

Empirical formula	$C_{51}H_{33}BBiClF_{24}N_2$	Index ranges	$-15 \leq h \leq 16$
Formula weight	1385.03		$-18 \leq k \leq 18$
Temperature (K)	100.00		$-22 \leq l \leq 21$
Crystal system	triclinic	Reflections collected	106684
Space group (number)	$P\bar{1}$ (2)	Independent reflections	12320
a (Å)	12.515(2)		R_{int} = 0.0545
b (Å)	14.102(3)		R_{sigma} = 0.0278
c (Å)	16.268(4)	Completeness to	
α (°)	75.219(6)	Θ = 25.242°	99.9%
β (°)	67.921(7)	Data / Restraints / Parameters	12320/78/781
γ (°)	77.582(5)	Goodness-of-fit on F^2	1.043
Volume (Å^3)	2549.7(9)	Final R indices	R_1 = 0.0289
Z	2	[I$\geq 2\sigma$(I)]	wR_2= 0.0642
ρ_{calc} (gcm^{-3})	1.804	Final R indices	R_1 = 0.0335
μ (mm^{-1})	3.637	[all data]	wR_2 = 0.0659
F(000)	1348	Largest peak/hole [eÅ^{-3}]	0.87/−1.28
Crystal size (mm^3)	0.176×0.14×0.044		
Crystal colour	orange	Internal ID (crystallographer)	1835 (CG)
Crystal shape	block		
Radiation	MoK_α (λ=0.71073 Å)		
2Θ range (°)	4.07 to 56.18 (0.75 Å)		

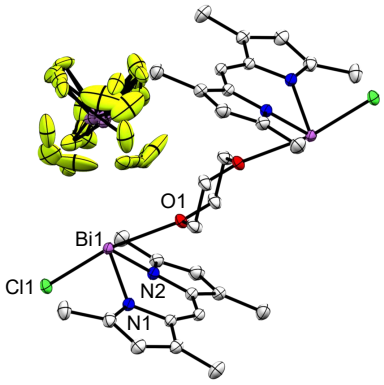


Figure 399: X-ray solid-state structure of **1Bi$^+$[SbF$_6$]** with thermal ellipsoids were set to a 50% probability level. Hydrogen atoms were omitted for clarity. Chlorine atoms are shown in green, flourine atoms in lime green, carbon atoms in grey, nitrogen in blue, oxygen atoms in red, bismuth and antimony in dark magenta. Selected bond lengths [Å] Bi1−Cl1 2.5284(4), Bi1−O1 2.6537(13), Bi1−N2 2.2101(13), Bi1−N1 2.1834(13) and bond angles [°] Cl1−Bi1−O1 169.95(5), N1−Bi1−Cl1 93.27(4), N1−Bi1−Cl1 93.27(4), N1−Bi1−O1 79.31(5), N2−Bi1−O1 79.30(5), N1−Bi1−N2 83.87(8).

Table 45: Crystallographic data and structure refinement of **1Bi$^+$[SbF$_6$]** (Figure 399).

Empirical formula	$C_{30}H_{38}Bi_2Cl_2F_{12}N_4O_2Sb_2$		$-17 \leq h \leq 19$
Formula weight	1447.00	Index ranges	$-29 \leq k \leq 28$
Temperature (K)	100.00		$-13 \leq l \leq 11$
Crystal system	monoclinic	Reflections collected	28198
Space group (number)	$C2/m$ (12)	Independent reflections	4037
a (Å)	12.2573(11)		R_{int} = 0.0369
b (Å)	18.998(2)		R_{sigma} = 0.0216
c (Å)	8.8845(8)	Completeness to	
α (°)	90	Θ = 25.242°	99.9%
β (°)	99.757(3)	Data / Restraints / Parameters	4037/348/196
γ (°)	90	Goodness-of-fit on F^2	1.045
Volume (Å^3)	2039.0(4)	Final R indices	R_1 = 0.0183
Z	2	[I$\geq 2\sigma$(I)]	wR_2= 0.0460
ρ_{calc} (gcm^{-3})	2.357	Final R indices	R_1 = 0.0196
μ (mm^{-1})	10.135	[all data]	wR_2 = 0.0466
F(000)	1344	Largest peak/hole [eÅ^{-3}]	1.13/−1.39
Crystal size (mm^3)	0.325×0.082×0.04		
Crystal colour	red	Internal ID (crystallographer)	1801 (CG)
Crystal shape	plank		
Radiation	MoK_α (λ=0.71073 Å)		
2Θ range (°)	4.29 to 68.23 (0.63 Å)		

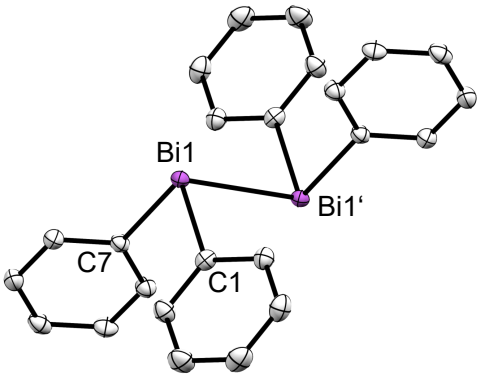


Figure 400: X-ray solid-state structure of Bi_2Ph_4 with thermal ellipsoids were set to a 50% probability level. Hydrogen atoms were omitted for clarity. Carbon atoms are shown in grey and bismuth atoms in dark magenta. Selected bond lengths [Å] Bi1−C1 2.067(2), Bi1−C1 2.067(2) and bond angles [°] C1−Bi1−Bi1' 91.56(6), C7−Bi1−Bi1' 94.81(6), C7−Bi1−C1 92.57(8).

Table 46: Crystallographic data and structure refinement of Bi_2Ph_4 (Figure 400).

Empirical formula	$C_{24}H_{20}Bi_2$	Index ranges	$-16 \leq h \leq 16$
Formula weight	726.36		$-8 \leq k \leq 8$
Temperature (K)	100.00		$-24 \leq l \leq 24$
Crystal system	monoclinic	Reflections collected	51592
Space group (number)	$P2_1/n$ (14)	Independent reflections	3472
a (Å)	11.4108(13)		R_{int} = 0.0379
b (Å)	5.7309(4)		R_{sigma} = 0.0152
c (Å)	16.4271(17)	Completeness to	
α (°)	90	Θ = 25.242°	99.9%
β (°)	104.565(4)	Data / Restraints / Parameters	3472/0/118
γ (°)	90	Goodness-of-fit on F^2	1.064
Volume (Å^3)	1039.71(18)	Final R indices	R_1 = 0.0146
Z	2	[I$\geq 2\sigma$(I)]	wR_2= 0.0331
ρ_{calc} (gcm^{-3})	2.320	Final R indices	R_1 = 0.0168
μ (mm^{-1})	16.906	[all data]	wR_2 = 0.0342
F(000)	660	Largest peak/hole [eÅ^{-3}]	1.09/−0.71
Crystal size (mm^3)	0.088×0.042×0.028		
Crystal colour	orange	Internal ID (crystallographer)	1814 (CG)
Crystal shape	block		
Radiation	MoK_α (λ=0.71073 Å)		
2Θ range (°)	4.99 to 63.08 (0.68 Å)		

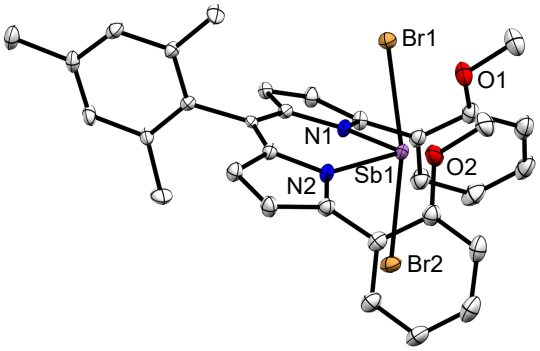


Figure 401: X-ray solid-state structure of **7Sb^{Br}** with thermal ellipsoids were set to a 50% probability level. Hydrogen atoms were omitted for clarity. Bromine atoms are shown in orange, carbon atoms in grey, nitrogen in blue, oxygen atoms in red and antimony in dark magenta. Two independent half-molecules are present in the unit cell from which only one is displayed above. Selected bond lengths [Å] Sb1−Br1 2.7076(5), Sb1−Br2 2.7608(5), Sb1−O1 2.932(3), Sb1−O2 2.905(3), Sb1−N1 2.090(3), Sb1−N2 2.089(3) and bond angles [°] Br1−Sb1−Br2 167.607(17), O2−Sb1−O1 120.99(9), N1−Sb1−Br1 86.32(10), N1−Sb1−Br2 84.64(10), N1−Sb1−N2 86.35(13).

Table 47: Crystallographic data and structure refinement of **7Sb^{Br}** (Figure 401).

Empirical formula	$C_{32}H_{29}Br_2N_2O_2Sb$		
Formula weight	755.14	2Θ range (°)	3.912 to 58.498
Temperature (K)	100.00	Completeness to Θ	
Crystal system	orthorhombic	Index ranges	$-21 \leq h \leq 21$
Space group (number)	Pnma		$-55 \leq k \leq 55$
a (Å)	15.7678(6)		$-19 \leq l \leq 16$
b (Å)	40.1150(14)		
c (Å)	13.8588(5)	Reflections collected	81995
α (°)	90	Independent reflections	12087
β (°)	90		R_{int} = 0.0501
γ (°)	90		R_{sigma} = 0.0374
Volume (Å^3)	8766.0(6)	Data / Restraints / Parameters	12087/0/556
Z	12	Goodness-of-fit on F^2	1.209
ρ_{calc} (gcm^{-3})	1.717	Final R indices	R_1 = 0.0463
μ (mm^{-1})	3.711	[I≥2σ(I)]	wR_2= 0.0981
F(000)	4464	Final R indices	R_1 = 0.0548
Crystal size (mm^3)	0.16×0.12×0.04	[all data]	wR_2 = 0.1009
Crystal habitus	clear blue plate	Largest peak/hole [eÅ^{-3}]	2.26/−1.25
Absorption correction	multi-scan	Internal ID (crystallographer)	8882f/8049_3d (GS)
Tmin; Tmax	0.6271; 0.7465	CCDC number	**2493718 2410512**
Radiation	MoK_α (λ=0.71073 Å)	device type	STOE IPDS 2T

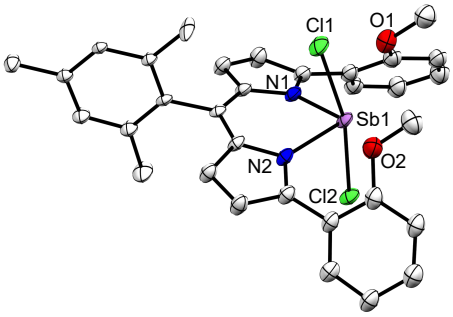


Figure 402: X-ray solid-state structure of **7Sb^{Cl}** with thermal ellipsoids were set to a 50% probability level. Hydrogen atoms were omitted for clarity. Chlorine atoms are shown in green, carbon atoms in grey, nitrogen in blue, oxygen atoms in red and antimony in dark magenta. The molecule resides on a crystallographic mirror plane consisting of the mesityl ring, antimony and the two chlorine atoms, resulting in the "left" and "right" part of the molecule being equivalent. Two independent half-molecules are present in the unit cell from which only one is displayed above. Selected bond lengths [Å] Sb1−Cl1 2.561(3), Sb1−Cl2 2.579(3), Sb1−O1 2.8161(3), Sb1−N1 2.133(6) and bond angles [°] Cl1−Sb−Cl2 166.98(10), O2−Sb1−O1 123.78(1), N1−Sb1−Cl1 85.58(18), N1−Sb1−Cl2 84.96(18), N1−Sb1−N2 86.7(3).

Table 48: Crystallographic data and structure refinement of **7Sb^{Cl}** (Figure 402).

Empirical formula	$C_{32}H_{29}N_2O_2Cl_2Sb$		
Formula weight	666.22	2Θ range (°)	3.752 to 58.498
Temperature (K)	100.00	Completeness to Θ	99.9%
Crystal system	monoclinic	Index ranges	$-14 \leq h \leq 14$
Space group (number)	$P2_1/n$		$0 \leq k \leq 19$
a (Å)	10.9031(15)		$0 \leq l \leq 26$
b (Å)	14.0770(18)		
c (Å)	19.118(3)	Reflections collected	8238
α (°)	90	Independent reflections	8238
β (°)	95.418(5)		R_{int} = ?
γ (°)	90		R_{sigma} = 0.0602
Volume (Å^3)	2921.2(7)	Data / Restraints / Parameters	8238/394/400
Z	4	Goodness-of-fit on F^2	1.184
ρ_{calc} (gcm^{-3})	1.515	Final R indices	R_1 = 0.0845
μ (mm^{-1})	1.159	[I≥2σ(I)]	wR_2= 0.1969
F(000)	1344	Final R indices	R_1 = 0.0929
Crystal size (mm^3)	0.13×0.11×0.06	[all data]	wR_2 = 0.2024
Crystal habitus	clear reddish pink plate	Largest peak/hole [eÅ^{-3}]	3.87/−3.83
Absorption correction	multi-scan	Internal ID (crystallographer)	8048 (GS)
Tmin; Tmax	0.6032; 0.7463	CCDC number	**2410514**
Radiation	MoK_α (λ=0.71073 Å)	device type	Bruker D8 Venture

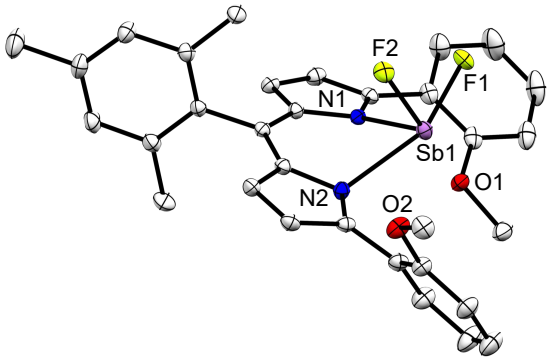


Figure 403: X-ray solid-state structure of **7Sb^{F}**. Thermal ellipsoids were set to a 50% probability level. Hydrogen atoms and one non-coordinating molecule of THF were omitted for clarity. Two units of **7Sb^{F}** form a dimer *via* short contacts. Fluorine atoms are shown in lime green, carbon atoms in grey, nitrogen in blue, oxygen atoms in red and antimony in dark magenta. Selected bond lengths [Å] Sb1−F1 1.9675(16), Sb1−F2 1.9320(16), Sb1−N1 2.117(2), Sb1−N2 2.430(2) and bond angles [°] F1−Sb1−F2 84.86(7), F1−Sb1−N1 84.80(8), F1−Sb1−N2 156.70(7), F2−Sb1−N2 78.94(7), N1−Sb1−N2 78.45(8).

Table 49: Crystallographic data and structure refinement of **7Sb^{F}** (Figure 403).

Empirical formula	$C_{64}H_{66}F_4N_4O_5Sb_2$		
Formula weight	1338.74	2Θ range (°)	4.8 to 58.5
Temperature (K)	100.00	Completeness to Θ	99.8%
Crystal system	triclinic	Index ranges	$-11 \leq h \leq 11$
Space group (number)	$P-1$		$-17 \leq k \leq 16$
a (Å)	8.7160(4)		$0 \leq l \leq 19$
b (Å)	12.9837(7)		
c (Å)	14.4902(7)	Reflections collected	8071
α (°)	111.545(2)	Independent reflections	8071
β (°)	101.756(2)		R_{int} = ?
γ (°)	91.143(2)		R_{sigma} = 0.0339
Volume (Å^3)	1485.12(13)	Data / Restraints / Parameters	8071/39/403
Z	1	Goodness-of-fit on F^2	1.114
ρ_{calc} (gcm^{-3})	1.497	Final R indices	R_1 = 0.0368
μ (mm^{-1})	0.977	[I≥2σ(I)]	wR_2= 0.0942
F(000)	680	Final R indices	R_1 = 0.0456
Crystal size (mm^3)	0.14×0.06×0.04	[all data]	wR_2 = 0.0999
Crystal habitus	clear dark violet plank	Largest peak/hole [eÅ^{-3}]	2.03/−0.79
Absorption correction	multi-scan	Internal ID (crystallographer)	8092 (GS)
Tmin; Tmax	0.673367; 0.746440	CCDC number	**2410515**
Radiation	MoK_α (λ=0.71073 Å)	device type	Bruker D8 Venture

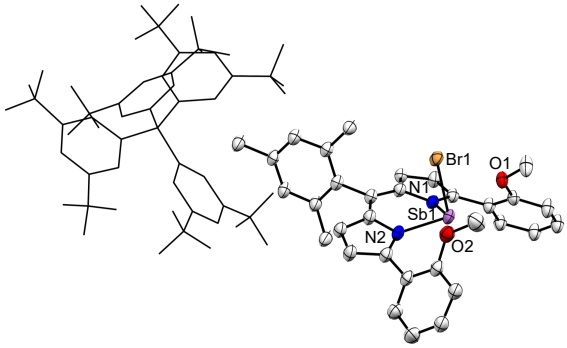


Figure 404: X-ray solid-state structure of **7Sb$^+$[BArF]**. Thermal ellipsoids were set to a 50% probability level. Hydrogen atoms were omitted and [BArF]$^-$ counterion depicted in wireframe-style for clarity. Bromine is shown in orange, carbon atoms in grey, nitrogen in blue, oxygen atoms in red and antimony in dark magenta. Selected bond lengths [Å] Sb1−Br1 2.5095(17), Sb1−O1 2.7106(5), Sb1−O1 2.6553(6), Sb1−N1 2.103(11), Sb1−N2 2.104(12) and bond angles [°] N1−Sb1−Br1 93.3(3), N2−Sb1−Br1 91.9(3), N1−Sb1−N2 85.9(4).

Table 50: Crystallographic data and structure refinement of **7Sb$^+$[BArF]** (Figure 404).

Empirical formula	$C_{32}H_{41}BBrF_{24}N_2O_2Sb$		
Formula weight	1538.46	2Θ range (°)	4.518 to 50.5
Temperature (K)	100.00	Completeness to Θ	99.2%
Crystal system	triclinic	Index ranges	$-15 \leq h \leq 15$
Space group (number)	P-1		$-18 \leq k \leq 18$
a (Å)	12.985(3)		$-19 \leq l \leq 19$
b (Å)	15.558(3)		
c (Å)	15.967(2)	Reflections collected	20722
α (°)	77.031(12)	Independent reflections	11291
β (°)	88.600(15)		R_{int} = 0.1269
γ (°)	89.868(16)		R_{sigma} = 0.1450
Volume (Å^3)	3142.5(10)	Data / Restraints / Parameters	11291/798/861
Z	2	Goodness-of-fit on F^2	1.095
ρ_{calc} (gcm^{-3})	1.626	Final R indices	R_1 = 0.1301
μ (mm^{-1})	1.192	[I≥2σ(I)]	wR_2= 0.2861
F(000)	1524	Final R indices	R_1 = 0.2048
Crystal size (mm^3)	0.14×0.1×0.04	[all data]	wR_2 = 0.3374
Crystal habitus	violet plate	Largest peak/hole [eÅ^{-3}]	1.69/−1.56
Absorption correction	multi-scan	Internal ID (crystallographer)	8489_3dn (GS)
Tmin; Tmax	0.3798; 0.9558	CCDC number	**2410513**
Radiation	MoK_α (λ=0.71073 Å)	device type	STOE IPDS 2T

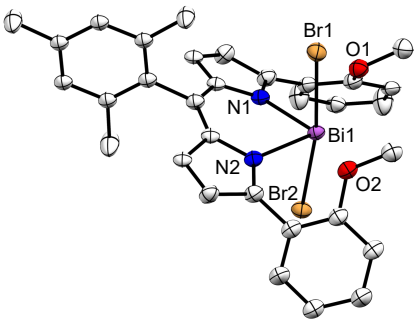


Figure 405: X-ray solid-state structure of **7Bi^{Br}**. Thermal ellipsoids were set to a 50% probability level. Hydrogen atoms were omitted for clarity. Bromine is shown in orange, carbon atoms in grey, nitrogen in blue, oxygen atoms in red and bismuth in dark magenta. The molecule resides on a crystallographic mirror plane consisting of the mesityl ring, bismuth and the two bromine atoms, resulting in the "left" and "right" part of the molecule being equivalent. Two independent half-molecules are present in the unit cell from which only one is displayed above. Selected bond lengths [Å] Bi1−Br1 2.781(4), Bi1−Br2 2.848(4), Bi1−O1 2.727(13), Bi1−N1 2.265(15) and bond angles [°] Br1−Bi1−Br2 171.55(12), O1−Bi1−O2 128.7(6), N1−Bi1−Br1 85.5(4), N1−Bi1−Br2 88.2(4), N1−Bi1−N2 82.6(8).

Table 51: Crystallographic data and structure refinement of **7Bi^{Br}** (Figure 405).

Empirical formula	$C_{32}H_{29}BiBr_2N_2O_2$		
Formula weight	842.37	2Θ range (°)	3.602 to 50.5
Temperature (K)	100.00	Completeness to Θ	99.4%
Crystal system	monoclinic	Index ranges	$-13 \leq$ h ≤ 13
Space group (number)	$P2_1/m$		$-16 \leq$ k ≤ 16
a (Å)	11.1336(4)		$-22 \leq$ l ≤ 22
b (Å)	14.0406(5)		
c (Å)	19.1261(7)	Reflections collected	6091
α (°)	90	Independent reflections	6091
β (°)	93.697(3)		R_{int} = 0.215
γ (°)	90		R_{sigma} = 0.0183
Volume (Å^3)	2983.62(19)	Data / Restraints / Parameters	6091/542/393
Z	4	Goodness-of-fit on F^2	1.213
ρ_{calc} (gcm^{-3})	1.875	Final R indices	R_1 = 0.0845
μ (mm^{-1})	8.619	[I$\geq 2\sigma$(I)]	wR_2= 0.2588
F(000)	1616	Final R indices	R_1 = 0.0900
Crystal size (mm^3)	0.18×0.16×0.05	[all data]	wR_2 = 0.2706
Crystal habitus	clear reddish pink plate	Largest peak/hole [eÅ^{-3}]	5.97/−3.10
Absorption correction	multi-scan	Internal ID (crystallographer)	8174 (GS)
Tmin; Tmax	1.0000; 1.0000	CCDC number	**2410516**
Radiation	MoK_α (λ=0.71073 Å)	device type	STOE IPDS 2T

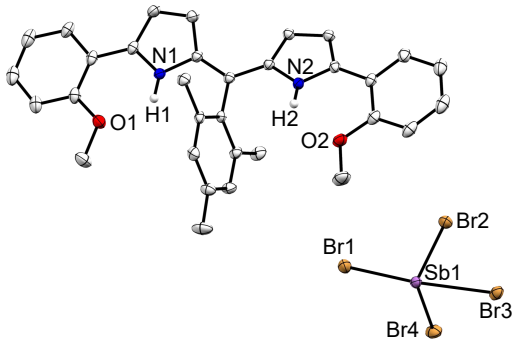


Figure 406: X-ray solid-state structure of **L7-HSbBr**. Thermal ellipsoids were set to a 50% probability level. Non-nitrogen-bound hydrogen atoms were omitted for clarity. Bromine is shown in orange, carbon atoms in grey, nitrogen in blue, oxygen atoms in red and antimony in dark magenta. Selected bond lengths [Å] Sb1−Br1 2.6417(4), Sb1−Br2 2.5225(4), Sb1−Br3 2.9941(4), Sb1−Br4 2.6128(4), Sb1−Br3' 3.0182(4) and bond angles [°] Br1−Sb1−Br3 174.674(12), Br2−Sb1−Br1 91.088(11), Br2−Sb1−Br3 86.358(10), Br2−Sb1−Br4 94.220(12).

Table 52: Crystallographic data and structure refinement of **L7-HSbBr** (Figure 406).

Empirical formula	$C_{32}H_{31}Br_4N_2O_2Sb$		
Formula weight	916.98	2Θ range (°)	3.764 to 64.186
Temperature (K)	102.00	Completeness to Θ	99.9%
Crystal system	monoclinic	Index ranges	$-16 \leq h \leq 18$
Space group (number)	$P2_1/n$		$-34 \leq k \leq 33$
a (Å)	12.5701(7)		$-19 \leq l \leq 19$
b (Å)	23.1023(13)		
c (Å)	13.3436(8)	Reflections collected	102541
α (°)	90	Independent reflections	12406
β (°)	113.371(2)		R_{int} = 0.0644
γ (°)	90		R_{sigma} = 0.0396
Volume (Å^3)	3557.0(4)	Data / Restraints / Parameters	12406/0/375
Z	4	Goodness-of-fit on F^2	1.092
ρ_{calc} (gcm^{-3})	1.712	Final R indices	R_1 = 0.0398
μ (mm^{-1})	5.298	[I$\geq 2\sigma$(I)]	wR_2= 0.0873
F(000)	1776	Final R indices	R_1 = 0.0517
Crystal size (mm^3)	0.24×0.22×0.15	[all data]	wR_2 = 0.0913
Crystal habitus	metallic bluish green block	Largest peak/hole [eÅ^{-3}]	1.43/−1.08
Absorption correction	multi-scan	Internal ID (crystallographer)	8302f (GS)
Tmin; Tmax	0.6628; 0.7463		
Radiation	MoK_α (λ=0.71073 Å)	device type	Bruker D8 Venture

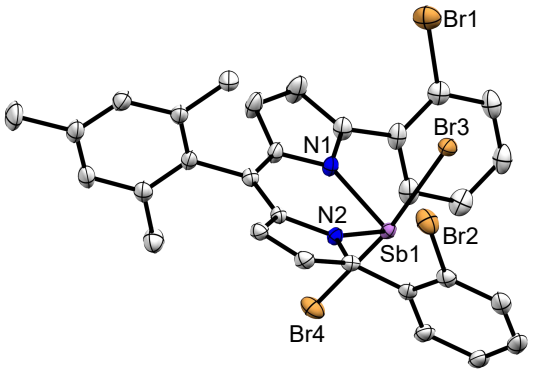


Figure 407: X-ray solid-state structure of **8Sb^{Br}**. Thermal ellipsoids were set to a 50% probability level. Hydrogen atoms were omitted for clarity. Bromine is shown in orange, carbon atoms in grey, nitrogen in blue and antimony in dark magenta. Selected bond lengths [Å] Sb1−Br3 2.6568(3), Sb1−Br4 2.7351(3), Sb1−N1 2.0983(19), Sb1−N2 2.0945(19) and bond angles [°] Br3−Sb1−Br4 171.637(10), N1−Sb1−Br3 87.40(6), N1−Sb1−Br4 85.69(6), N2−Sb1−N1 85.68(7).

Table 53: Crystallographic data and structure refinement of **8Sb^{Br}** (Figure 407).

Empirical formula	$C_{30}H_{23}Br_4N_2Sb$		
Formula weight	852.89	2Θ range (°)	5.226 to 55.998
Temperature (K)	100.00	Completeness to Θ	99.9%
Crystal system	monoclinic	Index ranges	$-21 \leq h \leq 21$
Space group (number)	$P2_1/c$		$-16 \leq k \leq 16$
a (Å)	16.1435(7)		$-20 \leq l \leq 18$
b (Å)	12.2827(5)		
c (Å)	15.7393(6)	Reflections collected	85665
α (°)	90	Independent reflections	7045
β (°)	110.892(2)		R_{int} = 0.0385
γ (°)	90		R_{sigma} = 0.0185
Volume (Å^3)	2915.7(2)	Data / Restraints / Parameters	7045/1/337
Z	4	Goodness-of-fit on F^2	1.040
ρ_{calc} (gcm^{-3})	1.943	Final R indices	R_1 = 0.0229
μ (mm^{-1})	6.450	[I≥2σ(I)]	wR_2= 0.0554
F(000)	1632	Final R indices	R_1 = 0.0256
Crystal size (mm^3)	0.38×0.12×0.1	[all data]	wR_2 = 0.0565
Crystal habitus	clear red plank	Largest peak/hole [eÅ^{-3}]	2.51/−0.79
Absorption correction	multi-scan	Internal ID (crystallographer)	8207f (GS)
Tmin; Tmax	0.5278; 0.7463		
Radiation	MoK_α (λ=0.71073 Å)	device type	Bruker D8 Venture

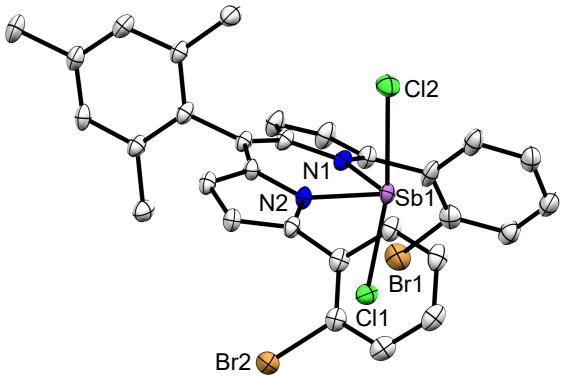


Figure 408: X-ray solid-state structure of **8Sb^{Cl}**. Thermal ellipsoids were set to a 50% probability level. Hydrogen atoms were omitted for clarity. Bromine is shown in orange, chlorine atoms in green, carbon atoms in grey, nitrogen in blue and antimony in dark magenta. Selected bond lengths [Å] Sb1−Cl1 2.4990(16), Sb1−Cl2 2.5561(17), Sb1−N1 2.099(5), Sb1−N2 2.099(5) and bond angles [°] Cl1−Sb1−Cl2 168.70(6), N1−Sb1−Cl1 86.53(14), N1−Sb1−Cl2 84.61(14), N2−Sb1−N1 86.32(1).

Table 54: Crystallographic data and structure refinement of **8Sb^{Cl}** (Figure 408).

Empirical formula	$C_{30}H_{23}Br_2Cl_2N_2Sb$		
Formula weight	763.97	2Θ range (°)	4.306 to 58.548
Temperature (K)	100	Completeness to Θ	99.5%
Crystal system	monoclinic	Index ranges	$-21 \leq h \leq 21$
Space group (number)	P21/c		$-16 \leq k \leq 16$
a (Å)	15.7079(7)		$-21 \leq l \leq 21$
b (Å)	12.2881(4)		
c (Å)	15.5151(7)	Reflections collected	16625
α (°)	90	Independent reflections	7604
β (°)	109.294(4)		R_{int} = 0.0411
γ (°)	90		R_{sigma} = 0.0438
Volume (Å^3)	2826.5(2)	Data / Restraints / Parameters	7604/1/338
Z	4	Goodness-of-fit on F^2	1.038
ρ_{calc} (gcm^{-3})	1.795	Final R indices	R_1 = 0.0693
μ (mm^{-1})	4.015	[I≥2σ(I)]	wR_2= 0.1858
F(000)	1488	Final R indices	R_1 = 0.0885
Crystal size (mm^3)	0.3×0.147×0.02	[all data]	wR_2 = 0.2037
Crystal habitus	red plate	Largest peak/hole [eÅ^{-3}]	3.89/−1.79
Absorption correction	multi-scan	Internal ID (crystallographer)	8048 (GS)
Tmin; Tmax	0.0733; 0.5511		
Radiation	MoK_α (λ=0.71073 Å)	device type	STOE IPDS 2T

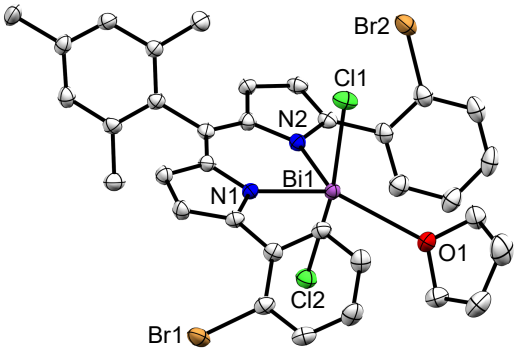


Figure 409: X-ray solid-state structure of **8Bi^{Cl}**. Thermal ellipsoids were set to a 50% probability level. Hydrogen atoms and one non-coordinating unit of THF were omitted for clarity. Bromine is shown in orange, chlorine atoms in green, carbon atoms in grey, nitrogen in blue, oxygen in red and bismuth in dark magenta. Selected bond lengths [Å] Bi1−Cl1 2.6881(12), Bi1−Cl2 2.6275(12), Bi1−O1 2.756(3), Bi1−N1 2.230(4), Bi1−N2 2.234(4) and bond angles [°] Cl1−Bi1−Cl2 172.11(4), Cl1−Bi1−O1 103.46(8), Cl2−Bi1−O1 83.68(8), N1−Bi1−Cl1 86.93(10), N1−Bi1−Cl2 85.36(10), N1−Bi1−O1 141.13(12), N2−Bi1−N1 82.22(13).

Table 55: Crystallographic data and structure refinement of **8Bi^{Cl}** (Figure 409).

Empirical formula	$C_{38}H_{39}BiBr_2Cl_2N_2O_2$		
Formula weight	995.39	2Θ range (°)	3.874 to 55.996
Temperature (K)	123	Completeness to Θ	100.0%
Crystal system	orthorhombic	Index ranges	$-18 \leq h \leq 18$
Space group (number)	$Pbca$		$-21 \leq k \leq 18$
a (Å)	14.0635(3)		$-41 \leq l \leq 41$
b (Å)	16.5942(3)		
c (Å)	31.6713(5)	Reflections collected	68801
α (°)	90	Independent reflections	8916
β (°)	90		R_{int} = 0.0759
γ (°)	90		R_{sigma} = 0.0332
Volume (Å^3)	7391.21(22)	Data / Restraints / Parameters	8916/0/427
Z	8	Goodness-of-fit on F^2	1.055
ρ_{calc} (gcm^{-3})	1.789	Final R indices	R_1 = 0.0439
μ (mm^{-1})	7.09	[I≥2σ(I)]	wR_2= 0.1202
F(000)	3872	Final R indices	R_1 = 0.0497
Crystal size (mm^3)	0.28×0.21×0.1	[all data]	wR_2 = 0.1264
Crystal habitus	clear red block	Largest peak/hole [eÅ^{-3}]	1.89/−4.15
Absorption correction	multi-scan	Internal ID (crystallographer)	8038 (GS)
Tmin; Tmax	0.0651; 0.1475		
Radiation	MoK_α (λ=0.71073 Å)	device type	STOE IPDS 2T

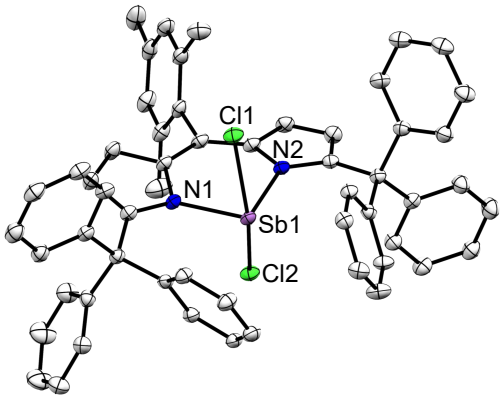


Figure 410: X-ray solid-state structure of **10Sb^{Cl}**. Thermal ellipsoids were set to a 50% probability level. Hydrogen atoms and non-coordinating units of THF were omitted for clarity. Chlorine atoms are shown in green, carbon atoms in grey, nitrogen in blue and antimony in dark magenta. Two independent molecules are present in the unit cell from which only one is displayed above. Selected bond lengths [Å] Sb1−Cl1 2.5530(7), Sb1−Cl2 2.5707(7), Sb1−N1 2.138(2), Sb1−N2 2.144(2) and bond angles [°] Cl1−Sb1−Cl2 153.54(2), N1−Sb1−Cl1 83.49(7), N1−Sb1−Cl2 80.18(7), N2−Sb1−N1 93.51(9).

Table 56: Crystallographic data and structure refinement of **10Sb^{Cl}** (Figure 410).

Empirical formula	$C_{132}H_{130}Cl_4N_4O_5Sb_2$		
Formula weight	2237.69	2Θ range (°)	3.818 to 58.5
Temperature (K)	100	Completeness to Θ	99.9%
Crystal system	triclinic	Index ranges	$-15 \leq h \leq 15$
Space group (number)	P-1		$-20 \leq k \leq 20$
a (Å)	11.6042(8)		$-22 \leq l \leq 22$
b (Å)	14.8342(13)		
c (Å)	16.5472(14)	Reflections collected	165297
α (°)	88.963(3)	Independent reflections	14631
β (°)	70.953(3)		R_{int} = 0.0827
γ (°)	89.777(3)		R_{sigma} = 0.0404
Volume (Å^3)	2692.0(4)	Data / Restraints / Parameters	14631/676/707
Z	1	Goodness-of-fit on F^2	1.081
ρ_{calc} (gcm^{-3})	1.380	Final R indices	R_1 = 0.0467
μ (mm^{-1})	0.661	[I≥2σ(I)]	wR_2= 0.1186
F(000)	1160	Final R indices	R_1 = 0.0580
Crystal size (mm^3)	0.3×0.1×0.08	[all data]	wR_2 = 0.1252
Crystal habitus	clear pink needle	Largest peak/hole [eÅ^{-3}]	1.09/−1.48
Absorption correction	multi-scan	Internal ID (crystallographer)	7969g (GS)
Tmin; Tmax	0.6478; 0.7461		
Radiation	MoK_α (λ=0.71073 Å)	device type	Bruker D8 Venture

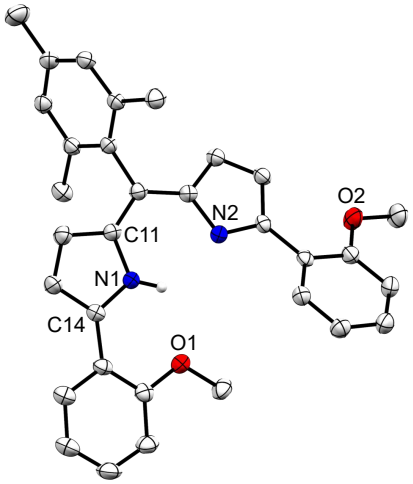


Figure 411: X-ray solid-state structure of **L7**. Thermal ellipsoids were set to a 50% probability level. Non-nitrogen-bound hydrogen atoms were omitted for clarity. Carbon atoms are shown in grey, oxygen in red and nitrogen in blue. Selected bond lengths [Å] N1−C11 1.383(3), N1−C14 1.364(3) and bond angles [°] Cl14−N1−C11 110.6(2).

Table 57: Crystallographic data and structure refinement of **L7** (Figure 411).

Empirical formula	$C_{32}H_{20}N_2O_2$		
Formula weight	474.58	2Θ range (°)	4.108 to 55.998
Temperature (K)	103	Completeness to Θ	99.9%
Crystal system	orthorhombic	Index ranges	$-11 \leq h \leq 11$
Space group (number)	$P2_12_12_1$		$-13 \leq k \leq 13$
a (Å)	8.5110(4)		$-37 \leq l \leq 37$
b (Å)	10.5686(6)		
c (Å)	28.6880(17)	Reflections collected	85372
α (°)	90	Independent reflections	6223
β (°)	90		R_{int} = 0.1244
γ (°)	90		R_{sigma} = 0.0554
Volume (Å^3)	2580.5(2)	Data / Restraints / Parameters	6223/0/333
Z	4	Goodness-of-fit on F^2	1.039
ρ_{calc} (gcm^{-3})	1.222	Final R indices	R_1 = 0.0465
μ (mm^{-1})	0.076	[I≥2σ(I)]	wR_2= 0.0929
F(000)	1008.0	Final R indices	R_1 = 0.0751
Crystal size (mm^3)	0.3×0.06×0.03	[all data]	wR_2 = 0.1076
Crystal habitus	clear dark red plank	Largest peak/hole [eÅ^{-3}]	0.17/−0.26
Absorption correction	multi-scan	Internal ID (crystallographer)	8573f (GS)
Tmin; Tmax	0.6129; 0.7464		
Radiation	MoK_α (λ=0.71073 Å)	device type	STOE IPDS-2T

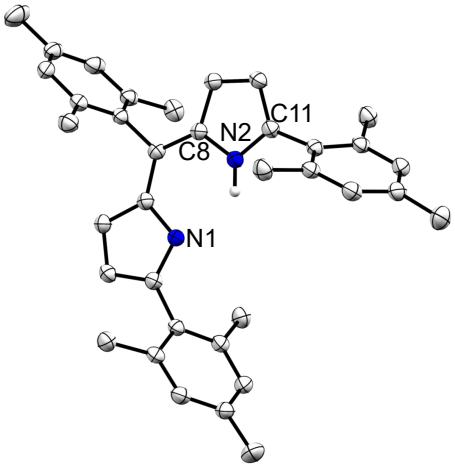


Figure 412: X-ray solid-state structure of **L9**. Thermal ellipsoids were set to a 50% probability level. Non-nitrogen-bound hydrogen atoms were omitted for clarity. Carbon atoms are shown in grey and nitrogen in blue. The molecule resides on a crystallographic mirror plane consisting of the methene carbon and the mesityl ring, resulting in the "left" and "right" part of the molecule being equivalent. Selected bond lengths [Å] N2−C8 1.3866(17) , N2−C11 1.3407(17) and bond angles [°] Cl11−N2−C8 108.10(11).

Table 58: Crystallographic data and structure refinement of **L9** (Figure 412).

Empirical formula	$C_{36}H_{38}N_2$		
Formula weight	498.68	2Θ range (°)	3.97 to 55.996
Temperature (K)	123	Completeness to Θ	95.3%
Crystal system	monoclinic	Index ranges	$-11 \leq h \leq 11$
Space group (number)	C2/c		$-18 \leq k \leq 19$
a (Å)	8.9043(6)		$-25 \leq l \leq 27$
b (Å)	15.0920(7)		
c (Å)	21.0010(14)	Reflections collected	6744
α (°)	90	Independent reflections	3138
β (°)	102.248(5)		R_{int} = 0.0209
γ (°)	90		R_{sigma} = 0.0232
Volume (Å^3)	2757.9(3)	Data / Restraints / Parameters	3138/0/180
Z	4	Goodness-of-fit on F^2	1.045
ρ_{calc} (gcm^{-3})	1.201	Final R indices	R_1 = 0.0482
μ (mm^{-1})	1.04	[I≥2σ(I)]	wR_2= 0.1279
F(000)	1072	Final R indices	R_1 = 0.0625
Crystal size (mm^3)	0.21×0.2×0.18	[all data]	wR_2 = 0.1373
Crystal habitus	clear orange block	Largest peak/hole [eÅ^{-3}]	0.30/−0.19
Absorption correction	multi-scan	Internal ID (crystallographer)	8033 (GS)
Tmin; Tmax	0.4626; 0.5104		
Radiation	MoK_α (λ=0.71073 Å)	device type	STOE IPDS-2T

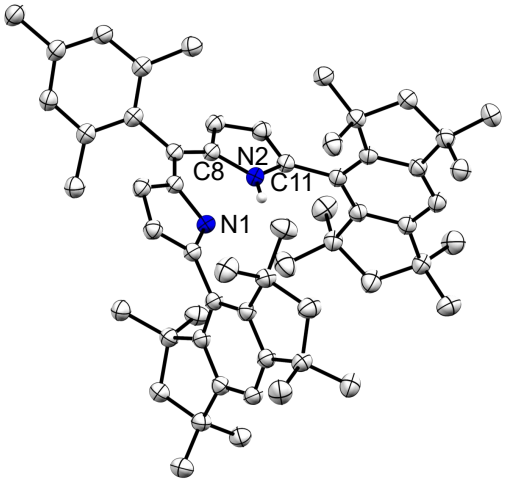


Figure 413: X-ray solid-state structure of **L11**. Thermal ellipsoids were set to a 50% probability level. Non-nitrogen-bound hydrogen atoms were omitted for clarity. Carbon atoms are shown in grey and nitrogen in blue. The molecule resides on a crystallographic mirror plane consisting of the methene carbon and the mesityl ring, resulting in the "left" and "right" part of the molecule being equivalent. Selected bond lengths [Å] N2−C8 1.3942(19), N2−C11 1.335(2) and bond angles [°] Cl11−N2−C8 108.35(13).

Table 59: Crystallographic data and structure refinement of **L11** (Figure 413).

Empirical formula	$C_{58}H_{74}N_2$		
Formula weight	827.24	2Θ range (°)	4.27 to 55.992
Temperature (K)	100	Completeness to Θ	98.3%
Crystal system	monoclinic	Index ranges	$-19 \leq h \leq 22$
Space group (number)	$C2/c$		$-15 \leq k \leq 15$
a (Å)	17.2996(8)		$-31 \leq l \leq 30$
b (Å)	11.5254(4)		
c (Å)	23.9268(10)	Reflections collected	12136
α (°)	90	Independent reflections	5585
β (°)	100.605(3)		R_{int} = 0.0375
γ (°)	90		R_{sigma} = 0.0358
Volume (Å^3)	4689.2(3)	Data / Restraints / Parameters	5585/0/283
Z	4	Goodness-of-fit on F^2	1.051
ρ_{calc} (gcm^{-3})	1.132	Final R indices	R_1 = 0.0552
μ (mm^{-1})	0.064	[I≥2σ(I)]	wR_2= 0.1413
F(000)	1744	Final R indices	R_1 = 0.0754
Crystal size (mm^3)	0.1×0.053×0.02	[all data]	wR_2 = 0.1572
Crystal habitus	clear orange block	Largest peak/hole [eÅ^{-3}]	0.48/−0.32
Absorption correction	integration	Internal ID (crystallographer)	8002 (GS)
Tmin; Tmax	0.9930; 0.9986		
Radiation	MoK_α (λ=0.71073 Å)	device type	STOE IPDS-2T

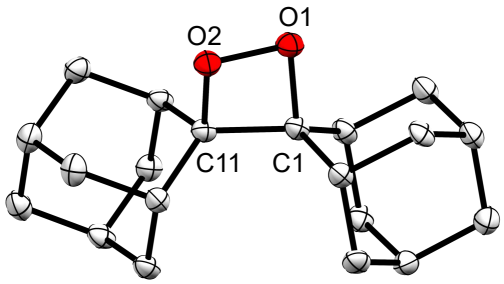


Figure 414: X-ray solid-state structure of **39**. Thermal ellipsoids were set to a 50% probability level. Hydrogen atoms were omitted for clarity. Carbon atoms are shown in grey and oxygen atoms in red. Selected bond lengths [Å] O1−O2 1.509(3), O1−C1 1.481(3), O2−C11 1.483(3) and bond angles [°] C1−O1−O2 89.17(16), C11−O2−O1 88.31(17).

Table 60: Crystallographic data and structure refinement of **39** (Figure 414).

Empirical formula	$C_{20}H_{28}O_2$		
Formula weight	300.42	2Θ range (°)	4.586 to 55.996
Temperature (K)	102	Completeness to Θ	99.7%
Crystal system	monoclinic	Index ranges	$-24 \leq h \leq 24$
Space group (number)	$P2_1/c$		$-12 \leq k \leq 12$
a (Å)	18.4527(13)		$-17 \leq l \leq 17$
b (Å)	9.8104(6)		
c (Å)	13.1780(8)	Reflections collected	71510
α (°)	90	Independent reflections	5535
β (°)	105.687(3)		R_{int} = 0.0784
γ (°)	90		R_{sigma} = 0.0335
Volume (Å^3)	2296.7(3)	Data / Restraints / Parameters	5535/0/199
Z	4	Goodness-of-fit on F^2	1.057
ρ_{calc} (gcm^{-3})	0.869	Final R indices	R_1 = 0.0822
μ (mm^{-1})	0.054	[I≥2σ(I)]	wR_2= 0.2696
F(000)	656	Final R indices	R_1 = 0.0960
Crystal size (mm^3)	0.16×0.08×0.07	[all data]	wR_2 = 0.2837
Crystal habitus	clear colourless block	Largest peak/hole [eÅ^{-3}]	0.58/−0.58
Absorption correction	multi-scan	Internal ID (crystallographer)	8301f (GS)
Tmin; Tmax	0.6917; 0.7463	CCDC number	**2410517**
Radiation	MoK_α (λ=0.71073 Å)	device type	Bruker D8 Venture

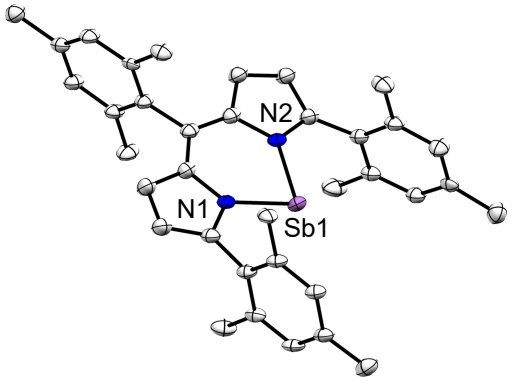


Figure 415: X-ray solid-state structure of **9Sb**. Thermal ellipsoids were set to a 50% probability level. Hydrogen atoms were omitted for clarity. Carbon atoms are shown in grey, nitrogen atoms in blue and antimony in dark magenta. Selected bond lengths [Å] Sb1−N1 2.083(9), Sb1−N2 2.096(9) and bond angles [°] N1−Sb1−N2 85.7(3).[xvii]

Table 61: Crystallographic data and structure refinement of **9Sb** (Figure 415).

Empirical formula	$C_{36}H_{37}N_2Sb$		
Formula weight	619.42	2Θ range (°)	4.158 to 50.492
Temperature (K)	100.00	Completeness to Θ	94.7%
Crystal system	monoclinic	Index ranges	$-9 \leq h \leq 9$
Space group (number)	$P2_1/n$		$-32 \leq k \leq 31$
a (Å)	8.051(3)		$-13 \leq l \leq 16$
b (Å)	27.946(10)		
c (Å)	13.821(5)	Reflections collected	14537
α (°)	90	Independent reflections	5308
β (°)	96.117(11)		R_{int} = 0.1231
γ (°)	90		R_{sigma} = 0.1672
Volume (Å^3)	3092.1(19)	Data / Restraints / Parameters	5308/330/362
Z	4	Goodness-of-fit on F^2	1.136
ρ_{calc} (gcm^{-3})	1.331	Final R indices	R_1 = 0.1035
μ (mm^{-1})	0.918	[I≥2σ(I)]	wR_2= 0.2334
F(000)	1272.0	Final R indices	R_1 = 0.1377
Crystal size (mm^3)	0.6×0.12×0.02	[all data]	wR_2 = 0.2534
Crystal habitus	orange needle	Largest peak/hole [eÅ^{-3}]	2.00/−1.47
Absorption correction	multi-scan	Internal ID (crystallographer)	8834 (GS)
Tmin; Tmax	0.4962; 0.7465		
Radiation	MoK_α (λ=0.71073 Å)	device type	Bruker D8 Venture

[xvii] Single crystals were grown from a saturated benzene solution and obtained by L. Mohr during a research internship.

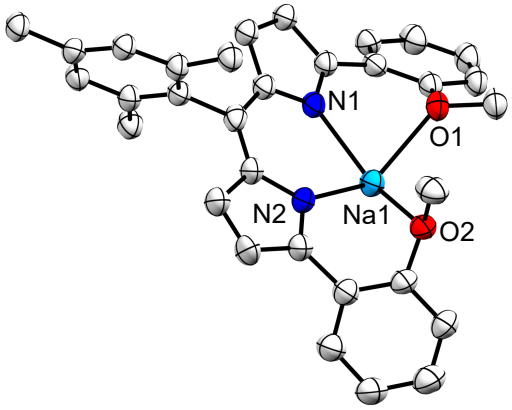


Figure 416: X-ray solid-state structure of **L7^{Na}**. Thermal ellipsoids were set to a 50% probability level. Non-coordinating benzene unit and hydrogen atoms were omitted for clarity. Sodium is shown in teal, carbon atoms in grey, nitrogen in blue and oxygen atoms in red. Selected bond lengths [Å] Na1−O1 2.424(3), Na1−O2 2.374(3), Na1−N1 2.309(3), Na1−N2 2.309(3) and bond angles [°] O2−Na1−O1 100.98(10), N1−Na1−N2 81.79(11).

Table 62: Crystallographic data and structure refinement of **L7^{Na}** (Figure 416).

Empirical formula	$C_{35}H_{32}N_2NaO_2$		
Formula weight	535.61	2Θ range (°)	3.038 to 55.998
Temperature (K)	100.00	Completeness to Θ	100.0%
Crystal system	monoclinic	Index ranges	$-20 \leq h \leq 20$
Space group (number)	$I2/a$		$-21 \leq k \leq 21$
a (Å)	15.6445(11)		$-33 \leq l \leq 33$
b (Å)	15.9518(15)		
c (Å)	25.024(2)	Reflections collected	31629
α (°)	90	Independent reflections	7461
β (°)	98.394(6)		R_{int} = 0.1636
γ (°)	90		R_{sigma} = 0.1052
Volume (Å^3)	6178.0(9)	Data / Restraints / Parameters	7461/0/367
Z	8	Goodness-of-fit on F^2	1.016
ρ_{calc} (gcm^{-3})	1.152	Final R indices	R_1 = 0.0890
μ (mm^{-1})	0.083	[I≥2σ(I)]	wR_2= 0.2217
F(000)	2264.0	Final R indices	R_1 = 0.1514
Crystal size (mm^3)	0.32×0.31×0.01	[all data]	wR_2 = 0.2725
Crystal habitus	clear red plate	Largest peak/hole [eÅ^{-3}]	0.35/−0.34
Absorption correction	multi-scan	Internal ID (crystallographer)	8748_pl (GS)
Tmin; Tmax	0.5808; 0.8679		
Radiation	MoK_α (λ=0.71073 Å)	device type	STOE IPDS 2T

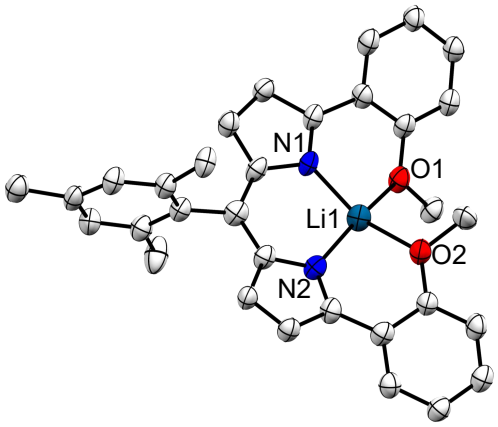


Figure 417: X-ray solid-state structure of **L7^{Li}**. Thermal ellipsoids were set to a 30% probability level. Second independent molecule and hydrogen atoms were omitted for clarity. Lithium is shown in dark teal, carbon atoms in grey, nitrogen in blue and oxygen atoms in red. Two independent molecules are present in the unit cell from which only one is displayed above. Selected bond lengths [Å] Li1−O1 2.032(15), Li1−O2 2.011(15), N1−Li1 1.911(16), N2−Li1 1.966(16) and bond angles [°] O2−Li1−O1 96.9(6), N1−Li1−N2 95.5(6).

Table 63: Crystallographic data and structure refinement of **L7^{Li}** (Figure 417).

Empirical formula	$C_{35}H_{32}LiN_2O_2$		
Formula weight	480.51	2Θ range (°)	6.654 to 160.98
Temperature (K)	100.15	Completeness to Θ	99.9%
Crystal system	monoclinic	Index ranges	$-16 \leq$ h ≤ 16
Space group (number)	$P2_1/c$		$-32 \leq$ k ≤ 31
a (Å)	13.019(2)		$-17 \leq$ l ≤ 19
b (Å)	25.731(4)		
c (Å)	15.969(2)	Reflections collected	53731
α (°)	90	Independent reflections	10996
β (°)	103.779(10)		R_{int} = 0.4118
γ (°)	90		R_{sigma} = 0.2609
Volume (Å^3)	5195.5(13)	Data / Restraints / Parameters	10996/3/678
Z	8	Goodness-of-fit on F^2	0.970
ρ_{calc} (gcm^{-3})	1.229	Final R indices	R_1 = 0.1267
μ (mm^{-1})	0.594	[I$\geq 2\sigma$(I)]	wR_2= 0.2865
F(000)	2032	Final R indices	R_1 = 0.2824
Crystal size (mm^3)	0.43×0.05×0.02	[all data]	wR_2 = 0.3889
Crystal habitus	clear reddish pink needle	Largest peak/hole [eÅ^{-3}]	0.35/−0.30
Absorption correction	multi-scan	Internal ID (crystallographer)	8860v_pl (GS)
Tmin; Tmax	0.4473; 0.7543		
Radiation	CuK_α (λ=1.54178 Å)	device type	Bruker D8 Venture

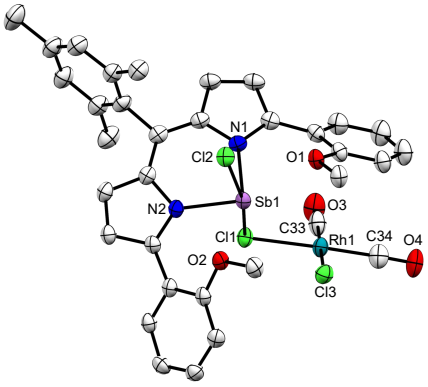


Figure 418: X-ray solid-state structure of **Rh1**. Thermal ellipsoids were set to a 50% probability level. Hydrogen atoms were omitted for clarity. Chlorine atoms are shown in green, carbon atoms in grey, nitrogen in blue, oxygen atoms in red, antimony in dark magenta, and rhodium in green-blue. Selected bond lengths [Å] Sb1−Cl1 2.8888(8), Sb1−Cl2 2.4335(8), Sb1−N1 2.120(3), Sb1−N2 2.120(3), Rh1−Cl1 2.3694(9), Rh1−Cl3 2.3535(9), Rh1−C33 1.843(4), Rh1−C34 1.836(4), O3−C33 1.127(5), O4−C34 1.139(5) and bond angles [°] Cl2−Sb1−Cl1 163.55(3), N1−Sb1−Cl1 80.22(8), N1−Sb1−Cl2 87.44(8), Cl3−Rh1−Cl1 90.94(3), C33−Rh1−Cl1 88.63(12), C34−Rh1−Cl3 88.43(13), C34−Rh1−C33 92.06(17).

Table 64: Crystallographic data and structure refinement of **Rh1** (Figure 418).

Empirical formula	$C_{34}H_{29}Cl_3N_2O_4RhSb$		
Formula weight	860.6	2Θ range (°)	3.788 to 55.998
Temperature (K)	100	Completeness to Θ	100.0%
Crystal system	triclinic	Index ranges	$-10 \leq h \leq 11$
Space group (number)	P-1		$-15 \leq k \leq 15$
a (Å)	8.4780(4)		$-24 \leq l \leq 24$
b (Å)	11.3666(5)		
c (Å)	18.6143(9)	Reflections collected	20494
α (°)	95.154(4)	Independent reflections	8088
β (°)	98.778(4)		R_{int} = 0.0506
γ (°)	107.070(3)		R_{sigma} = 0.0438
Volume (Å^3)	1677.38(14)	Data / Restraints / Parameters	8088/0/412
Z	2	Goodness-of-fit on F^2	1.063
ρ_{calc} (gcm^{-3})	1.704	Final R indices	R_1 = 0.0544
μ (mm^{-1})	1.577	[I≥2σ(I)]	wR_2= 0.1471
F(000)	852	Final R indices	R_1 = 0.0588
Crystal size (mm^3)	0.22×0.1×0.05	[all data]	wR_2 = 0.1528
Crystal habitus	clear light red plank	Largest peak/hole [eÅ^{-3}]	1.48/−2.66
Absorption correction	multi-scan	Internal ID (crystallographer)	8738_b (GS)
Tmin; Tmax	0.4865; 0.7453	CCDC number	**2493713**
Radiation	MoK_α (λ=0.71073 Å)	device type	STOE IPDS 2T

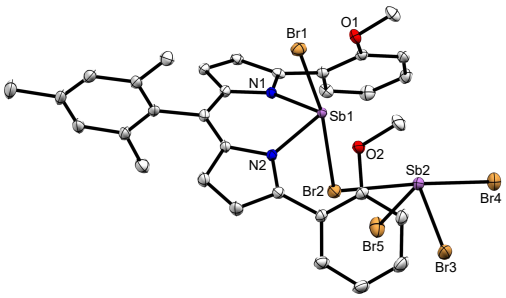


Figure 419: X-ray solid-state structure of **Sb1**. Thermal ellipsoids were set to a 50% probability level. Non-coordinating unit of CH_2Cl_2 and hydrogen atoms were omitted for clarity. Bromine atoms are shown in orange, carbon atoms in grey, nitrogen in blue, oxygen atoms in red and antimony in dark magenta. Selected bond lengths [Å] Sb1−Br1 2.5822(4), Sb1−Br2 2.9538(4), Sb1−N1 2.107(2), Sb1−N2 2.106(2), Sb2−Br2 2.8884(4), Sb2−Br3 2.5171(4), Sb2−Br4 2.6929(4), Sb2−Br5 2.5278(4) and bond angles [°] Br1−Sb1−Br2 171.068(11), N1−Sb1−Br1 89.94(6), N1−Sb1−Br2 81.86(6), Br3−Sb2−Br2 83.849(11), Br3−Sb2−Br4 91.483(12), Br3−Sb2−Br5 95.899(14), Br5−Sb2−Br2 87.250(12), Br5−Sb2−Br4 92.487(12).

Table 65: Crystallographic data and structure refinement of **Sb1** (Figure 419).

Empirical formula	$C_{33}H_{31}Br_5Cl_2N_2O_2Sb_2$		
Formula weight	1201.55	2Θ range (°)	5.152 to 56
Temperature (K)	102	Completeness to Θ	99.8%
Crystal system	triclinic	Index ranges	$-11 \leq h \leq 11$
Space group (number)	P-1		$-19 \leq k \leq 19$
a (Å)	8.5670(5)		$-21 \leq l \leq 21$
b (Å)	15.0691(10)		
c (Å)	16.4222(11)	Reflections collected	119065
α (°)	113.766(3)	Independent reflections	9000
β (°)	97.952(2)		R_{int} = 0.0595
γ (°)	99.147(2)		R_{sigma} = 0.0263
Volume (Å^3)	1866.9(2)	Data / Restraints / Parameters	9000/6/420
Z	2	Goodness-of-fit on F^2	1.032
ρ_{calc} (gcm^{-3})	2.137	Final R indices	R_1 = 0.0234
μ (mm^{-1})	6.974	[I≥2σ(I)]	wR_2= 0.0579
F(000)	1140	Final R indices	R_1 = 0.0263
Crystal size (mm^3)	0.13×0.07×0.04	[all data]	wR_2 = 0.0595
Crystal habitus	clear yellow plate	Largest peak/hole [eÅ^{-3}]	1.84/−1.60
Absorption correction	multi-scan	Internal ID (crystallographer)	8630f (GS)
Tmin; Tmax	0.5957; 0.7464	CCDC number	**2493717**
Radiation	MoK_α (λ=0.71073 Å)	device type	Bruker D8 Venture

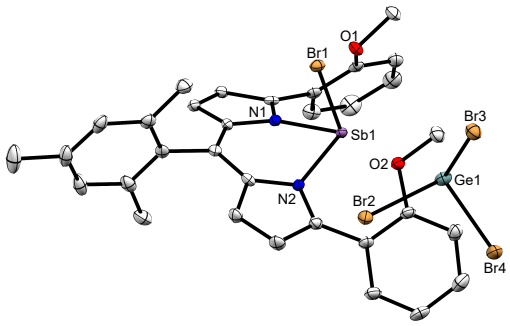


Figure 420: X-ray solid-state structure of **Ge1**. Thermal ellipsoids were set to a 50% probability level. Hydrogen atoms were omitted for clarity. Bromine atoms are shown in orange, carbon atoms in grey, nitrogen in blue, oxygen atoms in red, germanium in grey-green and antimony in dark magenta. Selected bond lengths [Å] Sb1−Br1 2.5650(4), Sb1−N1 2.119(2), Sb1−N2 2.115(2) and bond angles [°] N1−Sb1−Br1 90.56(7), N2−Sb1−Br1 90.35(7), N2−Sb1−N1 83.65(9).

Table 66: Crystallographic data and structure refinement of **Ge1** (Figure 420).

Empirical formula	$C_{32}H_{29}Br_4GeN_2O_2Sb$		
Formula weight	987.55	2Θ range (°)	3.84 to 55.998
Temperature (K)	100	Completeness to Θ	99.9%
Crystal system	triclinic	Index ranges	$-11 \leq h \leq 11$
Space group (number)	P-1		$-18 \leq k \leq 18$
a (Å)	8.3683(5)		$-19 \leq l \leq 19$
b (Å)	13.8330(9)		
c (Å)	14.9731(9)	Reflections collected	90690
α (°)	95.559(2)	Independent reflections	8019
β (°)	97.234(2)		R_{int} = 0.0593
γ (°)	102.871(2)		R_{sigma} = 0.0285
Volume (Å^3)	1662.22(18)	Data / Restraints / Parameters	8019/0/384
Z	2	Goodness-of-fit on F^2	1.051
ρ_{calc} (gcm^{-3})	1.973	Final R indices	R_1 = 0.0264
μ (mm^{-1})	6.556	[I≥2σ(I)]	wR_2= 0.0586
F(000)	948	Final R indices	R_1 = 0.0353
Crystal size (mm^3)	0.2×0.08×0.02	[all data]	wR_2 = 0.0623
Crystal habitus	clear light green plank	Largest peak/hole [eÅ^{-3}]	0.98/−0.79
Absorption correction	multi-scan	Internal ID (crystallographer)	8739f (GS)
Tmin; Tmax	0.5809; 0.7463	CCDC number	**2493715**
Radiation	MoK_α (λ=0.71073 Å)	device type	Bruker D8 Venture

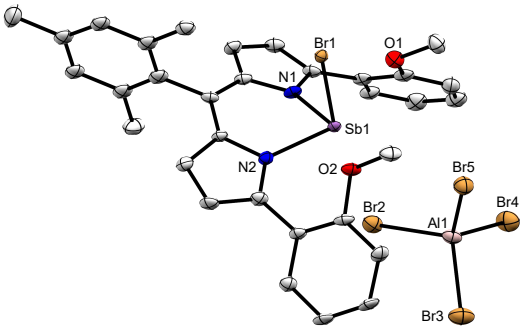


Figure 421: X-ray solid-state structure of **Al1**. Thermal ellipsoids were set to a 50% probability level. Hydrogen atoms were omitted for clarity and only the main layer of the Sb atom (93% occupancy) is shown. Bromine atoms are shown in orange, carbon atoms in grey, nitrogen in blue, oxygen atoms in red, aluminum in pale rose and antimony in dark magenta. Selected bond lengths [Å] Sb1−Br1 2.5053(12), Sb1−N1 2.123(6), Sb1−N2 2.117(6) and bond angles [°] N1−Sb1−Br1 92.64(16), N2−Sb1−Br1 91.40(16), N2−Sb1−N1 83.9(2).

Table 67: Crystallographic data and structure refinement of **Al1** (Figure 421).

Empirical formula	$C_{32}H_{29}AlBr_5N_2O_2Sb$		
Formula weight	1021.85	2Θ range (°)	3.724 to 56
Temperature (K)	100	Completeness to Θ	99.8%
Crystal system	triclinic	Index ranges	$-13 \leq h \leq 13$
Space group (number)	$P\text{-}1$		$-17 \leq k \leq 17$
a (Å)	10.2989(7)		$-18 \leq l \leq 18$
b (Å)	13.1541(10)		
c (Å)	13.8208(10)	Reflections collected	62474
α (°)	69.873(3)	Independent reflections	8362
β (°)	80.556(3)		R_{int} = 0.0575
γ (°)	86.196(3)		R_{sigma} = 0.0466
Volume (Å^3)	1734.1(2)	Data / Restraints / Parameters	8362/96/429
Z	2	Goodness-of-fit on F^2	1.177
ρ_{calc} (gcm^{-3})	1.957	Final R indices	R_1 = 0.0654
μ (mm^{-1})	6.613	[I≥2σ(I)]	wR_2= 0.1338
F(000)	980.0	Final R indices	R_1 = 0.0829
Crystal size (mm^3)	0.44×0.2×0.05	[all data]	wR_2 = 0.1421
Crystal habitus	metallic reddish green plate	Largest peak/hole [eÅ^{-3}]	1.97/−1.44
Absorption correction	multi-scan	Internal ID (crystallographer)	8881f (GS)
Tmin; Tmax	0.3707; 0.7463	CCDC number	**2493714**
Radiation	MoK_α (λ=0.71073 Å)	device type	Bruker D8 Venture

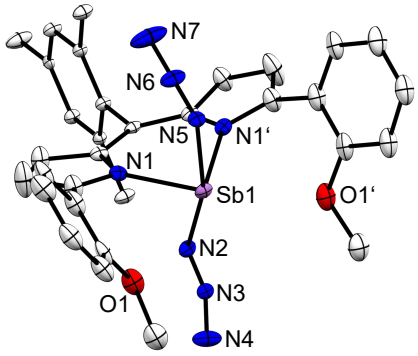


Figure 422: X-ray solid-state structure of **7Sb^{N3}**. Thermal ellipsoids were set to a 50% probability level. Hydrogen atoms and disorder in azide substituent were omitted for clarity. Carbon atoms are shown in grey, nitrogen in blue, oxygen atoms in red and antimony in dark magenta. The molecule resides on a crystallographic mirror plane consisting of the mesityl ring, antimony and the azide substituents, resulting in the “left” and “right” part of the molecule being equivalent. Selected bond lengths [Å] Sb1−N1 2.106(8), Sb1−N2 2.275(12), Sb1−N5 2.276(10), N3−N4 1.12(2), N5−N6 1.169(15) and bond angles [°] N1−Sb1−N1’ 85.7(4), N2−Sb1−N5 162.7(4).

Table 68: Crystallographic data and structure refinement of **7Sb^{N3}** (Figure 422).

Empirical formula	$C_{32}H_{29}N_8O_2Sb$		
Formula weight	679.38	2Θ range (°)	3.944 to 51.998
Temperature (K)	100	Completeness to Θ	99.7%
Crystal system	orthorhombic	Index ranges	$0 \leq h \leq 20$
Space group (number)	Pnma		$0 \leq k \leq 16$
a (Å)	16.420(3)		$0 \leq l \leq 16$
b (Å)	13.309(3)		
c (Å)	13.286(3)	Reflections collected	3095
α (°)	90	Independent reflections	3095
β (°)	90		R_{int} = 0.1707
γ (°)	90		R_{sigma} = 0.0693
Volume (Å^3)	2903.4(10)	Data / Restraints / Parameters	3095/221/234
Z	4	Goodness-of-fit on F^2	1.311
ρ_{calc} (gcm^{-3})	1.554	Final R indices	R_1 = 0.0969
μ (mm^{-1})	0.996	[I≥2σ(I)]	wR_2= 0.1763
F(000)	1376	Final R indices	R_1 = 0.1284
Crystal size (mm^3)	0.12×0.04×0.005	[all data]	wR_2 = 0.1865
Crystal habitus	clear intense red plate	Largest peak/hole [eÅ^{-3}]	3.98/−2.81
Absorption correction	multi-scan	Internal ID (crystallographer)	8579g (GS)
Tmin; Tmax	0.519735; 0.746545		
Radiation	MoK_α (λ=0.71073 Å)	device type	Bruker D8 Venture

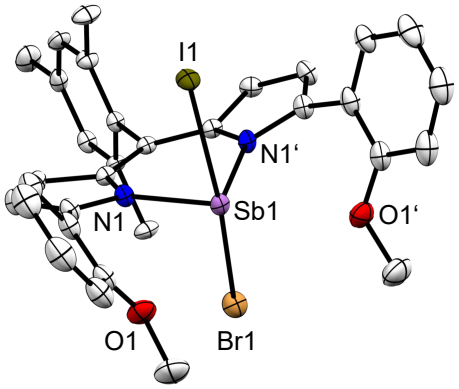


Figure 423: X-ray solid-state structure of **7Sb^{BrI}**. Thermal ellipsoids were set to a 50% probability level. Hydrogen atoms were omitted for clarity. Carbon atoms are shown in grey, bromine in orange, iodine in olive green, nitrogen in blue, oxygen atoms in red and antimony in dark magenta. The molecule resides on a crystallographic mirror plane consisting of the mesityl ring, antimony and the halide substituents, resulting in the “left” and “right” part of the molecule being equivalent. Selected bond lengths [Å] Sb1−I1 3.002(2), Sb1−Br1 2.759(9), Sb1−N1 2.090(2) and bond angles [°] Br1−Sb1−I1 166.3(3), N1−Sb1−I1 83.50(8), N1−Sb1−Br1 86.5(2) N1−Sb1−N1’ 86.82(11).

Table 69: Crystallographic data and structure refinement of **7Sb^{BrI}** (Figure 423).

Empirical formula	$C_{32}H_{29}BrIN_2O_2Sb$		
Formula weight	802.13	2Θ range (°)	4.934 to 55.996
Temperature (K)	100	Completeness to Θ	99.8%
Crystal system	orthorhombic	Index ranges	$-20 \leq h \leq 20$
Space group (number)	$Pnma$		$-17 \leq k \leq 17$
a (Å)	15.8400(8)		$-18 \leq l \leq 17$
b (Å)	13.4472(7)		
c (Å)	13.9335(7)	Reflections collected	59890
α (°)	90	Independent reflections	3729
β (°)	90		R_{int} = 0.0596
γ (°)	90		R_{sigma} = 0.0233
Volume (Å^3)	2967.9(3)	Data / Restraints / Parameters	3729/14/213
Z	4	Goodness-of-fit on F^2	1.116
ρ_{calc} (gcm^{-3})	1.795	Final R indices	R_1 = 0.0261
μ (mm^{-1})	3.348	[I≥2σ(I)]	wR_2= 0.0559
F(000)	1560	Final R indices	R_1 = 0.0317
Crystal size (mm^3)	0.16×0.12×0.06	[all data]	wR_2 = 0.0579
Crystal habitus	clear dark red block	Largest peak/hole [eÅ^{-3}]	0.52/−0.44
Absorption correction	multi-scan	Internal ID (crystallographer)	9183f (GS)
Tmin; Tmax	0.7012; 0.7463		
Radiation	MoK_α (λ=0.71073 Å)	device type	Bruker D8 Venture